Bidirectional Charging Systems and Battery Lifetime Modeling for Vehicle-to-Grid Applications

Zur Erlangung des akademischen Grades eines

DOKTORS DER INGENIEURWISSENSCHAFTEN (Dr.-Ing.)

von der KIT-Fakultät für Elektrotechnik und Informationstechnik des
Karlsruher Instituts für Technologie (KIT)

angenommene

DISSERTATION

von

M.Sc. Matthias Luh

Tag der mündlichen Prüfung:	11.09.2024
Hauptreferent:	Prof. Dr. rer. nat. Marc Weber
Korreferent:	Prof. Dr.-Ing. Marc Hiller

Acknowledgments

The research presented in this dissertation was carried out during my time as a PhD student in the Electronic Packaging and Interconnects (AVT) department at the Institute for Data Processing and Electronics (IPE) at the Karlsruhe Institute of Technology (KIT). Without the support of numerous people and organizations, this work would not have been possible, which is why I would like to express my gratitude at this point.

First, I thank Prof. Dr. rer. nat. Marc Weber for giving me the opportunity to pursue a PhD under his supervision and for his support and guidance in finishing this thesis, which I increasingly appreciated over time. I want to thank Prof. Dr.-Ing. Marc Hiller for co-refereeing my thesis and for his valuable feedback and impulses, especially for the power electronics part of my research.
I particularly thank Dr.-Ing. Thomas Blank, my supervisor and head of our working group, for countless fruitful discussions, his feedback, ideas, and support, for the freedom and opportunities he gave me in my research and personal development, and for his confidence in my work.

Moreover, I would like to thank the German Research Foundation (Deutsche Forschungsgemeinschaft, DFG) for the financial funding of my work within the research training group "Energy Status Data" and Prof. Dr.-Ing. Klemens Böhm for the management of this group, for creating a framework for continuous interdisciplinary exchange and professional development, and for the support of our research.
Furthermore, I want to thank Anthony Britto, Kaleb Phipps, and Matthias Wolf for their professional and enjoyable cooperation in our self-organized study group.

I am incredibly grateful for the valuable discussions and support of my current and former colleagues, particularly Felix Steiner, Helge Wurst, Henrik Herzenstiel, Hongpeng Zhang, Jonas Sievers, and Dr.-Ing. Simon Bischof, as well as numerous other colleagues of other research groups at our university. Without you, this work would not have been possible, and the time would not have been nearly as great as it was.
Thanks also go to all the students I worked with. Notably, the work of Benedikt Rzepka, Johann Kraft, Marek Lutz, and Yannick Fritsch was valuable for the research of my thesis and the self-organized study groups, and I very much enjoyed the cooperation.

A precious contribution often overlooked is the professional work of our workshop and laboratory staff, with whom it was pleasant to work. I want to thank Alexander Bacher, Jennifer Derschang, and our former colleague Uwe Bauer for their magical PCB assembly and rework skills. Thank you, Benjamin Leyrer, Peter Hoffmann, Peter Schöck, and Tibor Piller, for helping me out countless times, no matter how demanding the requests were.
Further, I thank Dr.-Ing. Marc Schneider for his advice and the 3D printing of several challenging objects, as well as our administration, which supported me in any organizational matters, and Daniel Kompalla for his fast and competent IT support.

My research and daily work have been significantly boosted by a multitude of brilliant open-source and freeware programs, libraries, tools, websites, and publicly available datasets, most of which are based on the voluntary contributions of thousands of developers, as well as research teams and organizations that make them freely available. A big thanks for that!

Words cannot possibly express my gratitude toward my family, who always was understanding and supported me, to my friends, who made me enjoy every minute spent with them and offered advice, and most importantly, my girlfriend, Verena. She always believed in me, supported me in every possible way, was sympathetic, and motivated me in challenging times. Thank you!

Kurzfassung

Um den menschengemachten Klimawandel zu begrenzen, werden dringend kurzfristig umsetzbare Lösungen gesucht, welche die Transformation zu einer emissionsarmen Zukunft ermöglichen. Im Zuge des weltweiten Ausbaus der erneuerbaren Energien und der Elektrifizierung des Verkehrssektors wird die Sicherstellung eines zuverlässigen Betriebs der Stromnetze eine zunehmende Herausforderung. Dies liegt nicht zuletzt an den erhöhten Anforderungen, die sich aus der volatileren Stromerzeugung und dem steigenden Stromverbrauch durch die Elektromobilität ergeben.
Das intelligente, bidirektionale Laden von Elektrofahrzeugen (Vehicle-to-Grid, V2G) kann einen essenziellen Beitrag dazu leisten, sowohl den Anteil an erneuerbaren Energien im Strommix zu erhöhen als auch Mobilitätsbedürfnisse emissionsarm zu erfüllen. Obwohl diese Idee bereits wohlbekannt ist, stehen der Umsetzung noch immer viele Hürden im Weg. Dazu zählen höhere Kosten für bidirektionale Ladegeräte und Bedenken hinsichtlich einer potenziell schnelleren Batteriealterung.

In dieser Thesis stelle ich Lösungsansätze für diese Probleme und Erkenntnisse zu den Ungewissheiten vor, welche die Nutzung des Potenzials von V2G beschleunigen und verbessern können. Zum einen wurde hocheffiziente Leistungselektronik für ein V2G Ladesystem entwickelt und charakterisiert. Aus der Literatur bekannte Ansteuerungsverfahren für die verwendeten weich schaltenden Topologien wurden für den Betrieb mit Siliciumcarbid Halbleitern angepasst, um in breiten Betriebsbereichen hohe Effizienzen von mehr als 96 % zu erzielen und die Schaltfrequenz zu steigern. Dadurch kann eine Reduktion von Kosten, Gewicht und Bauraum erreicht werden.
Zum anderen wurden netzdienliche Regelverfahren hergeleitet, in der Hardware implementiert und validiert, welche den robusten Betrieb eines regenerativen Energiesystems unterstützen und dadurch höhere Einnahmen erzielen können. Dazu gehören eine Spannungs- und Frequenzregelung, die dynamische Stabilisierung der Netzfrequenz durch Nachbildung einer elektronisch geregelten virtuellen Schwungmasse sowie die Reduktion der Phasenasymmetrie im Stromnetz.
Außerdem wurde einer der bisher umfangreichsten frei verfügbaren Batteriealterungsdatensätze generiert und publiziert [J1], [R1]. Dieser umfasst Kapazitäts- und Impedanz-Messdaten von 228 Rundzellen, welche etwa 450 Tage mit 76 verschiedenen Testbedingungen betrieben wurden. Auf Grundlage dieses Datensatzes wurde ein gut wiederverwendbares Batteriealterungsmodell hergeleitet. Mithilfe des Modells wurden verschiedene V2G Ladestrategien untersucht, welche die Batteriealterung im Vergleich zum konventionellen Laden sogar reduzieren können.

Abstract

Addressing anthropogenic climate change requires solutions for a transformation to a low-emission future that can be implemented in the short term. As the world progresses toward the expansion of renewable energy sources (RES) and the electrification of the transportation sector, ensuring reliable operation of electricity grids becomes a significant challenge. This is not least because of the growing requirements resulting from increasingly volatile electricity generation and rising electricity consumption due to electromobility.
The intelligent, bidirectional charging of electric vehicles (Vehicle-to-Grid, V2G) can contribute substantially to both increasing the share of RES in the electricity mix and satisfying mobility needs with low emissions. Although this idea is already well known, its implementation still faces many obstacles. Among these are higher costs for bidirectional chargers and concerns regarding potentially faster battery aging.

In this thesis, I propose solutions to these problems and insights into the uncertainties that can accelerate and improve the exploitation of the potential of V2G.
Firstly, highly efficient power electronics for a V2G charging system were developed and characterized. Control methods for soft switching topologies known from the literature were adapted for the operation with silicon carbide semiconductors to achieve high efficiencies of more than 96% in wide operating ranges and to increase the switching frequency. As a result, the cost, weight, and size can be reduced.
On the other hand, grid-supporting control methods were derived, implemented in the hardware, and validated, which support the robust operation of a regenerative energy system and can thus generate higher revenues. This includes voltage and frequency control, dynamic stabilization of the grid frequency by emulating an electronically controlled virtual inertia, and the reduction of phase unbalance in the electricity grid.
Moreover, one of the most comprehensive freely available battery aging datasets to date was generated and published [J1], [R1]. It includes capacity and impedance measurement data from 228 cylindrical cells operated for approximately 450 days under 76 different test conditions. A well-reusable battery aging model was derived from this dataset. The model was employed to analyze various V2G charging strategies, which can even reduce battery degradation compared to conventional charging.

Contents

1 Introduction

According to the Intergovernmental Panel on Climate Change (IPCC), urgent and effective actions are needed to mitigate human-induced climate change and limit global warming, including a rapid decrease in greenhouse gas (GHG) emissions [1, pp. 24, 40]. Among all options, replacing fossil fuel power plants with RES has one of the highest potentials for emission reduction [1, p. 38].

The transition from a fossil-based to a renewable electricity system poses several challenges, particularly in regions where geographic conditions allow only low capacities of dispatchable RES, such as hydroelectric plants, and mature, affordable storage technologies like pumped hydroelectric energy storage (PHES). In an electricity system based on a high share of volatile RES like solar and wind power, alternative storage systems, demand-side management (DSM), and sector coupling are required to ensure a reliable supply regardless of fluctuating electricity generation and seasonal variations. Even though the expansion of RES is advancing worldwide, progress in the field of electrical energy storage is still very slow in many countries. For example, battery electric storage systems (BESSs) offer the possibility to store electrical energy, typically over a period of a few hours to days. However, despite rapid developments in recent decades, they are still relatively expensive and resource-intensive.

Another promising option for emission reduction is coupling the electricity and mobility sectors with electric vehicles (EVs). While the utilization of EVs increases the demand for electricity in the first place, intelligent, grid-serving charging of these vehicles creates flexibility to adapt the electricity demand to the available supply. Their contribution becomes even more significant if EVs are not only charged but their batteries are also used to feed back energy into the electricity grid, similar to a stationary BESS. The concept of bidirectional charging, known as “Vehicle-to-Grid” (V2G) or “Vehicle-Grid Integration” (VGI), has already been recognized decades ago [2]. Since then, there have been numerous demonstrators and field experiments, many of which are summarized by Ravi and Aziz [3] and Everoze [4]. Nevertheless, only a small number of EVs on the market currently support V2G.

Sovacool et al. [5], Noel et al. [6], Ghazanfari and Perreault [7], Ravi and Aziz [3], and an initiative for bidirectional charging in Germany [8] discuss many opportunities of V2G, but also barriers which prevented its widespread adoption, for example:

- **Customer-oriented aspects:** Confusion, lack of understanding or misinformation about V2G and its potential positive and negative impacts or EVs in general; range anxiety and the preference to have a fully charged EV at all times; lack of transparency in V2G programs and distrust against its operators; uncertainty about how V2G will influence the EV range at a particular time (e.g., in case of unforeseen trips); inconvenience; unawareness or undervaluation of cost savings from V2G; concerns or uncertainty regarding the impact on battery lifetime.
- **Financial aspects:** Higher capital cost for the communication and control infrastructure as well as the electronics required for bidirectional charging; high expectations regarding revenues from V2G; high investment risks due to uncertainty in regulation and future electricity price volatility; difficult access to the electricity market for "prosumers", hindering V2G business models.
- **Technical aspects:** Until recently, a lack of standards for and thus the availability of bidirectional charging and communication infrastructure and, up to date, a fragmentation of standards and regional differences between them; higher cost and complexity of bidirectional charger infrastructure (e.g., power electronics, control, and communication); higher weight and volume of bidirectional chargers (depending on the implementation).

The time window to mitigate climate change is closing at a breathtaking pace. Solutions that can be implemented in the short term are urgently needed to achieve a transition to low-emission energy and transportation systems. Even though there are still obstacles, V2G can play an essential role in accomplishing this goal.
Therefore, in this doctoral thesis, I want to address some of the barriers that prevented V2G from becoming established on the market and explore the chances of V2G for a future energy system. Specifically, the following objectives were defined for the thesis:

- Development and characterization of highly efficient and flexible bidirectional V2G charger power electronics with comparable cost, weight, and volume to unidirectional chargers
- Derivation of power electronic control strategies that enhance the robustness of electricity grids and support increasing the share of RES to reduce emissions
- Analysis of the practical feasibility of these control strategies and their limitations on a power hardware-in-the-loop (PHIL) test bench
- Investigation of the impact of V2G on battery lifetime and identification of recommendations to reduce battery aging

As illustrated in Figure 1.1, this thesis is divided into three parts. The first part outlines the energy and mobility transition to provide background information on the coupling of these sectors through Vehicle-to-Grid. Furthermore, an overview of the field of V2G is given.
The second part focuses on power electronics for V2G. After a summary of suitable topologies and control algorithms, a V2G charger prototype and the results of its operation are presented.
The third part evaluates a battery aging study. It provides the fundamentals of lithium-ion batteries, their aging, and a review of existing aging models and datasets. Finally, the aging experiment and its results, the derived aging model, and its application to simulate the impact of V2G on battery degradation are discussed.

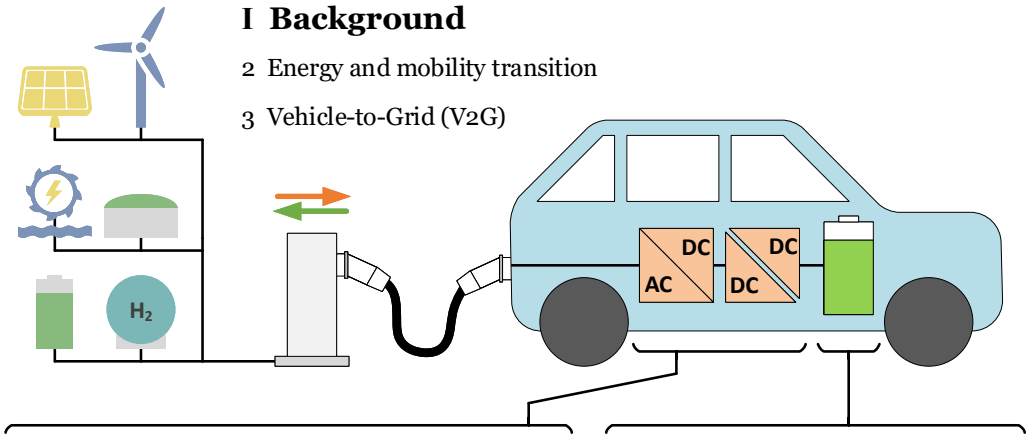

Figure 1.1: Graphical abstract of this thesis

Part I

Background

2 Energy and mobility transition

V2G couples the electricity and mobility sectors. This chapter provides an overview of the motivation, possible implementation, and challenges of the energy transition and the electrification of the transport sector to support identifying opportunities and requirements of V2G.

At present, only a small portion of global energy consumption is provided by RES or nuclear energy. This can be seen in Figure 2.1a, which shows the global primary energy consumption by energy source over time. The overall demand approximately doubled in the last 40 years and

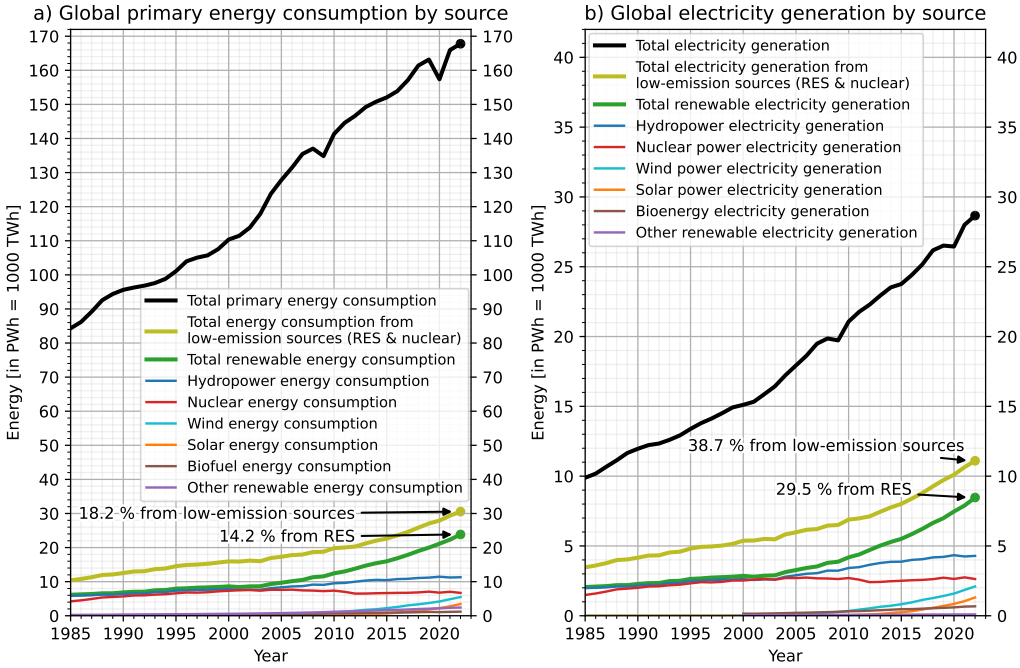

Note: The primary energy consumption of non-fossil sources (RES, nuclear, and their share in the total primary energy consumption) in the left graph is calculated using the "substitution method": Not the actual energy output (e.g., electricity) generated by RES/nuclear power is used, but a higher value that equivalents to the primary energy that a thermal fossil fuel power plant would have needed to generate the same amount of energy output.

Figure 2.1: Global a) primary energy consumption and b) electricity generation by source. Data compiled by *Our World in Data* [9] (CC BY 4.0), interactive version online: [10, 11]. Original data from *Ember* [12, 13] (CC BY 4.0), *Energy Institute* [14], *U.S. Energy Information Administration (EIA)* [15].

reached about 170,000 TWh in 2022. The share of low-emission sources in the primary energy demand rose to 18.2%, but the majority is still sourced from fossil fuels — mainly oil, coal, and gas. While the energy generated by nuclear power slightly declined in the last 20 years, RES experienced significant growth and accounted for 14.2% of primary energy demand in 2022.
Their increase can be seen more clearly in Figure 2.1b, which depicts the global electricity generation by energy source over time. In the electricity sector, 29.5% of energy was generated by RES, and 38.7% when also including nuclear power. Hydropower generation increased relatively linearly since 1950, and solar and wind power have grown exponentially in recent decades. Nevertheless, the majority of energy in the electricity sector is still generated by fossil fuels as well.

This is a problem for two reasons. Firstly, fossil fuel reserves on our planet are finite: According to a report from *BP* in 2021, proven reserves of coal, oil, and gas will last only 139, 54, and 49 years, respectively, at the current rates of consumption [16, pp. 16, 34, 46]. Consequently, alternative solutions to replace these finite, fossil resources must be found and implemented at some point.
However, the more urgent problem is climate change: The majority of anthropogenic (i.e., human-induced) GHG emissions are caused by burning fossil fuels and through industrial processes that release CO_2 into the atmosphere [17, pp. 6f.]. In its sixth assessment report of 2021, the IPCC states that the increase in GHG concentrations, which is observed in the atmosphere, is undoubtedly the result of human activities and that these GHGs are by far the primary cause of the observed global warming [18, p. 4, 7]. Exceeding a temperature rise of significantly more than 1 to 1.5°C above the pre-industrial level increases the risks and frequencies of weather extremes such as heatwaves, severe droughts, and extreme rainfall events [18, p. 15]. Even worse, it could also trigger climate tipping points, many of which accelerate global warming even further [19]. Therefore, in order to mitigate climate change, these emissions would have to decrease rapidly. The 195 parties of the United Nations Framework Convention on Climate Change (UNFCCC) that signed the Paris Agreement [20] obliged themselves to attempt to limit global warming to 1.5°C relative to the pre-industrial level [21, p. 3].

Figure 2.2 shows historical GHG emissions and possible CO_2 emission paths to limit global warming to 1.5 or 2.0°C. The historical emission data was compiled by *Our World in Data* [23], and the future trends are based on the carbon budgets calculated by the IPCC [18, p. 29].
Even though it has been known to the public for more than 40 years that man-made climate change exists and should be urgently prevented [27], human-induced GHG emissions are still not even close to the course necessary to reach the Paris Agreement. If global CO_2 emissions were to fall linearly from 2022 on, they would have to reach net zero as early as 2034 to reach the target temperature of 1.5°C with a likelihood of 67% (green solid line in Figure 2.2). Comparing the development of historical emissions with the trajectories necessary to comply with the budgets,

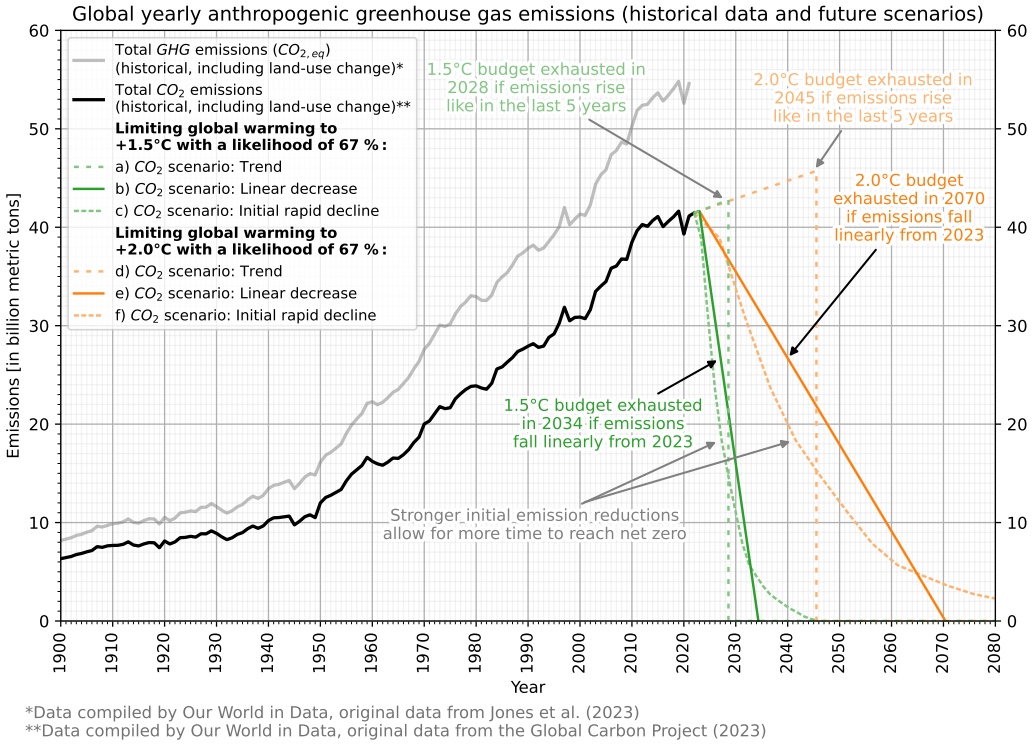

Figure 2.2: Human-caused GHG and CO_2 emissions in the past and future scenarios to meet the 1.5°C or 2.0°C targets of the Paris Agreement [21] with a likelihood of 67%. Historical emission data compiled by *Our World in Data* [22, 23] (CC BY 4.0). Original data: Jones et al. [24, 25] (CC BY 4.0), *Global Carbon Project* [26] (CC BY 4.0). Remaining emission budgets for future scenarios from the *IPCC* [18, p. 29].

it becomes unmistakably clear that rapid and effective measures to reduce emissions need to be realized as soon as possible.

Reducing emissions can be achieved with sufficiency, efficiency, and renewable energy, as illustrated in Figure 2.3 (also compare [1, pp. 957-959]):

- **Sufficiency:** Avoiding demand for useful energy (or other resources) in the first place, e.g., by living in a smaller home, heating to a lower room temperature, sharing resources like cars, avoiding trips, or reducing consumption of goods.
- **Efficiency:** Improving the energy efficiency (e.g., of buildings, vehicles, appliances) and all conversion processes in between, i.e., reducing the primary energy demand without altering the useful energy output.
- **Renewable energy (RE):** Sourcing the remaining primary energy demand from RES, such as solar, wind, hydro-, geothermal, or biomass power plants, instead of fossil fuels.

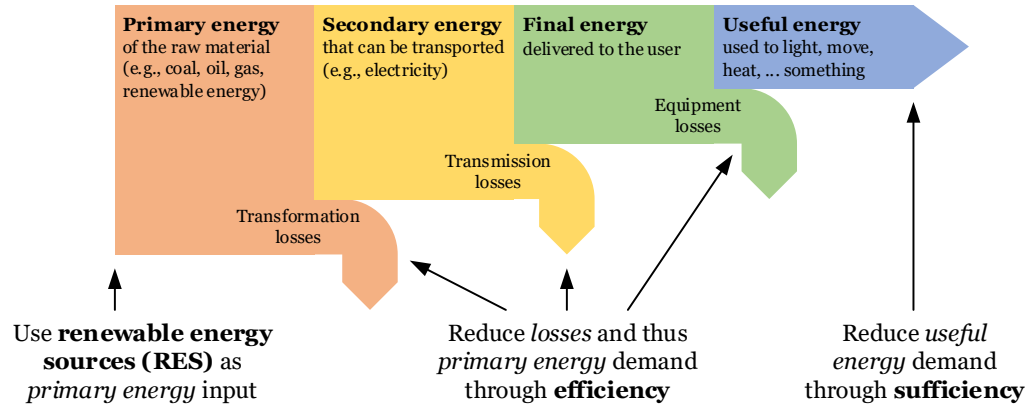

Figure 2.3: Primary/secondary/final/useful energy and how to reduce emissions with renewable energy, efficiency, and sufficiency. Own graphic based on the chart and description from [28].

2.1 Energy transition

Of all the mitigation options presented by the IPCC [1, p. 38], renewable energy sources, particularly solar and wind power, have the highest potential to reduce GHG emissions in the current decade. RES can power the existing electricity grid and thus reduce the emissions of all machines and appliances already connected to it. However, RES can also reduce emissions in the transport sector, particularly through the electrification of vehicles, and the emissions in the heating sector, e.g., through heat pumps. Often, the electrification of these sectors can also reduce the overall primary energy demand — especially if the electricity grid is powered by a high share of RES [29, p. 835f.]. For example, while the well-to-wheel efficiency of internal combustion engine vehicles (ICEVs) powered by fossil fuels ranges from 11 to 37%, EVs powered by solar and wind power reach a well-to-wheel efficiency of 39 to 72%, according to Albatayneh et al. [30]. This results in a reduction of the primary energy demand by a factor of approximately 2 to 3.5. Similarly, heat pumps can reduce primary energy demand and emissions, particularly when powered predominantly with RES. While the efficiency of gas furnaces ranges from 78 to 97%, the coefficient of performance (COP)[1] of heat pumps typically lies between 2.3 and 5, according to Self et al. [31]. This allows for a primary energy demand reduction of a factor of up to 3 to 5.

[1] The COP is the ratio of useful thermal energy output to electric energy input, i.e., a metric for efficiency. It can significantly exceed 100% since the electricity (input energy) is not used to heat the space directly but to transport heat from the environment into the heated space (output energy).

Other sectors, currently or in general, cannot simply be electrified, for example, iron ore reduction, the production of chemicals such as ammonia, or long-distance shipping and aviation [32, 33]. However, RES can decarbonize these sectors with power-to-X (PtX), e.g., power-to-gas (PtG) or power-to-liquid (PtL): Fossil fuels are substituted with synthetic fuels that were produced using RES, e.g., hydrogen (H_2), methane (CH_4), ammonia, or synthetic gasoline, diesel, and kerosene.

Regardless of how much the primary energy demand can be reduced through sufficiency and efficiency, it is crucial for rapid and effective mitigation of emissions to meet the remaining primary energy demand by renewables as quickly as possible. Since the cost of RES, such as solar and wind power, as well as storage technologies like lithium-ion (Li-ion) batteries, declined rapidly in the past decades, they became cost-competitive or even have a lower levelized cost of energy (LCOE) than fossil and nuclear power plants [1, p. 12], [34]. In addition to appropriate energy policy measures, this is probably the main reason why electric energy generated by RES globally almost doubled in the past decade, as shown in Figure 2.1b. This increase is driven in particular by the exponential growth of electricity generated from solar and wind power.

2.1.1 Renewable electricity generation and demand

"Electricity systems powered predominantly by renewables are becoming increasingly viable" [1, p. 28], according to the IPCC. Breyer et al. [35] review literature on 100% RE systems: Most of the studies conclude that energy systems based on 100% RES are technically and financially viable worldwide. About 50 studies on energy systems based on 100% (or almost 100%) RE are listed by Brown et al. [29, p. 842]. Meschede et al. review studies on 100% RE systems for islands and conclude that they are "technically feasible and economically viable" [36, p. 25] both on small and big islands. The 2023 global renewable status report of REN21 summarizes that of the 146 countries with net-zero GHG emission targets (among which China, the US, India, Brazil, Japan, Canada, the EU, and many others), 94 countries have RE targets across all sectors, 25 of which for 100% RE [37, p. 24]. More than 170 countries had at least some form of target to increase the share of RE [37, p. 27]. Some countries, islands, or regions already reached 100% RE in the electricity grids for a longer period or even continuously [38, p. 196]. However, most of them rely on hydropower, which is subject to geographical conditions and thus not transferable to many other regions.

In regular operation, fossil, nuclear, biomass, geothermal, and most hydroelectric power plants can adjust their electricity generation power relatively flexibly to a desired value up to the nominal capacity of the power plant. Therefore, these types of power plants are categorized as dispatchable power plants. Conversely, the maximum available generation power of intermittent power plants (solar, wind, wave, or tidal power) depends on external factors (e.g., weather, time of the day,

season of the year, tides). Hence, the generated power cannot be arbitrarily increased to the nominal power of the plant most of the time. However, typically, it can be reduced in any case.
If a highly renewable, low-emission energy system shall be operated with a high share of intermittent RES, other solutions have to be implemented to match this volatile energy generation with the momentary demand reliably. Several possibilities exist, which can or have to complement each other, as addressed by Breyer et al. [35, p. 78189]. They are outlined in Figure 2.4[2] using the letters *A* to *G*, which are described in the following list:

A. **Increased RES capacity:** With larger RE capacities, electricity demand exceeds generation less frequently and with lower intensity.

B. **Cross-border electricity trade:** Increased energy exchange with neighboring countries reduces regional differences in weather-dependent electricity generation (also compare [29, p. 837]). Geographic advantages of other regions (e.g., conditions that allow large pumped storage capacities) can be used more effectively, too.

C. **Demand response (DR):** Part of the electricity demand can also be shifted in time because it is not always important when exactly the energy is used. For instance, heat pumps are often supplemented by thermal storage systems that can store heat for several hours to decouple electricity use and heat demand. Electric passenger cars typically only need to charge a few hours a week but are not in use the majority of the time. If long charging opportunities exist frequently, the charging process could be scheduled or temporarily interrupted. Some industrial consumers (e.g., cold stores) or household appliances could also antedate or postpone part of their electricity demand.

D. **Sector coupling / power-to-X (PtX):** Linking different energy sectors (e.g., the electricity sector with the heat, transport, or industry sectors) is crucial for highly renewable energy systems [45]. Not only can other sectors benefit from low-emission electricity sources such as photovoltaic, wind, and hydropower, but the electricity sector can also benefit from the flexibilities of other areas of energy demand. This can significantly reduce peak electricity demand, curtailed RE generation, and residual load [46]. Synthetic gases and fuels can be

[2] Figure 2.4 is based on the historical generation and demand data in Germany in 2022 from SMARD ("Bundesnetzagentur | SMARD.de", CC BY 4.0) [39]. In this relatively simple approach, the generation data is linearly scaled to the respective RES expansion targets of the current governing coalition [40, 41] (see Figure 2.5), considering past installation capacity data from the German Federal Network Agency [42], the German Federal Ministry for Economic Affairs and Climate Action (BMWK) [43], and SMARD [39]. The yearly electricity demand was estimated at 720 TWh in 2030 and 975 TWh in 2040, which is calculated based on a linear interpolation from the current overall electricity demand (483 TWh in 2022 [39]) and the estimated future loads of scenario B (high electrification) of the latest network development plan of the transmission system operators (TSOs) [44, p. 70]. For future load, the electricity demand, power-to-heat (PtH), and 50% of the power-to-hydrogen demand (representing hydrogen used for industry and mobility) are included. The electricity generation and demand of storage systems (BESS, PHES, and the rest of the power-to-hydrogen demand, representing hydrogen used for electricity generation) are excluded.

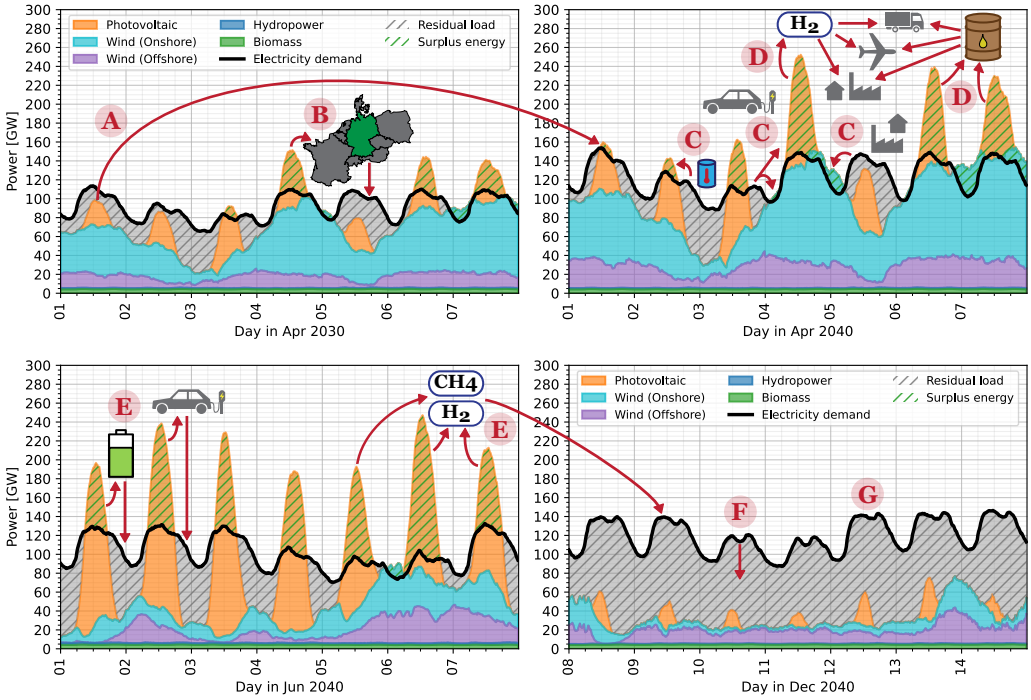

Figure 2.4: Possible future renewable electricity generation and demand in Germany — using 2022 data from "Bundesnetzagentur | SMARD.de" (CC BY 4.0) [39], linearly scaled to projections of RES capacity and demand in 2030 and 2040 — and methods to decrease non-renewable energy use

produced predominantly when surplus energy from RES is available, stored, and used at a later point in time, for example, in the transport, heat, and industry sectors. However, even though the electrification of other sectors can reduce primary energy demand and improve RES integration, it significantly increases overall electricity demand. Thus, a much higher RE capacity is needed than would be required just to cover conventional electricity consumption.

E. **Storage systems:** Short-term energy storage systems — such as PHES, stationary BESS, or EVs supporting V2G — can store excess energy for later points in time. They are particularly useful if comparably low amounts of energy need to be stored and returned very frequently (compare June 2040 in Figure 2.4). However, especially if seasonal conditions cause more extended periods of low RE generation (seen in the week of December 2040 in Figure 2.4), so-called long-term storage systems are more suitable. In this case, fuel cells or gas-fired power plants can use hydrogen and methane generated during periods of high surplus energy or imported from other regions.

F. **Efficiency and sufficiency:** Similar to an increased RES capacity, decreasing energy demand can also help to increase the overall share of RES and reduce emissions.

G. **Backup power plants:** On the path toward a 100% RE system, fossil fuel-powered plants can be used as a backup, possibly supplemented with carbon capture and storage (CCS) or carbon capture and use (CCU) systems.

2.1.2 Renewable energy and storage expansion in Germany

The historical development of photovoltaic (PV) and wind power plant capacities [42, 43] and their planned expansion [40, 41] in Germany is shown in Figure 2.5. Although the timing for the expansion targets tends to be delayed to be well in line with the remaining carbon budget (compare Figure 2.2), for the first time, these recently introduced targets reach levels necessary for a 95 to 100% renewable energy system as analyzed by several studies [47–54].
Although the share of renewable energy in the electricity sector is already about 50% [55], it is planned to increase the PV capacity by a factor of five and wind power by more than a factor of three. This is because the decarbonization of all sectors will significantly increase the overall electricity demand, likely by a factor of two or more in comparison to 2022 [39], [47, pp. 28-33], [48, pp. 23f.], [52, pp. 24f.].

In the past, energy storage systems mainly improved the operation of different conventional power plants. They allowed their cost-optimal dispatch, e.g., increasing the share of base load power plants with low marginal cost (such as nuclear and coal plants) and decreasing the use of more expensive peaking plants (especially gas turbines) [56, pp. 721, 725]. There was no need for extensive electricity storage systems: The portion of renewable energy that had to be curtailed because parts of the electricity grid were congested was very small (2.7% in 2021 [57, p. 175]), and various dispatchable power plants could adjust their power flexibly enough to match generation and demand. However, in the transition to a highly renewable energy system, there is a paradigm shift from the concept of dispatchable power plants covering base and peak load to an energy system with largely volatile electricity generation, a more flexible demand side, and substantially expanded short and long term storage [48, p. 30], [35, p. 78189].

For a long time, pumped hydroelectric energy storage (PHES) systems were the only significant type of electrical storage system used in the grid [56, p. 721], [58, p. 7]. The capacity of PHES located in Germany[3] is currently in the range of 37–40 GWh with both a pump and generation power of about 6 GW [58–62]. While PHES systems have been used in Germany for over a century,

[3] PHES systems with an additional storage capacity of about 15–20 GWh and a power of roughly 3 GW operating entirely or partly for the German electricity market are located in Austria and Luxembourg [59, p. 38].

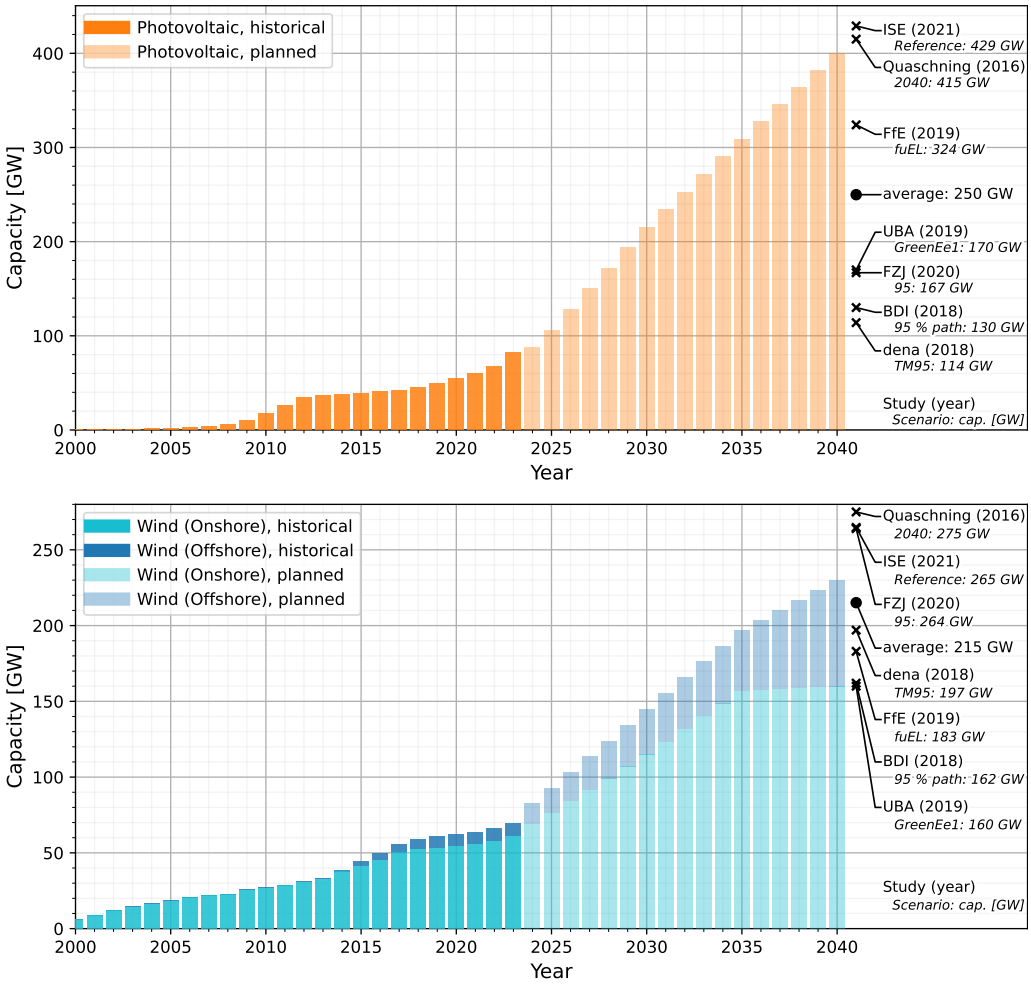

Figure 2.5: Historical [42, 43] and planned [40, 41] installation capacities for photovoltaic (top) and wind (bottom) power in Germany with capacities necessary for (nearly) 100% renewable energy systems according to studies of Quaschning [47], *ISE* [48, 49], *FfE* [50], *UBA* [51], *FZJ* [52], *dena* [53] and *BDI* [54]

their expansion stagnated about 40 years ago [63, p. 421]. Even though the potential for currently planned or possible future PHES projects is remarkable, many of these projects came to a halt, and some existing PHES plants were (at least temporarily) shut down due to poor profitability as well as unfavorable energy economic and policy framework conditions. Most importantly, at least until the end of 2021, the price spread on the electricity market and the revenues for regulating reserve power were very low, which is an unfavorable condition for all types of storage systems in the grid. In addition, storage systems in Germany have to pay a quite significant grid

charge[4], further decreasing profitability. Other barriers are concerns and restrictions because of environmental protection and the acceptance by residents [59, 60, 63, 65, 66].

In recent years, there has been a significant increase in stationary battery storage in Germany. This can be seen in the development of overall power (orange curve) and capacity (green and yellow curves) of stationary battery systems shown in Figure 2.6. In April 2024, about 13.0 GWh of home, industrial, and large-scale battery systems combined were installed, most of which were lithium-ion battery systems [67, 68]. In the last five years, the average yearly capacity growth rate was approximately 60% — if it persists, the BESS capacity could exceed that of PHES located in Germany (blue line) by 2026.
Figure 2.6 also contains projections of stationary battery capacity (green and yellow points) for future energy systems with a 95% (*FfE* [50, p. 300], *FZJ* [52, pp. 31f.]) and 100% (*ISE* [48, pp. 29f.], [69]) reduction of greenhouse gas emission in all sectors compared to 1990. The studies of *ISE* [48, 69] and *FZJ* [52] also include projections of usable mobile battery capacities from EVs supporting V2G (red points). The historical development of the total estimated battery capacity of all battery electric vehicles (BEVs) and plug-in hybrid electric vehicles (PHEVs) registered in Germany (gray curve) is shown for comparison [70, 71]. More than 2.33 million BEVs and PHEVs were registered on January 1, 2024 [72], with a combined EV battery capacity of about 100 GWh [71]. This capacity is an order of magnitude higher than that of all stationary battery systems and already more than 2.5 times the storage capacity of all PHES located in Germany.

Besides PHES, stationary and mobile battery storage systems, other technologies exist. Examples are compressed air energy storage (CAES), sensible or latent heat storage, flywheel, electromagnetic or capacitor energy storage systems, and synthetic gases or fuels produced with renewable energy (i.e., PtX) that can later used in fuel cells or thermal power plants to generate electricity again [58, 59, 73–75]. Although none of these technologies currently contribute any significant storage capacity to the German electricity grid, it is expected that at least some of them will also undergo massive expansion in the coming decades. Namely, both the potential and future demand for long-term storage that can be provided with hydrogen and methane reservoirs is immense [48, pp. 16, 29, 33f., 49], [52, pp. 32-38], [58].

As of 2024, all storage systems located in Germany combined could only feed in approximately 14 GW (ca. 27% of the average electricity demand) and would last no longer than four hours on average at maximum feed-in power[5]. This is not sufficient for future energy systems with a high share of volatile RES. The future generation and demand examples in Figure 2.4 (considering the expansion targets shown in Figure 2.5) illustrate the situation: There are significant energy

[4] after a transitional period during which they are exempt from the grid charge, see §118 EnWG, section 6 [64]
[5] PHES: 6 GW / ca. 40 GWh [58–62], BESS: 8.4 GW / 13 GWh [67, 68], electricity demand: 458 TWh in 2023 [39]

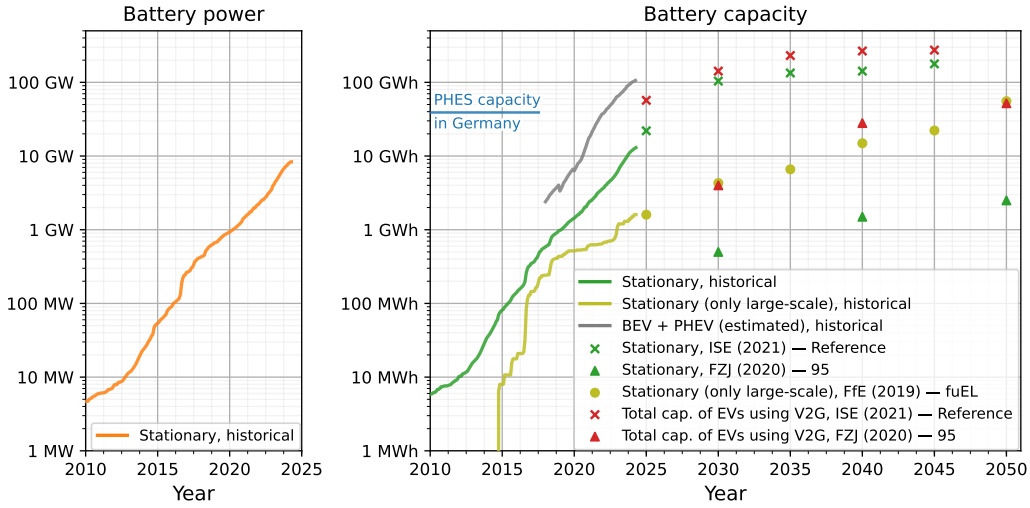

Figure 2.6: Historical development of BESS power (orange) and capacity (green and yellow curves) in Germany (data: Figgener et al. [67, 68], CC BY 4.0) with stationary (green and yellow points) and V2G (red points) battery capacity projections for highly renewable energy systems according to studies of *ISE* [48, 69], *FfE* [50], and *FZJ* [52]. Capacity of PHES located in Germany (blue line) [58–62] and cumulative BEV and PHEV battery capacity (gray curve, data: Hecht et al. [70, 71], CC BY 4.0) for reference.

surpluses at some times and high residual loads at other times, both often in the range of 100 GW or more for several hours or even days. It quickly becomes evident that storage systems will have to play a much more relevant role in the following decades, especially when aiming for a 100% GHG-neutral energy system.

2.2 Electric vehicles

Worldwide, the transport sector accounted for 15% of the global GHG emissions in 2019 [17, p. 8]. In Germany, it even accounted for 20% of the national emissions in 2022, of which about 98% are caused by road traffic [76, pp. 7, 23]. Since 1990, the GHG emissions of the German transport sector have barely decreased at all [77, p. 315], [76, p. 24], which is problematic for climate change mitigation.

As described in [78, pp. 14-16], the “transformation of the transport sector”, with the goal of its decarbonization, can be divided into the “mobility transition” and the “energy transition in transport”. The mobility transition refers to the reduction of energy demand in the transport sector — substituting, reducing, or shortening trips and shifting to less energy-intensive forms of transportation (e.g., from planes to rapid trains or from cars to public transport or bikes). On the

other hand, the energy transition in the transport sector addresses the shift from carbon-intensive fossil fuels to almost carbon-free sources for the remaining energy demand (e.g., the shift from internal combustion engine vehicles (ICEVs) to EVs). Due to their high efficiency and the ability to be charged by RES, EVs play a central role in both the reduction of primary energy demand and the reduction of GHG emissions in the transport sector [17, p. 32], [78, pp. 44f.]. The emissions of BEV passenger cars are already significantly lower than those of ICEVs. With the ongoing energy transition and improvements in battery cell production and lifetime, their emissions will continue to fall [79–83].

2.2.1 Classification of electric vehicles

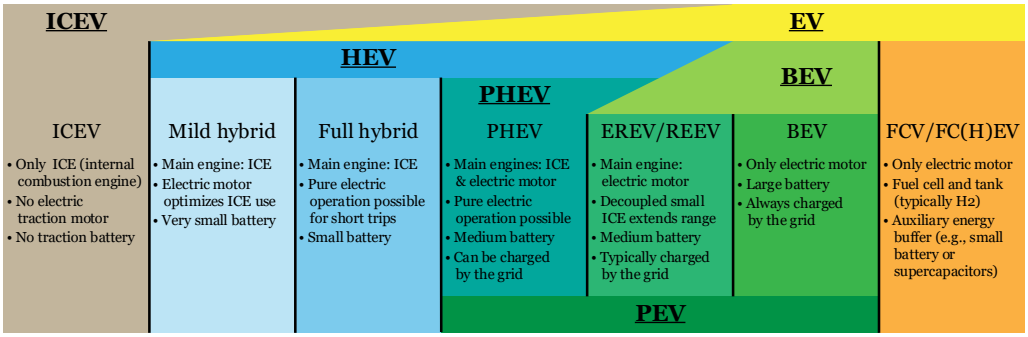

Figure 2.7: A possible classification of ICEVs, EVs, hybrid electric vehicles (HEVs), PHEVs, BEVs, plug-in electric vehicles (PEVs), and fuel cell electric vehicles (FCEVs)

Electric vehicles (EVs) can be divided into hybrid electric vehicles (HEVs), plug-in hybrid electric vehicles (PHEVs), battery electric vehicles (BEVs), and fuel cell electric vehicles (FCEVs), as shown in Figure 2.7 and described in [84, pp. v, 1-3., 53-62, 137-148]. While a BEV only uses a battery as its primary energy storage (e.g., a lithium- or sodium-ion battery), HEVs are electric vehicles powered by multiple energy sources, typically fuel burned in an internal combustion engine (ICE) and a battery. Different HEV variants exist, such as mild or full hybrid vehicles, as well as extended-range electric vehicles (EREV) / range-extended electric vehicles (REEV). PHEVs are HEVs that can be charged by a plug, i.e., the battery can be charged by the electricity grid and not only with energy from braking or the ICE. The term plug-in electric vehicle (PEV) is sometimes used when considering both PHEV and BEV. On the other hand, an FCEV uses fuel cells to convert energy stored in fuels into electricity used for driving. Often, the energy is buffered with an additional battery, which is why some authors refer to it as a fuel cell hybrid electric vehicle (FCHEV). While this thesis focuses on BEVs, much of the discussion and results around V2G can also be transferred to PHEVs that have a significant battery capacity.

2.2.2 EV charging

The EV charging infrastructure standards applicable in Germany are summarized in [85–87]. IEC 61851-1 [88], which covers conductive charging via cables, specifies four EV charging modes, as shown in Figure 2.8. In modes 1, 2, and 3 ("AC charging"), the EV is connected to the alternating current (AC) grid. The onboard charger (OBC) in the vehicle converts the AC voltage into a direct current (DC) voltage to charge the battery. The charger is typically galvanically isolated.

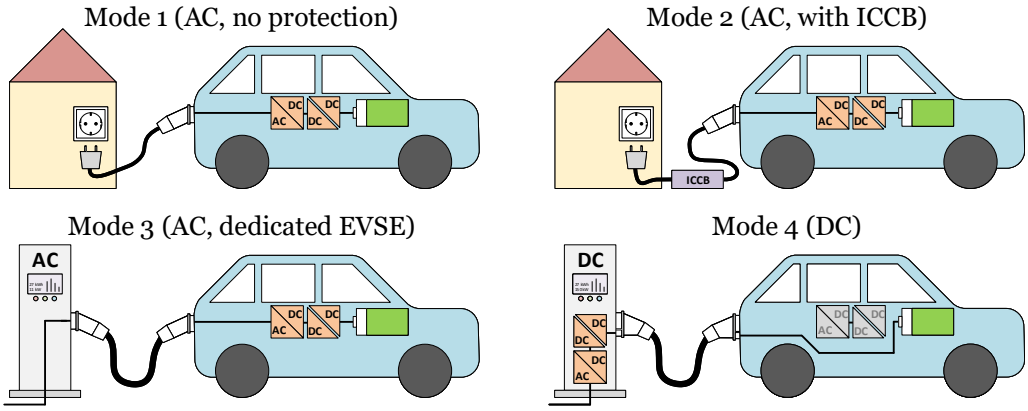

Figure 2.8: Conductive EV charging modes according to IEC 61851-1

- In **mode 1**, there is no communication between vehicle and infrastructure and no added safety layer in the cable. Vehicles and users have to rely on the safety mechanisms installed in the infrastructure. Therefore, this charging mode is forbidden in some countries.
- In **mode 2**, an In-Cable Control Box (ICCB), sometimes called an In-Cable Control and Protection Device (IC-CPD), is integrated into the cable. It communicates with the vehicle (e.g., to limit the charging current) and protects against electric shocks with a residual-current device (RCD) as well as by monitoring the protective earth (PE) wire.
- In **mode 3**, a dedicated, usually permanently installed electric vehicle supply equipment (EVSE), i.e., an AC charging station, is responsible for protection and communication to the EV.
- In **mode 4** ("DC charging"), the power electronics device that converts AC into DC is located in a stationary charging system. The direct current is transferred to the battery through the cable — the onboard charger is not used.

Since an OBC is located in the vehicle at all times, its weight and volume are more constrained than stationary DC chargers, and thus, the maximum charging power for AC charging is typically

low. For fast charging (e.g., on longer trips), DC chargers are more suitable. Since public DC chargers typically serve a high number of customers, they can also be more expensive than an OBC, which inherently only serves one EV.

Figure 2.9 shows a variety of other possibilities to charge EV batteries, also summarized in [89]:

- Besides the conductive charging modes, EVs could also be charged using **wireless power transfer (WPT)** while parking or driving, as specified in the series of standards IEC 61980. Although not yet broadly commercialized for EV charging, this technology is gaining momentum [90].
- Charging with **pantographs**, also called Automatic Connection Devices (ACDs), mounted on the vehicle or the station, is already used for some electric buses in Europe [91–93].
- Connecting an EV to **catenaries (overhead wires)** while driving can drastically decrease the necessary battery capacity if the coverage of overhead wires on the route is good[6].
- Another alternative is **battery swapping**: Instead of charging it while in the EV, the empty battery is removed from the car and charged stationarily. In the meantime, the EV can continue to drive with another battery that is already charged. The first EV manufacturer has been offering commercial battery swapping in China since 2018 [98] and opened its first battery swap station in Germany in 2022 [99].

One of the first non-proprietary fast charging standards was CHAdeMO (derived from "Charge de Move"). In 2011, several hundred chargers were installed in Japan [100], and Europe's first CHAdeMO charger followed in 2012 [101]. The competing standard was the Combined Charging System (CCS), which combined the vehicle inlet for AC and DC charging. The CCS standard prevailed in Europe, with its type 2 plug for AC and combo 2 plug for DC charging [102, 103]. Most EV models and charging networks in North America also support CCS (type 1 and combo 1 plug). However, several automakers have recently announced that they will support the North American Charging Standard (NACS) in this region in the future [103]. In China, on the other hand, the GB/T charging standards are used[7]. Although numerous CHAdeMO stations exist in Europe and the USA, with few exceptions, this standard is mainly used by new EVs in Japan. It is foreseeable that CHAdeMO will play a minor role outside Japan in the future [104].

In Germany, all public AC charging stations need at least one CCS "Type 2" and all public DC stations at least one CCS "Combo 2" connection due to the "Ladesäulenverordnung" (charging

[6] One historical example is the "trolleybus" [94]. As of 2020, almost 300 trolleybus systems were in operation worldwide [95]. Several pilot projects in Germany have also investigated the use of overhead wires for the electrification of truck traffic, with systems that are easier to handle and less constrained for driving [96, 97].

[7] The "GB" standards are the national standards of the People's Republic of China. The "T" is used for standards that are recommended but not mandatory.

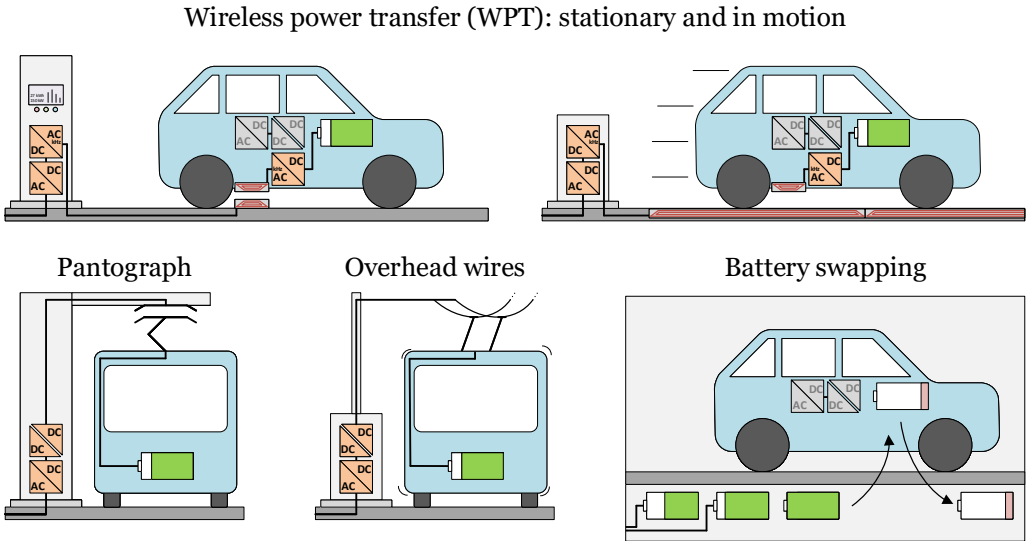

Figure 2.9: Alternatives to conductive EV charging: wireless charging and battery swapping

station regulation) of 2016 [105], [86, pp. 21-23]. As a result, CCS Type 2 and Combo 2 connectors became the most common ones for charging stations installed and new vehicles registered in Germany.

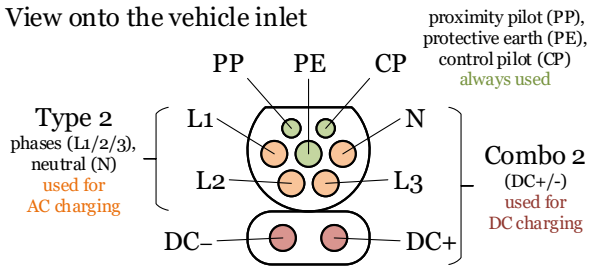

Figure 2.10: Pinout of the Combined Charging System (Type 2 / Combo 2 connector)

Figure 2.10 shows the pinout of the combined Type 2 and Combo 2 connector on the vehicle side, as specified in the standards IEC 62196-2 and IEC 62196-3 [106–109]. For single, two, or three-phase AC charging, power transfer takes place over pins L1/2/3 and N. For DC charging, the DC+/– pins are used to transfer power. The protective earth (PE), as well as the communication pins proximity pilot (PP) and control pilot (CP), are connected in both charging modes. The PP pin is used to detect a cable connection and — using a resistor coding between the PP and PE pins — its nominal current rating. The CP pin is used to exchange information between EV and EVSE,

i.e., the charging station. In the basic form of communication, the EVSE generates a pulse width modulation (PWM) signal between the CP and PE pins, which the EV evaluates. The duty cycle of the PWM provides information on the maximum current that the EVSE can deliver or if the digital communication interface shall be used instead. The EV modulates the PWM amplitude to signal its state to the EVSE.
This simple form of communication is only sufficient for basic AC charging, but not if more information needs to be exchanged between EV and EVSE, such as for:

- **DC charging:** An isolation check is coordinated before the charging process starts, and the EVSE needs to know the battery voltage and current limits.
- **Plug and Charge (PnC):** If both EVSE and EV support PnC, the payment process can be handled automatically without user intervention — the user does not have to authenticate himself with a charging card/chip or other payment methods before the charging begins.
- **V2G power transfer:** If the EV transmits energy back to the grid, EVSE and EV need to exchange more information, for example, on tariff schemes and their capabilities, requirements, and needs.

In these cases, data is exchanged based on the power line communication (PLC) standard "HomePlug Green PHY" as specified in the series of standards ISO 15118. The high-frequent PLC signal is modulated onto the CP pin in addition to the existing PWM signal to enable advanced bidirectional data exchange between EVSE and EV.

In many scenarios, the EVSE or EV also need to exchange data with other entities, for example:

- to transmit information about charging sessions for billing purposes,
- to remotely monitor or control charging stations,
- to provide feedback about the grid state to other entities,
- to dynamically adjust the charging or discharging power, for instance:
  - due to temporarily limited grid capacities,
  - to optimize self-consumption of RES like PV systems,
  - to minimize electricity costs when using dynamic tariff schemes,
  - to minimize GHG emissions of the charging session considering dynamic specific emissions of the electricity mix,
  - to offer ancillary services such as grid frequency control.

While the communication standards between EVSE and EV are relatively well developed and have already penetrated the market considerably, communication with other entities — such as energy management system (EMS), charge point operator (CPO) / charge system operator (CSO),

distribution system operator (DSO) or transmission system operator (TSO), electromobility service provider (EMSP), electricity market or aggregators — is still subject to many uncertainties. Among the most popular communication standards used for these purposes are Open Charge Point Protocol (OCPP) [110], EEBUS [111], OpenADR [112] as well as the ones specified in IEEE 2030.5 [113], IEC 60870-5-104 [114], and the series of norms IEC 63110. IEC 61850 is also worth mentioning since it currently covers the automation of electricity grid equipment and Distributed Energy Resources (DER) and might be extended for the communication between charging points and the electricity grid (IEC TR 61850-90-8) [115]. IEC 63382 (in development) will cover the grid integration of EVs as well [115].
An overview of the standards, in which context they are used, how they compare against each other, and examples of their use cases can be found in [115–123]. The TÜV Rheinland Consulting GmbH and its project partners give a good overview of applicable communication standards related to smart and bidirectional charging in Germany in their white paper about EV charging control from 2022. For the communication with an EVSE, they recommend ISO 15118-20 for the EV, OCPP (IEC 63110) for the CSO, and EEBUS (VDE-AR-E 2829-6, VDE-AR-E 2122-1000, and soon IEC 63380) for the EMS and Smart Meter Gateway (SMGW) [124, p. 13, 18]. On a European level, this is discussed in [123].

2.2.3 Development of electric mobility in Germany

About 49.1 million passenger cars were registered in Germany at the beginning of 2024, of which only 1.41 million (2.9%) were BEVs and 0.92 million (1.9%) were PHEVs [72]. Moreover, there were about 5 million motorcycles (of which 1.2% were BEVs), 85 thousand buses and coaches (3.1% BEVs), 3.7 million trucks (2.1% BEVs), and 2.4 million tractor units (0.05% BEVs) [72].

On average, there were 582 registered passenger cars per 1000 inhabitants in Germany [125]. The car density is lower in large cities compared to other districts, as shown in Figure 2.11a (also compare [126, pp. 35, 69]). The situation is reversed when considering the density per area: The density (Figure 2.11b) as well as the total number of passenger cars (Figure 2.11c) in large cities is by magnitudes higher than in rural districts due to the higher population density (Figure 2.11d). The share of BEVs among all registered cars is particularly high in large cities (see Figure 2.11e), in addition to some outlier districts where major car brands are located[8]. In general, the BEV share is lower in the states of former East Germany, except for the Berlin region. The differences for PHEVs are not quite as distinct, as shown in Figure 2.11f. The disparity could be explained by the fact that most EVs are still relatively expensive and are consequently mainly bought or leased

[8] e.g., 11.3% in Wiesbaden (*Opel* in Rüsselsheim), 9.4% in Wolfsburg and 5.4% in Braunschweig (*Volkswagen*), 5.25% in Böblingen and 5.0% in Stuttgart (*Mercedes-Benz* and *Porsche*)

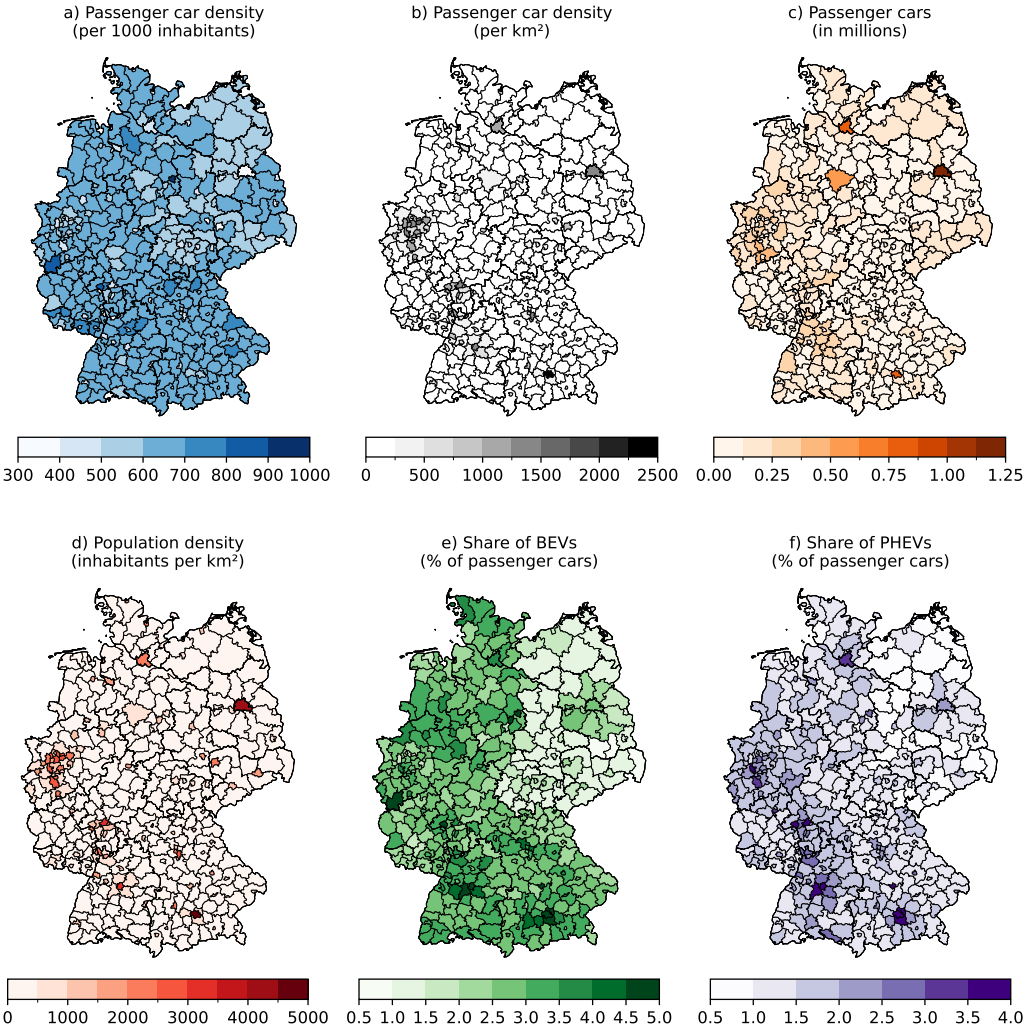

Figure 2.11: Passenger car density a) per capita and b) area, c) total number of passenger cars, d) population density and e) share of BEVs (scale limited to 5%) and f) PHEVs (scale limited to 4%) in the districts of Germany at the beginning of 2024. Vehicle and population data: *KBA* [125]. Cartographic data: ©GeoBasis-DE / *BKG* 2023, Data license Germany – attribution – Version 2.0 (dl-de/by-2-0), dataset: https://gdz.bkg.bund.de/index.php/default/digitale-geodaten/verwaltungsgebiete/verwaltungsgebiete-1-2-500-000-stand-31-12-vg2500-12-31.html [127].

by wealthier people. There is a high correlation between average salaries (compare [128], [129, pp. 8f.]) and BEV shares in the districts. As EVs tend to become cheaper, these regional differences could diminish in several years.

The market share of newly bought and registered BEVs has substantially risen in the last five years. According to recent forecasts, the inventory of EVs is expected to increase significantly in the following years, as summarized in Figure 2.12. Predictions for 2030 range from less than a

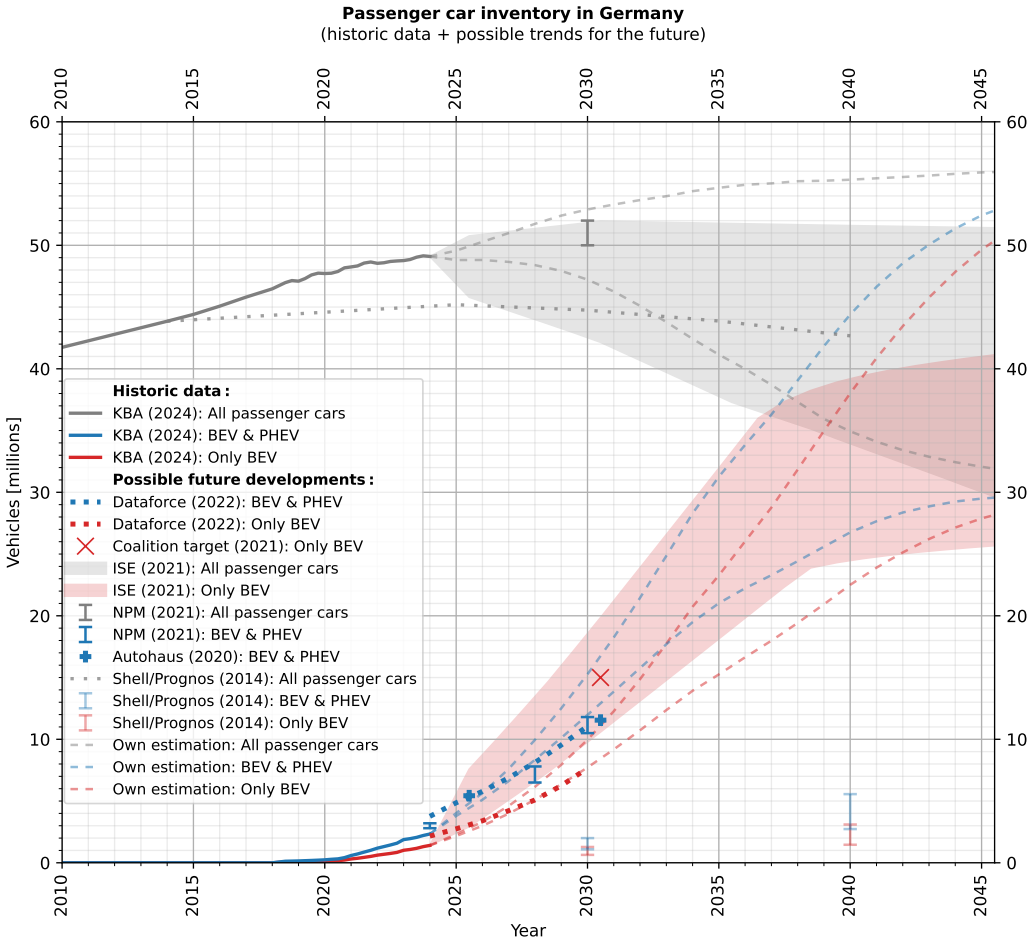

Figure 2.12: Development of the passenger vehicle fleet in Germany and its electrification — historical data from *KBA* [72, 130–134] and future projections from *Dataforce* [135], the coalition agreement of the current government in Germany [136, p. 27], *Fraunhofer ISE* [48, p. 19], [137], *NPM* [138], *Autohaus*/Borscheid [139], *Shell*/*Prognos* [140, pp. 63f.] and own estimations based on historical data and the development of market shares [141]

million BEVs[9] [140, pp. 63f.] to almost 20 million BEVs [48, p. 19], [137].

[9] Older studies, such as those by *Prognos* and *Shell* in 2014 [140], tend to underestimate the disruption of EVs and the development of the car inventory in general. Their projection of 1 million EVs in 2030 was already reached in 2022.

Even though the electrification of the transport sector is predicted to reduce primary energy demand significantly, it will contribute to a considerable increase in electricity demand in the future. For example, if 50 million passenger cars were BEVs, their average consumption was 22 kWh/100 km, including charging losses, and their average yearly driving distance was 14700 km (compare [126, p. 4]), the additional electricity demand would be 161.7 TWh per year. This corresponds to a 33.5% increase in electricity demand[10] compared to 483 TWh in 2022 [39].

The battery capacity of the more than 200 different passenger BEV models available in the German market in 2023 ranges from approximately 6 kWh to 108 kWh [143]. Based on calculations of Hecht et al. [70, 71], the average battery capacity of all battery electric cars registered in Germany until July 2022 was approximately 52 kWh[11].
The power of typical OBCs ranges from 3.6 kW to 22 kW [144, 145]. In July 2022, almost all BEVs in Germany had an 11-kW OBC[12], and their maximum DC charging capability averaged roughly 82 kW, according to Hecht et al. [70].

Alongside the growth in the EV inventory, the charging infrastructure is also expanding: There were more than 95,000 public AC charging points (most of which have a power rating of 11 or 22 kW) and more than 18,000 public DC charging points (most of which have a maximum power of 50, 150, or 300 kW) in Germany as of March 2024 [146]. However, the actual charging power is also limited to the maximum charging capability of the vehicle, which depends on the EV model and factors such as battery temperature and State of Charge (SoC). An unheated battery at cold winter temperatures or high SoCs typically prevents a high charging power.
The current government in Germany aims for one million public charging points for 15 million EVs by 2030 [136, pp. 27, 51f.]. However, some experts are of the opinion that significantly fewer public charging points are sufficient to reach this ambitious vehicle electrification target [147].

[10] The estimation is rather pessimistic because a high number of EVs and a high average consumption [142] are assumed, and decreased electricity demand from reduced fossil fuel production, distribution, and provision is not considered.
[11] about 755,000 BEVs [70, fig. 1] with an estimated total battery capacity of 39.4 GWh [70, fig. 2]
[12] the average was 8.7 kW

3 Vehicle-to-Grid (V2G)

This chapter explores the diverse aspects of V2G to build an understanding of its dependencies and interrelationships. Alongside the motivation and general operating principle, applications are presented, economic and social aspects are outlined, and advantages, disadvantages, and barriers are discussed.

3.1 Motivation and concept

With the rapid development of electric mobility in Germany, charging millions of EVs is increasingly becoming a challenge for the energy system, especially the distribution grids. While the overall increase in electric energy demand is moderate — even if all passenger cars in Germany were EVs — the peak power demand of the charging sessions could significantly exceed the present capabilities of the grid. A common concern is that this could be an issue, especially in the evening, when many people come home from work and plug in their electric cars to charge [148, pp. 24f.]. Several approaches exist to solve this problem and guarantee the safe and reliable operation of the electricity grid and the ramp-up of electric mobility.

3.1.1 Smart charging

An EV only supports *unidirectional charging* if it can solely recharge energy from a charging station but not discharge the battery again, i.e., return energy to the grid. For *conventional* (i.e., uncontrolled) unidirectional charging, the vehicle is connected to the station, and the charging process (i.e., power flow from the grid to the battery) starts immediately. The vehicle charges up to a preset charging limit or until the user ends the charging session. In contrast, *smart unidirectional charging* is influenced by other conditions (e.g., departure time, variable electricity prices, grid state, battery degradation). The charging process does not necessarily start immediately and also not inevitably until the vehicle is fully charged. The objective is not to charge the battery as quickly as possible but to provide other benefits (e.g., for the electricity grid, the battery, or the user) in this process. The advantages of grid-serving charging of EVs were already recognized in

the early 1980s [149].
Smart charging is sometimes referred to as "V1G", e.g., by the Charging Interface Initiative e.V. (CharIN), which further distinguishes between "controlled" and "cooperative" charging [150].

Why smart charging can be beneficial or even necessary for integrating EVs into the grid will be explained using examples from the *Netze BW GmbH*, a large DSO in Germany. In various field studies, the company investigated the effect of higher penetrations of EV charging on the grids [151]. Since 2018, there have been four projects: The "E-Mobility-Allee" [152, 153], the "E-Mobility-Carré" [154, 155], the "E-Mobility-Chaussee" [156, 157], and the "NETZlabor Intelligentes Heimladen" (Grid Lab Intelligent Home Charging) [158]. Within the projects, the DSO tested the effects of (also see Figure 3.1):

- Uncontrolled ("natural") charging: EV owners charge their car whenever they want — typically, the EV starts to charge as soon as it is plugged in until it is fully charged or the battery SoC reaches a defined level [154, p. 56].
- Static charging management: The maximum available charging power is limited at certain times based on a fixed schedule [156, p. 82].
- Dynamic charging management: The maximum power is limited based on real-time measurements and communication between EV, EVSE, and grid infrastructure, for instance:
  - when the grid conditions, e.g., the power rating of the customers' grid connection, require a decrease in electricity demand ("grid-compatible charging") [156, pp. 82-84],
  - to prevent congestion in the distribution grid ("grid-serving charging") [156, p. 84],
  - to improve stability and prevent congestion in the European transmission grid ("system-serving charging") [156, p. 84], or
  - to reduce electricity costs for charging based on variable tariff rates ("market-oriented charging") [156, p. 85].
- Stationary battery systems: A BESS installed in the distribution grid and controlled by the DSO, either with fixed or dynamic charging and discharging schedules [156, pp. 66-81].
- Line regulators: Active adjustment of the grid voltage with an electronic regulation system. The device can be placed in a distribution cabinet, for example, in remote areas with long line distances that would otherwise have too high voltage deviations [156, pp. 58-65].
- Simultaneous charging: In stress tests, all EVs are charged simultaneously on purpose, e.g., to test the effectiveness of previously mentioned measures [152, pp. 32-37] [158].

The field tests have shown that the maximum charging power of all EVs in the investigated grids combined (and thus the simultaneity factor) is usually much lower than initially feared —

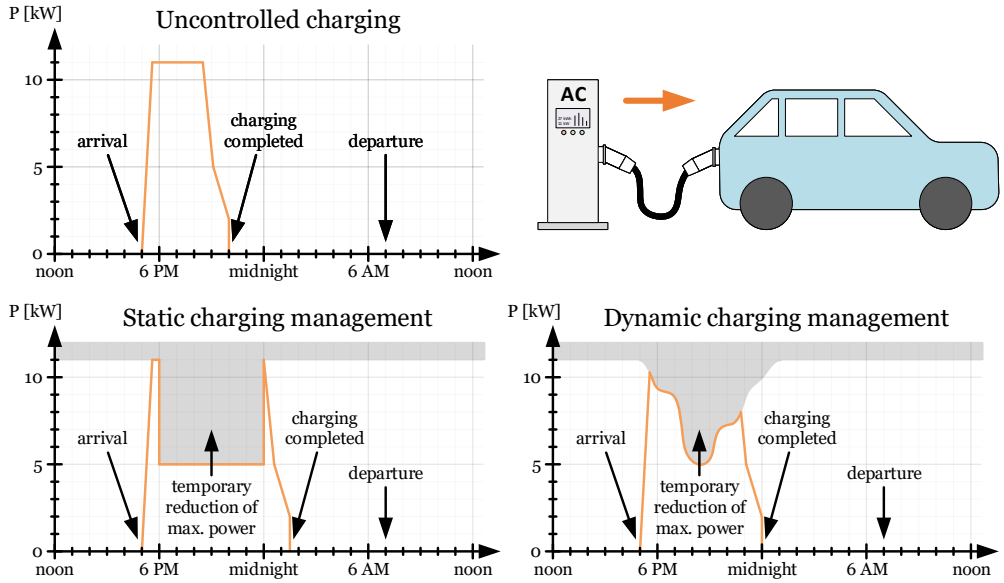

Figure 3.1: Unidirectional charging of an EV: conventional, uncontrolled charging (top) and smart charging with static (bottom left) or dynamic (bottom right) charging management

especially if a high number of EVs is considered. A possible explanation is that people's lifestyles are much more different than sometimes anticipated. For example, not everyone comes home from work at the same time; some people work part-time, in shifts, or at home, or use other modes of transportation for their daily commute, have a vacation, are on parental leave, or are retired. Moreover, not everyone charges their EV every day.
In the first project, the maximum simultaneity factor was 50%, but only 0.1% of the time. During 73% of the time, none of the ten EVs in the project was charging at all [152, pp. 24, 29]. The highest simultaneity factor in the second study with 58 EVs was even lower, with 22.4% [154, pp. 59]. In a third, smaller experiment with eight EVs in a rural area, a maximum of six simultaneous charging processes (i.e., 75%) took place [156, pp. 59]. The combined charging power was highest between approximately 6 PM and midnight in all projects, with peaks at around 9 PM [152, p. 26], [154, pp. 58], [156, pp. 128].

Even though the simultaneity factor was relatively low, for high penetration of EVs, it is essential to reduce the share of conventional, uncontrolled charging processes to avoid, postpone, or at least reduce a costly expansion of the grid and electrical installation of the customers. Expanding the energy system for a very high share of uncontrolled charging sessions might be conceivable. However, it is highly questionable whether the low added value justifies the significant additional costs of such an electricity system that is considerably oversized for the majority of the time.

Instead, more innovative solutions yield cost-optimal results without affecting EV charging satisfaction noticeably.
In all completed field studies of *Netze BW*, load management (i.e., DR/DSM) proved to be the most effective option of all the measures investigated [152, p. 24], [154, p. 92], [156, p. 132]. The studies focused on private charging points, where, according to the DSO, around 70% of charging sessions take place [154, p. 19]. In this environment, the EVs are typically connected to the charger for much longer than they need to charge. Therefore, the potential for controlled charging was high, but the influence on EV utilization was minimal. About 90% of the participants did not feel restricted by it, and many did not even notice a difference at all [152, p. 24], [154, p. 66], [156, p. 129]. While in the most recent field study, all participants wanted to have an opportunity to charge their car immediately on demand, this option was only used once in the whole experiment [156, p. 101].
In the largest investigation, the peak load on the grid side could be reduced from 98 kW to 40 kW through dynamic charging management, which would also have allowed the vehicles to be supplied via the grid connection of the building that existed before the study [154, pp. 78, 80].

Despite the success, several challenges were mentioned in the field experiments. For example, some EVs only charge with one or two phases, in general, or toward the end of the charging process — this can cause high asymmetries in the grid voltages [152, pp. 30-33], [154, pp. 84-89], [156, pp. 119-123]. Moreover, alternatives to controlled charging that reduce demand peaks without influencing the charging process (such as stationary battery systems) have significantly higher investment and operating costs. In addition, a BESS needs more space and is currently not allowed to be operated by DSOs [156, pp. 80f., 132]. While a BESS could reduce peak loads and improve voltage stability and asymmetry [156, pp. 78-81], optimal dimensioning is difficult if it is the only means to limit peak demand. If the storage is too small, significant demand peaks can occur once the battery is fully discharged, as seen in the "E-Mobility-Carré" project. On the other hand, a larger battery is more expensive and often not used at all [154, p. 71]. Due to the high cost of a BESS, a grid expansion might sometimes even be the cheaper option [156, p. 81].

Smart (unidirectional) charging management [159–161] is becoming increasingly common in Europe. In Norway, by far the leader in electric mobility per inhabitant [162], smart meters were already installed in 97% of households in 2019 [163], and 84% of the grid users have dynamic electricity tariffs [164, p. 22], [165], providing good preconditions for smarter charging. Since July 2022, all new private charging points sold in the UK must have "smart functionality" [166]. In Germany, AC charging points for private households, municipalities, and companies have been heavily subsidized if they feature interfaces for communicating with the energy system, for example, to reduce charging power [167–169]. However, widespread deployment of smart meters is not planned until around 2030 [170], which will likely delay the use of charging management.

3.1.2 Bidirectional charging (Vehicle-to-Grid)

Smart charging can improve grid stability or the utilization of RES by offering flexibility through an adjustment of the electricity demand profile. In limiting the peak load, it enables a higher number of EVs in the grid than uncontrolled charging. However, an even higher potential can be unlocked when the vehicles also provide their battery storage to feed back energy into the grid — comparable with a stationary BESS. This concept is called *bidirectional charging* or Vehicle-to-Grid (V2G) and sometimes also Vehicle-Grid Integration (VGI).
An illustration is given in Figure 3.2: The EV arrives at 5 PM and departs at 7 AM the next day, as in the previous examples in Figure 3.1. Similarly, the EV shall charge sufficient energy from the grid — Grid-to-Vehicle (G2V) or forward power transfer (FPT) — to ensure that the user's mobility needs are not negatively affected. However, to support the grid at certain times of high demand in the evening hours, energy is fed back from the EV into the grid as well — V2G or reverse power transfer (RPT). As in the previous examples, the battery has sufficient energy when the user departs. However, the RPT capability of a limited number of EVs could help to integrate even more EVs into the grid than possible with controlled charging alone.

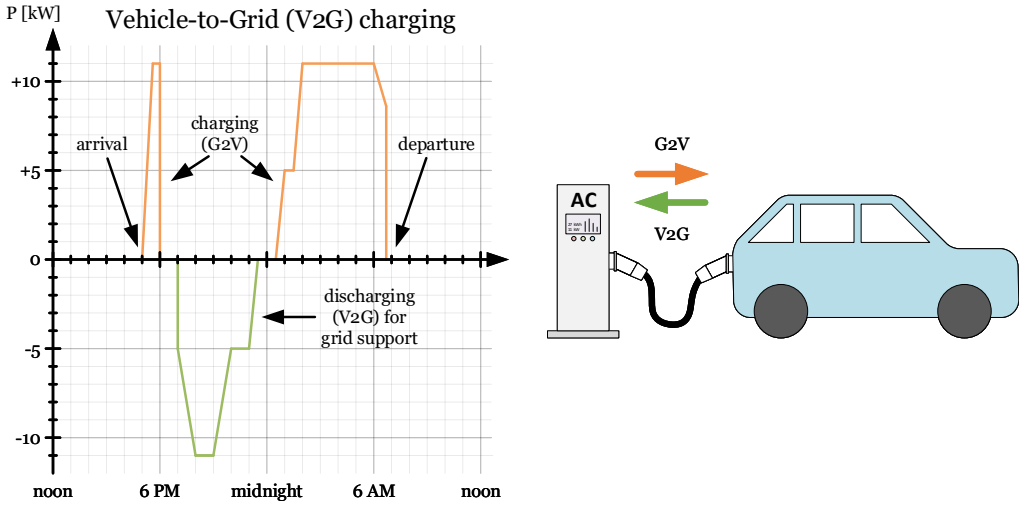

Figure 3.2: Bidirectional charging of an EV

Grid support and the prevention or reduction of grid reinforcement measures for the transition to EVs are only one part of the motivation for V2G. Another important driver is the storage capacity needed for the energy transition. It is also conceivable that V2G will contribute to stabilizing the grid by providing ancillary services, such as frequency and voltage control. Until now, they have been handled primarily by conventional large-scale power plants, which are expected to be phased

out as part of the energy transition. Because of these promising prospects, it is an appealing idea to make the already existing EV batteries accessible for grid-serving purposes when the vehicles are not in use and have access to bidirectional charging points, for example, at home or work.

The fundamental concept of V2G was identified more than 25 years ago, which makes it surprising that it is still not widely used. One factor is the unsteady development of electric mobility in general. The first EVs were already invented in the 19th century. However, ICEVs became dominant at the beginning of the 20th century [171]. Driven by regulations such as the California Air Resources Board's (CARB) "Zero-Emission Vehicle (ZEV) Program" of 1990 [172], automakers developed new battery and hybrid electric vehicles such as the GM EV1, which was introduced in 1996 [171]. One year later, Kempton and Letendre first published the concept of Vehicle-to-Grid [2, 173]. The authors recognized that V2G could be beneficial for integrating renewables by providing storage. Other advantages named were the use of EVs for peak load generation or grid support, e.g., to reduce grid expansion (decentralized energy transition) or through frequency control. However, the development of EVs stalled when the ZEV targets were suspended after lobbying by the automotive and oil industries and a lawsuit [172, 174, 175], and only recently began to gain momentum again[1].
Even though the benefits of V2G were recognized early on, the delays in the EV market development and the generally high cost and low storage capacity of batteries in the past may also have caused V2G to remain largely irrelevant for a long time. Nevertheless, research in the field of V2G has progressed significantly since then. In addition to theoretical investigations, simulations, and prototypes, there have been an increasing number of field studies and model projects, proving that V2G is not just an exciting concept but will very likely be an integral part of future electricity grids.

[1] At the time of the V2G study, it was mandated that by 2003, 10% of passenger cars sold by automakers in California shall be ZEVs [2, 176]. This target was not met until 2021 [177].

3.2 Fields of application

After outlining the general principle of bidirectional charging, this chapter aims to show how, where, and when V2G can be used. Besides potential use cases and their respective technical requirements, suitable vehicle classes, charging locations, and charger types are discussed.

3.2.1 Use cases of V2G

Bidirectional charging is often distinguished by the environment in which it is used or the energy consumer type powered by it:

- **Vehicle-to-Load (V2L):** An electrical load (e.g., a device or machine) is powered by the EV battery using a single- or three-phase socket inside or outside the vehicle.
- **Vehicle-to-Vehicle (V2V):** Energy is exchanged from one EV to another[2], e.g., to share energy with stranded EVs with empty batteries so they can reach the next charging station.
- **Vehicle-to-Home (V2H):** The EV shares energy within the home, i.e., behind the meter (BTM). No energy flows from the EV to the grid. In commercial or industrial environments, or if energy is delivered to multiple homes (e.g., within an apartment building), the terms **Vehicle-to-Building (V2B)** or **Vehicle-to-Community (V2C)** are used instead.
- **Vehicle-to-Grid (V2G):** Energy is also shared with the public electricity grid, i.e., front of the meter (FTM).
- **Vehicle-to-X (V2X):** An umbrella term for the applications mentioned in this list.

From a hardware perspective, there are typically few differences between these types of bidirectional charging. Therefore, V2G is mainly used as a general term in this thesis, independent of the exact application.

In these environments, there are different use cases, i.e., purposes for which smart and bidirectional charging are used. A non-exhaustive overview of these use cases and services — most of which can be found in the literature, e.g., [7, 8, 178–182], [183, pp. 10-19] — is presented in Table 3.1.

[2] using a V2L/V2V adapter since the standard type 2 cable used for AC charging has one female and one male end, so it cannot directly be connected between two vehicles

Table 3.1: Overview of V1G and V2X use cases and services

Description	Environment*	Type	Capabilities
Increase degree of PV self-consumption and self-sufficiency (e.g., home storage system)	P, C, I	V1G or V2H/B	$P^{-}_{(ph)}$, C_E $P^{+/-}_{(ph)}$, C_E
Minimize electricity cost from the grid (with time-of-use or dynamic tariffs)	P, C, I	V1G or V2H/B/G	P^{-}, $C_{E/P}$ $P^{+/-}$, $C_{E/P}$
Electricity trading / arbitrage (e.g., day-ahead, intraday)	esp. P, I	V2G	$P^{+/-}$, C_A
Virtual power plant	P, C, I	V2G	$P^{+/-}$, C_A
Energy sharing	esp. P	V2G	$P^{+/-}$, $C_{E/A}$
Peak shaving / valley filling (load shifting)	P, C, I	V1G	P^{-}, $C_{E/G}$
Peak shaving (through power feed-in)	P, C, I	V2B/G	P^{+}, $C_{E/G}$
Grid congestion management (e.g., redispatch / virtual power line)	P, C, I	V2G	$P^{+/-}$, $C_{A/G}$
Energy transport (e.g., using energy charged at work to power the home)	esp. P	V2H/B	$P^{+/-}$, C_E
RES surplus energy charging	P, C, I	V1G	P^{-}, C_E
RES maximization	P, C, I	V2G	$P^{+/-}$, C_E
CO_2-minimized charging	esp. P	V1G	P^{-}, C_E
CO_2 emission minimization[3]	esp. P	V2G	$P^{+/-}$, C_E
Demand response (e.g., interruptible load)	P, C, I	V1G	P^{-}, $C_{A/G}$
Capacity reserve (to avoid blackouts)	P, C, I	V2G	P^{+}, $C_{A/G}$
Battery lifetime maximization	P, C, I	V1G or V2H/B/G	P^{-}, BM $P^{+/-}$, BM
Virtual inertia (VI)	P, C, I	V2G	$P^{+/-}$, $\dot{f}$, HSC
Primary frequency control	P, C, I	V2G	$P^{+/-}$, HSC
Secondary & tertiary frequency control	P, C, I	V2G	$P^{+/-}$, C_A
Voltage control	P, C, I	V2G	$Q^{+/-}_{ph}$
Low-voltage, high-voltage, and fault ride-through (LVRT, HVRT, FRT)	P, C, I	V2G	$Q^{+/-}_{ph}$, HSC, FRT
Reactive power compensation	I	V2B	$Q^{+/-}_{(ph)}$, $C_{E/G}$
Oscillation damping	esp. I	V2G	$P^{+/-}_{(ph)}$, HSC
Harmonic cancellation	I	V2B/G	$P^{+/-}_{(ph)}$, HSC

(continued on next page)

Table 3.1 (continued)

Description	Environment*	Type	Capabilities
Blackout recovery (black start capability)	P, C, I	V2G	P^+, C_G
Backup power supply	P, C, I	V2L/H/B	P^+_{ph}, $Q^{+/-}_{ph}$, C_E, HSC, FRT
Electricity generator / mobile power supply	P, C, I	V2L	P^+_{ph}, $Q^{+/-}_{ph}$

* P = private (typically at home), C = commercial (e.g., at the charging station of a supermarket, or using a car-sharing or a company's fleet), I = industrial (e.g., at the charging station for factory employees)

Multiple use cases mentioned in Table 3.1 could be used (some even at the same time) to pursue one or a balanced mix of multiple strategies, for example, minimizing electricity or overall costs, maximizing revenue[4], prolonging battery life [180], minimizing user dissatisfaction [185], or reducing emissions[5].
The electrical and information technology capabilities of the bidirectional charging unit mentioned in the use case overview in Table 3.1 are explained in Table 3.2.

Table 3.2: Overview of electrical and information technology capabilities for different V1G and V2X use cases and services

Capability	Description
P^+	V2G — active power feed-in control (phase-independent, i.e., arbitrarily — e.g., symmetrical or only on some phases)
P^+_{ph}	V2G — active feed-in demand control (phase-specific, i.e., typically asymmetric)
P^-	G2V/V1G — active power demand control (phase-independent)
P^-_{ph}	G2V/V1G — active power demand control (phase-specific)
$Q^{+/-}$	reactive power provisioning (phase-independent)
$Q^{+/-}_{ph}$	reactive power provisioning (phase-specific)
$\dot{f}$	high-speed, smooth frequency derivation calculation
C_E	communication to the EMS
C_P	communication to the electricity provider

(continued on next page)

[3] e.g., charging when marginal/average emissions are low and discharging when they are high — other GHG and particle emissions causing climate change and adverse health effects could also be considered [183, pp. 43-47], [184]

[4] In contrast to minimizing costs, maximizing revenue (by providing as many profitable use cases as possible) could have a greater impact on battery life, which would also increase costs more.

[5] If the battery is discharged at a time of high average (or marginal) emissions and recharged at a time of lower ones, even negative emissions can be attributed to the EV [186, p. 174], [181, p. 87].

Table 3.2 (continued)

Capability	Description
C_A	communication to an aggregator
C_G	communication to the grid (local substation or DSO/TSO)
HSC	high-speed, low-latency control (in the order of milliseconds)[6]
FRT	fault ride-through (over-voltage and over-current capability/handling, robustness)
BM	prognostic modeling of battery aging [4, p. 27], [187, pp. 344f.]

In some applications, whether the power must be controlled phase-dependently (i.e., usually asymmetrically) or can be set independently (e.g., symmetrically or on an arbitrary phase) depends on how the power is calculated in the electricity meter. This can be phase-related or balanced, i.e., feed-in on one phase and consumption on another are offset against each other.
Bidirectional chargers will likely experience significantly higher usage compared to unidirectional chargers. Thus, its power electronics need to have higher reliability and longevity. Low power losses in standby, idle, and partial load are crucial in applications where the charger is active for long periods without delivering significant energy. Examples of these applications are frequency control or the use of an EV as a home storage system.

3.2.2 Suitable vehicle types

Private passenger cars are not utilized most of the time: On average, they are only used for 3% of the day in Germany [126, p. 4]. At all times, more than 50% of private passenger cars are parked at home, and more than 70% are either at home or at work, according to studies in Germany [126, pp. 76f.] and the US [189]. On average, they are parked at home for more than 20 hours and at work for a little less than 2 hours per day in Germany [126, p. 76], as shown in Figure 3.3.
The average daily driving distance per private passenger car is 40 km [126, pp. 4, 70]. With a relatively conservative consumption estimation of 20 kWh/100 km (without charging losses), this equivalents to an energy demand from the battery of 8 kWh. As mentioned in Chapter 2.2.3, the mean battery capacity of today's BEVs is about 52 kWh. Thus, only around 15% of the average battery capacity is used on a daily basis (see Figure 3.3a). As these are mean values, some vehicles certainly travel much longer distances and need more energy from the battery. On the other hand, 40% of passenger cars are not used at all on an average day, according to the

[6] Some stationary home storage systems have reaction times of more than two and settling times of more than ten seconds [188, p. 38]. However, reaction times of only a few milliseconds are needed in some use cases.

aforementioned mobility study [126, pp. 4, 70]. According to *Dena* and *Prognos*, in 40% of cases, the daily travel distance of passenger cars is less than 20 km, and only in 12% of cases, it is 100 km or longer [129, p. 8].
In order to recharge the 56 kWh of energy consumed in a week, the BEV needs to be connected to an 11 kW charger for about 6 hours (or about 9 hours to a 7.2 kW charger). So, the vehicle needs to be charged less than 4% (or 6%) of the overall parking time, as shown in Figure 3.3b/c.

Larger EVs — such as electric trucks, tractor units, buses, and coaches — might also be used for V2G. They typically have much larger battery capacities, which is beneficial for their usage as an energy storage for the grid. However, since these vehicles are mainly used commercially, they are usually utilized much more intensively. Not only do they drive and charge significantly more, but they are also used more frequently, which hinders the use of bidirectional charging applications in many cases. On the other hand, they might have more deterministic and predictable driving patterns (e.g., departure time and route length), which could help to get the most out of V2G in some instances.
Motorhomes are an exception: In many cases, they are only used seasonally, i.e., for a few months of the year, and have long parking periods outside the season (as well as at campsites). There were almost 840,000 motorhomes registered in Germany at the beginning of 2023 [190]. Even though there are currently almost no battery electric models, future BEV or PHEV versions could also be equipped with V2G capability. The bidirectional charging system would have the advantage of being able to power sockets in the motorhome even without access to an electricity grid (V2L). Since the battery can be used as large energy storage, together with a solar system on the roof and exterior walls, this would enable longer stays away from electricity grids and still allow occupants to use electricity.

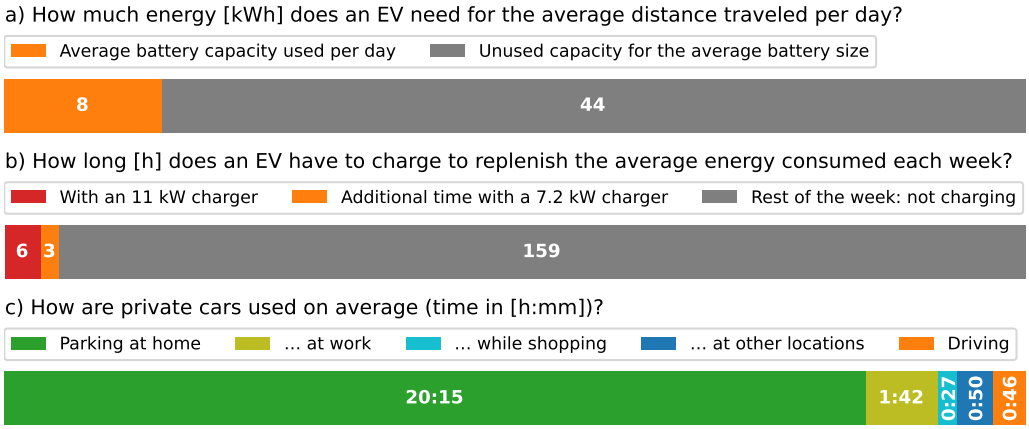

Figure 3.3: Summary of the average private passenger BEV usage in Germany

In some countries, dedicated school buses are used to take students to school and back home again. These buses usually have much lower utilization rates and drive shorter daily distances than those used in public transport. Therefore, they are well suited for V2G applications. The V2G charging company *Nuvve* has already been offering V2G services for school buses in the US since 2020 [191–193].

Smaller EVs — such as electric motorcycles, scooters, and e-bikes — have significantly lower battery capacities and tend to be more price-sensitive. The cost overhead for V2G and the relatively low revenue could prevent V2G from being established in these applications.

Since the application in passenger cars appears to have the highest potential, only these vehicles are discussed below. However, the discussion and results can usually be applied to other vehicle categories as well.

3.2.3 Suitable charging locations and occasions

Charging points at which drivers want to recharge energy as quickly as possible, e.g., DC fast chargers used during long-distance trips, are very unsuitable for most V2G applications with RPT. Instead, smart charging management should ensure that all vehicles charge as fast as the EV, EVSE, and grid connection allow.

AC and DC chargers at shopping centers and supermarkets typically also serve customers with relatively short charging times. They offer the possibility to deliver significant amounts of energy while drivers can fulfill everyday duties, which is particularly beneficial for people without opportunities to charge at home or work. In these cases, it is likely that most customers do not want to discharge the battery but also charge it as quickly as possible. Moreover, the number of such charging points is limited, and — from a broader perspective — instead of being used for discharging, providing as much energy as possible to as many customers as possible would be more helpful. The situation is different if supermarket parking lots are also made available for charging EVs at night, which is particularly useful in densely populated areas (compare [147]). In this case, the EVs of nearby residents that park and charge there for longer periods overnight could also be charged with DR/V1G or offer V2G services.

Other public charging spots with longer parking times, e.g., near leisure activities, might be more suitable for V2G. However, the average time vehicles are located there is relatively small (compare Figure 3.3c). Exceptions are parking facilities at train stations or airports, where passenger cars are typically parked for several hours or even weeks.

At the place of work or education, on the other hand, most cars rest for several hours. Charging at work is particularly helpful for people without access to private charging points. Since BEVs have

not yet prevailed in this target group, this could also help the electrification of passenger cars in general. Using V2G at work can be particularly interesting for EV users with full-time positions and charging options at or near the workplace since their vehicles are usually parked for more than eight hours. This means that, on average, enough energy for an entire week can be provided by just one unidirectional charging session (compare Figure 3.3b). If less energy needs to be recharged per session (e.g., because the EV can be charged several times a week or drives less than the average vehicle), the additional time can be used to coordinate the V1G or V2G charging process with the employer's EMS, so that there are benefits for the company (or CPO) as well. The same applies if the EV can charge faster (e.g. if EV and EVSE support AC or DC charging with more than 11 kW). Large, often flat roof areas and sheltered parking lots also facilitate the installation of relatively cheap large-scale PV systems. They could be combined with smart uni- or bidirectional charging systems to reduce the cost of charging and offer peak shaving or other functionalities for the company.
In Germany, 70.1% of employees had full-time jobs in 2019 [194], and 45% of jobholders worked at large businesses in 2020 [195]. These companies often have dedicated parking lots near or on the site, facilitating the installation of many charging points for employees.
Vehicle fleets of businesses could be V2G-capable as well. In many cases, they remain at the company the majority of the time, offering high temporal flexibility for energy to be charged and discharged — especially at night or during weekends. If the vehicles are booked in advance, the charging management can also consider this to ensure the EVs are charged in time.
Similarly, car-sharing operators offering EVs have fleets of vehicles often booked in advance, sometimes with dedicated charging points distributed in cities. While the energy of individual cars used for V2G might be comparatively low to allow spontaneous bookings, the car-sharing operator could aggregate all its vehicles. As a result, large car-sharing operators could provide high cumulative charging and discharging power and even trade it on electricity markets.

Using V2G when charging at home has the highest potential: This is where private passenger cars spend by far the most time (84% on average), as already addressed in Figure 3.3c. In this environment, V2G could be used primarily at private but also at public or shared/semi-public[7] charging points. In Germany, there were about 41.7 million apartments at the end of 2021. As shown in Figure 3.4a/b, 12.94 million buildings had one apartment, 3.17 million buildings had two (containing a total of 6.33 million apartments), and 3.25 million buildings had three or more apartments [196, p. 10]. Hence, 46% of the apartments are in single- or two-family[8] houses, where private charging opportunities exist in many cases.

[7] e.g., parking lots/garages of apartment buildings

[8] Depending on the definition, a house with two apartments might also be called a "single-family house" — here, it is referred to as a "two-family house".

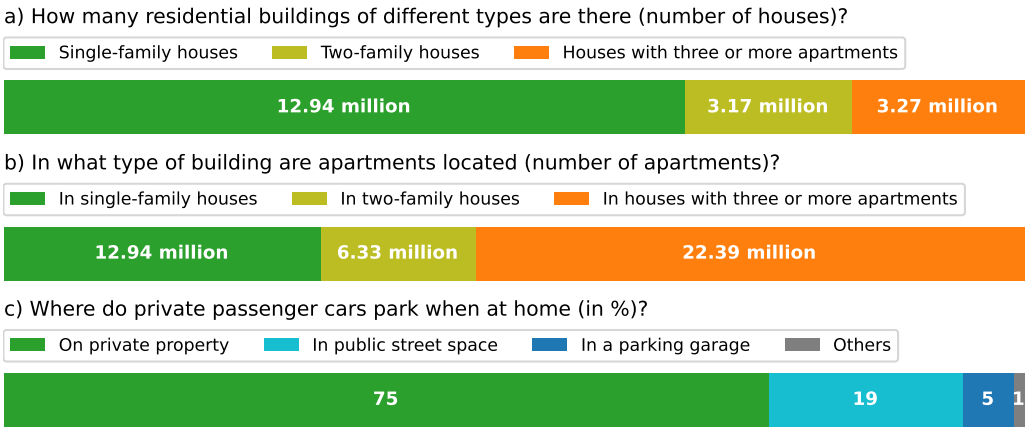

Figure 3.4: Where do people park their passenger cars in Germany when they are at home [126, pp. 76f.], and in what type of residential building do they live [196, p. 10]?

On average, 75% of cars park on private property when at home (see Figure 3.4c), ranging from 40% in large cities to 90% in rural areas [126, pp. 76f.]. While parking on private ground does not automatically guarantee that EV owners will be able to install their own (bidirectional) charging points, in many cases, it is possible — especially at single-family homes or semi-detached buildings. According to a survey from Bozem et al. carried out in 2013, 83% of single-family households in Germany had a private parking space, of which 85% (i.e., about 70% of single-family households in total) had access to electricity [197, pp. 52f.]. In multi-family houses, only 55% had a private parking space, of which 50% had access to electricity at that time (i.e., only a total of about 27% of all households in multi-family houses) [197, pp. 52f.]. In total, around 17 to 19 million households in Germany have a private parking space with access to electricity, which would potentially allow installing an own charging point and thus use V2G at home.

There are additional limitations for buildings with many apartments, mainly found in densely populated cities [129, p. 13] (also see Figure A.1 in the appendix). Even if private car parking spaces exist, it is likely that the grid connection does not allow each resident to have its own dedicated charging point — at least not without heavily limiting the maximum charging power with dynamic load management. Therefore, sharing charging points might be financially more efficient. In this case, it is unlikely that EV owners are interested in using V2G services since it is more convenient to charge as much energy as possible whenever the EV has the opportunity to charge.

3.2.4 Suitable charger types

There are three main charging types for V2G, as shown in Figure 3.5:

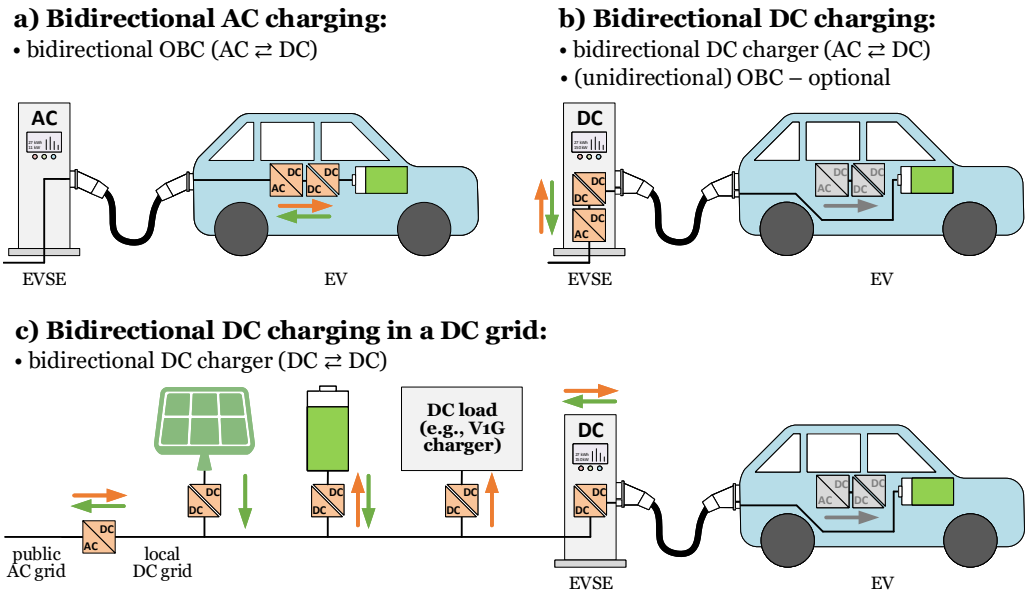

Figure 3.5: V2G charging options: a) AC charging with an OBC, b) DC charging with a dedicated DC charging station, c) charging in a DC grid with a DC/DC converter or an integrated multi-port inverter for PV, BESS, and EV

a) Bidirectional AC charging: BEVs have a built-in OBC, allowing users to charge at the numerous public AC charging points and using an AC home charger. This OBC needs bidirectional power electronics hardware to support V2G. It is usually more expensive than a conventional, unidirectional OBC and thus not standard in vehicles sold in the past. However, the added cost for bidirectional charging is comparatively small.

The communication messages for bidirectional power transfer (BPT) defined in ISO 15118-20 need to be supported in the software of the OBC controller to exchange information with the EVSE. The PLC hardware required for this information exchange is defined in ISO 15118-3 and is already present in BEVs since it is also required for unidirectional DC charging.

For AC charging, the EVSE is, in simplified terms, a power outlet with added protection features and a communication interface. Compared to a unidirectional AC charger, a bidirectional EVSE also needs to support the BPT communication messages. The required power line communication hardware is sometimes already present in unidirectional AC EVSEs. An AC charger is typically inexpensive, and there are almost no additional hardware costs to support bidirectional charging.

b) Bidirectional DC charging: The OBC is unused. The EV essentially only needs to support the communication messages required for V2G, so the added costs to support V2G are very low. However, there are significant additional costs in the EVSE: Instead of the power electronics of the OBC, an additional external DC charger is used, including the bidirectional power electronics.

c) Bidirectional DC charging in a DC grid: It is also conceivable to integrate multiple DC sources and loads — such as a PV system, a BESS, and unidirectional or bidirectional EV chargers — to a combined DC system [198, pp. 4f.], [199, p. 20]. This could be realized by a hybrid inverter with multiple DC ports or a distributed DC grid.
On the EV side, this is equivalent to bidirectional DC charging (Figure 3.5b). For the EVSE, the cost would be reduced since only a bidirectional DC/DC charger is required.
The overall system cost can also be reduced compared to individual PV and BESS inverters and EV charging devices since fewer power electronics components are needed. The bidirectional grid-tie inverter could potentially be sized smaller and is consequently less expensive than the sum of all inverters otherwise required since energy is shared across the DC bus. Moreover, there are fewer conversion processes, e.g., between the PV system and the EV, which increases efficiency.

From the perspective of an EV original equipment manufacturer (OEM), bidirectional DC charging (Figure 3.5b/c) is preferred since the V2G capability of the EV is inexpensive and easy to implement. Compared to unidirectional charging, the added complexity in the EV is low. Technical aspects of the AC grid, such as grid codes, standards, tests, certifications, and their regional differences, do not need to be considered. According to interviews and panel discussions with car and charger manufacturers[9], some BEV OEMs are even considering omitting the OBCs in the future. Advantages for the OEM are reduced weight, space, complexity, development cost, and EV price. An EV driver user could only use AC chargers if an additionally acquired mobile charger is carried along.

The situation is different from the perspective of an EV user. If the user plans to acquire an EV, a PV system, and a BESS, a combined bidirectional DC charging system (Figure 3.5c) might be the most cost-effective solution. However, if a PV system is already present or not an option, there are two possibilities: The OBC of the EV supports bidirectional charging (Figure 3.5a), or a dedicated bidirectional DC charging station is required (Figure 3.5b).
Although a bidirectional OBC is more expensive than a unidirectional OBC, the added cost for V2G support is relatively small. The hardware cost of a bidirectional AC EVSE is low as well. On the other hand, a dedicated DC charger requires an entirely new and costly power electronics device in addition to the OBC typically already installed in an EV. From the user perspective,

[9] at the IQPC Ultra Fast Charging Systems in Berlin in 2019, the Vehicle-2-Grid Conference in Münster in 2022, and the 25th European Conference on Power Electronics and Applications (EPE'23) in 2023; also compare [200, 201]

buying an EV that supports bidirectional AC charging is most likely financially more advantageous than buying an EV with a unidirectional OBC and an additional V2G-capable DC charger.

Another aspect is that bidirectional OBCs produced by large OEMs are very likely to be cheaper than dedicated bidirectional DC chargers of charging equipment manufacturers: OEMs can cost-efficiently manufacture them at remarkably high volumes, there is no need for an additional user interface or a visually appealing housing and the sale of the OBC (and the related revenue) is not core to the business model. In addition, it is conceivable that AC chargers that are already installed and support software updates will become compatible with V2G charging.
Moreover, modifying OBCs for bidirectional AC charging (Figure 3.5a) is less resource-intensive than having two separate chargers: the unidirectional OBC and a bidirectional external DC charger.

3.3 Interdisciplinary perspectives

Vehicle-to-Grid is a broad subject area that links electrical engineering, computer science, economic, legal, political, social, and other disciplines. For a better understanding and the development of effective solutions, it is beneficial to consider the requirements, challenges, and findings of other domains. Therefore, the following section provides an overview of selected research topics from other disciplines on V2G.

3.3.1 Economic analysis

Literature on economic aspects of V2G addresses how high the additional cost for bidirectional charging is compared to unidirectional charging and what the expected revenues or other non-financial advantages of the different applications (i.e., use cases, environments, and services offered) are. Some studies also analyze the impact on the energy system's overall cost or which influence different tariff systems or operational strategies have on V2G usage.

Noel et al. give an overview of the economic aspects of bidirectional charging [183, ch. 4]: Compared to unidirectional charging, there are higher investment costs for the bidirectional charger (i.e., power electronics, control, and communication interfaces) and — depending on the service — dedicated metering hardware. Computational investment and operating costs for an EMS and an aggregator may also occur. The operating cost strongly depends on regional (e.g., country-specific) characteristics, such as energy market design, taxation, electricity tariff systems, prices, and price spreads [183, pp. 7, 94-100]. Whether there are costs associated with faster battery aging and how high they are is a very complex issue (also see Chapter 6.3.2 and

Chapter 7.3). In addition to the types of services provided, battery degradation cost also depends on whether and how the aging is considered in the operational strategy. In general, the authors conclude that V2G is cost-effective, even with conservative cost assumptions.

Over time, there has been a wide range of publications about cost-benefit analyses and the profitability of different V2G services provided by single or fleets of EVs in specific regions, for example, in Germany [178, 202–206], [207, p. 48-61], Sweden [202], European countries [206, 208], or various US states [186, 209].
Heilmann and Friedl [210] review more than 300 studies focusing on the economic benefits of smart and bidirectional charging. The authors analyze and compare assumptions and other input factors of the studies and give an overview of expected revenues for various applications, which vary significantly. The effects of different assumptions for input factors on revenue — such as battery lifetime, RES share, and electricity price — are discussed in detail. "Secondary frequency control and load leveling" [210, p. 11] can generate the highest revenue, according to the review. V2G is expected to generate more income than smart unidirectional charging alone. Increasing power and efficiency is beneficial as well.

While primary frequency control is most profitable according to several studies, its market is relatively small: Of the 3 GW of primary control reserve in Central Europe, 562 MW were provided by Germany in 2021 [57, p. 226]. Using 11 kW V2G chargers, this power could be provided by less than 52 thousand EVs, i.e., the market would quickly be saturated. In the Frequency Containment Reserve (FCR) market, V2G-capable EVs also heavily compete with stationary BESSs [211]. In some countries, the revenue from primary reserve is already low without BESSs and V2G, e.g., in Sweden, where frequency control is typically delivered by hydropower plants [202].
Other authors report that peak shaving, increased self-consumption of solar power, and, in general, providing multiple services in parallel result in maximum profit [178]. The final reports of some field studies (see Chapter 3.4.1) also include statements about the economic viability of different investigated applications.

In addition to regional differences in attainable revenues, the economic analysis is highly dependent on the assumptions made for the expenditures. Due to higher battery and hardware costs in the past, earlier studies often conclude that V2G is not profitable or only under specific circumstances [203, 204]. However, costs related to battery aging and power electronics are very likely to decrease further in the future as both batteries and bidirectional chargers become more mature, durable, and less expensive to purchase. On the other hand, with a higher share of RES and the need for storage systems, the expected revenue is likely to increase — especially since cheap storage systems such as PHES are not abundantly available and peak power plants (e.g., fossil or synthetic gas power plants) remain expensive (as modeled in [206]).

In summary, V2G requires additional investment costs compared to conventional charging, but particularly recent studies reveal that there are viable business models.

3.3.2 Social aspects

In most studies on V2G, user-oriented aspects are often neglected or only covered superficially and simplified, as elaborated by Sovacool et al. [212]. However, a few publications specifically address these topics, such as what different kinds of EV users think about V2G or what concerns and needs affect bidirectional charging. Other studies analyze how many people are willing to use V2G under which circumstances, what influences user acceptance, and how it can be improved. Some authors also address the costs and benefits for society as a whole.

Baumgartner et al. [213] provide a systematic literature review of publications that include user aspects of smart and bidirectional charging. They discuss the literature and divide it into categories (e.g., user behavior, benefits, barriers, ...), disciplines (e.g., Engineering, Economics, Computer Science, ...), research topics, and stakeholders. The authors observe that most studies focus on engineering aspects, and interdisciplinary work between technical and non-technical domains is relatively scarce. Little research focuses on the "human dimension" of smart charging and V2G. Moreover, few qualitative studies exist that, for example, attempt to analyze what motivates users to use or reject V2G. In another study [214], the authors review and discuss different influences and perceptions of smart charging and V2G on users. In a survey, they asses the willingness to pay for bidirectional charging tariffs, the minimum driving range with which users still feel comfortable, and motivation to use V2G. The study also focuses on differences between experienced and inexperienced EV users, which influences suitable V2G tariffs and strategies (e.g., focusing on grid stability or carbon-neutral charging). In the survey, users expected high savings of around 40% for V2G compared to regular charging. The minimal driving range expected despite V2G discharging was around 200 km. By comparison, many studies investigating profitability or optimal strategies for V2G utilization often assume much lower minimal driving ranges, e.g., 50 to 125 km, which might be too low for users to feel comfortable in practice.

Van Heuveln et al. [215] analyze which factors impact user acceptance of V2G. In addition to a literature search, they provide detailed insight into interviews with EV drivers from the Netherlands. The most essential elements for or against V2G adoption were:

- **adequate compensation:** revenue covering more than the cost of battery wear, free parking, or significantly cheaper charging,
- **battery degradation:** a concern in almost every interview, especially when the EV was privately bought and not leased,

- **range anxiety:** not having enough driving range because the battery is not sufficiently charged, especially for unplanned trips,
- **transparency:** regarding the battery SoC and degradation, energy flows, and revenue,
- **a user-friendly interface:** minimizing discomfort and overhead for the user, but with the ability to control charging and discharging at all times.

Noel et al. [6] analyze barriers to V2G in Nordic countries (Denmark, Finland, Iceland, Norway, and Sweden), which they gathered through interviews with experts in different domains (energy, transportation, finance, and information technology) and institutions (e.g., governmental and regulatory institutions, science, industry, civil organizations). They identified different categories and clusters, some of which are closely related to user acceptance (e.g., skepticism and lack of trust that other stakeholders control their EV and battery, high complexity, concerns, and uncertainty regarding battery degradation).

In their book "Vehicle-to-Grid: A Sociotechnical Transition Beyond Electric Mobility", Noel et al. [183, ch. 6] devote an entire chapter to consumer and societal aspects of V2G, including a discussion of literature and surveys on this topic. Among many other findings, they note that (at the time of writing) most consumers lack knowledge about V2G and its benefits — education about V2G and its advantages could significantly increase acceptance. Depending on the conditions of the contract, expected revenue from users may outweigh realizable earnings, and especially contracted conditions — such as a fixed number of hours that the EV needs to be plugged in — deteriorate user acceptance substantially. However, according to a study [216] discussed in the book, if users were not significantly affected by range and contracted conditions, there was a high acceptance even without remuneration. Keeping the inconvenience at a minimum regarding autonomy and the complexity of the user interface[10] is another crucial factor for the successful adoption of V2G. The authors also give examples of how knowledge and acceptance can further be improved [183, pp. 162], e.g., by highlighting the advantages for society and the environment, considering or at least not neglecting the "value of conspicuousness and status" [183, p. 161] and visibility of V2G (even if it increases cost), with information campaigns and pilot projects, or by first focusing on a particular target group, which over time can help to promote V2G to a broader audience. Another promising example is that consumers could be guided to V2G by first experiencing convincing V2L/V2X use cases that fulfill their personal needs or even enable previously unimaginable applications (e.g., connecting power tools or hobby equipment to the

[10] Some studies propose complex user interfaces requiring detailed input on trip planning each time the EV is connected to a charger. While users should be able to change settings, such as desired minimum driving ranges at certain times, the daily effort should be minimized for higher acceptance. For example, V2G could be used with the default settings whenever a user plugs in the EV, while a simple "charge now" button could let it charge as fast as possible instead.

EV in remote locations). This offers the opportunity to experiment with different bidirectional charging applications — effortlessly and without obligations or external intervention.

3.3.3 Scheduling and optimization

Another research domain focuses on the optimal usage of V2G, i.e., how and with which algorithms energy flow can be controlled. This could be for one or multiple EVs or a mix of EVs and other assets, forming a Virtual Power Plant (VPP). Authors address different objectives, e.g., revenue maximization or cost minimization, emission reduction, self-consumption, grid stabilization, peak load reduction, or congestion management. Examples of boundary conditions are the availability and emissions of generators, electricity prices, grid stability, the user's needs, as well as battery SoC, State of Power (SoP), and degradation.
Algorithms for optimizing smart and bidirectional charging processes are summarized in [3, pp. 15-18] and [179, 217–224]. Algorithm types often discussed in the literature include mixed-integer linear, mixed-integer nonlinear, or dynamic programming; genetic and rule-based algorithms; particle swarm and ant colony optimization; Lagrangian relaxation; fuzzy logic or model predictive control; artificial neural networks; supervised and reinforcement learning.

3.4 Path to commercialization

In recent years, V2G has not merely remained the subject of research but is also increasingly being trialed in practice. Moreover, the first commercial bidirectional chargers and EVs with bidirectional charging support have appeared on the market, and it is foreseeable that V2G will soon be widely used. This chapter provides an overview of this development by summarizing the findings of field experiments and trends in the commercialization of V2G chargers. Moreover, the future flexibility potential of smart and bidirectional charging is outlined.

3.4.1 V2G field experiments

Field experiments evaluate if and how well different V2G use cases work in practice. They reveal barriers, limitations, and issues in different domains that need to be addressed and allow the evaluation of the overall system's responsiveness, efficiency, and reliability. Some studies also investigate the acceptance and impressions of participants, e.g., if they felt restricted by V2G.

Fifty V2G pilot projects worldwide and conclusions with "lessons learned" are presented in a report by Everoze from 2018 [4]. The authors visit ten selected projects and give a short

yet exceptionally detailed insight into the services provided and the partners, beneficiaries, and customers involved. They also assign service, technology, and market readiness levels to the projects and their investigated services. They summarize that V2G is valuable, particularly when aggregated and mixed with different assets (e.g., stationary batteries and DR) to improve availability. Services such as frequency response and the time-shifting of energy, especially in areas with time- or load-variable electricity tariffs, provided higher value than services affecting the distribution grid, such as local constraint management or peak reduction, reactive power, or voltage regulation. These DSO services are rarely investigated and have a lower readiness level — their value tends to be uncertain but generally lower, and it is highly specific depending on the exact location in the grid. V2G can provide services significantly longer and potentially with higher revenue than unidirectional smart charging because most services can not only be provided until the EV is fully charged. User acceptance plays a subordinate role in most projects: Minimally accepted SoC and user comfort remain largely unexplored. However, it was identified that consumer behavior is diverse and can be very unforeseeable. A wide variety of customer types can be beneficial for V2G, e.g., privately owned or rented vehicles of diverse consumers as well as business or car-sharing fleets. The remaining challenges mentioned are that V2X hardware is still expensive and rare, commercially relatively immature, and inefficient in partial load operation. Requirements and processes for grid connection are heterogeneous, extremely complicated, and, in some regions, lengthy. Depending on country-specific circumstances, there are high costs for special measurement equipment to provide grid services. Double grid charges for storage systems — and thus V2G — are due in some countries, e.g., Germany, Denmark, and the Netherlands. Furthermore, tariff components that depend on the exact energy usage are difficult to assess because it is not trivial to distinguish if energy is used for storage or driving. Although battery degradation from V2X generally seems lower than from driving, it needs to be considered in the services. Pilot projects in new markets, adequate grid connection standards, V2X charger cost reduction, and data are viable for a successful implementation of V2G.

In a more recent publication, Ravi and Aziz [3] present more than 50 projects and give an overview of various investigated services. The authors compare different hardware and control architectures, name standards related to V2G, categorize the services, name associated objectives and constraints, give an outlook on the market potential, and discuss challenges. Major issues are:

- **cost and revenue:** in particular, the higher cost for bidirectional charging and communication hardware, battery wear, and EVs in general, as well as uncertainty in markets and revenues,
- **social challenges:** e.g., inconvenience, confusion, lack of trust, range anxiety,
- **regulatory issues and standards:** communication protocols, grid connection, double taxation of storage systems (also see [183, pp. 124f.]),

- **technical issues:** battery degradation, energy losses during operation and in idle, limited storage capacity, cybersecurity, and, in general, successful integration of RES, storage systems, and V2G into the grid.

The European Network of Transmission System Operators for Electricity (ENTSO-E) gives an overview of European smart and bidirectional charging projects in which TSOs were involved [148, pp. 41-48]. Another brief overview is given by the recent publication of Jaman et al. [225]. The authors also give detailed technical insight into a V2G testing system using a CCS Combo 2 interface, e.g., the ISO 15118 communication protocol and messages, efficiency, and reaction times of the test setup.

The interactive and frequently updated database on v2g-hub.com gives an overview of more than 140 V2X projects worldwide [226]. The projects can be shown on a map or timeline and can be filtered, e.g., by country, EV and EVSE manufacturer, DSO/TSO and aggregator involved, by service provided, or by charging method (AC or DC) used. The database and some of the project reports can be downloaded as well.

3.4.2 EVs and chargers supporting V2G

An extensive market overview of commercial bidirectional charging stations can be found in Table A.1 (page 269) of the appendix. The broader commercialization of bidirectional charging began in 2012 in Japan, whereby the applications focused mainly on V2L and V2H [227]. The early development of these systems was primarily driven by the Fukushima disaster in 2011 [4, p. 10]. In Japan, the CHAdeMO standard was well established. Consequently, bidirectional DC charging was already standardized by CHAdeMO in 2014 [101, 225].
Many of the models listed in Table A.1 are also promoted with the benefits of V2L/V2H in case of disasters in mind. One of the earliest commercially available V2H chargers was the *LEAF to Home* DC charger by *Nissan*, introduced in Japan in 2012. It allows charging a *Nissan Leaf* EV when the customer's solar panels generate power or electricity prices are low and discharging it when prices are high. It can also power residential homes using the EV battery to provide backup power in case of blackouts [228]. Until January 2017, approximately 4,000 of the V2H systems were sold in Japan, according to *Nissan* [4, 229]. *Nichicon*, the company that built the chargers for the LEAF to Home system, claims that it holds a 90% market share in V2H systems in Japan. They produce 1,000 V2H devices per month as of January 2023 and want to increase production significantly [230]. Even though V2H systems are relatively mature in Japan compared to the rest of the world and have been on the market for about a decade, the technology has not yet gained great traction. Mitsubishi Electric even stopped selling V2H devices in 2021 since they (as BEVs in general) did not sell well in Japan [230].

In Europe, there were virtually no public V2G charging points at the beginning of 2024, and V2H has not yet emerged for private charging either. However, the outstanding benefits of V2X have also been recognized in Europe and the US in recent years. It is becoming increasingly apparent that bidirectional charging is gradually moving from research projects and field studies to the market around the world: New fields of application and business models are explored in practice, and more vehicles and charging stations support V2G, or at least V2H and V2L. The bidirectional capability of EV chargers has been introduced in the CCS standard in 2022 [231, 232]. Consequently, numerous manufacturers have recently announced bidirectional AC and DC CCS chargers, particularly for the European and American markets. Interestingly, in North America and Japan, V2L and V2H are often advertised considering their benefits during blackouts (e.g., by Ford [233]). In Europe, however, the focus is more on advantages such as increased self-consumption of electricity from own PV systems, income from electricity trading, or the contribution to the energy transition. By 2024, approximately 30–40 V2G charger models are expected to be on the market, as shown in Table A.1. EVs that support V2G are listed in [234, 235].

3.4.3 Future smart and bidirectional charging potential

Although EVs still only account for a fraction of the vehicle inventory, their theoretical flexibility potential is already considerable. Public charging points currently have a combined capacity of a couple of gigawatts (see Chapter 2.2.3) and could temporarily reduce their power during critical grid congestion. Nevertheless, residential or work-related charging points offer a greater flexibility potential, as discussed in Chapter 3.2.3. However, the number and combined capacity of these (predominantly AC) charging points are more challenging to assess due to a lack of public data[11], which makes it difficult to estimate their potential flexibility contribution.

Between November 2020 and the end of 2021, about 690,000 home chargers[12] were installed through a subsidy program of the Federal Ministry for Digital and Transport (BMDV) [147, 237]. The combined power of these chargers alone is about 7.6 GW. While they were not required to support bidirectional AC charging, a communication interface supporting curtailing or postponing charging, as well as a software update capability, was mandatory [168]. Therefore, it is conceivable that some chargers funded through the program will support V2G charging in the future[13].

In the long term, it can be expected that the majority of EV owners who can install residential chargers will make use of them due to the cost advantages over public charging points. The

[11] However, local DSOs can estimate the quantity, power, and local distribution of charging points since they need to be informed about the installation of chargers of up to 12 kVA and have to approve chargers with higher power [236].

[12] For comparison, about 684,000 BEV and 567,000 PHEV passenger cars were registered in Germany on January 1, 2022 [72].

[13] A more recent program for PV surplus charging even explicitly subsidized bidirectional chargers [238]

authors of a study by *Prognos* and *dena* estimate that between 12.0 and 13.9 million parking spaces are feasible to be equipped with private charging infrastructure by 2030 — around 88% of which will be at single- or two-family houses [129, p. 18]. Using 11 kW chargers, the overall installed power of these private charging points would be around 140 GW.
Before being widely adopted by people without private charging opportunities, it is likely that in the near future, EVs will continue to be predominantly used if residential chargers exist [126, p. 80], [129, pp. 20, 25, 28]. Since the potential for V2G is particularly high for private charging points, it is crucial that the V2G technology is deployed to the market as quickly as possible to achieve high penetration of bidirectional charging applications.

The studies of *ISE* [48] and *FZJ* [52] analyzing RE system scenarios for Germany estimate that V2G will contribute to the electricity grid as significant energy storage in the future (red markers in Figure 3.6). "Scenario 95" of the *FZJ* study assumes that BEVs will only account for 26% of the passenger car transport performance by 2050[14], and 10% of the overall BEV battery capacity will be used for V2G [52, pp. 31f., 65f.]. According to the *ISE* study, in which the anticipated development of the BEV fleet is relatively progressive, 10% of BEV owners will use V2G in the future [48, p. 29], [239, p. 19]. The studies do not discuss the temporal availability and usable fraction of the battery capacity in detail.

Estimates of the future V2G potential are difficult to determine since they depend on a variety of factors in a highly dynamic field. Even though the battery capacity and lifetime, range, cost, charge rate, and variety of EVs have improved tremendously, it is still uncertain if and how fast BEVs and V2G will gain broad acceptance. Retrospectively, older studies vastly underestimate the momentum of the EV market ramp-up, particularly the number of BEVs sold and their average range and battery capacity[15].

Several EV manufacturers have recently announced bidirectional charging support in Europe and the US, some even as software updates for existing models. As in Japan, the first applications focus on V2H, e.g., to increase PV energy self-consumption or use EV batteries in case of blackouts. After the normative, legal, and fiscal uncertainties for bidirectional AC charging and V2G use cases have been clarified [8], V2G can become more affordable for the mainstream. Further acceleration of market penetration can be accomplished if business models are established that allow EVs to collectively participate in the electricity market, i.e., as a "prosumer" community[16]. The rising share of volatile RES and the phase-out of fossil fuel power plants will increase the

[14] Instead, a high share of FCEV and PHEV is anticipated, which is not indicated by current sales trends. The authors estimate that around 3.5% of the passenger car transport performance will be satisfied by BEVs by 2030. However, as shown in Figure 2.12, this is almost certainly already reached in 2024.

[15] As of 2023, several mass-market BEV models already have ranges of 600 km or more [143], which was deemed almost impossible by several automotive experts 15 years earlier [240].

[16] The company *Sonnen GmbH* has already been doing this with home storage systems for several years [241, 242].

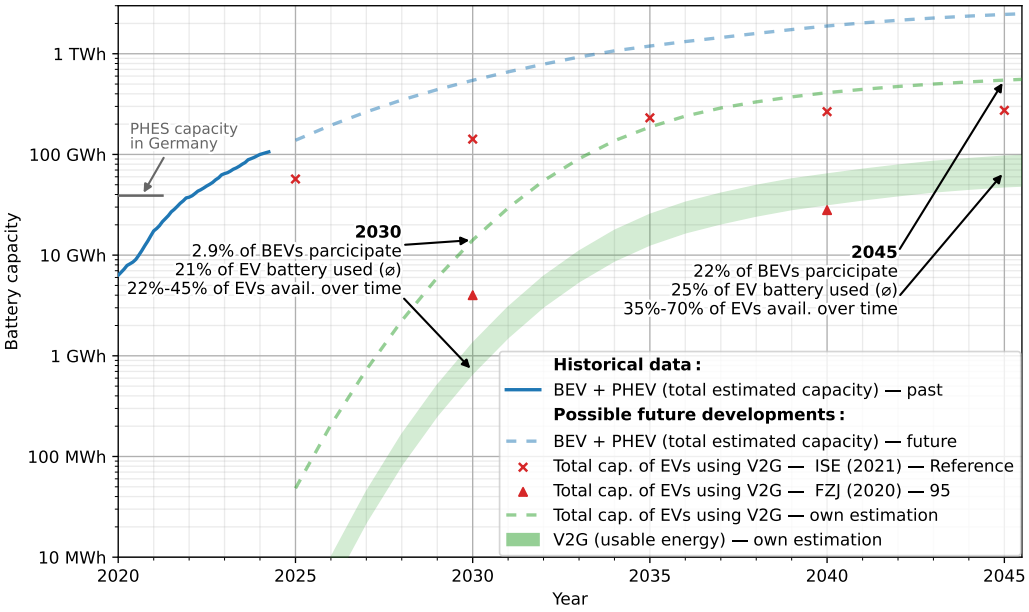

Figure 3.6: Estimated historical cumulative BEV and PHEV battery capacity (blue solid curve, data: Hecht et al. [70, 71], CC BY 4.0) and possible future scenarios for battery and usable V2G capacities based on Figure 2.12 (total: blue dashed line, participating in V2G: green dashed line, usable at any time: green area) as well as projections according to studies of *ISE* [48, 69] and *FZJ* [52] (red points)

demand for storage and, thus, its revenue in the electricity market. However, even in the long term, it is unlikely that the majority of EV owners will be able or willing to use V2G. Many EV users have no opportunity to connect their cars to charging stations frequently, and many might stay opposed to other stakeholders "controlling" their EVs. Furthermore, most likely, only a fraction of the capacity will be used for V2G to minimize inconvenience and degradation.

In the alternative scenario presented in Figure 3.6 (green curves), 22% of BEV users will use V2G by 2045, 25% of the battery can be used for V2G on average, and 35 to 70% of the vehicles participating are connected to charging stations over the course of time. Based on this example, EVs with a combined capacity of more than 14 GWh could use V2G by 2030 — however, only 0.7 to 1.3 GWh would be available (depending on day and time). In 2045, EV passenger cars with almost 550 GWh would participate and contribute with 48 to 96 GWh over time. This is up to 2.5 times the capacity of all PHES in Germany. Other vehicle types, such as electric buses, trucks, or motorhomes, might provide additional capacity. Regardless of the considerable potential, much more short and long-term storage capacity is needed for a successful energy transition with more than 95% RES. Therefore, even though the potential of V2G is immense, it can only be one of many solutions for the energy transition.

3.5 Opportunities and barriers

Vehicle-to-Grid offers a multitude of opportunities. Nevertheless, many barriers and disadvantages still must be overcome before the technology can become established. This chapter will summarize these aspects before moving on to the technical details of power electronics and control.

3.5.1 Advantages and opportunities

As has been shown in many studies mentioned in Chapter 3.3.1, bidirectional charging can decrease the cost of ownership for an EV through added revenue or cheaper charging [3, p. 4], [7], [183, p. 38]. As a result, various business models are emerging, for example, for aggregators (e.g., electricity providers) that bundle the power of many vehicles to trade energy on the electricity market [3, p. 4], [7, p. 3].

If the additional income from V2G reduces the cost of EVs even more compared to ICEVs, another advantage is that this could accelerate the market penetration of EVs themselves [8, p. 21] and, therefore, decrease primary and fossil energy use [183, p. 43]. For most countries, reduced fossil energy use also decreases dependency on costly fossil fuel imports, which is also a geostrategic advantage [175, pp. 1096, 1102].

The flexibility and storage capacity that V2G can offer in addition to V1G allows for the cost-effective integration of more RES into the grid, thus decreasing emissions in both the electricity and mobility sectors. This can not only reduce GHG but also particle emissions, which mitigates climate change and adverse health effects [5, p. 389], [7], [183, pp. 38-47], [148, p. 31].

If EVs charge electricity during periods of low “marginal emissions” in the grid and discharge when emissions are high, even negative emissions can be attributed to the EV [186, p. 174], [181, p. 87], potentially enabling CO_2 certificate trading as an added revenue stream. Similarly, if EVs predominantly charge when inexpensive excess energy of RES is available and discharge energy during periods of high residual load (i.e., with high marginal electricity cost), not only emissions but also the overall electricity cost for all consumers is reduced.

According to Noel et al. [183, pp. 35f.], the power and energy costs of V2G are lower compared to other storage technologies, such as BESS, PHES, CAES, and PtG. Moreover, the reaction time and round trip efficiency of V2G are better than or competitive with other storage systems.
If a high market penetration of V2G can be achieved, the usable power and energy capacity might soon exceed that of PHES and stationary BESS (compare Figures 2.6 and 3.6), offering a compelling way to increase the storage capacity needed for the energy transition significantly.

The distributed storage capacity and flexibility of V2G, along with advanced use cases to offer ancillary services (e.g., voltage and frequency regulation, capacity reserve, redispatch, black start capability), can significantly improve the stability, robustness, and resilience of the grid (both interconnected grids and microgrids). Thus, it can reduce the number and duration of blackouts while also decreasing the system cost [3, p. 4], [7], [183, pp. 38, 42], [148, pp. 27-29].

If the bidirectional charger is capable of being used as a backup power supply in an "islanded" V2B/V2B/V2L operation separated from the grid, the EV can provide electricity during blackouts for several days, depending on battery capacity, SoC, and electricity demand.

In combination with a smart distribution grid, V2G can reduce peak load and improve voltage quality, thus avoiding, postponing, or reducing costly electricity grid and peak generation expansion [7, pp. 3f.], [8, p. 22], [175, p. 1098], [148, pp. 27-32].

V2G uses the already existing battery capacity of EVs. If V2G is used instead of additional stationary storage systems or electricity generators, the usage of critical conflict minerals and other resources can be reduced. Depending on the implementation, this can decrease overall cost [5, pp. 384f.] and the number of skilled workers needed in the energy transition[17].

For EV users that operate local RES, such as PV or micro wind turbine systems, V2G — as a replacement or supplement to stationary storage systems — increases self-consumption and sufficiency and decreases electricity demand from the grid [7], [148, p. 32].

While increased battery degradation is mainly seen as a disadvantage of bidirectional charging, several studies discussed in Chapter 6.3.2 have shown that with suitable operational strategies, battery lifetime can even be increased with V2G.

Customer satisfaction may also increase through bidirectional charging, not only through added revenue from V2G services or cost savings from V2H but also by enabling previously unthought opportunities with V2H or V2L [183, pp. 153-155]. One could use private passenger cars as a backup power source during blackouts or disasters or as a mobile power generator for camping or other leisure activities in remote areas.

V2L can also add benefits to construction site, fire-fighting, ambulance, and other municipal vehicles, e.g., by replacing the need for or reducing the use of gasoline or diesel generators and thus reducing cost, emissions, smell, noise, and maintenance.

[17] Suppose a homeowner wants to install a new solar system, a home charger for PV surplus charging, and battery storage. If the EV supports V2H using AC (dis)charging, there is almost no extra work needed to install a bidirectional charger instead of a (smart) unidirectional charger to use the EV as a storage system. However, additional effort is needed to install a stationary storage system, which typically also has a significantly lower storage capacity than an EV.

3.5.2 Disadvantages and barriers

A major obstacle for V2G is the higher investment cost for the bidirectional power electronics [3, pp. 14, 21], [5, p. 391], [6], [183, pp. 94-97] (compare Chapter 4.1). However, the added cost for bidirectional AC charging is significantly lower than for bidirectional DC charging (see Chapter 3.2.4):
Compared to a unidirectional OBC, a bidirectional OBC for AC charging needs AC/DC and DC/DC converters capable of transferring power into both directions, which causes higher expenses for the required semiconductors and their control (little to medium extra cost). The EVSE for bidirectional AC charging needs PLC hardware for communication to the EV, which many AC charging points support regardless (i.e., no or minor extra cost for a bidirectional AC EVSE). However, many EVs are only "V2G-ready" for bidirectional DC charging, which requires a separate bidirectional DC charger (high extra cost) in addition to the already existing unidirectional onboard AC charger.
In summary, the added cost for power electronics, especially for bidirectional DC charging, is significant. Decreasing this cost and integrating the V2G capability in the OBC is crucial for high market penetration.
In any case, the investment cost for bidirectional charging, as opposed to conventional charging, is further increased by the communication interfaces needed for meaningful applications[18] [3, pp. 14, 21], [5, p. 391], [183, pp. 94]. If this communication already exists for smart/controlled charging, no added hardware cost for bidirectional charging arises.

Depending on the topology of the bidirectional charger, it might have a higher weight and volume than a unidirectional charger. This is primarily a concern in OBCs, where space and weight are limited. However, this is usually less important for BEVs than for PHEVs or ICEVs. Because of recuperation, part of the additional energy needed for acceleration can be recovered while braking. Since electric motors are smaller than comparable ICEs and, unlike a fuel tank, batteries are mostly placed under the vehicle, more space is available for other electronics or luggage.

Achieving high efficiency in the whole V2G system for charging and discharging is a challenge as well [183, pp. 72-74], like in all energy storage systems. Compared to unidirectional charging, the energy is converted twice (for charging and for discharging), so high power electronics or battery losses affect potential revenue. In most V2G use cases, the bidirectional charger only operates in part load. For example, if the EV is used as a PV home storage system, to minimize electricity cost from the grid, or for V2L, the discharge power might often only be in the range of 100 to 500 W — which is only 0.5 to 2.3% of the nominal load of a 22 kW charger. While battery energy efficiency is high for such low operating powers, the power electronics efficiency is usually

[18] e.g., to the grid, an EMS, or an aggregator

extremely low [243, p. 17f.]. For example, if the charging or discharging efficiency is 80%, the round-trip efficiency is 64%, i.e., more than a third of the energy is lost. Therefore, achieving high (dis)charging efficiency at part load or in idle/standby (e.g., for frequency regulation) is crucial for V2X use cases in which the charger is often in light load operation [244].

Compared to unidirectional OBCs, V2G chargers must have a longer service life. While conventional chargers are only active for a few hours a week, many V2G use cases benefit from the charger being active as often as possible. This places a higher strain on the hardware.

V2G increases inconvenience for users [3, p. 21], [5, pp. 392f.], [175], [183, pp. 142-144]. While an average EV only needs to charge a few hours on an AC charger each week (compare Figure 3.3), for many V2G and V2H use cases, it is beneficial if the EV is connected to a charger as often as possible, which means that the user would have to regularly plug in the EV (e.g., once or twice a day) instead of just occasionally (e.g., once or twice a week).
Even though the EV is regularly connected to the charger, as the battery is often discharged instead of charged, many users might be uncomfortable with the uncertainty of the range the EV has at a particular point in time. Uncertainty and range anxiety can lead to stress and frustration, especially among less experienced EV drivers. The smart charging company *Virta* recommends providing the user with forecasted (dis)charging profiles and the option to charge manually, opt out, and set limits for a minimum SoC [245]. If users realize that they are in control and there is transparency for them at all times, this might also reduce distrust against V2G operators and stakeholders that seem to "control" their EV battery — another obstacle for V2G adoption.
There is a conflict of objectives between the minimum range that should be available to the user at all times, the usable capacity for V2G applications, and increased battery aging. Setting the minimum guaranteed range too low might cause problems when the EV user takes trips spontaneously or without announcing it to the V2G charger. Setting it too high reduces V2G capacity and thus revenue, and it can also increase battery degradation at very high SoCs.

Whether and how much battery lifetime is decreased or increased through V2G is a very controversial topic and depends on the exact operational strategy, as discussed in Chapter 6.3.2 and Chapter 7.3.3. Regardless of whether V2G actually degrades the battery faster, uncertainty and concerns about it and the perception by potential users that battery lifetime decreases is a significant hurdle of V2G [3, pp. 14, 20f.], [5, pp. 391, 393f.], [6, 7], [183, pp. 66-71]. As the cost of batteries gradually decreases and their lifetimes increase, the concerns regarding battery degradation and its related cost might play a minor role in the future. In the meantime, for successful adoption of V2G, it is crucial that battery degradation can be modeled, quantified, and transparently communicated to the EV owner and the operational strategy is adjusted to consider and thus minimize aging (also compare [4, p. 27], [187, pp. 344f.]).

V2G adds much complexity in addition to smart or conventional unidirectional EV charging. The complexity affects not only the development and operation of all components involved but also user adoption. Currently, most people are unaware of what bidirectional charging is and lack an understanding of the interrelationships, motivations, advantages, and disadvantages of V2G. Unawareness, confusion, distrust, and misinformation of V2G and EVs in general hinder market adoption [3, pp. 14, 21], [5, pp. 393f.], [6, 175], [183, pp. 141-144].

While the added cost for V2G is lower than the cost of stationary storage systems, building large-scale BESS might be faster and less complicated since many individual EV owners need to be convinced to provide V2G to achieve the same power and energy rating of the large-scale storage system [183, pp. 35-37].

Several studies conducting interviews with potential V2G users show that there are high expectations for revenue but an unawareness or undervaluation of cost savings or other benefits [3, p. 21], [5, pp. 390-392], [183, pp. 142-144]. If there are only marginal savings from V2G, users might prefer to avoid the complexity of V2G. Therefore, bidirectional charging might first gain a foothold with use cases that do not focus on revenue [183, pp. 152-155], e.g., higher self-sufficiency through V2H with own PV plants, emission reduction, or the non-monetary benefits of V2L.

Privacy, data protection, and cybersecurity are further concerns for V2G [3, pp. 20f.], [183, pp. 206f.]. Stakeholders involved in the V2G ecosystem could collect information about mobility, electricity use, and living behavior of EV users. Hackers attacking aggregators that control a large V2G fleet could harm EV users or destabilize the grid. However, excessive security requirements for the infrastructure could significantly delay the introduction of V2G, as is the case with the deployment of SMGWs in Germany, which will continue to be delayed until approximately 2032 [170], [8, pp. 9, 35f.].

Until recently, there was a lack of suitable and interoperable standards for bidirectional DC charging via CCS. Still, there are regional differences and a high fragmentation of standards as well as normative, fiscal, and legislative gaps [7], [8, pp. 7, 29f.], [183, pp. 118-130]. For example, local grid standards and their parameters cannot sufficiently be communicated to the OBC under ISO 15118-20:2022 [232, 234], hindering flexible grid-compliant or even grid-supporting bidirectional AC charging. However, it is expected that the standards will be improved in the near future [246].
Some use cases, such as VI, grid voltage stabilization, peak shaving in the distribution grid, LVRT, and FRT, are currently not incentivized, standardized, or mandated for EV chargers. Therefore, there is no business model or advantage for EV users at the moment. These advanced cases might take longer before being adopted [183, pp. 122-124], [8, p. 9].

Fiscal barriers exist as well [3, p. 22], [183, pp. 124f.], [8, p. 34]: As previously mentioned, some states tax energy stored and fed back to the grid or charge grid fees twice, drastically reducing revenue or even ruining the use case's financial feasibility. In addition, it is hard to determine which energy has been used for driving (i.e., should be taxed) and which is only temporarily stored to be discharged to the grid (excluding losses) at a later point in time (i.e., ideally, it should not be taxed).
Charging energy at the workplace (for free or with reduced industry tariffs) and discharging this energy at home (for private use) is not properly regulated yet and may be treated as tax evasion, even though this use case is exceptionally useful from a technical standpoint.

Even though EVs have existed for a long time, electrification of passenger cars has only gained momentum in the last five to ten years. Therefore, EVs and EVSEs are comparatively immature, and many challenges still exist in their reliability and interoperability. In the past, it seemed that many manufacturers first focused on delivering products that work at all instead of focusing on more advanced features like V2G or at least V2L. Therefore, almost no EVs and EVSEs support bidirectional charging at the moment. However, as the products on the market become more mature and several manufacturers have announced plans to launch V2X products, several bidirectional charging use cases will likely gain significance in the following years [8, pp. 19f.].

For investors, V2G-related companies, and users, the high uncertainty regarding future electricity prices, standards, and regulations is a significant reason why V2G develops slowly [3, pp. 21f.], [7], [183, pp. 118-130], [8, p. 29]. In addition, market access for prosumers is still challenging in many countries [183, p. 99], [8, p. 8], [148, p. 36]. The ongoing standardization, regulatory clarity, and simplification for V2G in tax legislation, as well as initial subsidies for V2G chargers, tax credits, reduced grid fees, or a sensibly designed feed-in tariff for grid support, could foster the market ramp-up (also compare [3, p. 22], [7, p. 12]).

Subsidies in V2G systems and their revenue tend to support wealthier people, who are often not dependent on financial support. EVs still have a significantly higher investment cost than (new or used) ICEVs, and V2H or V2G can primarily be used by people with private parking spaces, i.e., primarily by wealthier people who can afford to live in their own house instead of an (often rented) apartment in a multi-family home without opportunities to charge. At the same time, V2G could reduce the operating cost of EVs significantly, encouraging the use of private cars over public transport, shared cars, and bicycles or causing rebound effects, e.g., more and longer distances driven with EVs. Moreover, money spent by the government on V2G programs cannot be spent on better public transport and cycling infrastructure (also compare [183, pp. 203-211]).

Part II

Vehicle-to-Grid charging system

4 Fundamentals: power electronics and control

In this thesis, the power electronics and control of a highly efficient and flexible V2G charger prototype were developed and analyzed. This section provides the necessary theoretical background. After a brief comparison of suitable inverter and converter topologies, the power electronics topologies used in the prototype are explained in detail. Afterward, control algorithms for grid-connected inverters are discussed, and ancillary services to improve the robustness of the electricity grid are presented.

4.1 Power electronics for bidirectional EV charging

Conventional, unidirectional charging systems convert the AC voltages and currents of the electricity grid into a DC voltage and current to charge the battery. A bidirectional V2G charging system also needs to be capable of transferring power back from the DC battery to the AC grid. The operation, requirements, and possible topologies of EV chargers are described, for example, in [144, 198, 199, 247–253].

High charging and discharging efficiency, especially in part load, are crucial for many V2X applications [183, pp. 72-74], [244].

On the battery side, the maximum and minimum battery voltages, as well as the maximum charge and discharge currents or powers of the battery, must be respected. For an OBC, these parameters are defined by the EV battery, primarily by the cell chemistry and model, as well as the number of cells connected in series and parallel. A stationary DC charger must respect the parameters communicated by the EV. For a high level of interoperability, standardized voltage classes have been established for stationary DC chargers, e.g., 200–500 V (to support systems colloquially called “400 V systems”) and 200–920 V (to also support so-called “800-V systems”) for passenger cars [251, 254] and up to 1250 V for “Megawatt Charging” used for commercial vehicles [255].

On the grid side, the charger must not exceed the maximum permissible current (depending on the grid connection, fuse protection, and cable) — e.g., for AC charging, in the range of 6 to 63 A (typically 10 to 32 A) in Europe and up to 80 A in North America [88, 144]. Energy should

generally be drawn or injected with a high power and displacement factor, i.e., close to 1, with low reactive and harmonic components. This is assured by power factor correction (PFC).
The charger should operate at the mains voltages and frequencies normally present and should not break in the event of temporary over- or under-voltages. The North American CCS type 1 and NACS charging systems allow only single-phase (120 V) or split-phase (240 V) charging. In many other regions, two- or three-phase charging is also possible, which is beneficial for achieving a higher charging power [144], [154, p. 84].

4.1.1 Comparison of AC/DC converter topologies

If charging with more than one phase shall be supported, the OBC can be set up modular or centralized, as shown in Figure 4.1 and described by Jankovic et al. [145]. In modular chargers, there is one charging module per phase. Using a switching matrix or rewiring the modules depending on the EV market region also allows paralleling modules to achieve higher maximum currents in single-phase applications while maintaining low asymmetry in three-phase grids. Centralized chargers have a single power electronics unit that supports three-phase charging. Single-phase charging can also be supported using a switching matrix, e.g., by connecting the line and neutral conductors to the phase inputs of the three-phase inverter (compare [252, pp. 51507f., Figure 4]). While typically needing a higher number of switches, single-phase charger modules have a lower DC link voltage, which allows the use of semiconductors and filters with lower voltage ratings.

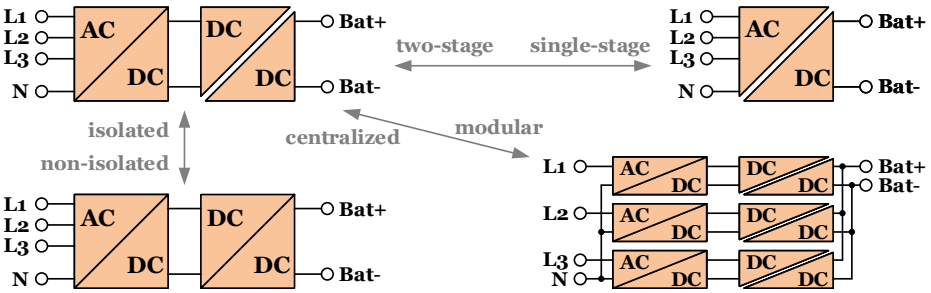

Figure 4.1: Classification of EV charger topologies

For improved safety, high voltage (HV) battery systems in EVs are galvanically isolated from the low voltage (LV) system, e.g., the auxiliary LV battery and the vehicle chassis. This can protect against electric shocks and reduce the risk of fire, even in the case of faults, such as isolation faults due to humidity, contaminants, or broken connectors. While charging, the chassis is connected to the PE conductor. EV charging systems (on- and off-board) often galvanically isolate the DC/battery side from the AC grid as well, among others, to maintain isolation from the chassis,

as described in [86, pp. 56-59], [251, 256] (also see ISO 6469-3, ISO 17409, IEC 61851-1, and IEC 61851-23).
The galvanic isolation is usually implemented with a medium-frequency transformer in the DC/DC converter [256]. Some single-stage AC/DC converters also offer integrated galvanic isolation [257]. Using grid frequency transformers for isolation is unsuitable for OBC since they would have a volume and weight several orders of magnitude higher than the medium-frequency transformer (compare [258, Fig. 1]). However, for DC charging parks with multiple fast charging points, a medium to low voltage transformer — typically needed either way — can provide galvanic isolation for all charging points of the charging park using an isolé terre (IT) distribution system [144]. In contrast, wireless charging naturally provides galvanic isolation.
If no galvanic isolation is present while charging, the user must be protected against touch currents flowing through the human body because of touch voltages present at the EV chassis or other accessible parts of the vehicle, as discussed by Wang et al. [256]. Most importantly, common mode (CM) voltages and currents introduced by the charger into the grid, the battery, and the vehicle chassis need to be minimized, which is particularly challenging in non-isolated chargers. CM currents injected into the grid could accidentally trip the RCD — or, in North America, the ground fault circuit interrupter (GFCI) — which would interrupt charging. In addition, other appliances in the grid could be disturbed. CM currents through the vehicle chassis could also disturb other electronics in the EV.
Non-isolated chargers are generally cheaper and need less space and weight. On the other hand, isolated chargers naturally insert a high common mode impedance between the EV battery system and the grid. Thus, they facilitate the reduction of CM currents and touch voltages and improve electromagnetic interference (EMI), thus offering superior safety. Nevertheless, non-isolated OBCs could increasingly become established on the market.

OBC systems can consist of dedicated power electronics systems or can be integrated into the existing hardware of the EV, which potentially reduces cost, space, and weight [144, 248, 256]. For example, some topologies allow the use of the traction inverter and motor windings for charging and only require a minimum set of added components. Typically, integrated chargers are non-isolated.

The battery can be charged with single-stage or two-stage chargers. In the first step of two-stage chargers, the AC grid voltage is rectified to an interim DC link voltage. In the second step, a DC/DC converter provides the desired voltage and current for the battery. Single-stage converters rectify the AC voltages and provide the desired battery voltage and current in one step. The HV traction battery charger may also contain the power electronics used to charge the LV battery [259].

A variety of single-phase AC/DC converters for modular EV chargers are compared in Table 4.1 and Figure 4.2. Centralized three-phase AC/DC converters are shown in Table 4.2 and Figure 4.3.

Table 4.1: Comparison of single-phase AC/DC converter topologies for modular EV chargers: number of power transistors (T) and diodes (D) and their breakdown voltage level, bidirectional power transfer capability (V2G)

Figure	Name	References	T	D	Voltage	V2G
4.2a	Conventional boost PFC	[250, 260]	1	5	medium	–
4.2b	Interleaved boost PFC	[144, 248]	2	6	medium	–
4.2c	Semi-bridgeless dual-boost PFC	[260–262]	2	4	medium	–
4.2d	Bridgeless boost PFC	[261]	2	2	medium	–
4.2e	Bridgeless boost PFC with a bidirectional/AC switch	[261]	2	4	medium	–
4.2f	Totem-pole bridgeless boost PFC with diode rectification	[145, 260, 261]	2	2	medium	–
4.2g	Totem-pole bridgeless boost PFC with active/synchronous rectification (H4)	[144, 260, 263, 264]	4	0	medium	✓
4.2h	Three-level T-type neutral point clamped inverter (3L-TNPC)	[265]	4	0	high	✓
4.2i	Five-level T-type NPC inverter	[266, 267]	8	0	med.[*1]	✓
4.2j	Three-level I-type NPC inverter (3L-NPC) / diode-clamped inverter	[268]	4	2	medium	✓
4.2k	Five-level I-type NPC inverter	[267]	8	4	low	✓
4.2l	Three-level flying capacitor inverter	[268]	4	0	medium	✓

*1 4 switches with medium voltage rating, 4 switches with low voltage rating

The simplest single-phase PFC topologies (Figure 4.2a–f) contain a minimum of active switches and can only charge but not discharge the EV battery. An example of a bidirectional AC/DC topology is the totem-pole bridgeless boost PFC with active rectification (Figure 4.2g). Only one of the two half bridges needs to be switched with high frequency — the other can be operated with grid frequency. Using different semiconductor switches, such as gallium nitride (GaN) and silicon (Si) metal-oxide-semiconductor field-effect transistors (MOSFETs), can minimize conduction and switching losses at comparatively low cost [260]. Further single-phase topologies are discussed by Faraji et al. [269] and Akhtar et al. [270].

The simplest bidirectional, centralized, three-phase topology is the two-level voltage source inverter (VSI), shown in Figure 4.3m. If the neutral conductor is also connected to a half bridge, the phase currents can be controlled arbitrarily. An example is shown in Figure 4.3n, but this can also be applied to other topologies. Individually controlling phase currents is typically not required for EV charging systems but could be used to reduce voltage and current asymmetries

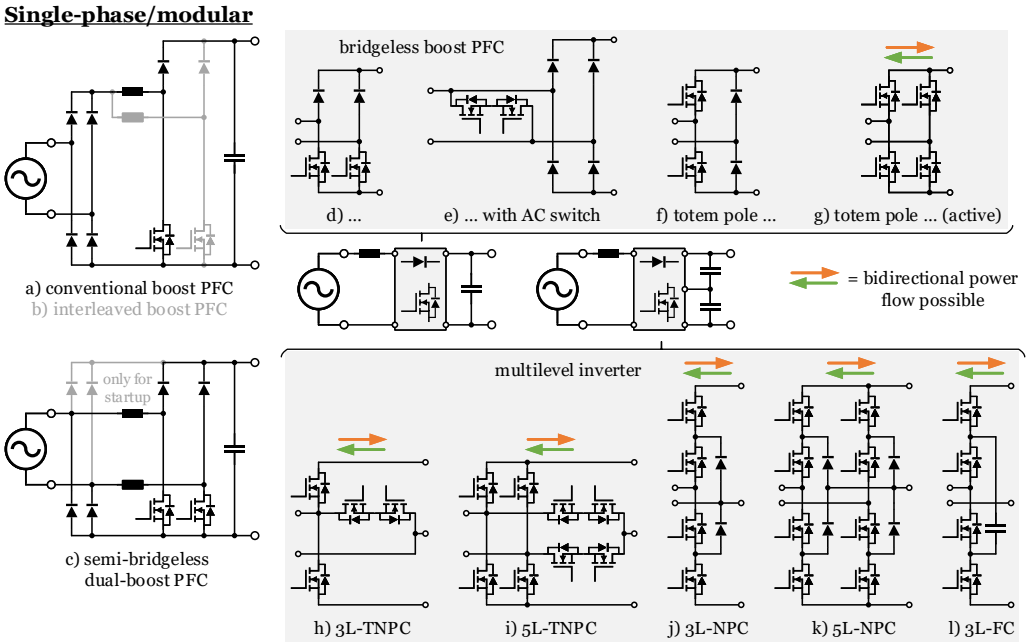

Figure 4.2: Comparison of single-phase AC/DC converter topologies for modular EV chargers

in grids [271], e.g., in battery or PV inverters, particularly in microgrids. As long as the sum of the three phase currents is zero at all times, three-leg topologies can also support grid balancing, although not as well as four-leg topologies.

The hard-switching three-phase two-level voltage source inverter (VSI) can be extended by auxiliary switches that are connected between the center points of the half bridges and a split DC link capacitor to enable soft switching (Figure 4.3o). The resulting auxiliary resonant commutated pole inverter (ARCPI) is explained in Chapter 4.1.4. Soft switching eliminates switching losses, increasing partial load efficiency and allowing higher switching frequencies. As a result, the current ripple in the AC filter and the voltage ripple in the DC filter are lower when using the same components, or smaller filters can be used for the same ripple requirement.

An example of an integrated, unidirectional, non-isolated single-stage AC/DC converter is shown in Figure 4.3q. The topology is used in the 43 kW OBC of the first generation of the *Renault Zoe* [256]. The traction motor windings are used as a filter between the already existing motor inverter and an additional current source rectifier (CSR). Further integrated, mostly non-isolated charger topologies are described by Zhang et al. [272] and Rivera et al. [144].

Examples of unidirectional three-level AC/DC converters are different types of Vienna rectifiers (Figure 4.3s-v). Bidirectional three-level inverters (neutral point clamped (NPC), T-type neutral point clamped (TNPC), active neutral point clamped (ANPC), and flying capacitor inverters)

are shown in 4.3w-z. The corresponding single-phase variants are shown in 4.2h-l. If both the phase and neutral conductor of a single-phase inverter are connected to a three-level leg, a total of five switching states are possible, which is why some authors refer to them as a five-level inverter [266, 267].

Table 4.2: Comparison of three-phase AC/DC converter topologies for centralized EV chargers: number of power transistors (T) and diodes (D), breakdown voltage level, and bidirectional power transfer capability (V2G)

Figure	Name	References	T	D	Voltage	V2G
4.3m	Three-phase two-level voltage source inverter (2L-VSI / B6 bridge)	[144, 247]	6	0	high	✓
4.3n	Three-phase two-level four-leg VSI	[273]	8	0	high	✓
4.3o	Auxiliary resonant commutated pole inverter (ARCPI)	[274], [C1], [C2]	12	0	high[*1]	✓
4.3p	Three-phase buck-type current source rectifier (CSR)	[198]	6	6[*2]	high	–
4.3q	Three-phase two-level CSR with an interleaved boost converter (type 1)	[144, 256, 272]	6/12[*3]	6[*2]	high	–
4.3r	Modular multilevel converter (MMC) with half bridges / full bridges	[275]	$\geq$24	0	low	✓
4.3s	Vienna rectifier (type 1)	[247, 276]	3	18	medium	–
4.3t	Vienna rectifier (type 2)	[276]	6	12	medium	–
4.3u	Vienna rectifier (type 3, Y)	[145, 276]	6	6	high[*4]	–
4.3v	Vienna rectifier (type 3, Δ)	[276]	6	6	high	–
4.3w	Three-level T-type NPC inverter (3L-TNPC)	[199, 252]	12	0	high[*5]	✓
4.3x	Three-level I-type NPC inverter (3L-NPC) / diode-clamped inverter	[199, 248]	12	6	medium	✓
4.3y	Three-level active neutral point clamped inverter (3L-ANPC)	[199, 277]	18	0	medium	✓
4.3z	Three-level flying capacitor inverter	[278]	12	0	medium	✓

*1 6 main switches with high voltage and current rating, 6 auxiliary switches with medium voltage and current rating
*2 if reverse blocking transistors (e.g., RB-IGBTs) are used, no additional diodes are needed
*3 since the existing motor inverter is used, only 6 additional transistors are needed
*4 diodes with high voltage rating, switches with medium voltage rating
*5 6 switches with high voltage rating, 6 switches with medium voltage rating

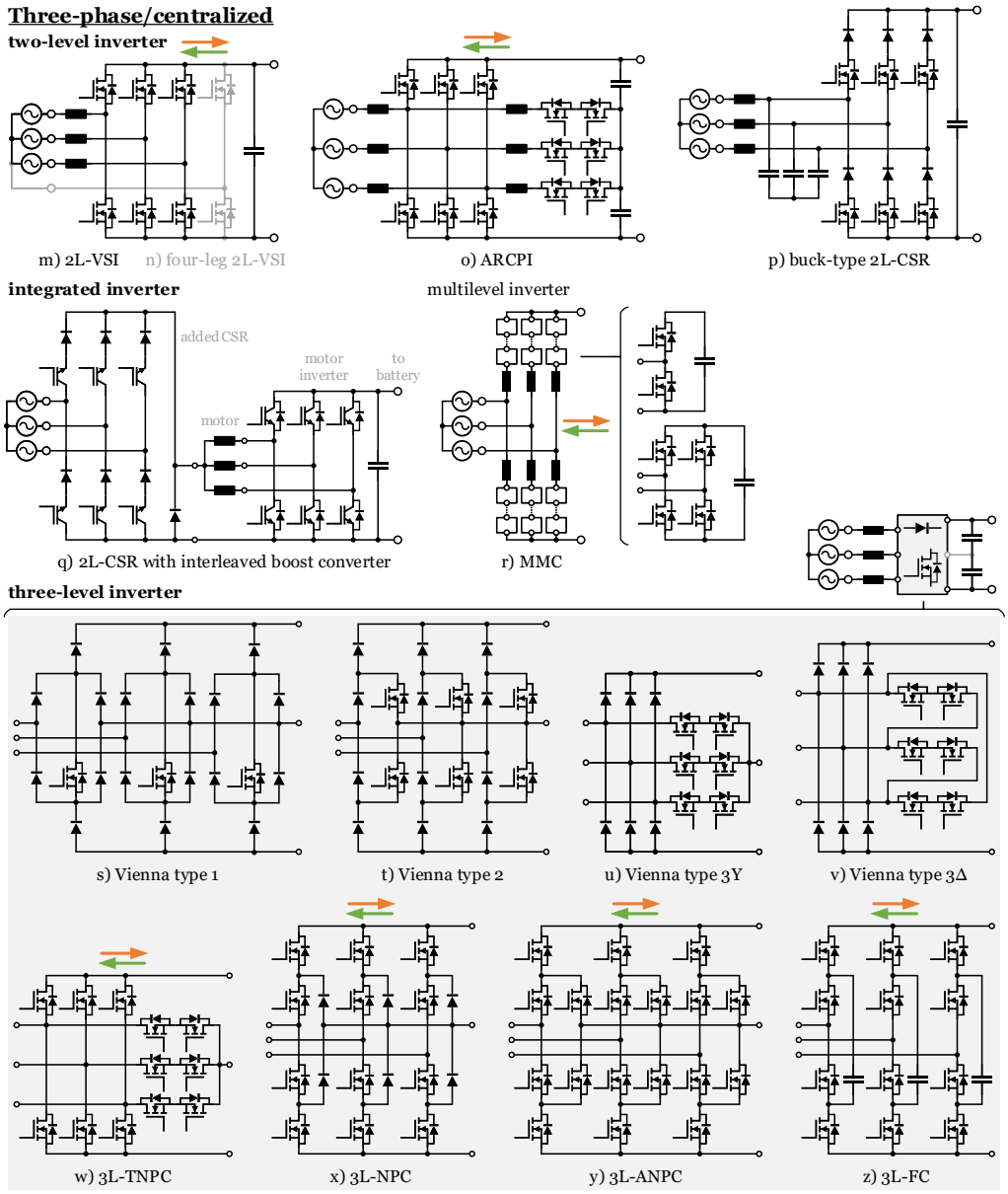

Figure 4.3: Comparison of three-phase AC/DC converter topologies for centralized EV chargers

The modular multilevel converter (MMC) shown in Figure 4.3r consists of multiple similar modules connected in series. The modules can comprise, for instance, half bridges or full bridges.

Figure 4.4a shows an advantage of multilevel inverters: While two-level inverters only allow two discrete switching states per leg ($+\frac{V_{DC}}{2}$ and $-\frac{V_{DC}}{2}$), three-level inverters allow three states ($+\frac{V_{DC}}{2}$, 0, and $-\frac{V_{DC}}{2}$). Lower voltage swings across the semiconductors reduce switching losses compared to a hard-switching two-level topology when using the same switching frequency. In addition, the current ripple in the AC filter inductor is lower, so smaller filters can be used. Semiconductors in multilevel inverters are typically exposed to lower voltages. This allows the use of cheaper components with a smaller breakdown voltage rating or reaching higher input or output operating voltages with components of the same voltage class.
However, a higher number of components increases the complexity of the power electronics, e.g., the power module and the printed circuit board (PCB). For example, semiconductor switches in this voltage class require isolated gate drivers, increasing the cost per transistor. The higher switch count also increases the complexity of the controller, which may require a more powerful and, thus, more expensive processor. Therefore, depending on the implementation, the overall cost of multilevel inverters is often higher compared to a two-level inverter.

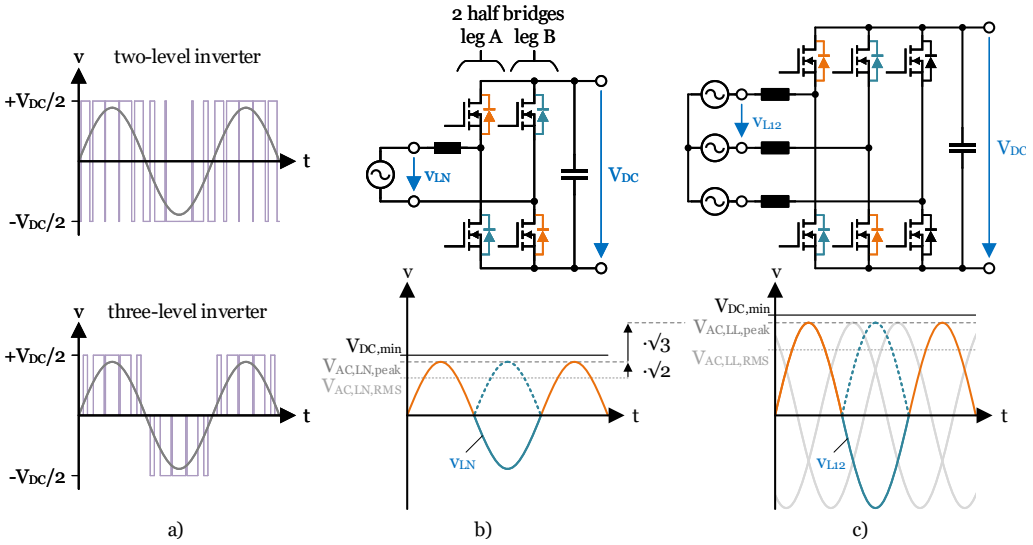

Figure 4.4: a) Comparison of switching patterns for two-level and three-level inverters. Minimum DC link voltage for b) single-phase and c) three-phase topologies

Modular single-phase chargers typically require a higher number of semiconductor components. For example, a three-phase charger with three (bidirectional) totem-pole bridgeless boost PFCs (Figure 4.2g) needs twelve transistors. In contrast, a centralized three-phase, two-level VSI (Figure 4.3m) only needs six switches. On the other hand, the voltage rating of the centralized inverter needs to be higher. For a VSI, the minimum DC link voltage $V_{DC,min}$ and, thus, the

voltage rating of the semiconductors, DC link filters, and other components depend on the AC grid voltage. In the European electricity grid, the root mean square (RMS) grid voltage $V_{AC,RMS}$ is 230 V (line-neutral) for single-phase and 400 V (line-line) for three-phase grids, with a tolerance of up to +10%/−15% [279, 280]. This results in a minimum DC link voltage of at least 360 V for single-phase and 625 V for three-phase inverters (see Equations 4.1a–c and Figure 4.4b/c). However, as indicated by V_{margin}, the DC link voltage should be higher (e.g., +10%) to allow a stable operation despite dead time and imperfect controller behavior.

$$V_{DC,min} = V_{AC,RMS,max} * \sqrt{2} + V_{margin} \tag{4.1a}$$

$$V_{DC,min,1ph} = 230\ V * 110\% * \sqrt{2} + V_{margin} \approx 360\ V + V_{margin} \tag{4.1b}$$

$$V_{DC,min,3ph} = 400\ V * 110\% * \sqrt{2} + V_{margin} \approx 625\ V + V_{margin} \tag{4.1c}$$

4.1.2 Comparison of DC/DC converter topologies

Forouzesh et al. [281] comprehensively review DC/DC converters and discuss isolated/non-isolated, uni-/bidirectional, voltage-/current-fed, hard-/soft-switching, and single-/multi-stage topologies. A review of DC/DC converters focusing on EV charging and V2G is presented in [198, 253, 282–284].

Selected DC/DC converter topologies are shown in Table 4.3 and Figure 4.5. Among the most popular non-isolated DC/DC converters are the buck (Figure 4.5a) and boost (Figure 4.5b) converters. Active switches can be used instead of diodes to reduce conduction losses and allow bidirectional operation. This results in the circuit of Figure 4.5c, a bidirectional buck or boost converter, depending on the direction of power transfer. It is used in the non-isolated, integrated OBC topology shown by Zhang et al. [272] and in stationary DC charging topologies presented by Rivera et al. [144].
Interleaved converters (e.g., Figure 4.5d) can increase power and decrease current and voltage ripple. In addition to these benefits, three-level inverters (e.g., Figure 4.5e) can also reduce switching losses and the required voltage class of the semiconductors.
A cascaded buck-boost converter capable of reducing or increasing the voltage level in both directions of power transfer is shown in Figure 4.5f.
Non-isolated and isolated variants of SEPIC, Zeta, or Ćuk converters, as well as isolated flyback and forward converters [285], [286, pp. 1044-1050], [287, pp. 281-290, 303f.] are primarily used for low-power applications. Some of these topologies might still be relevant for light electric vehicles (LEVs), possibly through interleaving or cascading multiple converters, as discussed by Akhtar et al. [270].

Table 4.3: Comparison of DC/DC converter topologies for EV charging: number of power transistors (T) and diodes (D), bidirectional power transfer capability (V2G), galvanic isolation (isol.), soft-switching capability (soft)

Figure	Name	References	T	D	V2G	isol.	soft
4.5a	Buck converter	[287, pp. 182f.]	1	1	–	–	–
4.5b	Boost converter	[287, pp. 196f.]	1	1	–	–	–
4.5c	Bidirectional buck converter (→) / bidirectional boost converter (←)	[144, 281]	2	0	✓	–	–
4.5d	Bidirectional interleaved buck (→) / boost (←) converter	[144, 284]	≥4	0	✓	–	–
4.5e	Three-level buck (→) / boost (←) conv.	[144]	4	0	✓	–	–
4.5f	Cascaded bidirectional buck-boost conv.	[288]	4	0	✓	–	–
4.5g	Push-pull converter (full wave rectifier)	[287, p. 297]	2	2	–	✓	–
4.5h	Push-pull converter (full bridge rectifier)	[289]	2	4	–	✓	–
4.5i	Half bridge converter (full wave rectifier)	[287, pp. 291f.]	2	2	–	✓	–
4.5j	Phase-shifted full bridge (PSFB)	[144]	4	2/4	–	✓	–
4.5k	LLC converter	[144, 290, 291]	2/4	2/4	–	✓	✓
4.5l	LC-series/LC-parallel converter for wireless charging	[90, 292]	2/4	2/4	–	✓	✓
4.5m	Dual active bridge (DAB)	[258, 282]	8	0	✓	✓	(✓)
4.5n	Bidirectional LLC converter	[252, 293, 294]	4/6/8	0	✓	✓	(✓)
4.5o	CLLC converter	[258, 295, 296]	4/6/8	0	✓	✓	✓
4.5p	CLLLC converter	[252, 258, 297]	4/6/8	0	✓	✓	✓
4.5q	DAB converter with LCL resonant tank	[282]	8	0	✓	✓	✓
4.5r	Three-phase DAB	[258]	12	0	✓	✓	(✓)

Most isolated DC/DC topologies exhibit a similar structure, as shown in the second row of Figure 4.5. Input and output filters comprising a capacitor (for voltage-fed converters), an inductor (for current-fed converters), or both can be used, further described by Forouzesh et al. [281, p. 9147]. The "inverter" topology on the input side, typically containing one to six semiconductor switches, chops the DC voltage into an alternating voltage. The power is transferred galvanically isolated by a transformer. Depending on the topology, a resonant circuit is inserted between the inverter and rectifier stage, sometimes consisting of the transformer itself. Afterward, the voltages and currents are rectified and filtered. For bidirectional chargers, another inverter stage is used at the output instead of the passive rectifier.

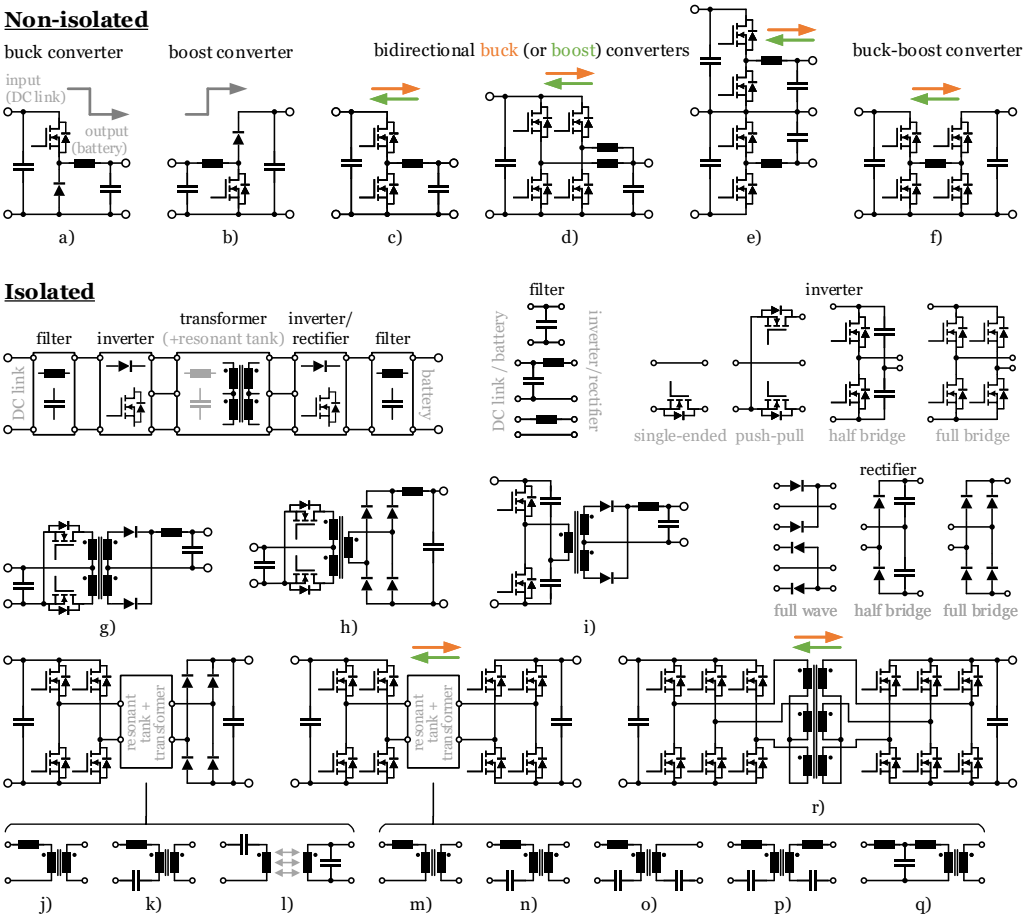

Figure 4.5: Comparison of DC/DC converter topologies for EV chargers — inverter and rectifier naming convention according to [287, p. 275f.], filters for voltage- and current-fed converters described in [281, p. 9147]

A simple isolated DC/DC topology suitable for unidirectional EV charging is the phase-shifted full bridge (PSFB), shown in Figure 4.5j. The inductance at the primary side of the transformer stage can be a discrete component or the leakage inductance of the transformer. If the secondary-side rectifier is replaced with active switches to allow a bidirectional operation, the dual active bridge (DAB) is obtained (Figure 4.5m). It allows soft switching in certain operation ranges, which permits using a higher switching frequency and, thus, smaller filter components and a smaller transformer [258].

The LLC converter (Figure 4.5k) is a resonant DC/DC converter that features zero-voltage switching (ZVS) on the input inverter stage and zero-current switching (ZCS) on the output rectifier stage [291, p. 19]. Thus, it eliminates switching losses almost entirely. The LLC converter is

named after the components of the resonant circuit: An inductance (L), the transformer with its primary inductance (L), and a capacitance (C) connected in series in the primary-side circuit. The leakage inductance of the transformer can be increased by design to replace a discrete inductor component. In this case, only the transformer and the capacitors form the resonant tank. As in most of the presented isolated topologies, different configurations for the inverter and rectifier stages are possible, as discussed in [290]. If a half bridge is used at the input and a full-wave rectifier is used at the output, only two transistors and two diodes are needed.
While the conventional LLC converter is unidirectional, it can also be operated bidirectionally with active secondary-side switches (Figure 4.5n). However, the achievable output voltage and power ranges are limited in reverse operation, and higher switching losses than in forward mode occur [293]. A series capacitance can be added to the secondary side to improve RPT, which yields the CLLC converter in Figure 4.5o. If the secondary-side inductance is significant (e.g., because of a transformer with large secondary-side leakage or a discrete inductance), the topology is also called a CLLLC converter (Figure 4.5p) [297, 298], [C3]. However, some authors also call it a CLLC [252, 299], symmetric CLLC [258], or a bidirectional LLC topology [300].
Apart from the LLC-based topologies, other resonant tank configurations are available, such as the LCL-T series-parallel resonant converter in Figure 4.5q. More resonant tanks are discussed in [301, 302], [C3]. The resonant converters presented so far are called “conventional resonant” or “full-resonant” converters. In contrast, “quasi-resonant” and “multi-resonant” topologies use zero-current and zero-voltage switches to obtain soft switching in topologies that conventionally have a hard-switching behavior (e.g., buck, boost, Ćuk, Zeta, and SEPIC converters) [287, pp. 347-350], [286, pp. 1041-1134], [303]. Another class of “quasi-square-wave converters” (QSC) is presented by Vorperian [304].

Wireless chargers for resonant inductive power transfer (RIPT) use a structure similar to conventional resonant DC/DC converters. However, the DC/DC converter and the transformer are split into a transmitting side (in the EVSE) and a receiving side (in the EV). A topology using an LC-series resonant filter at the transmitter side and an LC-parallel filter at the receiver side is shown in Figure 4.5l. Other unidirectional topologies for WPT are presented in [90, 292], and bidirectional topologies are investigated in [305, 306]. WPT with capacitive coupling using a resonant “class E^2 converter” is demonstrated in [307].

4.1.3 Comparison of hard- and soft-switching topologies

Figure 4.6 compares the switching transition of hard and soft switching MOSFETs. The red curves show the behavior of a FET in a hard-switching half bridge. The green curves show the transition of a FET in a soft-switching half bridge in an ARCPI. The advantages of the soft-switching topology are significantly reduced overshoots and lower $\frac{\mathrm{dv}}{\mathrm{dt}}$ transients. However, the

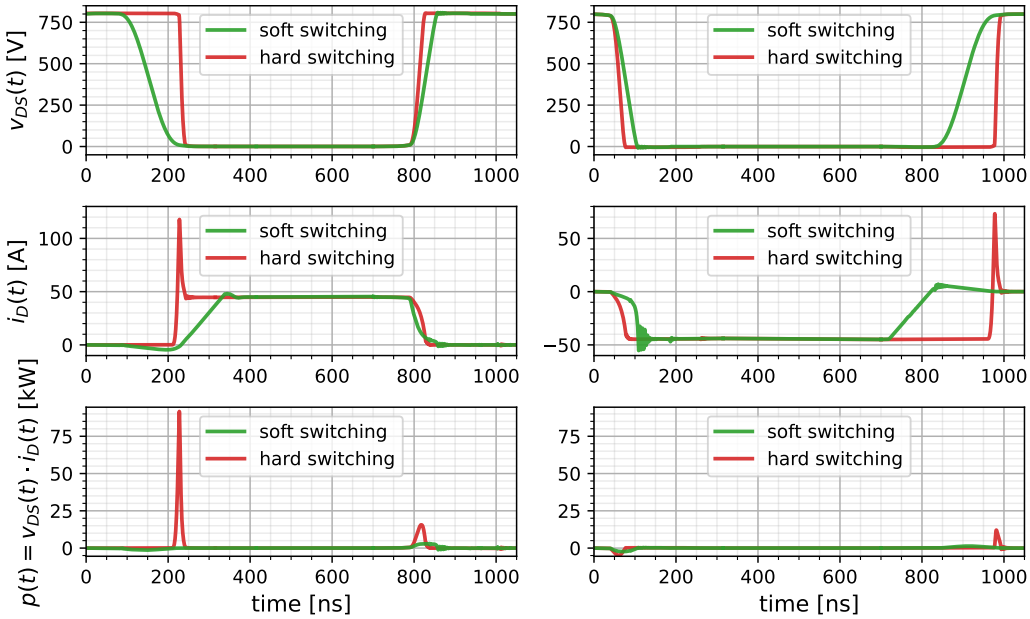

Figure 4.6: Simulated switching behavior of MOSFETs in a hard-switching (red) and soft-switching (green) half bridge during turn-on and turn-off with positive drain current (left) and negative drain current (right)

switching transition takes longer, so the timing to obtain the desired duty cycle needs to be adjusted accordingly. The product of the drain-source voltage and the drain current in the MOSFETs is significantly lower in the soft-switching topology than in the hard-switching topology. Therefore, the dissipation power during the switching transition and, thus, the switching losses are lower. This can also be observed in the resulting switching loci in Figure 4.7. In the simulated example, the soft-switching topology reduces switching losses in the half bridge by more than 95%.

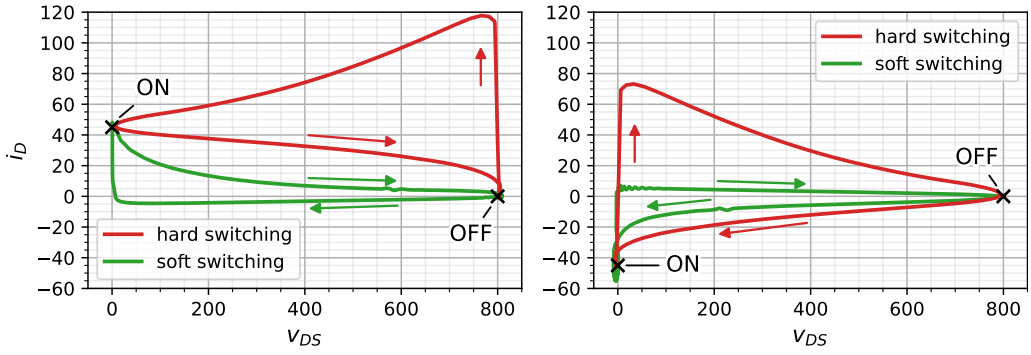

Figure 4.7: Switching loci of simulated MOSFETs in a hard-switching (red) and soft-switching (green) half bridge during turn-on and turn-off with positive drain current (left) and negative drain current (right)

4.1.4 Auxiliary Resonant Commutated Pole Inverter (ARCPI)

The ARCPI — used in the V2G test bench presented in Chapter 5 — is a two-level VSI. In the three-phase configuration shown in Figure 4.8, it is comparable to a hard-switching B6 bridge and generally controlled with similar PWM patterns, e.g., space vector modulation (SVM). However, an auxiliary circuit is used during the switching transition periods to obtain ZVS.

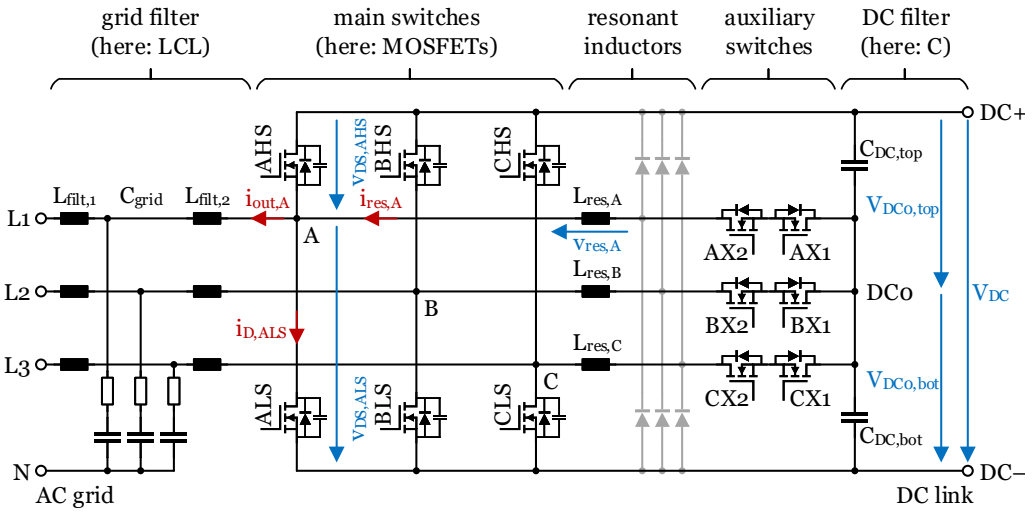

Figure 4.8: Simplified equivalent circuit of the ARCPI

The switching behavior of the ARCPI is described comprehensively in [274, 308–311] and [C1]. There are three different commutation cases, which are shown in Figure 4.9. The transitions are explained for half bridge A. In all three cases of the example, the low-side MOSFET ALS is turned on at the beginning, so its drain-source voltage $v_{DS,ALS}$ is low. During the switching transition that is shown, ALS shall be turned off, and the high-side MOSFET AHS shall be turned on. The three cases are distinguished by the polarity and magnitude of the half-bridge output current i_{out}, indicated by a red arrow in Figure 4.8. Since the output current $i_{out,A}$ flows through the inductor of the grid filter $L_{filt,2}$, which is significantly larger than the resonant inductor $L_{res,A}$, it stays approximately constant during the switching transition. The DC link voltages $V_{DC0,top} \approx V_{DC0,bot} \approx \frac{V_{DC}}{2}$ are assumed to be constant during the switching transition as well.

In **case 1**, the output current $i_{out,A}$ is positive. Consequently, the drain current of the low-side FET ALS $i_{D,ALS}$ is negative initially. The switching transition is initiated by turning on auxiliary FET AX1 at t_1, as indicated by the number "1" at the bottom of Figure 4.9. Since $v_{DS,ALS} \approx 0$ and $V_{DC0,bot} \approx \frac{V_{DC}}{2}$, there is a positive voltage $v_{res,A}$ from node DC0 to node A. Therefore, as soon as AX1 is turned on, a current $i_{res,A} > 0$ begins to build up through the body diode of AX2 and the

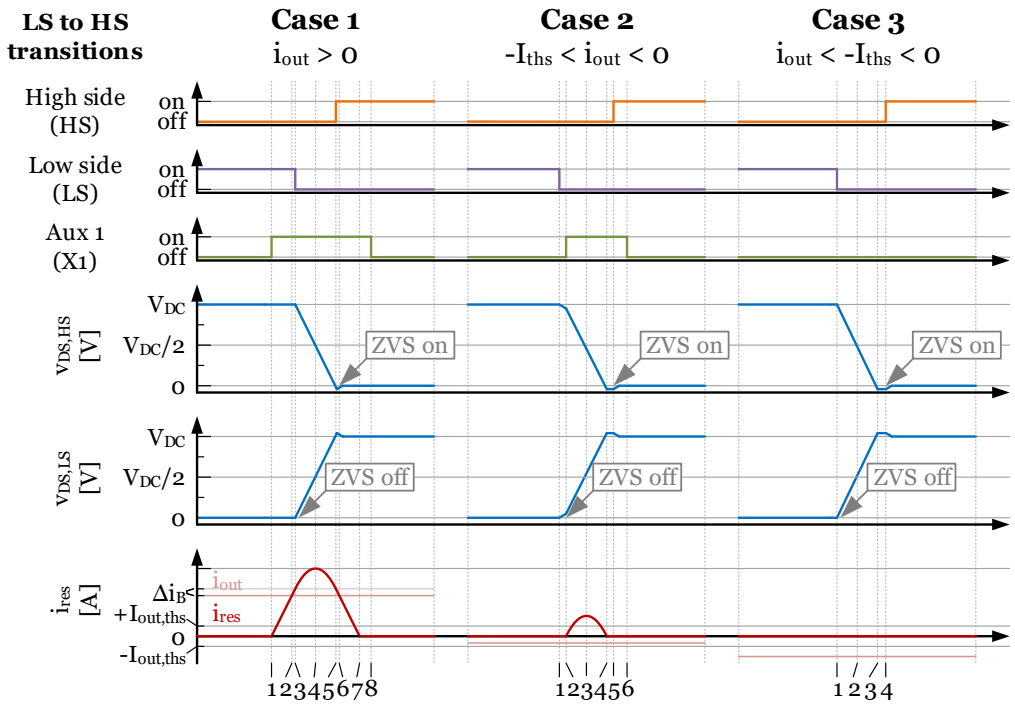

Figure 4.9: Switching transitions in the ARCPI: Gate signals for the high-side, low-side, and auxiliary switches, drain-source voltage of the high-side and low-side MOSFETs, half-bridge output and resonant current — adapted from [C1]

resonant inductor $L_{res,A}$. The low-side FET ALS, which previously carried $i_{out,A}$, is kept turned on, so its drain-source voltage stays zero, and the current $i_{res,A}$ increases linearly. It exceeds the magnitude of $i_{out,A}$ at t_2, at which point the drain current $i_{D,ALS} = i_{res,A} - i_{out,A}$ through ALS becomes positive. ALS is turned off shortly after, at t_3, after an additional "boost current" Δi_B is built up. A soft-switching turn-off transition is obtained since both its drain-source voltage and drain current are relatively low. From now on, the current $i_{res,A} - i_{out,A} > 0$ charges the parasitic capacitance of ALS and discharges the capacitance of AHS. As a result, $v_{DS,ALS}$ increases, and $v_{DS,AHS}$ decreases. Since the voltage $v_{res,A}$ between DC0 and node A also decreases, the increase of $i_{res,A}$ slows down. After t_4, the potential at node A is larger than at DC0, so the current through the inductor $L_{res,A}$ starts to decrease. The voltage $v_{DS,ALS}$ continues to increase until it exceeds V_{DC}, and $v_{DS,AHS}$ becomes negative at t_5. As a result, the body diode of AHS conducts the remaining current $I_{res,A} - i_{out,A} > 0$. The high-side FET AHS is turned on between t_5 and t_6. Since its drain-source voltage $v_{DS,AHS}$ was approximately zero, it turned on with ZVS. After the current $i_{res,A}$ declined to zero at t_7, AX1 is turned off at t_8. Additional low-power diodes, marked in gray in Figure 4.8, can be inserted between the resonant tank inductors, the auxiliary switches

and DC+/– to let a remaining $i_{res,A} \neq 0$ decay without oscillations.
In **case 2**, the output current $i_{out,A}$ is negative but relatively small. At t_1, ALS is turned off to initiate the switching transition. Since $i_{out,A}$ is negative, the positive current $i_{D,ALS}$ charges the parasitic capacitance of ALS while the capacitance of AHS is discharged. However, the switching transition is very slow due to the small current magnitude. Therefore, if ALS is turned off quickly, very low switching losses occur (nearly ZVS). To speed up the transition, AX1 is turned on at t_2. Similar to case 1, a positive current $i_{res,A}$ builds up until t_3, supporting the transition. At t_4, $v_{DS,AHS}$ becomes negative, and thus, the body diode of AHS starts to conduct a current. It is turned on at t_5 with ZVS. AX1 is turned off afterward, at t_6.
In **case 3**, the output current $i_{out,A}$ is negative and larger than the threshold current $I_{out,ths}$. At t_1, ALS is turned off. As in case 2, the positive current $i_{D,ALS}$ charges the parasitic capacitance of ALS and discharges the capacitance of AHS. However, the transition is significantly faster. Therefore, a soft turn-off of ALS can only be achieved if it turns off very quickly. The switching transition takes place without the auxiliary circuit. Starting at t_3, the body diode of AHS conducts the output current. At t_4, AHS is turned on with ZVS, as in the previous cases.

The transitions from the high-side to the low-side MOSFET are similar to the cases presented in the example. However, the other auxiliary FET X2 is used instead of X1, and the polarity of i_{out} needs to be reversed, e.g., case 3 applies if $0 < I_{ths} < i_{out}$.

Since the resonant inductors and auxiliary switches only conduct current during switching transitions, they can be designed for a much smaller RMS current than the main switches and the grid filter. However, the auxiliary switches experience higher peak currents than the main switches. The resonant inductors barely increase cost since — besides their small RMS rating — they have a much smaller component value than the filter inductors.
Compared to a 2L-VSI, the ARCPI is slightly more expensive in the first place since it needs additional switches, gate drivers, and resonant inductors, and it has a higher control complexity. However, it is significantly more efficient across all operating areas because of reduced switching losses. This allows for increased switching frequencies and, thus, reduced grid filter size. Lower losses can also decrease the cost of cooling components. Therefore, depending on the design, the ARCPI can be even cheaper and more compact than a conventional 2L-VSI.
Compared to most bidirectional three-level VSI, the ARCPI has a lower switch count. Like the almost similar-looking 3L-TNPC, it needs twelve active switches. However, the six auxiliary switches of the ARCPI can be smaller than the six switches of the 3L-TNPC connected to the split DC link capacitor due to a lower RMS current. Using the same switching frequency, the grid filter of a 3L-TNPC faces lower current ripples than a similarly sized filter of an ARCPI since the former experiences smaller voltage steps than the latter. However, the ARCPI has even lower switching losses than the 3L-TNPC and can thus operate at a higher switching frequency to achieve the same current ripple rating at higher efficiency.

4.1.5 CLLLC converter

The CLLLC converter used in the V2G test bench described in Chapter 5 is a bidirectional, isolated, resonant DC/DC converter. It is explained in detail in [C3]. An equivalent circuit diagram (ECD) of a CLLLC converter with full bridges on both sides is shown in Figure 4.10. The resonant tank consists of a transformer (T) with its primary inductance (L_p) and a turns ratio of 1:n, and an inductance (L_{res1}, L_{res2}) and a capacitance (C_{res1}, C_{res2}) on both the primary and secondary side of the transformer. If the transformer (highlighted in yellow) is designed with purposely large and suitable stray inductances, L_{res1} and L_{res2} are formed as parasitic inductances of the transformer, and no additional inductors are needed. MOSFETs are used as transistors (Q1–Q8). They include intrinsic body diodes and parasitic capacitances C_{DS} between their drain and source terminals. The voltage-fed converter comprises capacitors on the DC input and output (C_{DC1}, C_{DC2}) to stabilize the voltage. When used in a bidirectional EV charger, one side of the converter (DC1) is the common DC link connected to the bidirectional AC/DC converter (compare Figure 4.1). The other side (DC2) is connected to the battery, typically via relays.

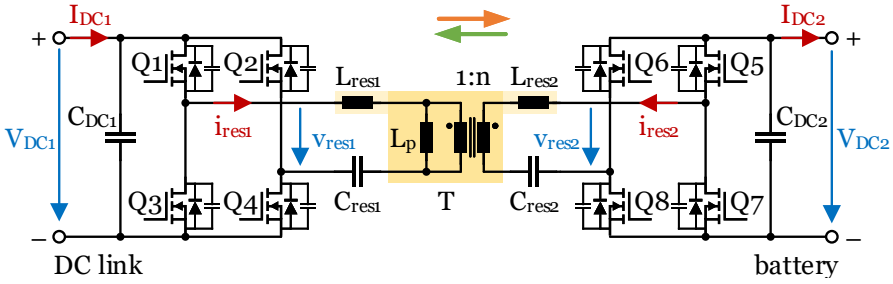

Figure 4.10: Simplified equivalent circuit of the CLLLC converter

Figure 4.11 shows the operating principle and switching behavior of the converter. If power is transferred from DC1 to DC2 (charging/G2V), the primary side half bridges are operated complementary: Q1/Q4 and Q2/Q3 are turned on and off with the switching frequency f_{sw} and a duty cycle of 50%. The generated trapezoidal voltage wave excites the resonant circuit, and an approximately sinusoidal current flows through the resonant tank. On the output side, the current is rectified either passively, with the body or additional discrete power diodes, or actively, by turning on the MOSFETs whenever the diode would conduct the current (synchronous rectification, SR).

At the beginning of Figure 4.11 ($t = 0\ \mu s$), MOSFETs Q1 and Q4 are turned off, and Q2 and Q3 are turned on. As a result, v_{res1} equals $-V_{DC1}$. Q2 and Q3 are turned off at t_1 (first red dotted line), just before the resonant tank current i_{res1} becomes positive. The negative current i_{res1} charges the parasitic capacitances of Q2 and Q3 and discharges the ones of Q1 and Q4. As a

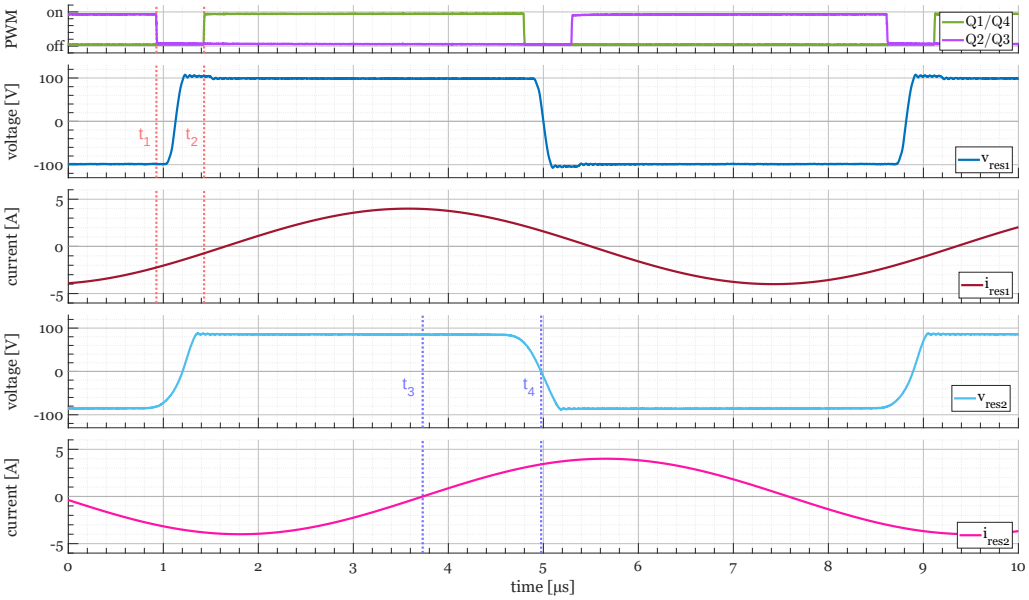

Figure 4.11: Switching behavior of the CLLLC converter in G2V mode: Gate signals for Q1/Q4 and Q2/Q3, primary side voltage v_{res1}, primary side current i_{res1}, secondary side voltage v_{res2}, secondary side current i_{res2}

result, v_{res1} becomes positive during the dead time. As soon as v_{res1} becomes larger than V_{DC1}, the body diodes of Q1 and Q4 conduct the resonant tank current. Right after, at t_2, Q1 and Q4 are turned on. Since the voltage at turn-on was almost zero, ZVS was achieved.
On the secondary side, if i_{res2} is negative (and no synchronous rectifying is used), the body diodes of Q5 and Q8 conduct the current. At t_3 (first blue dotted line), i_{res2} becomes positive. After this point, the parasitic capacitances of Q5 and Q8 are charged, and the ones of Q6 and Q7 are discharged due to the positive current i_{res2}. The polarity of v_{res2} reverses at t_4, and shortly after, the body diodes of Q6 and Q7 naturally take over the current flow without hard switching.

The transfer gain is the ratio between output and input voltage. It depends on the output load $R_{load,DC}$ and can be controlled by varying the switching frequency f_{sw}. In order to analyze the transfer gain, the converter can be simplified by the first harmonic approximation (FHA), in which only the power transferred with the fundamental sinusoidal component of the switching frequency is considered [C3]. The full bridge at the input is modeled as a sinusoidal voltage source with the amplitude $\hat{V}_{res1,1}$, as shown in Equation 4.2. The output side, including the rectifier, output filter, and load, is modeled as a resistive load $R_{load,AC}$ (Equation 4.3). The resulting ECD is shown in Figure 4.12.

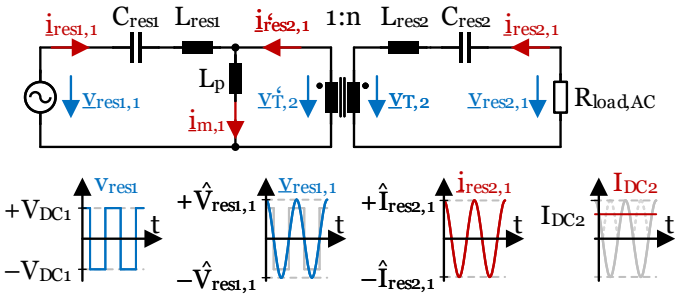

Figure 4.12: FHA model of the CLLLC converter

$$\hat{V}_{res1,1} = \frac{4}{\pi} \cdot V_{DC1} \tag{4.2}$$

$$R_{load,AC} = \frac{8}{\pi^2} \cdot R_{load,DC} \tag{4.3}$$

The resulting overall transfer gain M_{G2V} for charging (G2V/FPT) is shown in Equation 4.4, and the gain for discharging (V2G/RPT) in Equation 4.5.

$$M_{G2V} = n \cdot \frac{F_{x1}^2 \cdot (m_1 - 1)}{\sqrt{(F_{x1}^2 m_1 - 1)^2 + (\frac{Q_2}{F_{x2}})^2 \cdot (1 - F_{x1}^2 m_1 - F_{x2}^2 m_2 + F_{x1}^2 F_{x2}^2 (m_1 + m_2 - 1))^2}} \tag{4.4}$$

$$M_{V2G} = \frac{1}{n} \cdot \frac{F_{x2}^2 \cdot (m_2 - 1)}{\sqrt{(F_{x2}^2 m_2 - 1)^2 + (\frac{Q_1}{F_{x1}})^2 \cdot (1 - F_{x1}^2 m_1 - F_{x2}^2 m_2 + F_{x1}^2 F_{x2}^2 (m_1 + m_2 - 1))^2}} \tag{4.5}$$

$$F_{x1} = \frac{f_{sw}}{f_{res1}} \qquad f_{res1} = \frac{1}{2\pi\sqrt{L_{res1} C_{res1}}}$$

$$F_{x2} = \frac{f_{sw}}{f_{res2}} \qquad f_{res2} = \frac{1}{2\pi\sqrt{L_{res2} C_{res2}}}$$

$$m_1 = \frac{L_{res1} + L_p}{L_{res1}} \qquad Q_1 = \frac{\sqrt{L_{res1}/C_{res1}}}{R_{load,AC}}$$

$$m_2 = \frac{L_{res2} + n^2 \cdot L_p}{L_{res2}} \qquad Q_2 = \frac{\sqrt{L_{res2}/C_{res2}}}{R_{load,AC}}$$

Examples of the transfer gain characteristics for G2V and V2G operation under different load conditions as a function of the switching frequency are shown in Figure 4.13. At a fixed input voltage, the output voltage decreases with higher output power and higher switching frequency. In the gray area, also called the “capacitive area”, no ZVS can be achieved. Since this can quickly overheat or even destroy the converter, this area is usually avoided in operation.

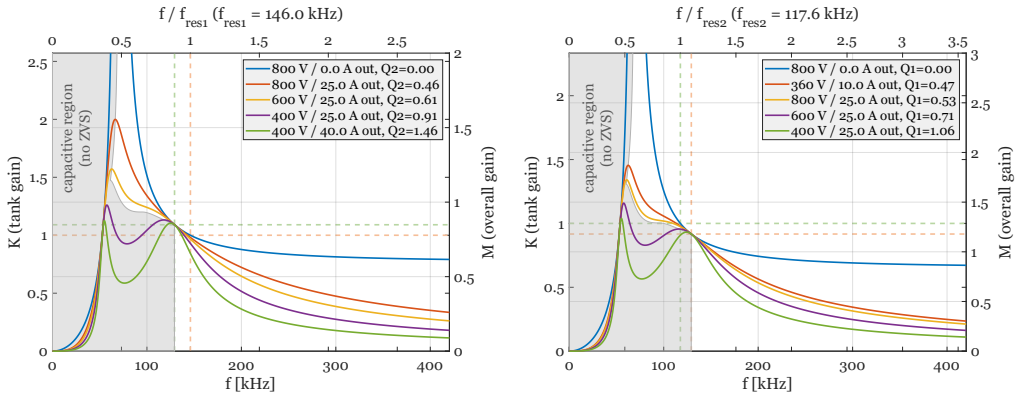

a) G2V operation / charging

b) V2G operation / discharging

Figure 4.13: Transfer gain of the CLLLC converter at different load conditions according to the FHA model

The CLLLC converter is a very efficient, galvanically isolated, bidirectional DC/DC converter. Compared to a DAB, it can almost completely eliminate switching losses under all operating conditions. Consequently, the switching frequency can be higher while maintaining superior efficiency, and thus, the isolating transformer may be more compact. Additional resonant inductors and capacitors are needed on both the primary and the secondary side. This increases component count and design complexity compared to an LLC converter. However, a bidirectional LLC converter has increased switching losses and a limited operating range in the reverse direction. A bidirectional LLC might be preferable for low-power RPT, such as for V2L. However, for V2H and V2G with a higher reverse power rating, the CLLLC is more suitable [C3].

4.2 Control algorithms for grid-connected inverters

This chapter presents control structures that grid-connected inverters can use to feed energy into the grid or even actively contribute to its stabilization.

4.2.1 Grid-following and grid-forming inverters

AC/DC converters of unidirectional EV chargers are rectifiers operated with a comparatively simple PFC control. In contrast, V2G chargers can feed power into the electricity grid, acting as inverters as well. Grid-connected inverters can be divided into grid-following inverters (GFLIs) and grid-forming inverters (GFMIs) [312–317]. A GFLI can feed power into an electricity grid, following the grid voltage and frequency provided by other generators. Therefore, it relies on the presence of an existing grid. An example is a small residential PV inverter in an interconnected network, in which large synchronous generators in thermal power plants control the grid frequency. In contrast, a GFMI actively contributes to grid stability by providing the grid voltage and frequency. GFMIs can operate in grids on their own. Examples are battery inverters in PV-fed microgrids.
Some authors further distinguish GFLIs into grid-feeding and grid-supporting inverters [312, 313]. A grid-feeding inverter is a regular GFLI, which typically maximizes output power while maintaining a high power factor (i.e., no reactive output power). On the other hand, grid-supporting inverters can support the grid, for example, by adjusting the active and reactive power output to stabilize grid frequency and voltage.
Most present inverter-based resources (IBRs) in interconnected grids are GFLIs. However, due to the rising share of mostly inverter-based RES and the phase-out of thermal power plants with their synchronous generators, there is a growing need for a significant share of GFMIs to maintain a stable and reliable grid operation with 100% IBRs [314, 317, 318].

GFLIs are often modeled as current sources and GFMIs as voltage sources [312–314, 316, 317, 319, 320], as shown in Figure 4.14. A GFLI estimates the grid frequency and phase, typically by a phase-locked loop (PLL). Based on an active power setpoint P^{set} and a reactive setpoint Q^{set} (often zero), as well as the measured grid voltage and the estimated phase, the controller determines the direct current i_d and quadrature current i_q components. The semiconductor switches are controlled by a PWM to feed the currents into the grid at the point of common coupling (PCC). A grid-supporting inverter may consider the grid voltage and frequency and adjust the injected current to support their stabilization.
On the other hand, the GFMI directly generates a voltage phasor. The resulting current that flows into the grid — and thus, the active and reactive power — is determined by the differences between the inverter and grid voltage phasors and the inverter and grid impedances. The GFMI's primary goal is maintaining a stable grid voltage and frequency. In regular operation, GFMIs of RES or storage systems typically also consider the active power setpoint P^{set} to adjust the power output based on available generation potential or a dispatch schedule [315, 317].

However, the boundaries between GFL and GFM sometimes cannot be easily drawn with the aforementioned definition, as different inverter topologies and control methods can make it

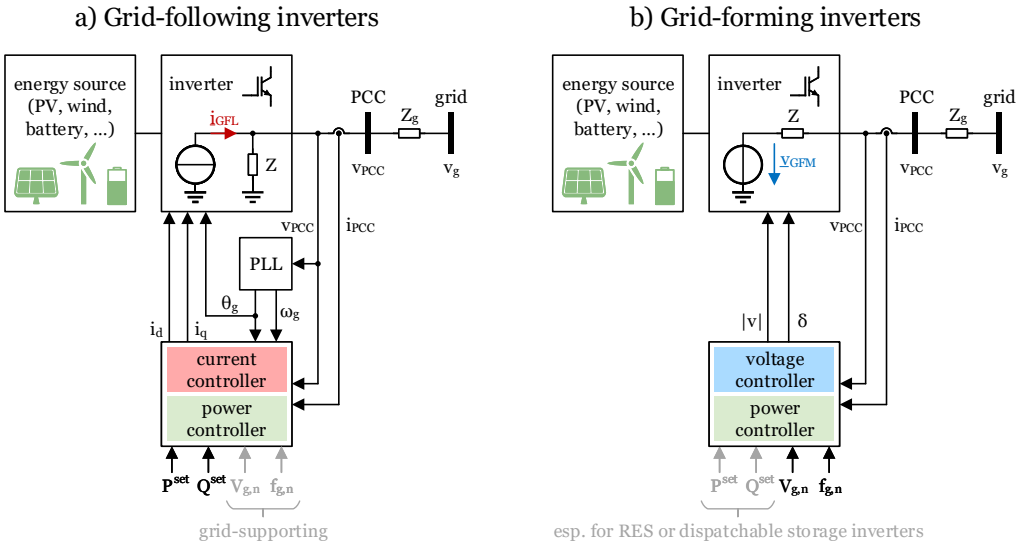

Figure 4.14: Simplified structure of a) grid-following and b) grid-forming inverters

difficult to differentiate between them. For a clear distinction of GFMI, independent of the exact inverter and control topology, the UNIFI consortium recommends using specifications and requirements of its capabilities [315]. In another report, it compares requirement-based definitions found in other publications [317]. For example, the ENTSO-E defines three classes of IBRs [318]: Class 1 IBRs, comparable with grid-following inverters, are only required to withstand certain regular grid conditions, such as the complete voltage and frequency range, and provide basic functionality, such as unity power factor control ($Q^{set} = 0$) and the reduction of power output at over-frequency. Class 2 IBRs, comparable with grid-supporting inverters, shall support voltage- and frequency-support, damping, fault current injection, and FRTs. Class 3 IBRs, comparable with grid-forming inverters, shall be able to sustain grid operation even during abnormal and emergency states without any synchronous generators in the grid. The inverter must create the grid voltage independently, contribute to system inertia, dampen harmonics, and reduce imbalances.

RES inverters typically try to maximize active power output, e.g., based on the available solar irradiation or wind speed. Therefore, GFL control is more common in these inverters. Increasing their active power output based on grid-supporting or grid-following control is only possible with an additional energy buffer or enough headroom during regular operation. For example, instead of operating at the maximum power point, the inverter could operate with reduced output power in regular operation [318, p. 37]. However, the reactive power can also be adjusted at the maximum output power as long as the inverter's current limit is not exceeded.

GFM control is more common in BESS inverters. Other readily available examples are the inverters in static synchronous compensators (STATCOMs) or high-voltage direct current (HVDC) converter stations [314, pp. 1, 37f., 64].

Adding grid-forming capabilities to an inverter typically increases cost: The hardware requires a higher current rating, the control is more complex, and thus, the development is more expensive. Therefore, it is unlikely that cost-sensitive inverters such as the ones in V2G chargers will be grid-forming. However, it is conceivable to add grid-supporting capabilities to the inverter that are supported by the hardware with minimum added cost.

4.2.2 Grid synchronization and control

Grid-following and grid-supporting inverter controllers need to estimate the grid frequency and phase, which is typically done using a PLL. Different structures for grid synchronization are compared in [321–325] and [326, pp. 43-89, 169-202]. Some of the most commonly discussed methods for three-phase inverters are the Synchronous Reference Frame (SRF), the Double Second-Order Generalised Integrator (DSOGI), and the Decoupled Double Synchronous Reference Frame (DDSRF) PLLs [327, 328].

The SRF-PLL, shown in Figure 4.15, is one of the simplest methods to track the grid frequency and phase. The three-phase AC voltages v_a, v_b, and v_c are transformed by the amplitude-invariant Clarke transformation (Equation 4.6a) to obtain the corresponding two-phase voltages v_α and v_β and the zero-sequence component v_0. Afterward, the voltages of this stationary reference frame are transformed to the voltages v_d and v_q in the rotating positive-sequence reference frame by using the Park transformation (Equation 4.6b).

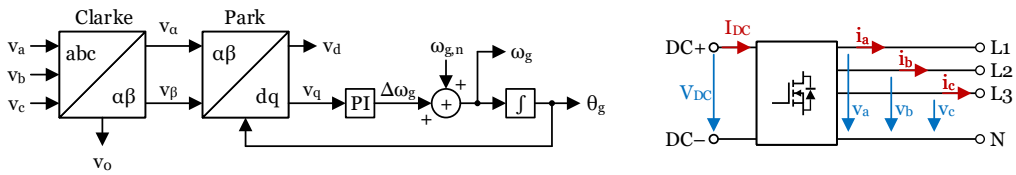

Figure 4.15: Simplified structure of the SRF-PLL (left) and definition of voltage and current measurements (right)

$$\begin{bmatrix} x_\alpha \\ x_\beta \\ x_0 \end{bmatrix} = \begin{bmatrix} \frac{2}{3} & -\frac{1}{3} & -\frac{1}{3} \\ 0 & \frac{1}{\sqrt{3}} & -\frac{1}{\sqrt{3}} \\ \frac{1}{3} & \frac{1}{3} & \frac{1}{3} \end{bmatrix} \begin{bmatrix} x_a \\ x_b \\ x_c \end{bmatrix} \tag{4.6a}$$

$$\begin{bmatrix} x_d \\ x_q \end{bmatrix} = \begin{bmatrix} \cos(\theta_g) & \sin(\theta_g) \\ -\sin(\theta_g) & \cos(\theta_g) \end{bmatrix} \begin{bmatrix} x_\alpha \\ x_\beta \end{bmatrix} \tag{4.6b}$$

Since v_d is aligned to the grid voltage phasor, its orthogonal component v_q shall be zero. It is fed into a PI controller to eliminate any remaining error $v_q \neq 0$, as seen in Figure 4.15. The output of the PI controller is the estimated offset of the angular frequency $\Delta\omega_g$ to the nominal grid frequency $\omega_g = 2\pi f_g$. The estimated grid frequency is integrated to obtain the grid phase θ_g, which is fed back to the Park transformation. Under ideal conditions in steady state, the PLL tracks the grid frequency and phase perfectly, and thus, v_q is zero.
The currents can be transformed with the Clarke and Park transformation as well. The rear part of Figure 4.15, in which the phase θ_g is determined using the q-component, is omitted.

The transformation is also illustrated in Figure 4.16 with symmetric, ideal grid voltages. The voltages v_a, v_b, and v_c, which have a phase shift of 120°, can be represented by one voltage phasor $\underline{v}$ in the phasor diagram (orange arrow). The angle between the phasor and the a- or the α-axis is the grid phase θ_g. The individual grid voltages can be derived by projecting the phasor to the axes a, b, and c (turquoise, red, and green arrows in the phasor diagram in Figure 4.16a). The voltages v_α and v_β of the stationary two-phase reference frame can be derived similarly (purple and yellow arrows in Figure 4.16b). There is no zero-sequence component v_0 in balanced grids. The phasor can also be projected onto the dq reference frame, which rotates with the angular grid frequency ω_g (Figure 4.16c). As mentioned, the d-axis rotates with the voltage phasor. Therefore, in steady state, v_d equals the grid voltage amplitude $\hat{V}_g$, and v_q is zero.

The SRF-PLL works well in symmetric, undistorted grids. However, in unbalanced grids or with harmonic distortions, the performance of the SRF-PLL deteriorates [322, 324], [326, pp. 182f.]. Different PLLs have been developed to improve the behavior under realistic and even severely impaired conditions. Two examples are the DSOGI- and the DDSRF-PLL shown in Figure 4.17. According to some authors, the DSOGI-PLL is superior [329]. Others identify comparable results [324, 330] or attribute better performance to the DDSRF-PLL [322, 323] or entirely other topologies (e.g., [325]). In this thesis, the DDSRF-PLL (Figure 4.17b) is used.

The transformations of the DDSRF-PLL will be explained using Figure 4.17b and Figure 4.18. Each step is labeled by a purple circled capital letter (A-E). Similarly to the SRF-PLL, the DDSRF-PLL transforms the grid voltages v_a, v_b, and v_c (A) to the stationary αβ reference frame (B) using the Clarke transformation. The resulting components v_α, v_β, and v_0 for an unbalanced

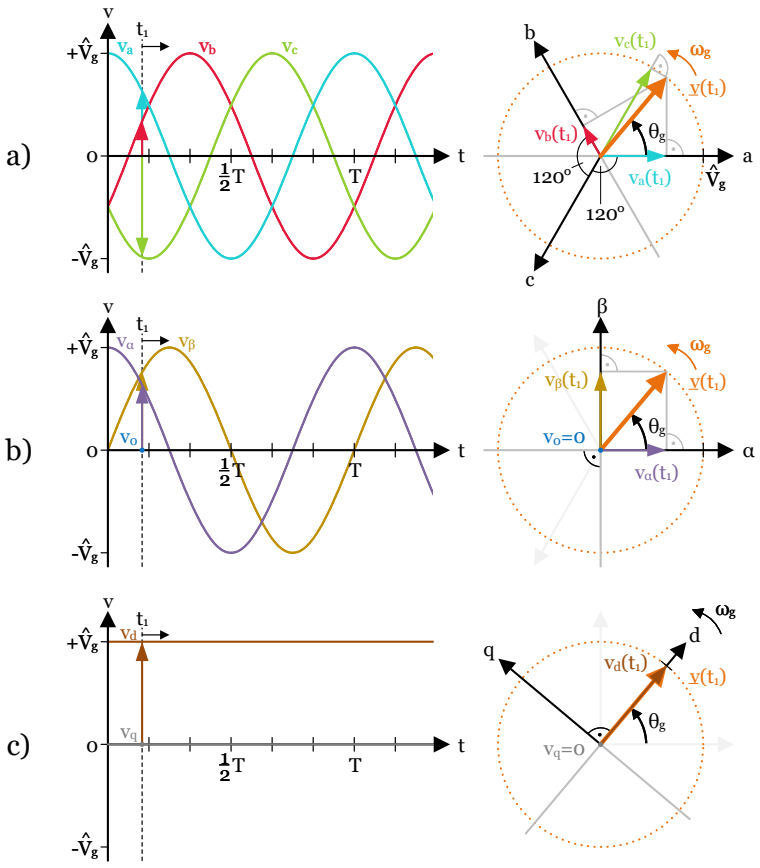

Figure 4.16: a) Symmetric three-phase grid voltages v_a, v_b, and v_c and their voltage phasor $\underline{v}$ at t_1, b) representation in the stationary αβ reference frame, and c) the rotating dq reference frame

grid are shown in Figure 4.18a/b.

In the next step, these components are transformed into both a positive (+) and a negative (−) sequence reference frame (C). In the DDSRF-PLL, both transformations use the same grid phase θ_g but with different signs, which results in Equation 4.7. The positive-sequence reference frame rotates with the grid frequency, and the negative one rotates with the negative grid frequency.

$$\begin{bmatrix} x_{d+} \\ x_{q+} \\ x_{d-} \\ x_{q-} \end{bmatrix} = \begin{bmatrix} \cos(\theta_g) & \sin(\theta_g) \\ -\sin(\theta_g) & \cos(\theta_g) \\ \cos(-\theta_g) & \sin(-\theta_g) \\ -\sin(-\theta_g) & \cos(-\theta_g) \end{bmatrix} \begin{bmatrix} x_\alpha \\ x_\beta \end{bmatrix} = \begin{bmatrix} \cos(\theta_g) & \sin(\theta_g) \\ -\sin(\theta_g) & \cos(\theta_g) \\ \cos(\theta_g) & -\sin(\theta_g) \\ \sin(\theta_g) & \cos(\theta_g) \end{bmatrix} \begin{bmatrix} x_\alpha \\ x_\beta \end{bmatrix} \tag{4.7}$$

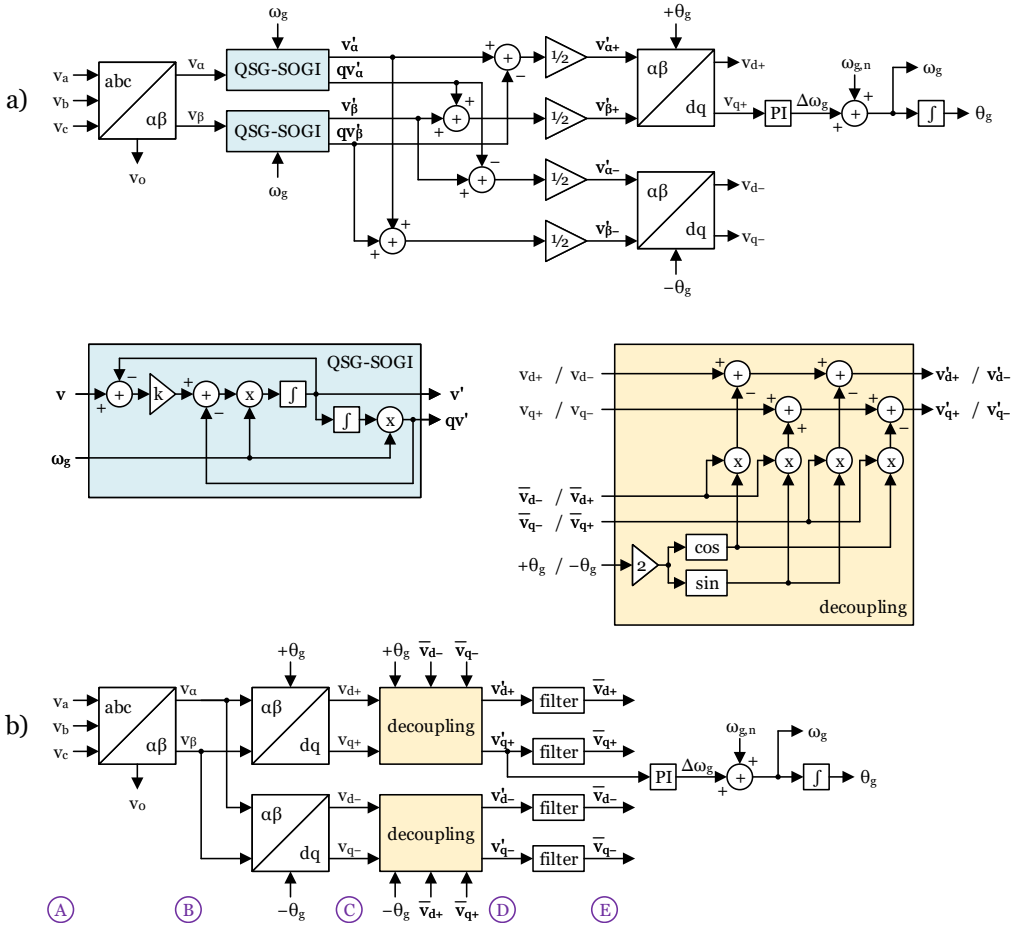

Figure 4.17: a) DSOGI-PLL, b) DDSRF-PLL

In a balanced grid in steady state, $v_{d+} = \hat{V}_g$ and $v_{q+} = 0$. In an unbalanced grid, v_{d+} and v_{q+} are not constant but oscillate with twice the grid frequency. The negative-sequence components v_{d-} and v_{q-} oscillate even under balanced conditions. This is because any DC signal in one reference frame is seen as an oscillating signal in the other reference frame. Since both frames rotate in opposite directions with grid frequency, the difference between their rotations is twice the grid frequency.

A decoupling network cancels out the oscillations (see Figure 4.17b and Equations 4.8a–d). The decoupled components v'_{d+}, v'_{q+}, v'_{d-}, and v'_{q-} are derived (D), which are constant in steady state under both balanced and unbalanced conditions. The decoupling network subtracts components

of the opposing reference frame, in which the oscillation is filtered out. Typically, low-pass filters (LPFs) are used for this purpose, which yields $\bar{v}_{d+}$, $\bar{v}_{q+}$, $\bar{v}_{d-}$, and $\bar{v}_{q-}$ (E).

$$x'_{d+} = x_{d+} - \bar{x}_{d-}\cos(2\theta_g) - \bar{x}_{q-}\sin(2\theta_g) \tag{4.8a}$$

$$x'_{q+} = x_{q+} + \bar{x}_{d-}\sin(2\theta_g) - \bar{x}_{q-}\cos(2\theta_g) \tag{4.8b}$$

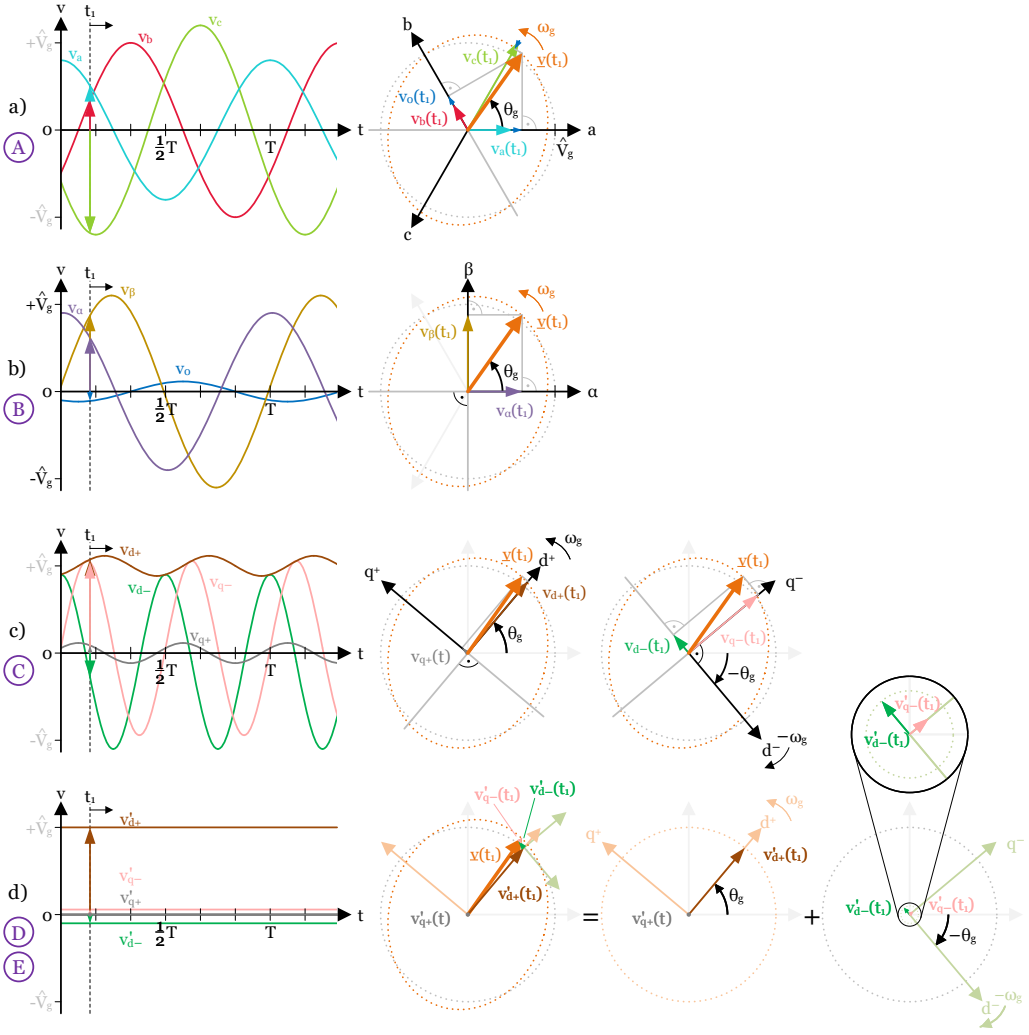

Figure 4.18: a) Unbalanced three-phase grid voltages v_a, v_b, and v_c and their voltage phasor $\underline{v}$ at t_1, b) representation in the stationary αβ reference frame, c) the rotating positive- and negative-sequence dq reference frames, and d) the decoupled v_{d+}, v_{q+}, v_{d-}, and v_{q-} components in the DDSRF-PLL

$$x'_{d-} = x_{d-} - \bar{x}_{d+}\cos(-2\theta_g) - \bar{x}_{q+}\sin(-2\theta_g)$$
$$= x_{d-} - \bar{x}_{d+}\cos(2\theta_g) + \bar{x}_{q+}\sin(2\theta_g) \quad (4.8c)$$
$$x'_{q-} = x_{q-} + \bar{x}_{d+}\sin(-2\theta_g) - \bar{x}_{q+}\cos(-2\theta_g)$$
$$= x_{q-} - \bar{x}_{d+}\sin(2\theta_g) - \bar{x}_{q+}\cos(2\theta_g) \quad (4.8d)$$

The trajectory of the voltage phasor $\underline{v}$ follows an ellipse in an unbalanced grid condition. Its path can be derived by geometrically adding the decoupled vectors $\vec{v}_+$ and $\vec{v}_-$ of the positive and negative reference frames, as shown in Figure 4.18d.
For grid phase estimation, the unfiltered v'_{q+} component is fed into a PI controller (Equation 4.9), comparable to the SRF-PLL.

$$G_{PI}(s) = K_p + \frac{K_i}{s} \quad (4.9)$$

Typically, the filtered components ($\bar{x}_{d+/q+/d-/q-}$) are used for voltage and current control since the unfiltered components ($x'_{d+/q+/d-/q-}$) oscillate during sudden changes (e.g., voltage sags). However, the filtered components limit the controller dynamic, depending on the filter type and order. Revelo and Silva [331] use a notch filter (NF) to derive $\bar{i}_{d+/q+/d-/q-}$ using the DDSRF-PLL, which can improve the controller performance compared to an LPF.

The basic control structure for a GFLI with DDSRF-PLL can be seen in Figure 4.19 [C2]. The sign of the decoupling term (marked in blue) depends on the sign convention of the grid current. Here, the inverter is treated as a power source, as shown in Figure 4.15.

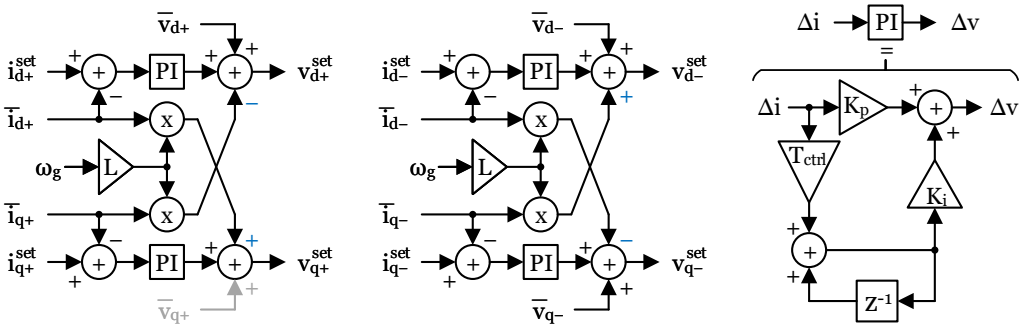

Figure 4.19: Simplified structure of a dual reference frame current controller (left), including PI controllers (right)

In the simplest approach, the negative-sequence currents i^{set}_{d-} and i^{set}_{q-} are zero, and the positive-sequence current i^{set}_{d+} can be set proportionally to the active power and i^{set}_{q+} according to the reactive power. Revelo and Silva [331] present different methods to use both positive and negative-sequence

currents, for example, to balance voltages or currents or to minimize power oscillations during asymmetric voltage faults.

The resulting voltage setpoints are transformed back to the stationary reference frame using the inverse Park and Clarke transformations according to Equations 4.10. The resulting vector is applied to the inverter output by driving the switches with a PWM pattern based on SVM.

$$\begin{bmatrix} x_\alpha \\ x_\beta \end{bmatrix} = \begin{bmatrix} \cos(\theta_g) & -\sin(\theta_g) & \cos(\theta_g) & \sin(\theta_g) \\ \sin(\theta_g) & \cos(\theta_g) & -\sin(\theta_g) & \cos(\theta_g) \end{bmatrix} \begin{bmatrix} x_{d+} \\ x_{q+} \\ x_{d-} \\ x_{q-} \end{bmatrix} \tag{4.10a}$$

$$\begin{bmatrix} x_a \\ x_b \\ x_c \end{bmatrix} = \begin{bmatrix} 1 & 0 & 1 \\ -\frac{1}{2} & \frac{\sqrt{3}}{2} & 1 \\ -\frac{1}{2} & -\frac{\sqrt{3}}{2} & 1 \end{bmatrix} \begin{bmatrix} x_\alpha \\ x_\beta \\ x_0 \end{bmatrix} \tag{4.10b}$$

4.2.3 Ancillary services

The safe, stable, and reliable operation of the electricity grid requires a variety of ancillary services. These are listed and described in [57, pp. 218-220], [332, pp. 58-70], [333, 334], and [C2].

Ancillary services related to frequency control are Frequency Containment Reserve (FCR), Frequency Restoration Reserve (FRR) with automatic (aFRR) and manual (mFRR) activation, as well as replacement reserve (RR). They ensure that generation and demand power are in balance in regular operation and during sudden frequency variations, for example, because of the outage of a large power plant or the separation of the European interconnected grid due to failures. Their interaction after an abrupt frequency drop is explained using the example in Figure 4.20 (also compare [57, 335–342]). A frequency increase is faced with an opposing reaction.

Before t_0, the grid is in steady-state operation with $f_g = f_{g,n} = 50\ Hz$. At t_0, a significant loss of generation power causes an imbalance between electricity generation and demand. The response to this consists of several stages:
In the present electricity grid, a large share of generation is provided by synchronous generators in conventional thermal or hydropower plants, which are powered by a mechanical steam or hydroelectric turbine. Since the demand in the grid is now larger than the generation power, the electrical load on the remaining generators and, thus, the mechanical load on the turbines is larger. This causes turbines to release kinetic energy from their rotating mass and thus slow down. Since

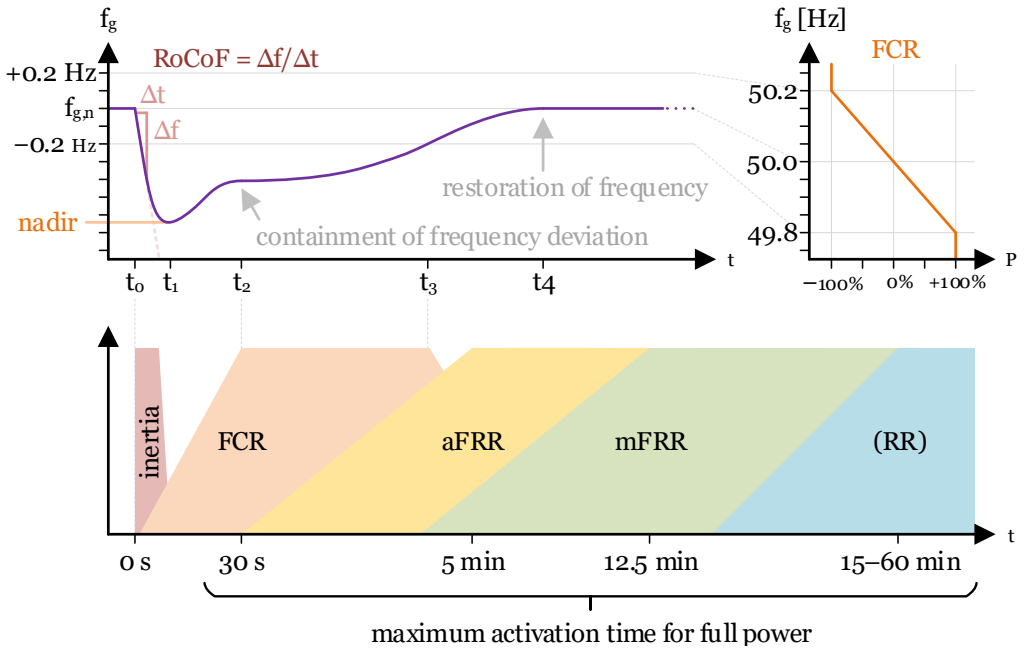

Figure 4.20: Illustration of a frequency drop in the electricity grid and reaction by different stages of frequency control

their mechanical rotational speed is tightly coupled with the electrical grid, the frequency in the electricity grid also drops. The Rate of Change of Frequency (RoCoF) is limited by the inherent mechanical **inertia** of all turbine generators, synchronous condensers, and motors synchronously connected to the grid at the time of the event. The kinetic energy E_{kin} in a turbine generator can be expressed by Equation 4.11. S_n is the nominal apparent power, H is the inertia constant, J is the moment of inertia, and ω_n the nominal angular velocity of the generator [339, pp. 15f.].

$$E_{kin} = S_n H = \frac{1}{2} J \omega_n^2 \tag{4.11}$$

Typical values for inertia constants of thermal and hydroelectric power plants lie in the order of 0.5 to 6 s, and the kinetic energy is in the range of 1 to 9 GWs [342, p. 4]. The overall system inertia of large interconnected networks such as the Central European electricity grid lies in the order of several hundred to thousands of gigawatt seconds (GWs) and varies over time [339, p. 43], [340, p. 78], [343]. The maximum permissible RoCoF lies in the range of 0.5 to 4 Hz/s [340, p. 8], which is only reached in severe events and only lasts for a few seconds [344, p. 30].
As soon as the frequency in the synchronous grid in Continental Europe deviates by more than 10 mHz, all units in the grid providing **FCR** (“primary control”) need to react with a change of generation power. The required power is proportionally scaled based on the frequency deviation

to the nominal frequency. At or above a deviation of 200 mHz, the maximum FCR power needs to be provided, as seen in the top right side of Figure 4.20. The full power is activated automatically, must be available after 30 seconds at the latest, and needs to be provided for up to 15 minutes [338], [337, pp. 57-62], [57, p. 223]. In Continental Europe, the overall FCR capacity is 3 GW, 562 MW of which were provided in Germany in 2021 [57, p. 226]. FCR limits the maximum frequency drop (nadir at t_1) and returns the frequency to a quasi-stationary operating point at t_2. If a failure impaired the grid balance, the frequency typically remains below the initial frequency.
In the next step, **aFRR** ("secondary control") is automatically activated in the load-frequency control area of the TSO(s) in which the failure occurred. This relieves the units providing FCR (after t_3) so they can be used for new deviations, and it shall restore the grid frequency to its nominal value (at t_4). The full power needs to be active within 5 minutes after the event and needs to be provided for up to 15 minutes. About 2 GW of aFRR were tendered in Germany in 2021 [57, pp. 223, 227].
For the support or relief of the aFRR units, **mFRR** ("tertiary control") can be dispatched manually. Manual FRR is used for longer-lasting issues in particular. The full capacity must be available within 15 minutes and can be dispatched in 15-minute intervals. Around 1100 MW of positive and 600 MW of negative[1] tertiary mFRR were tendered on average in Germany in 2021 [57, pp. 223, 227]. In some European countries, **RR** is an additional measure to replace mFRR.

These frequency control capabilities are supplemented by further means, such as deactivating interruptible loads and PHES, as well as load shedding below critical under-frequency limits. Small generators such as photovoltaic and battery inverters can operate in a limited frequency sensitive mode (LFSM), in which they reduce or increase the power feed-in or demand above or below the normal frequency range [345–347].
In a future electricity grid with a high share of IBRs, these frequency control measures must be implemented by the inverters, even in regular grid operation. On the one hand, the typically ultra-fast reaction times of inverters could significantly improve frequency stability. On the other hand, the lack of mechanical inertia of inverter-based generators, such as wind or PV generators, is a challenge.

Synthetic inertia, also called virtual inertia (VI), is one possible solution to face transient frequency stability with a lack of mechanical inertia in the future [339, p. 20], [340, p. 26f., 41f.]. Different topologies to provide synthetic inertia are reviewed in [348–352]. They can be divided into topologies that model the behavior of synchronous generators, topologies based on swing equations, and variants that implement a frequency-power relationship. A simple variant with a frequency-power relationship is the Virtual Synchronous Generator (VSG) [348, pp. 9f.], shown in

[1] positive reserve: increase generation or reduce demand, negative reserve: reduce generation or increase demand

Figure 4.21. The measured frequency deviation Δf to the nominal grid frequency $f_{g,n}$ is multiplied with the damping constant k_D for FCR, and its derivative $\frac{d}{dt}\Delta f$ is multiplied with the inertia constant k_I to provide synthetic inertia. Therefore, the VSG is essentially a PD controller intended to reduce the frequency deviation Δf. However, when used in grid-following inverters, the VSG does not directly influence the grid frequency. Instead, it only supports other conventional power plants or grid-forming inverters in maintaining the grid frequency by reducing the power variations in the grid that caused the frequency variation.

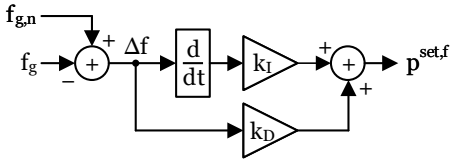

Figure 4.21: Simplified structure of the VSG

While frequency control mainly covers the grid's short-term stability, additional measures are necessary for long-term stability. With different forms of congestion management, the transmission and distribution system operators make sure that the energy demand can be fulfilled without exceeding the safe operating limits of the grid infrastructure, e.g., power ratings of transformers or power lines. This includes redispatch, countertrading, feed-in and demand side management, peak-shaving and valley-filling, the disconnection of interruptible loads, or the provisioning of capacity reserves. TSOs also need to compensate for the energy losses in the transmission system through additional generation [57, p. 218], [333, 334].

In the unlikely case of a blackout, the grid must be restored. This requires some of the power plants to be black-start capable and support the grid restoration process. The power plant needs to start and run without an external power source, and the restoration needs to be coordinated by the TSO [57, p. 540], [333, 334]. For inverter-based systems, this could be implemented using a grid-forming inverter with a battery storage system.

Voltage regulation is another important aspect of the stable operation of the electricity grid. This includes avoiding over- and under-voltages in the transmission and distribution grid by providing or compensating reactive power, as well as reducing imbalances in the distribution grid [333, 334]. Particularly in weak, remote grids, the voltage quality can be impaired without additional measures. In these instances, a significant voltage difference occurs between periods of high demand, e.g., when many EVs are charged in evening hours, and periods of low demand, for example when PV systems feed energy into the grid at noon. Asymmetric demand or generation, e.g., caused by single- or two-phase EV chargers and small single-phase PV systems, further intensifies the problem [156, pp. 26, 34, 46f.].

Possible solutions include flexible alternating current transmission systems (FACTS), transformers with tap changers, and line regulators. Similar to PV inverters and stationary battery systems, V2G fleets could also provide reactive or active power to regulate the voltage in the distribution grid [156, pp. 56f.], [334], [347].
Power quality measures such as oscillation or harmonic damping improve voltage and frequency stability. Low-frequent local or inter-area oscillations caused by disturbances like transmission line faults can cause power outages. Therefore, they must be avoided and damped when occurring [333].

Another essential aspect of grid stability is the transient behavior during abnormal over- or under-voltage conditions, e.g., caused by switching operations or short-circuit faults. If too many generators disconnect because of under-voltage events due to nearby or distant short circuits, a significant share of generation would be missing after the fault, leading to frequency stability issues. Instead, generators should be capable of injecting sufficient fault currents at critical under-voltage events. This allows over-current protections to trip, helping to clear temporary faults or to isolate affected segments so that the remaining segments can continue operation [314, pp. 20f.], [317]. The LVRT, HVRT, and FRT capabilities are typically not remunerated ancillary services but rather required in grid codes [334]. An overview of such requirements can be found in [353, pp. 3-7] and [332, pp. 51-53].
Depending on the use case, IBRs should detect a loss of the grid and shut down (“anti-islanding”) or intentionally continue to operate in islanded operation and later resynchronize. The first case allows grid operators to safely turn off the grid segment for maintenance and repair. The latter case reduces the adverse effects of outages by providing emergency power after a fault [314, pp. 22], [317], [334].

Many of the ancillary services could also be implemented with bidirectional or partly even with unidirectional EV chargers [3, 7, 148]. Some ancillary services, such as primary frequency control and some forms of congestion management, have already been successfully tested in field experiments, as summarized by Paul Reynolds et al. [4].

5 Vehicle-to-Grid charger prototype

This chapter presents the development and characterization of a bidirectional battery charger for V2G applications. The focus is on the power electronics hardware and control. The communication interfaces between the EV, EVSE, and EMS are not part of this thesis (see Figure 5.1).

The V2G charger aims to serve as a powerful and flexible test platform to investigate different V2G use cases. It shall be able to transfer power in both directions, i.e., G2V and V2G, with a power of up to 22 kW. The hardware is intended to be operated in the European 230/400 V three-phase grid. However, single-phase operation and the use with lower grid voltages, e.g., 120 V, shall also be possible with derated power. The charger should be able to charge batteries with a voltage range of about 250 to 800 V. A very high efficiency over wide operating ranges, i.e., also in partial or light load operation, is desirable.

As discussed in Chapter 4.1.1, EV batteries are isolated from the vehicle chassis for safety reasons, and most chargers maintain this isolation while connected to the grid. Since V2G chargers are expected to be connected to the grid for a considerable amount of time, the investigated charger should also be isolated. Because of this requirement, a two-stage charger using an AC/DC and a galvanically isolated DC/DC converter was selected. Resonant converters are preferred since they eliminate switching losses, which is particularly useful for obtaining high efficiency even in light load conditions. Based on these considerations, a three-phase ARCPI topology was selected for the AC/DC stage and a CLLLC converter for the DC/DC stage.

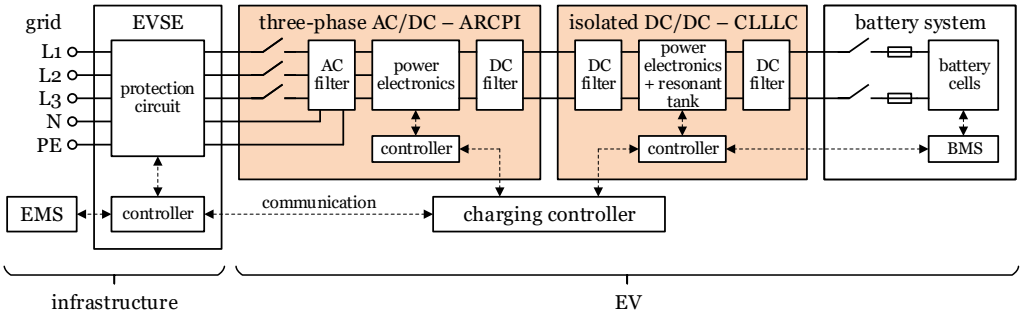

Figure 5.1: Simplified diagram of the investigated V2G charging system in case of bidirectional AC charging using the OBC — the AC/DC and DC/DC converters (highlighted in orange) are the focus of this work

5.1 Design and optimization of the DC/DC converter

The CLLLC converter used for the V2G test platform was initially designed in a master's thesis [354]. Within the scope of the present doctoral thesis, the converter was further enhanced, e.g., to support dynamic dead times and synchronous rectifying for higher efficiency and output power [C3], to work smoothly together with the AC/DC converter developed in this thesis, to allow a quick and automatic transition between the charging and discharging modes for dynamic V2G operation, and to be controlled with a graphical user interface on a computer, emulating the charging controller in Figure 5.1.

The naming convention used for the converter is shown in Figure 5.2. In forward operation (FWD), energy is transferred from DC1 to DC2, and the battery is charged (G2V). DC1 is the "input" or "primary side", and DC2 is the "output" or "secondary side". I_{DC1} and I_{DC2} are positive.
In backward operation (BWD), energy is transferred from DC2 to DC1, and the battery is discharged (V2G). Now, DC2 is the "input" or "primary side", and DC1 is the "output" or "secondary side". I_{DC1} and I_{DC2} are negative.

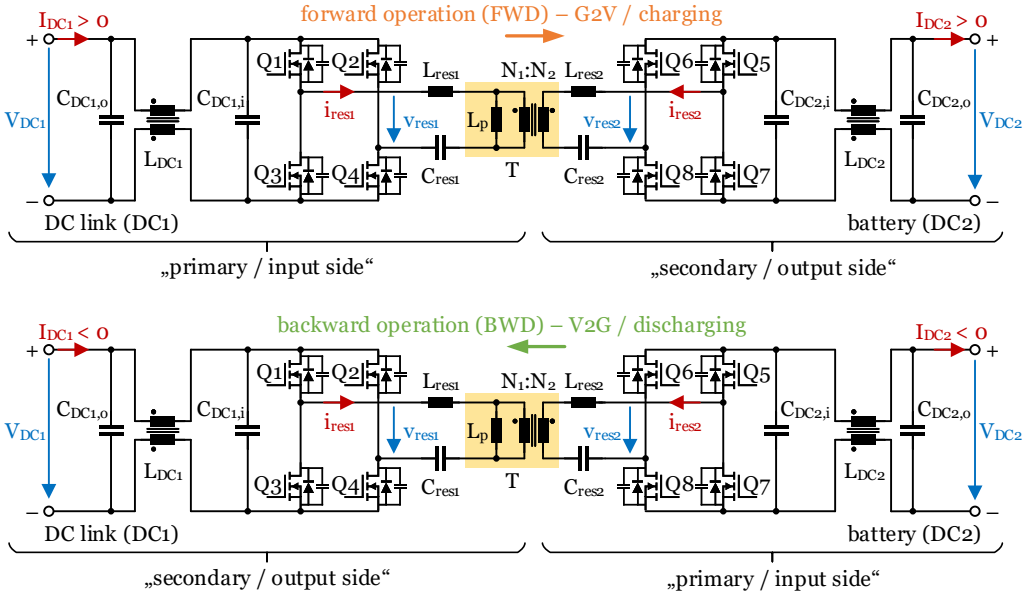

Figure 5.2: Simplified schematic of the CLLLC prototype with current sign and naming convention used in this thesis

5.1.1 Power electronics

The CLLLC prototype is shown in Figure 5.3. The assembled board in Figure 5.3a consists of a main board, a controller board (Figure 5.3b) mounted on top, and eight individual gate-driver boards (Figure 5.3c) placed under the main board. The gate drivers control the MOSFET full bridges inside the power module (Figure 5.3d). The power module is detachable to compare different module variants. The arrangement of the final assembly with the power module, gate driver boards, controller board, resonant tank, and the CLC filters in the DC links can be seen in Figure 5.3e from the top and Figure 5.3f from the side.

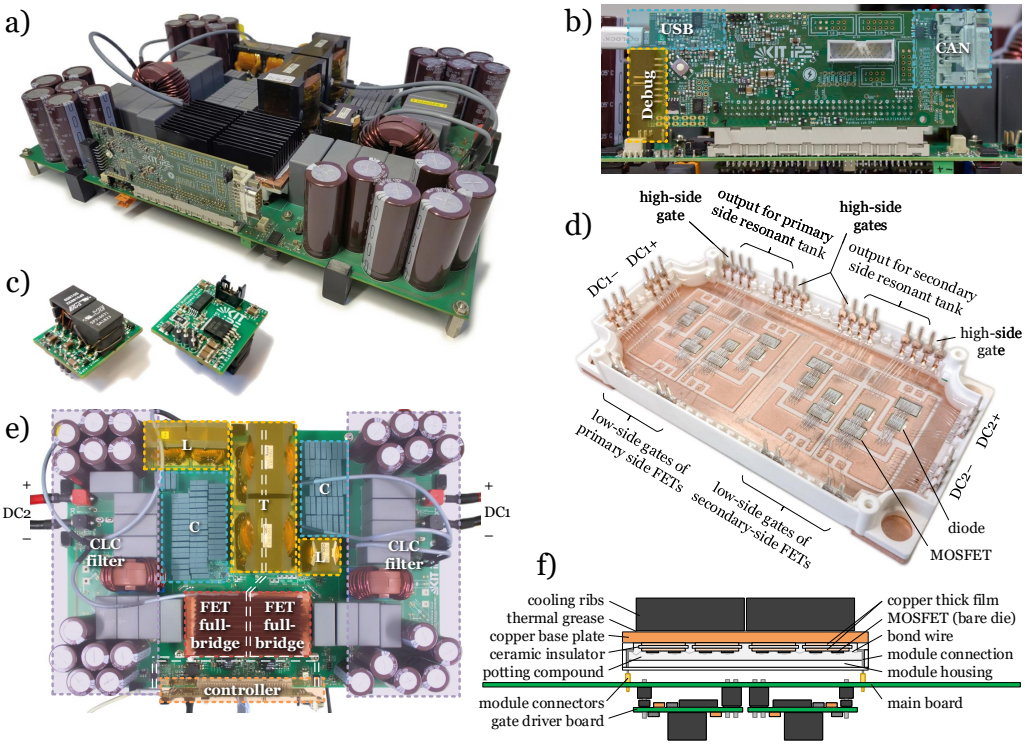

Figure 5.3: a) Photo of the CLLLC converter prototype, b) view onto the controller board with external communication interfaces, c) gate driver boards, d) power module comprising diodes and MOSFETs, e) overview of the main board with functional sections, f) side view of the assembly with power module, main board, and gate driver boards — images b)-f) are based on [354, pp. 66-69, 80, 134], rearranged and extended (own work, CC BY 4.0)

Due to the lack of commercially available suitable transformers, the resonant tank consists of discrete resonant inductors rather than an integrated transformer with appropriately designed

leakage inductances. The latter would have been preferred because it saves space, weight, and overall cost. The CLC filter on the DC1 link to the AC/DC converter, shown in Figure 5.2 and Figure 5.3e, is not necessarily required since the inverter also has a large DC capacitance. It was added to allow stand-alone operation of both converters in other applications. The component values for the resonant tank[1] and the CLC filters are shown in Table 5.1. The filter inductor is a common mode (CM) choke whose stray inductance functions as a differential mode (DM) inductance to filter the input and output currents.

Table 5.1: Component values used in the CLLLC prototype shown in Figure 5.2

resonant tank	L_{res1} = 15 µH	C_{res1} = 79.2 nF	N_1:N_2 = 7:9	f_{res1} = 146 kHz
	L_{res2} = 16 µH	C_{res2} = 114.4 nF	L_p = 50 µH	f_{res2} = 117.6 kHz
CLC filters	$C_{DC1,o}$ = $C_{DC1,i}$ = $C_{DC2,i}$ = $C_{DC2,o}$ = 284 µF			
	$L_{DC1,DM}$ = $L_{DC2,DM}$ = 9 µH		$L_{DC1,CM}$ = $L_{DC2,CM}$ = 1.5 mH	

Different power modules were compared. All modules consist of two full bridges comprising eight *Cree/Wolfspeed CPM3-1200-0013A* silicon carbide (SiC) MOSFETs ($V_{DS} = 1200\ V, R_{DS,on} \approx 13\ m\Omega$). Some of the modules also include *Cree/Wolfspeed CPW5-1200-Z050B* or *Rohm S6305* SiC Schottky diodes ($V_R = 1200\ V, V_F \approx 1.1\ V$) mounted anti-parallel to the FETs to reduce the forward voltage drop compared to the intrinsic body diodes of the MOSFETs ($V_{SD} \approx 3.6\ V$ when turned off). This is relevant on the primary side in the last phase of the dead time, just before the MOSFETs turn on with ZVS (also see V_{res1} between $t = 1.2 \ldots 1.5\ \mu s$ in Figure 4.11 on page 76). It is even more important on the secondary side if the diodes passively rectify the output current of the resonant tank for the DC link. The secondary-side MOSFETs can also be used actively by implementing synchronous rectifying. In this case, the conduction losses further decrease since the drain-source voltage in the on-state is significantly reduced.

The converter measures 38 x 28 x 8.5 cm^3 and weighs 5.36 kg, including the main, controller, and gate driver boards, as well as the power module and filters. External cables, a housing, and a cooling fan needed for high-power operation are not included. Based on a maximum continuous power of 15 kW, the power density of the inverter prototype is 1.66 kW/dm^3 or 2.80 kW/kg.

[1] The resonant tank is designed for a wide operating range, even under light load conditions. Among others, this is achieved by comparatively large $C_{res1/2}$ values. However, the large $C_{res1/2}$ values cause high oscillating reactive currents in the primary circuit. As it turned out, light load operation can also be handled well with a discontinuous burst operation. Therefore, lower $C_{res1/2}$ values would be recommended for the next design iteration.

5.1.2 Controller

A functional overview of the controller board and its connection to the main board with measurement signals and power supply is shown in Figure 5.4. The microprocessor used is an *Infineon AURIX TriCore TC275C* with three cores. Core 0 is responsible for the control loop of the DC/DC converter, the Controller Area Network (CAN) communication to the battery system, and the CAN and Universal Asynchronous Receiver/Transmitter (UART) communication to the charging controller, which is emulated by a computer. Core 1 collects all measurement signals via Serial Peripheral Interface (SPI) buses and converts them for the control loop. Core 2 takes care of the synchronous rectifying of the secondary side.

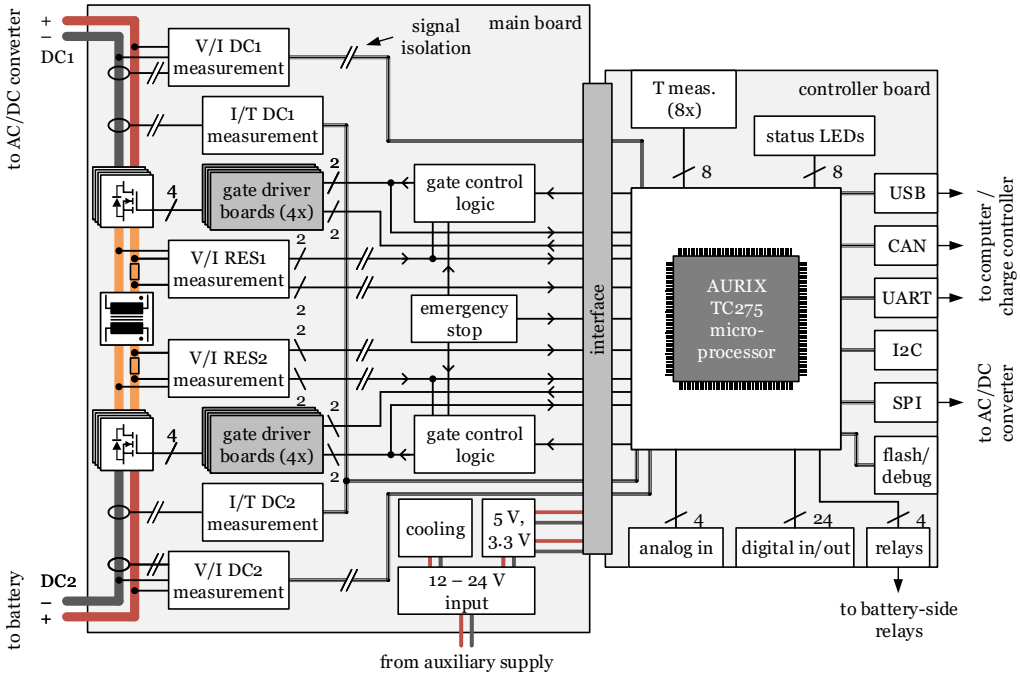

Figure 5.4: Overview of the signals from and to the DC/DC controller — image based on [354, p. 79], rearranged and extended (own work, CC BY 4.0)

The control loop is executed with a relatively slow controller frequency of 4 kHz. It starts with the measurement acquisition via the SPI buses. The data is converted and then processed by the CLLLC controller. The manipulated variable is the switching period T_{sw} of the primary-side full bridge. It is dynamically adjusted based on the deviation of the measured DC1 and DC2 voltages and currents to their respective setpoints. The new switching period setting is immediately applied at the end of the control loop.

The switching period was used as the manipulated variable instead of the switching frequency because its relationship to the transfer gain is more linear (compare Figure 5.5). Since sud-

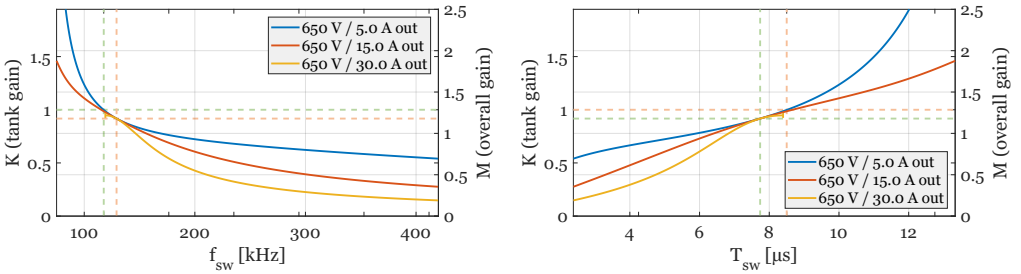

a) Gain as a function of the switching **frequency**

b) Gain as a function of the switching **period**

Figure 5.5: Transfer gain of the CLLLC converter in V2G operation according to the FHA model

den switching period changes can cause high inrush currents into the resonant tank, a simple I-controller is used instead of a PID controller. The switching frequency is limited from 80 to 420 kHz in the forward direction (G2V) and 75 to 420 kHz in the backward direction (V2G). The higher the output voltage and current shall be, the lower the switching frequency has to be. On the other hand, if the output power is too low for the highest switching frequency, the converter operates discontinuously. Small switching bursts are applied with the maximum switching frequency to control the output effectively and efficiently. The start-up procedure and voltage or current overshoots are handled separately.

In unidirectional operation (either G2V or V2G), the charging controller sets the power transfer direction and setpoint values. A simplified control diagram for this mode of operation is shown in Figure 5.6. The controlled variables are the maximum output voltage and current, for example, based on the battery's maximum charging limits. Optionally, the minimum input voltage and maximum input current can also be controlled. The controller seamlessly chooses the limiting

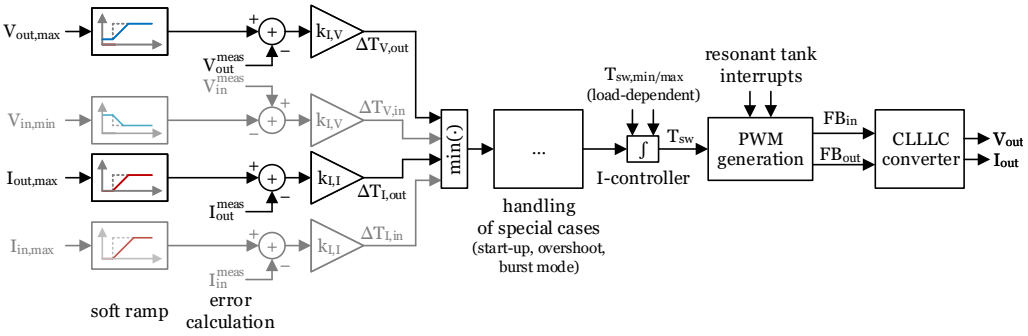

Figure 5.6: Simplified controller structure in unidirectional operation mode

variable by using the minimum of the respective calculated ΔT_{sw} values. If any value exceeds the limit, this results in a negative ΔT_{sw}, i.e., an increase of the switching frequency and, thus, a reduction of the transferred power. The resulting value for ΔT_{sw} is added to the last switching period to obtain the new period T_{sw} for PWM generation of the primary side, i.e., the input side. The secondary-side full bridge (FB_{out}) is either turned off for passive rectification (as implemented in [354]) or actively driven to support synchronous rectification (developed in this thesis).

When the DC/DC converter is operated with an inverter that determines the power flow, the converter can be operated in an additionally implemented dynamic bidirectional mode. The corresponding control diagram is shown in Figure 5.7. In this mode, the CLLLC converter determines the power transfer direction and power level based on the DC1 link voltage between the inverter and the converter, as well as the DC2/battery voltage, as shown in the bottom right box of the diagram. If the inverter draws power from the grid, the DC1 voltage rises, so the DC/DC converter needs to charge the battery to stabilize V_{DC1}. In the opposite case, the inverter feeds power into the grid. Thus, the DC1 voltage falls, and the converter needs to discharge the battery. The power is reduced if the battery reaches the maximum or minimum allowed voltages. The tolerated voltage and current setpoint ranges are configured statically. The DC1 voltage range should be selected relatively tight around or equal to the nominal DC1 voltage. The DC2 voltages can be selected based on the minimum and maximum allowed battery voltages. The minimum (negative/discharging) and maximum (positive/charging) permissible currents for the common DC1 and the DC2/battery links are selected as current limits.

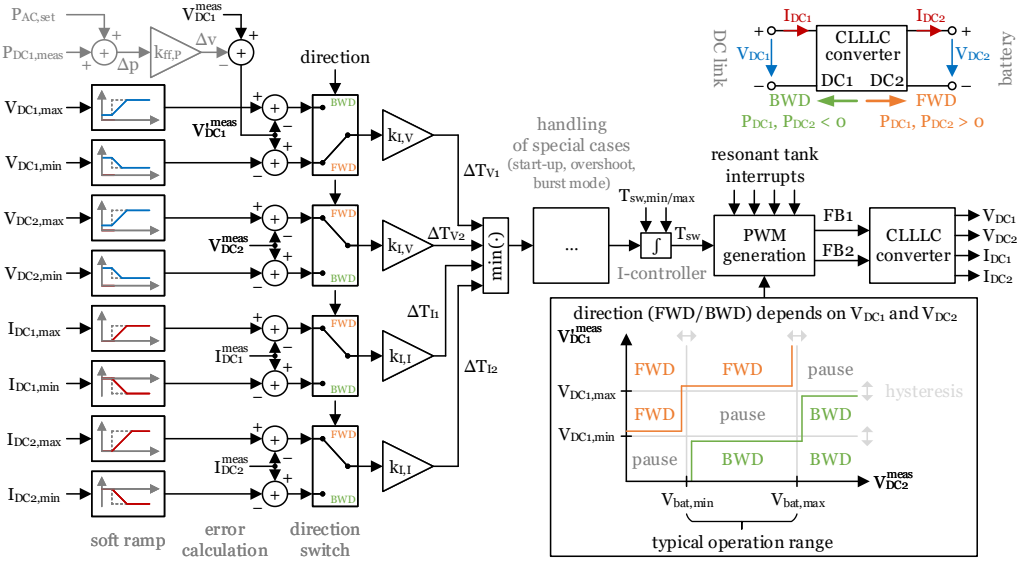

Figure 5.7: Simplified controller structure in the dynamic bidirectional operation mode

For an improved overall power transfer dynamic and to reduce DC1 voltage deviations, the inverter can communicate its power setpoint to the DC/DC converter so both devices can adjust the transferred power simultaneously. This was realized using a galvanically isolated high-speed SPI bus between the two controllers. A cyclic redundancy check (CRC) and a counter value are added to the data packet to detect data corruption. The DC/DC converter requests the AC power setpoint from the inverter in every control loop. Next, the power difference Δp between the DC1 power measured by the DC/DC converter and the AC power setpoint of the inverter is calculated. However, the transferred power of the CLLLC converter cannot be influenced directly but is controlled by the switching frequency, which is selected based on the voltage and current setpoints. Therefore, Δp is multiplied with a control factor $k_{ff,P}$ and subtracted from the measured DC1 voltage before it is fed into the controller as V'^{meas}_{DC1} to adjust the power accordingly. The resulting $\Delta v = k_{ff,P} \cdot \Delta p$ is limited to ±30 V to avoid an excessive reaction of the voltage controller.
If the inverter increases the power fed into the grid ($P^{set}_{AC} > 0$), and the momentary power transferred by the CLLLC converter and flowing out of the DC1 link ($P^{meas}_{DC1} < 0$) is not large enough, V'^{meas}_{DC1} will be reduced. This causes the converter to switch to the backward mode (if not already done) and decrease the switching frequency to increase the magnitude of the DC1 power $|P^{meas}_{DC1}|$. In contrast, if the inverter decreases the power fed into the grid or increases the power drawn from the grid, V'^{meas}_{DC1} is increased. As a result, the converter decreases $|P_{DC1}|$ in backward operation or switches into forward power transfer operation and increases P_{DC1}, if necessary.

The DC/DC converter can be configured and started using its UART interface via the USB connector. The most important commands to control the converter are shown in Appendix A.3. Measurements and states are sent via UART every second. The converter also transmits its measurements and states via the CAN interface. This information can be visualized on a *LabVIEW* interface on the computer, as shown in Figure A.2 in Appendix A.3. The interface shows the input and output voltages, currents, and powers, the switching frequency, efficiency, error states, and several component temperatures for two converters.

5.1.3 Dynamic dead time generation

The principle of ZVS in the CLLLC converter is to let the primary-side resonant tank current i_{res} drive the transition of the full bridge output voltage v_{res} of the primary side (compare v_{res1} between t_1 and t_2 in Figure 4.11). However, the slew rate of v_{res} is dependent on the output load. The resulting minimum dead time required for soft switching also depends on the input voltage.
Two different load conditions are compared in Figure 5.8. Power is transferred in the forward direction from DC1 to DC2. In Figure 5.8a and c, the output power is large, so the resulting primary-side transition, in this example v_{res1}, is fast. The optimal turn-on time for MOSFETs Q1 and Q4 is highlighted in green in Figure 5.8a. It is reached as soon as the v_{res1} transition

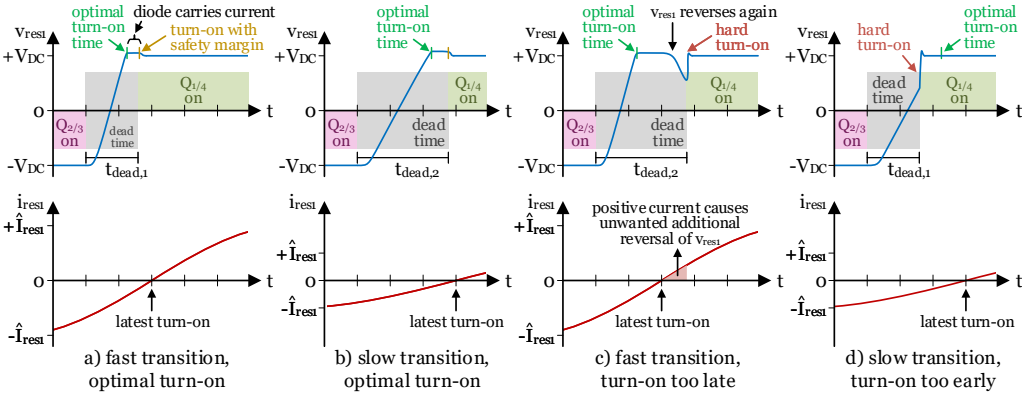

Figure 5.8: Switching transition under two different load conditions: a) optimal dead time $t_{dead,1}$ for the fast transition, b) optimal dead time $t_{dead,2}$ for the slow transition, c) using $t_{dead,2}$ for the fast transition causes hard switching, d) using $t_{dead,1}$ for the slow transition causes hard switching

is complete, i.e., v_{res1} exceeds V_{DC}. If the MOSFETs turn on earlier, no ZVS is achieved. If they turn on later, the rectifier diodes conduct the current i_{res1} while the FETs are still off, which increases conduction losses compared to turned-on MOSFETs. A small safety margin can be included to ensure ZVS is achieved, as marked in yellow. This results in dead time $t_{dead,1}$.

In Figure 5.8b and Figure 5.8d, the output power is lower, so the switching transition takes longer. The optimal turn-on time of Q1 and Q4 is marked in green in Figure 5.8b. The resulting dead time, including a safety margin, is $t_{dead,2}$. It is significantly longer than in the previous case.

ZVS cannot be achieved in many instances if a fixed dead time is used. For example, using the optimal dead time $t_{dead,2}$ of the light-load condition (Figure 5.8b) for the higher output power (Figure 5.8a) results in the switching transition shown in Figure 5.8c. The transition is completed long before Q1 and Q4 are turned on, which increases conduction losses during the switching transition. More importantly, since the primary-side resonant tank current changes sign before these FETs are turned on, the resonant tank voltage starts an additional, unwanted transition, and no ZVS can be achieved.

On the other hand, if the optimal dead time $t_{dead,1}$ for the high-power condition is used for light load, the transition of v_{res1} is not completed by the time Q1 and Q4 are turned on. As a result, the soft switching transition is interrupted, which partly causes a hard turn-on as well.

The solution to this problem is a dynamic adjustment of the primary-side dead time. The controller calculates the timing based on the direction of power flow, the switching frequency f_{sw}, the input voltage $V_{DC,in}$, and output load $R_{load} = \frac{V_{DC,out}}{I_{DC,out}}$. This is an extension to the controller presented in [354] and significantly increases efficiency and reduces EMI due to unwanted hard switching transitions.

5.1.4 Synchronous rectifying

Another improvement compared to [354] is the implementation of synchronous rectifying on the secondary side. Instead of the passive rectification, where only the diodes of the output side rectify the secondary-side resonant tank current, the MOSFETs are turned on whenever these diodes would conduct the current. This reduces voltage drops across the semiconductors and thus significantly decreases conduction losses. There are commercial synchronous rectifying integrated circuits (ICs) that measure the drain-source voltage across the MOSFET to detect periods in which the FET shall be turned on. However, the ICs found do not support the operation with the required output voltage of 800 V or more. Therefore, another concept was implemented, which is shown in Figure 5.9.

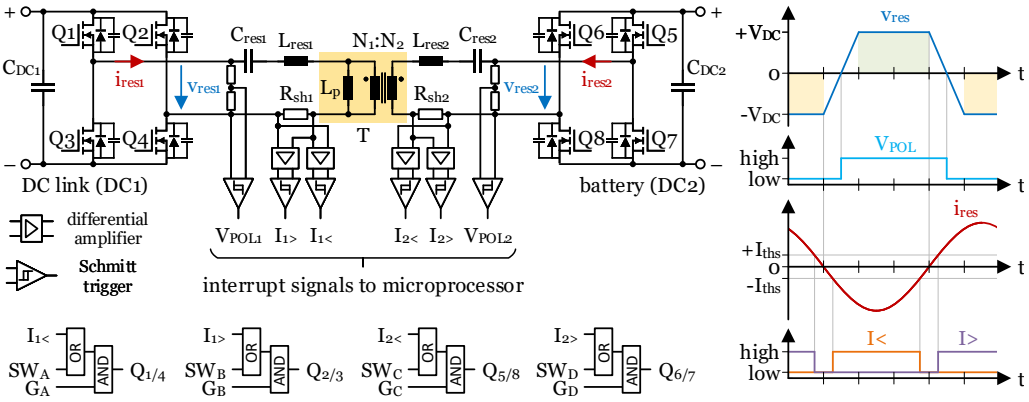

Figure 5.9: Resonant tank voltage and current signals to microprocessor and gate drivers used for synchronous rectifying

Schmitt trigger comparators are placed on both sides of the resonant circuit to let the microprocessor detect the polarity of the voltage v_{res} and the current i_{res}. Additionally, the current signals $I_{1/2<>}$, which determine whether the resonant tank currents are above or below a defined threshold, are connected to the gate drivers via logic gates. The three operating modes shown in Table 5.2 were implemented.

Table 5.2: Operating modes of the CLLLC gate drivers

$G_{A/B/C/D}$	$SW_{A/B/C/D}$	$I_{1/2<>}$	Description
0	–	–	FET turned off
PWM	1	–	FET controlled by PWM of microprocessor (e.g., primary side)
timer	0	HW	FET controlled by synchronous rectifying HW, gated by SW

In the first mode, the MOSFET is turned off. This can be used when the converter is off or on the output side if passive rectifying is used. In the second mode, only the microprocessor determines the MOSFET behavior with a PWM signal. This is used on the primary side. In the third mode, the software (SW) of the microprocessor determines when the synchronous rectifying hardware (HW) circuit shown in Figure 5.9 is allowed to turn on the MOSFET.
Synchronous rectifying is only used when the voltage and current signals can be detected reliably, and it benefits efficiency, which is the case above a certain voltage and current threshold. In this case, each edge of the secondary-side V_{POL} signal triggers the execution of an interrupt service routine (ISR) in the microprocessor. In the ISR, the $G_{A/B/C/D}$ signal of the respective secondary-side FETs is enabled for a certain period. A timeout value of 33% of the switching period minus a constant dead time of 150 ns was used in the prototype. During this time, the FET turns on whenever the respective current signal $I_{1/2<\!/\!>}$ is HIGH. However, the turn-on of the MOSFETs is delayed by the ISR call and the propagation delay of the gate driver, which causes the FETs to turn on slightly later than permitted by the V_{POL} signal.
For example, if power is transferred from DC1 to DC2 in forward mode, a rising V_{POL2} edge triggers the microprocessor, which enables the G_C signal. The FETs Q5 and Q8 are turned on while G_C and $I_{2<}$ are HIGH. The FETs turn off as soon as $I_{2<}$ becomes LOW or the microprocessor timeout clears the G_C signal. Ideally, the MOSFETs are turned on during the periods marked in light green in the v_{res} curve in Figure 5.9. Similarly, a falling V_{POL2} edge makes the microprocessor turn on the G_D signal. The FETs Q6 and Q7 are turned on while G_D and $I_{2>}$ are HIGH, ideally in the time frame marked in yellow in Figure 5.9.

5.2 Simulation of the AC/DC converter

As part of this thesis, a new ARCPI prototype was developed. Before designing the prototype, the inverter was simulated in *LTspice* and *MATLAB*/*Simulink*, among others. The *LTspice* simulation focused on the optimization of the ARCPI switching transition timings, using only one arm of the ARCPI and simulated time frames of typically less than 20 µs. The *MATLAB*/*Simulink* models were used to compare and optimize different PLLs and grid controllers of the inverter, i.e., using time horizons of multiple seconds. Instead of the ARCPI, only a simple 2L-VSI / B6 bridge was modeled using the *Simscape* “Specialized Power Systems” Library in *Simulink*. This has the advantage that the soft switching transitions do not have to be modeled in detail. Instead, a simplified switch model is used to speed up the simulation significantly.

5.2.1 ARCPI switching behavior

The *LTspice* model shown in Figure 5.10 was used to test the general principle of operation of the auxiliary circuit[2], to compare different values for the resonant components, and to optimize the switching behavior for the first operation of the prototype. Only one half bridge is simulated. The DC link is supplied by the constant voltage source on the left side. On the half-bridge output ("HB_A" on the right side), there is a constant current source that is set to different positive or negative values to emulate the switching cases described in Chapter 4.1.4.

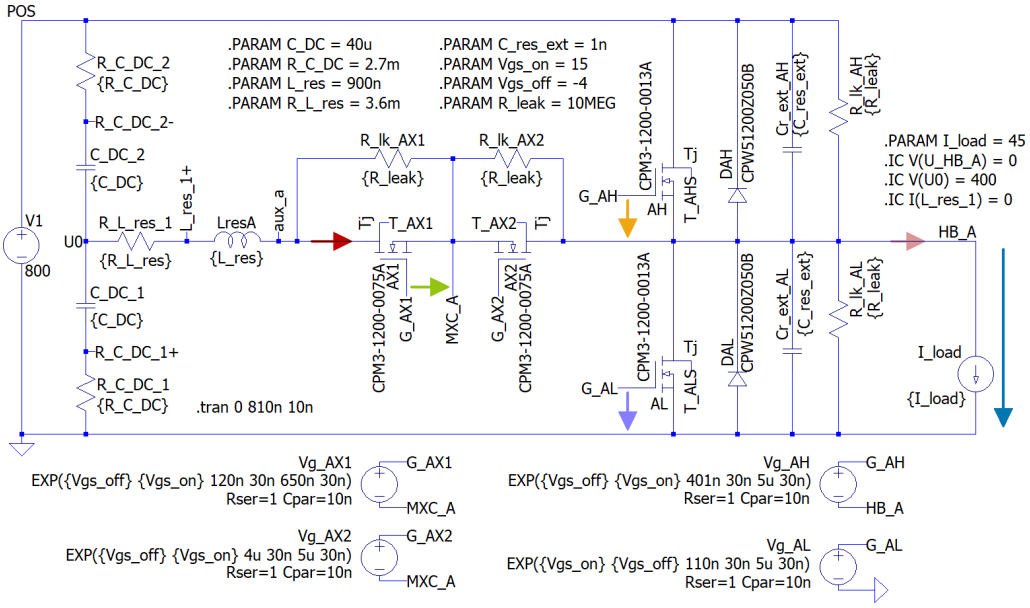

Figure 5.10: *LTspice* model of one ARCPI arm used to optimize switching patterns

The simulation models of the MOSFETs and diodes to be used in the prototype are provided by the manufacturer, *Cree/Wolfspeed*. For the main MOSFETs "AL" and "AH", the *CPM3-1200-0013C* model was selected. Both *CPM3-1200-0075A* and *CPM3-0900-0065B* were tested for the auxiliary FETs "AX1" and "AX2". Optionally, *CPW5-1200-Z050B* diodes ("DAL" and "DAH") are used anti-parallel to the main MOSFETs to reduce diode voltage drop during dead time.
The resonant capacitance is formed by the nonlinear parasitic drain-source capacitance of the main MOSFET ($C_{GD} \approx 270\ pF$ at 800 V [355]), the parasitic anode-cathode capacitance of the

[2] The simulation model shows the circuit used in the prototype. However, as will be explained later, it is recommended to change the order of the resonant inductors and auxiliary FETs as opposed to the circuit diagram shown, i.e., to connect "AX1" and "AX2" to "U0" and "LresA" between the auxiliary FETs and the main bridge output "HB_A".

diode ($C_{AC} \approx 170\,pF$ at 800 V [356]), and a discrete capacitor ($C_{res,ext} = 1\,nF$), which extends the otherwise very short transitions times. This results in $C_{res,total} \approx 1.44\ nF$ at 800 V. The parasitic semiconductor capacitances are nonlinear — the capacitance increases at lower voltages, which has to be considered in the switching pattern generation. For example, at 100 V, the overall capacitance is $C_{res,total} \approx 2\ nF$. The use of a significant constant external capacitance reduces this nonlinearity. A resonant inductor value L_{res} of 900 nH was chosen to simulate a 1 µH inductor with a -10% decrease due to saturation and component tolerance.
The FETs are controlled by the pulse voltage sources shown at the bottom of Figure 5.10, which emulate the gate driver behavior using exponential rise and fall curves. A DC link voltage of 800 V was selected. Each side of the split DC link capacitor is 40 µF in the simulation, which was sufficient to keep the potential "U0" stable. Leakage resistors with 10 MΩ were placed between various nodes to speed up and stabilize the simulation.

The results for the simulation of the three switching cases using the *CPM3-1200-0075A* auxiliary FETs are shown in Figure 5.11. In case 1, a load current of +45 A was applied. This corresponds approximately to the peak current expected at 32 A_{RMS} at the grid connection, which is reached at the maximum output power of 22 kVA in a 230/400 V grid. Auxiliary FET AX1 is used to allow a ZVS transition from the low-side FET AL to the high-side FET AH. AX2 remains off, and only its body diode is used. In case 2, the output current is -5 A. AX1 supports the switching transition. In case 3, the output current is -35 A, and no auxiliary FETs are used because the output current itself allows a ZVS transition. The transitions from the high side to the low side, which use AX2,

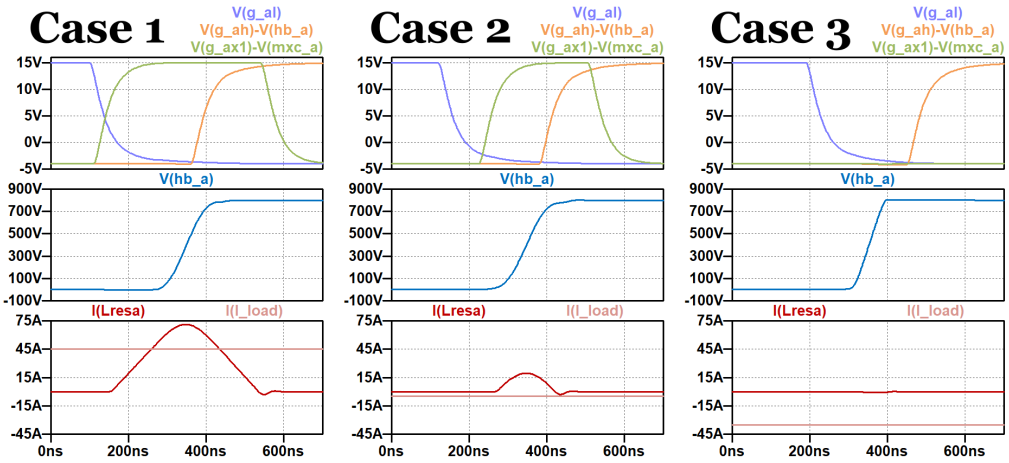

Figure 5.11: *LTspice* simulation results of the three switching cases discussed in Chapter 4.1.4. From top to bottom: Gate-Source voltages of the low side (purple), high side (orange), and AX1 FET (green), voltage between the half-bridge output and DC- (blue), load current (light red) and current through the auxiliary circuit (red) — the direction of the load and auxiliary circuit currents is indicated in Figure 5.10.

are not shown because they are symmetric to the cases discussed here with reversed current signs. The gate driver timings were optimized manually to obtain ZVS at turn-off and turn-on while keeping the current through the auxiliary circuit at relatively low levels. Contrary to the operation described in the literature (see Chapter 4.1.4), no boost current was used since almost perfect ZVS switching could be achieved without a boost current. This helps to minimize the average and peak currents and, thus, the power losses through the auxiliary circuit.
The dead time between turn-off and turn-on of the main MOSFETs is 260 ns in the examples. The maximum slope $\frac{\mathrm{dV_{DS}}}{\mathrm{dt}}$ of the FETs is approximately $8.1\ \frac{\mathrm{kV}}{\mu\mathrm{s}}$ in case 1, about $7.5\ \frac{\mathrm{kV}}{\mu\mathrm{s}}$ in case 2, and $10.7\ \frac{\mathrm{kV}}{\mu\mathrm{s}}$ in case 3. In the last case, it cannot be influenced by the gate drivers, but only by using a different $C_{res,ext}$.

As mentioned, the main MOSFET and the anti-parallel diodes nearly achieve ZVS, so there are almost no switching losses. Their conduction losses can be roughly estimated by assuming that for each phase and at each point in time, exactly one main FET is in line with the output current. Using the RMS inverter output current of 32 A present at nominal power and the datasheet value $R_{DS,on}$ of 13 mΩ at $V_{GS} = 15\ V$ and $T_j = 75°C$ [355], the conduction (and thus overall) power losses in all main FETs add up to 40 W:

$$\begin{aligned} P_{loss,main,3ph} &\approx P_{loss,main,3ph,cond} \approx 3 \cdot R_{DS,on,main} \cdot I_{out,RMS}^2 \\ &= 3 \cdot 13\ m\Omega \cdot (32\ A)^2 \approx 39.9\ W \end{aligned} \tag{5.1}$$

The auxiliary circuit faces different losses depending on the momentary output current. All auxiliary FETs turn on and off with ZCS, so their switching losses are negligible. The highest conduction losses occur at high output currents, where cases 1 and 3 alternate at the two switching operations from the low side to the high side and vice versa. The highest auxiliary FET current occurs in the simulated case 1, with a peak of 71.1 A. From t = 100 to 600 ns, the RMS current I(Lresa) is 40.4 A, according to *LTspice*. Using datasheet values of $R_{DS,on}$ of 90 mΩ at $V_{GS} = 15\ V$, $I_D = 40\ A$, and $T_j = 75°C$ for the auxiliary FETs [357], the conduction (and thus overall) losses during this switching transition time frame of 500 ns are approximately 147 W for one auxiliary FET:

$$P_{loss,AX1,peak}(I_{out}(t_i)) \approx R_{DS,on,aux} \cdot (I_{aux,RMS}(I_{out}))^2 \tag{5.2a}$$

$$P_{loss,AX1,peak}(45\ A) \approx 90\ m\Omega \cdot (40.4\ A)^2 \approx 146.9\ W \tag{5.2b}$$

According to the simulation, the average losses are slightly higher than the calculated ones — 178 W during the 500 ns time frame, i.e., 89 µJ per switching transition.
The other auxiliary FET remains turned off with $V_{GS} = -4\ V$. According to the datasheet, the drain-source voltage across the body diode is −6.67 V at $I_D = -40.4\ A$, which corresponds to

momentary losses of 270 W of one auxiliary FET according to Equation 5.3b. The simulated losses are also 270 W (or 135 µJ per transition).

$$P_{loss,AX2,peak}(I_{out}(t_i)) \approx V_{SD,off,aux} \cdot I_{aux,RMS} \tag{5.3a}$$

$$P_{loss,AX2,peak}(45\ A) = 6.67\ V \cdot 40.4\ A \approx 269.5\ W \tag{5.3b}$$

The same switching transition is simulated for a hard-switching topology without the auxiliary circuit to illustrate the advantage of soft switching. In this case, the combined switching loss energy for the high and low-side main MOSFETs of one phase is approximately 1.41 mJ. That is more than six times higher than the loss energy in the auxiliary circuit of the soft switching topology ($89\ \mu J + 135\ \mu J = 224 \mu J$).

Since the auxiliary circuit is only used once per switching period, the average conduction losses in the auxiliary circuit are only $\frac{500\ ns}{10\ \mu s} = 5\%$ of the previously calculated losses when using a switching frequency of 100 kHz. Therefore, the worst-case auxiliary FET losses for the auxiliary circuits of one phase are 20.8 W using datasheet values and 22.4 W in the simulation.

$$P_{loss,AX1+AX2,avg}(I_{out}(t_i)) = (P_{loss,AX1,peak} + P_{loss,AX2,peak}) \cdot \frac{t_{transition}}{T_{sw}} \tag{5.4a}$$

$$P_{loss,AX1+AX2,avg}(45\ A) = (146.9\ W + 269.5\ W) \cdot \frac{500\ ns}{10\ \mu s} \approx 20.8\ W \tag{5.4b}$$

On average, the mean overall losses of the auxiliary FETs are smaller since the operating point investigated in the calculations is only reached during the output current peak at point d in Figure 5.12. The simulation is repeated for all points shown in Figure 5.12 to calculate the average losses presented in Table 5.3. In summary, the overall auxiliary FET losses at nominal output power are approximately 14 W for one phase and 42 W for all three phases.

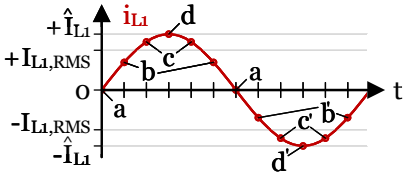

Figure 5.12: One period of the grid current and points used for the auxiliary FET loss calculation in Table 5.3

As shown in Figure 5.11, the switching behavior in the *LTspice* simulation looked fine for the *CPM3-1200-0075A* auxiliary FET simulation model. However, when using the *CPM3-0900-0065B* model as an alternative, significant oscillations were found in the auxiliary current and the voltage across the auxiliary FETs right after they were turned off at the end of the switching

Table 5.3: Auxiliary FET loss calculation at different points in time using the maximum RMS output current of 32 A

	$i_{out}(t_i)$	$P_{loss,\ AX1+AX2,\ avg,\ datasheet}$	$P_{loss,\ AX1+AX2,\ avg,\ simulation}$
a	0.0 A	6.5 W	9.0 W
b	22.2 A	9.7 W	10.1 W
c	38.7 A	17.3 W	18.1 W
d	45.0 A	20.8 W	22.4 W
mean ($\frac{a+2b+2c+d}{6}$)		13.5 W	14.6 W

transition. As discussed in [C1], a likely reason for this is that at the end of the switching transition, the reverse recovery charge of the auxiliary FET excites the additional resonant circuit formed by the resonant inductor and the parasitic capacitance of the auxiliary FET. While this oscillation is small in Figure 5.11, it is very prominent when using the *CPM3-0900-0065B* simulation model (see Figure 5.13).

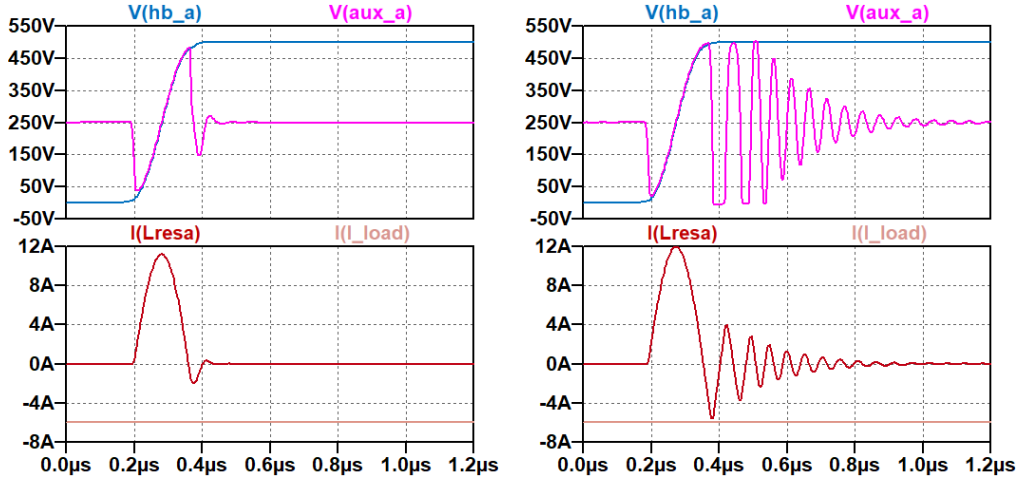

a) CPM3-1200-0075A: oscillations highly damped

b) CPM3-0900-0065B: oscillations poorly damped

Figure 5.13: Behavior of the switching transition using two different MOSFET simulation models under otherwise same conditions — location of measurement signals shown in Figure 5.14a

As was later discovered using the prototype, unlike in the simulation, the ringing is also present when using the *CPM3-1200-0075A*. A solution to quickly eliminate the ringing is to change the order of the auxiliary FETs and the resonant inductors, as shown in Figure 5.14. Unfortunately, this was only detected after the prototype was built and could not be tested in a new revision due to time constraints, as an extensive redesign of the electronics would have been necessary.

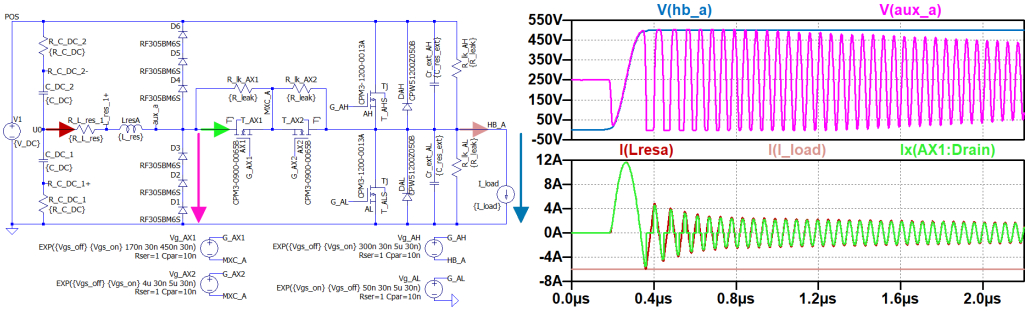

a) Resonant inductor connected to “U0” (DC0), auxiliary FETs placed at the half-bridge output (as in the prototype): severe oscillations

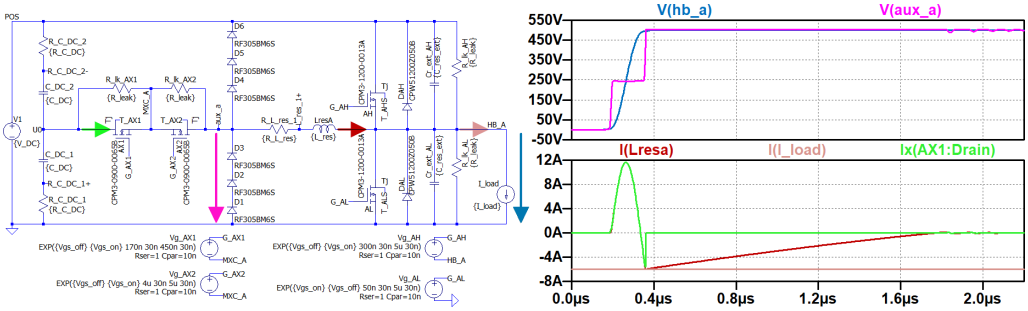

b) Auxiliary FETs connected to “U0” (DC0), resonant inductor placed at the half-bridge output (recommended): no oscillations

Figure 5.14: Effect of the component placement in the auxiliary circuit — diodes from “aux_a” to “POS” (DC+) and ground (DC−) clamp the “aux_a” potential within the DC link potentials

5.2.2 DDSRF-PLL

The Decoupled Double Synchronous Reference Frame (DDSRF) PLL presented in Chapter 4.2.2 was implemented in a *MATLAB* script to find and evaluate suitable filter settings under regular and impaired grid conditions. A block diagram of the most promising PLL structure presented in the following and implemented in the prototype is shown in Figure 5.15.

A second-order LPF is used to derive the filtered voltages $\bar{v}_{d+/q+/d-/q-}$ used for the decoupling network and the converter control algorithm. The filter is necessary to cancel out the second harmonic of the grid frequency from the reference frames rotating in opposing directions. The grid frequency f_g derived from the unfiltered decoupled voltage v'_{q+} is filtered by a fourth-order LPF. This yields a smooth signal $\bar{f}_g$ that is used for the grid frequency and virtual inertia (VI) control algorithm.

The grid angle is an output of the PLL, which is also needed in the decoupling and Park transformations of the PLL. In the time-discrete PLL implemented in the simulation and the prototype, the grid angle of the previous cycle i–1 is used in the current cycle i to solve this cyclic dependency. However, the angle will change from one to the next control loop cycle. The

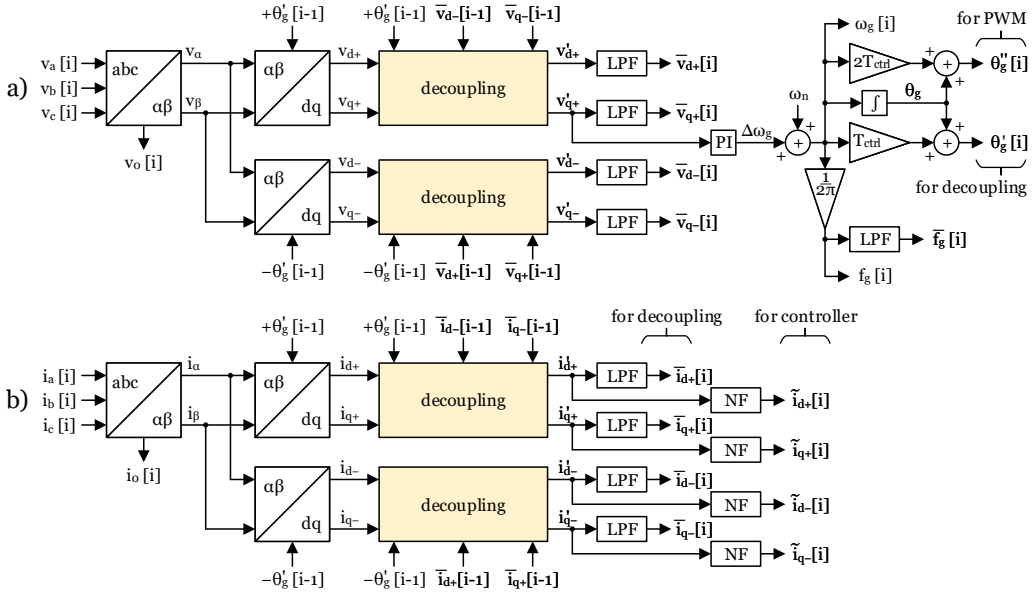

Figure 5.15: DDSRF-PLL implemented in the *MATLAB* simulation and the prototype

projected phase difference during one control loop period $\Delta\theta_g = \omega_g T_{ctrl}$ is added to the grid angle to compensate for this inaccuracy. This results in the projected grid angle of the next cycle $\theta'_g \approx \theta_g[i+1]$ used for the transformations. In the prototype, the measurements needed for the PLL are captured in cycle i, the PLL measurements are processed in the controller in cycle i+1, and the PWM is applied in cycle i+2. Consequently, the reverse Park transformation needed for the PWM uses the projected grid angle $\theta''_g[i] \approx \theta_g[i+2]$ shifted by two control loop periods.
For the decoupling of the current signals (Figure 5.15b), a second-order LPF is used, similar to the voltage decoupling. However, unlike in the literature discussed in Chapter 4.2.2, a notch filter (NF) is proposed to filter the decoupled currents $i'_{d+/q+/d-/q-}$ to derive the current signals $\tilde{i}_{d+/q+/d-/q-}$ that are used by the current controller. This hybrid approach was chosen to improve the current controller performance while maintaining robustness in the decoupling structure.
The filter settings are described in detail in [C2] and summarized in Table 5.4. The angular cut-off frequencies ω_c and the NF bandwidth ω_{BW} are given relative to the nominal angular grid

Table 5.4: Low-pass and notch filter settings for the voltage (v), current (i), and frequency (f) filters in the DDSRF-PLL implemented in the simulation and the prototype

$LPF_{v/i}$		**NF_i**			**LPF_f**			
ω_c	Q	ω_c	ω_{BW}	Q	$\omega_{c,1}$	$\omega_{c,2}$	Q_1	Q_2
$0.42 \cdot \omega_{g,n}$	0.35	$2 \cdot \omega_{g,n}$	$0.3 \cdot \omega_{g,n}$	$\frac{\omega_c}{\omega_{BW}}$	$0.16 \cdot \omega_{g,n}$	$0.08 \cdot \omega_{g,n}$	0.45	0.35

frequency $\omega_{g,n} = 2\pi \cdot 50\ Hz$. The factors K_p and K_i of the PI controller estimating the grid phase are calculated as described in [358, pp. 4f.] and [C2]:

$$\omega_{natural} = \frac{\ln\left(\frac{1}{\delta \cdot \sqrt{1-\zeta^2}}\right)}{t_s \cdot \zeta} \tag{5.5a}$$

$$K_p = 2\zeta \frac{\omega_{natural}}{\hat{V}_{g,n}} \tag{5.5b}$$

$$K_i = \frac{\omega_{natural}^2}{\hat{V}_{g,n}} \tag{5.5c}$$

The nominal grid voltage amplitude $\hat{V}_{g,n}$ is $\sqrt{2} \cdot 230$ V. The damping ratio ζ was set to 0.247. When excited by a step response, the PI controller shall reach an error band of 10% after a settling time of 0.168 s, i.e., $\delta = 0.1$ and $t_s = 0.168$. This yields $K_p \approx 0.0854$ and $K_i \approx 9.6765$.

Several grid events were simulated, such as sudden or gradual voltage or frequency variations, unbalanced grids, harmonics, noise, measurement offsets, and frequency reversals. Selected scenarios are shown in Figure 5.16. The grid voltages $v_{a/b/c}$ shown in the first row vary according to the events and are used as input for the PLL.
The resulting resulting direct (d) and quadrature (q) components for the positive (+) and negative ($-$) reference frames are shown in rows two to five. The raw, unfiltered signals $v_{d+/q+/d-/q-}$ are displayed in yellow, the decoupled signals $v'_{d+/q+/d-/q-}$ in turquoise, and the filtered signals $\bar{v}_{d+/q+/d-/q-}$ in dark blue. For comparison, the signals $v_{d/q}$ derived by a regular SRF-PLL with similar PI controller settings are visualized with dashed red lines along with $v_{d+/q+}$.
The "regular" grid voltage amplitude is represented by v'_{d+}. On the other hand, v'_{q+} is controlled to be zero. Put simply, the lower its amplitude, the better the phase estimation. Any deviation to 0 V indicates a phase error and causes a correction of the estimated grid frequency and phase. The decoupled negative-sequence signals $v'_{d-/q-}$ represent asymmetric grid voltage components. In steady state (e.g., before $t = 0.03\ s$ in Figure 5.16a), all decoupled (v') and filtered ($\bar{v}$) positive- and negative-sequence signals are constant. The raw positive-sequence voltages $v_{d+/q+}$ are also constant in a symmetric grid. However, the raw negative-sequence voltages $v_{d-/q-}$ always oscillate since the grid voltage phasor is rotating with twice the grid frequency from the perspective of the negative-sequence reference frame (compare Chapter 4.2.2). Therefore, the decoupled voltages are filtered with LPFs.
However, this introduces a significant delay in the filtered signals when the grid voltages vary. This can be seen in Figure 5.16a. At $t = 0.03\ s$, the grid voltage is reduced from 100% to 80% of the nominal grid voltage. Afterward, it is increased to 110% at $t = 0.13\ s$. While the signals $v_{d/q}$ generated from the SRF-PLL (red) and the raw positive-sequence voltages $v_{d+/q+}$ of the DDSRF-PLL (yellow) perfectly represent the actual grid voltages, the low-pass filtered signals

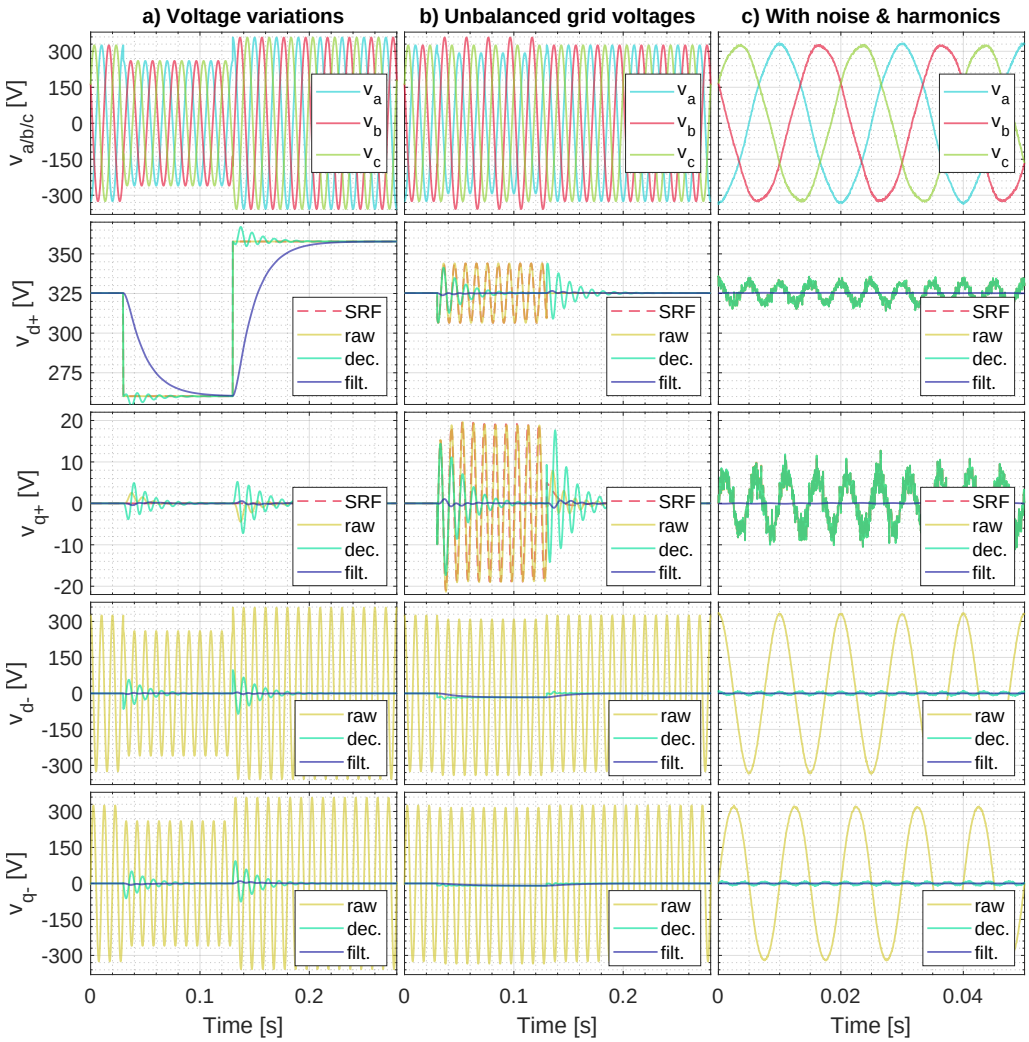

Figure 5.16: DDSRF-PLL *MATLAB* simulation results: a) grid voltage variations, b) unbalanced grid voltages, c) grid voltages with noise and harmonics — from top to bottom: grid voltages, positive-sequence direct and quadrature components, negative-sequence direct and quadrature components

(dark blue) experience significant delay. This causes a perturbation in the decoupled signals of the opposing reference frame (turquoise), which uses these filtered signals for decoupling. With the selected LPF settings, the filtered voltage signal v_{d+} reaches 80% of the applied voltage step after 42 ms.

While introducing significant delay in step responses, the DDSRF-PLL is advantageous under asymmetric grid conditions, as shown in Figure 5.16b. $\hat{V}_a$ is reduced to 90%, and $\hat{V}_c$ is increased

to 110% from $t = 0.03\ s$ to $0.13\ s$. During this period, the SRF-PLL and the raw DDSRF-PLL signals experience significant oscillations persisting until the grid is symmetric again. The asymmetry cannot be represented in the SRF-PLL. However, after a brief perturbation, the decoupled signals $\mathrm{v_{d-/q-}}$ of the DDSRF-PLL accurately reflect the asymmetry (here: $v_{d+} \approx 325\ V$, $v_{q+} = 0\ V$, $v_{d-} \approx -16\ V$, and $v_{q-} \approx -9\ V$).
The grid voltages are symmetric in the third example (Figure 5.16c). However, noise and a fifth harmonic component with an amplitude of 2% of the nominal grid voltage are introduced to represent more realistic input signals for the PLL. The distortions can clearly be seen in the raw and decoupled signals of the DDSRF-PLL and the signals of the SRF-PLL, which are all almost identical. However, the filtered components of the DDSRF-PLL are almost constant, potentially allowing for a more robust grid control.

While the impairment of the reaction time caused by the low-pass filtering could be tolerable for the grid voltages, it is desirable to avoid this delay for the current signals for a better current controller performance. Therefore, for the current signals, a pure low-pass filtered approach, as used for the voltage signals (Figure 5.15a), is compared with the hybrid filter method (Figure 5.15b). Figure 5.17a shows the output of the PLLs if only LPFs are used, i.e., the filtered signal corresponds to $\bar{\mathrm{i}}_{\mathrm{d+/q+/d-/q-}}$. In contrast, Figure 5.17b shows the notch filtered signals $\tilde{\mathrm{i}}_{\mathrm{d+/q+/d-/q-}}$ derived using the hybrid filter method. In both cases, the inverter starts in standby operation with 0 A and ramps up to a symmetric three-phase current with an amplitude of $\hat{i}_{a/b/c} = 12\ A$ at $t = 0.03s$. Afterward, the currents become asymmetric with $i_c = 0$ and $i_a = -i_b$. Noise is added to represent more realistic input signals impaired from grid disturbances, switching operation, and analog-to-digital converter (ADC) measurement.
As shown in Figure 5.15a, the raw and decoupled positive reference frame signals follow the grid current amplitude well, and the low-pass filtered current experiences a significant delay. In contrast, the notch-filtered signal is almost identical to the decoupled signal in Figure 5.15b. During the transition to asymmetric operation at $t = 0.15\ s$, the low-pass filtered signals remain very stable, but the notch-filtered signals are disturbed for a brief moment. However, the perturbation is smaller in amplitude than the decoupled signal. A comparable oscillation can be seen in the notch-filtered negative-sequence signal when the positive-sequence currents change at $t = 0.03s$ in the last two rows of Figure 5.15b. At the same time, the negative-sequence signal follows the negative-sequence current transition at $t = 0.15\ s$ very well.
In summary, the notch-filtered signals may experience oscillations during sudden current changes in the opposing reference frame. However, they are expected to improve the achievable controller reaction time in case of deviations from the measured to the desired current within the same reference frame. Therefore, the hybrid filter is implemented in the prototype.

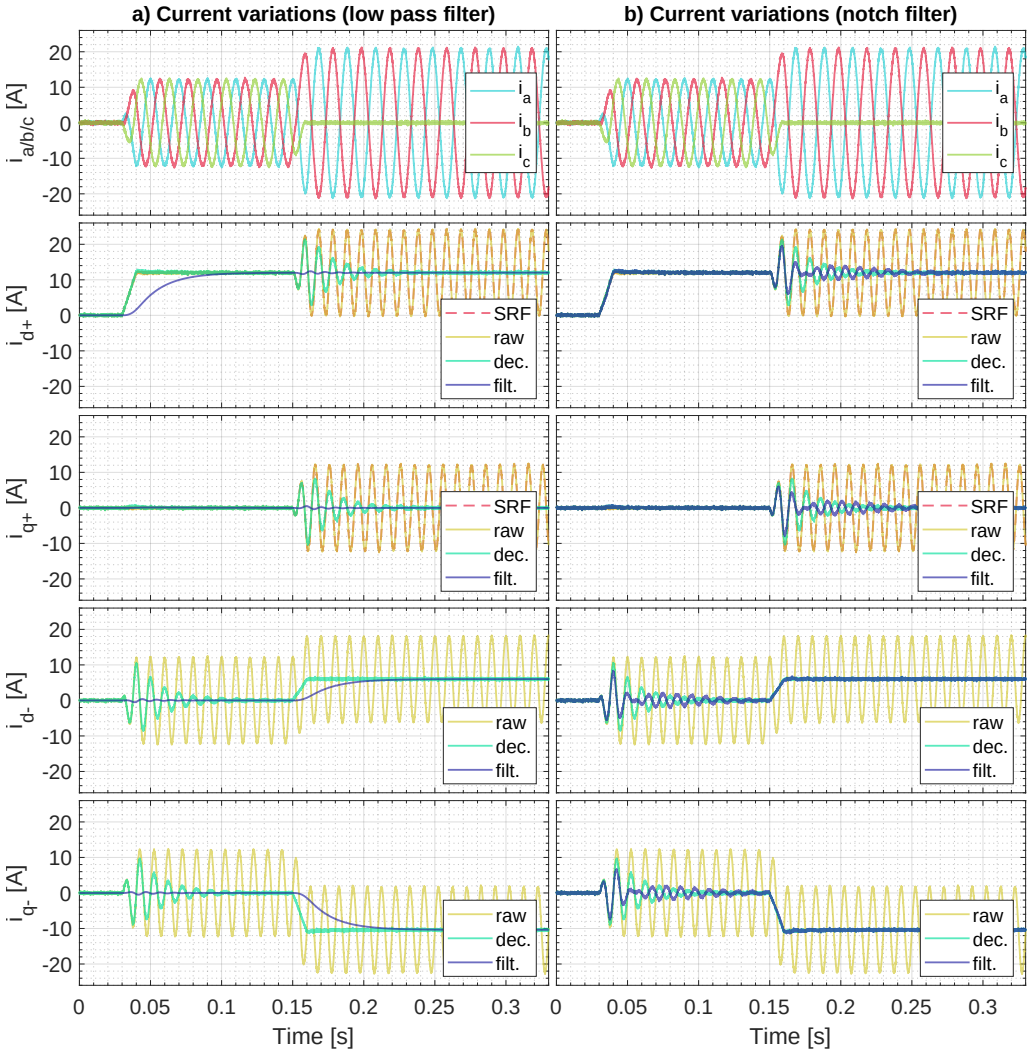

Figure 5.17: DDSRF-PLL *MATLAB* simulation results: a) current variations with noise (low-pass filter output), b) current variations with noise (notch filter output)

The reaction of the raw and filtered estimated grid frequency signals f_g and $\bar{f}_g$ to frequency steps and ramps is shown in Figure 5.18. The unfiltered signal follows the actual frequency very well. Nevertheless, for more robust frequency control and smooth VI emulation even under severely disturbed grid conditions, the filtered frequency shall be used for these control algorithms.

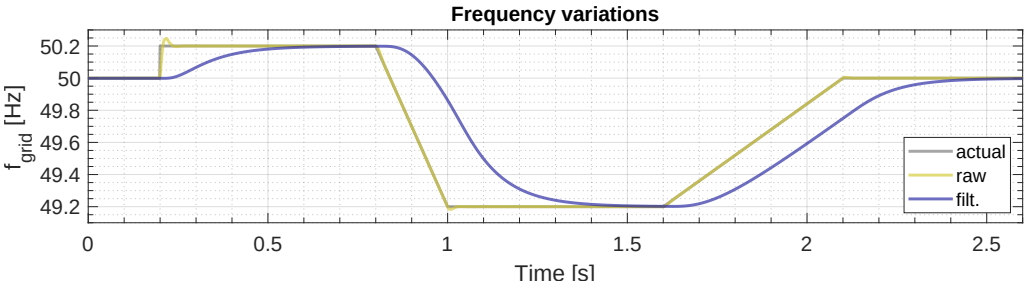

Figure 5.18: DDSRF-PLL *MATLAB* simulation result: frequency variations — raw and low-pass filtered outputs

5.3 Design of the AC/DC converter prototype

The ARCPI prototype shown in Figure 5.19 was developed and characterized in this thesis.

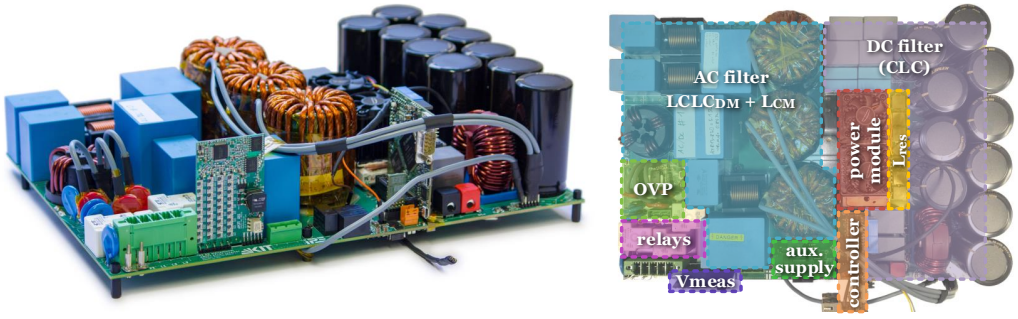

Figure 5.19: a) Photo of the ARCPI converter prototype, b) functional sections of the main board

It comprises a power module, resonant circuit, DC and AC filters, an over-voltage protection (OVP) circuit, grid-side main and pre-charge relays, a controller board, and measurement electronics. A block diagram of the components involved in the power flow is also shown in Figure 5.20. The power electronic and filter circuit is depicted in more detail in Figure 5.21.
The AC filter component values are $C_{grid,1} = 4.7\ \mu F$, $L_{grid,1} = 15\ \mu H$, $C_{grid,2} = 20\ \mu F$, $L_{grid,2} \approx 320\ \mu H$. Due to a lack of commercial components, $L_{grid,2}$ was custom-designed and -built using four stacked *DMEGC DH571060* iron-nickel powder cores and 25 windings with a 700x0.1 mm Litz wire. Various values for the series resistances of $C_{grid,1/2}$ were compared. They support damping oscillations when the load resistance of the AC side is low, for example, when little or no power is transferred in V2L mode. Eventually, resistors with an effective value of 1.25 Ω (4.5 W power rating) for $C_{grid,1}$ and 1.1 Ω (10 W rating) for $C_{grid,2}$ were used. The inductor L_{CM} has a common mode inductance of 750 µH.

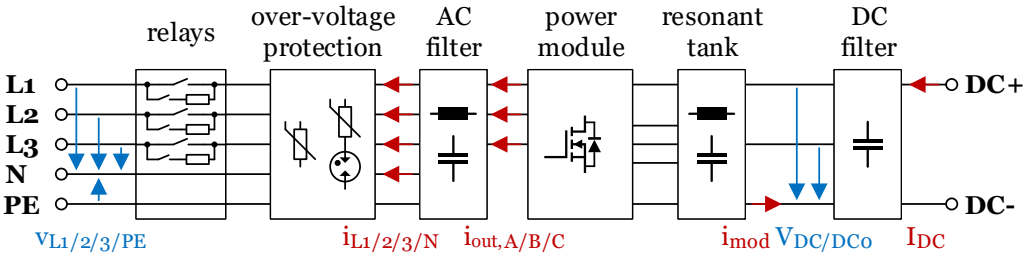

Figure 5.20: Functional blocks of the ARCPI prototype with voltage and current measurements

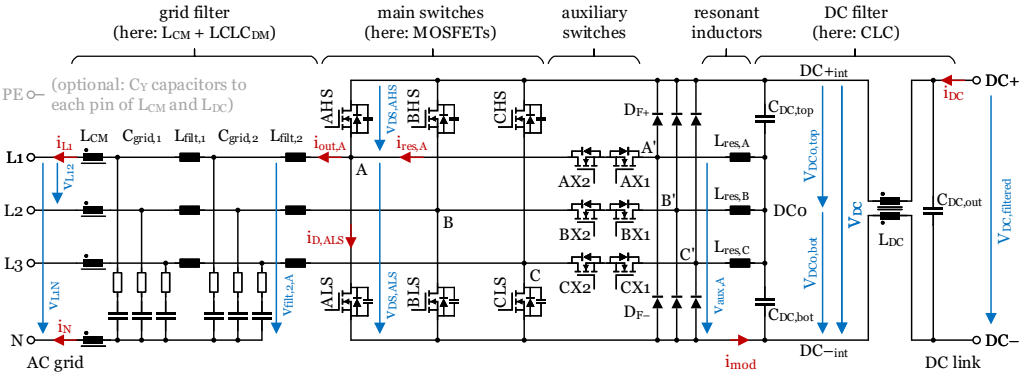

Figure 5.21: Simplified schematic of the power electronics with current sign and naming convention used in this thesis

The split DC filter capacitances $C_{DC,top/bot}$ consist of electrolytic and foil capacitors with an overall capacitance of $C_{top} = C_{bot} \approx 3.46\ mF$. $C_{DC,out}$ (10 µF) consists of foil capacitors. The effective capacitance from DC+ to DC− is approximately 1.73 mF. L_{DC} has a 1.5 mH common mode and an 8 µH differential mode inductance per winding.
Three surface-mount device (SMD) inductors with an overall inductance of 990 nH were connected in series to form L_{res}. Low-loss NP0 ceramic SMD capacitors with an effective capacity of $C_{res,ext} = 1\ nF$ were added to the PCB close to the power module.

The inverter measures 35.5 x 25 x 10 cm^3 and weighs 8.25 kg, including the main, controller, measurement, and gate driver boards, the power module with cooling fans, AC and DC filters, pre-charge and discharge resistors, and grid-side relays. External cables and a housing are not included. Based on the maximum continuous power of 22 kW, the power density of the prototype is 2.48 kW/dm^3 or 2.67 kW/kg.

5.3.1 Configuration and operation

Similar to the DC/DC converter, the AC/DC converter can be configured and operated using a UART interface. The most relevant commands are summarized in Appendix A.5. Important measurements and states are transferred via UART and CAN. They can also be visualized with a *LabVIEW* interface on a computer, as shown in Figure 5.22. Beside the AC and DC voltages, currents, and powers, the frequency, efficiency, and various temperatures and states are shown. Moreover, the temporal course of the positive-, negative-, and zero-sequence voltages and currents, as well as the grid frequency, are visualized.

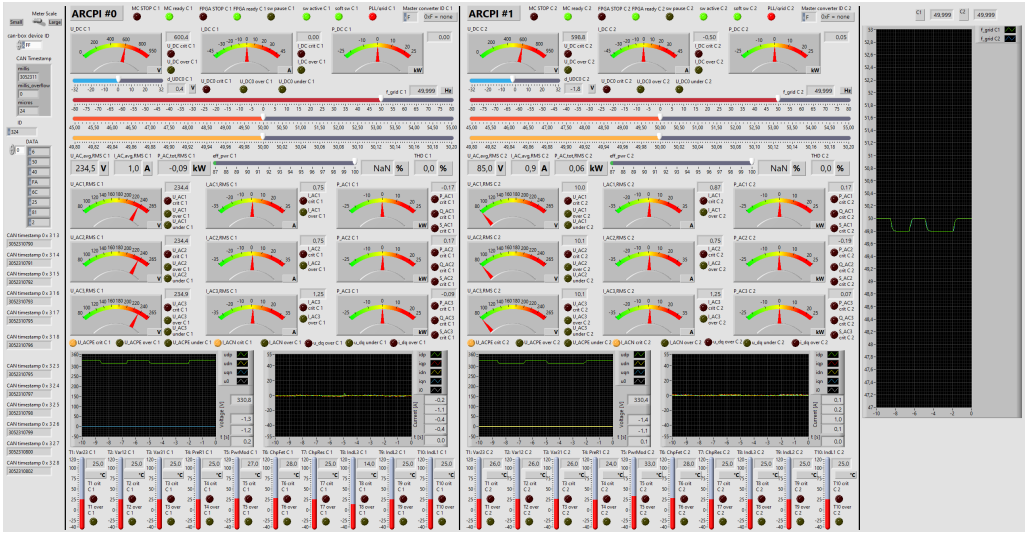

Figure 5.22: *LabVIEW* interface to visualize the ARCPI converter measurements and states received via CAN

5.3.2 Power module

Custom power modules for the ARCPI prototype were designed and manufactured in-house (compare [C1]). Two of the modules are shown in Figure 5.23. The module was conceptualized as part of this thesis, and the manufacturing was carried out by colleagues at our institute.
An *Infineon EconoPACK2* was used as housing. Similar to the simulation presented in Chapter 5.2.1, all modules contain six *Cree/Wolfspeed CPM3-1200-0013A* SiC MOSFETs ($V_{DS} = 1200\ V, R_{DS,on} \approx 13\ m\Omega$ [355]) used for the main MOSFETs (A/B/C LS/HS). *Cree/Wolfspeed CPM3-0900-0065B* ($V_{DS} = 900\ V, R_{DS,on} \approx 65\ m\Omega$ [359]) and *Cree/Wolfspeed CPM3-1200-0075A* ($V_{DS} = 1200\ V, R_{DS,on} \approx 75\ m\Omega$ [357]) were compared for the six auxiliary FETs that

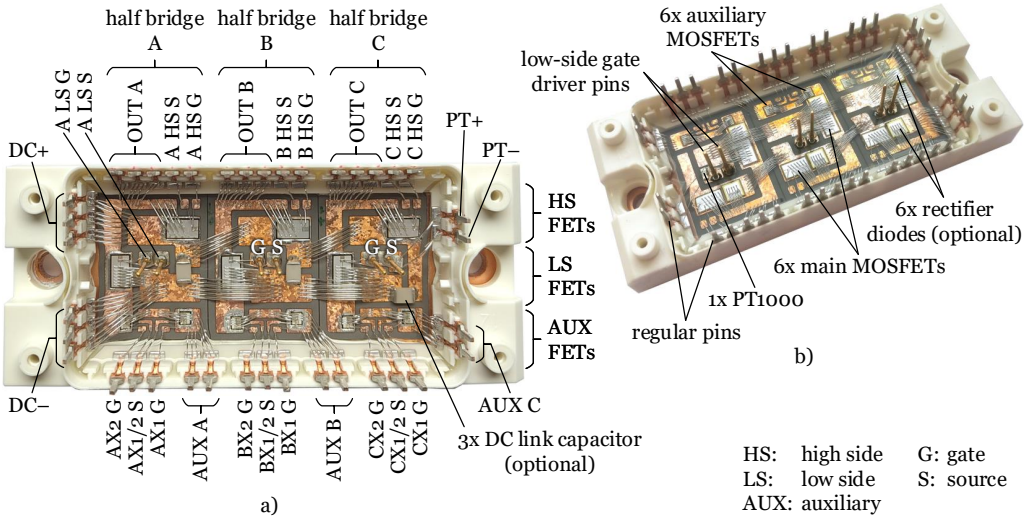

Figure 5.23: Photos of the power module used in the ARCPI prototype: a) with internal DC link capacitors and without rectifier diodes, b) with rectifier diodes and without internal DC link capacitors

are also included in the module (AX/BX/CX 1/2). A sinterable PT1000 temperature sensor by *Heraeus* was placed inside the module to estimate its internal temperature.
In addition, some of the modules contain rectifier diodes, internal DC link capacitors, or both. For the rectifier diodes, six *Cree/Wolfspeed CPW5-1200-Z050B* SiC diodes ($V_R = 1200\ V, V_F \approx 1.1\ V$ [356]) were placed anti-parallel to the main MOSFETs. Optionally, three DC link capacitors (*KYOCERA AVX 1812GA102JAT1A*, 1 nF, 2 kV, −55 to 125°C, C0G dielectric), one per half-bridge, were placed inside the power module close to the half bridges.

The power module is detachable from the main board to simplify testing different module variants. A gate driver board that controls the MOSFETs is connected to the main board from the other side. The receptacles for the power module pins that need to be connected to the gate driver board are both press-fit to the main board and soldered to the gate driver board. The assembly is illustrated in Figure 5.24, and the bottom side of the gate driver board is shown in Figure 5.25d.

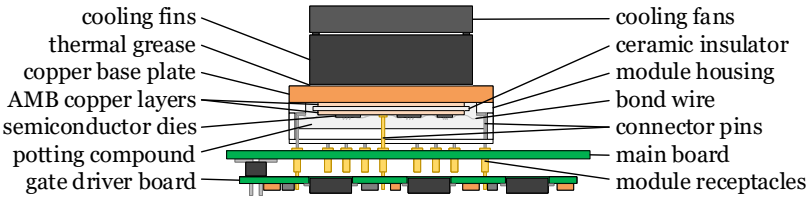

Figure 5.24: Side view of the assembly with power module, main board, and gate driver boards

5.3.3 Controller hardware and software

The custom-designed separate controller board, shown in Figure 5.25a/b, is placed on the main board, as seen in Figure 5.19. It comprises both an *Infineon AURIX TriCore TC375AA* micropro-

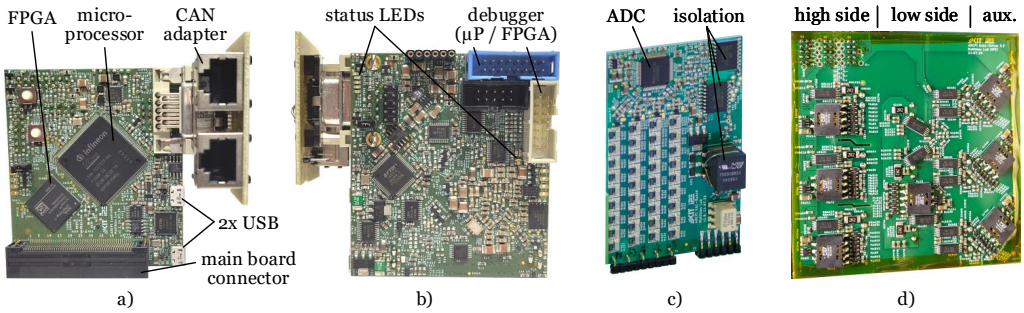

Figure 5.25: a) Top and b) bottom side of the controller board, c) AC voltage sense board, d) gate driver board below the main board

cessor with three cores and a *Xilinx Spartan-7 XC7S50* field-programmable gate array (FPGA). An overview of the functional blocks of the microprocessor and FPGA is shown in Appendix A.4. Core 0 of the processor is responsible for the UART and CAN communication used to control and configure the AC/DC converter and send measurements and states to the charge controller. Core 1 uses SPI to communicate with the FPGA and the DC/DC converter and processes measurement signals. Core 2 runs the control loop, executed with $f_{ctrl} = 20\ kHz$. The FPGA communicates to all ADCs via SPI and calculates derived signals. For example, the DDSRF-PLL and an RMS calculation are implemented on the FPGA to calculate grid-related measurements from the grid current sensors, as well as the voltage measurements obtained from the grid voltage ADC board shown in Figure 5.25c. The communication to each ADC and the subsequent measurement signal processing run mostly in parallel. Afterward, the FPGA synchronously transmits all measurements and states to the microprocessor using three parallel 50 MHz SPI buses. A CRC is added to detect data corruption. The FPGA receives the desired duty cycles calculated by the microprocessor control loop for the three half bridges and controls the gate drivers of the FETs accordingly.

The basic controller structure, shown in Figure 5.26, is relatively similar to conventional controller structures known from grid-following inverters. The DDSRF-PLL described in Chapter 5.2.2 was used in the prototype. The remaining parts will be explained in the following chapters.

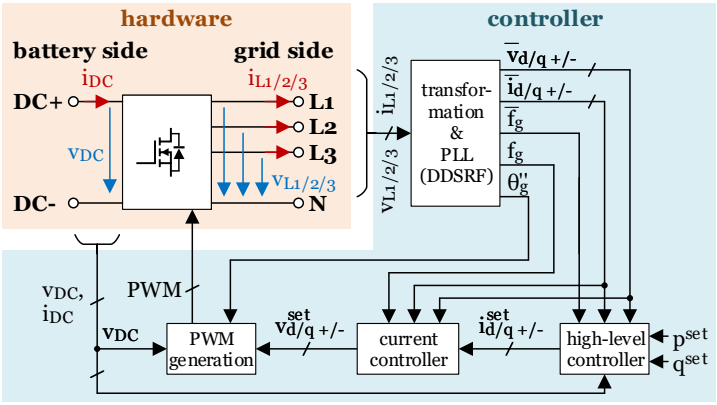

Figure 5.26: Overview of the AC/DC converter controller structure — adapted from [C2]

5.3.4 PWM generation

The microprocessor determines one duty cycle for each of the three half bridges and sends the values to the FPGA. Thus, it can control the inverter similarly to a conventional 2L-VSI / B6 bridge. The FPGA operates the auxiliary circuits of the ARCPI, so it needs to calculate the switching points of the main and auxiliary FETs, considering optimal dead times and auxiliary circuit timing. The PWM signals for the gate drivers, shown in Figure 5.25d, are applied by the FPGA in the following cycle.

The optimal turn-on and turn-off times for the main and auxiliary MOSFETs were calculated by a *MATLAB* script and then verified and optimized experimentally. The script considers the effective resonant capacity, including the external capacitors and the voltage-dependent parasitic capacity of the FETs and diodes. The time differences between the reference PWM and the FET turn-on and turn-off times, shown in Figure 5.27, are stored in LUTs in the FPGA. The optimal timing depends on the DC link voltage and the momentary output current of the corresponding phase, as shown in Figure 5.28. It is calculated using increments of 32 V for the DC link voltage

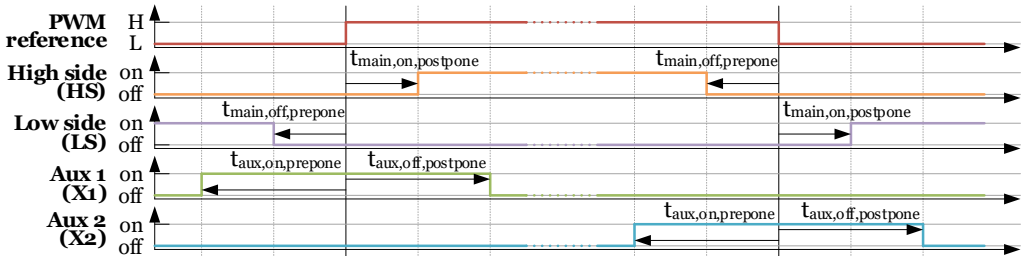

Figure 5.27: Main and auxiliary FET timing derived from the reference PWM by the FPGA — adapted from [C1]

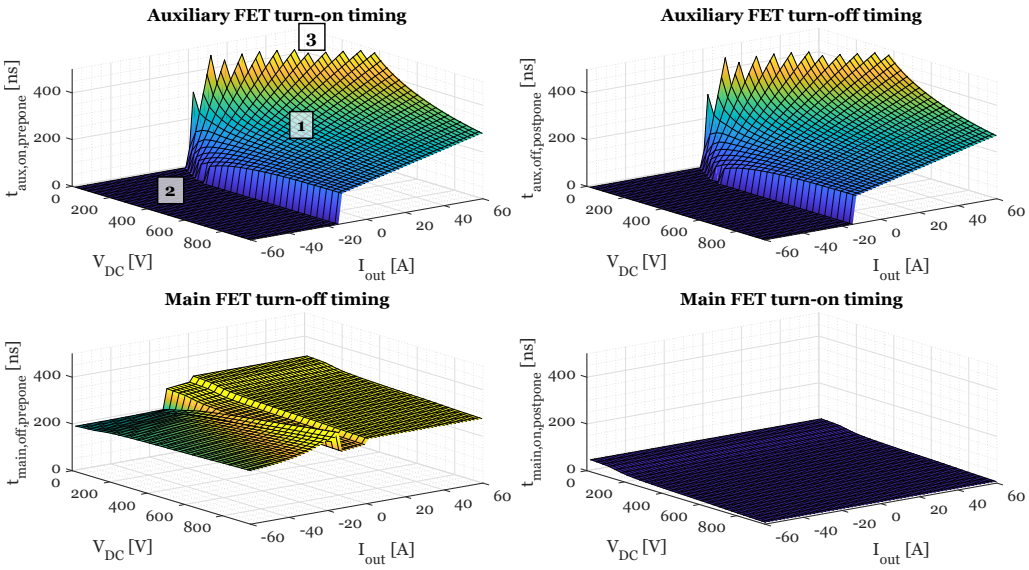

Figure 5.28: Visualization of the DC link voltage and output current dependent main and auxiliary MOSFET timing lookup table (LUT) — adapted from [C1]

and 2 A for the output current. In the operating conditions marked with a "1" in Figure 5.28, soft switching is achieved using the auxiliary MOSFETs (compare cases 1 and 2 in Figure 5.11). In area 2, they are not used since soft switching occurs naturally when the dead time is sufficiently long (case 3 in Figure 5.11). Soft switching would take too long in the instances marked with a "3" in Figure 5.28. Therefore, a hard switching transition is used instead. Since this only affects the operation at DC link voltages below 400 V, it is irrelevant for most practical applications.
The first and last PWM cycles at turn on and turn off of the inverter and very high and very low duty cycles that would cause incomplete soft switching transitions are treated specially to obtain ZVS in these cases, too.

5.3.5 Current controller

The current controller is shown in Figure 5.29. It is comparable to the controller already presented in Figure 4.19 of Chapter 4.2.2 but was extended with setpoint ramps that limit the maximum rate of change of the applied setpoints to typically 200 A/s to improve controller stability.
Compared to Figure 4.19, the PI controllers feature an anti-windup logic, an integration limiter, and an over-current controller. The simplified structure is depicted in Figure 5.30. The anti-windup logic prevents a further increase of the integral part i_{sum} if the maximum achievable output voltage amplitude is already reached. In this case, a further increase of the desired output

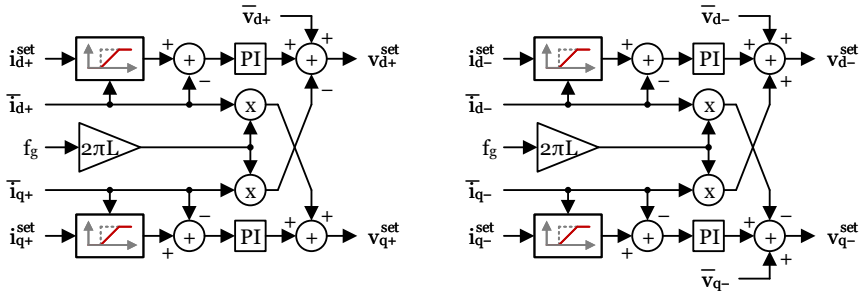

Figure 5.29: Double reference frame current controller implemented in the prototype

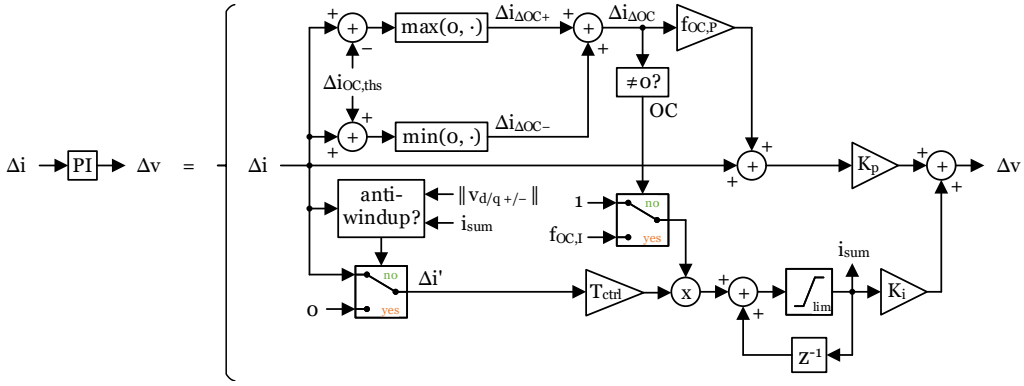

Figure 5.30: Extended PI controller used in the current controller

voltage has no further effect, and the controller only allows holding or decreasing i_{sum}. The integral part is also limited to a maximum value to prevent excessive current overshoots.
If the measured current deviates unusually much from the setpoint ($|\Delta i| > \Delta i_{OC,ths}$), the integration is intensified by the factor $f_{OC,I}$. Moreover, an additional proportional term $f_{OC,P} \cdot \Delta i_{\Delta OC}$ is added to the current error Δi to increase the controller speed for the over-current part $|\Delta i_{\Delta OC}| = |\Delta i| - \Delta i_{OC,ths}$. This is particularly useful during sudden events such as short circuits or abrupt grid voltage variations since the filtered grid voltage signals lag behind the actual grid voltages, as discussed in Chapter 5.2.2. The over-current threshold $\Delta i_{OC,ths}$ is set to 1.25 A, the additional proportional factor $f_{OC,P}$ is 6, and $f_{OC,I}$ is 3.

The current control factors K_p and K_i were initially dimensioned according to the magnitude optimum [360, pp. 46-56] (“Betragsoptimum”). For this purpose, the simplified control loop shown in Figure 5.31a is used. It consists of a regular PI controller (see Equation 5.6), a dead time element representing the time-discrete PWM applied to the power electronic circuit, a first-order lag (PT1) element for the AC grid filter, a PT1 element for the analog measurement filter, and a

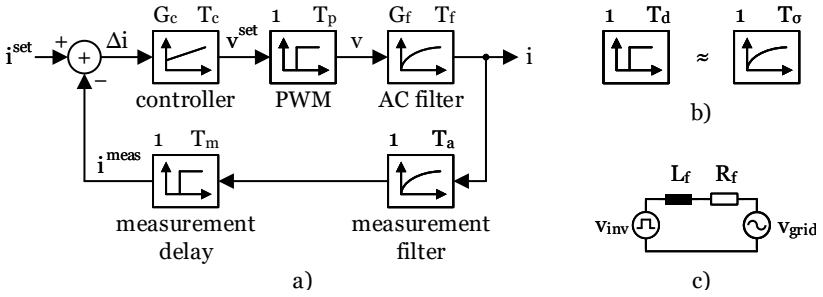

Figure 5.31: Simplified model to determine the current controller parameters: a) control loop, b) approximation of dead time elements with first-order lag (PT1) elements, c) simplified grid filter model

dead time element representing the data acquisition delay. The notch filter from the DDSRF-PLL is neglected.

$$G_{ctrl}(s) = K_p + K_i \frac{1}{s} = G_c \cdot \left(\frac{1 + sT_c}{sT_c} \right) \qquad \textit{with} \quad G_c = K_p \ , \quad T_c = \frac{K_p}{K_i} \tag{5.6}$$

The dead time elements can be approximated with PT1 elements [360, pp. 54f.], as shown in Figure 5.31b. In this case, the dead time T_d equals the time constant T_σ of the PT1 element. As previously described, the measurement of cycle i–1 is used in control cycle i to calculate the PWM duty cycle value of cycle i+1. Therefore, both T_p and T_m can be approximated with $T_{ctrl} = 50\ \mu s$. The cut-off frequency of the analog low-pass filter for the current measurement is significantly higher than the control loop period T_{ctrl} because the FPGA uses oversampling to acquire the current measurement, i.e., $T_a \ll T_m$. Therefore, the measurement filter is ignored for the controller design ($T_a \approx 0$).
For the AC filter, the simplified model shown in Figure 5.31c is used, which results in:

$$G_f = \frac{1}{R_f} \ , \qquad T_f = \frac{L_f}{R_f} \tag{5.7}$$

The resistance R_f is approximated by the overall series resistance of the grid filter and the $R_{DS,on}$ of a main MOSFET, which results in $R_f = 41\ m\Omega$. Similarly, the sum of filter inductances yields $L_f = 335\ \mu H$. The resulting time constant T_f is approximately 8.17 ms. Since $T_p \ll T_f$ and $T_m \ll T_f$, T_p and T_m can be combined to $T_{\sigma,i} \approx T_p + T_m \approx 2T_{ctrl}$ (compare [360, pp. 46f.]). The resulting simplified open-loop transfer function of the process is:

$$G_{o,i}(s) = \frac{i^{meas}(s)}{v^{set}(s)} \approx \frac{1}{1 + sT_p} \cdot \frac{G_f}{1 + sT_f} \cdot \frac{1}{1 + sT_a} \cdot \frac{1}{1 + sT_m} \approx \frac{G_f}{1 + sT_f} \cdot \frac{1}{1 + sT_{\sigma,i}} \tag{5.8}$$

Using the magnitude optimum (compare [360, p. 52]), the resulting PI controller parameters are:

$$G_c = \frac{T_f}{2G_f T_{\sigma,i}} \quad , \qquad T_c = T_f \tag{5.9a}$$

$$\text{or} \qquad K_p = G_c = \frac{L_f}{4T_{ctrl}} \quad , \qquad K_i = \frac{G_c}{T_c} = \frac{R_f}{2T_{\sigma,i}} = \frac{R_f}{4T_{ctrl}} \tag{5.9b}$$

The controller settings were tested on the prototype. Based on the measurement results, the parameters were adjusted to reduce oscillations and improve stability. The actual current controller factors used in the prototype in regular operation are:

$$K_{P,d+} = K_{P,q+} = \overbrace{0.2}^{\text{empirical factor}} \cdot \overbrace{\frac{L_f}{4T_{ctrl}}}^{\text{magnitude optimum}} = 0.335\,\frac{V}{A} \tag{5.10a}$$

$$K_{I,d+} = K_{I,q+} = 0.4 \cdot \frac{R_f}{4T_{ctrl}} = 82\,\frac{V}{A \cdot s} \tag{5.10b}$$

$$K_{P,d-} = K_{P,q-} = 0.6 \cdot \frac{L_f}{4T_{ctrl}} = 1.005\,\frac{V}{A} \tag{5.10c}$$

$$K_{I,d-} = K_{I,q-} = 0.8 \cdot \frac{R_f}{4T_{ctrl}} = 164\,\frac{V}{A \cdot s} \tag{5.10d}$$

5.3.6 DC link voltage controller

A DC link voltage controller is needed to maintain the desired voltage v_{DC} when the DC port of the inverter is not connected to a laboratory power supply. The implemented controller is shown in Figure 5.32. The DC link voltage can be kept at a constant voltage ($v_{DC}^{set,lo} = v_{DC}^{set,hi}$)

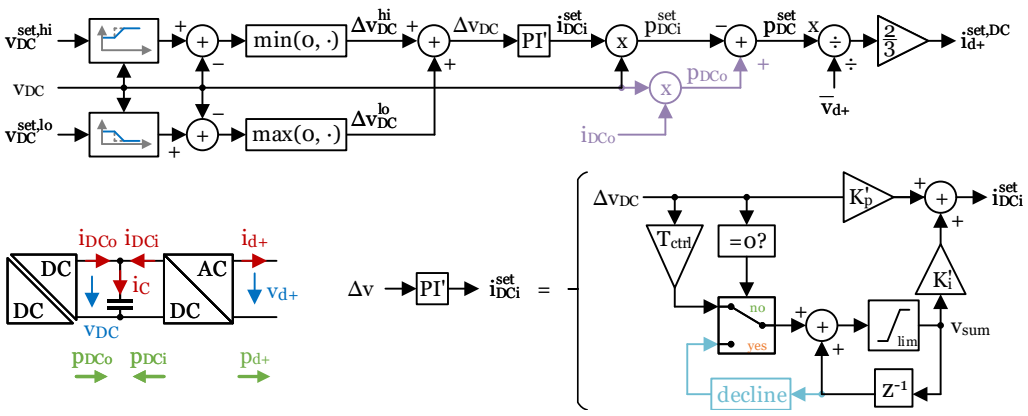

Figure 5.32: DC link voltage controller and simplified diagram of the sign conventions

or in a range ($v_{DC}^{set,lo} < v_{DC} < v_{DC}^{set,hi}$). If the inverter supplies a load or an external converter that determines the power flow, feedforward control of the output power p_{DCo} can be enabled for improved voltage stability (purple in Figure 5.32). The power, which is fed into the DC link of the inverter, is calculated with the inverter's voltage and output current measurements. Together with the output of the PI controller, the power setpoint to maintain the DC link voltage p_{DC}^{set} is formed. The setpoint current $i_{d+}^{set,DC}$ determined by the DC link controller is calculated using the positive-sequence direct voltage, i.e., the main voltage component of the grid. Similar to the current controller, the integral component of the PI controller is limited to a maximum value.
If the AC/DC and DC/DC converters are used in conjunction, and the inverter determines the power flow, the DC link voltage control should be handled by the DC/DC converter, as described in Chapter 5.1.2. However, the CLLLC converter's output power dynamic is very limited. If the AC/DC converter requests a sudden AC power increase, this would cause the DC link voltage between the converters to drop significantly, so the inverter could not fulfill the desired power transfer. Therefore, both the AC/DC and DC/DC converters control the DC link voltage. While the inverter is responsible for larger transient deviations caused by quick output power variations, the DC/DC converter shall adjust the transferred power as soon as possible to take over voltage control. However, this means that the power setpoint requested by the inverter may be applied to the grid with a delay, limited by the capability of the CLLLC converter to adjust its output power. For the combined DC link control, the feedforward control of the inverter (purple in Figure 5.32) is disabled. The integral part of the inverter's DC link controller needs to decline when the DC link voltage is in the desired range to let the DC/DC converter take over control. This is achieved by enabling the light blue "decline" block in Figure 5.32. The DC1 voltage setpoint of the DC/DC converter has to be configured within the allowed DC link voltage range of the inverter.
During the initial characterization of the charging system, both converters were operated together with independent DC voltage controls. Without communication between the two converters, the DC link voltage stability and overall power transfer responsiveness had significant room for improvement. Therefore, the feedforward control already described in Chapter 5.1.2 was implemented. This allows the DC/DC converter to adjust the transferred power simultaneously with the inverter to improve the dynamic behavior.

For the dimensioning of the inverter's DC link voltage PI controller, the simplified model shown in Figure 5.33 is used. The open-loop transfer function of the process is described by Equation 5.11.

$$G_{o,v}(s) = \frac{v_{DC}^{meas}(s)}{i_{d+}^{set,DC}(s)} \approx \frac{G_i}{1+sT_i} \cdot \frac{G_f}{sT_f} \cdot \frac{1}{1+sT_a} \cdot \frac{1}{1+sT_m} \approx \frac{G_f \cdot G_i}{sT_f} \cdot \frac{1}{1+sT_{\sigma,v}} \quad (5.11)$$

T_i is the time constant of the inverter, which reflects the delay caused by the current controller. When neglecting the nonlinear behavior of the setpoint ramps and considering the adjusted K_P

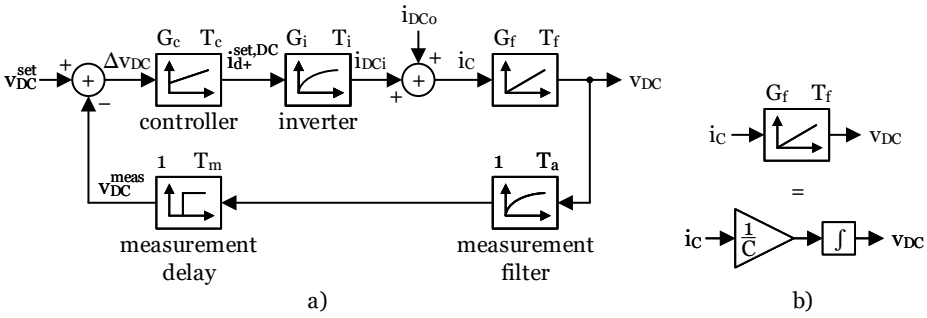

Figure 5.33: Simplified model to determine the DC link voltage controller parameters: a) control loop, b) DC link filter voltage and currents, c) DC link filter model

factors of the current controller (Equation 5.10a), the non-compensable delay relevant for the DC link voltage controller is estimated to:

$$T_{\sigma,v} \approx T_i + T_a + T_m = \frac{2T_{\sigma,i}}{0.2} + T_a + T_m \approx \frac{4T_{ctrl}}{0.2} + 2T_{ctrl} = 22T_{ctrl} = 1.1\ ms \quad (5.12)$$

Using the symmetric optimum (compare [360, p. 62]), the resulting PI controller parameters are:

$$G_c = \frac{T_f}{2G_f G_i T_{\sigma,v}}\ , \qquad T_c = 4T_{\sigma,v} \quad (5.13a)$$

$$\text{or} \qquad K_p = G_c = \frac{C}{2G_i T_{\sigma,v}}\ , \qquad K_i = \frac{G_c}{T_c} = \frac{C}{2G_i T_{\sigma,v} \cdot 4T_{\sigma,v}} = \frac{C}{8G_i T_{\sigma,v}^2} \quad (5.13b)$$

The DC link capacitance C of the inverter is approximately 1.74 mF. The gain of the inverter G_i, i.e., the ratio between i_{DCi} and $i_{d+}^{set,DC}$, depends on the grid and DC link voltages. For a grid voltage of 230 V_{RMS} and a DC link voltage of 600 V, G_i is -0.813. Using the symmetric optimum yields:

$$K_{P,v} = \frac{C}{44G_i T_{ctrl}} \approx -0.9726\ \frac{A}{V}\ , \qquad K_{I,v} = \frac{C}{3872G_i T_{ctrl}^2} \approx -221.1\ \frac{A}{V \cdot s} \quad (5.14)$$

However, the variable grid and DC voltages are already considered in the controller part behind the PI controller, as shown in Figure 5.32. Therefore, G_i does not need to be included in the PI controller settings used in the prototype.
The controller parameters derived from the symmetric optimum were tested in the prototype and adjusted to reduce oscillations and improve behavior when used in conjunction with the DC/DC converter. The values used in the prototype (compare Figure 5.32) are $K'_{P,v} = 0.075$ and $K'_{I,v} = 1.125$.

When the converter starts operation with a discharged DC link from the AC grid, the pre-charge relays depicted in the "relay" block in Figure 5.20 are used. In the first phase, the DC link is passively charged through the 50 Ω resistors of the pre-charge circuit (one per phase) and the rectifier diodes of the power module. Once charged to 70% of the minimum required DC link voltage ($70\% \cdot \sqrt{6} \cdot V_{LN,RMS,max}$), the active phase of the pre-charge starts. The pre-charge relays with the resistors remain active, but the MOSFETs are pulsed through a PWM. The DC link voltage controller applies a negative i_d-current to reach the desired output voltage. The controllers consider the reduced maximum achievable current and the adapted controller settings due to the pre-charging resistors. The grid currents and the DC link voltage are checked for plausibility during the pre-charge process, and the inverter is turned off in case of implausibilities such as unusually small or high currents or timeouts.

5.3.7 Frequency control and virtual inertia

The Virtual Synchronous Generator (VSG) described in Chapter 4.2.3 was realized in the microprocessor to reduce frequency variations in the electricity grid with the V2G charger. The structure of the implemented VSG is shown in 5.34. It supports Frequency Containment Re-

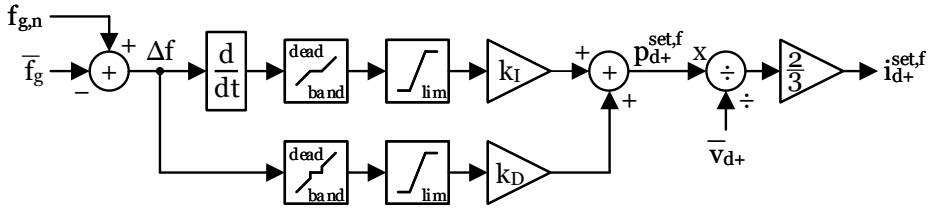

Figure 5.34: Simplified structure of the VSG implemented in the prototype

serve (FCR) by adjusting the output power of the inverter proportional to the deviation Δf to the nominal grid frequency $f_{g,n}$. This relationship is determined by the factor k_D. Synthetic inertia is provided by controlling the output power proportional to the derivative $\frac{d}{dt}\Delta f$, adjusted by the factor k_I. In the prototype, both factors are configurable by the user via the UART interface. The default settings are $k_D = 4.0\ \frac{kW}{Hz}$ and $k_I = 1.0\ \frac{kW \cdot s}{Hz}$.
Inside a dead band of ±10 mHz, the FCR of the VSG is inactive. Outside the dead band, the output power is proportional to the frequency deviation. The maximum Δf processed by the FCR term is set to ±1.5 Hz, i.e., the output power will not be altered further if the deviation is even larger. The inertia term also has a dead band (2 mHz/s), outside which the output power is adjusted linearly, i.e., continuously and without steps. The dead band prevents activation of the inertia term from noise alone. The derivative is limited to 2 Hz/s.

A simple method to calculate the derivative of the grid frequency in the control loop executed with 20 kHz ($T_{ctrl} = 50\ \mu s$) is shown in Equation 5.15.

$$\text{Simple discrete derivative:} \qquad \frac{d}{dt}\Delta f = \frac{\Delta f[i] - \Delta f[i-1]}{T_{ctrl}} \tag{5.15}$$

The frequency in interconnected grids changes very slowly. Even during severe grid fault events, e.g., a decline of 1 Hz/s, the frequency difference between two control loop executions is negligibly small. Even though the filtered grid frequency is used, VI control would be extremely prone to quantization and measurement noise, as well as oscillations in the measured frequency caused by the interaction of the inverter and the grid with the PLL. Hence, an improved method to calculate the frequency derivative is used, which is shown in Figure 5.35. During each control

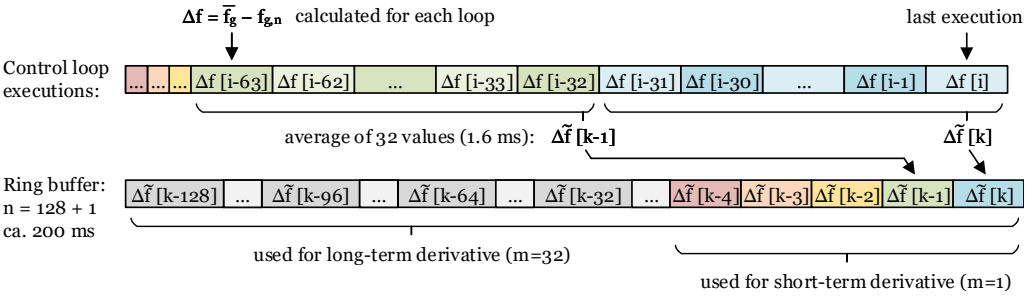

Figure 5.35: Extended filter for the derivative calculation of the virtual inertia term

loop execution in the microprocessor, the difference Δf between the filtered grid frequency $\bar{f}_g$ calculated by the FPGA to the nominal grid frequency $f_{g,n}$ is determined. For every 32 control cycles, an average value $\Delta\tilde{f}$ calculated from these cycles is stored in a ring buffer. Similar to oversampling, this increases the resolution of the frequency deviation value while reducing its temporal resolution.

Using the five-point discrete derivative finite impulse response (FIR) filter shown in Equation 5.16, a long-term and a short-term derivative value are calculated using the last 129 ($m = 32$) and the last five ($m = 1$) values of $\Delta\tilde{f}$, respectively.

$$x_m[k] \approx \frac{\Delta\tilde{f}[k-4m] - 8 \cdot \Delta\tilde{f}_m[k-3m] + 8 \cdot \Delta\tilde{f}[k-m] - \Delta\tilde{f}[k]}{12 \cdot m} \tag{5.16}$$

The absolute maximum number is selected and converted back to the base unit Hz/s:

$$y_m[k] = \frac{1}{32 \cdot T_{ctrl}} \cdot \begin{cases} x_{32}[k], & \text{if } |x_{32}[k]| > |x_1[k]| \\ x_1[k], & \text{otherwise} \end{cases} \tag{5.17}$$

This value is fed into a simple first-order infinite impulse response (IIR) LPF with $\beta = 0.03$ to determine the final value $\bar{y}_m$ used for the virtual inertia term:

$$\frac{d}{dt}\Delta f[k] \approx \bar{y}_m[k] = \beta * y_m[k] + (1-\beta) * \bar{y}_m[k-1] \tag{5.18}$$

5.3.8 Grid voltage control

The V2G charger shall also stabilize the local grid voltages during regular operation and temporary faults. In case of a transient low-voltage fault, the inverter shall remain connected and support the grid voltage by injecting reactive current (LVRT). The maximum fault duration, the minimum AC voltage for which the inverter needs to sustain operation, and the relationship between grid voltage and required reactive power vary depending on the grid code. Examples are shown in [353, pp. 3-7].
The simple grid voltage controller shown in Figure 5.36a was implemented. It feeds in reactive power based on an LUT or function of the grid voltage. This reactive power setpoint is converted into a setpoint for the positive-sequence quadrature current i_{q+}.

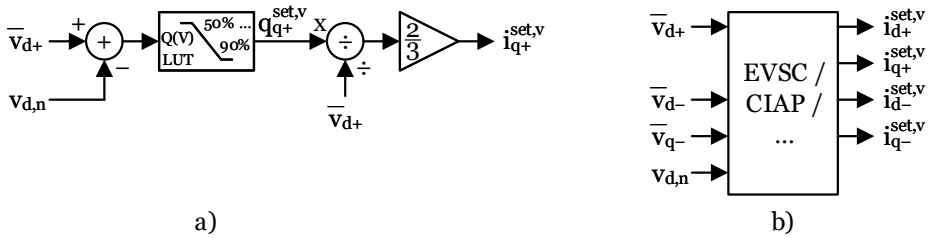

Figure 5.36: a) Simple grid voltage controller for symmetric reactive power provisioning, b) voltage controller for asymmetric current injection

The nominal grid voltage $v_{d,n}$ and the maximum provided reactive power can be configured using the UART interface. In the current implementation, no reactive power is supplied at 90% of the nominal grid voltage, and the maximum reactive power is supplied at 50% of the nominal voltage.

The simple controller might not deliver desirable results during severe asymmetric voltage faults. Various methods that use positive- and negative-sequence currents to pursue different equalization objectives are presented by Revelo and Silva [331]. For example, in the "constant instantaneous active power" (CIAP) method, the current setpoints for $i_{d+/q+/d-/q-}$ are chosen so that the transferred power remains constant despite the asymmetric voltages. In the prototype, this would ensure continuing a steady power transfer with the CLLLC converter. On the other hand, the "equalizing voltage sequence control" (EVSC) strategy tries to reduce the asymmetry of grid

voltages using negative-sequence currents. While increasing power oscillations through the converters, this method prioritizes grid support.
Both the CIAP and EVSC strategies were implemented in the microprocessor of the prototype. Since $i_{d+/q+/d-/q-}$ can be arbitrarily chosen, further strategies could be implemented on the developed flexible controller platform with minimal effort (compare Figure 5.36b). However, the inverter ratings need to be respected, and the amplitude of negative-sequence currents might be limited due to the resulting active power oscillations at twice the grid frequency. These oscillations need to be absorbed by the DC link capacitor or an improved, highly dynamic power transfer behavior of the DC/DC converter.

5.4 Experimental setup

First, the DC/DC converter developed in the master's thesis [354] was enhanced and further characterized in this thesis. Next, the newly developed AC/DC converter was tested independently to verify and optimize the functionality of the switching procedures and control algorithms. Finally, the complete V2G charging system consisting of the inverter and the DC/DC converter was jointly used in a PHIL test bench to validate its operation.

5.4.1 DC/DC converter

The fundamental operation of the CLLLC converter has already been analyzed up to a power level of 3.5 kW and maximum voltages of 200 V in [354]. As part of the present thesis, the efficiency was improved by introducing load-dependent dead times and implementing synchronous rectifying. Moreover, the converter was characterized at higher voltages and output power. For the efficiency measurements, two test setups were selected. First, the converter was operated with fixed power load resistors and later an electronic load, as shown in Figure 5.37a. This also enabled an easy verification of the theoretical transfer gain since the output is modeled through a load resistance in the FHA model. Afterward, both sides of the converter were connected to the power supply, as shown in Figure 5.37b. This facilitates validating the bidirectional operation without the use of two individual bidirectional power supplies, which were not available at the time of characterization. As the energy flows in a loop, the HV power supply unit only needs to provide the power losses of the converter. However, the tests are limited to a transfer gain of one, so the converter could not be tested at full power in forward operation.
General voltage and current measurements were gathered with a *Tektronix MSO58* oscilloscope with *TMDP0200* and *THDP0200* HV differential probes. The probes were connected to test points on the PCB. *Pico Technology TA018* current clamps were used for current measurements.

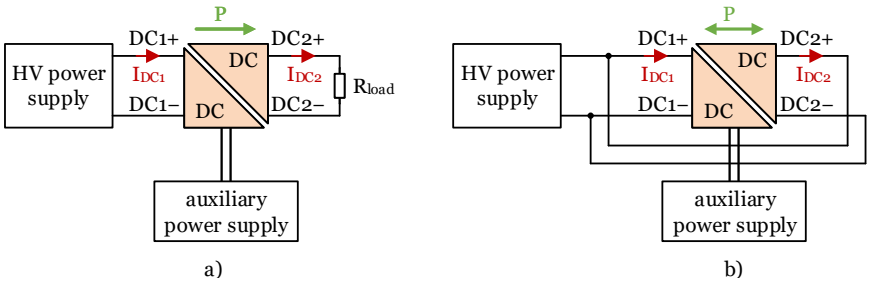

Figure 5.37: Experimental setup for the CLLLC converter characterization: a) unidirectional operation with load resistors or an electronic load, b) bidirectional operation with one power supply

They were typically attached around the DC1+ and DC2+ power cables connected to the converter. The efficiency was determined with a *Hioki PW3390* high-precision power analyzer using *CT6862-05* current sensors. Usually, the smallest possible measurement range was selected to improve accuracy, and the DC1+ and DC2+ power cables connected to the converter were routed through the sensor to measure the currents I_{DC1} and I_{DC2}. The voltage probes of the power analyzer were connected to the DC+ and DC− plugs of the cable connected to the converter. Thus, the measured efficiency considers all losses on the PCB up to and including the contact resistances of the external plugs connected to the converter.
The controller, gate drivers, cooling fans, and all other analog and digital circuits on the board are powered by an external 12 V auxiliary power supply. The auxiliary power demand is not included in the efficiency measurements captured by the power analyzer (“power electronics efficiency”), so it needs to be factored in afterward to determine the “overall efficiency”.
Thermal images were captured with a *FLIR A655sc* long-wave infrared camera.

5.4.2 AC/DC converter

For the initial commissioning of the inverter, the individual functions, such as measurement data acquisition and communication between the FPGA and microprocessor, were tested without power transmission (compare Figure 5.38a). After successful completion, an operation with a constant current $i_{L1} = -i_{L2}$ at the AC outputs was implemented, shown in Figure 5.38b. This allowed the output current to be varied incrementally at different DC link voltages to verify the simulated switching behavior and optimize the timing where necessary (compare Chapter 5.3.4). Next, the inverter was supplied with a DC power supply to transfer power to load resistors, as depicted in Figure 5.38c. The V2L operation of the inverter could be tested using a simple grid-forming mode, and the proper functionality of the PLL could be verified. Finally, the grid-following operating modes were implemented and analyzed. For the experiments, the inverter was not connected to the public electricity grid to avoid damage to both the inverter and the

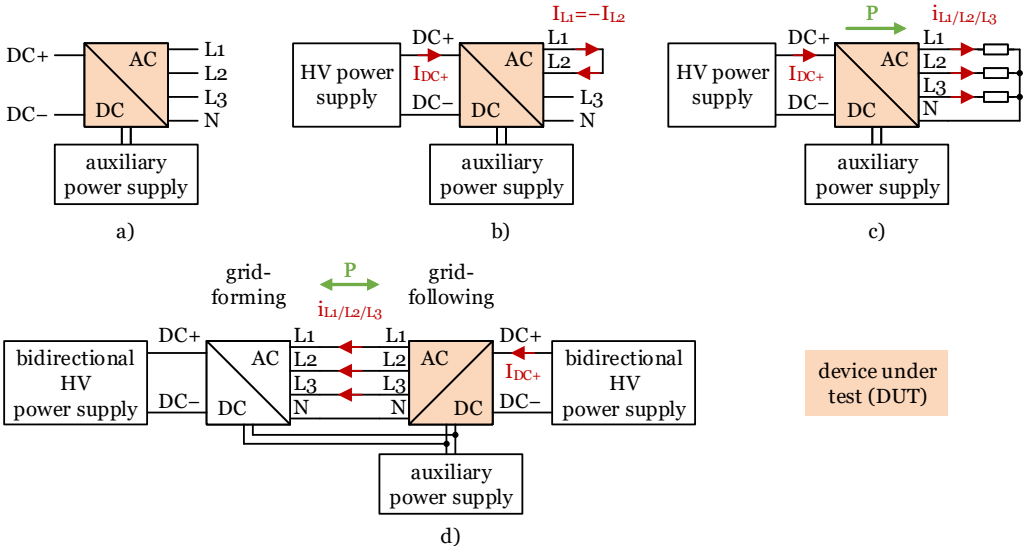

Figure 5.38: Experimental setup for the ARCPI characterization: a) commissioning of basic functionality, b) optimization of switching behavior, c) unidirectional grid-forming mode, d) bidirectional grid-following operation

local infrastructure in case of malfunctions. Instead, two ARCPI prototypes were operated in an AC-coupled configuration, as illustrated in Figure 5.38d. One inverter forms a grid (GFMI) by generating sinusoidal three-phase voltages. The other inverter is the device under test (DUT), which connects to the emulated grid and operates as a GFLI. This allowed testing the control algorithms in detail since the grid frequency and voltages could be arbitrarily chosen, and initial tests could also be run at lower voltages.

The measurement equipment used for the DC/DC converter characterization was also used for the inverter experiments. Similarly, general voltage measurements were captured using test points on the PCB, and the DC voltages for the efficiency measurement were taken from the DC+ and DC− plugs of the cable connected to the inverter. Since the contacts of the AC plugs were not accessible, the voltage probes of the power analyzer were connected to test pins soldered to the contacts of the AC power receptacles below the PCB to measure all phase-to-neutral voltages. Hence, the measured efficiency considers all losses on the PCB up to (and including) the contact resistances of the external DC plugs but excluding the AC plugs connected to the converter. Besides the power electronics, the prototype board includes the DC and AC filters, OVPs, and relays, so their losses are also included. The AC cables coming from the inverter could be directly connected to a three-phase power outlet of the infrastructure, and the DC cables can be connected to the DC/DC converter. Similar to the DC/DC converter, an external auxiliary power supply is needed to power the controllers, gate drivers, analog and digital circuits, and cooling fans. The auxiliary power demand must also be considered to determine the overall efficiency.

5.4.3 Power hardware-in-the-loop test bench

Finally, both converter systems were used in conjunction on a PHIL test bench to test their application in a V2G charging system. Two methods were used. In the first example shown in Figure 5.39a, the test setup already presented in Figure 5.38d was extended by the DC/DC converter. A bidirectional HV power supply feeds the first ARCPI, which emulates the grid. The

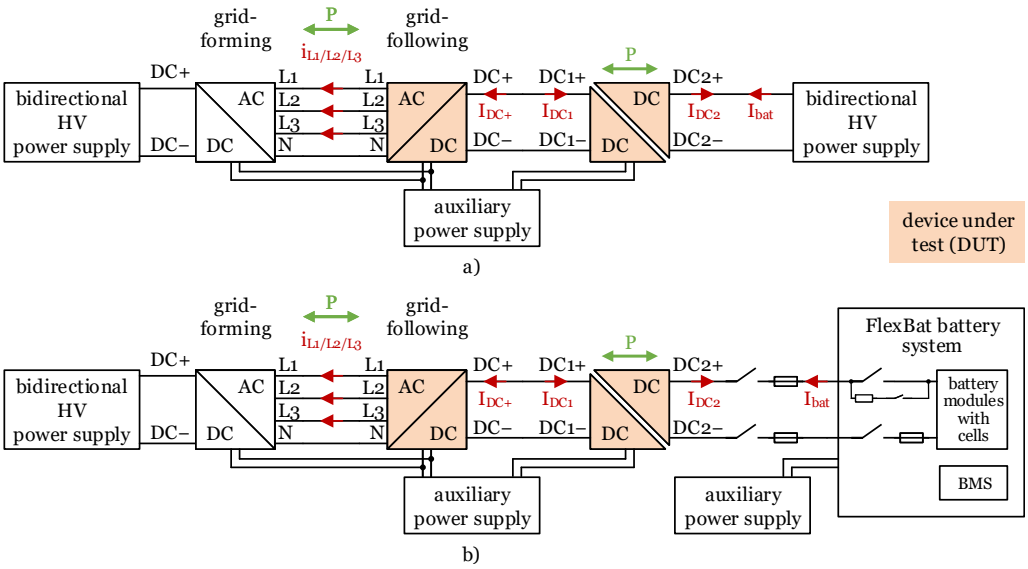

Figure 5.39: Experimental setup for the PHIL test bench: a) using a bidirectional power supply to emulate the EV battery, b) using the *FlexBat* battery system [361] to emulate the EV battery

investigated V2G charger, comprising an ARCPI and a CLLLC converter, is connected between the emulated grid and another bidirectional HV power supply. The voltage of the latter supply can be adjusted to the battery voltage of interest.

In the second case, an actual battery system is charged or discharged by the V2G system. For this purpose, the *FlexBat* battery system developed in a preceding dissertation at the institute [361] was used. It is a stand-alone battery system with a battery management system (BMS) and protection components such as relays. The *FlexBat* system only requires an auxiliary power supply for operation and can be controlled via CAN, which the CLLLC converter handles. As an additional layer of protection during the experiments, the V2G charger was also equipped with fuses and relays that the DC/DC converter controls. Therefore, the resulting setup is comparable to an external DC V2G system (see Figure 3.5b in Chapter 3.2.4).

The same measurement equipment as in the previous experiments was used. Since only eight oscilloscope channels were available, the three AC phase-to-neutral voltages, three AC phase

currents, one DC voltage, and one DC current were measured. Depending on the type of measurement, the DC1 or DC2/battery voltage and current were recorded with the oscilloscope. The efficiency measurement always considers the overall efficiency of both the AC/DC and DC/DC converter.

A photo of the PHIL test bench with the DUTs, the battery system, power supplies, measurement systems, and the computer from which the test bench is controlled is shown in Figure 5.40.

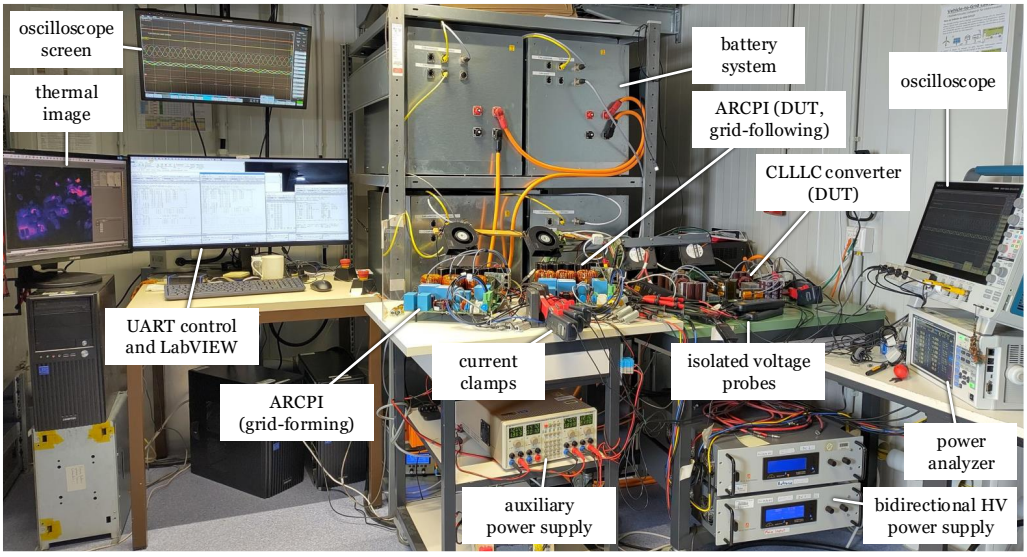

Figure 5.40: Photo of the PHIL test bench

5.5 Results and discussion

In this chapter, the measurement results gathered with the V2G charging system hardware are presented and discussed.

5.5.1 DC/DC converter

First, the transfer gain of the CLLLC converter is analyzed. Then, the optimized switching behavior of the converter with dynamic dead times and synchronous rectification (SR) is discussed. Finally, the efficiency of the converter in different operating modes is presented.

The switching-frequency-dependent transfer gain of the CLLLC converter, i.e., the ratio between the output to the input voltage, was measured using fixed input voltages and different output load resistors. A comparison of the measured and the theoretical gains calculated with the FHA for the same operating points is shown in Figure 5.41. The G2V transfer gain for other input voltages and the general switching transition characteristics are presented in [C3] and [354].

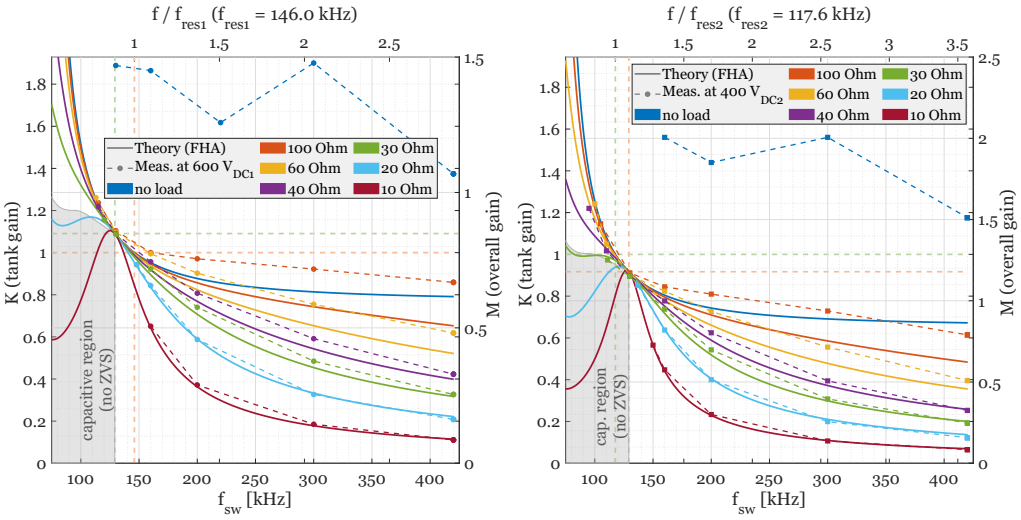

a) G2V/FWD with 600 V input (DC1) voltage

b) V2G/BWD with 400 V input (DC2) voltage

Figure 5.41: Theoretical (FHA) vs. measured gain of the CLLLC converter prototype at different output loads

The measured gain matches the theoretical one well for high output power, i.e., load resistances below 40 Ω (which is 10 A at 400 V). However, the measured ratio becomes increasingly higher toward lower output loads, i.e., output resistances of 60 Ω and larger. In an open-circuit operation with no load, the transfer gain is less consistent and almost twice as high as in the theoretical FHA model. Possible explanations are the influence of higher harmonics and parasitic capacitances in the transformer and the PCB, which impact the transfer behavior when the power is very low.
In a practical application, the converter does not operate with a fixed switching frequency but adjusts the frequency or interrupts switching using a discontinuous burst operation to obtain the desired output voltage and current. Therefore, the unexpected high transfer gains at low loads are not an issue. For example, with an input voltage of 600 V and no output load, an output voltage of 50 V, i.e., an overall gain of 0.083, can be reached in the G2V direction using the discontinuous operating mode. For comparison, the theoretical gain is 0.615 for this operating point at the maximum switching frequency of 420 kHz. Using an input voltage of 200 V and an output load resistor of 10 Ω, an output voltage of 10 V, i.e., a transfer gain of 0.05, could be realized in V2G

with discontinuous operation. However, the voltage ripple is 0.9 V in this example, which is slightly higher than in continuous operation.

The CLLLC converter prototype initially operated with a fixed dead time of 500 ns (compare [354, p. 97]). It was later reduced to 350 ns since the dead time was too long to ensure soft switching transitions in some cases (see Figure 5.8c). However, the shorter dead time caused partially hard switching transitions for other operating points (compare Figure 5.8d). Therefore, as part of this thesis, a dynamic dead time generation was implemented, as presented in Chapter 5.1.3. For this purpose, the switching transition was empirically analyzed for multiple input voltages ranging from 100 to 800 V, multiple output loads ranging from 10 Ω to open-circuit operation, and the allowed switching frequency range of up to 75 to 420 kHz for both G2V and V2G operation. Next, the minimal, optimal, and maximal dead times for soft switching were determined for the operating points. Examples of different optimal dead times in V2G operation are shown in Figure 5.42. The first two rows show the digital signals sent to the gate drivers of the primary side (DC2 in V2G operation). The last row shows the output voltage of the full bridge (v_{res2}, in cyan), shown in the schematic in Figure 5.9. The blue vertical lines mark the times when the MOSFETs Q6 and Q7 start to turn off, considering the propagation delay t_{pd} of the isolated gate drivers. Similarly, the gray vertical lines show where Q5 and Q8 start to turn on with the dead time selected in the respective example. In addition, the earliest (red), optimal (green), and — if applicable — the latest (yellow) turn-on times of the complementary MOSFETs Q5 and Q8 are shown. If the FETs are turned on before the earliest turn-on time, the soft switching transition is interrupted, and thus, switching losses occur. When turning on after the latest turn-on time (as is the case in Figure 5.42a), the resonant tank current changes its sign before the complementary FETs turn on, and thus, v_{res2} starts to reverse a second time during the dead time, causing switching losses as well. Ideally, the FETs should turn on at the earliest times (red line)

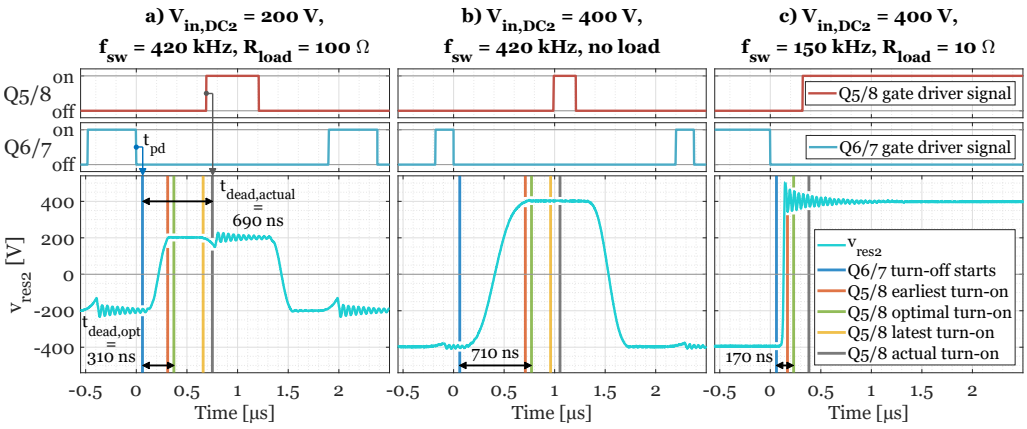

Figure 5.42: Examples of the optimal dead time determined for different V2G operating points

to minimize conduction losses. However, the “optimal” turn-on times (green) include a minimal delay to account for variations in the transition speed, e.g., caused by quickly changing switching frequencies or temperature and component variations in the resonant tank or MOSFETs.
In the first case (Figure 5.42a), the resulting minimum dead time is approximately 250 ns, the optimal dead time was determined to be 310 ns, and the maximum dead time is approximately 600 ns. In the example, the actually used dead time of 690 ns was too long, so it had to be corrected. In the second case (Figure 5.42b), the optimal dead time is about 710 ns. The dead time used in this example was 990 ns, which is also too long. While the transition from a negative to a positive voltage v_{res2} still looks fine, the complementary transition at around 1.5 µs causes switching losses, as v_{res2} starts to reverse at 2.15 µs before MOSFETs Q6 and Q7 turn on. Therefore, the dead time needed to be decreased as well. In the last example (Figure 5.42c), the optimal dead time is very short since the slew rate of v_{res2} is very high. The dead time of 320 ns used in the example is unnecessarily long and was reduced as well.
The optimal dead times determined through the measurements for various output loads and input voltages are shown in Figure 5.43. The functions that determine the optimal dead time

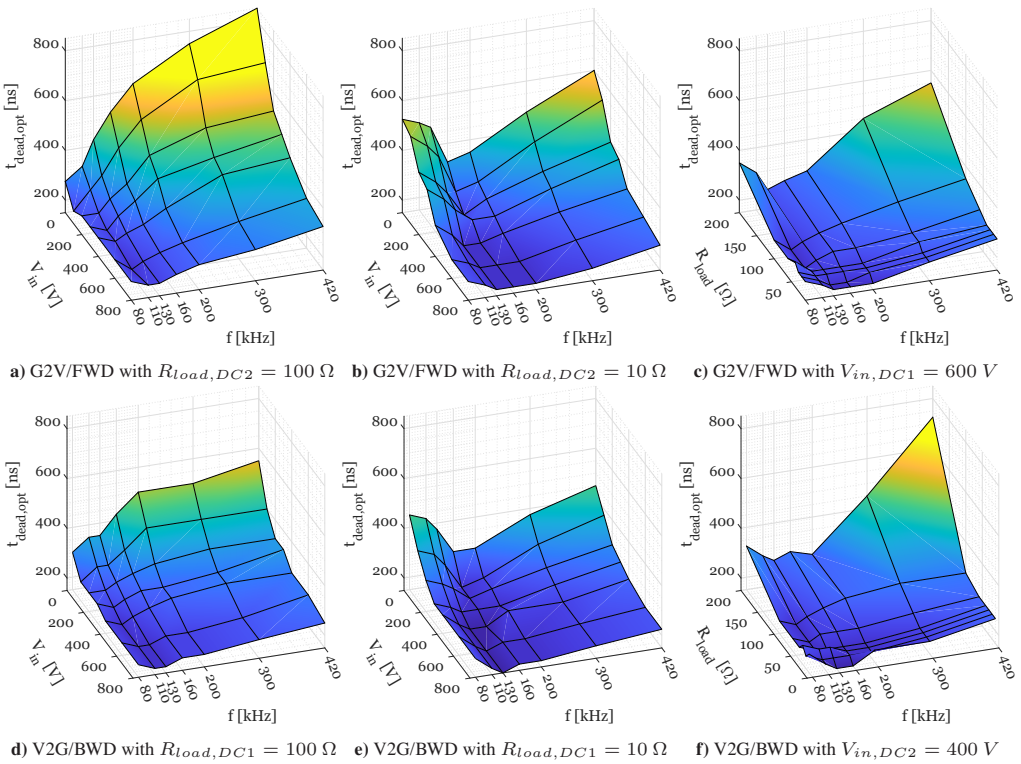

a) G2V/FWD with $R_{load,DC2} = 100\ \Omega$ **b)** G2V/FWD with $R_{load,DC2} = 10\ \Omega$ **c)** G2V/FWD with $V_{in,DC1} = 600\ V$

d) V2G/BWD with $R_{load,DC1} = 100\ \Omega$ **e)** V2G/BWD with $R_{load,DC1} = 10\ \Omega$ **f)** V2G/BWD with $V_{in,DC2} = 400\ V$

Figure 5.43: Optimal dead times measured at various input voltages and output loads

$t_{dead,G2V}(V_{in}, R_{load}, f_{sw})$ and $t_{dead,V2G}(V_{in}, R_{load}, f_{sw})$ based on the momentary operating condition were implemented in the microprocessor using the measured optimal values and constraints.

Another relevant improvement of the CLLLC converter's efficiency is the implementation of synchronous rectification in this thesis. Instead of passive rectification using the body diodes of the secondary side MOSFETs or additional anti-parallel Schottky diodes, the FETs are controlled to rectify the secondary-side resonant tank current actively. The functionality of the realized switching patterns is illustrated in the measurements in Figure 5.44. For a better understanding of the switching processes and signals described in the following, Figure 5.9 may be used for reference. The DC1 voltage is 600 V, and a 20 Ω load resistor is connected to DC2. The converter is operated in G2V/forward mode, in which the primary side MOSFETs Q1/Q4 and Q2/Q3 are driven complementarily (shown in the first two rows of Figure 5.44), resulting in the resonant tank voltage v_{res1} depicted in the third row of the figure (yellow curve). At the given switching frequency of 148 kHz, this results in the resonant tank voltage v_{res2} on the DC2 side (cyan curve

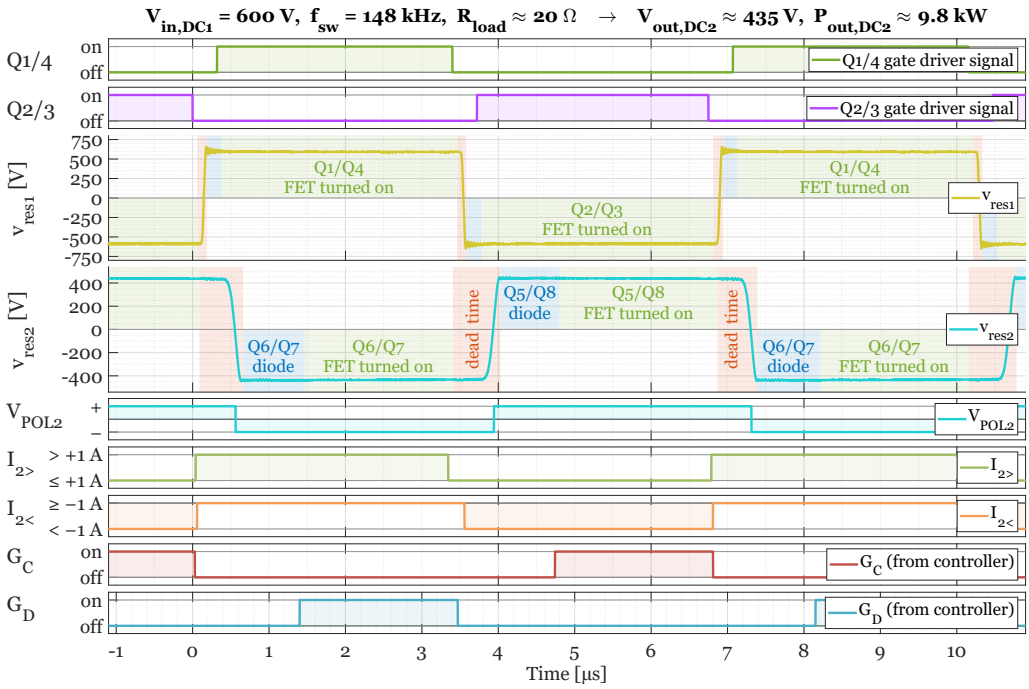

Figure 5.44: G2V operation with synchronous rectification — from top to bottom: gate driver signals to Q1/4 and Q2/3, resulting resonant tank voltages v_{res1} and v_{res2}, detected voltage polarity V_{POL2} and current sign signals ($I_{2>}$ for positive and $I_{2<}$ for negative currents i_{res2}), gating signals G_C and G_D during which FETs Q5/Q8 and Q6/Q7 turn on if the respective $I_{2</>}$ signal is active

in the fourth row). The digital signal V_{POL2} routed to the microprocessor (shown in the fifth row) reflects the polarity of v_{res2} very well.
In the prototype, the secondary-side resonant tank current i_{res2} cannot be measured readily using an oscilloscope. However, the digital signals $I_{2>}$ and $I_{2<}$ passed to the microprocessor and the SR logic circuit indicate the polarity of i_{res2}. Neglecting the hysteresis, $I_{2>}$ is active when i_{res2} is larger than 1 A, and $I_{2<}$ is active when the current is below -1 A. The signals are shown in the sixth and seventh rows.
As explained in Chapter 5.1.4, the V_{POL2} signal triggers an ISR in the microprocessor, which enables the gating signals G_C and G_D shown in the last two rows until a timeout is reached (here, after a maximum on-time of 2.08 µs) or the $I_{2</>}$ signals are cleared. G_D is activated on a falling edge of V_{POL2} and cleared when the processor detects that $I_{2>}$ becomes inactive. Similarly, G_C is activated by a rising edge of V_{POL2} and deactivated when $I_{2<}$ is cleared. The logic gates used for SR turn on MOSFETs Q6 and Q7 when both $I_{2>}$ and G_D are active and turn on MOSFETs Q5 and Q8 when both $I_{2<}$ and G_C are active.
In the background of the two resonant tank voltage signals, the colored areas indicate the necessary minimum dead time (red) and when the high-side or low-side MOSFETs are turned on (green), already considering the propagation delay of the gate drivers. The FETs are disabled in the blue areas, but the body diodes conduct a current.
As shown in the background of the third row in Figure 5.44, the primary-side MOSFETs are turned on most of the time due to the optimized dynamic dead-time generation. In the analyzed operating point, the necessary dead times (red areas) are very short, and there are only brief periods during which the diodes conduct the resonant tank current i_{res1} (blue areas).
When using passive rectification, only the body diodes would conduct the secondary side current i_{res2}. Thanks to SR, the FETs support the diodes most of the time, as shown in the green areas in the fourth row of the figure. This reduces the secondary side conduction losses significantly since the forward voltage drops from around 3 V (body diode) or 1 V (Schottky diode) to less than 0.6 V (MOSFETs turned on). However, it can be seen that the diodes Q6/Q7 and Q5/Q8 are still carrying the current for a considerable amount of time (blue areas) since the timing for SR is not optimal.
This is because the ISRs of the microprocessor add a significant delay to the signal chain. Even though the ISRs were prioritized and optimized, the overall latency for activating the gating signals (e.g., the delay between a falling edge of V_{POL2} and a rising edge of G_D) is around 600 to 850 ns (roughly 10% of the switching period in this operating point). The latency for clearing the gating signals (e.g., the delay between a falling edge of $I_{2>}$ and a falling edge of G_D — if not already cleared through the expiry of the gating timer) is around 250 to 300 ns. Beside the instructions inside the ISR needed to start or stop the timer for the gating signal, the latency is a result of several processor cycles needed for arbitration and interrupt routing, context save and jump instructions, and signal rise and fall times of the incoming and outgoing signals. The latency

could be significantly improved if the signals were directly routed through a modified logic gate circuit without the detour via the microcontroller's ISR. For the newly developed ARCPI, an FPGA was used as a result of these findings to significantly improve timing while maintaining flexibility for the logic circuit.

The converter efficiency was investigated with and without synchronous rectification as well as with and without the use of additional anti-parallel SiC Schottky rectifier diodes. An efficiency comparison[3] for G2V/forward operation with a constant input voltage of 220 V and a fixed output load of approximately 10 Ω for a switching-frequency-dependent output power of 0.5 to 3 kW is shown in Figure 5.45.

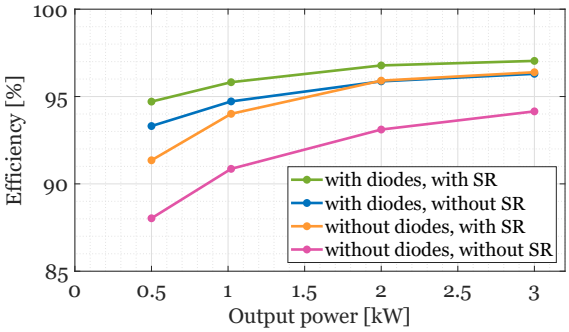

Figure 5.45: CLLLC power electronics efficiency with and without SiC Schottky diodes or SR at $V_{DC1} \approx 220\ V$ and $R_{load,DC2} \approx 10\ \Omega$, excluding auxiliary power needed for the controller and cooling — based on [C3, Fig. 16]

As expected, the module without additional Schottky diodes faces the highest losses if SR is disabled (pink curve), resulting in the lowest efficiency of the converter. The module with Schottky diodes and activated SR (green curve) experiences significantly smaller losses, which improves efficiency considerably. The modules with Schottky diodes and inactive SR (blue curve) and without Schottky diodes and active SR (orange curve) have comparable losses at an output power of 2 and 3 kW. At lower output power, the module with Schottky diodes is more efficient. With perfect SR timing, the Schottky diodes are expected to make no difference if SR is activated. However, because of the latency previously described, the additional diodes improve efficiency by about 1% to 3% in the measurements compared to the modules without diodes that use SR (orange and green curves).

[3] Note: Unlike the other efficiency measurements, the efficiencies in Figure 5.45 were not measured with a power analyzer since it was not available at the time of investigation. Instead, the efficiency $\eta = P_{out}/P_{in}$ was calculated using the input power $P_{in} = V_{in} \cdot I_{in}$, and the output power $P_{out} = V_{out}^2/R_{load}$, whereby the voltages and currents were measured by the oscilloscope, and R_{load} was measured in advance using a precision resistance meter. Therefore, the efficiency measurements are less accurate.

The comparison of the graphs with and without SR shows that the efficiency of unidirectional LLC converters can also be increased if FETs with SR are used on the output side instead of or in addition to rectifier diodes. If the increased efficiency and the resulting electricity cost savings alone can justify using FETs and implementing SR on the output side, the additional expense of transforming the unidirectional to a bidirectional DC/DC converter is no longer substantial.
Thermal images captured during the experiments with 1 kW output power are shown in Figure 5.46. The ambient temperature, input voltage, output load, and active cooling setup using fans are similar in all cases to obtain comparable test conditions. In Figure 5.46a, the operation was stopped before reaching a steady-state temperature to avoid damage due to overheating since no temperature sensor is present in the CLLLC converter module. In the other cases, the measurement was stopped when no noticeable increase in the power module temperature could be detected. This was the case after 4 minutes in Figure 5.46b/c and 3 minutes in Figure 5.46d.

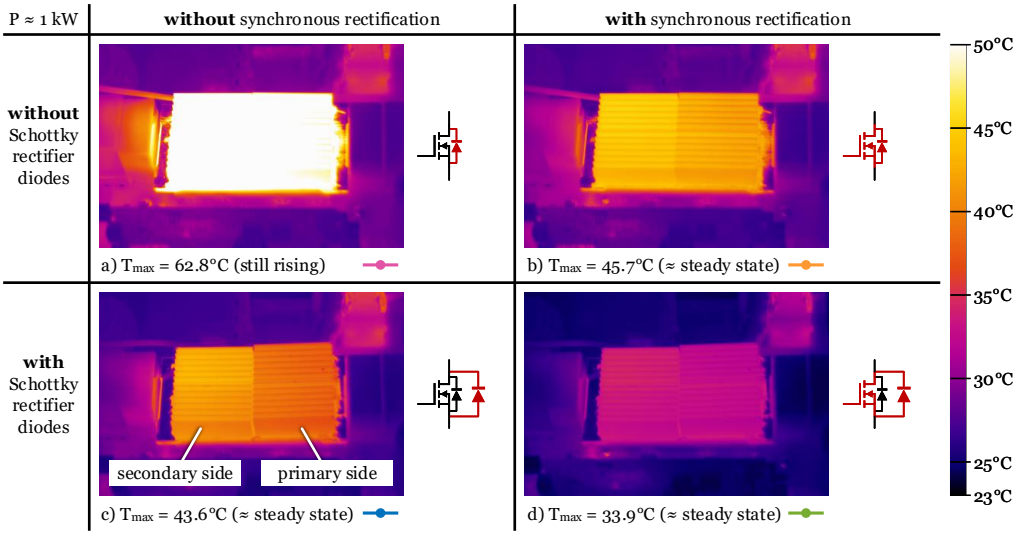

Figure 5.46: Comparison of thermal images of the actively air-cooled cooling ribs of the power module at $P \approx 1\ kW$ and $T_{ambient} \approx 23°C$ with and without diodes or SR — based on [Fig. 16 C3]

Even though the output power $P_{out} \approx 1\ kW$ is equivalent in all cases, the differences in power losses in the module can be seen impressively. Interestingly, it is also apparent that the heat sinks on the left-hand side of the module, above the secondary-side MOSFETs, are warmer in all cases. This confirms that the losses on the output side are higher than on the input side.

The efficiency of the CLLLC inverter prototype with rectifier diodes and SR was investigated in more detail. For this purpose, the "overall efficiency" $\eta_{overall}$ calculated by Equation 5.19b is used, which considers the auxiliary power P_{aux} needed to supply the controller and cooling fans.

$$\eta_{power} = \frac{P_{out}}{P_{in}} = \frac{V_{out} \cdot I_{out}}{V_{in} \cdot I_{in}} = \begin{cases} \frac{V_{DC2} \cdot I_{DC2}}{V_{DC1} \cdot I_{DC1}}, & \text{in G2V/FWD operation} \\ \frac{V_{DC1} \cdot I_{DC1}}{V_{DC2} \cdot I_{DC2}}, & \text{in V2G/BWD operation} \end{cases} \tag{5.19a}$$

$$\eta_{overall} = \frac{P_{out}}{P_{in} + P_{aux}} \tag{5.19b}$$

The power electronics efficiency η_{power} was measured by the power analyzer, and $\eta_{overall}$ was calculated afterward, considering the auxiliary power demand. The converter's standby power consumption is approximately 2.6 W. During active operation, a fan cools the power module, and the gate drivers are active, which increases the power demand to $P_{aux} \approx 10\ W$.

The efficiency for different operating points is shown in Figure 5.47. All measurements captured within the specified transfer gain range that the converter was designed for [354, p. 61] were included, i.e., all measurements for which M_{G2V} is between 0.32 and 1.6, and M_{V2G} lies between 0.625 and 3.125. The two left diagrams show the measurement results collected in G2V opera-

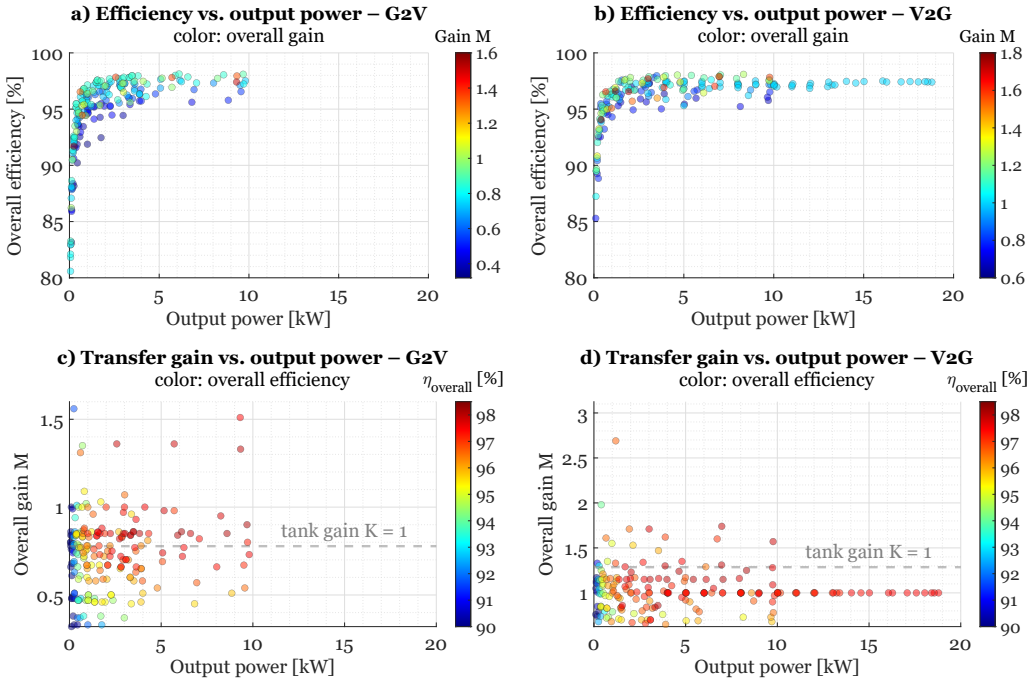

Figure 5.47: Overall CLLLC converter efficiency in G2V and V2G operation

tion, and the right diagrams represent V2G operation. The upper diagrams show the efficiency as a function of the converter's output power P_{out}. Besides the output power, the efficiency depends on the input and output voltage level and the resulting overall transfer gain M. This gain is represented by the color of the measurement points in the two upper diagrams to visualize the gain-dependency of the efficiency. The same measurement points are shown differently in the lower diagrams (Figure 5.47c/d): M is shown on the y-axis, and the efficiency is displayed as the color of the measurement points.

The efficiency typically lies in the range of 95% to 98%. The maximum efficiency ($P_{power} = 98.28\%$ / $P_{overall} = 98.12\%$) was measured in G2V operation with $V_{in} \approx 400\ V$ and $V_{out} \approx 340\ V$ at 6.1 kW. The efficiency is 97.4% at the highest output power that could be measured with the test setup (18.8 kW in V2G operation, $V_{in} = V_{out} \approx 800\ V$). The overall efficiency is also good in light-load operation. For example, for an output power exceeding 2% of the maximum rating (i.e., 400 W), $P_{overall}$ is still above 90%. The efficiency only falls below 85% if the output power is lower than 200 W (1% of the maximum rating). This highlights the advantage of soft-switching compared to hard-switching topologies since the switching losses of the latter significantly decrease their efficiency in light-load operation.

In the prototype, the efficiency is generally higher for high output powers and voltages and around or above the resonant tank gain $K \approx 1$. The efficiency is significantly smaller at very low gains or high switching frequencies, which hints that there are some switching-frequency-related losses even though the topology uses ZVS and ZCS. Furthermore, the maximum output power is limited at very low or high gains. For the highest efficiency, it is thus advisable to design CLLLC converters specifically for the battery and grid voltages occurring in the application.

In some V2X use cases, such as for V2L or if the EV battery is used as a PV home storage replacement, the converter will frequently have to deliver a low output power in the range of 50 W to 1 kW. In this case, designing the converter for a lower maximum power capability (e.g., 11 kW) and reducing standby and cooling power demand to improve the efficiency in these light-load operating points might be beneficial.

As explained in Chapter 5.4.1, no bidirectional power supplies were available during characterization, so either load resistors were used, or the converter's input and output sides were connected to transfer power in a loop. In the latter case, the experiments were inevitably limited to the transfer gain $M = 1$. As seen in Figure 5.41, this restricted the G2V operation to comparatively low output loads and only allowed high-power tests in V2G operation. The efficiency remained between 96.8 and 97.5% for these operating conditions above 10 kW. The prototype could not reach the specified maximum output power of 20 kW since the over-current protection was triggered due to unexpectedly high currents in the primary side resonant tank. A possible explanation is that the resonant tank inductors or transformers saturated, possibly also due to an uneven current distribution between the two parallel-connected transformers of the CLLLC prototype. Moreover, the reactive current in the resonant tank that is circulating but not used for

effective power transfer is relatively high in the prototype. On the one hand, this is because the prototype was not designed with custom-made inductive components but using a very limited set of readily available and suitable transformers and inductors. On the other hand, the converter was designed to operate in a broad input and output voltage range at low to high output load (compare Figure 5.41), which results in a resonant tank design with comparatively high reactive current components. Thanks to the successfully implemented light-load burst mode, significantly lower transfer gains can be reached compared to the theoretical FHA transfer gain (also compare [354, pp. 88, 117]). Therefore, a future revision of the converter could be designed with an optimized resonant tank for a narrower gain range with reduced reactive current components, for example, through an increased L_p.

A thermal image of the CLLLC converter prototype in operation using a power module with Schottky diodes and activated SR at an output load of 6.35 kW is shown in Figure 5.48. The image also provides insight into the approximate loss distribution. While the resonant tank capacitors, the DC filters, and even the transformers stay relatively cool, the resonant tank inductors and particularly the power module are the warmest components. For permanent operation at the maximum power output, the cooling concept for the power module needs to be improved. Moreover, a custom-designed and efficiency-optimized transformer that also includes the primary- and secondary-side inductances is beneficial to reduce power losses and improve energy density (compare [354, pp. 62, 127]).

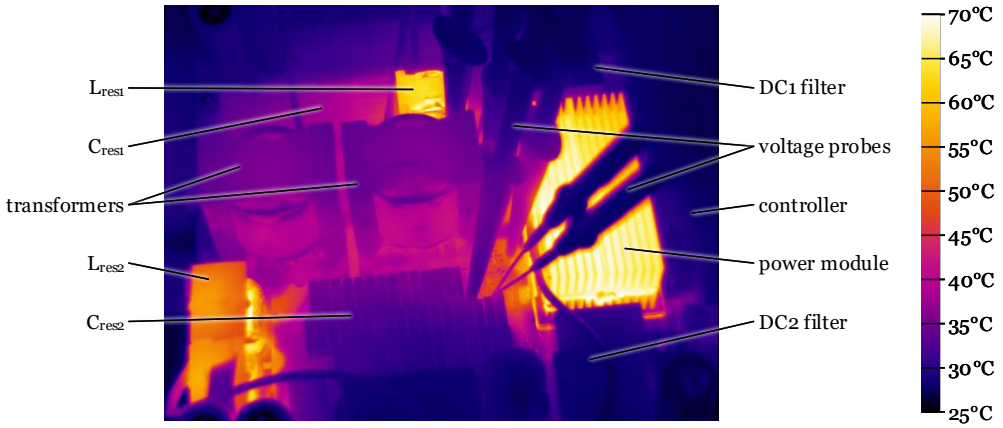

Figure 5.48: Thermal image of the actively air-cooled CLLLC power electronics with diodes and SR after approximately 7 minutes of operation at $P \approx 6.35\ kW$, $V_{in} = V_{out} = 340\ V$, and $T_{ambient} \approx 23°C$

5.5.2 AC/DC converter

In this chapter, the soft switching procedures of the ARCPI prototype are analyzed in detail. Next, the performance of the control algorithms is investigated, ranging from active and reactive power control to asymmetric current injection, grid voltage control, and frequency control. Finally, the inverter efficiency is presented.

For the soft switching behavior analysis, the drain-source voltage of a low-side main MOSFET is measured for the three cases presented in Chapter 4.1.4 and simulated in Chapter 5.2.1 — once for a turn-off and once for a turn-on transition. The results are shown in Figure 5.49 and described in the following. Figure 5.21 may be used to support locating the signals in the schematic.
The reference PWM timing requested from the microprocessor for half-bridge "A" is shown in the first row. The four gate driver signals that the FPGA generates from the reference timing for the low-side (ALS), high-side (AHS), and the outer (AX1) and inner (AX2) auxiliary FETs of half-bridge A are shown in the second to fifth rows. At a DC link voltage of 300 V (shown in the sixth row), this results in the switching transition of the low-side main FET ALS, shown in the seventh row in green. The dead time, i.e., the time during which both main MOSFETs are turned off, is marked by the light red area.
In the low-to-high transition of case 1 (first column), MOSFET ALS starts to turn off at marker 1. Its channel is fully turned off after approximately 150 ns, i.e., while the voltage remains near 0 V, resulting in a ZVS turn-off procedure. Shortly after, at $t \approx -100\ ns$, the drain-source voltage of the ALS FET sharply rises due to the auxiliary circuit. The low-to-high transition ends before the complementary high-side FET AHS is turned on at marker 2. It also turns on with ZVS since its drain-source voltage ($V_{DS,AHS} = V_{DC} - V_{DS,ALS}$) was near 0 V at the end of the dead time, i.e., at $t \approx +100\ ns$.
Similar ZVS turn-on and turn-off procedures occur in all cases. However, when observed closely, it can be seen that no perfect ZVS turn-on is obtained in case 1. This is demonstrated in the high-to-low transition of case 1 in the fourth column. ALS turns on at $t \approx +100\ ns$ (marker 3) when its drain-source voltage is still 11 V, i.e., 3.7% of the DC link voltage is still present. This is due to the proposed optimized soft-switching procedure, in which a boost current in the auxiliary circuit is usually not used. It slightly increases switching losses but significantly reduces the resonant current I_{res} through the auxiliary circuit. As a result, the conduction losses in the auxiliary FETs are reduced, compensating for the negligible switching losses in the main FETs. Since the maximum current through the auxiliary circuit is reduced, the FET rating can be smaller. A boost current is only used when the DC0 potential is not centered, i.e., $|V_{DC0,top} - V_{DC0,bot}| > \Delta V_{DC0,ths} = 3\ V$. In this case, a small additional boost current is built up for balancing. This is realized by turning on the auxiliary FET 110 ns earlier (increase $t_{aux,on,prepone}$) and turning off the main FET 35 ns later (decrease $t_{main,off,prepone}$) than defined in the optimal timing LUTs. This boost

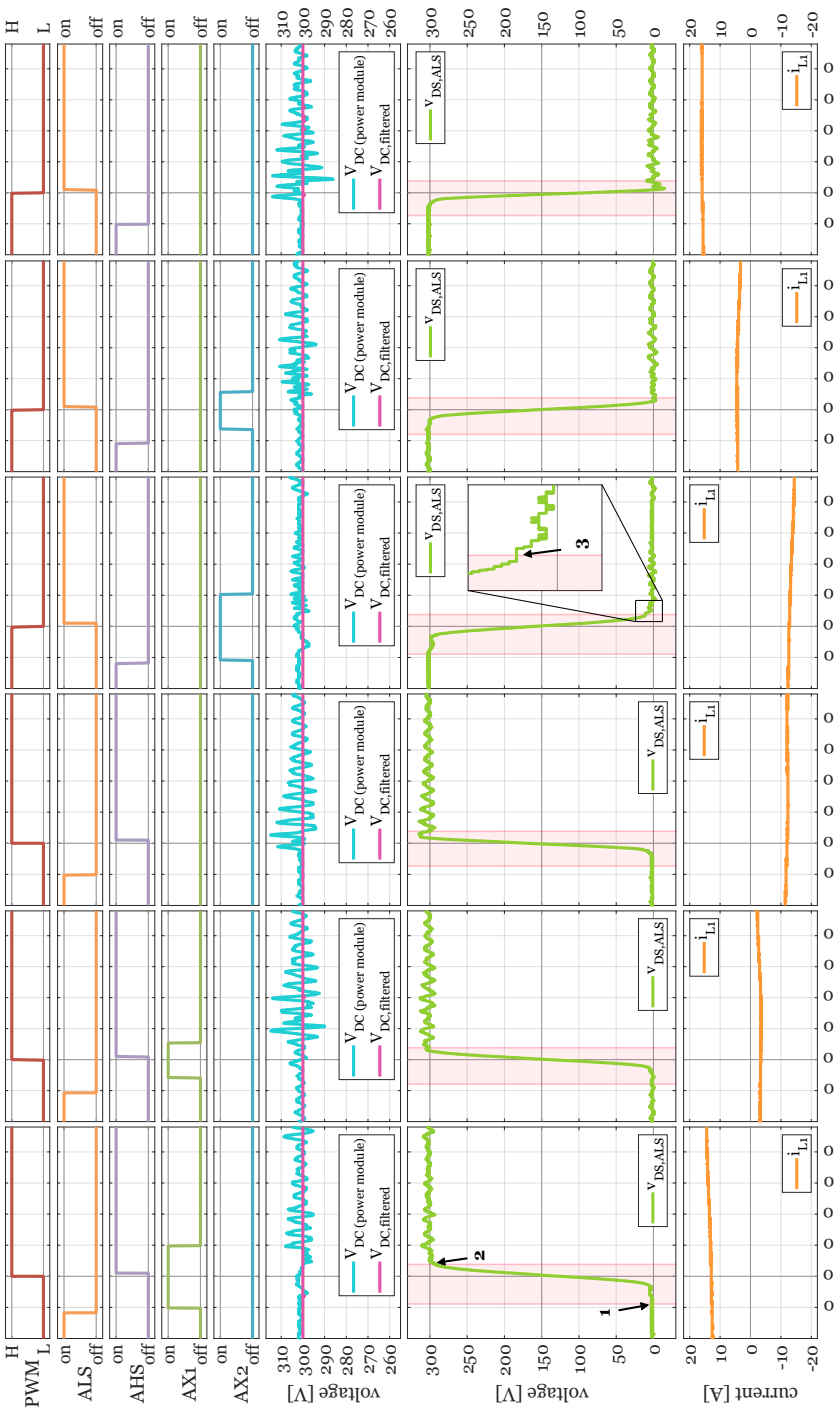

Figure 5.49: Soft-switching transitions of the main MOSFETs in the ARCPI prototype, from top to bottom: reference PWM signal, gate signals of the low-side (LS), high-side (HS), and auxiliary switches (X1, X2) of half-bridge A, DC link voltage measured close to the power module and filtered DC link voltage measured at the DC terminal, drain-source voltage of the low-side FET with dead time (red area), AC grid current of phase L1 — adapted from [C1]

current is only used if it supports balancing the DC link. For example, if $V_{DC0,bot} > V_{DC0,top}$, the timing of AX1, BX1, and CX1 can be adjusted to increase a positive $i_{res,A/B/C}$, which discharges $C_{DC,bot}$ and charges $C_{DC,top}$ and thus balances the split DC link capacitors. Likewise, the timing of AX2, BX2, and CX2 can be altered to intensify a negative $i_{res,A/B/C}$, which balances the capacitors if $V_{DC0,bot} < V_{DC0,top}$. However, if the output current is large ($|I_{out}| > 25\ A$), no boost current is used to limit the maximum auxiliary circuit current. The balancing kept the DC link voltages stable and symmetrical during the experiment with the specified settings.
Due to ZVS, the over- and undershoot of the drain-source voltage is low. This is confirmed by Figure A.5 in Appendix A.6, which shows an overlay of all switching transitions captured at a constant DC voltage of 200 V and an AC voltage of 60 V_{RMS} while the AC output terminals were connected to three 5 Ω load resistors as shown in Figure 5.38c.

While the drain-source voltages of the main FETs transition smoothly, there is an issue with oscillations in the auxiliary circuit in the prototype, as already discussed in Chapter 5.2.1. The oscillations present in the simulations can also be measured in the prototype, which is shown in Figure 5.50, using power modules with *CPM3-0900-0065B* auxiliary MOSFETs. The green curve is a measurement of the drain-source voltage of the low-side MOSFET ALS. The red signal is $v_{aux,A}$, measured between point A' (i.e., the drain connection of AX1) and $DC-_{int}$, as shown in Figure 5.21.
The soft switching transition of $v_{DS,ALS}$ looks as intended. The turn-on of the auxiliary switches also works well, as seen in the red signal at $t = -0.03\ \mu s$ and $t = 3.77\ \mu s$. However, a large oscillation with a frequency of about 15 MHz is induced when switching off the auxiliary FETs. As analyzed using the simulations in Chapter 5.2.1, a likely reason is that the reverse recovery charge of the auxiliary MOSFETs excites the resonant circuit formed by the resonant inductor and the parasitic capacity of the switched-off auxiliary FETs. The measured oscillation looks comparable to the one in the simulation using the *CPM3-0900-0065B* auxiliary FETs at the same operating condition (see Figure 5.13). However, unlike in the simulation, power modules using *CPM3-1200-0075A* auxiliary FETs experienced similar oscillations.
The freewheeling diodes $D_{F+/-}$ (see Figure 5.21) were added to minimize the impact and avoid

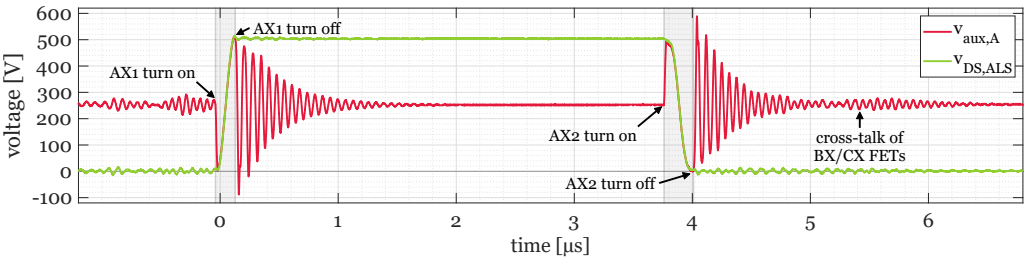

Figure 5.50: Drain-source voltage of FET ALS (green), oscillations of $v_{aux,A}$ (red) at $V_{DC} = 500\ V, i_{L1}(t = 0) = -6\ A$

damaging over-voltages across the auxiliary FETs. Apart from short transient overshoots below the DC− or above the DC+ potential right after the auxiliary FETs turn off, the potential of A' stays within the DC+/− potentials because of the diodes. Nevertheless, the oscillations cannot be damped adequately. As mentioned in Chapter 5.2.1, the problem can be solved by swapping the positions of the resonant inductors and the auxiliary FETs. In this case, the current in the inductor caused by the reverse recovery charge can decay through the freewheeling diodes between the resonant inductors and the auxiliary FETs as well as the body diodes of the main MOSFETs even though the auxiliary FETs are turned off.

In the following, the implemented high-level controllers that determine the active and reactive power fed into or drawn from the grid will be analyzed (compare Figure 5.26). For this purpose, two inverters are connected, as shown in Figure 5.38d. The DC voltage of both inverters is 600 V. One inverter emulates a three-phase grid with an AC voltage of 230 V_{RMS} and a frequency of 50 Hz. It uses a power module with *CPM3-1200-0075A* auxiliary FETs and additional rectifier diodes. The other inverter is the DUT, on which the following controller settings are applied. Its power module contains the same auxiliary FETs but no extra rectifier diodes.

First, the DUT's active power setpoint (p^{set}) is increased from 0 to +15 kW, emulating discharging an EV battery (V2G, grid feed-in). The reactive power setpoint q^{set} stays zero. The resulting DC and AC voltages and currents measured at the DUT are shown in Figure 5.51a. The new setpoint

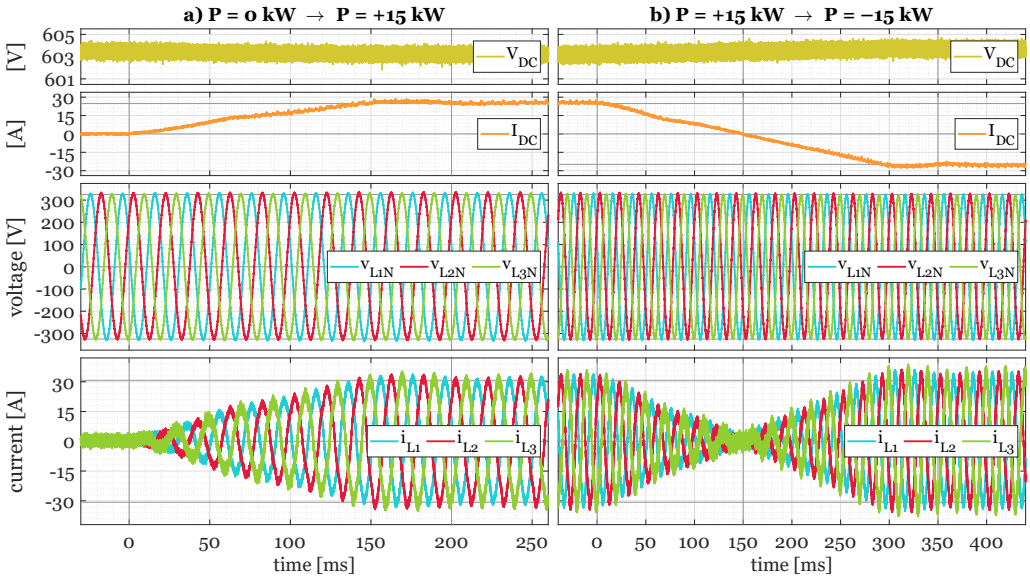

Figure 5.51: ARCPI prototype DC and AC voltages and currents: a) setpoint step from 0 kW to +15 kW (V2G), b) setpoint step from +15 kW (V2G) to −15 kW (G2V)

is applied at $t \approx 0\ ms$. The power is ramped up with 100 kW/s. Therefore, the final value is first reached after around 150 ms and remains stable after approximately 200 ms. The primary reason for ramping up the power comparatively slowly is that in the final V2G charger setup, the CLLLC converter will be connected to the inverter, so it must ramp up its power synchronously. However, the CLLLC converter power cannot be adjusted quickly, so the inverter limits the output power slew rate. Moreover, a slower current ramp rate reduces overshoots caused by the PI current controller of the ARCPI, as well as oscillations in the measured positive- and negative-sequence currents caused by the filters in the DDSRF-PLL (compare Chapter 5.2.2).

Next, a setpoint step from +15 kW (V2G) to −15 kW (G2V) is applied, as shown in Figure 5.51b. The new setpoint is reached after approximately 300 ms and remains stable after about 350 ms. In Figure 5.52a, the setpoint is set back to 0 kW again. A setpoint ramp is also applied here if the inverter is not shut off abruptly but continues operation with 0 kW. In this example, the final value is reached after about 150 ms.

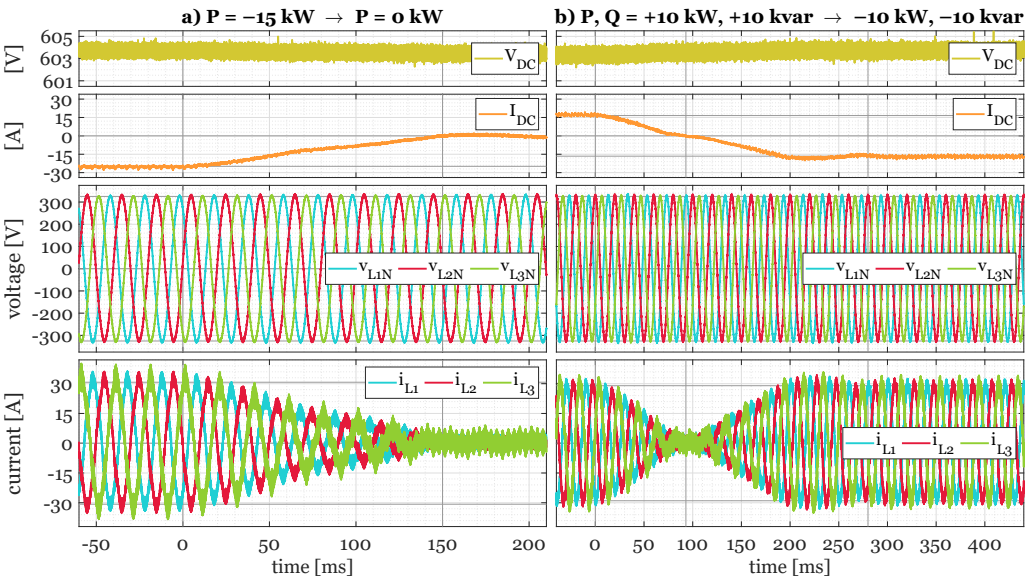

Figure 5.52: ARCPI prototype DC and AC voltages and currents: a) setpoint step from −15 kW (G2V) to 0 kW, b) setpoint step from +10 kW, +10 kvar (V2G, inductive load) to −10 kW, −10 kvar (G2V, capacitive load)

The inverter was also operated at full load (±22 kW) in G2V and V2G direction. The measurement results of the power analyzer are summarized in Table A.4 in Appendix A.6. Besides DC, AC phase, and AC average or sum voltages, currents, and powers, the power factor (P.F.), total harmonic distortion (THD), the components of the fifth and seventh harmonics of the current, the efficiency (η), and the DC ripple current (ΔI) are shown.

In Figure 5.52b, both active and reactive power are used. A setpoint step from +10 kW (V2G) and +10 kvar (inductive load[4]) to −10 kW (G2V) and −10 kvar (capacitive load) is shown. The power reverses at 90 ms. The new setpoint is first attained after around 200 ms with a slight overshoot and stabilizes after approximately 280 ms.

Because of the dual reference frame PLL, the inverter can also draw or feed in asymmetric currents, which is demonstrated in Figure 5.53. Instead of constant power, constant direct and

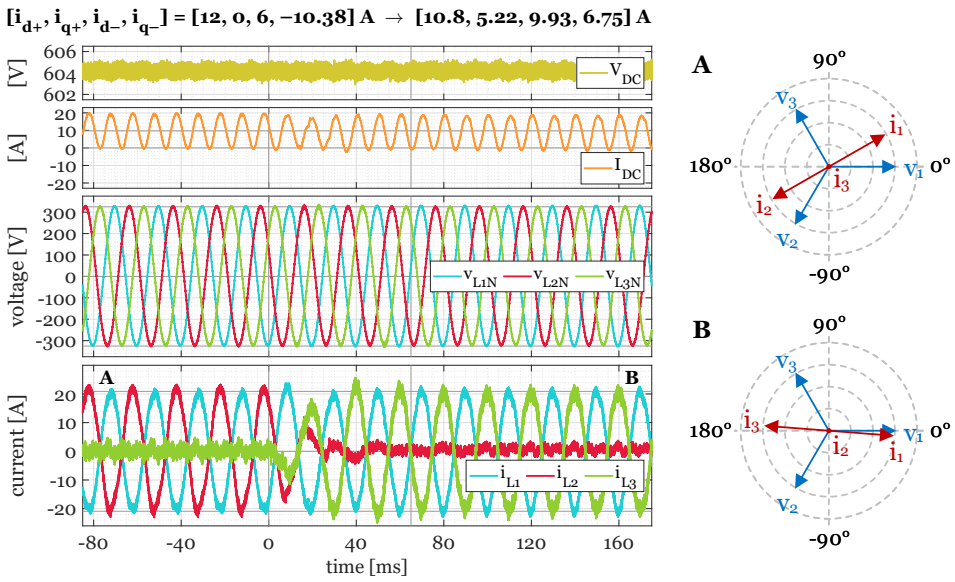

Figure 5.53: DC and AC voltages and currents (left) and vector diagram of the power analyzer (right): setpoint step with asymmetric currents

quadrature current setpoints are requested for both reference frames. In part A of the diagram ($t < 0\ ms$), the setpoint currents are $i_{d+} = 12\ A$, $i_{q+} = 0\ A$, $i_{d-} = 6\ A$, and $i_{q-} = -10.38\ A$. With this configuration, the current i_{L3} is eliminated, and i_{L1} is 14.8 A_{RMS} with a phase angle of 30°. A limitation of this three-leg inverter topology is that only the currents in the three phases, but not the neutral conductor, can be controlled. Therefore, the sum of the three currents $i_{L1/2/3}$ needs to be zero. Consequently, i_{L2} is $-i_{L1}$ in the first example.
A new setpoint is applied at $t = 0\ ms$ with $i_{d+} = 10.8\ A$, $i_{q+} = 5.22\ A$, $i_{d-} = 9.93\ A$, and $i_{q-} = 6.75\ A$. The currents settle after about 65 ms. In part B, the resulting current amplitudes are similar, but this time, i_{L2} is eliminated, the phase angle of i_{L1} is −4.4°, and i_{L3} is $-i_{L1}$.
For more degrees of freedom in current control, a fourth half-bridge could be added for the neutral

[4] Note: The reactive power sign convention in the ARCPI controller is complementary to that of the power analyzer.

conductor, or three single-phase ARCPI systems could be operated in parallel. This way, all three currents can be adjusted individually. For example, a three-phase operation in which only one phase is used or active power is exchanged between phases would be possible.

Next, the grid voltage controller is analyzed by provoking a low-voltage ride-through (LVRT). In Figure 5.54a, the inverter initially feeds 1.5 kW into the grid. The AC voltage controller is configured to feed in negative reactive power when the grid voltage drops: At 50% of the nominal voltage, the reactive power setpoint is -2 kvar. At $t \approx 0\ ms$, the grid-forming inverter reduces its AC voltage setpoint from 230 V to 115 V with 5 V/ms. As a reaction, the grid-following inverter (DUT) increases the reactive power setpoint to -2 kvar (capacitive load). However, the controller needs approximately 210 ms to reach a steady state. Since the direct and quadrature voltages measured by the DDSRF-PLL are filtered with an LPF, the resulting voltages $\bar{v}_{d+/q+/d-/q-}$ lag the actual grid voltage (also shown in the simulation in Figure 5.16). As follows from the controller diagram in Figure 5.29, this causes the inverter to apply a voltage v_{d+}^{set} that is significantly higher than required to reach the current setpoint. As a result, over-currents quickly build up in the first 30 ms. However, they are successfully limited by the over-current control module presented in Figure 5.30.
Apart from the slow AC and DC current oscillations between 0 and 200 ms, there is a significant ringing with a frequency of about 2.1 kHz, particularly near $t \approx 10\ ms$. This is likely caused by an interaction of the over-current controller with the AC filter, particularly $L_{filt,2}$ and $C_{filt,2}$, stimulated by the AC voltage drop.

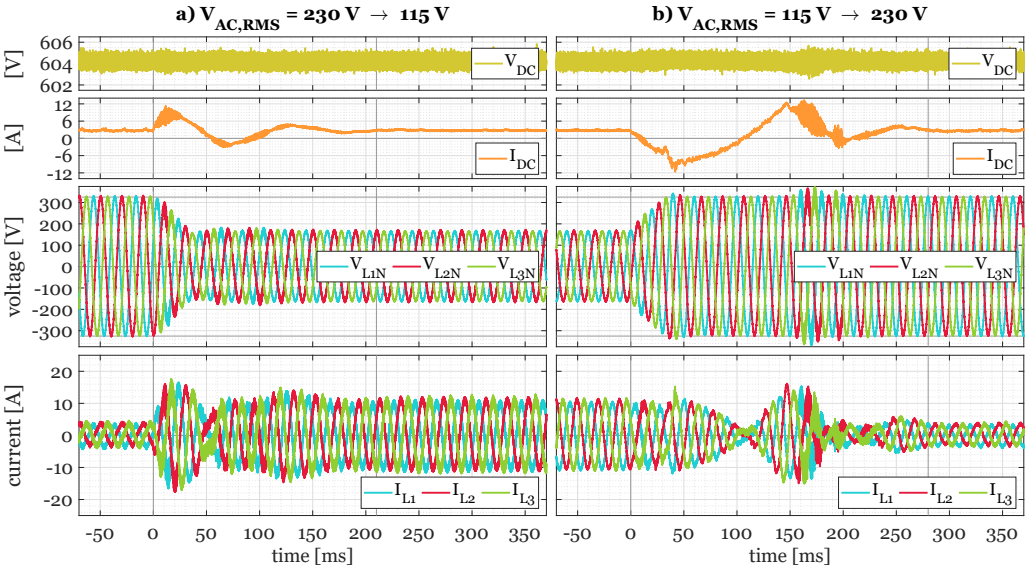

Figure 5.54: Grid voltage control: a) AC voltage drop from 230 V to 115 V, b) recovery to 230 V

In Figure 5.54b, the low-voltage fault emulated by the grid-forming inverter is cleared, and the voltage rises back to 230 V. Consequently, the DUT omits the reactive power fed into the grid and returns to its purely active power setpoint. The currents are stable after approximately 280 ms. This time, the voltages $v^{set}_{d+/d-/q-}$ (see Figure 5.29) are lower than required to reach the current setpoint due to the voltage LPF of the PLL, so the inverter temporarily even draws power.
The LVRT event was also captured with the power analyzer. The extracted signals are shown in Figure A.6 in Appendix A.6. During the voltage drop, the DUT supplies a positive reactive power to the grid-forming inverter. This means that the DUT draws negative reactive power, i.e., it has a capacitive load behavior, which increases the grid voltage. The active power is maintained during the event.
If steeper grid voltage slopes are generated or the DUT operates with significantly higher output power before a low-voltage event, the inverter will disconnect and turn off due to over-currents. However, the voltage regulation works reliably for slow voltage variations, for example, due to a variation of grid load during the day. For a more robust ride-through during fast, transient events, the control algorithms need to be improved. This could be achieved by using a different filter structure for the voltages generated by the DDSRF-LPF or an entirely different PLL topology (e.g., the DSOGI-PLL — see Chapter 4.2.2). Moreover, the over-current controller branch could be optimized, and the AC filter and controller settings could be tuned to reduce ringing.
Nevertheless, the presented LPF and NF configuration for the voltages and currents determined by the DDSRF-PLL yielded smoother results and was significantly less prone to overshoots or oscillations in regular grid conditions compared to other configurations tested using only LPFs or only NFs or substantially faster filter settings. While the output power change rate and the immunity to transient voltage faults are limited because of the filters, they are sufficient for charging and most V2G applications that support grid stability.

The inverter can also react to asymmetric grid voltages by purposefully injecting or drawing asymmetric currents. This can be used to reduce grid asymmetries or minimize oscillations of the transferred power caused by the voltage imbalance. An example is shown in Figure 5.55, in which the grid phase voltages were set to 60 V, 120 V, and 90 V by the GFMI. For $t < 0\ ms$ in Figure 5.55a, regular active power control with a setpoint of +2 kW (V2G) is used. The grid-side inverter currents are symmetric since only the current i_{d+} is utilized, and all other components are zero. However, due to the voltage imbalance, the transferred power oscillates between approximately 1.2 and 2.8 kW. At $t = 0\ ms$, the inverter transitions into the CIAP control presented by Revelo and Silva [331], which was adapted and implemented in the inverter. The direct and quadrature current components of the positive and negative sequence are adjusted to transfer a constant active power despite the large voltage imbalance. The output power reaches a steady state after approximately 30 ms.

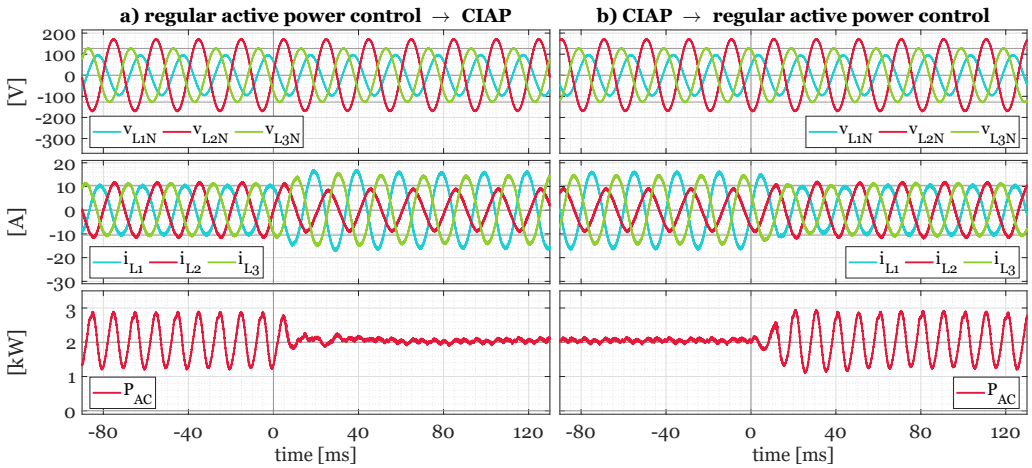

Figure 5.55: Grid voltage control: Asymmetric current injection during voltage imbalance: a) transition from regular to CIAP control, b) returning to regular control

Figure 5.55b shows the transition from CIAP to regular control. The currents become symmetric after approximately 25 ms, and the active power begins oscillating again.

Next, the frequency controller is analyzed. A large frequency drop that occurred after a system split of the Central European electricity grid on July 24, 2021, was emulated on the GFMI. Frequency data of the Hernani substation in Spain was taken from a report on the incident [344, pp. 96f.]. The data was modified five seconds after the start of the event, i.e., after the nadir (minimum frequency), to return to the frequency present before the event faster. The grid-forming inverter starts with 230 $V_{AC,RMS}$ and a frequency of 49.96 Hz present just before the event. The DUT's power setpoint is -5 kW, i.e., the inverter draws 5 kW from the grid.
Three runs were carried out. In Figure 5.56a, only Frequency Containment Reserve (FCR) is activated in the DUT with $k_D = 6\ \frac{kW}{Hz}$. Virtual inertia (VI) is disabled, i.e., $k_I = 0\ \frac{kW \cdot s}{Hz}$. In Figure 5.56b, the FCR is disabled, and only the VI is activated, with $k_D = 0\ \frac{kW}{Hz}$ and $k_I = 2\ \frac{kW \cdot s}{Hz}$. In Figure 5.56c, both FCR and VI are enabled with $k_D = 6\ \frac{kW}{Hz}$ and $k_I = 2\ \frac{kW \cdot s}{Hz}$.
In all cases, the frequency event starts at $t = 0\ s$. The GFMI follows the programmed frequency profile (f_g^{set} in the figure) open-loop without responding to the varying power of the DUT, assuming that the grid frequency is fixed and cannot be changed by the individual inverter. The actual frequency measured by the power analyzer is displayed as f_g^{meas}. The frequency profile obtained from the report contains oscillations three to five seconds after the event starts, which are reproduced by the GFMI accurately. The oscillations are caused by local transients at the substation where the measurement originates — potentially voltage oscillations due to significant load shedding at 49.0 and 48.7 Hz [344, pp. 30-32, 73f.]. The strong oscillations are useful to check whether the VI controller remains stable even during severe incidents.

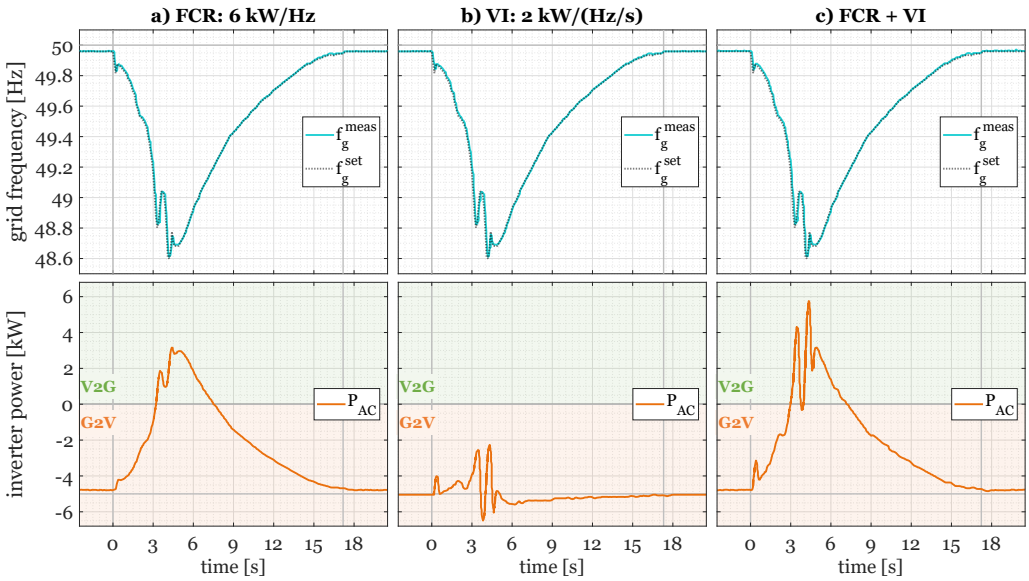

Figure 5.56: Grid frequency drop and inverter reaction with a) frequency control, b) virtual inertia, c) both

In Figure 5.56a, the FCR controller of the DUT adjusts the inverter power adequately. The larger the frequency deviation from 50 Hz, the more the power drawn from the grid is reduced compared to the setpoint of -5 kW. Since the frequency already deviates at the start ($t < 0\ s$), the actual power magnitude is slightly lower than 5 kW before the incident. Between 3.2 and 7.5 s, the DUT even feeds in power into the grid, with a seamless transition between G2V and V2G operation. Unlike in the conventional FCR control presented in Chapter 4.2.3, the inverter is configured to further adjust its power outside the control band of 49.8 to 50.2 Hz as long as a predefined limit is not exceeded. The ratio between the frequency deviation and the measured power variation is approximately 6 $\frac{\mathrm{kW}}{\mathrm{Hz}}$, i.e., as configured. The power profile is a little smoother than the frequency profile due to the low-pass filtering of the measured grid frequency. The power lags behind the frequency by about 0.1 seconds.

In Figure 5.56b, only VI is active, and the inverter adjusts the power according to the frequency slope. For slow frequency changes, such as between six and fifteen seconds, the factor between the frequency derivation and the inverter power adjustment is at about 2 $\frac{\mathrm{kW{\cdot}s}}{\mathrm{Hz}}$, as expected. Even though the oscillation at around $t = 4\ s$ is also reflected in the inverter output power, the factor is only about 1 $\frac{\mathrm{kW{\cdot}s}}{\mathrm{Hz}}$ for this oscillation. The significant damping likely comes from the additional low-pass filters used in the smooth frequency derivative calculation. If no filtering was used in the frequency estimation and the calculation of its derivative, the output power would be adjusted very harshly. Since the power adjustment also affects the grid voltages at the inverter output, there is a risk of negatively influencing the frequency estimation in the PLL and ultimately causing an

unstable VI control in case of such extreme events. Thus, damping rapid frequency oscillations with filtering can be beneficial. However, the additional LPFs also increase the delay between the frequency profile and the resulting power response to approximately 0.25 s, which is higher than in the FCR control.
Both FCR and VI are enabled in Figure 5.56c. The initial power response at $t \approx 0.5\ s$ is significantly higher than when only using FCR, and the output power adjustment in the nadir is also larger. Thus, the combined controller can reduce frequency variations in the grid more effectively and increase its robustness in case of such extreme events.
However, the effects of a large number of inverters with VI control on grid stability have yet to be investigated. Ideally, the control parameters can be adapted to the grid conditions at runtime, e.g., to the capacity of grid-supporting inverters active in the grid or the local grid impedance.

Finally, the efficiency of the ARCPI prototype was investigated. The DUT uses a power module with *CPM3-1200-0075A* auxiliary FETs, internal capacitors, and no rectifying diodes. The power electronics efficiency η_{power} (Equation 5.20a) was measured by the power analyzer. The overall efficiency $\eta_{overall}$, considering the power demand for the controller and cooling, was calculated afterward with Equation 5.20b.

$$\eta_{power} = \frac{P_{out}}{P_{in}} = \begin{cases} \frac{P_{DC}}{P_{AC}}, & \text{in G2V operation} \\ \frac{P_{AC}}{P_{DC}}, & \text{in V2G operation} \end{cases} \tag{5.20a}$$

$$\eta_{overall} = \frac{P_{out}}{P_{in} + P_{aux}} \tag{5.20b}$$

The standby power consumption of the ARCPI prototype with cooling and relays turned off is approximately 5.2 W. The power demand increases to 13.2 W during active operation due to the grid-side relays and two fans mounted onto the power module. An external fan was added for prolonged operation at higher power, so P_{aux} increases to a maximum of 20.4 W depending on the required cooling power. The power electronics and overall efficiencies measured at an AC voltage of 230 V_{RMS} and a DC link voltage of 600 V are shown in Figure 5.57.
The efficiency is typically above 98% and almost identical in G2V and V2G directions. For typical charging powers of 7 to 22 kW, the overall efficiency is almost constant at around 99%. The maximum power electronics efficiency is 99.26% at 12 kW in V2G operation, which results in a 99.09% overall efficiency. At maximum load, η_{power} is 98.96%, and $\eta_{overall}$ is 98.97% in either direction. The efficiency at light load is also good. The overall efficiency only falls below 97% for an output power of less than 2 kW. At 200 W (less than 1% of the nominal power), $\eta_{overall}$ is still approximately 77% in G2V and 80% in V2G mode.

The inverter was also operated with high output power for extended periods to inspect the temperature development of its components over time. An example is shown in Figure 5.58,

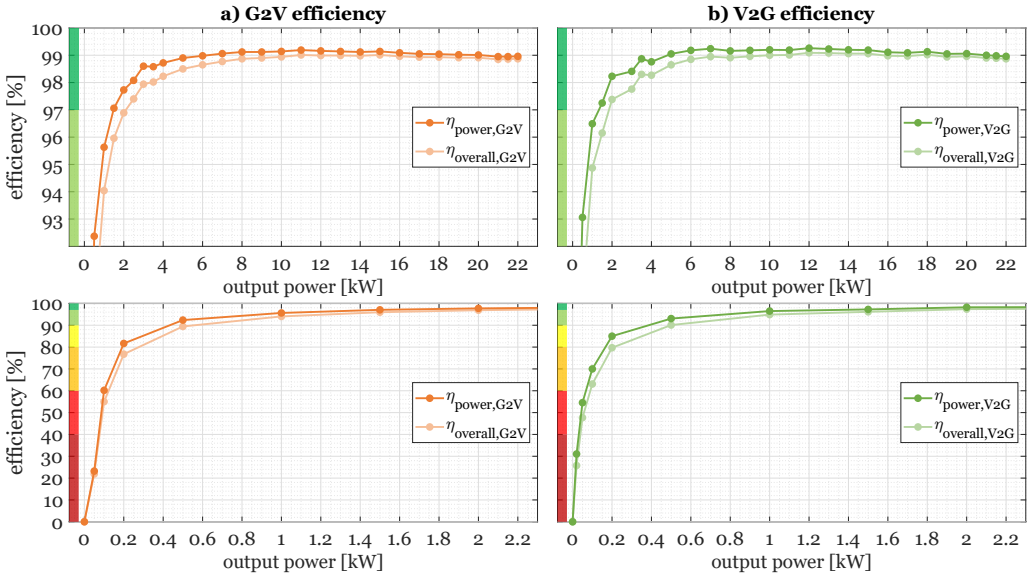

Figure 5.57: G2V and V2G efficiency of the ARCPI prototype over the entire power range (top) and at low load (bottom)

where the GFMI and the DUT are operated with a constant power of 15 kW. The original thermal image is shown on the left side, and an overlay with a photo to facilitate identifying components is displayed on the right side. After 11 minutes of operation, the hottest component, one of the grid-side relays, reaches a temperature of 60°C. At that time, the cooling fins of the power module only have about 44°C.

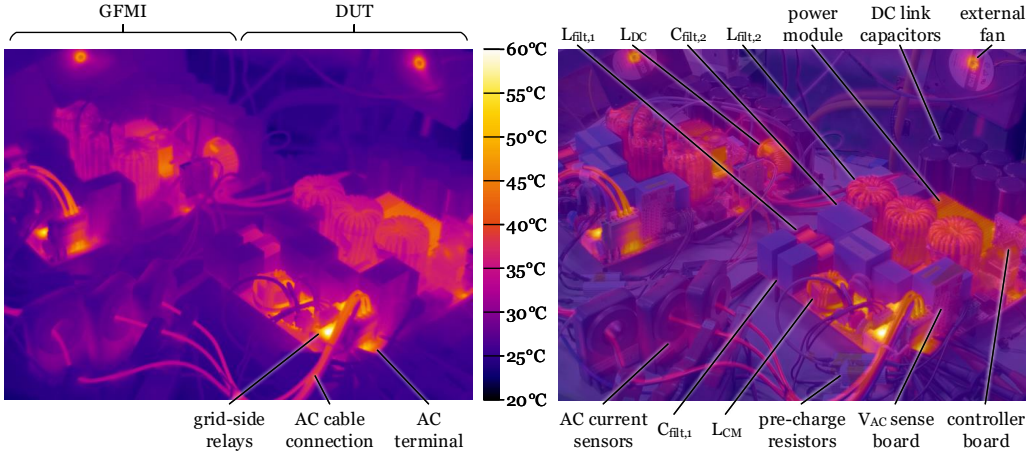

Figure 5.58: Thermal image of the ARCPI prototypes (GFMI + DUT) after 11 minutes of operation at $P = +15\ kW$ (V2G), $V_{AC} = 230\ V$, $V_{DC} = 600\ V$, and $T_{ambient} \approx 23°C$ (left: original, right: overlay of a photo)

5.5.3 Power hardware-in-the-loop test bench

After the functionality of the AC/DC and DC/DC converters have been validated individually, they are connected to be operated as a V2G charger to inspect the combined controller performance and efficiency. The AC side of the ARCPI DUT is connected to a grid-following inverter again, and its DC side is linked to the DC1 port of the CLLLC DUT. Initially, the CLLLC converter's DC2 port is connected to the *FlexBat* battery system, as shown in Figure 5.39b. This setup is comparable to its use as a stationary DC V2G charger.

The inverter's DC link needs to be pre-charged from the AC grid for power-up, as described at the end of Chapter 5.3.6. This is demonstrated in Figure 5.59. The steps of the start-up procedure mentioned in the figure are also indicated by the purple numbers in Figure 5.60. In the first phase, between $t = 0\ s$ and $t \approx 0.5\ s$, the DC link is charged passively via the pre-charge resistors shown in the "grid-side relays" block of Figure 5.60. The MOSFETs are turned off, but a current that is limited through the pre-charge resistors is rectified by the body diodes of the FETs or external rectifier diodes, if available. In the second phase, between $t \approx 0.5\ s$ and $t \approx 1.0\ s$, the MOSFETs are controlled to charge the DC link to its setpoint value through the pre-charge circuit. Afterward, the main relays are turned on so the inverter is properly connected to the grid. When the main relays are safely turned on, the pre-charge relays open again. Moreover, the supply voltage of the main relays is lowered to save energy. The inverter is now ready for operation so that the battery can be connected.

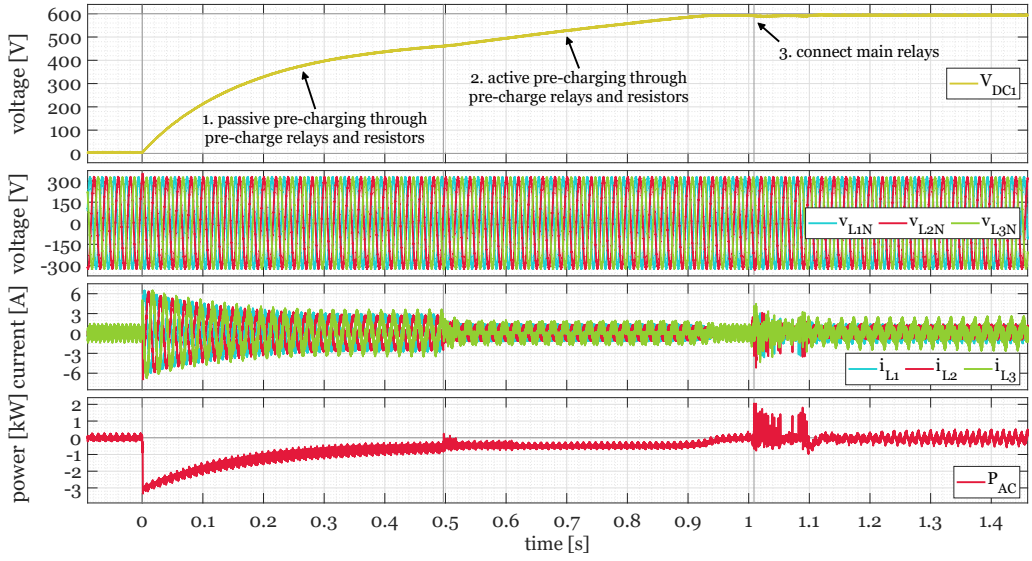

Figure 5.59: Pre-charging of the inverter-side DC link (DC1) from the grid

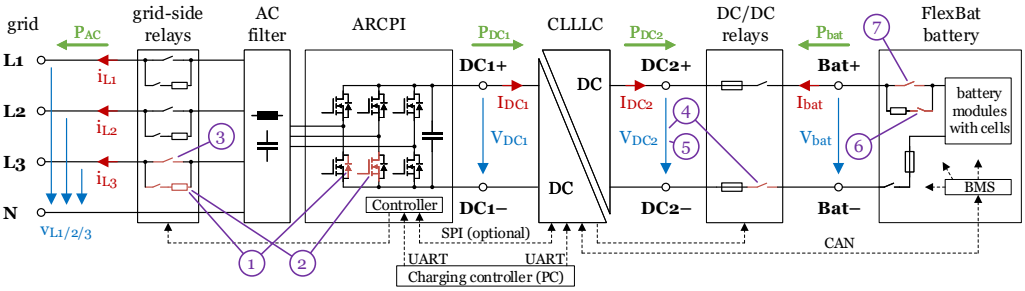

Figure 5.60: Overview of the steps and components involved in the pre-charging procedure

The CLLLC converter communicates to the *FlexBat* battery system via CAN and signals that the inverter is ready. Once the *FlexBat* system is ready, the converter is expected to apply a test voltage of 50 V to confirm that the communication and voltage measurement of the BMS work. The DC/DC relays are closed, and the test voltage is applied at $t = 0\ s$ in Figure 5.61. The *FlexBat* system confirms the test voltage and requests the CLLLC converter to apply the battery voltage, which is about 390 V in this example. The CLLLC converter applies the voltage at $t = 4\ s$. Since no load is connected, the converter operates in the light-load burst mode, which produces slight periodic overshoots. At $t = 14.4\ s$, the BMS acknowledges the voltage and connects its own pre-charge relays. At $t = 19.6\ s$, the main relays of the battery are connected, so the battery is ready to be charged or discharged by the V2G charging system.

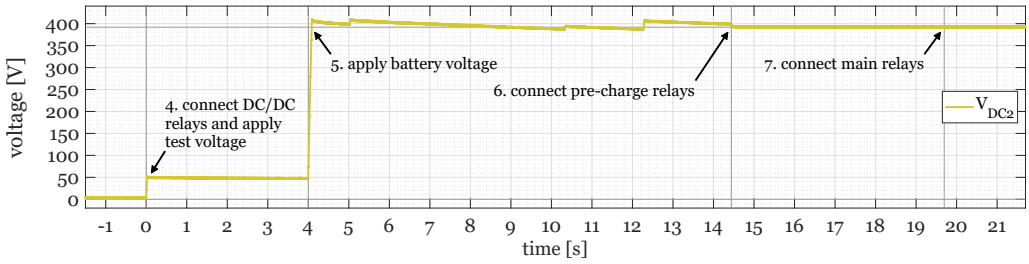

Figure 5.61: Pre-charging of the battery-side DC link (DC2) with connection to the *FlexBat* battery system

In Figure 5.62a, the inverter starts to draw 2 kW from the grid at $t = 0\ ms$ to charge the *FlexBat* battery. The AC power first reaches the setpoint after 35 ms and stabilizes after approximately 130 ms. In this and the following examples, the inverter and converter did not communicate with each other via SPI (as shown in Figure 5.60) to smoothly synchronize the transmitted power. The DC/DC converter adjusted its power independent of the inverter with the objective of keeping V_{DC1} constant. Because this relatively slow control causes oscillations in the DC1 link, the battery power P_{bat} increases irregularly in the first 30 ms before stabilizing (see Figure 5.62a). In the new operating point, the combined power electronics efficiency of the AC/DC and DC/DC converter

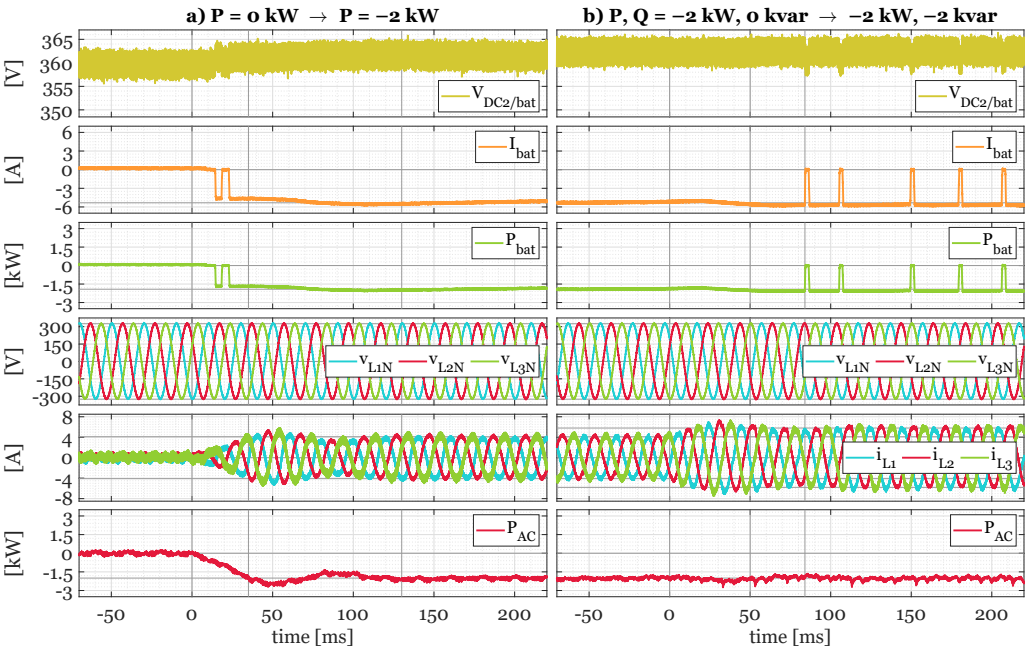

Figure 5.62: V2G charger connected to the *FlexBat* system: a) setpoint step from 0 to −2 kW (charge battery), b) addition of −2 kvar reactive power (capacitive load) — from top to bottom: DC2/battery voltage, current, and power, AC voltages, currents, and active power

measured by the power analyzer is 94.69%.

In Figure 5.62b, a reactive power of −2 kvar (capacitive load) is added at $t = 0\ ms$. The inverter power is stable after 50 ms. The CLLLC converter operates near the maximum switching frequency at the given voltage ratio since the output power is only 2 kW. Triggered by the load change, it temporarily transitions into the discontinuous operation mode (light-load burst mode) at $t \approx 85\ ms$. This introduces a harmless ripple to the battery current, which increases efficiency compared to operating at an otherwise higher necessary switching frequency. Even though the AC current amplitudes are higher due to the additional reactive power, the efficiency rises to 94.93%. However, the converter returns to the continuous mode after several seconds, as shown in Figure 5.63a.

In Figure 5.63b, the active and reactive power setpoint is reset to zero. While the AC power is reduced, the CLLLC converter stabilizes the common DC1 voltage, which is not shown due to a lack of oscilloscope channels. Due to the reduced AC power, V_{DC1} decreased. Therefore, the converter temporarily even discharges the battery again between 60 and 105 ms to increase V_{DC1} to its nominal setpoint again. The AC and DC powers stabilize after about 150 ms.

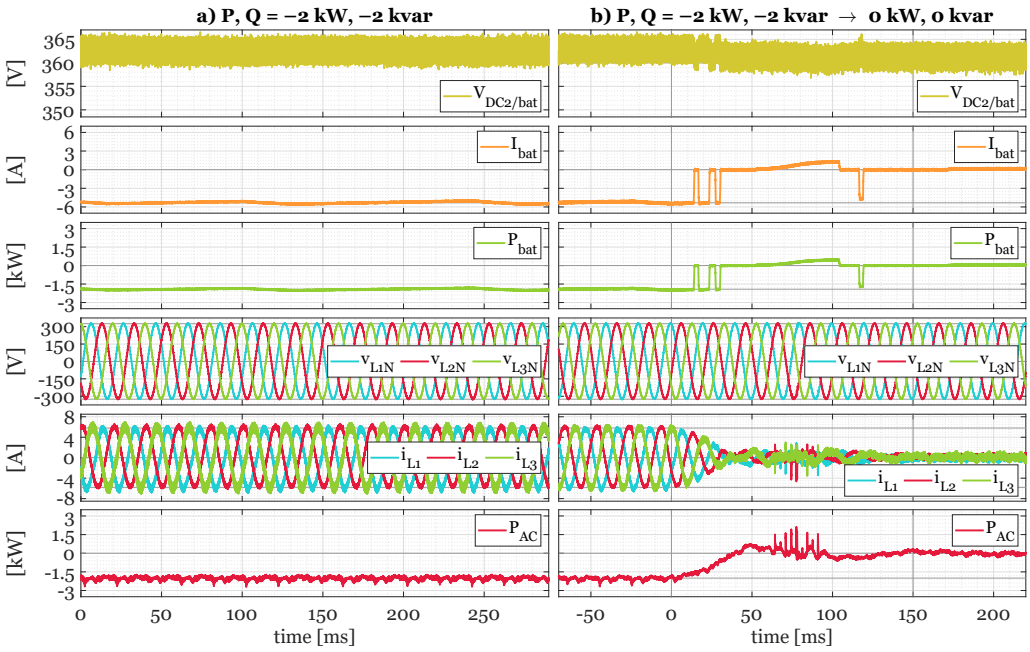

Figure 5.63: V2G charger connected to the *FlexBat* system: a) stable operation in continuous switching mode at −2 kW (charge battery) and −2 kvar (capacitive load), b) setpoint step to 0 kW and 0 kvar

The CLLLC converter was designed for a higher battery voltage. Its transfer gain is not ideal for use with the *FlexBat* battery system. For stable operation at 230 V grid voltage, a nominal DC1 voltage of at least 600 V is required. The maximum battery voltage of the *FlexBat* system is approximately 400 V. This results in a minimum transfer gain M of 1.5 for the CLLLC converter in V2G operation. As shown in Figure 5.41, this requires a very low switching frequency below the resonant frequency f_{res2}. In the current implementation of the CLLLC controller, the converter starts at the highest switching frequency and reduces it gradually until the voltage or current setpoint is reached. This limits the controller speed for operating points with low switching frequencies. More importantly, the maximum output power is limited at $f_{sw} < f_{res1/2}$ due to the risk of hard switching transitions in the capacitive region. Therefore, the following experiments were carried out with a bidirectional power supply with a higher voltage setting at output DC2 instead of the battery (compare Figure 5.39a).

Figure 5.64a shows a setpoint step from +2 kW/+2 kvar (discharge battery, inductive load) to −2 kW/−2 kvar (charge battery, capacitive load). Unlike in the previous figures, the internal DC1 voltage is measured instead of V_{DC2} since the bidirectional power supply at DC2 keeps V_{DC2} at a stable voltage of 440 V. The CLLLC converter is configured to control V_{DC1} to 600 V. The inverter only adjusts its AC power when the voltage is lower than 590 or above 610 V.

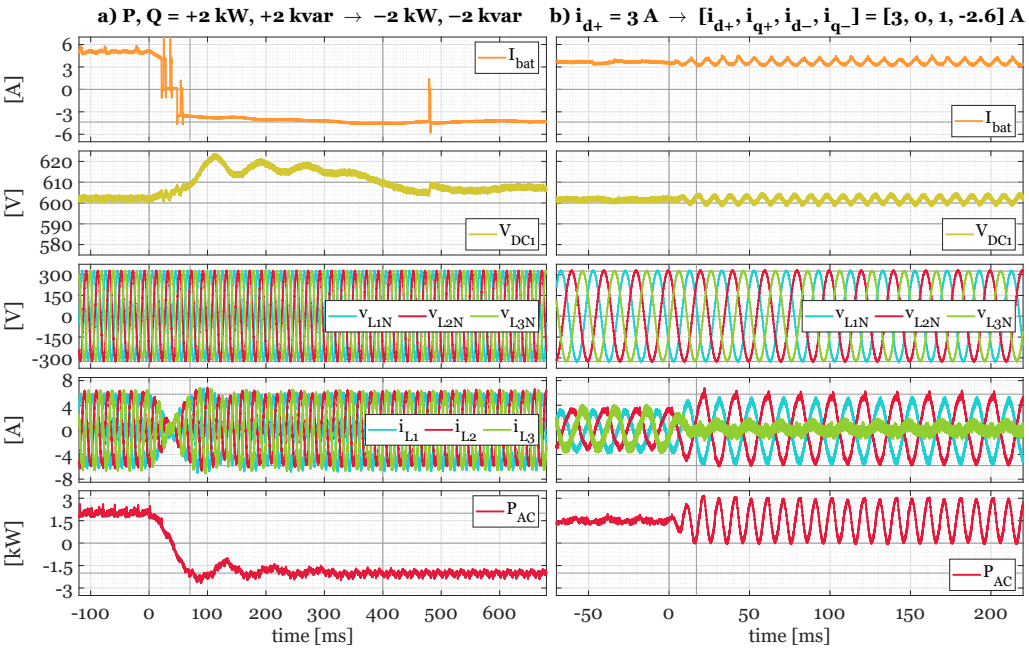

Figure 5.64: V2G charger connected to a bidirectional power supply: a) setpoint step from +2 kW/+2 kvar (V2G, inductive load) to −2 kW/−2 kvar (G2V, capacitive load), b) transition from symmetric to asymmetric operation — from top to bottom: "battery" current, DC1 voltage, AC voltages, currents, and active power

The AC power transitions from −2 kW to +2 kW in 70 ms and stabilizes after approximately 340 ms. Due to the power reversal, the DC1 voltage rises. As a reaction, the DC/DC converter changes the power transfer direction within 50 ms and increases the output current to reach the desired DC1 voltage. Since the converter's controller is comparatively slow and V_{DC1} increases above the maximum tolerated limit, the inverter temporarily reduces the AC power near $t \approx 130\ ms$. The nominal DC1 voltage range is reached again after 400 ms.

In the following, V_{DC2} is set to 460 V. In Figure 5.64b, the inverter transitions from a symmetric current of $i_{d+} = 3\ A$ to an asymmetric setpoint current with $i_{d+} = 3\ A$, $i_{q+} = 0\ A$, $i_{d-} = 1\ A$, and $i_{q-} = -2.595\ A$, which minimizes i_{L3}. Since the average AC power is similar, the new setpoint is reached after less than 20 ms. Due to the asymmetric AC currents, the injected active power oscillates. The capacitors in the DC1 link absorb part of it. Since the CLLLC converter reacts to the DC1 voltage level, it also adjusts the transferred current, but a ripple of ±3 V remains. For a significantly higher asymmetric output power or unfavorable load conditions, the converter's DC link control is not fast enough, and V_{DC1} oscillates stronger. As a result, the inverter cannot apply the desired currents since its DC link control intervenes by adjusting i_{d+} to keep V_{DC1} in the tolerated range.

In Figure 5.65a, a new setpoint is applied at $t = 0\ ms$ using $i_{d+} = 2.7\ A$, $i_{q+} = 1.3\ A$, $i_{d-} = 2.5\ A$, $i_{q-} = 1.7\ A$. Again, the AC currents reach their new setting within 20 ms since the average power remains similar. The CLLLC converter corrects the slightly increased V_{DC1} using three short switching interruptions and proceeds in continuous operation after around 80 ms.

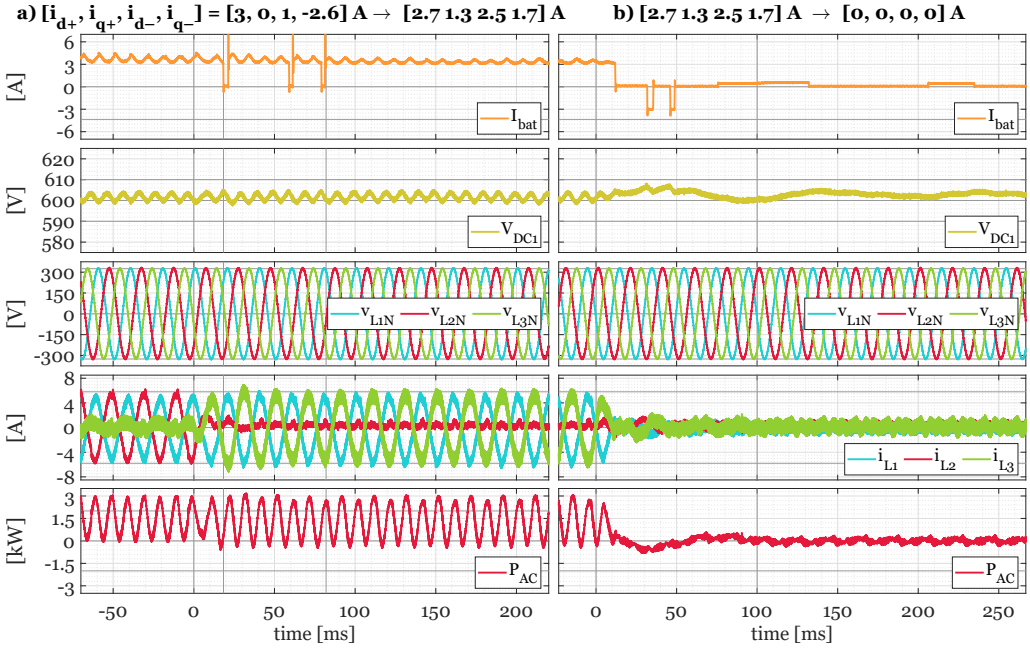

Figure 5.65: V2G charger connected to a bidirectional power supply: a) asymmetric current setpoint step, b) setpoint step to 0 A

In Figure 5.65b, a setpoint in which all currents $i_{d+/q+/d-/q-}$ are zero is applied. The AC power fully stabilizes after around 100 ms. Since the inverter's MOSFETs are still active afterward, there are small but non-negligible conduction and switching losses that would slowly drain the DC link. The power to cover these losses and keep the DC link voltage near the target value is delivered by the DC/DC converter because the AC power setpoint is zero. The CLLLC converter operates in light-load mode and only transfers power occasionally using its maximum switching frequency because the power demand is extremely low. An example is shown between 205 ms and 235 ms. Since no AC power is transferred, the switching operation could be turned off, but as a result, the grid-side LCL filter would draw reactive power from the grid. For sustained operation without power transfer, both the FETs and the grid-side relays can be turned off, which significantly reduces standby losses. In this case, the inverter needs to pre-charge the DC link again to reconnect to the grid, which takes one to two seconds before the regular operation can be continued. However, for many V2G use cases, this increased reaction time is sufficient.

In Figure 5.66, the FCR and VI control is activated in the V2G charger, using $k_D = 2\ \frac{kW}{Hz}$ and $k_I = 1\ \frac{kW \cdot s}{Hz}$. The inverter's AC power is set to -2 kW (G2V). At $t = 0\ s$, the frequency event described in the previous chapter is applied by the GFMI. The AC power applied by the

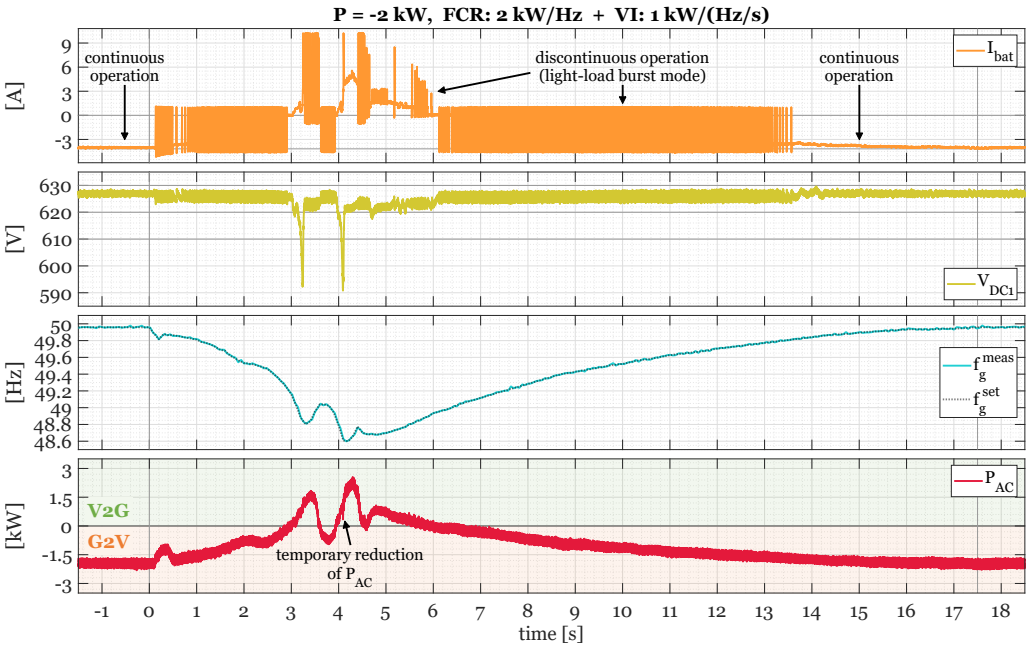

Figure 5.66: Grid frequency drop and V2G charger reaction with activated FCR and VI

inverter looks as expected. Similar to the stand-alone operation of the inverter, the controller delay between the frequency curve and the power reaction is between 0.1 and 0.2 seconds due to the frequency filters. Generally, the CLLLC converter's DC link control works well. However, during the transition from G2V to V2G power transfer direction at $t \approx 3.2\ s$ and $t \approx 4.1\ s$, the DC link voltage transiently drops by about 19 V below the target range of 610 to 630 V. In the latter case, the inverter reduces its power by approximately 0.6 kW for about 20 ms to prevent a further decline of V_{DC1}. This can be seen by the tiny downward spike in P_{AC} at $t \approx 4.1\ s$. Nevertheless, the V2G charger can support grid frequency stabilization well.

In the previous experiments, the CLLLC converter only adjusted its output power based on the V_{DC1} and V_{DC2} measurements. The communication between the two devices for feedforward control of the inverter's setpoint power to the DC/DC converter was not implemented at that time, i.e., $k_{ff,P} = 0$ in Figure 5.7 of Chapter 5.1.2. However, the results presented so far have shown that this feedforward control would be beneficial in supporting the V_{DC1} voltage regulation of the

otherwise relatively slow CLLLC converter controller. Based on these findings, the communication between the converters and the feedforward control was implemented.

First, various factors $k_{ff,P}$ were analyzed, starting at lower DC1 voltages, as shown in Figure 5.67. The desired V_{DC1} range is set to 90 V to 110 V in the ARCPI (highlighted in green) and to 100 V in the CLLLC converter. The DC2 voltage is set to 80 V by the bidirectional power supply, and an AC voltage of 25 V_{RMS} is supplied by the GFMI. The controller performance without feedforward control ($k_{ff,P} = 0$, shown in Figure 5.67a) is compared to the performance with enabled feedforward control using $k_{ff,P} = 0.1\frac{V}{W}$ (Figure 5.67b). For this purpose, a setpoint jump from 0 to +150 W (V2G) is applied, i.e., the inverter shall feed power into the grid.

Even before the setpoint is applied, the DC/DC converter occasionally transfers power to keep V_{DC1} near its setpoint of 100 V. Without feedforward control, the converter starts power transfer 11 ms after the setpoint step is applied. Due to the leading ramp-up of the AC power, the DC link voltage falls to 82 V, i.e., about 8.9% below the lower target value. Consequently, the inverter's DC link controller reduces power transfer near $t \approx 70\ ms$ until V_{DC1} returns to the target range. The AC and DC power synchronize after approximately 80 ms and reach their target value about 160 ms after the setpoint step.

With feedforward control, the CLLLC converter restarts power transfer within less than a millisecond after the inverter receives the new setpoint, even before V_{DC1} falls below 100 V. Because

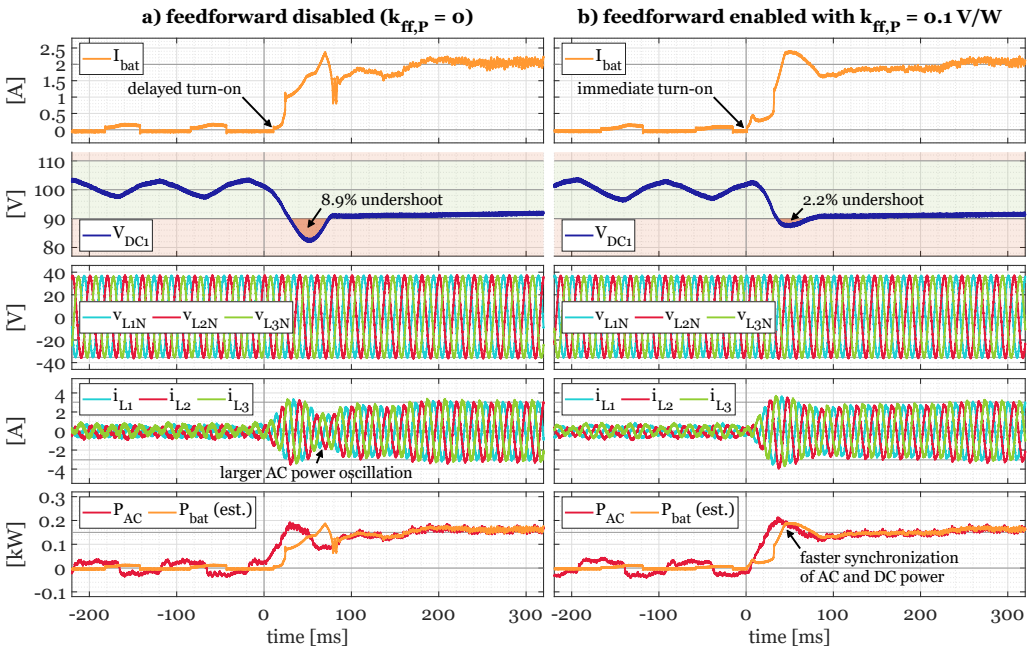

Figure 5.67: DC1 voltage control: a) without and b) with feedforward of the AC power setpoint to the CLLLC converter

the converter was prepared to the expected DC link drop, V_{DC1} only falls to 88 V, i.e., about 2.2% below the lower threshold of the target range. The AC and DC power synchronize between 50 to 80 ms after the setpoint step is applied and settle after approximately 120 ms.
This clearly shows that the feedforward control of the inverter's power setpoint improves the DC link voltage stability and controller performance. Unfortunately, no further measurements with activated feedforward control could be conducted because the CLLLC converter's power module broke with a bridge short circuit during a test with a higher DC link voltage. The breakdown voltage of the semiconductors was impaired due to solder residues in the power module prototype, and the CLLLC converter prototype does not feature a quick over-current detection for the power module. Due to time constraints, further modules could not be assembled.

The estimated overall efficiency of the V2G charging system, including the power losses in the ARCPI and the CLLLC converter prototypes, as well as the auxiliary power demand for the controllers and cooling fans, is shown in Figure 5.68. The overall system efficiency was

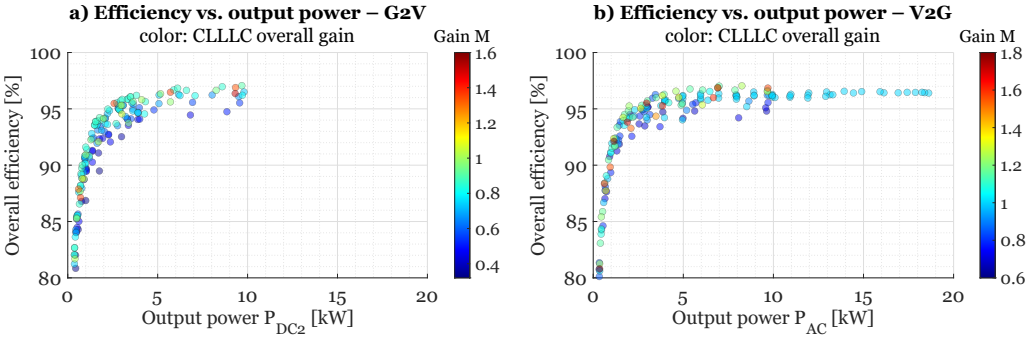

Figure 5.68: Estimated overall V2G charging system efficiency (ARCPI + CLLLC converter) in G2V and V2G operation

calculated for each CLLLC converter efficiency measurement i (see Figure 5.47), using $P_{DC1}[i]$, $P_{DC2}[i]$, and $\eta_{power,CLLLC}[i]$ of the measurements as well as the constant $P_{aux,CLLLC}$. Moreover, an LUT for each ARCPI efficiency measurement k (compare Figure 5.57) was created, containing $\eta_{power,ARCPI}(P_{DC1}[k])$ and $P_{aux,ARCPI}(P_{DC1}[k])$. The resulting overall efficiency is calculated by Equation 5.21, using linear interpolation for $\eta_{power,ARCPI}(P_{DC1}[i])$ and $P_{aux,ARCPI}(P_{DC1}[i])$.

$$\eta_{overall,G2V}[i] = \frac{|P_{DC2}[i]|}{\frac{|P_{DC1}[i]|}{\eta_{power,G2V,ARCPI}(P_{DC1}[i])} + P_{aux,ARCPI}(P_{DC1}[i]) + P_{aux,CLLLC}} \tag{5.21a}$$

$$\eta_{overall,V2G}[i] = \frac{|P_{DC1}[i]| \cdot \eta_{power,G2V,ARCPI}(P_{DC1}[i])}{|P_{DC2}[i]| + P_{aux,ARCPI}(P_{DC1}[i]) + P_{aux,CLLLC}} \tag{5.21b}$$

The estimated overall system efficiency, including auxiliary power demand, is above 94% for most operating points. It only falls below 85% for an output power of less than 0.6 kW. The highest overall efficiency is 97.06% at 9.7 kW in G2V and 97.04% at 8.25 kW in V2G direction. At the highest V2G output power of 18.6 kW, the overall efficiency is 96.4%.

5.6 Summary

Affordable bidirectional chargers are essential for the successful adoption of V2G. In Chapter 5, the design and characterization of highly efficient bidirectional power electronics for use in stationary and onboard V2G chargers were presented. By using SiC MOSFETs in the presented soft-switching topologies, both the efficiency and switching frequency can be increased, reducing the necessary filtering and cooling efforts and saving cost, weight, and space.
An existing CLLLC converter prototype was significantly improved by enhancing its efficiency to more than 98% through dynamic dead time adjustment and synchronous rectification. A newly developed ARCPI prototype with optimized switching patterns for SiC MOSFETs reached excellent efficiencies beyond 99%. In a PHIL test bench, different operation modes and ancillary services that can improve the robustness of electricity grids powered by a high share of renewable energy sources and experiencing increased demand from new consumers, such as EVs and heat pumps, were investigated. Several control algorithms could successfully be validated with the prototype, including active and reactive power, frequency, virtual inertia, and grid voltage control. The typical reaction time of the system is below 0.2 seconds. The combined operation of the converters was also validated by charging and discharging a real HV Li-ion battery system. The estimated overall efficiency of the V2G charging system, including auxiliary power demand, is between 95% and 97% for most operating points. It remains satisfactory even for a light load operation, which is crucial for its use in V2L or V2H applications.
While V2G charging hardware tends to be more expensive and complex, the results indicate that if bidirectional charging systems replace unidirectional OBCs, they can enhance efficiency and thus reduce electricity costs while offering a wide range of opportunities to create additional revenue and benefits for grid stability and the energy transition.

Part III

Battery degradation

6 Fundamentals: lithium-ion batteries

Although lithium-ion batteries have evolved rapidly in recent decades, many users are still concerned about battery aging. This raises skepticism about V2G and EVs in general. In this thesis, a battery aging study was conducted to reduce uncertainties related to battery degradation caused by V2G. This chapter provides the theoretical background on Li-ion batteries and their degradation and comprehensively reviews aging data and models.

Batteries are electrochemical energy storage devices that have become indispensable to our lives. In addition to proven applications in smartphones, cameras, laptops, power tools, toys, or medical products, the focus has shifted increasingly to applications in electromobility and stationary energy storage. In these cases, no single-use battery cells ("primary cells") are used, only rechargeable ones ("secondary cells"), which are considered exclusively in the following.

A simplified example of the structure of an EV battery system is shown in Figure 6.1 (also compare [362, pp. 180f., 311], [363, pp. 25-27, 238f.], [364, pp. 167f.], and [365]). The battery (or "battery system" / "battery pack") typically consists of several serially connected battery modules. Each module consists of multiple cells connected in series, in some EVs also in parallel. A BMS monitors, protects, balances, and controls the battery. It is often divided into a

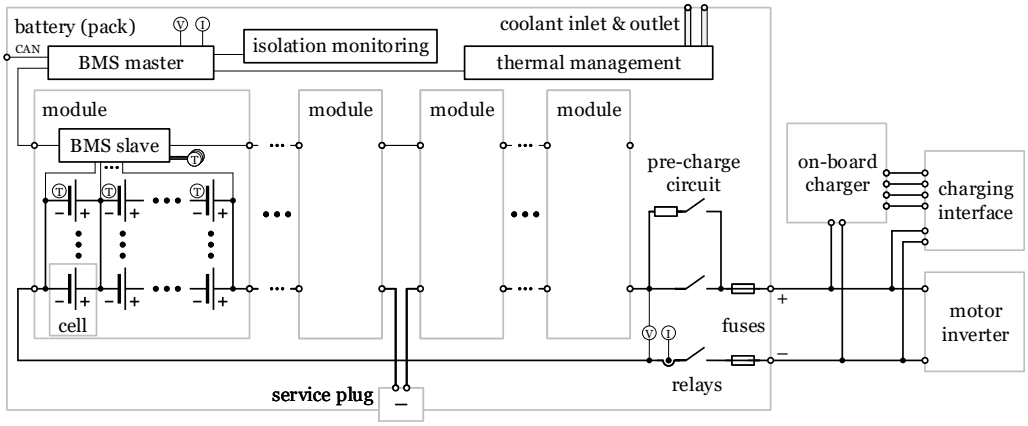

Figure 6.1: Simplified structure of an EV battery (example)

BMS master and multiple BMS slaves. While the BMS slaves are typically responsible for cell voltage and temperature measurement and cell balancing, the BMS master collects and processes all information from the battery and communicates with other controllers in the EV. Among others, the master is responsible for the control of the main and pre-charge relays, the battery voltage and current measurement, SoC, State of Health (SoH), remaining useful life (RUL), and State of Power (SoP) estimation of the battery pack, isolation monitoring, and the thermal management of the battery (i.e., cooling and heating of the cells). In addition to the relays, the battery output is protected with fuses. It is connected to the motor inverter and other HV loads, as well as to the OBC (for AC charging) and the charging interface (for DC charging).

6.1 Battery types and chemistries

While in the past, lead-acid (PbA), nickel-metal hydride (NiMH), and lithium-ion batteries (LIBs) have been used, current EVs almost exclusively use various types of Li-ion cells [366, p. 7]. Sodium-ion batteries (SIBs) are a promising "post-lithium" alternative, which could soon be used for low to medium-range EVs. They use less critical raw materials that are abundantly available and thus cheaper [367, 368] but are not covered in this thesis.

Rechargeable LIBs are available in three major form factors, which are shown in Figure 6.2: cylindrical, prismatic, and pouch cells [364, pp. 105f.], [369, p. 20]. Inside the housing, they

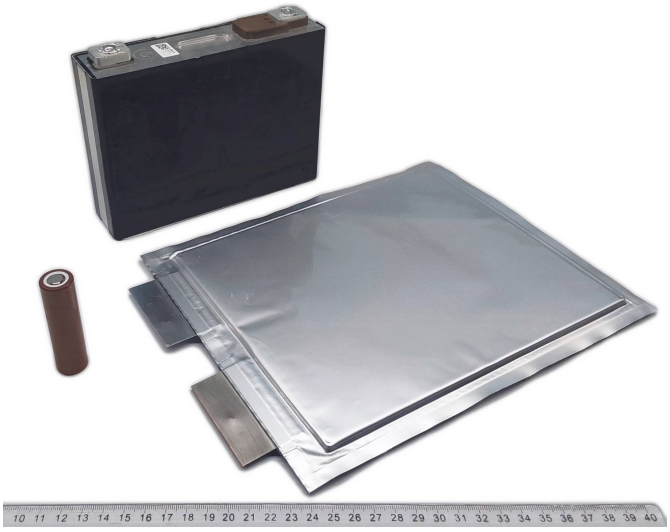

Figure 6.2: Typical form factors of rechargeable Li-ion battery cells: cylindrical (left), prismatic (top), pouch (right)

consist of one rolled or multiple stacked layers, each comprising pairs of positive and negative electrodes with separators in between [370, p. 927-929], as seen in Figure 6.3. The positive electrode — connected to the positive contact terminal of the cell — serves as a cathode when discharging and as an anode when charging the cell. However, it is commonly just named "cathode". Similarly, the negative electrode is called "anode" [364, pp. 22f.].

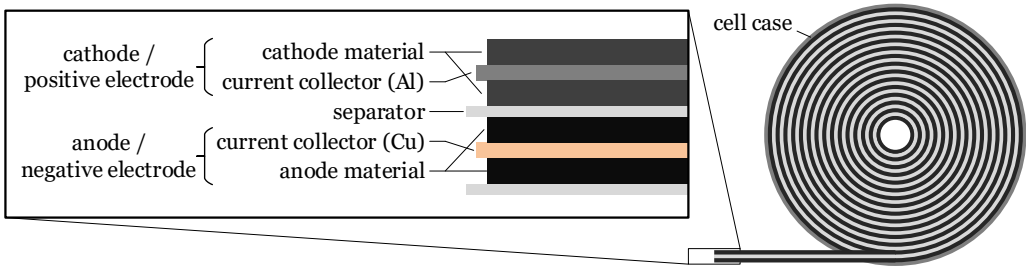

Figure 6.3: Simplified structure of a cylindrical Li-ion cell

The electrodes consist of current collectors that are coated with different materials. In LIBs, the anode is a thin copper foil typically coated with graphite. Alternative materials are, for example, lithium titanium oxide (LTO), structures doped with or based on silicon, or metallic lithium (Li) [364, pp. 22f., 44, 54f.], [369, p. 16]. The cathode is an aluminum foil that can be coated with different lithium compounds. Examples are lithium cobalt oxide (LCO), nickel manganese cobalt (NMC), nickel cobalt aluminum (NCA), lithium manganese oxide (LMO), and lithium iron phosphate (LFP) [364, pp. 22f.], [369, p. 17].

The cell is filled with an electrolyte that can transport the Li-ions when the cell charges or discharges. While in conventional LIBs, the electrolyte is fluid, in lithium-polymer batteries, the electrolyte is solid or in the form of a gel [371]. Gel-like electrolytes can be found in the batteries of many mobile devices. Solid-state batteries (SSBs) with a solid electrolyte are promising for EVs due to their safety, higher energy density, and fast charging capability [372]. However, the technology is still relatively immature. The separator isolates the positive and negative electrodes but is permeable for Li-ions [364, p. 14], [369, pp. 19f.].

When graphite-based anodes are used, a solid electrolyte interphase (SEI) is formed between the anode material and the electrolyte. The growth of the SEI layer is strongest in the first cycles of the battery cell's life but continues throughout the lifetime of the cell. The SEI is also permeable for Li-ions but blocks electrons. It consumes Li-ions and decomposes the electrolyte, and thus significantly contributes to cell aging [373, 374]. On the cathode side, a cathode-electrolyte interphase (CEI) / solid permeable interphase (SPI) can be formed, especially for cells with higher voltage levels above around 4 V [375] (also compare Figure 6.4). The CEI may even improve the safety and stability of the cell [376].

Different LIB chemistries are compared in Table 6.1. LCO and LMO were among the first

Table 6.1: Comparison of Li-ion cell chemistries according to [364, 368, 370, 377–385] — from good (++) to bad (——)

cathode material	LCO $LiCoO_2$	LMO $LiMn_2O_4$	LFP $LiFePO_4$	NCA $LiNi_xCo_yAl_{1-x-y}O_2$	NMC/NCM $LiNi_xMn_yCo_{1-x-y}O_2$	LMO, NMC, ...
anode material			graphite C			LTO $Li_4Ti_5O_{12}$
gravim. energy density	+	+/○	○/—	++	++/+	——
volum. energy density	○	○	—	++	++/+	——
power density	○	++/+	++/+	++/+	+	+/○
fast charging	+	○	+	+	+	++
nominal voltage	+ (3.6 V)	++ (3.7–3.8 V)	○ (3.2–3.3 V)	+ (3.6–3.7 V)	+ (3.6–3.7 V)	—— (2.2–2.4 V)
lifespan	○	—	++/+	+/○	+	++
thermal stability	——	—	+	—	○	++
safety	—	+/○	++	○	+/○	++
afford-ability	—	○	+	○	○	——

commercialized LIBs at the beginning of the 1990s. LCO cells are often used in portable devices such as smartphones, cameras, and laptops. LMO batteries are used in power tools and some EVs, often blended with NCA or NMC. NCA and NMC batteries are particularly successful in EVs because of their high energy density [371]. LFP cells are very safe and thus often used in home storage systems. Due to their high safety and because their energy density has improved in recent years, they have increasingly become a viable solution for many EVs as well. In recent years, they have become a cheaper alternative to NCA and NMC cells and also feature a higher cycle life [368, 371, 386]. Cells with LTO anode materials have a significantly lower energy density and are more expensive. However, they are very safe, can be operated in a wide temperature range and charged quickly, and have an exceptionally long cycle life. Possible applications are electric buses and medical devices [380].

It should be noted that the assessment in Table 6.1 is subject to change since the development of LIBs is very dynamic. New materials, compositions, and production processes are developed and then improved. The characteristics of the cells, such as lifetime, charging rate, and energy density, are enhanced. While improved production processes and the economy of scale reduce cost, global supply chain issues and increased demand for particular materials significantly impact the cost of different chemistries. The cost of batteries declined by more than 97% since the beginning of the 1990s, with a decrease of about 19% per doubling of the cumulative battery capacity [34]. Although recent temporary shortages of raw materials and inflation increased battery prices, in the long term, the price of batteries is expected to fall further, below 100 USD/kWh on a battery pack level [386, 387].

6.2 Operation of lithium-ion batteries

The operation of an LIB is explained using Figure 6.4: When discharging, positively charged lithium ions deintercalate from the graphite structure at the negative electrode (anode). An electron is released into the copper current collector of the negative electrode. The Li-ion flows through the electrolyte and passes the separator membrane. It is then intercalated into the metal oxide (or metal phosphate) compound at the positive electrode (cathode) using an electron from the aluminum current collector. Electrons cannot pass the electrically isolating separator — instead, they pass the external load, which results in an electrical current flow.
The procedure is reversed when charging the battery: Electrons flow from the positive electrode to the negative electrode. At the same time, lithium ions deintercalate from the cathode compound, pass the separator in the electrolyte, and intercalate into the graphite structure [364, pp. 14f., 61].

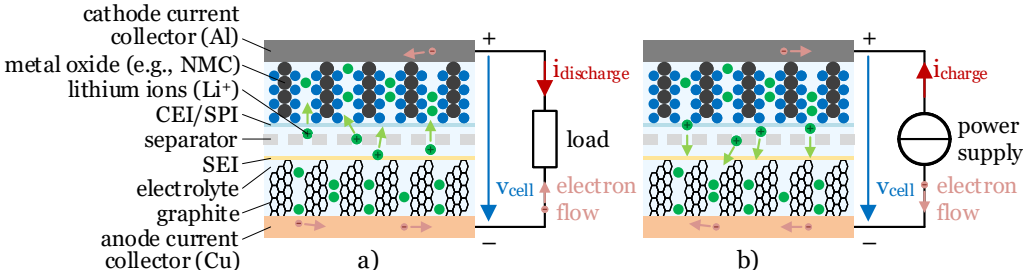

Figure 6.4: Principle of operation of a Li-ion cell: a) discharging, b) charging (based on [364, Fig. 2.1] and [388, Figure 2])

Particularly for automotive batteries, there are high safety requirements to avoid hazards such as fires and explosions [362, pp. 183f., 303-321]. Nevertheless, the safe operating area (SOA) of the

battery cells needs to be respected at all times to contain safety risks and avoid excessive battery degradation. This includes maintaining a safe voltage, current, and temperature range.

Li-ion cells are often charged using the "CC/CV" method shown in Figure 6.5a. In this example, the cell is almost empty with a State of Charge (SoC) near 0% before charging. It is charged with a constant current (CC) between t_1 and t_2 (see numbered gray lines). As the SoC increases, the voltage at the cell terminals rises to the maximum end-of-charge (EOC) voltage at t_2. From there on, the current needs to be decreased to respect the maximum voltage of the battery cell. The cell is therefore charged with a constant voltage (CV). The current decreases approximately exponentially. For practical reasons, the charging process is ended once the cell current declines below a cut-off current at t_3. The cell reached an SoC of about 100%.

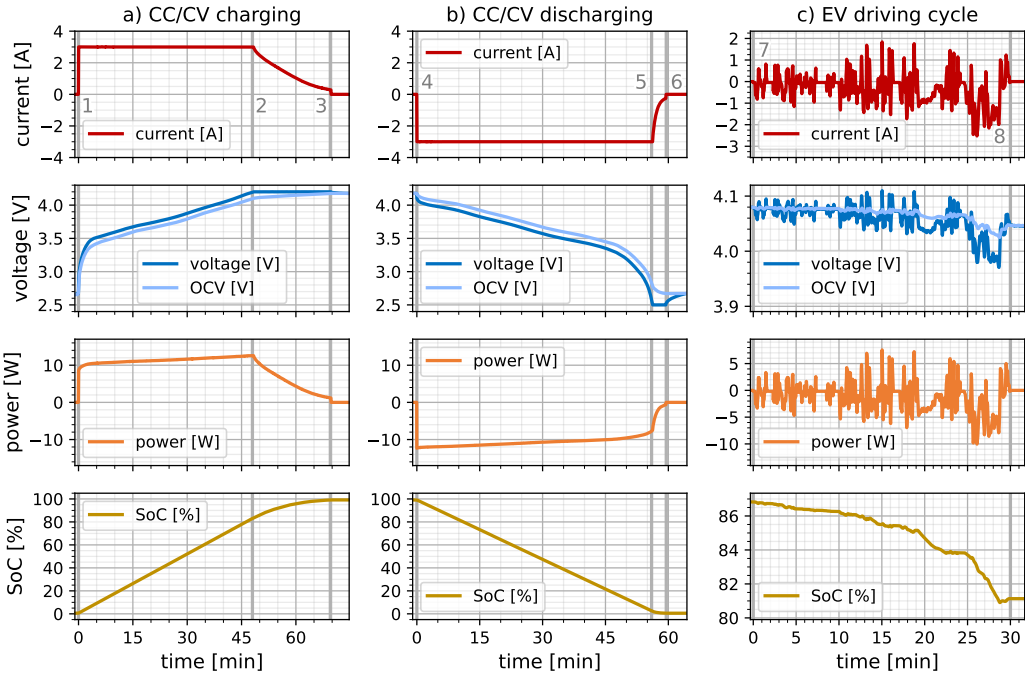

Figure 6.5: Cell current, terminal and open-circuit voltage (OCV), power, and SoC of a Li-ion NMC cell — a) CC/CV charging, b) CC/CV discharging, c) discharging in the WLTP driving cycle

The Li-ion cell in the example is an NMC cell with a nominal capacity of 3 Ah. It is charged with a C-rate of 1 C, i.e., the charging current is 3 A (see Equation 6.1).

$$\textit{C-rate} = \frac{\textit{cell current [A]}}{\textit{nominal cell capacity [Ah]}} \qquad \textit{in } [C] = \left[\frac{1}{h}\right] \tag{6.1}$$

If the cell were charged with 1 C from an SoC of 0 to 100%, the charging process would take an hour; for 2 C, it would take half an hour, and so on. However, due to the CV phase, the last phase of the charging process takes significantly longer if the cell is to be fully charged (see SoC curve at the bottom of Figure 6.5a). A fast charging curve for EV batteries can look different. For example, the charging current could be dynamically adjusted based on the temperature and SoC of the battery cells to avoid overheating and lithium plating.

In Figure 6.5b, the cell is discharged using a CC/CV profile. Between t_4 and t_5, the current is constant at a discharge rate of 1 C. Between t_5 and t_6, the discharge current is reduced to respect the cell's minimum end-of-discharge (EOD) voltage. Here, the current decreases significantly faster in the CV phase than in the charging process. After discharging is stopped ($I_{cell} = 0$ at $t > t_6$), the terminal voltage of the cell relaxes and increases to the open-circuit voltage (OCV).

In most applications, the discharging current is not constant. For example, in Figure 6.5c, a cell is discharged using simulated driving conditions of an EV. For this purpose, a power is applied to the cell that it would experience in an EV battery using a Worldwide Light-duty Test Cycle (WLTC) of the Worldwide harmonized Light vehicles Test Procedure (WLTP) [389]. The simulated EV starts driving at t_7 and stops at t_8 at the end of the WLTC.

Unlike the cell current or terminal voltage, the SoC cannot be measured directly. Instead, it has to be estimated. Simple approaches are "coulomb counting" and using OCV measurements with an LUT. For the coulomb counting method, the cell current is integrated to calculate the electrical charge (measured in Ah) discharged from or charged into the cell. With the help of the nominal capacity, the remaining discharge or charge can be estimated. However, an initial estimation of the SoC is needed. Moreover, current sensor inaccuracy or an offset can deteriorate the estimation over time. The available discharge varies with temperature and age of the cell, which is difficult to factor in if only the current is used as a measured variable. As an alternative or complement, the OCV of the cell can be measured when the cell is relaxed or estimated during operation. Using an OCV curve over the SoC of the cell stored in advance in an LUT, the SoC can be estimated with minimal deterioration over time. However, the OCV is hard to estimate in a dynamic cell operation, and coulomb counting offers more accurate results. Alternative approaches are Kalman filters, impedance monitoring, and machine learning. While they are more complex to implement, they can offer significantly improved accuracy [390, 391], [363, pp. 67-86].

In many applications, the relevant indicator for the "battery level" is not the SoC but the State of Energy (SoE). While the SoC is the ratio of the estimated remaining charge (in Ah) to the usable capacity of the cell, the SoE is the ratio of the estimated remaining energy (in Wh) to the overall usable energy. Similar to the SoC, the SoE of a fully charged battery is 100%, and that of a fully discharged battery is 0%. The SoE is useful in applications such as EV batteries or BESS since the energy (Wh) delivered, not the charge (Ah), is relevant.

The difference between the SoC at the start and the end of the discharging process is typically referred to as the Depth of Discharge (DoD) [220, 392–396]. If the cell is discharged from an SoC of 80% to 60%, then $DoD = \Delta SoC = SoC_{start} - SoC_{end} = 20\%$. This convention will also be used in the following. However, some authors also define the DoD as the "complement" to the SoC, i.e., $DoD = 1 - SoC$ [380, 397, 398].

Another important metric for the operation is the State of Power (SoP), which can be "defined as the ratio of peak power to nominal power" [363, p. 24]. In EVs, it estimates the maximum available power that can be drawn from or fed into the battery, e.g., for acceleration or fast charging. The maximum discharge power for acceleration might be limited at low SoCs, and the maximum charging power (e.g., for regenerative braking) is limited at very high SoCs. The maximum available power might be reduced due to cold temperatures or an aged battery.

6.3 Battery aging

The performance of battery cells deteriorates over time. This degradation is revealed by a reduction in the usable capacity and an increase in the impedance or internal resistance of the cell. This occurs when charging or discharging the battery ("cyclic aging") but also over time, even when the battery is not in use ("calendar aging"). Both aging types can take place simultaneously, but their causes differ [399].

Calendar aging is often expressed as a function of time. On the other hand, cyclic aging depends on charge transfer in the cells. While cyclic aging is sometimes also indicated as a function of time, it is mostly described as a function of charge throughput (Ah) or cycles (N). However, a "cycle" may have different meanings and is sometimes not defined unambiguously. For example, if a 3 Ah cell is operated in an SoC window of 25 to 75% with a DoD of 50%, a cycle may refer to the "operating cycle" (25%→75%→25%), in which — using an idealized, new cell — a charge of 1.5 Ah is charged and then discharged. Alternatively, a cycle may refer to an equivalent full cycle (EFC), i.e., the charge and discharge of the nominal cell capacity (3 Ah). In the example, it is equivalent to two operating cycles of a new cell. However, if the cell loses usable capacity, more and more operating cycles are needed to obtain one EFC. Therefore, the use of the charge throughput (Ah-throughput) and the derived EFCs are less ambiguous than the use of operating cycles. Ah-throughput and EFCs can be measured by integrating the current through the cell, even under realistic operating conditions with variable currents and arbitrary SoC profiles. The charge throughput may refer to the charge charged into (Ah_c) or discharged from the cell (Ah_d) or the sum of both.

The State of Health (SoH) is an indicator of the aging of the battery. It is typically defined as the ratio of the aged, usable battery capacity to its original, nominal capacity. For a new cell,

the SoH is 100%. Theoretically, if no more charge could be drawn from a completely destroyed cell regardless of its SoC, the SoH would be 0%. However, for practical applications, the end of life (EOL) of the battery is reached long before, for example, at an SoH of 80% [363, pp. 23f., 95]. If using this criterion, a 3 Ah / 10 Wh cell would reach its EOL if the usable discharge under the reference conditions is less than 2.4 Ah or 8 Wh for a fully charged cell, depending on if the SoH is calculated charge- or energy-based.
A typical development of the SoH over the number of EFCs is shown in Figure 6.6. At the beginning of life (BOL), the SoH is 100%. The decline is relatively steep in the first few hundred cycles and then relaxes. In the "knee region", the SoH begins to decrease steeper again [394, p. 699] — in this example, after about 1100 cycles. The 80% EOL criterion is reached after about 1260 cycles, and after less than 300 additional cycles, another 20% capacity loss occurs.

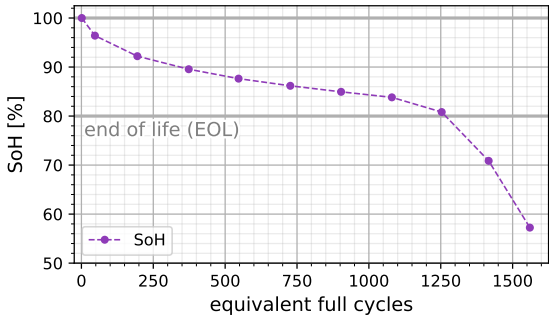

Figure 6.6: Typical development of the SoH of a Li-ion cell — here: NMC cell cycled at 25°C, 1 C charging, 1 C discharging, SoC from 10% to 100%, CC/CV charging and discharging with 1/10 C cut-off current

Modern NMC cells achieve about 2000 full cycles under regular conditions before their SoH reaches 80%. In an EV with a usable range of 400 km, this roughly represents 800,000 km. LFP cells can even exceed 5000 cycles, corresponding to a driven distance of 2 million kilometers [368]. With this lifetime, the battery could clearly outlive the life of a private passenger EV, making the use for additional applications such as V2G or a second life as stationary storage more interesting.

Another indicator of battery aging is the cell impedance. For example, an internal resistance increase by a factor of two can be defined as an EOL criterion for use in an EV [363, p. 95]. The higher resistance can limit fast charging or cause derating while driving the EV because of increased heat generation in the battery.
The cell impedance is dependent not only on age but also on excitation frequency, temperature, and SoC. It can be measured using electrochemical impedance spectroscopy (EIS) in galvanostatic or potentiostatic mode. When using a galvanostatic EIS (GEIS), the cell is excited by a sinusoidal current of a fixed frequency. At the same time, the amplitude and phase shift of the resulting sinusoidal voltage that is superimposed on the OCV of the cell is measured. With a potentiostatic

EIS (PEIS), the cell is excited with a sinusoidal voltage (with a DC offset equal to the OCV), and the resulting sinusoidal current amplitude and phase shift are measured. The measurement is repeated for other frequencies, for example, in the range of 10 mHz to 10 kHz. GEIS is more suitable for characterizing electrochemical storage devices with low impedances, such as Li-ion cells [400, 401]. Figure 6.7 illustrates the principle of a GEIS and shows an example of a measurement for a Li-ion cell. A four-point measurement ensures that only the impedance of the cell and not that of the cable is measured.

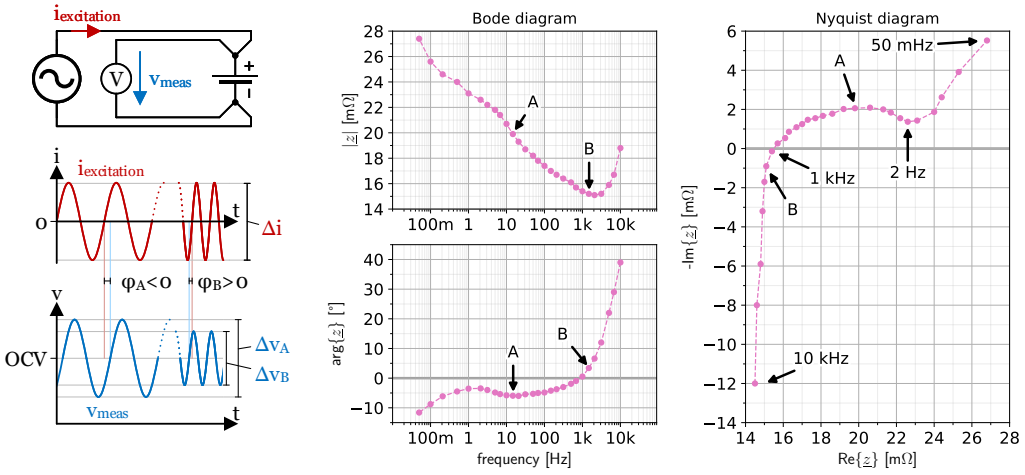

Figure 6.7: Principle of a galvanostatic EIS measurement (left), measurement results in a Bode (center) and Nyquist diagram (right)

6.3.1 Degradation mechanisms and dependencies

A good overview of different causes for various aging mechanisms, their degradation modes, and consequences is given by Lin et al. [388, Figure 3] and in [374, 394, 402–405]. Aging mechanisms are also discussed in detail in [399, 406–409]. Three different modes of aging can be observed: loss of lithium inventory (LLI), loss of active material (LAM), and conductivity loss (CL) [403, 405].

LLI refers to the loss of Li-ions that are available for the charging and discharging process. Li-ions may be consumed by side reactions, such as SEI growth or lithium plating and dendrite formation. Thus, they can no longer be used in the intended reactions and effectively reduce the battery capacity. LAM is the loss of “active” material, i.e., other compounds that take place in the chemical reactions required for the operation of the battery cell. This concerns the active material in the cathode (e.g., the NMC compounds) and the anode (e.g., graphite). If active

material is not available for lithium intercalation or the electrolyte is degraded, this reduces the effective cell capacity and increases the impedance. Some authors also include structural changes or defects of inactive material to LAM [405]. Examples of such non-active components are the current collectors, binders, conductive additives, the separator, and the electrolyte [370, pp. 904f., 918]. Other authors also explicitly list the "loss of electrolyte" as a dedicated degradation mode [388, 404]. CL refers to the degradation of components that reduce the conductivity, e.g., binder decomposition or the corrosion of current collectors [405, p. 139].

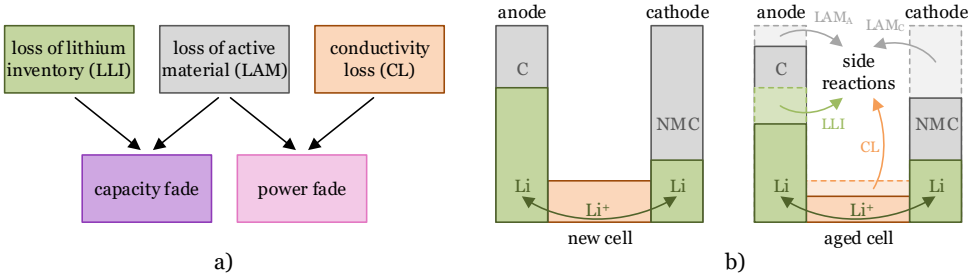

Figure 6.8: a) Relationship between degradation modes and their consequences, b) simplified dual tank model to illustrate the degradation modes (extended version based on [404, Fig. 4])

Figure 6.8a illustrates the relation between the LLI, LAM, and CL degradation modes and their consequences (capacity and power fade). Figure 6.8b shows a simple "dual-tank model" to demonstrate the consequences of different aging modes. Anode and cathode materials can be modeled as tanks that can store lithium. The cell capacity is determined by the amount of available lithium and the size of the anode and cathode tanks. LAM on the anode and cathode side and LLI consume the material through side reactions and thus reduce the capacity. Side reactions can also consume materials responsible for conductivity. This impedes lithium and electron transport and thus increases resistance and available power [404].

The underlying mechanisms of degradation are manifold and depend on the operating conditions of the cell, particularly the temperature, the SoC and DoD, and the charging and discharging current. The relationship between degradation causes, mechanisms, and modes is shown in Figure 6.9. Degradation occurs even under ideal conditions, i.e., low charging and discharging rates and moderate temperatures and SoCs. Among the most common aging mechanisms in these cases is SEI growth. Other examples are electrode particle fracture and reduced electrode porosity through mechanical wear due to cycling. Beyond ideal conditions, degradation is sped up — for example, because of side reactions (e.g., the dissolution of electrolyte and binder) or increased mechanical wear caused by chemical reactions. An operation outside the SOA can drastically reduce lifetime or even permanently destroy the battery cell, as described in [374, 388, 405, 408, 411].

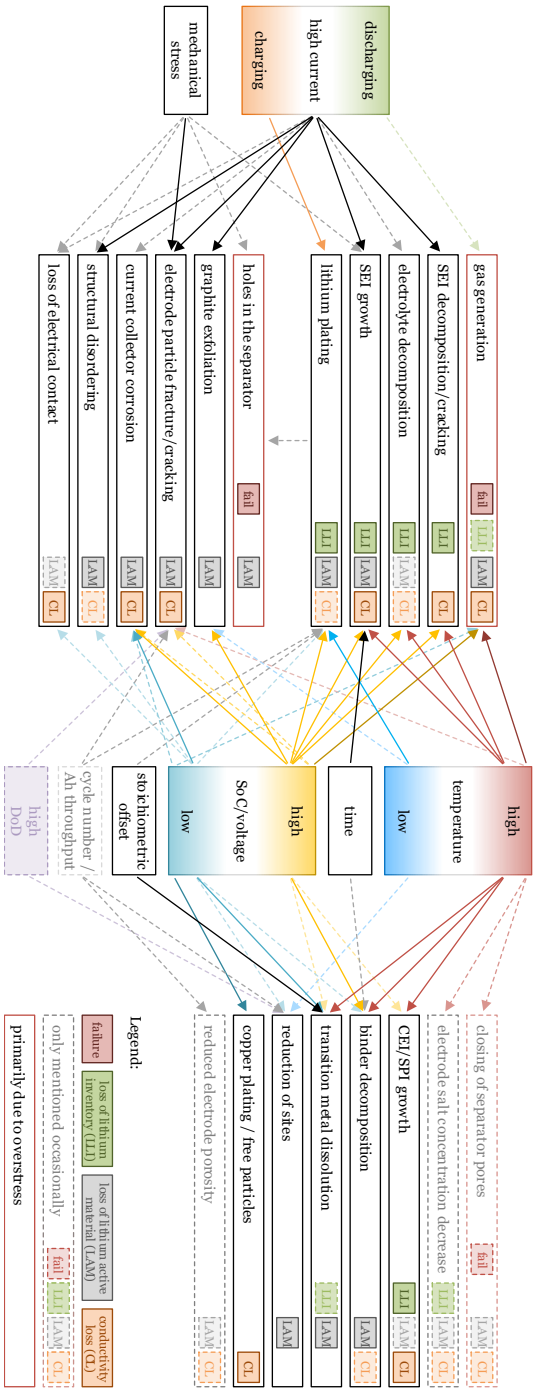

Figure 6.9: Degradation causes, mechanisms, and modes according to [374, 388, 394, 399, 402–410]

For example, if the cell temperature is too high, the cell ages significantly faster. At some points, unwanted chemical reactions can destroy the cell (e.g., electrolyte/binder decomposition, separator melting) or even cause a thermal runaway.
When cycling at low temperatures, the cell also ages faster. If a cold cell is charged too fast, lithium plating in the cell can reduce usable capacity and ultimately cause internal short circuits because of dendrite formation. Charging with high current rates can also cause lithium plating at moderate temperatures, particularly if the cell already aged significantly [412–415].
Over-currents, in general, can grow or decompose the SEI, crack electrode particles, corrode the current collectors, disorder the cathode structure, or cause graphite exfoliation and contact loss.
Over-charging the cell or applying sustained over-voltages can generate heat and decompose the electrolyte or the cathode, producing gases inside the cell and even bursting its housing. It can also destroy the SEI or cause graphite exfoliation. Over-discharging ("deep discharging") or sustained under-voltages can corrode and dissolve the anode, which can cause copper plating and dendrite formation.
External short circuits or mechanical stress, such as deformation or penetration of the cell, must be avoided since they can quickly destroy the cell.

Thus, for the safe operation of the battery, it has to be protected against inadmissible operation. The lifetime of the battery can be extended if the cells are operated within conditions that minimize aging processes. This implies that the degradation mechanisms need to be understood, modeled, and considered in the operating strategy.

6.3.2 Battery degradation caused by V2G

Since the battery is a significant cost factor in EVs, its lifetime is often explicitly considered in the context of V2G, e.g., in studies covering its economic aspects or optimal scheduling. As mentioned in Chapter 3.3.2, low battery degradation, adequate compensation for it, and transparency about the degradation caused by V2G are essential factors for user acceptance. In addition to developing longer-lasting cells, reducing the hurdle of battery aging due to V2G involves two key requirements. The first is quantifying battery degradation in the development of business cases and operational strategies, e.g., during simulation, comparison, and optimization of different variants. This reduces battery degradation and, thus, the cost of V2G in the first place. Second, the actual deterioration or improvement of the SoH attributed to V2G compared to a conventional operation over the lifetime of the battery should be estimated. This improves transparency for V2G users and allows for suitable compensation.

Thompson [394], Leippi et al. [220], and Bui et al. [395] give an overview of how V2G affects battery degradation, which dependencies and aging mechanisms exist, and which methods and

modeling approaches are used in research and industry to analyze the effects of V1G and V2G on cell lifetime.

In literature focusing on battery degradation of smart and bidirectional charging and its associated cost, typically, very simple battery wear models are used:
In many instances (e.g., [186, 202, 204, 416–420]), it is assumed that a fixed amount of energy (Wh) or charge (Ah) can be extracted from the battery or a corresponding fixed number of cycles can be attained before the battery reaches its EOL, independent of temperature, time, SoC, DoD, and charge and discharge rates. The replacement cost of the battery is usually proportionally attributed to any energy drawn from the battery, resulting in a fixed price per energy or charge unit taken from the battery.
In addition, a higher charging or discharging current or power is penalized in some studies [421, 422], V2G operation is factored in with a fixed, smaller penalty compared to driving [423, 424], or temperature is added as a dependency in addition to the (dis)charging current [425].
Some authors only penalize charging power (e.g., a term proportional to the square of the power) independent of the overall energy throughput or other conditions [426, 427]. Others only use the DoD as a dependency for degradation [398].
In most of these models, V2G — by definition of the aging model used — causes higher battery degradation because of increased cycling. The positive effect of a lower SoC on calendar aging is neglected. It is not surprising that studies using those simplified models conclude that the higher energy throughput of V2G causes (often much) more degradation if the underlying aging model prescribes precisely that. If the battery replacement cost was assumed to be high, which is particularly the case in older studies, many authors found that V2G is not profitable — or only under specific circumstances.
Lunz et al. [428] argue that because EVs are not in use the majority of the time, the cells experience pure calendar aging more often than cyclic aging. Based on a small set of experimental aging measurements, they derive a relatively simple model considering calendar aging effects, e.g., its SoC dependency. Because of its low calendar aging, the V2G use case had a lower battery degradation cost than all other uncontrolled or smart unidirectional charging methods analyzed in the study, even before considering additional electricity cost benefits.

On the other hand, some authors use more advanced models [178, 244, 392, 393, 396, 429–433]. Petit et al. [430] calibrate their model to existing measurement results of two cell chemistries: NCA and LFP. They note that V2G has different effects on the battery life depending on the chemistry: In contrast to LFP cells, NCA cells are more susceptible to cyclic rather than calendar aging. Uddin et al. [180, 187] conducted aging tests with NCA cells and derived a model from them. Their smart charging algorithm only allows V2G utilization if it prolongs battery lifetime. As a result, not all EVs make use of V2G, but those that do experience a capacity fade reduction of up to 9.1% in the first year of the simulation.

Dubarry et al. [434] and Bui et al. [395] perform a relatively large number of calendar and cycling aging tests. In the first study [434], temperature and SoC were varied for calendar aging tests. Accelerated driving and V2G profiles were applied to the cells at room temperature to investigate the effects of cyclic aging. The authors conclude that V2G significantly decreases cell life. The second study [395] considers different temperatures and SoC levels for calendar and different temperatures and discharge current rates for cyclic aging to generate a semi-empirical cell degradation model. The derived model is then applied to different charging and V2G strategies. V2G could even extend cell lifetime significantly in some scenarios as opposed to conventional charging. Charging with a combined V1G/V2G strategy extended lifetime in all scenarios.

To summarize, V2G can lead to less battery aging compared to uncontrolled charging according to some studies — e.g., Uddin et al. [180] and [178, 395, 428, 432] — and more aging according to most others — e.g., Dubarry et al. [434]. In a collaborative publication [187], the authors of the aforementioned publications [180, 434] discuss why their studies lead to seemingly contradictory results. In short, "unintelligent" V2G that maximizes energy profits alone can lead to significantly higher aging. However, if battery degradation is considered in the V2G algorithm, both battery aging can be reduced and energy profit optimized reasonably. However, this requires detailed prognostic/marginal battery degradation models that allow the algorithm to consider aging in the decision-making process (also compare [4, p. 27]).

6.3.3 Battery aging models

As mentioned, battery degradation is often modeled very simply in the literature outside of the electrochemistry domain. Presumably, the same applies to most (especially small) companies that focus on battery applications rather than cell development and production. This may be due to the lack of publicly available, comprehensive, yet easily reusable battery aging models. Literature on cell degradation mechanisms is widely available. However, understanding and applying the findings typically requires expert knowledge in the field of electrochemistry. Publications on degradation models exist in great numbers as well. Unfortunately, other researchers or companies often cannot easily reuse the model to analyze or optimize battery aging in their own applications. For example, in many instances, the model or its parameter values are not shared in the studies or only in three-dimensional plots, which makes reading the values painful and error-prone. Other studies only analyze specific dependencies, e.g., only cyclic or calendar aging, or there are significant differences in the cell chemistry of the publication and the one of interest. Moreover, many results are not part of open-access publications, which hinders using results outside academia. In order to find models that researchers and developers can reuse in areas that focus on battery applications, this section takes a step back and gives an overview of general battery aging models, i.e., not specifically tailored to V2G.

The classification of battery degradation models is ambiguous in the literature since the boundaries are sometimes blurred, models are used in conjunction with each other, or they can be classified using different criteria. One could distinguish between electrochemical/physics-based, equivalent circuit, (semi-)empirical, and machine learning models [396, 435–439]:

- **Electrochemical** or **physics-based models** describe the fundamental aging mechanisms considering the chemical reactions inside the cell, e.g., SEI layer growth or lithium plating. The methods often require a profound understanding of the underlying processes and range from models on the atomic/molecular scale to single particle models that significantly reduce complexity [435–437, 440].
- **Equivalent circuit models (ECMs)** replicate the cell in the form of an ECD, for example, using voltage sources, resistors, capacitors, and Warburg elements. The degradation of the cell, particularly the impedance increase and power fade, can be tracked by estimating the ECD values, e.g., with the help of EIS, pulse patterns, or Kalman filters with parameter estimation [396, 437, 438, 441, 442]. While ECMs help estimate the SoH using measurement data of aged cells, they can typically not be used to simulate the aging effect of different operational strategies without actual data measurements under this condition.
- **Empirical models**, also known as performance-based models, treat the cell as a black box. Typically, mathematical equations are fitted to experimental results of accelerated cell aging tests. While purely empirical models use arbitrary functions, **semi-empirical models** consider electrochemical or physics-based theory as guidance, e.g., by using Arrhenius, Tafel, or Wöhler equations to find suitable fitting functions [396, 437, 438, 443].
- **Machine-learning-based aging models** are often considered as a separate class, although they overlap with empirical ones. They range from statistical approaches, such as Gaussian process regressions or support vector machines, to deep learning models, such as various forms of neural networks. They can predict the SoH, RUL, or other aging-related parameters [435, 438, 444, 445]. Like ECMs, they are usually used with real-world measurement data, e.g., measurements of the first hundred operating cycles.

Battery degradation models are reviewed in [220, 374, 394, 439, 446]. Further studies are listed in [447]. Physics-based / electrochemical models are discussed in [443] and [448, pp. 35f.]. SoH and RUL estimation methods are reviewed in [449, 450]. However, most of the SoH and RUL estimation models also rely on actual measurements of a cell to estimate its current or future degradation. This means that the models cannot be used to simulate cell aging before data for this specific operating condition was collected.
Tools that support battery degradation modeling are the open-source package *PyBAMM* [451], which includes electrochemical models, and NREL's *BLAST* software [452] (only the *BLAST-lite* version is open-source), which uses the *NREL model* described further below.

Battery aging models often quantify the degradation through the reduction of usable capacity (Q) or an increase of capacity losses (Q_L). This can be expressed as an absolute value (Ah) or a percentage (%) of the nominal capacity, the initial capacity under a reference condition, or the initial capacity under the operating condition. The power fade, or a resistance or impedance increase, can be modeled as an alternative or in addition. Other models return the lifetime of the cell (L) — e.g., in years — or the number of achievable cycles (N) — operating cycles or equivalent full cycles (EFCs) — until a certain EOL criterion is reached.

A comparison of empirical Li-ion battery degradation models is presented in Table 6.2. It is indicated if the publication is published under open-access conditions (✓) or at least available online (•), e.g., as a preprint. The next column shows if example values for the model equations are shown to easily reuse the model (✓), or if only part of the values are provided or they can at least be reconstructed with additional effort (•). It is also indicated if the authors provide an impedance/resistance/power fade model in addition to a capacity aging model, which is the focus of this review. Moreover, the number and type of calendar and cyclic capacity loss dependencies are stated. Common stress factors (herein called "parameters") for calendar aging are:

- time (t),
- temperature (T),
- State of Charge (SoC), State of Energy (SoE), or voltage (V).

Common cyclic parameters are:

- number of cycles (N, under the operating condition or as EFCs), or charge (Ah) or energy (Wh) throughput (general, or only for charging or discharging: $Ah_{c/d}$),
- time-dependent, minimum, mid/average, or maximum SoC or voltage during cycling ($SoC/V_{t/min/mid/max}$),
- Depth of Discharge (DoD, typically defined as $DoD = SoC_{max} - SoC_{min}$) or the energy-related DoD_E (defined as $DoD_E = SoE_{max} - SoE_{min}$),
- general/charging/discharging current or C-rate ($C/C_c/C_d$).

The table does not include simple models that only consider time or the number of cycles.
The relationship between calendar and cyclic capacity aging is also shown. Often, all terms representing the individual calendar aging dependencies of each parameter i are multiplied: $Q_{L,cal} = \prod f_{t,i}(\cdot)$. The same applies to all cyclic aging dependencies: $Q_{L,cyc} = \prod f_{N,i}(\cdot)$. The overall calendar and capacity losses are typically added to determine the overall capacity losses: $Q_L = Q_{L,cal} + Q_{L,cyc}$.

Table 6.2: Review of (semi-)empirical Li-ion battery degradation models

Sources	Open access	Example values	Z/R/P model	Num. cal. parameters	Calendar parameters	Num. cyc. parameters	Cyclic parameters	Calendar ($f_{t,i}$) / cyclic ($f_{N,i}$) aging relationship	Notes
[453, 454]	–	–	–	0	–	2	Ah, DoD	$Q_L=\prod f_{N,i}(\cdot)$	
[455]	–	✓	–	0	–	2	N, T	$Q_L=\prod f_{N,i}(\cdot)$	
[456, 457]	–	✓	–	0	–	2	N, T	$Q_L=f_{N,1}(T, N)+f_{N,2}(T, N)$	
[458]	–	–	–	0	–	3	N, T, C_d	$Q_L=f_{N,1}(T)\cdot f_{N,2}(T, C)\cdot f_{N,3}(N)$	
[459]	–	✓	–	0	–	3	N, SoC_{mid}, DoD	$Q_L=\prod f_{N,i}(\cdot)$	
[425]	–	✓	–	0	–	3	Wh_c, T, C_d	$Q_L=f_{N,1}(C_d)\cdot f_{N,2}(T, C_d)\cdot f_{N,3}(Ah)$	
[460]	•	✓	–	0	–	3	Ah, T, C_d	$Q_L=f_{N,1}(T, C_d)\cdot f_{N,2}(Ah)$	
[461]	–	•	–	0	–	4	t, T, C, DoD	$Q_L=f_N(t, T, C, DoD)$	L
[397]	–	✓	–	0	–	4	N, SoC_t, DoD, C	$Q_L=\prod f_{N,i}(\cdot)$	
[462]	–	✓	–	0	–	4	Ah_c, T, SoC_{mid}, C	$Q_L=f_{N,1}(T, C)\cdot f_{N,2}\cdot(SoC)\cdot f_{N,3}(Ah)$	
[463]	–	✓	✓	0	–	4	Ah_c, T, SoC_{mid}, DoD	$Q_L=f_{N,1}(T, SoC_{mid}, DoD)\cdot f_{N,2}(Ah_c)$	
[464]	•	✓	–	0	–	4	t, V, C_c, C_d	$Q_L=\int\sum f_{N,i}(\cdot)\,dt$	
[465]	✓	✓	✓	0	–	4	T, DoD, C_c, C_d	$N=\prod f_{N,i}(\cdot)$	
[466]	–	✓	–	0	–	5	N, T, V_{max}, DoD, C	$Q_L=f_{N,1}(DoD, C, V_{max})\cdot f_{N,2}(T, C)\cdot f_{N,3}(N)$	
[467]	–	✓	–	0	–	5	T, SoC_{mid}, DoD, C_c, C_d	$N=f_{N,1}(T)\cdot f_{N,2}(C_d)\cdot f_{N,3}(C_c)\cdot f_{N,4}(SoC_{mid}, DoD)$	
[468]	•	✓	–	0	–	5	N, T, SoC_t, SoH, t_{cyc}	$L=f_{N,1}(N, T, SoC_t, t_{cyc})\cdot f_{N,2}(SoC_t)\cdot f_{N,3}(SoH)$	X
[469]	✓	•	–	0	–	6	Ah_d, T, C_d, $C_{c,co}$, C_d, DoD	$Q_L=f_N(Ah_d, T, DoD, C_c, C_{c,co}, C_d)$	
[470]	–	✓	–	0	–	6	N, T, V_{max}, V_{min}, C_d, C_c	$Q_L=N\cdot\sum f_{N,i}(\cdot)$	
[471]	–	✓	–	0	–	6	N, T, SoC_{mid}, DoD, C_d, C_c	$Q_L=f_{N,1}(T, DoD, C_c, C_d)\cdot f_{N,2}(SoC_{mid})\cdot f_{N,3}(N)$	
[472]	–	–	–	3	t, T, SoC	0	–	$Q_L=\prod f_{t,i}(\cdot)$	
[473]	–	✓	–	3	t, T, SoC	0	–	$dQ_L/dt=f_{t,1}(T, SoC)\cdot f_{t,2}(Q_L, T)$	L
[474]	–	✓	✓	3	t, T, SoC	0	–	$Q_L=f_{t,1}(T, SoC)\cdot f_{t,2}(t, T)$	
[475]	–	✓	–	3	t, T, SoC	0	–	$Q_L=f_t(t, T, SoC)$	L
[434]	•	✓	–	3	t, T, SoC	0	–	$Q_L=f_t(t, T, SoC)$	
[476]	•	✓	✓	3	t, T, V	0	–	$Q_L=f_t(t, T, V)$ — 6 different models compared	★
[477]	✓	✓	✓	3	t, T, SoC	0	-	$Q_L=f_t(t, T, SoC)$	
[478]	✓	•	–	4	t, SoC, SoC_t, C			*(differential equation system — see paper)*	M
[479]	–	✓	–	4	t, T, SoC, C			$Q_L=f(t, T, SoC, C)$	M
[480]	–	✓	✓	4	t, T, SoC, C			$Q_L=f(t, T, SoC, C)$	M
[481]	–	✓	–	5	t, T, SoC, C_c, C_d			$Q_L=f(t, T, SoC, C_c, C_d)$	M

(continued on next page)

Table 6.2 (continued)

Sources	Open access	Ex. values	Z/R/P model	Num. cal. p.	Cal. param.	Num. cyc. p.	Cyc. param.	Calendar ($f_{t,i}$) / cyclic ($f_{N,i}$) aging relationship	Notes
[482]	–	✓	✓	2	t, T	2	N, T	$Q_L=\prod C_{L,cal}+\prod C_{L,cyc}$	
[433]	✓	–	–	3	t, T, SoE	1	Wh	$Q_L=f_t(t, T, SoE)+f_N(Wh)$	
[483]	–	✓	✓	3	t, T, V	1	N	$Q_L=\prod f_{t,i}(\cdot)+f_N(N)$	
[484]	–	✓	✓	2	t, SoC	3	N, SoC_{mid}, DoD	$Q_L=\prod f_{t,i}(\cdot)+\prod f_{N,i}(\cdot)$	
[485]	–	✓	–	2	t, T	3	Ah_d, T, C	$Q_L=\prod f_{t,i}(\cdot)+f_N(T, C)\cdot Ah_d$	★
[486]	–	–	–	3	t, T, SoE	2	N, DoD_E	$Q_L=\prod_i f_{t,i}(\cdot)+\sum_k f_N(DoD_E)$	
[395]	✓	•	–	3	t, T, SoC	2	Ah, C_d	$Q_L=\prod f_{t,i}(\cdot)+\prod f_{N,i}(\cdot)$	L
[487]	–	–	–	3	t, T, SoC	3	Ah, T, C	$Q_L=f_t(t, T, SoC)+f_N(Ah, T, C)$	
[488]	•	•	–	3	t, T, SoC	3	Ah, T, C_d	$Q_L=\prod f_{t,i}(\cdot)+f_{N,1}(T, C_d)\cdot Ah$	
[489]	–	✓	✓	3	t, T, SoC	3	t, DoD, C	$Q_L=\prod f_{t,i}(\cdot)+\prod f_{N,i}(\cdot)$	
[490, 491]	–	✓	✓	3	t, T, V	3	Ah, V_t, DoD	$Q_L=\prod f_{t,i}(\cdot)+f_{N,1}(V_t, DoD)\cdot f_{N,2}(Ah)$	
[430]	•	✓	–	3	t, T, SoC	3	Ah, T, C	$dQ_L/dt=\begin{cases} d/dt\{f_N(Ah, T, C)\} & \text{if cell in use} \\ d/dt\{f_t(t, T, SoC)\} & \text{else} \end{cases}$	L, ★
[492]	✓	✓	–	3	t, T, V	3	N, T, DoD	$Q_L=\prod f_{t,i}(\cdot)+\prod f_{N,i}(\cdot)$	
[493]	–	•	–	3	t, T, SoC	4	N, T, SoC_{mid}, DoD	*(see paper)*	
[432, 494]	–	✓	–	3	t, T, SoC	4	N, DoD, SoC, T	$Q_L=\prod f_{t,i}(\cdot)+\sum_k\prod_i f_{N,i}(\cdot)$	
[439]	✓	✓	–	3	t, T, V_-	4	N, SoC_t, DoD, C	$Q_L=f_t(t, T, V_-)+f_N(N, SoC_t, DoD, C)$	V
[495, 496]	✓	✓	✓	3	t, T, SoC	4	N, T, SoC_{mid}, DoD	$Q_L=\prod f_{t,i}(\cdot)+\prod f_{N,i}(\cdot)$	
[396]	✓	•	–	3	t, T, SoC	5	N, T, SoC_{mid}, DoD, C	$Q_L=f_t(t, T, SoC)+f_N(N, T, SoC_{mid}, DoD, C)$	L
[497]	✓	✓	–	3	t, T, SoC	5	N, T, SoC_{mid}, DoD, C_c	*(see paper)*	
[498]	✓	✓	–	3	t, T, V_-	5	Ah, Ah_c, T, SoC_t, C_c	$QL=f_t(t, T, V_-)+f_N(Ah, Ah_c, T, SoC_t, C_c)$	V
[499, 500]	✓	–	✓	4	t, T, V, DoD	4	N, T, V_t, DoD	$Q=\min(\prod f_{t/Li,i}(\cdot), \prod f_{N/sites,i}(\cdot))$	★, Y
[501]	•	✓	✓	5	t, T, V, V_-, DoD_{max}	4	N, Ah_d, T, DoD	$Q=\min(Q_{Li}(\ldots), Q_{neg}(\ldots), Q_{pos}(\ldots))$	V, Y
This work	✓	✓	–	3	t, T, V	6	Ah, T, V_t, V_-, C_c, C_d	(*described in Chapter 7.2 of this thesis*)	V

i index for each aging parameter dependency

k index for each charge/discharge cycle

L some or all dependencies are not modeled by a continuous function but by a discrete LUT

M combined model or no differentiation between calendar and cyclic aging

V V_- is the SoC- or OCV-dependent potential of the negative electrode

X t_{cyc} is the duration of a charge-discharge cycle

Y the "Li" term corresponds to LLI, "neg" and "pos" to LAM in the negative or positive electrode, "sites" to the dominant LAM in one of the electrodes

★ often used in the literature, explained below

These models differ significantly in some cases. They vary in complexity and accuracy and were derived using different cell types and test conditions. However, there are commonly used building blocks that model temperature, voltage, or DoD dependency (compare [498, 499]):

$$\text{Arrhenius dependency:} \quad \exp\left(\frac{-E_a}{R_g}\cdot\left(\frac{1}{T}-\frac{1}{T_{ref}}\right)\right) \quad \rightarrow a\cdot\exp\left(\frac{b}{T}\right) \tag{6.2a}$$

$$\text{Tafel dependency:} \quad \exp\left(\frac{e\cdot F}{R_g}\cdot\left(\frac{OCV}{T}-\frac{V_{ref}}{T_{ref}}\right)\right) \quad \rightarrow c\cdot\exp\left(d\cdot\frac{V}{T}\right) \tag{6.2b}$$

$$\text{Wöhler dependency:} \quad \left(\frac{DoD}{DoD_{ref}}\right)^f \tag{6.2c}$$

T is the temperature (in K), OCV is the open-circuit voltage (in V), and DoD is the Depth of Discharge (in Ah or %) to which the battery cell is exposed. They are time- or cycle-dependent in real applications but are often kept constant in the experiments used to derive degradation models. R_g is the universal gas constant, and F is the Faraday constant. The activation energy E_a, T_{ref}, V_{ref}, DoD_{ref}, and a–f are constants to be fitted.
In literature using battery degradation models, often one of the following is used:

- Smith et al. [499, 500] (sometimes called *"NREL model"*):

$$Q = min(Q_{Li}, Q_{sites}) \tag{6.3a}$$

$$Q_{Li} = b_0 + b_1\cdot t^{0.5} \tag{6.3b}$$

$$Q_{sites} = c_0 + c_1\cdot N \tag{6.3c}$$

  The factors b_1 and c_1 depend on temperature, OCV, and DoD. Both are obtained by multiplying Arrhenius, Tafel, and Wöhler functions. The decrease of Q_{Li} models the LLI, for example, because of SEI growth. Q_{sites} reflects the lack of sites/locations for Li-ions to intercalate into, e.g., because parts of the metal oxide or graphite are not available anymore. In another model variant [501], the site losses for both electrodes are modeled separately.

- Wang et al. [485]:

$$Q_L = Q_{L,cyc} + Q_{L,cal} \tag{6.4a}$$

$$Q_{L,cyc} = (a\cdot T^2 + b\cdot T + c)\cdot\exp\left((d\cdot T + e)\cdot C\right)\cdot Ah_d \tag{6.4b}$$

$$Q_{L,cal} = f\cdot\exp\left(\frac{-E_a}{R_g\cdot T}\right)\cdot t^{0.5} \tag{6.4c}$$

  Cyclic losses are represented by multiplying a second-order temperature polynomial, an exponential term considering the temperature and C-rate, and the discharging throughput. Calendar losses are modeled with the Arrhenius equation and a $\sqrt{\text{t}}$-dependency.

- Ecker et al. [476]: Different calendar aging models are compared using experimental data, each containing variants of the base voltage and temperature dependency:

$$f_{cal}(T,V) = a^{\left(\frac{V-V_{ref}}{\Delta V}\right)} \cdot b^{\left(\frac{T-T_{ref}}{\Delta T}\right)} \tag{6.5}$$

  V_{ref}, ΔV, T_{ref}, and ΔT are arbitrarily chosen, and a and b are fitting constants. The function $f_{cal}(T, V)$ is multiplied with t, $\sqrt{t}$, log(t), or a combination of them to obtain the capacity loss $Q_{L,cal}$.

- Petit et al. [430]: The time derivatives of the following base models allow the model to be applied under varying conditions. Only one of the two aging modes is used at a time, depending on the current magnitude through the cell.

$$Q_{L,cyc} = B_{cyc}\,[C] \cdot \exp\left(\frac{-E_{a,cyc} + a \cdot |C|}{R_g \cdot T}\right) \cdot Ah^{z_{cyc}} \tag{6.6a}$$

$$Q_{L,cal} = B_{cal}\,[SoC] \cdot \exp\left(\frac{-E_{a,cal}\,[SoC]}{R_g \cdot T}\right) \cdot t^{z_{cal}[SoC]} \tag{6.6b}$$

  Lookup tables are used for B_{cyc}, B_{cal}, $E_{a,cal}$, and z_{cal}, i.e., the factors are different depending on the C-rate or SoC and were fit using experimental data. For C-rates and SoCs other than the ones investigated, interpolation can be used to obtain these factors.

Most models do not consider the knee region, where the SoH declines rapidly, often after around 80%, as already shown in Figure 6.6. Under regular operating conditions, the LLI aging mode dominates initially, e.g., because of SEI growth, which can be modeled relatively well. Toward the knee region, other aging modes prevail, such as LAM through graphite site losses in the anode [394, p. 699] or lithium plating, even in moderate conditions [412].
The effects depend on different stress factors and thus need to be modeled differently, as in the *NREL model*. Accurate modeling of all of these aging modes is beneficial for model accuracy toward the EOL and supports estimating the value of an EV battery for second-life applications.

The empirical models are based on accelerated aging experiments using real battery cells. Modeling the influence of a wide range of different parameters is cost-intensive since an extensive set of cells must be aged under different conditions, requiring test equipment with many measurement channels. Unsurprisingly, many empirical models only focus on specific aspects of aging, collected with a limited amount of parameter sets.
However, a degradation model that considers both calendar and cyclic aging is required to accurately estimate the influence of EV driving cycles and different charging and V2G strategies on battery aging. The calendar aging model should consider the SoC or voltage since it is impacted by V2G. The temperature should also be considered to model the effects of charging and V2G during

different seasons and times of the day or to identify the requirements for thermal management during V2G operation. A cyclic battery aging model for EVs should consider the number of cycles or the Ah-throughput, temperature, SoC or voltage and/or DoD, and the charging and discharging rates. Charging and discharging rates have different effects on battery lifetime. Charging with high currents significantly impacts battery lifetime, particularly at cold temperatures and high SoCs. However, no reusable model was found that considers all of these parameters (calendar aging: t, SoC or V, T; cyclic aging: Ah or N, T, C_c, C_d, DoD or V or SoC).
It is conceivable to merge several models, e.g., a calendar aging model of one study and a detailed cyclic model of another study. However, it is unlikely that the resulting model accurately reflects the aging behavior, e.g., because a different cell model or even chemistry was used to derive the model. Even if the same cell was selected in both experimental setups, the test conditions in the experiment might differ, e.g., the reference performance tests in which the remaining capacity was determined. Moreover, cyclic aging tests that last several months also include calendar aging effects, which might not be accurately represented in studies focusing on cyclic aging. Similarly, the reference performance tests of calendar aging experiments also introduce cyclic aging to cells, which is not considered in pure calendar aging models.

6.3.4 Battery aging datasets

A comprehensive battery aging dataset is required to generate battery degradation models that consider all of the mentioned aspects. Datasets on battery aging certainly exist from research facilities and cell and EV manufacturers. However, comprehensive datasets that would allow the derivation of reusable models are rarely published. Commercial manufacturers typically have no interest in making the data available to the public, particularly not for free, since the data collection is expensive and time-consuming, and the results may be confidential. Most experiments found in academic literature only contain a small number of cells and parameter variations. Moreover, published experimental results are often not available under open-access conditions, hindering their use outside academia. Authors describe and visually present selected results of aging experiments, but the result data (e.g., capacity fade over time and cycle life) or raw data (e.g., voltage, current, and temperature curves captured in the experiment with a temporal resolution in the order of seconds) to derive or validate custom models is usually not available. Reconstructing the data from figures is painful and error-prone, and requests to various authors to obtain the result data were unsuccessful.

To provide readers a basis for finding suitable data for their own applications, Table 6.3 gives an overview of datasets and experimental results from Li-ion battery aging tests found in the literature and data repositories (also compare [502–506]). The table has been carefully compiled at the end of 2023 to ensure accuracy and completeness. However, the possibility of oversights

or inaccuracies cannot be entirely ruled out despite careful examination. Several studies were excluded from the review because only one parameter was varied, less than five different parameter sets were tested, or only second-life batteries previously aged under unknown parameters were investigated. Question marks in the table indicate that the study could not be accessed or the information was not identifiable. The first row behind the sources indicates if the publication describing the data is available under open-access conditions (✓) or at least available online (•), e.g., as a preprint. The following row states if all (✓) or only selected (•) capacity aging results of the test matrix were presented in the publication. If a dataset is published (i.e., data can be copied and reused), the open-access availability is shown in the next column. Here, a bullet (•) may also indicate that the authors state that the data will be made available on request. It is indicated if result data (e.g., remaining capacity over time or cycles during check-ups) can be downloaded (✓) or at least copied manually (•), e.g., from a table or interactive chart. The "raw data" availability refers to cycling data (e.g., voltage and current over time in high temporal resolution).
The next section in the table shows the number of cells in the experiment, the number of parameter sets, the approximate maximum duration and cycle number that the cells were aged, and if the impedance increase or power fade was also investigated and presented in the study.
In the following, the number of parameter sets, the number and type of varied parameters, and the type of the test matrix are stated for both calendar and cyclic aging experiments.

A parameter set refers to a composition of parameters that define the aging condition, for example, $\{T_{cal} = 40°C, V_{cal} = 3.7\ V\}$ for a calendar aging cell. If a study investigates the effect of $n = 3$ different temperatures ($T_{cal} = \{10°C, 25°C, 40°C\}$) and $m = 2$ voltages ($V_{cal} = \{3.7\ V, 4.2\ V\}$) on calendar life, there are several ways to set up a test matrix. The combinations of all temperatures and all voltages could be analyzed, resulting in a completely populated test matrix (indicated by ● in the table), i.e., $n \cdot m = 6$ parameter sets in the example. Alternatively, a reference parameter set can be defined, e.g., $\{T_{cal,ref} = 25°C, V_{cal,ref} = 3.7\ V\}$. The effect of parameter variations is only explored by varying one parameter based on the reference parameter set (indicated by ⊙), resulting in $n + m - 1 = 4$ parameter sets. If more parameter sets are defined than using a reference test but fewer than in a full test matrix, this is marked with ◑. If fewer parameter sets than using a reference test are defined, i.e., multiple parameters are varied, it is indicated by ○.

Parameters investigated in calendar aging studies are temperature (T) and State of Charge (SoC) or voltage (V). Parameters varied in cyclic aging studies are temperature, State of Charge (SoC) limits (SoC/V_{min} and SoC/V_{max}), and, with them, the Depth of Discharge (DoD). Many studies define an average/center SoC (SoC_{mid}), i.e., the cycle ranges from $SoC_{min} = SoC_{mid} - \frac{DoD}{2}$ to $SoC_{max} = SoC_{mid} + \frac{DoD}{2}$. Some studies introduce additional micro-cycles (DoD_{μ}), whereby very small charge and discharge cycles are superimposed to larger cycles, emulating EV driving patterns. Further parameters are the charge (C_c) and discharge (C_d) current or C-rate, or a symmetric (or not clearly specified) current or C-rate (C). The CC charging phase may also have

multiple stages with different currents (e.g., $C_{c,1\text{-}4}$). Some authors vary the cut-off current in the CV phase of charging ($C_{c,co}$), the duration of the CV phase at charging or discharging ($t_{c/d,CV}$), or the rest duration after charging and discharging $t_{c/d,rest}$. In other studies, AC currents (C_{AC}) are superimposed with different frequencies (f_{AC}), or rectangular pulse patterns are applied using varying duty cycles ($duty_d$) or frequencies (f_{pulse}). Cyclic aging may also be interrupted with longer phases of calendar aging (duty). Different charge protocols (CP) may be analyzed, e.g., CC, CC/CV, and boost charging. Other studies investigate the charging strategy (CS) in specific applications, e.g., immediate, delayed, or V2G charging in EVs. Non-uniform current profiles (PRF) are sometimes applied to a cell, emulating real applications (e.g., EV driving cycles or energy trading). Many parameters, such as the current, SoC limits, DoD, or even temperature, are varied in these cases. This is useful for validation but complicates the attribution of aging to specific parameters if only arbitrary profiles are used for model generation. Single studies investigate the effect of different formation protocols in manufacturing (frm), mechanical pressure applied to the cells while cycling (p), and different check-up intervals (CU).

Table 6.3: Review of datasets and literature on experimental battery aging

Sources	Pub.		Data			Experiment						Calendar aging				Cyclic aging			
	Open access	Result plot/table	Open access	Result data	Raw data	Cell chemistry	Number of cells	Num. of param. sets	≈ max. duration	≈ max. cycles	Impedance aging	Num. of param. sets	Num. of param. varied	Parameters varied	Test matrix	Num. of param. sets	Num. of param. varied	Parameters varied	Test matrix
[507]	✓	✓	✓	•	–	various	6300	–	2500	–	–	–	–	–	–	–	–	–	–
[506]	–	✓	✓	✓	•	various	137	50+	–	–	–	–	–	–	–	–	–	–	–
[508]	–	–	✓	✓	✓	various	200+	–	–	–	✓	–	–	–	–	–	–	–	–
[509]	✓	✓	–	–	–	NMC (5x)	20	2	?	100	✓	0	0	–	–	2	1	DoD	⊙
[510, 511]	✓	–	✓	–	✓	various	18	3	?	?	–	0	0	–	–	3	1	T	⊙
[512]	•	✓	–	–	–	LFP/C	13	5	365	2400	–	0	0	–	–	5	1	C_d	⊙
[513]	✓	✓	✓	•	–	NCA/C	15	5	100	1200	✓	0	0	–	–	5	1	f_{AC}	⊙
[514]	✓	✓	–	–	–	LFP/C	6	6	?	3200	–	0	0	–	–	6	1	C_d	⊙
[515]	–	✓	–	–	–	NMC/C	?	7	70	638	–	0	0	–	–	7	1	T	⊙
[458, 516]	–	✓	–	–	–	? (2x)	66	8	?	450	–	0	0	–	–	8	1	C_d	⊙
[517, 518]	–	?	✓	–	✓	?	20	–	870	?	–	0	0	–	–	20	1	PRF	–
[519, 520]	•	✓	✓	✓	✓	LFP/C	124	72	?	2300	✓	0	0	–	–	72	1	C_c	◑
[521, 522]	✓	✓	✓	✓	✓	LFP/C	77	77	?	2700	–	0	0	–	–	77	1	C_d	⊙
[523, 524]	•	•	✓	✓	✓	LFP/C	237	224	16+	1200	–	0	0	–	–	224	1	C_c	◑
[525, 526]	•	✓	✓	✓	✓	NMC/C	6	3	347	1400	–	0	0	–	–	3	2	DoD, PRF	⊙
[527, 528]	✓	✓	✓	✓	✓	NMC/C-Si	10	4	690	?	✓	0	0	–	–	4	2	C_c, C_d	⊙
[529–531]	✓	✓	✓	✓	✓	NCA/C	12	4	1100	500+	✓	0	0	–	–	4	2	$C_{c/d}$, duty	●
[506, 532, 533]	✓	✓	✓	✓	✓	NMC/C	40	4	120	620	✓	0	0	–	–	4	2	T, frm	●
[534]	–	✓	–	–	–	NMC/C	?	6	?	3200	✓	0	0	–	–	6	2	SoC_{mid}, DoD	⊙

(continued on next page)

Table 6.3 (continued)

Sources	Pub.		Data			Experiment						Calendar aging				Cyclic aging			
	Open access	Result plt/tbl	Open access	Result data	Raw data	Cell chem.	Num. cells	Param. sets	≈ max. dur.	≈ max. cyc.	Imp. aging	Num. p. sets	Num. p. var.	Param. var.	Test matrix	Num. p. sets	Num. p. var.	Param. var.	Test matrix
[535, 536]	✓	✓	✓	✓	•	NMC/C-Si	17	6	?	2000	✓	0	0	–	–	6	2	T, SoC_{max}/DoD	●
[407]	✓	✓	–	–	–	LFP/C	14	7	540	10500	✓	0	0	–	–	7	2	T, PRF	◑
[537]	–	✓	–	–	–	NMC, NCA	?	8	?	3000	✓	0	0	–	–	8	2	T, C_c	◑
[538]	–	✓	–	–	–	NCA/C	18	9	150+	900	–	0	0	–	–	9	2	SoC_{mid}, DoD	⊙
[442, 539, 540]	✓	✓	–	–	–	NCA-LCO/C	24+	12	?	4500	✓	0	0	–	–	12	2	T(t), T(x)	◑
[541]	–	✓	–	–	–	NMC-NCA	45	18	?	1000	•	0	0	–	–	18	2	SoC_{mid}, DoD	◑
[542]	✓	✓	•	•	?	NCA-LNO/C-Si, NMC/C	?	23+	?	662	–	0	0	–	–	23+	2	T, C_c	◑
[543–545]	✓	•	✓	–	✓	LCO-NMC/C	77	8+	?	?	–	0	0	–	–	8+	2	C_c, C_d	◑
[546]	–	✓	–	–	–	LFP	6	6	180	12500	–	0	0	–	–	6	3	SoC_{max}/DoD, C_c, C_d	●
[459, 508]	–	✓	✓	✓	✓	LCO/C	16	8	500	850	–	0	0	–	–	8	3	SoC_{mid}, DoD, C_d	◑
[461]	–	✓	–	–	–	LMO	?	10	?	425	–	0	0	–	–	10	3	T, DoD, C_c	⊙
[547, 548]	✓	✓	✓	✓	✓	various	130	11	?	1300	✓	0	0	–	–	11	3	T, C_c, C_d	◑
[549]	–	✓	–	–	–	LMO	36	12	?	420	–	0	0	–	–	12	3	T, DoD, C_d	⊙
[506, 550]	✓	✓	✓	✓	•	various	66+	12	?	4000	–	0	0	–	–	12	3	T, DoD, C_d	◑
[464]	•	–	–	–	–	LFP	14	14	?	?	–	0	0	–	–	14	3	V_{min}, V_{max}/DoD, $C_{c/d}$	○
[456, 457, 551–553]	✓	✓	✓	✓	✓	LCO/C	192	24	150	800	✓	0	0	–	–	24	3	T, $C_{c,co}$, C_d	●
[554, 555]	•	•	✓	✓	✓	NMC/C	256	64	426	?	–	0	0	–	–	64	3	DoD, C_c, C_d	◑
[556, 557]	✓	–	✓	–	✓	?	88	?	?	120	✓	0	0	–	–	?	3	T, C_c, C_d	?
[465]	✓	✓	✓	–	–	LFP, NMC	10	5	?	3500+	–	0	0	–	–	5	4	T, DoD, C_c, C_d	○
[558]	✓	✓	–	–	–	LMO/C	?	11	190	2500	–	0	0	–	–	11	4	T, DoD, DoD_μ, C_d	◑
[559]	–	✓	–	–	–	various	?	14	?	1100	✓	0	0	–	–	14	4	V_{max}/DoD, C_c, CP, $CP_{setting}$	◑
[560]	–	✓	–	–	–	LFP/C	?	19	?	4831	✓	0	0	–	–	19	4	T, DoD, C_c, C_d	◑
[445, 561]	–	•	✓	✓	–	NMC/C	30	30	?	1100?	–	0	0	–	–	30	4	T, DoD, C_c, C_d	◑
[460]	•	•	–	–	–	LFP/C	107	54	190	5500	–	0	0	–	–	54	4	T, DoD, C_c, C_d	◑
[485]	–	•	–	–	–	LMO-NMC/C	120	58	550	2500	•	0	0		–	58	4	T, DoD, C_c, C_d	◑
[562, 563]	–	–	–	✓	✓	?	38	?	?	?	✓	0	0	–	–	?	4	T, V_{min}/DoD, C_d, $duty_d$	◑
[466]	–	•	–	–	–	LCO/C	?	?	?	3900	–	0	0	–	–	20?	4	T, V_{max}, V_{min}/DoD, $C_{c/d}$	◑
[564]	–	✓	–	–	–	NMC/C	39	13	?	1900	✓	0	0	–	–	13	5	T, DoD, C_c, C_d, CP	◑
[470]	–	✓	–	–	–	LFP/C	15+	15	?	200	✓	0	0	–	–	15	5	T, V_{min}, V_{max}/DoD, C_c, C_d	⊙
[469]	✓	•	–	–	–	LCO (2x)	96	16	?	300	–	0	0	–	–	16	5	T, DoD, C_c, $C_{c,co}$, C_d	◑
[506, 565, 566]	✓	✓	✓	✓	✓	NMC/C	31	27	?	750	✓	0	0	–	–	27	5	T, V_{max}/DoD, C_c, C_d, p	⊙
[563, 567–569]	✓	✓	•	✓	✓	LCO/C	28	4	90	900	✓	0	0	–	–	28	5	T, V_{min}, V_{max}/DoD, C_c, C_d	◑
[570]	✓	•	–	–	–	LFP/C (3x)	?	20+	?	11000	–	0	0	–	–	20+	6	T, SoC_{mid}, DoD, C_c, C_d, t_{CV}	◑
[571]	–	✓	–	–	–	NCA/C	36	18	?	950	–	0	0	–	–	18	7	T, V_{min}, V_{max}/DoD, C_c, C_d, $t_{c,CV}$, $t_{d,CV}$	◑
[463, 572]	–	–	✓	–	✓	NCA	116	37	730	2000+	–	0	0	–	–	37	7	T, SoC_{mid}, DoD, C_c, C_d, $duty_d$, f_{pulse}	◑

(continued on next page)

Table 6.3 (continued)

Sources	Pub.		Data			Experiment						Calendar aging				Cyclic aging			
	Open access	Result plt/tbl	Open access	Result data	Raw data	Cell chem.	Num. cells	Param. sets	≈ max. dur.	≈ max. cyc.	Imp. aging	Num. p. sets	Num. p. var.	Param. var.	Test matrix	Num. p. sets	Num. p. var.	Param. var.	Test matrix
[573, 574]	✓	✓	✓	•	–	various	429	7	150	–	–	7	2	T, SoC	◑	0	0	–	–
[575]	–	✓	–	–	–	LFP/C	27	9	250	–	✓	9	2	T, SoC	●	0	0	–	–
[475]	–	✓	–	–	–	LFP/C	27	9	800	–	–	9	2	T, SoC	●	0	0	–	–
[576, 577]	–	✓	–	–	–	various	108	9	1050	–	✓	9	2	T, SoC	●	0	0	–	–
[578]	–	✓	–	–	–	LFP/C	?	9	300	–	–	9	2	T, SoC	●	0	0	–	–
[579]	•	•	–	–	–	NMC	30	10	490	–	✓	10	2	T, SoC	◑	0	0	–	–
[473, 580]	✓	✓	–	–	–	LFP/C	33	11	480	–	✓	11	2	T, SoC	◑	0	0	–	–
[581]	•	✓	–	–	–	NCA	?	12	250	–	✓	12	2	T, SoC	●	0	0	–	–
[582]	✓	✓	–	–	–	NMC/C	25?	12	630	–	–	12	2	T, SoC	●	0	0	–	–
[477]	✓	✓	–	–	–	LCO-NCA/C	40	17	720	–	✓	17	2	T, SoC	◑	0	0	–	–
[583]	–	•	–	–	–	LCO/C, LNMO/C	?	19	450	–	•	19	2	T, V	◑	0	0	–	–
[508]	–	–	✓	✓	✓	?	144	36	220	–	✓	36	2	T, SoC	●	0	0	–	–
[584]	✓	•	–	–	–	NCA/C	?	48	290	–	–	48	2	T, V	◑	0	0	–	–
[585]	✓	✓	–	–	–	various	?	48	300	–	✓	48	2	T, SoC	●	0	0	–	–
[478, 586]	•	✓	–	–	–	NMC/C	36	12	120	120+	–	5	1	SoC	⊙	7	2	SoC_{mid}, DoD	⊙
[587]	–	•	–	–	–	NCA/C	?	15+	?	560	–	4	1	T	⊙	18	3	T, C_c, CP	◑
[476]	•	•	–	–	–	NMC/C	?	13	490	?	✓	10	2	T, V	◑	3	1	SoC_{mid}	⊙
[428]	–	•	–	–	–	NMC/C	45	15	365+		–	11	2	T, SoC	◑	4	1	SoC_{mid}	⊙
[588]	✓	✓	–	–	–	LFP/C	8	8	365	4500	✓	4	2	T, SoC	●	4	2	T, PRF	●
[483]	–	•	–	–	–	LFP, NMC	87	15	500	5000	✓	6	2	T, SoC	⊙	9	2	DoD, $C_{c/d}$	●
[589, 590]	✓	•	✓	✓	✓	NMC/C	36+	13	?	5400	–	6	2	T, SoC	◑	12?	2	C_{AC}, f_{AC}	◑
[591]	–	✓	–	–	–	LTO	24	12	730	>95k	✓	7	2	T, SoC	⊙	5	2	T, $C_{c/d}$	◑
[592]	•	✓	–	–	–	LFP/C	50	14	850	8000	✓	8	2	T, SoC	◑	6	2	DoD, $C_{c/d}$	⊙
[434]	•	✓	–	–	–	NCA/C	52	20	455	380	✓	8	2	T, SoC	⊙	12	2	CS_{home}, CS_{work}	●
[593]	•	•	–	–	–	LFP/C	?	21	330	1500+	–	9	2	T, SoC	●	12	2	T, $C_{c/d}$	●
[453, 472, 489]	–	✓	–	–	–	LFP/C	23+	23	630	5500	✓	10	2	T, SoC	◑	13	2	DoD, $C_{c/d}$	◑
[490, 491, 594]	–	•	–	–	–	NMC/C	108	36	520	4200	✓	14	2	T, SoC	⊙	22	2	SoC_{mid}, DoD	◑
[396, 487]	✓	✓	–	–	–	NMC (2x)	?	60	450	2300	–	40	2	T, SoC	●	20	2	T, $C_{c/d}$	●
[395]	✓	✓	–	–	–	NMC/C	201	67	434	2800	–	58	2	T, SoC	●	9	2	T, C_d	●
[482, 484, 495, 496]	✓	✓	–	–	–	LFP/C	39	13	720	7000	✓	5	2	T, SoC	⊙	9	3	T, SoC_{mid}, DoD	◑
[595]	–	✓	–	–	–	LFP/C (2x)	?	11	90	2300	–	6	2	T, SoC	⊙	7	3	T, SoC_{max}, SoC_{min}/DoD	⊙
[479]	–	•	–	–	–	NMC/C	?	27	95	?	–	9	2	T, SoC	●	18	3	T, SoC_{mid}, $C_{c/d}$	●
[596]	–	•	–	–	–	NMC	72	34	690	2900	–	9	2	T, SoC	●	25	3	T, DoD, C_d	◑
[597–603]	✓	✓	–	–	–	NC	148	36	147	?	✓	12	2	T, SoC	●	24	3	T, SoC_{mid}, DoD	●
[604]	–	•	–	–	–	NMC/C	40+	20	480	4800	✓	13	2	T, V	◑	7	3	T, Socmin, SoC_{max}/DoD	⊙
[501]	•	•	–	–	–	NMC/C	11	9	300	?	✓	4	2	T, SoC	⊙	5	4	T, DoD, C_c, duty	○
[605]	✓	•	–	–	–	LTO	45	20	730	11000	–	6	2	T, SoC	●	14	4	T, DoD, C_c, C_d	◑
[606]	✓	•	–	–	–	NMC/C (?x)	?	?	1020	5500	•	6	2	T, V	●	?	4	T, V_{max}/DoD, C_c, C_d	◑

(continued on next page)

Table 6.3 (continued)

Sources	Pub.		Data			Experiment						Calendar aging				Cyclic aging			
	Open access	Result plt/tbl	Open access	Result data	Raw data	Cell chem.	Num. cells	Param. sets	≈ max. dur.	≈ max. cyc.	Imp. aging	Num. p. sets	Num. p. var.	Param. var.	Test matrix	Num. p. sets	Num. p. var.	Param. var.	Test matrix
[607, 608]	–	✓	–	–	–	NMC/C	93	31	408	1300	✓	8	2	T, SoC	◑	23	4	T, SoC_{mid}, DoD, C_d	◑
[480]	–	✓	–	–	–	NMC-LMO/C, NCA/C	78	13	1200	?	✓	9	2	T, SoC	●	4	4	T, DoD, DoD_{μ}, $C_{c/d}$	⊙
[609, 610]	✓	✓	✓	–	✓	NMC/C-Si	70	35	420	3500	–	12	2	T, SoC	●	23	4	T, DoD, C_c, C_d	◑
[498]	✓	•	–	–	–	LFP/C	111	90	240	2800	–	54	2	T, SoC	●	36	4	T, $C_{c/d}$, CP, PRF	◑
[611]	✓	•	–	–	–	NCA	?	?	700	1000	✓	96	2	T, V	●	?	4	V_{min}, V_{max}/DoD, C_c, $C_{c,boost}$	◑
[612]	–	✓	–	–	–	LMO-NMC/C	107	19	640	?	✓	6	2	T, SoC	⊙	13	5	T, SoC_{mid}, DoD, PRF, $t_{c,rest}$	○
[180]	✓	✓	–	–	–	NCA/C	63	21	380	1400	✓	9	2	T, SoC	●	12	5	T, SoC_{max}, SoC_{min}/DoD, C_c, C_d	◑
[492, 493, 613–616]	✓	✓	–	–	–	NMC/C	158	46	1100	7000	•	10	2	T, SoC	◑	36	5	T, SoC_{mid}, DoD, C_c, C_d	◑
[497]	✓	✓	✓	✓	–	NMC/C	32	32	325	1000+	–	11	2	T, SoC	◑	19	5	T, SoC_{mid}, DoD, C_c, duty	◑
[617]	–	•	–	–	–	NMC/LTO	33	27	320	18000	–	12	2	T, SoC	◑	15	5	T, DoD, DoD_{μ}, $C_{c/d}$, PRF	◑
[481, 618–620]	✓	•	–	–	–	NMC-LMO/C, NMC/C	258	40+	500	350+	✓	16	2	T, SoC	◑	25	5	T, SoC_{mid}, C_c, C_d, duty	◑
[439, 621–624]	–	•	✓	•	–	LFP/C	114	38	885	13500	✓	17	2	T, SoC	◑	21	6	T, SoC_{mid}, DoD, C_c, C_d, CP	◑
[625, 626]	–	✓	✓	?	✓	NCA/C-Si	196	196	697	1500	✓	75	3	T, SoC, CU	◑	121	7	T, SoC_{mid}, DoD, C_c, C_d, PRF, CU	◑
This work: Chapter 7	✓	✓	✓	✓	✓	NMC/C-Si	228	76	449+	3700+	✓	16	2	T, V	●	60	6	T, V_{min}, V_{max}/DoD, C_c, C_d, PRF	◑

To summarize, most experimental results focus on just a few different parameters, e.g., temperature and SoC-dependent calendar aging or different charging protocols. While this is very helpful to analyze certain aspects of aging, it is less suitable for generating a universal degradation model. In some studies, many parameters are varied with a very small number of cells, so semi-empirical modeling is only possible by making many assumptions about the model. Even more extensive campaigns rarely publish result or raw data and often just present selected results in figures in the publications. Among the most promising experiments that investigate calendar and cyclic aging and are potentially suitable for generating an EV battery aging model are:

- *EVERLASTING* project [609, 610]: Calendar aging is tested at four temperatures (0, 10, 25, 45°C) and three SoCs (10, 70, 90%). Two different charging (0.5, 1 C) and discharging rates (0.5 to 3 C) are tested with a fixed SoC range of 10–90% at three to four temperatures. In another test, three different driving profiles with two DoD windows were applied to cells at one to four temperatures. Raw cycling data of the cells is openly available.
- Uddin et al. [180] investigate calendar aging at three temperatures (10, 25, 45°C) and SoCs (20, 50, 90%). Cyclic testing is performed at room temperature with two DoDs (30 and

80%) and two to three different discharge rates (0.4, 0.8, 1.2 C). The charge rate is fixed to 0.3 C. The derived model is validated with six different operating profiles with different temperatures, SoCs windows, charging, and discharging currents. Although no result data is available for download, plots for capacity decrease and resistance increase are shown.

- *Batteries2020* project [492, 493, 613], also used in [614–616]: No open data is available for this relatively comprehensive dataset. However, it could be extracted from the published result plots, which are given for most cells, except for temperatures below 25°C. DoDs from 10 to 100% with various SoC_{mid} settings are tested with a fixed charge ($\frac{1}{3}$C) and discharge (1 C) current at three different temperatures (25, 35, 45°C). Different charge ($\frac{1}{3}$, 0.5, 1, 2 C) and discharge rates ($\frac{1}{3}$, 1, 2 C) are investigated at a fixed SoC range of 10% to 90%.
- *MOBICUS* project [481, 618–620]: In this large project, many cells were tested under different conditions, but no data is available for download, and only a few results are presented in the publications. However, several results of one of the cell chemistries are presented in [620]: Calendar aging was performed at four different temperatures (0, 25, 45, 60°C) and up to five SoCs (0, 30, 65, 80, 100). Cyclic aging with two charging (1, 3 C) and discharging rates (1, 3 C) is presented at 0, 25, and 45°C for up to four SoC_{mid} values (30, 65, 80, and 90%). The DoD is not clearly identifiable, but the application in PHEVs indicates that only shallow cycling was performed (likely 10%, as used in [618, 619]).
- Data from Naumann et al. [621–624], also discussed in [439]: Three different SoC_{mid} values (25, 50, 75%) and seven DoDs were tested at 40°C. Other cells were cycled with three different charging rates (0.2, 0.5, 1.0 C) and four discharging rates (0.2, 0.5, 1.0, 2.0 C) at the same temperature. Three additional parameter sets with different DoDs were also tested at 25°C. The result data of most of the experiments is available for download.
- Data recently published by Wildfeuer et al. [626] (open access), described in [625]: Almost 200 NCA/C-Si cells are tested for nearly two years. Calendar aging tests are conducted at 20, 35, 50, 60°C, and random temperatures. Fifteen fixed, as well as alternating and random SoCs, are chosen. Cyclic aging is performed with seven DoDs using ten different SoC_{mid}, seven charging, and seven discharging rates. Moreover, alternating conditions, dynamic driving profiles, and the effect of different check-up intervals are investigated.

With the exception of the newest comprehensive dataset published by Wildfeuer et al. in 2023 [625, 626], the presented studies either are not well reusable, do not consider all desired parameters of calendar aging (SoC or V, T) and cyclic aging (T, C_c, C_d, DoD or V/SoC range), or do not cover conditions typically found in EVs (broad temperature range, fast charging, cell chemistries). Although the testing conditions between the experiments vary significantly, it is conceivable to merge data from different studies or at least use it to validate existing models. However, to develop a plausible EV battery aging model for investigating different V2G use cases, a new dataset was generated in this thesis, which is described in the following chapter.

7 Battery aging investigation

The objective of the investigation presented in this chapter is to compare different V2G use cases and strategies to provide insights into the effect of bidirectional charging on battery degradation and derive recommendations for the operation of V2G and EVs in general to prolong battery lifetime. Employing V2G use case simulations with an accurate battery aging model enables comparing a wide range of scenarios with different conditions without the use of actual batteries. This allows testing more applications and reduces the required time, cost, and other resources.
For this purpose, a battery aging simulation model is needed that can attribute degradation to specific causes and quantify battery aging under different conditions, even if no data from a battery operated under these conditions is available. A conceivable structure of such a model is shown in Figure 7.1. Internally, it consists of a set of equations or algorithms calculating degradation metrics such as remaining usable capacity and internal resistance or the frequency-dependent impedance based on input variables such as cell voltage, current, and temperature over the lifetime of the cell. This model could be used not only in simulations but also during the life of the battery (e.g., in V2G and EMS optimization algorithms) or in the BMS of the EV.

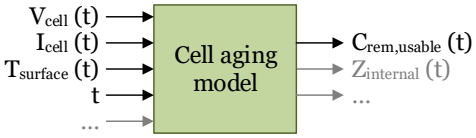

Figure 7.1: Objective: An easy-to-reuse cell aging model that can be used in simulations and during cell operation

The battery degradation models presented in Chapter 6.3.3 typically only focus on specific aspects. For example, some of them model cyclic aging but neglect calendar aging, or they assume that the cells are operated under the same condition over the lifetime of the battery. However, to simulate the aging of EV batteries, it is essential to consider varying operating conditions and account for calendar aging since the battery remains unused most of the time. Therefore, a new battery degradation model was derived as part of this thesis.
However, as discussed in the previous chapter, there is also a lack of publicly available data to generate such an aging model. Therefore, the accelerated battery aging experiment described in Chapter 7.1 was conducted to acquire a comprehensive battery aging dataset as a basis for the model. In the aging study, many parameters, such as temperatures, charging and discharging

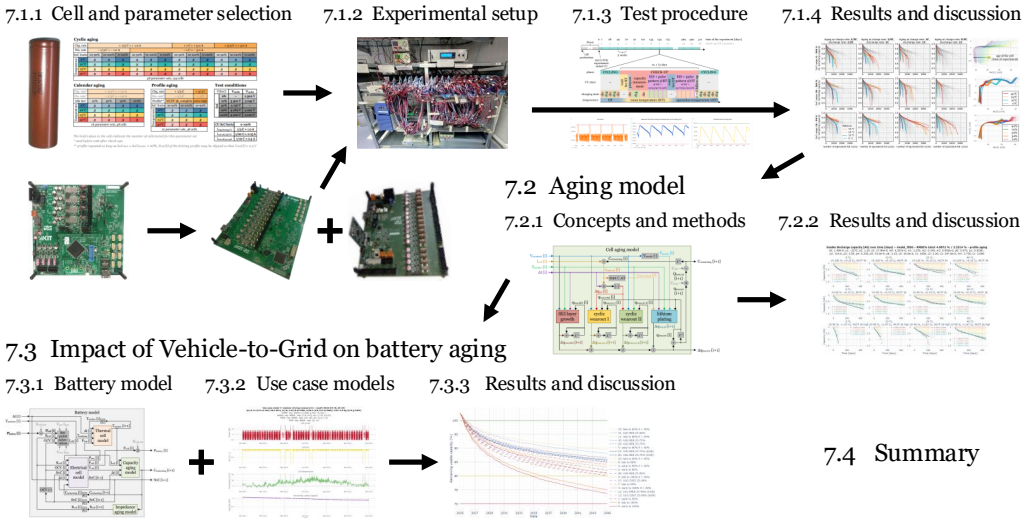

Figure 7.2: Graphical abstract of the battery aging investigation

rates, and SoC limits, were varied, and multiple cells were operated for each condition to improve statistical significance. Consequently, battery test equipment with hundreds of test channels was needed for the experiment. Commercial battery test equipment is costly, and no test environment was available that could have been reserved for several months to years. Therefore, a custom battery cell cycling and measurement data acquisition system presented in Chapter 7.1.2 was developed for this thesis. Next, the battery aging model described in Chapter 7.2 was derived from the data collected. Finally, the cell aging model was used to analyze battery degradation in different V2G use cases, as discussed in Chapter 7.3.

The battery aging result and raw log data, the aging model, and the V1G and V2G use case models summarized in Table 7.1 were made publicly available for free under *FAIR* (findable, accessible, interoperable, and reusable) conditions.

Table 7.1: Open-access publications, data, models, and software on battery aging generated within this thesis

Ref.	Description	Repository/Journal
[R1]	Battery aging data set	*RADAR4KIT*
[J1]	Description of the battery aging data set	*Nature Scientific Data*
[R2]	Python scripts for visualizing and analyzing the battery aging data	*GitHub*
[R3]	Python scripts used for the optimization of the battery aging model	*GitHub*
[R4]	Battery aging and V1G/V2G use case models	*GitHub*

7.1 Data collection

An extensive cycling experiment was conducted over a period of more than 600 days to obtain a comprehensive battery aging dataset. The cycling experiment and the results of the first 449 days of measurement data will be described in the following. Further technical details on how the openly available aging data [R1] was collected and processed and how it can be used are provided in [J1]. Scripts assisting in data analysis are published on *GitHub* [R2].

7.1.1 Cell and parameter selection

As the degradation model shall be used to determine aging in EV batteries, a battery cell similar to the cells typically used in modern EVs was selected for the experiment. Many different cell chemistries, form factors, and capacity ratings are used in the hundreds of EV models that are available at present. As mentioned in Chapter 6.1, commonly used chemistries in EVs are NMC, NCA, and LFP Li-ion cells. State-of-the-art LFP cells can reach very high cycle numbers (see Chapter 6.3), so the additional use of LFP batteries for V2G applications is uncritical and, thus, less relevant to be modeled. A comprehensive aging dataset using NCA cells was published recently by Wildfeuer et al. [625, 626]. On the other hand, a nickel-rich NMC cell was selected in the experiment described below. NMC cells are used in medium- to high-range EVs, where a high fraction of the battery capacity could potentially be used for V2G.
Although many EV batteries consist of individual cells with a relatively high capacity (e.g., in the range of 10–100 Ah), smaller cells were chosen for this investigation to limit the cycling and cooling hardware cost in the battery cycling test bench. Important aspects of the cell selection were a high energy density and charging power capability, a wide operating and charging temperature range, and high safety. Based on these considerations and a comparison of more than 150 cells from eight manufacturers available in 2021, the *LG INR18650HG2* was selected as a suitable test candidate. The specifications of this NMC/C+SiO cell (nickel manganese cobalt cathode, graphite silicon oxide anode) are summarized in Table 7.2.

The batch of 250 cells used in the experiment arrived on August 30, 2022. The presumed production date is November 26, 2020[1]. One of the cells was characterized in the following days, as summarized in Table 7.3. The measurements suggest that the cells are genuine. After cell preparation, the OCVs of all cells used in the experiment were measured at a temperature of 17.6-18.6°C (steady state) on September 19, 2022. The mean value was 3.5558 V (+0.0140 V/−0.0065 V)

[1] The codes lasered onto the cells are “DT331K262A_”, where “_” is one of 1-9, B, C, or D. The “T” indicates the production year of 2020, and the “331” reflects the day of the year.

Table 7.2: Properties of the selected battery cell *LG INR18650HG2* [627, 628] — adapted from [J1]

Form factor	18650 (cylindrical)	Nominal capacity	3000 mAh
Cathode material	$LiNi_xMn_yCo_{1-x-y}O_2$ (*"H-NMC" [628]*)	Voltage range	2.0–4.2 V (allowed) 2.5–4.2 V (used)
Anode material	Graphite with SiO	Nominal voltage	3.60 V
Weight	ca. 46 g	Usable energy	max. 11.0 Wh
Diameter	ca. 18.3 mm	Maximal current*	6.0 A (charging)
Height	ca. 65.0 mm		20.0A (discharging)
Energy density	240 Wh/kg 640 Wh/l	Temperature range*	−20 to +75°C (operation) −5 to +50°C (charging)

*Important: Please refer to the product specification provided by the manufacturer for details [627].

with a standard deviation of 0.0020 V. Considering the voltage range of 2.5 V (SoC = 0%) to 4.2 V (SoC = 100%) used in the experiment, this corresponds to an SoC of about 26.8% (+0.6%/−1.15%), using the OCV-SoC LUT shown in Table A.8 and Figure A.8.

Table 7.3: Measurement results of one of the cells shortly after arrival

Test (condition)	**Specification** [628]	**Actual**	**Test result (deviation)**
Color, appearance	brown	brown	pass (no anomalies detected)
Weight	44-45 g	45.75 g	pass
Impedance (1 kHz)	14-16 mΩ	14.2 mΩ	pass
Impedance (DC)	24-26 mΩ ("DC")	22.7 mΩ (0.05 Hz)	pass
Discharge capacity/energy (I_{chg} = 4.0 A to 4.2 V, $I_{chg,cut\text{-}off}$ = 100 mA, discharge to 2.5 V):			
I_{dischg} = 0.6 A	2.998 Ah / 11.0 Wh	2.925 Ah / 10.7 Wh	pass* (−2.42% / −2.64%)
I_{dischg} = 3.0 A	2.886 Ah / 10.3 Wh	2.889 Ah / 10.3 Wh	pass (+0.09% / +0.25%)
I_{dischg} = 5.0 A	2.884 Ah / 10.1 Wh	2.834 Ah / 9.7 Wh	pass* (−1.75% / −3.97%)

*Plausible with regard to previous calendar aging (ca. 1.75 years).

The cells were split into three groups to analyze three different modes of operation. One group of cells is charged and discharged continuously ("cyclic aging"), using different charging and discharging rates and voltage ranges. The second group rests at a defined voltage ("calendar aging"). The third group of cells is operated under different driving profiles typically found in EVs ("profile aging"). All tests are carried out at four different temperatures. An overview of all test conditions ("parameter sets") is shown in Figure 7.3. Three cells were used for each test condition to obtain a higher statistical relevance of the aging data and model. In total, 76 parameter sets and 228 cells were used in the main experiment.

Cyclic aging

Chg. rate		+ 1/3 C = + 1.0 A						+ 1 C = + 3.0 A			+ 5/3 C = + 5.0 A		
Dis. rate		− 1/3 C = − 1.0 A			− 1 C = − 3.0 A								
SoC limits		10-90%	10-100%	0-100%	10-90%	10-100%	0-100%	10-90%	10-100%	0-100%	10-90%	10-100%	0-100%
Temperature	0°C	3	3	3	3	3	3	3	3	3	3	3	3
	10°C	3	3	3	3	3	3	3	3	3	3	3	3
	25°C	3	3	3	3	3	3	3	3	3	3	3	3
	40°C	3	3	3	3	3	3	3	3	3	3	3	3
48 parameter sets, 144 cells													

Calendar aging

Chg. rate*		+ 1/3 C = + 1.0 A			
Dis. rate*		− 1/3 C = − 1.0 A			
Idle SoC		10%	50%	90%	100%
Temperature	0°C	3	3	3	3
	10°C	3	3	3	3
	25°C	3	3	3	3
	40°C	3	3	3	3
16 parameter sets, 48 cells					

Profile aging

Chg. rate		+ 1/3 C		+ 5/3 C
Dis. rate*		− 1/3 C		− 1 C
Profile**		WLTP 3b, complete		extra high
SoC limits		10-90%	10-100%	10-90%
Temperature	0°C	3	3	3
	10°C	3	3	3
	25°C	3	3	3
	40°C	3	3	3
12 parameter sets, 36 cells				

Test conditions

V(SoC)		$V_{cal,idle}$	$V_{cyc,lim}$
SoC	0%	–	2.500 V
	10%	3.300 V	3.249 V
	50%	3.736 V	–
	90%	4.089 V	4.092 V
	100%	4.200 V	4.200 V

CU SoC limits	0-100%
$I_{chg/dischg,CU}$	1/3 C = 1.0 A
$I_{cut-off,cal/CU}$	1/20 C = 0.15 A
$I_{cut-off,cyc/prf}$	1/10 C = 0.3 A

The bold values in the cells indicate the number of cells tested for this parameter set.
** used before and after check-ups*
*** profile repeated as long as $SoC_{start} \geq SoC_{lim,low} = 10\%$, $P_{cell}(t)$ of the driving profile may be clipped so that $V_{cell}(t) \geq 2.5$ V*

Figure 7.3: Test matrix for the aging investigation (three cells were used for each parameter set) — adapted from [J1]

Several other aging studies conduct measurements under a reference test condition (e.g., 25°C, 0–100%, +1 C/−1 C) and then only vary individual parameters (e.g., either temperature or charging rate). This allows for reducing the number of cells in the experiment. However, in this study, each temperature value was combined with each SoC value or range, and several charging and discharging currents were tested with the resulting combinations. This allows a more detailed examination of the interdependence of the parameters, for example, to observe the dependence of lithium plating on temperature, charging rate, and maximum SoC.

The selected parameter sets were a trade-off between a broad coverage of typical EV battery conditions and the cost and complexity of the experiment. For example, while additional cells could have also been discharged at −20°C, this would have required a dynamic adjustment of the cell temperature for charging since it is only allowed at higher temperatures. Selecting higher temperatures for cycling, such as +50°C, would pose a higher risk of thermal runaways, particularly when fast-charging severely aged cells, and thus require a suitable test environment capable of handling potentially destructive tests.

Besides the parameters tested, additional idle SoCs for the calendar aging cells and different DoD ranges for the cyclic aging cells would have been interesting. However, they would have significantly increased the cost and complexity of the experiment. For a more comprehensive selection of SoC ranges, other studies summarized in Table 6.3 can be considered.

Higher discharge rates were not used since they do not occur in the driving cycles under the

assumptions made for the EV battery capacity[2].
The driving profiles are based on the WLTC for Class 3b vehicles (i.e., typical passenger cars) of the WLTP [389]. The battery cell power was calculated using the *JRC Python Gearshift Calculation Tool* [629] and assumptions about the EV and battery characteristics. They are summarized in Table A.5 in Appendix A.7. The derived cell power profile is published in the *WLTP_Class_3b_cycle_power_profile.xlsx* spreadsheet along with the aging dataset [R1].

7.1.2 Experimental setup

A custom battery aging test bench was developed as part of this thesis. This allowed testing a large number of cells at a significantly lower investment cost than with a commercial cycling system. The test bench is shown in Figure 7.4, and a sketch showing all relevant components is provided in Figure A.9.

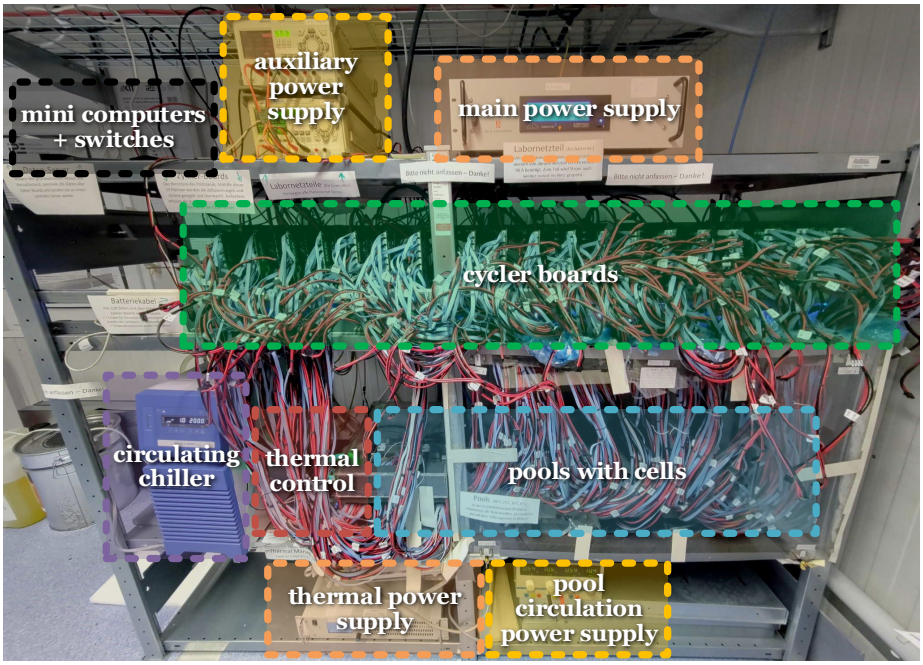

Figure 7.4: Test bench for the battery aging experiment — adapted from [J1]

[2] Higher discharge rates would be needed, e.g., when using small EV batteries, towing large trailers, driving uphill, or at significantly higher speeds than in the WLTP profile. This was not considered to reduce the number of cells in the experiment. Increased aging is unlikely since the battery is specified for much higher discharge rates.

The cycler boards are the core of the test bench. As seen in Figure 7.5, they control the charging and discharging of the cells using a DC/DC converter for each cell. The cycler boards measure the cell voltage, current, and temperature and derive other variables such as the estimated SoC, OCV, and the charge ΔQ since the charging or discharging began. The data is stored locally on an SD card and forwarded to *Raspberry Pi* mini computers. The *Raspberry Pi* receives the data, stores it on an SSD, and sends it to a web server via the MQTT protocol using a Python script. On the server, the data is converted and stored in an *InfluxDB* database. The data can be visualized online using a *Grafana* interface with a latency of around 1-2 seconds. While the cycling controller on the cycler board maintains a stable cell current or voltage, the cycling scheduler coordinates the transitions between charging, discharging, and dynamic operation. A master scheduler on a *Raspberry Pi* is responsible for the high-level control of the experiment. For example, it synchronizes all components during check-ups, in which the capacity of all cells is checked, or coordinates the restart of the test bench in the event of a power outage.

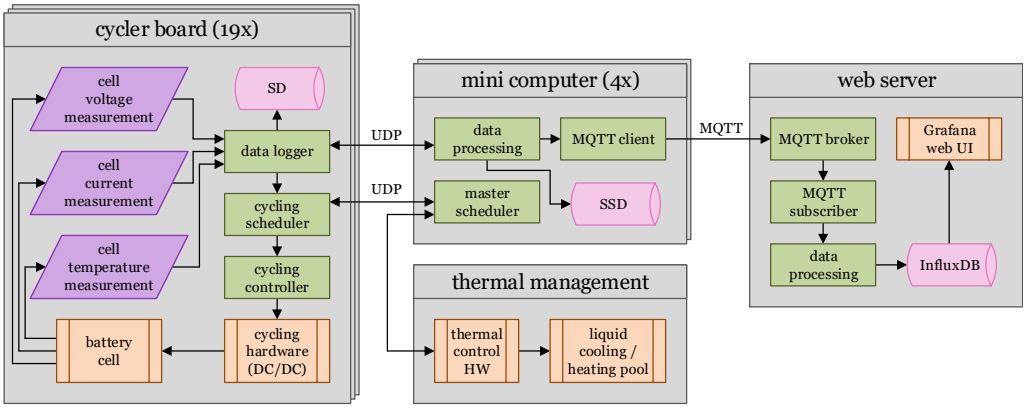

Figure 7.5: Battery data acquisition, transfer, and visualization — adapted from [C4] and [J1]

The cycler board is shown in detail in Figure 7.6. It can control up to 12 battery cells. The DC/DC converters that charge and discharge the cells are half bridges operating at a switching frequency of 500 kHz with two LC-filter stages at the output. This configuration allows a very smooth output voltage and current while maintaining a dynamic behavior, i.e., the cell current can be adjusted quickly. When charging the cell, the converters operate as buck-converters, and when discharging, they boost the cell voltage back to the main input voltage. The converter can also operate in dynamic modes, e.g., controlling the cell power according to a driving profile or injecting sinusoidal currents into the cell during EIS measurements.
The PWM signal for the DC/DC converters is generated by the high resolution timer (HRTIM) module of an *STMicroelectronics STM32G474* microcontroller. Thanks to the high temporal

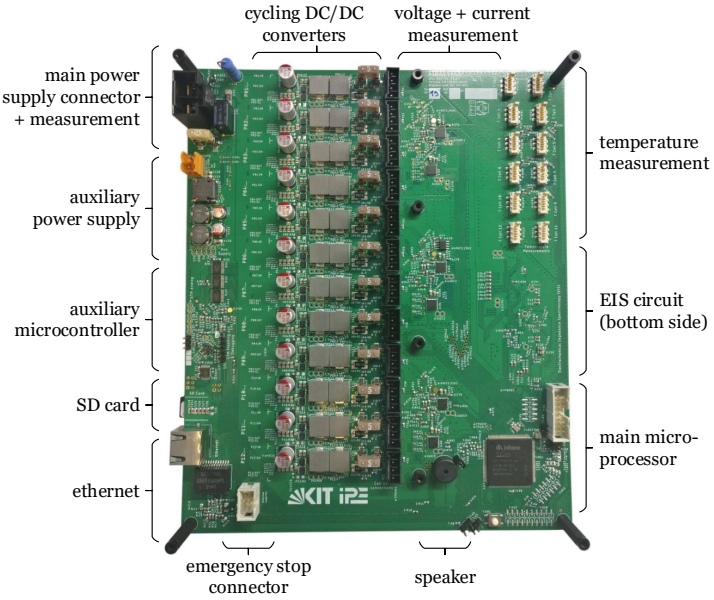

Figure 7.6: Battery cycler board responsible for cell charging and discharging as well as cell voltage, current, temperature, and impedance measurement — adapted from [J1]

resolution of the HRTIM, the desired duty cycle can be set with an accuracy of less than 184 ps or 0.01% of the switching period. While the auxiliary *STM32* microcontroller is responsible for PWM generation, most other tasks are coordinated by an *Infineon AURIX TriCore TC375AA* main microprocessor. For example, the main processor schedules the charging and discharging, controls the cell currents and voltages, acquires all measurements from external ADCs, stores the measurements and states on an SD card, and communicates with the mini computers via Ethernet. The cell voltages and currents are measured with 16-bit resolution ($\Delta V_{LSB} \approx 69\ \mu V$, $\Delta I_{LSB} \approx 343\ \mu A$). At typical operating conditions, the voltage can be measured with an accuracy of better than 0.05% and the current with better than 0.1% [C4]. The temperature is measured using negative temperature coefficient (NTC) thermistors connected to 12-bit ADCs. The temperature resolution is nonlinear but within $\Delta T_{LSB} < 0.05K$ in the relevant temperature range of -5°C to +45°C. The estimated accuracy is roughly within 1 K.

The 15 V main input voltage for cycling was provided by up to two paralleled bidirectional *Delta Elektronika SM 500-CP-90* power supplies, capable of supplying up to 180 A. The main power supply can be disconnected using a relay on the PCB, e.g., when the emergency stop switch is activated. A 12 V auxiliary power supply is used to power all circuits on the PCB, independent of the main power supply.

The predecessor of the cycler board, which has largely similar specifications, is presented in [C4] along with more details.

The cells are operated at four different temperatures. When battery cells are charged or discharged, their temperature rises due to power dissipation. The cells are stored in pools filled with liquid silicone oil to maintain a stable cell temperature. A cross-section of one of the pools is shown in Figure 7.7. Two NTC temperature sensors are fixed at opposing sides of the pool to measure the oil temperature. A circulating blade swirls the silicone oil to achieve a homogeneous temperature in the pool. The cells with the highest C-rates are placed right next to the circulating blade, and calendar aging cells are placed on the opposite side of the pool. A measurement electrode is placed in the pool to monitor the isolation resistance of the pool.

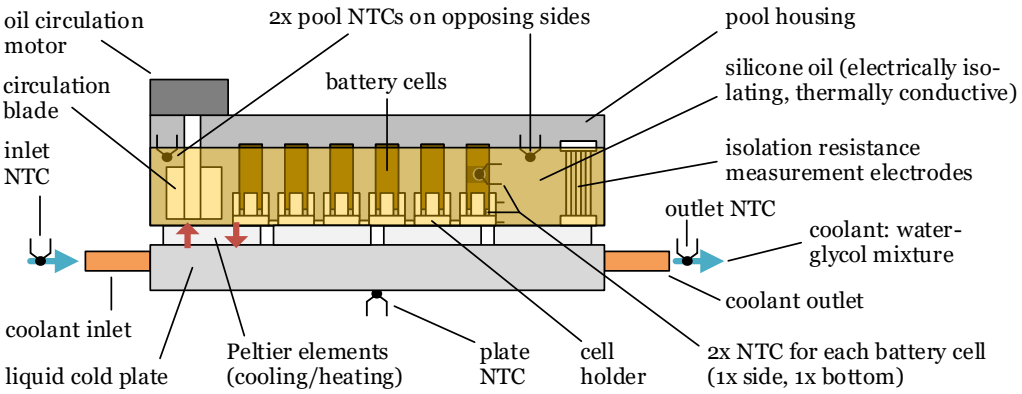

Figure 7.7: Illustration of one of the thermally controlled pools, including battery cells — adapted from [J1]

The cells are mounted on a 3D-printed structure. Their negative poles are at the bottom side. The positive pole is placed outside of the oil to avoid contamination of the cells' safety vents with oil. The cell temperature is measured using two temperature sensors per cell, as shown in Figure 7.8. One is fixed at the negative pole, and the other is placed at the side of the cell, approximately in

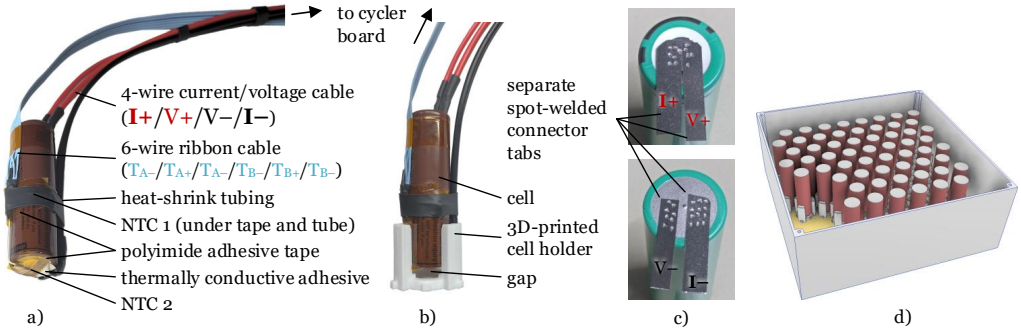

Figure 7.8: a) Assembly of the battery cell, b) cell mounted in an individual cell holder, c) spot-welded connector tabs for the four-wire measurement, d) sketch of cells mounted in the combined cell holder inside a pool — adapted from [J1]

the center. The cycler measures both temperatures and uses the average value, or the hottest of the two, in case the difference is larger than 3 K.
The pool temperature is regulated using Peltier elements that are placed below the pool with thermal grease. They allow a heat transfer in both directions so the pool can be heated or cooled. The other sides of the Peltier elements are mounted to a cold plate, through which a water-glycol mixture is circulated. The cold plates of the three coldest pools (0 to 25°C) are connected in a row and cooled by a circulating chiller, as shown in Figure 7.9. In regular operation, the coolant enters the cold plate of the coldest pool with a temperature of about −1°C and exits the cold plate of the warmest pool at approximately 6°C. Since the warm pool (40°C) only needs to be heated in regular operation, it is connected to a separate circuit mainly consisting of a pump, temperature sensors, and radiator fans that can exchange heat with the environment (usually 22-28°C) if necessary.

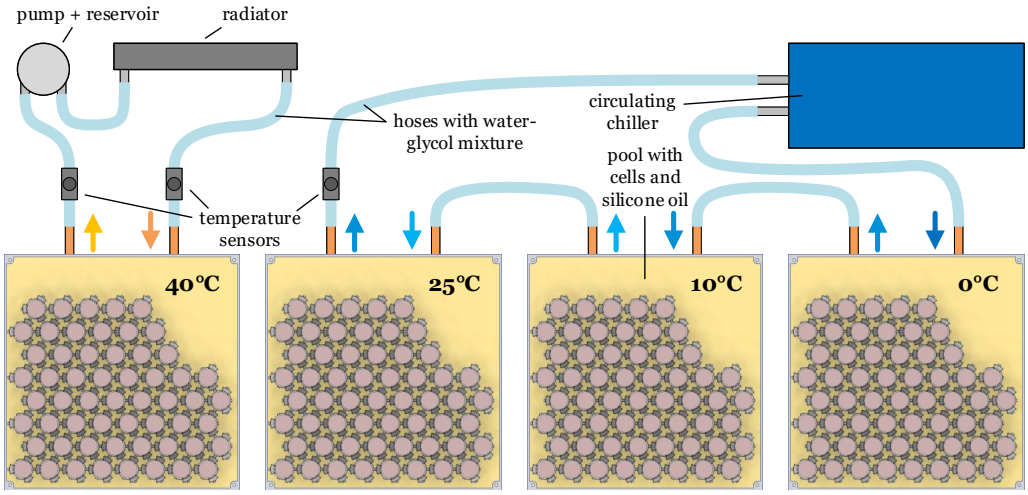

Figure 7.9: Overview of the components in the cooling circuits with coolant flows — adapted from [J1]

The thermal management controller board is shown in Figure A.10. It controls all Peltier elements using H-bridge DC/DC converters, the pumps and the fans using MOSFETs as power switches, and the circulating chiller using RS-232. Similar to the cycler board, the thermal management board stores its measurements and states on an SD card and sends them to a *Raspberry Pi*, where the data is also stored and forwarded to the web server.

7.1.3 Test procedure

Figure 7.10 provides an overview of the experimental test procedure. Most of the time, the cells remain in their operating condition, as defined in Figure 7.3. However, all cells are regularly

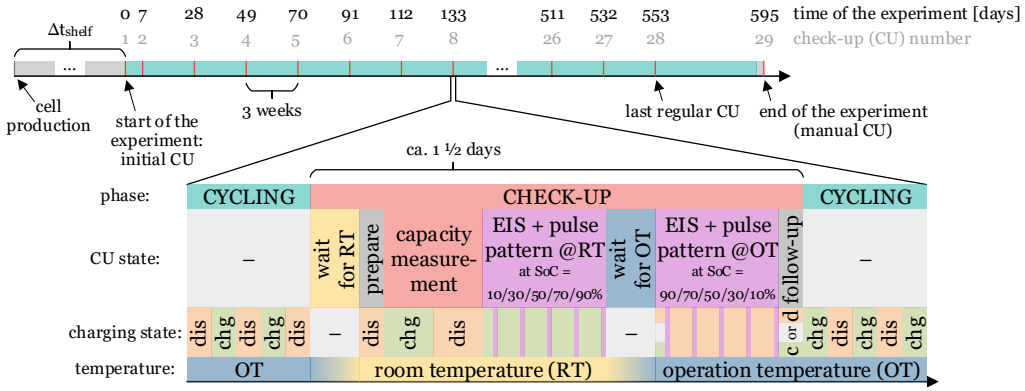

Figure 7.10: Test procedure and detailed view of a check-up routine — adapted from [J1]

benchmarked under comparable operating conditions with a check-up (CU), sometimes called a Reference Performance Test (RPT) in the literature.

When a CU starts, all cells complete their current cycling activity, ending with a discharge. When finished, the temperature for all cells is changed from their operating temperature (OT) to 25°C, referred to as room temperature (RT). The cells are charged or discharged to 2.6 V using their operational discharge and cut-off rate, shown in Figure 7.3. Next, they are discharged to 2.5 V using the check-up current rate of 1/3 C and the check-up cut-off current rate of 1/20 C.

The cells are then charged and discharged at RT using the check-up current and cut-off rates to determine their remaining usable capacities. Afterward, electrochemical impedance spectroscopy (EIS) is conducted at multiple SoCs (10/30/50/70/90%) to measure the frequency-dependent complex impedance of the cells at RT. The SoCs are reached by CC-CV charging to the OCV corresponding to the SoC of a new cell using Table A.8 in the Appendix. After each EIS, a current pulse pattern is applied to the cell to measure the voltage response in the time domain. The test conditions for the EIS and pulse pattern are summarized in Appendix A.7.

When all cells are finished, the temperature returns to their OT. The EIS and pulse measurements are repeated to obtain the impedance characteristics of the cell at their OT as well. Afterward, the cells are charged or discharged to their individual idle or lower operating SoC. The cyclic and profile aging cells continue with a charging process, and the calendar aging cells rest at their respective SoC. They are only recharged occasionally[3] if the voltage deviates by more than 5 mV.

[3] Note: Li-ion cells have an exceptionally low self-discharge rate. A voltage of 3.544 V ± 7 mV was measured at about 18°C for 16 unconnected cells on February 5, 2024, i.e., 504 days after the voltages were initially measured. The mean voltage is only less than 12 mV smaller than the mean voltage of the first measurement, so the self-discharge rate is significantly smaller than 1%/year. However, the cycling board introduces a leakage current in the order of 200 µA that gradually discharges the cells at roughly 50%/year. The leakage current is presumably mainly caused by the input bias currents of the current-sense amplifiers used in the cycler board. A conceivable solution to prevent this would be to separate the cells from the cycling circuit with relays if the cell is resting or reached its EOL.

The main experiment started on October 12, 2022, with the first CU. The second CU followed a week later, all others at intervals of 3 weeks until the last regular CU 28 starting on April 17, 2024. Due to a failure on the thermal management board, cycling was stopped on May 27, 2024. A manual check-up (CU 29) at room temperature was carried out between May 29 and June 1, 2024, marking the end of the experiment.
All cells are typically operated under the specified operating conditions until an end-of-life (EOL) condition of the cell is met. The operating temperature, C-rate, or SoC range is not altered over time. The capacity-based EOL_{cap} is reached if the estimated remaining usable capacity based on Equation 7.1 is smaller than 40% of the nominal capacity C_n of the cell in regular operation or less than 50% of C_n when measured in check-ups.

$$C_{rem,usable,est} = \left| \frac{\Delta Q}{SoC_{end} - SoC_{start}} \right| = \left| \frac{\Delta Q}{\Delta SoC} \right| \tag{7.1}$$

ΔQ is the charge processed in the last charging or discharging procedure. Using the cell terminal voltage and the LUT in Table A.8, SoC_{start} is determined just before the charging or discharging process starts, and SoC_{end} at the end, after a rest time of five minutes. Hence, the minimum rest period between charging and discharging operations or consecutive discharging profiles during regular operation and check-ups is five minutes.
The EOL_{imp} is reached if, for more than half of the EIS measurements (either at room or at operating temperature), the reference impedance Z_{ref} defined by Equation 7.2 is larger than three times the initial reference impedance $Z_{ref,init}$ measured in the first check-up. It is calculated using the average amplitude of the complex impedance $\underline{z}$ at four predefined, relatively arbitrary chosen frequencies.

$$Z_{ref} = \frac{|\underline{z}(10\ Hz)| + |\underline{z}(2.083\ Hz)| + |\underline{z}(0.5\ Hz)| + |\underline{z}(0.2083\ Hz)|}{4} \tag{7.2}$$

All measurements, derived variables, and states are logged every two seconds, forming the “LOG” dataset. After every charging or discharging procedure in regular operation, a check-up, or in other modes, an end-of-charge “EOC” data packet is stored. The “EIS” dataset includes the results of all EIS measurements, and the pulse pattern curves are stored in the “PULSE” dataset. In addition to the datasets collected during the experiment, configuration files (“CFG”) are defined before the experiment, which inform about the operating conditions. After the experiment, extended log files (“LOGEXT”) and post-processed log files (“LOG_AGE”) are derived. The latter can be used for modeling since they only include the most relevant variables with a lower temporal resolution, and data gaps are filled.

7.1.4 Results and discussion

Data collected by the test bench during the first 449 days of the experiment, i.e., until January 4, 2024, is presented in this chapter. The data is publicly available online [R1] and explained in a paper published in *Nature Scientific Data* [J1].

Before the experiment was started, the OCV of the cells used in the experiment (and one extra cell for test purposes) was measured at a temperature of around 18°C to find indications of production tolerances. As depicted in Figure 7.11a, the OCV ranged from 3.5418 to 3.5623 V (mean: 3.5558 V, standard deviation: 2.0 mV).

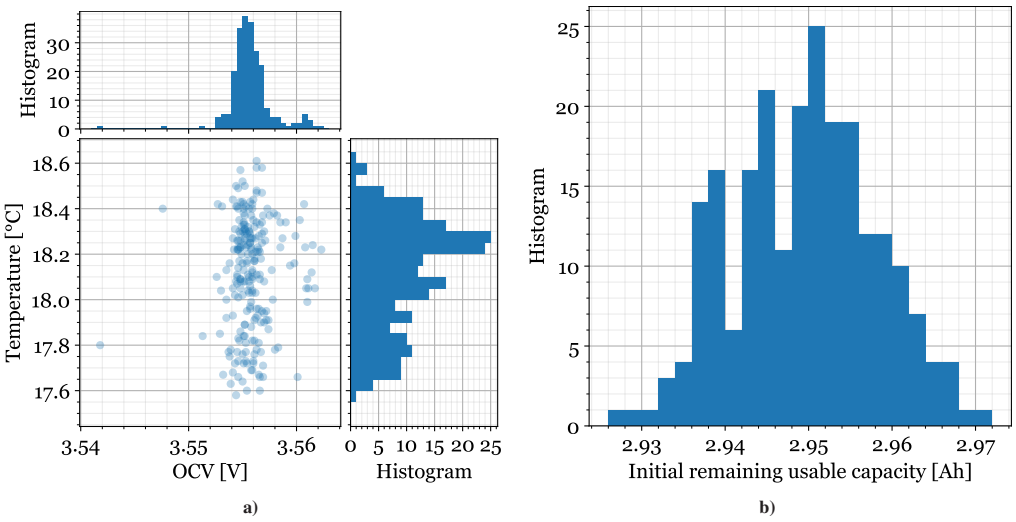

Figure 7.11: a) Initial OCV measured before the start of the experiment with steady-state temperature during the measurement, b) remaining usable discharge capacity measured in the first CU (i.e., before regular cycling) at 25°C — adapted from [J1]

As mentioned, the degradation of battery cells becomes apparent in a loss of usable capacity and an increase in impedance. However, the cell's usable capacity and effective impedance also depend on its operating condition (e.g., the temperature or current rate). Therefore, the test results collected during the CUs, in which all cells are characterized under comparable conditions, are used to analyze how different operating conditions affect aging. The initial remaining usable capacity of all cells measured at the beginning of the experiment is shown in Figure 7.11b. It was measured at 25°C in the first CU and ranged from 2.9263 to 2.9706 Ah (mean: 2.9495, standard deviation: 8.586 mAh, maximum deviation from mean: +0.72/−0.79%).

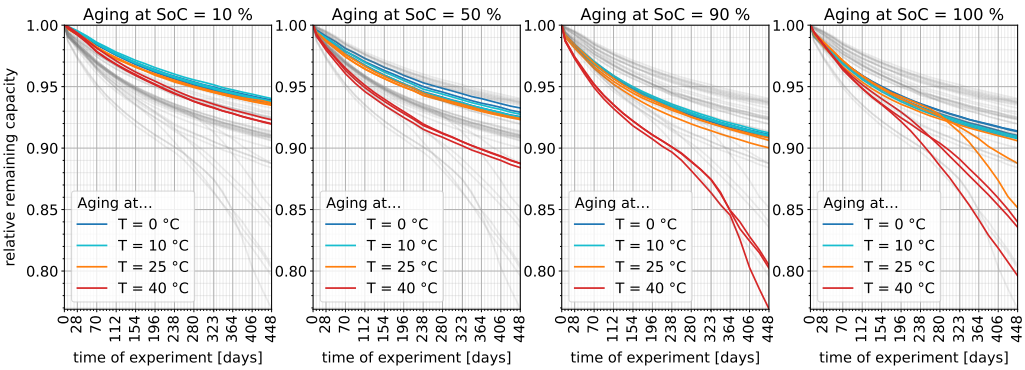

Figure 7.12: Development of the remaining usable capacity of all calendar aging cells as a function of time, relative to the first measurement of each cell, measured at room temperature in the check-ups — gray trajectories in the background: all calendar aging cells, i.e., overlay of cells aging at all SoCs and temperatures

The development of the remaining capacity for all calendar aging cells is shown in Figure 7.12. The x-axis represents the time since the start of the experiment in days. The y-axis depicts the relative remaining discharge capacity compared to the value collected in the first check-up, i.e., the capacity fade over time. The cells are divided into four graphs based on the SoC at which they rest during regular operation, from the lowest (10%) to the highest SoC (100%). Each trajectory represents one cell. The color of the trajectories indicates the operating temperature of the cells. Dark blue lines show the capacity fade of cells that rested at 0°C at the respective SoC. Turquoise lines represent cells at 10°C. Orange lines stand for 25°C, and red lines represent 40°C. In addition, the capacity fade of all other SoCs and temperatures is shown in the background of each graph in semi-transparent gray to assist the comparison of all calendar aging cells. It can be clearly seen that higher temperatures cause faster capacity fade. In general, higher SoCs cause more capacity losses as well. The fade is relatively high in the beginning and gradually slows down. For cells aging at 40°C and an SoC of 90% or 100% and the cell resting at 25°C and 100%, the capacity fade is significantly accelerated again after the remaining capacity falls below approximately 90% of the initial capacity.

In the literature, it is widely reported that the dominant aging mechanism for calendar aging cells is SEI layer growth, which is stronger at higher cell temperatures and voltages [374, p. 2212], [394, p. 696]. This behavior is also largely supported by the measurement data. However, it should be considered that the cells not only face calendar aging but also experience unavoidable cyclic aging due to the CUs. After 449 days, the cells aging at an SoC of 10% experienced about 43 equivalent full cycles (EFCs), while the cells at 100% passed 60 EFCs.

A rather unexpected result is that the capacity fade at an SoC of 90% tends to be noticeably higher than at 50 or 100% for cells resting at 40°C. Similar to this observation, multiple other aging studies also reported higher capacity fades at an SoC of 70 to 90% compared to smaller SoCs and

100% [611, p. 58], [625, p. 9], [630]. The exact reason for and characteristic of this effect in the experiment is uncertain. It might depend on the exact composition of the anode, cathode, and electrolyte material and the geometry of the cell and its electrode layers, particularly the size of the overhang causing a passive electrode effect [625, 630]. Keil [611, p. 58] even reported differences between cells of different production lots. Another uncertainty is which fraction of the capacity losses is reversible (as typical for the passive electrode effect) and could thus be recovered by suitable operating strategies, for example, applying a slow charge and discharge cycle or keeping the cells at another SoC for extended periods (compare [570]). In this context, the design of the experiment, particularly the check-ups, also influences the measured capacity, and the capacity loss in a real operation could be lower.

The capacity fade for all cyclic aging cells is presented in Figure 7.13. The relative remaining discharge capacity measured in the CUs, i.e., the capacity fade, is shown on the y-axis as a function of equivalent full cycles (EFCs) on the x-axis. It is calculated by dividing the average of

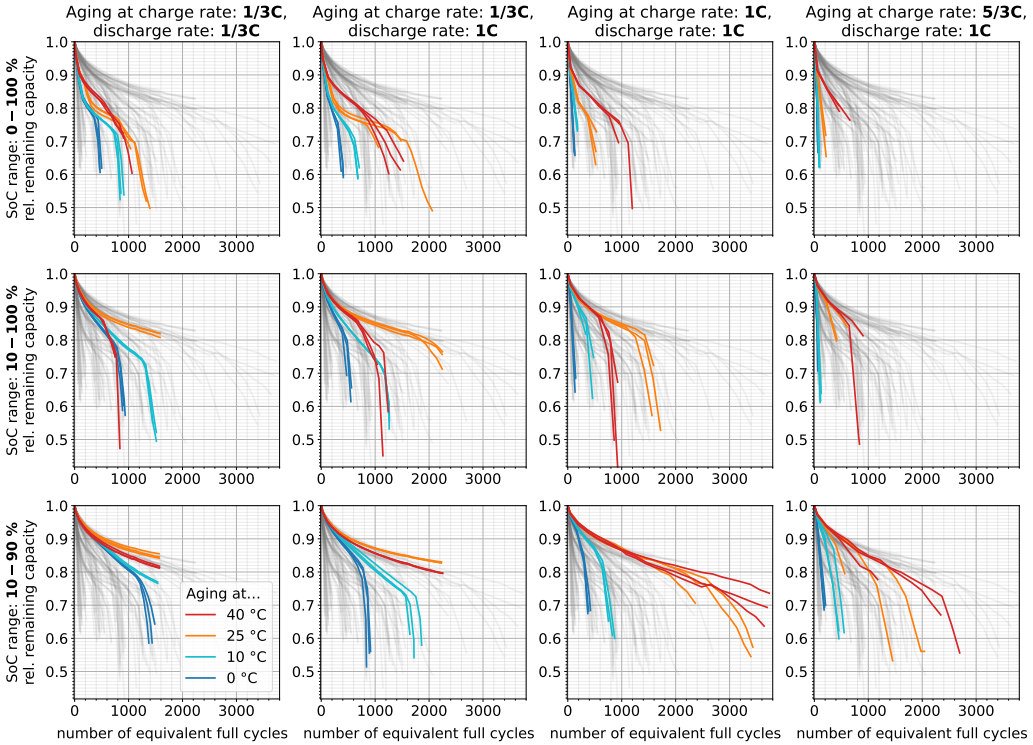

Figure 7.13: Development of the remaining usable capacity of all cyclic aging cells as a function of equivalent full cycles (EFCs), relative to the first measurement of each cell, measured while discharging at room temperature in the check-ups — data of all cyclic aging cells in gray in the background

the charged and discharged charge throughput by the nominal capacity C_n of the cell (3.0 Ah). Similar to the previous figure, the colors of the trajectories indicate the operating temperature of the cells (blue: 0°C, turquoise: 10°C, orange: 25°C, red: 40°C). The capacity fade of all other cyclic aging cells as a function of EFCs is shown in the background in gray. The parameter sets are subdivided according to the charge and discharge rate combinations (left: lowest charging and discharging rate, right: highest rates) and SoC ranges in which the cells are cycled during regular operation (from 0–100% in the top row to 10–90% in the bottom row). Data for all CUs collected in the first 449 days of the experiment is included. Most cells reached their EOL because the estimated remaining usable capacity was lower than 40% of the nominal capacity during cycling (compare Equation 7.1), or the BMS disabled the cell due to an overcharge event. This event typically occurs in the first regular operation charge procedure after a CU. In this case, the charge charged into the cell is either 5% larger than C_n or the estimated SoC reaches 125%, i.e., 25% more charge than expected could be charged into the cell. The reason for reaching the EOL, e.g., due to capacity fade, an overcharge, or repeated overtemperatures, is documented in the "Cycling Experiment Cell Overview" spreadsheet in the published dataset [R1] for each cell.

In contrast to the calendar aging cells, cycling at low temperatures causes the highest capacity losses, particularly at high C-rates and wide SoC ranges. Charging with high C-rates at low cell temperatures (e.g., 5/3 C at 0°C) has a devastating effect on the lifetime of the cell. In the most severe cases, when charging to 100% with the maximum charging rate (5/3 C) at 0°C, the remaining capacity was less than 70% of the nominal capacity after only 60 EFCs. When reducing the charging rate to 1/3 C and the SoC range to 10–90%, the cells at 0°C maintain an SoH of 70% for more than 800 EFCs.

The two groups of cells charging with the lowest charging rate of 1/3 C from 10 to 90% at a moderate temperature of 25°C maintain the highest capacity of all cyclic aging cells. After 449 days and over 1560 EFCs, the SoH of the cells also discharging with 1/3 C under this condition remains between 82.8 and 84.3%. The cells using the higher discharge rate of 1 C preserve 81.3 to 81.8% of their capacity in the more than 2220 EFCs completed during the same period.

High charging rates only resulted in a large number of EFCs if the temperature of the cell was sufficiently high (e.g., 40°C) and the end-of-charge voltage was limited below 4.2 V (100% SoC), i.e., 4.092 V (90% SoC) in the experiment. For cells cyclic between 10 and 90% with the highest charging rate and temperature, the SoH falls below 70% after 1200 to 2400 EFCs.

The remaining capacities for all cells aging with the WLTP driving profile are shown in Figure 7.14 as a function of EFCs and driving distance in the corresponding driving cycle. Similar to the cyclic aging cells, high charging rates significantly accelerate capacity fade if the cell is not warm enough. Slow charging to 100% also decreases lifetime, particularly for extreme temperatures.

The leading cause of the fast capacity fade at 40°C with an SoC limit of 100% is likely SEI layer growth. Lithium plating might dominate for low temperatures, even with moderate charging rates

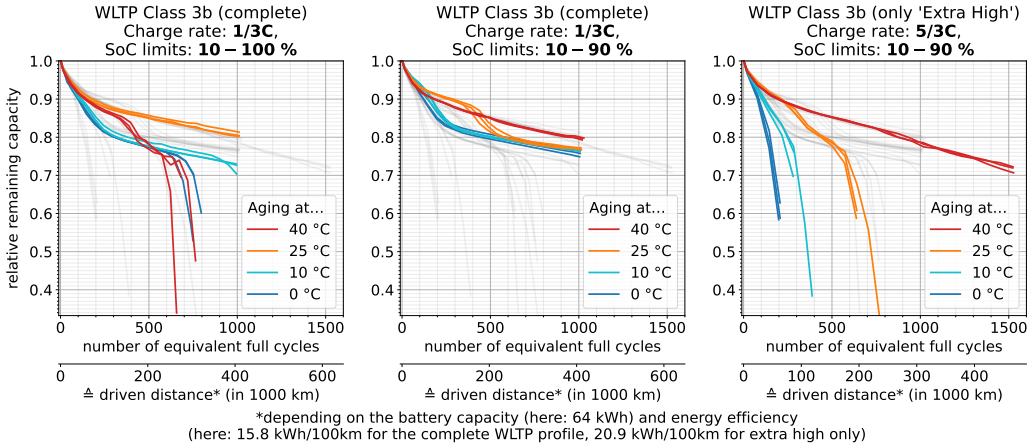

Figure 7.14: Development of the remaining usable capacity of all cells aging with the WLTP driving profile as a function of EFCs and driving distance, relative to the first measurement of each cell, measured while discharging at room temperature in the check-ups — data of all profile aging cells in gray in the background

(1/3 C at 0°C and 5/3 C at 0 to 25°C). At 40°C, a high charging rate has almost no detrimental impact on capacity fade compared to charging with 1/3 C, at least up to 1000 EFCs, or an SoH of around 80%. This highlights the importance of preheating the EV battery before fast charging. The emulated EV battery maintains 70% of the nominal capacity for at least 600 EFCs for all operating conditions except for cells fast-charging at temperatures below 25°C. This corresponds to a driving distance of more than 240,000 km in the complete WLTP profile or 180,000 km in the extra high WLTP profile. For less extreme conditions, e.g., a maximum charging limit of 90% or temperatures from 10 to 25°C, the battery even maintains 70% of C_n for more than 1000 EFCs or an equivalent of 400,000 km. The highest number of cycles is achieved if the cell rests at 25°C and cycles from 10–90% or 10–100%, or if it rests at 40°C and cycles from 10–90%. In this case, after 449 days and 1000 EFCs or 400,000 km, all cells still maintain approximately 80% of C_n. However, in real conditions, the cell experiences an additional capacity fade due to calendar aging, which is smaller under the accelerated test conditions of the experiments. On the other hand, the cell model and its chemistry is already approximately ten years old, as indicated by the data sheet and the technical specification of the cell [627, 628]. Even though newer, more powerful, and durable cells could not be acquired for this aging investigation, modern EV batteries will likely have a noticeably longer lifetime due to the rapid developments in battery research and production (compare [368, 606]).

The battery degradation is also apparent in an increase in impedance. Besides aging, the complex impedance of Li-ion battery cells strongly depends on the excitation frequency, temperature, and SoC. More than 35,000 EIS measurements were captured in the experiment. Selected results are presented in Figure 7.15. These and many other plots can also be inspected interactively in more

detail by opening the result plot examples in the published dataset [R1].
The impedance curves for all CUs are superimposed in the diagrams. As typical for EIS plots in the literature, the imaginary axis is inverted. For points above the real axis (negative $\mathrm{Im}\{\underline{z}\}$), the cell shows a capacitive behavior, and below the real axis (positive $\mathrm{Im}\{\underline{z}\}$), the impedance is inductive. In Figure 7.15a/b, the color of the curve indicates the time of the experiment, and in Figure 7.15c/d, it indicates the number of equivalent full cycles the cell completed. In Figure 7.15e, the color indicates the operating and measurement temperature during the EIS. In Figure 7.15f, it represents the SoC during the measurement. In all plots, the impedance is shown for a frequency of 10 kHz (lower left) to 50 mHz (upper right, highest impedance). The intersection of the real axis was measured at around 1 kHz independent of the temperature, age, and SoC. The local minimum (at $Re\{\underline{z}\} \approx 18m\Omega$ in Figure 7.15a) is at approximately 0.5–5 Hz. The impedance measurements at very high and very low frequencies (particularly above 2 kHz and below 0.5 Hz) are subject to larger measurement errors, as evident from several outliers.
Figure 7.15a shows the frequency-dependent impedance of the three calendar aging cells resting

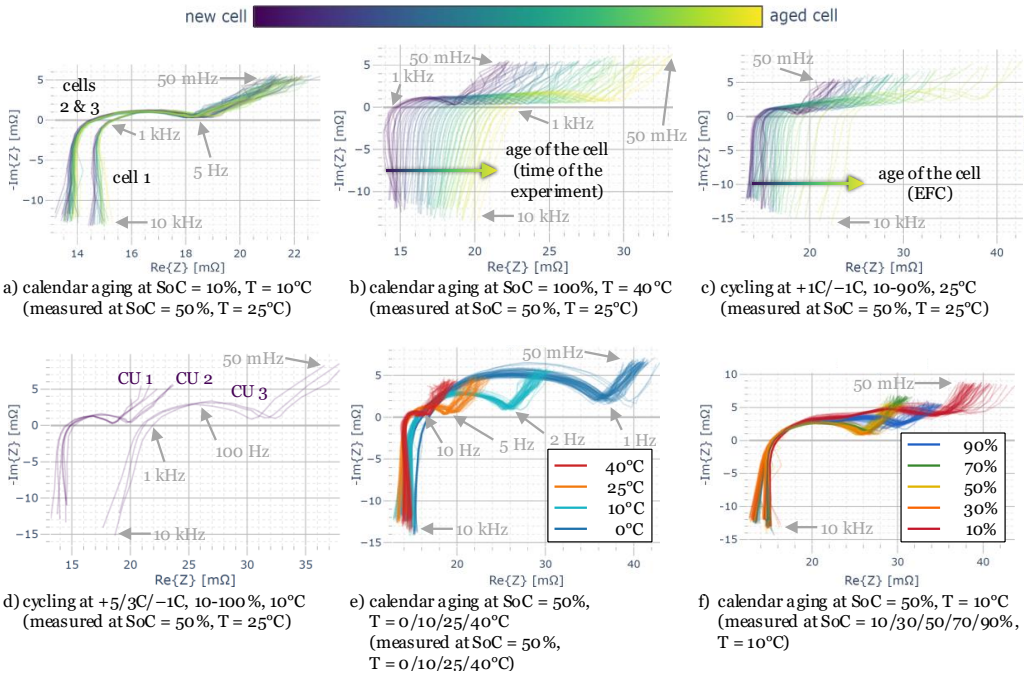

a) calendar aging at SoC = 10%, T = 10°C (measured at SoC = 50%, T = 25°C)

b) calendar aging at SoC = 100%, T = 40°C (measured at SoC = 50%, T = 25°C)

c) cycling at +1C/−1C, 10-90%, 25°C (measured at SoC = 50%, T = 25°C)

d) cycling at +5/3C/−1C, 10-100%, 10°C (measured at SoC = 50%, T = 25°C)

e) calendar aging at SoC = 50%, T = 0/10/25/40°C (measured at SoC = 50%, T = 0/10/25/40°C)

f) calendar aging at SoC = 50%, T = 10°C (measured at SoC = 10/30/50/70/90%, T = 10°C)

Figure 7.15: Selected electrochemical impedance spectroscopy (EIS) measurements: Color-coded aging dependency of the impedance (measured in the CUs at RT and 50% SoC) for parameter sets with different supposed dominant aging mechanisms: a) little impedance increase (but a considerable variation of initial impedance), b) significant SEI layer growth, c) intense cyclic aging, d) severe lithium plating. Color-coded dependency of e) cell temperature and f) SoC during the EIS measurement for calendar aging cells resting at 50% SoC and resting and measured at different operating temperatures (e) or 10°C (f).

at 10% and 10°C during regular operation. The impedances are measured in the CUs — in this example, at 25°C and an SoC of 50%. The calendar aging cell experiences minimal capacity fade, which is also reflected by the negligible impedance increase. However, it can be seen that the impedance of the cells in the experiment slightly differed even at the beginning of the experiment, by about 5.5% at 1 kHz.
The calendar aging cells resting at 100% and 40°C not only show a significant capacity fade but also a remarkable impedance increase, as seen in Figure 7.15b. At frequencies above 1 kHz, the complex impedance curves seem to be stretched along the real axis. The impedance magnitude $|\underline{z}|$ at 1 kHz increases from 14.4 mΩ to 23.0 mΩ, i.e., by 60%, in the first 449 days of the experiment. As for the capacity fade, the increase in impedance is likely mainly caused by SEI layer growth.
It is expected that cells cycling with $+/-1$ C from 10–90% at 25°C mainly experience cyclic aging, and calendar aging due to SEI layer growth is comparatively small. As shown in Figure 7.15c, the impedance also increases over the whole frequency range during the 3400 EFCs that the cell cycled in 449 days. Unlike the calendar aging cells, the capacitive part at lower frequencies around the local minimum at 1 Hz increases noticeably.
Among the cells for which severe lithium plating is expected to be the dominant aging mechanism are those charging with 5/3 C from 10–100% and discharging with 1 C at 10°C. The cells only survived three CUs, and their impedance increased significantly after only 108–126 EFCs at CU 3, as depicted in Figure 7.15d.
Figure 7.15e shows the temperature-dependency of the impedance during the measurement for all calendar aging cells resting at 50%. The temperature and SoC during the EIS measurement are similar to what the cells experience during regular operation, i.e., outside the check-up. The cells do not face a large capacity fade or impedance increase. However, the measurement temperature greatly influences the impedance: the colder the cell, the higher the impedance.
The dependency of SoC during the measurement is shown in Figure 7.15f for all calendar aging cells resting at 50% at 10°C. Again, the cells face little capacity or impedance increase over time, but the SoC significantly impacts the impedance. However, unlike the dependency of measurement temperature, the SoC-dependency of the impedance is only noticeable for frequencies below 1 kHz. The impedance amplitudes in the local minima at around 1 Hz are almost similar for the SoCs of 30, 50, and 70% but significantly higher for 90% and particularly 10%.

Since the EIS plots are relatively complex to analyze, the reference impedance Z_{ref} was calculated for each EIS measurement to reduce the result to one simple value (compare Equation 7.2 in Chapter 7.1.3). The development of the impedance over time or the EFCs is shown in Figure 7.16 to Figure 7.18. Individual outliers with significantly lower Z_{ref} values are caused by measurement errors in the EIS, for example, if one of the data points used for Z_{ref} has a lower or invalid value.
When comparing the development of Z_{ref} with the capacity trajectories of Figure 7.12 to Figure 7.14, it can be seen that these two symptoms of aging relate closely. For parameter sets and

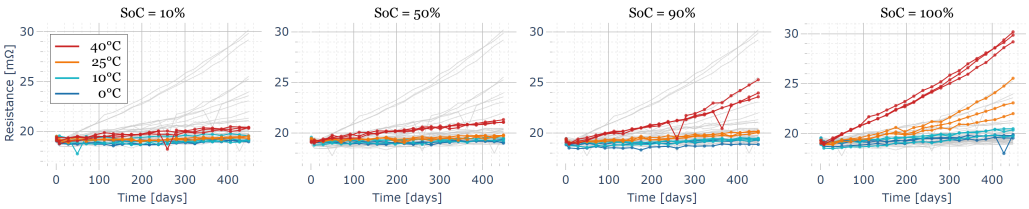

Figure 7.16: Development of the reference impedance of all calendar aging cells measured at 25°C

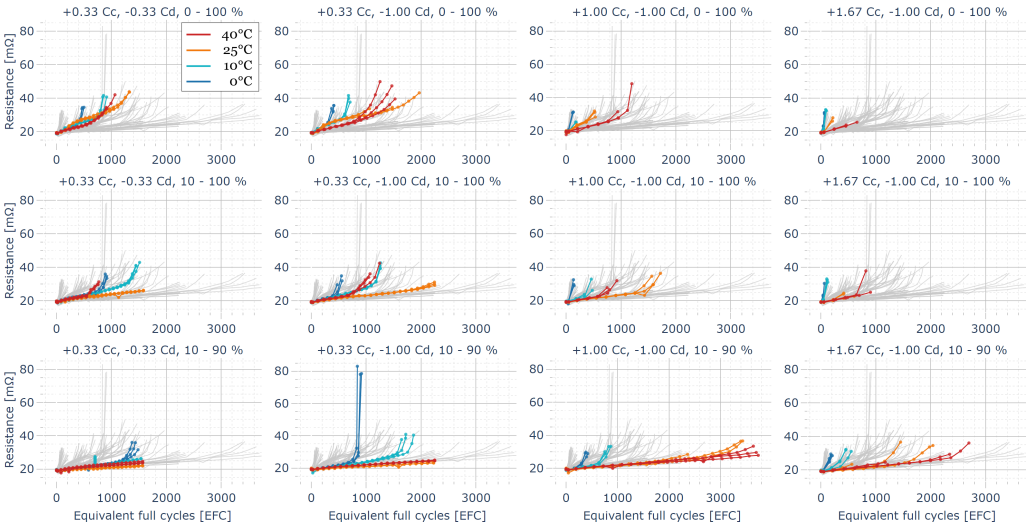

Figure 7.17: Development of the reference impedance of all cyclic aging cells measured at 25°C

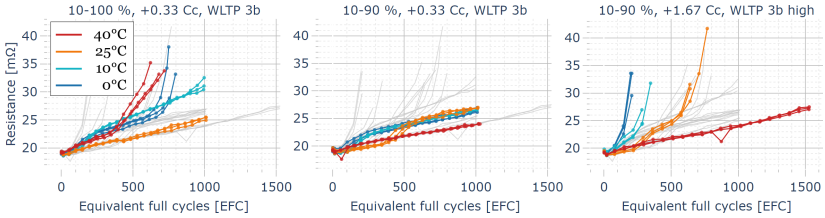

Figure 7.18: Development of the reference impedance of all cells aging with driving profiles measured at 25°C

times in the experiment, in which the capacity decreases faster, the impedance typically also increases faster. However, while the capacity decrease is often faster in the beginning and then slows down before rapidly accelerating again, the impedance generally increases relatively linearly most of the time. Nevertheless, just before the EOL, it also steeply increases. This can be seen when comparing the cells cycling with +1/3 C/−1 C from 0–100% at 40°C (red curves in the second column of the top row in Figure 7.13 and Figure 7.17). The capacity decreases strongly in the first 200 cycles, moderately up to around 800 EFCs, and then steeply again afterward.

However, impedance increases almost linearly from 0 to 800 EFCs and faster afterward.
Interestingly, the unexpected intense capacity loss for the calendar aging cell resting at 90% and 40°C compared to the cells at 50 and 100% (Figure 7.12) cannot be seen in the impedance development in Figure 7.16. Instead, the aging of impedance progresses as expected for calendar aging: the higher the temperature and SoC, the more severe the cell degradation. According to the literature, this can be attributed primarily to the higher growth rate of the SEI layer under these conditions.
The three cells cycling with +1/3 C/−1 C from 10–90% at 0°C experience by far the highest reference impedance increase (from 19 to about 80 mΩ), even though their capacity fade was not the highest measured of all cells.

The development of the impedance of the cells over time can also be analyzed using the pulse pattern measurements. The results for selected parameter sets are shown in Figure 7.19. Further, interactive plots are included in the published dataset [R1].

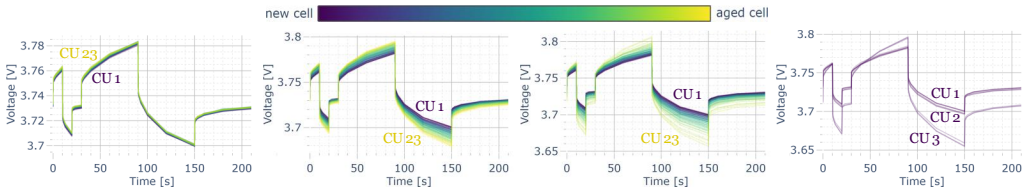

a) calendar aging at 10%, 10°C (measured at 50%, 25°C)
b) calendar aging at 100%, 40°C (measured at 50%, 25°C)
c) cycling at +1C/−1C, 10-90%, 25°C (measured at 50%, 25°C)
d) cycling at +5/3C/−1C, 10-100%, 10°C (measured at 50%, 25°C)

Figure 7.19: Cell voltage versus time during the pulse pattern measurement (current excitation shown in Figure A.7) at 50% SoC and 25°C — overlay of the measurements of all CUs and all cells of the presented parameter set

The dataset [R1] also includes raw log data ("LOGEXT") with a two-second resolution during the complete test period of each cell for various measurements, such as the cell voltage, current, temperature, charge, and energy, the estimated SoC and OCV, as well as operational states. A two-day extract of the log dataset for a cell during a check-up[4] is shown in Figure 7.20.

Many interesting phenomena can be analyzed in the log dataset that cannot be seen in the result datasets. For example, unusual current and voltage patterns were measured during some charging processes in which lithium plating is expected. Usually, a CC-CV charging process consists of a phase with a constant current until the maximum voltage is reached. Then, the constant voltage phase begins while the current declines (also compare Figure 6.5a). However, the currents and voltages look different in the two instances shown in Figure 7.21. In the first case, the current rises again during the CV phase (see arrows in Figure 7.21a). According to Ringler et al. [414],

[4] P063-1; S16:C05; CU 5 — i.e., parameter 063, cell number 1; slave 16, software channel 05 = hardware channel 6 of 12; December 21 to 23, 2022 — cyclic aging with +1 C/−1 C from 10–90% at 40°C

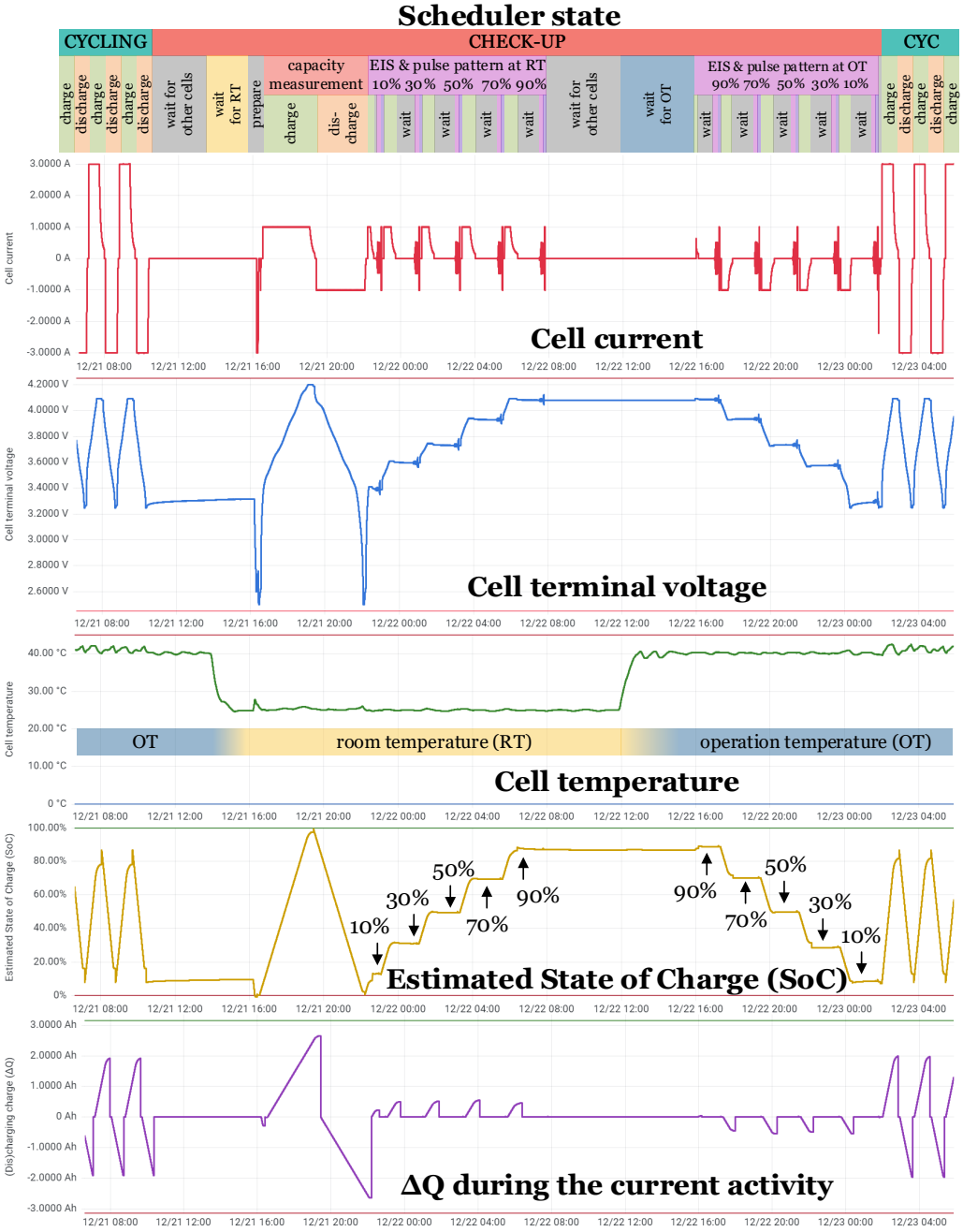

Figure 7.20: Selected raw log data variables during a complete check-up procedure — screenshot of the Grafana dashboard, annotated with scheduler state variables — adapted from [J1]

this behavior is an indication of lithium stripping, i.e., a reversal of the Li plating reaction. In the second case, the current increase in the initial CV phase is so intense that there is a second CC phase, followed by a second CV phase (see arrows in Figure 7.21b). In both cases, the cell temperature rises significantly — up to 17 K, even though the cells are liquid-cooled. In addition, the charge charged into the cells is larger than expected. Based on the charge added, the BMS of the cycler estimates an SoC of 125% before the charging process is stopped and the cell is permanently disabled for safety reasons.

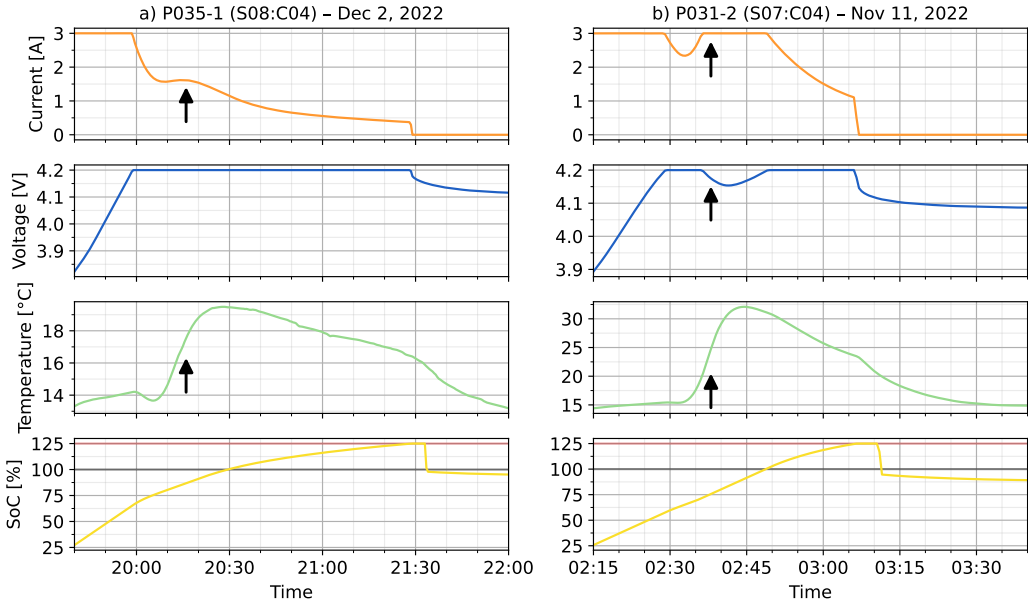

Figure 7.21: Unusual current and voltage patterns in the CC-CV charging process of cells for which lithium plating is expected (last cycles of two cyclic aging cells before the cells were permanently disabled) — a) 10°C, +1 C/−1 C, 10–100%, b) 10°C, +1 C/−1 C, 0–100%

Another event can be observed for a cell[5] charging with +1/3 C and discharging with −1 C between 10 and 100% at 10°C. On August 10, 2023, the measured cell voltage suddenly dropped from 4.04 V to approximately 0.4 V. This indicates that the cell was disconnected from the cell measurement electronics. However, a manual measurement revealed that it was properly connected to the cycler, but the cell itself became high-impedance, suggesting an internal open circuit. A comparison of the faulty cell with a new, almost unused cell (see Figure 7.22) indicates that the current interrupt device (CID) was activated. A CID and its interruption mechanism

[5] P034-3 (S09:C06), i.e., the third cell tested at parameter set 34, mounted to slave 9, SW channel 6 (= HW channel 7)

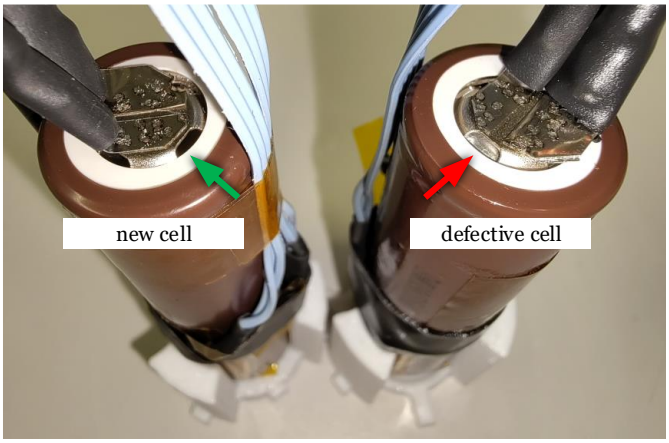

Figure 7.22: Comparison of the positive pole of a new, almost unused cell (left) with a faulty, high-impedance cell for which a CID interruption is suspected (right)

are visualized and described by Li et al. [631]. The device protects the cell by interrupting the current flow when the pressure inside the cell housing is too high. This can occur during a thermal runaway or when significant amounts of gas have been generated inside the cell, for example, due to over-currents (compare Figure 6.9).

The event occurred during a CU after the last EIS measurement at RT and an SoC of 90%. The cell was not used during and in the last 1 1/2 hours before the event, i.e., the cell current and power were zero. No temperature change was observed before, during, or after the event. The cell was not misused according to the BMS since the cell would have been disabled in this case. Therefore, an overcharge, an undercharge, or a thermal runaway can be excluded. However, small amounts of gas can also be generated during the regular operation of Li-ion cells [410]. The cell's estimated remaining usable discharge capacity during the CU was only 1.5762 Ah (SoH = 52.5%), i.e., the cell experienced severe aging during the 1260 EFCs that it cycled. Therefore, regular gas generation was likely the cause of this event.

Another cell, charging with +1/3 C and discharging with −1 C using an SoC range of 10 and 90% at 10°C, also experienced an open-circuit fault[6]. The cell was disabled due to severe capacity fade 40 days before the incident but still remained in the temperature-controlled pool. The event occurred during a temperature change from 10 to 25°C at the beginning of a CU. An activation of the CID due to thermal expansion of previously generated gas could explain this open-circuit fault. However, in contrast to the defective cell in Figure 7.22, the metal plate beneath the positive pole of the cell is barely deformed.

[6] P038-3 (S10:C03) on November 22, 2023 — SoH of 60% in the last CU, approximate SoH of 40% in the last regular cycle, after 1648 EFCs

7.2 Aging model

A semi-empiric battery degradation model for the capacity fade of Li-ion cells was derived using the data collected in the battery aging investigation. The model aims to address several limitations of many existing models (compare [394, p. 701]):

- **Dynamic operation:** For many (semi-)empirical battery aging models, equations or LUTs were fit to measurement results using the nominal, constant test parameters defined in the test matrix (see Figure 7.3) as an input, for example, $I = 3\ A$ and $T = 25°C$. Instead, the model developed in this thesis shall account for a dynamic operation with varying conditions — e.g., I(t), T(t) — by aiming to reconstruct the underlying aging mechanisms. This increases the chances for accurate modeling under realistic, dynamic operating conditions. Using log data with high temporal resolution instead of the constant nominal operating conditions as input also accounts for variations of the temperature in the test bench, e.g., caused by the self-heating due to power losses or local temperature variations in the pool, and by varying current rates, e.g., in the CV phase of the charging and discharging procedures.
- **Diversity:** The model uses aging data of 76 different test conditions collected from 228 cells as an input. Three different aging modes (calendar aging, cyclic aging, and EV driving profiles) were investigated, with varying temperatures, SoCs, DoDs, and independent charging and discharging rates. Because this dataset is one of the most comprehensive and diverse in the literature (compare Table 6.3), it has the potential to be accurate in a broader range of operating conditions than existing models (compare Table 6.2).
- **SoH limit:** While many models focus on the capacity fade until only 70 or 80% of the nominal capacity is left, this model uses aging data up to a minimum SoH of 40% and aims to model the capacity fade regardless of the SoH. This is particularly important for second-life applications.
- **Path dependency:** Although a capacity measurement of an aged battery gives information about the remaining capacity, it does not provide insight into how the capacity will develop during subsequent operation. Therefore, two aged cells with the same remaining usable capacity can have completely different remaining useful lives (RULs), even if operated under similar conditions. This can be considered if the aging model attributes degradation to the different underlying aging mechanisms instead of solely focusing on the remaining capacity as a state variable. If such a model is operated as a digital twin during the life of the EV, various second-life operating strategies could be simulated with it to estimate the RUL in a second-life application or how the operation could be adapted for optimal use. Information on the degradation model and its state variables reflecting past wear could also

be used in a digital product passport to provide valuable insight into the degradation of the battery or individual cells for their subsequent application.

- **Transferability:** The model is intended to facilitate transferability to other cells, among others, by explaining the function and meaning of individual fitting parameters. They could be fitted to similar cell chemistries using a much smaller number of reference measurements. However, the feasibility of a precise adaptation to other cells cannot be proven without further extensive investigations.

7.2.1 Concepts and methods

The fundamental concept of the proposed battery aging model is the calculation of an incremental capacity fade ΔQ_L for each time step Δt. ΔQ_L depends on the cell terminal voltage V_{cell}, the cell current I_{cell}, and the cell temperature. As previously discussed, the surface temperature of the cell was measured in the data used to parameterize the model (see Figure 7.8). Therefore, the temperature used to calculate ΔQ_L should also be the surface temperature $T_{surface}$. If the aging model is used in a simulation, a thermal model of the cell can be implemented in the application model to calculate the surface temperature of the cell from its operating conditions and the ambient or coolant temperature.

Different aging mechanisms are modeled: SEI layer growth, cyclic wearout, and lithium plating. The cyclic wearout is divided into two terms: a general term (I) and one that is only effective at low voltages (II). An individual capacity fade increment $q_{L,k}$ [i] is calculated for each aging mechanism k in every modeling step i. All losses are added to obtain the total loss (see Equation 7.3a). The model uses values relative to the nominal capacity C_n to facilitate adaptation to other cells (see Equation 7.3b). The remaining usable capacity is calculated by subtracting the total losses from the initial capacity C_{init}, which might be higher than the nominal capacity (see Equation 7.3c).

$$q_{L,tot}\left[i\right] = q_{L,SEI}\left[i\right] + q_{L,cyc,I}\left[i\right] + q_{L,cyc,II}\left[i\right] + q_{L,pl}\left[i\right] \tag{7.3a}$$

$$Q_{L,tot}\left[i\right] = C_n \cdot q_{L,tot}\left[i\right] \tag{7.3b}$$

$$C_{rem,usable}\left[i\right] = C_{init} - Q_{L,tot}\left[i\right] \tag{7.3c}$$

In battery modeling literature, SEI layer growth is typically purely attributed to calendar aging. The growth rate is high initially and then gradually slows down over time. Often, it is modeled with a $\sqrt{t}$, or more generally, a t^z dependency and a voltage- and temperature-dependent stress factor function f:

$$Q_{\mathrm{L,SEI/cal}} = f(T,V) \cdot t^z \tag{7.4}$$

However, this prevents modeling SEI layer growth under varying conditions. In this simplified model, the capacity losses would be reversed when the cell is first exposed to a large stress factor (e.g., high temperature) and then to a lower stress factor (e.g., a lower temperature). Some authors overcome this limitation by forming the derivative of Equation 7.4 with respect to time and applying the resulting ΔQ_L for each time step, using the respective operating conditions of this step [430].
Instead of a time-dependent SEI layer growth, the proposed model is time-invariant and instead uses prior SEI layer growth as a means to reduce the SEI loss growth rate over time. The underlying idea is that the potential to build up the SEI layer for a given operating condition is approximately identical at any point in time, but the actual growth rate depends on the existing SEI layer thickness. This results in the following equations:

$$f_{SEI}(T,V) = s_0 \cdot \exp\left(s_1 \cdot \left(\frac{1}{T} - \frac{1}{T_{ref,SEI}}\right)\right) \cdot \exp\left(s_2 \cdot (V - V_{ref,SEI})\right) \quad (7.5a)$$

$$g_{SEI}(T,V,q_{L,SEI}) = f_{SEI}(T,V) - s_3 \cdot q_{L,SEI} \quad (7.5b)$$

$$\Delta q_{L,SEI}[i] = \begin{cases} g_{SEI}[i] \cdot \Delta t[i], & \text{if } g_{SEI}[i] > 0 \\ 0, & \text{otherwise} \end{cases} \quad (7.5c)$$

$$q_{L,SEI}[i+1] = q_{L,SEI}[i] + \Delta q_{L,SEI}[i] \quad (7.5d)$$

Here, f_{SEI} is the "force" or potential to form the SEI, using an Arrhenius temperature dependency and an exponential voltage dependency. The growth rate g_{SEI} depends on f_{SEI} and the overall SEI losses accumulated to this point. Furthermore, $\Delta q_{L,SEI}[i]$ is the capacity loss increment for the discrete model step i. SEI decomposition and cracking are not modeled. Therefore, $\Delta q_{L,SEI}$ can only be positive. For a constant temperature and voltage, $q_{L,SEI}$ is an exponential function in the form $q_{L,SEI} = a\,(1 - \exp(-b \cdot t))$. T is the cell surface temperature in Kelvin, V is the cell terminal voltage in volts, and Δt is the time increment of the model step i in seconds, which can be variable. The fitting variables of the SEI growth model are described in Table 7.4.

Table 7.4: Explanation of SEI layer growth fitting variables

s_0	base SEI layer growth rate	higher s_0	$\rightarrow$ faster SEI growth / faster calendar aging
s_1	temperature dependency	higher $\lvert s_1 \rvert$	$\rightarrow$ steeper temperature dependency ($s_1 < 0$)
s_2	voltage dependency	higher s_2	$\rightarrow$ steeper voltage dependency
s_3	growth counterforce/limit	higher s_3	$\rightarrow$ SEI becomes more limited over time

$T_{ref,SEI}$ and $V_{ref,SEI}$ in Equation 7.5a can be arbitrarily chosen, but their value influences s_0. It is suggested to select values within the range of the experiment to facilitate automated or manual

fitting, for example, the temperature and voltage of the calendar aging reference parameter set — here: $T_{ref,SEI} = 298.15\ K$ (25°C) and $V_{ref,SEI} = 3.73\ V$ (OCV at 50% SoC). In this case, f_{SEI} equals s_0 at the reference operating point. This allows starting by fitting only s_0 and s_3 using the reference parameter set. Afterward, s_1 and s_2 can be fitted while introducing a temperature and voltage dependency. In this experiment, the fitting process was challenging because the calendar aging cells experienced significant cyclic losses due to the frequent CUs. Therefore, fitting SEI growth using calendar aging experiments with as few CUs as possible is recommended.

In the literature, cyclic aging is often modeled with a dependency on the number of cycles (or full cycles) N, the charge throughput Q_{tot} or "Ah" (i.e., the overall processed charge in Ah), or the energy throughput E_{tot} or "Wh" (in Wh):

$$Q_{\text{L,cyc}} = f(T, C, ...) \cdot N^z \tag{7.6a}$$

$$\text{or} \quad Q_{\text{L,cyc}} = f(T, C, ...) \cdot Ah_{tot}^z \tag{7.6b}$$

$$\text{or} \quad Q_{\text{L,cyc}} = f(T, C, ...) \cdot Wh_{tot}^z \tag{7.6c}$$

Typical dependencies selected for the stress factor function f are the temperature T and the C-rate C, usually regardless of whether the cell is charged or discharged. Sometimes, the DoD is also included. For cyclic aging, the exponent z is usually set to 1, i.e., the capacity fade is linear with respect to the number of cycles or the charge/energy throughput.
For the proposed model, cyclic aging is expected to depend on the processed charge (i.e., the number of lithium-ions passing through the separator and intercalating into the electrodes). However, due to capacity fade, the charge processed during a charge-discharge cycle changes over time. Therefore, a vaguely defined charge-discharge cycle N or the energy throughput E_{tot} is less suitable, and the charge throughput or number of equivalent full cycles (EFCs) is preferred. An argument against using EFCs is that the charge can differ when charging and discharging the cell since the coulomb efficiency is typically smaller than 1, particularly for severely aged cells. This complicates the definition of an EFC. Therefore, the proposed model uses a value related to the overall charge throughput, which includes both charging and discharging. More precisely, the relative charge q is defined for this purpose (compare Equation 7.7d). It is independent of the nominal capacity of the cell and also considers that a given charge quantity (e.g., 1 Ah) is more stressful to process for an aged cell with a smaller remaining capacity compared to a pristine cell. Instead of the cell current in ampere or the general C-rate (relative to the nominal cell capacity C_n), a "relative" C-rate c_{rel} is used to calculate the relative charge q while charging and discharging (see Equation 7.7d). The relative C-rate is calculated by dividing the cell current with the remaining usable capacity $C_{rem,usable}$ (Equation 7.7e).
The charging current significantly impacts cyclic aging, which is separately modeled in the lithium plating model. The discharge current influences aging indirectly through the cumulative charge

that depends on it. However, the measurement data of this study suggests that the discharge rate has no further direct impact on aging. While this is the case for the discharging rates of 1/3 and 1 C selected in this experiment, significantly higher discharge rates (e.g., 4 C) might have an additional, direct impact on aging, which this model does not cover. The underlying aging mechanisms could be SEI cracking, structural disordering, graphite exfoliation, or gas generation (see Figure 6.9).

According to the literature on battery aging, cycling with a higher DoD generally causes more degradation [494]. This is also confirmed by the dataset collected for this thesis. However, the voltage range at which the battery is operated using a certain DoD significantly impacts aging as well. For example, in an aging study of Zhu et al. [541], cells operated with a similar DoD of 20% faced vastly different capacity losses depending on the SoC window (e.g., 5-25%, 35-55%, or 75-95%). On the other hand, some cells tested with a significantly different DoD, but the same upper SoC limit (e.g., 25-85% vs. 65-85%, i.e., a DoD of 60% vs. 20%) faced relatively similar losses (see Fig. 1 and Fig. S3 in the supplementary data [541]). The cells cycling with a smaller DoD (65-85%) even experienced slightly higher capacity losses than those with a larger DoD (25-85%), presumably because they rested at higher voltages more often and thus experienced more SEI losses. Hence, it is questionable whether the differences in aging for different DoDs are really caused by the differences of the DoD itself or rather because the cell is operated throughout different voltage ranges for different DoD values. Based on these considerations, the proposed cyclic aging model does not consider DoD directly but, instead, the voltage difference to a reference voltage (see Equation 7.7a). The equation also includes an exponential term that accelerates aging after the characteristic tipping point around an SoH of 80%.

Similar to the measurement results of Zhu et al. (compare [541, Fig. 1]), the data presented in this work suggests that there are significantly higher losses for low voltages. This can be seen when comparing the capacity fade trajectories in Figure 7.13 for the SoC ranges of 0–100% and 10–100% at low charging rates of 1/3 C, for which no plating is expected. As a solution for this behavior, the proposed cyclic aging model is divided into a general cyclic aging term and a term that is only effective at low voltages (see Equations 7.8a–d). The cell terminal voltage instead of the SoC was chosen because, for most chemical reactions, the cell's voltage or the underlying internal potentials are expected to be more relevant than the SoC, which is more difficult to determine or even define accurately and uniquely.

The resulting general cyclic aging model is:

$$f_{cyc,I}(V, q_{L,tot}) = w_0 \cdot |V - V_{ref,cyc,I}| \cdot \exp\left(w_1 \cdot \max\left(0,\ q_{L,tot} - w_2\right)\right) \tag{7.7a}$$

$$g_{cyc,I}(V, q_{L,tot}, q_{L,cyc,I}) = f_{cyc,I}(V, q_{L,tot}) - w_3 \cdot q_{L,cyc,I} \tag{7.7b}$$

$$\Delta q_{L,cyc,I}\left[i\right] = \begin{cases} g_{cyc,I}\left[i\right] \cdot \Delta q\left[i\right], & \text{if } g_{cyc,I}\left[i\right] > 0 \\ 0, & \text{otherwise} \end{cases} \tag{7.7c}$$

$$\Delta q\left[i\right] = \left|c_{rel}\left[i\right]\right| \cdot \Delta t\left[i\right] \tag{7.7d}$$

$$c_{rel} = \frac{I_{cell}}{C_{rem,usable}} \tag{7.7e}$$

$$q_{L,cyc,I}\left[i+1\right] = q_{L,cyc,I}\left[i\right] + \Delta q_{L,cyc,I}\left[i\right] \tag{7.7f}$$

Similar to the SEI model, the cyclic aging growth rate $g_{cyc,I}$ is not linear but modeled using the force function $f_{cyc,I}$ and a counterforce proportional to previous cyclic capacity losses. Only irreversible losses are modeled here as well, i.e., $\Delta q_{L,cyc,I} > 0$. Again, V is the cell terminal voltage in volts, and Δt is the time increment of the model step i in seconds. The fitting variables w_0, w_1, w_2, and w_3 are presented in Table 7.5.

Table 7.5: Explanation of general cyclic wearout fitting variables

w_0	base wearout rate	higher w_0 $\rightarrow$ higher/faster cyclic aging
w_1	wearout acceleration	higher w_1 $\rightarrow$ aging accelerates faster
w_2	acceleration tipping point	higher w_2 $\rightarrow$ acceleration starts later / at higher q_L
w_3	wearout counterforce/limit	higher w_3 $\rightarrow$ wearout becomes more limited over time

$V_{ref,cyc,I}$ in Equation 7.7a was set to 3.73 V, which is the OCV of a new cell at an SoC of 50%. However, $V_{ref,cyc,I}$ could also be treated as a fitting variable, particularly for experiments in which significantly more SoC ranges and DoD variations have been investigated.

The additional cyclic aging model effective at low voltages is similarly calculated:

$$f_{cyc,II}(V,T) = c_0 \cdot \exp\left(c_1 \cdot \left(\frac{1}{T} - \frac{1}{T_{ref,cyc,II}}\right)\right) \cdot \max\left(0,\ c_2 - V\right) \tag{7.8a}$$

$$g_{cyc,II}(V,T,q_{L,cyc,II}) = f_{cyc,II}(V,T) - c_3 \cdot q_{L,cyc,II} \tag{7.8b}$$

$$\Delta q_{L,cyc,II}\left[i\right] = \begin{cases} g_{cyc,II}\left[i\right] \cdot \Delta q\left[i\right], & \text{if } g_{cyc,II}\left[i\right] > 0 \\ 0, & \text{otherwise} \end{cases} \tag{7.8c}$$

$$q_{L,cyc,II}\left[i+1\right] = q_{L,cyc,II}\left[i\right] + \Delta q_{L,cyc,II}\left[i\right] \tag{7.8d}$$

The fitting variables are described in Table 7.6. $T_{ref,cyc,II}$ in Equation 7.8a can be set to an arbitrary temperature in Kelvin (for example, equal to $T_{ref,SEI}$), but its value influences c_0.

In most semi-empirical models, lithium plating is not modeled at all (compare Table 6.2). The reason might be that it is very challenging to model, and operating conditions allowing lithium

Table 7.6: Explanation of fitting variables for cyclic aging at low voltages

c_0	base wearout rate	higher c_0	$\rightarrow$	higher/faster cyclic aging at low voltages
c_1	temperature dependency	higher $\lvert c_1 \rvert$	$\rightarrow$	steeper temperature dependency (here: $c_1 > 0$)
c_2	threshold voltage (in V)	higher c_2	$\rightarrow$	losses already occur at increased voltages
c_3	wearout counterforce/limit	higher c_3	$\rightarrow$	wearout becomes more limited over time

plating (e.g., charging at low temperatures using high charging rates and high SoC limits) should generally be avoided in regular operation. However, lithium plating can also occur in mild operating conditions for aged cells. It is expected to be the dominant driver of capacity fade after the knee point, after which the fade rate increases significantly [412]. As indicated by the measurement data, modeling lithium plating might be beneficial if the cell degradation should be analyzed below a minimum SoH of around 80 to 85%. As seen by analyzing the knee points in Figure 7.13, this is particularly the case if the cell is charged at low temperatures (10°C or below), high charging rates (1 C or above), or high SoCs (above 90% or 4.1 V for the investigated cell).
Unlike SEI layer growth, lithium plating is not limited over time but is even expected to accelerate. According to Yang et al., the reason could be "local pore clogging near the anode/separator interface" [412, p. 28], as well as decreased porosity and increased resistance through significant SEI layer growth (also compare [414]).
Generally, lithium plating can occur when the anode potential versus Li/Li+ is below 0 V. Under these circumstances, lithium can be deposited on the graphite particle surface instead of intercalating into it, often causing irreversible lithium losses [412–415]. The anode potential is decreased with increased charging currents (compare [415, Fig. 2]) or for higher internal resistances, which may occur due to lower temperatures, decreased anode porosity due to cyclic aging, or increased SEI layer resistance [412].
Based on these considerations and after comparing several modeling approaches using the dataset collected for this thesis, the following semi-empirical lithium plating model is proposed:

$$r_{eff}(T, q_{L,tot}) = \left(p_0 + \left(p_1 \cdot \max\left(0,\ p_2 - T\right)\right)^{p_3}\right) \cdot \exp\left(p_4 \cdot q_{L,tot}\right) \tag{7.9a}$$

$$\Phi_a(V, T, q_{L,tot}, c_{rel}) = \Phi^0_{a,est}\left(V\right) - r_{eff}(T, q_{L,tot}) \cdot c_{rel} \tag{7.9b}$$

$$g_{pl}(V, T, q_{L,tot}, c_{rel}) = p_5 \cdot \left(-\Phi_a(V, T, q_{L,tot}, c_{rel})\right) \cdot \lvert c_{rel} \rvert^{p_6} \tag{7.9c}$$

$$\Delta q_{L,pl}\left[i\right] = \begin{cases} g_{pl}\left[i\right] \cdot \Delta t\left[i\right], & \text{if } g_{pl}\left[i\right] > 0 \\ 0, & \text{otherwise} \end{cases} \tag{7.9d}$$

$$q_{L,pl}\left[i+1\right] = q_{L,pl}\left[i\right] + \Delta q_{L,pl}\left[i\right] \tag{7.9e}$$

The effective relative resistance r_{eff} is determined using a temperature-dependent term and a term that lets the resistance increase for rising overall capacity fade. Besides the exponential term in the cyclic aging model in Equation 7.7a, the increasing resistance in the plating model is an additional driver of accelerated aging after the tipping point. Again, T is the cell surface temperature in Kelvin. Since no reference electrode is available in the cells, the open-circuit (equilibrium) anode potential Φ_a^0 cannot be measured but has to be estimated. The anode potential presented in [632, Figure 3] was used as a baseline to derive an approximation LUT $\Phi_{a,est}^0(\mathrm{SoC})$. It was assumed that for an SoC of 0% (ideal OCV of 2.5 V), x in Li_xC_6 is 0.01, and for an SoC of 100% (OCV of 4.2 V), x is 0.96. For $x < 0.04$, the anode potential of [498, Figure A1] was used since no measurement values are shown for this range in [632, Figure 3]. This results in the $\Phi_{a,est}^0(\mathrm{SoC})$ dependency shown in Figure 7.23a. The LUT was then transformed to $\Phi_{a,est}^0(\mathrm{V_{cell}})$ using the SoC (OCV_{avg}) dependency shown in Figure A.8 and Table A.8 so the cell terminal voltage can be used as input[7]. Next, the piecewise linear approximation function shown in Equation 7.10 and Figure 7.23b was derived based on the LUT for faster modeling.

$$\Phi_{a,est}^0(V_{cell}) = \begin{cases} 2.5\ V - 0.5905 \cdot V_{cell} & \text{if } 4.095 < V_{cell} \\ 0.082\ V & \text{if } 3.83 < V_{cell} \leq 4.095 \\ 0.8906\ V - 0.2111 \cdot V_{cell} & \text{if } 3.65 < V_{cell} \leq 3.83 \\ 0.12\ V & \text{if } 3.5 < V_{cell} \leq 3.65 \\ 2.15\ V - 0.58 \cdot V_{cell} & \text{if } V_{cell} \leq 3.5 \end{cases} \tag{7.10}$$

As shown in Equation 7.9c, the lithium plating rate is calculated using the base rate p_5, the difference of the anode potential to 0 V, and a factor for the C-rate dependency (compare Equation 7.7e). If $p_6 > 1$, and the anode potential is negative, the plating rate is intensified for large relative C-rates above 1 C and reduced for smaller C-rates. Since lithium stripping, i.e., the "dissolution of plated lithium" [415, p. 44], is not modeled, the C-rate dependent factor helps consider that the overall irreversible plating losses might be much smaller at lower plating rates compared to larger rates. Part of the plated lithium might still intercalate into the graphite over time in moderate plating conditions. However, in extreme conditions (e.g., at 0°C and a charging rate of 5/3 C), the dataset suggests that larger plating rates seem to have a self-amplifying effect. A possible explanation could be that above a certain plating rate, the anode is clogged by plated lithium so heavily that

[7] Note: In the transformation, the cell terminal voltage V_{cell} was assumed to be equal to OCV_{avg} for simplicity. This estimation is not accurate but was chosen because the OCV and SoC estimations of the battery experiment data are even less accurate, particularly for aged cells. If a reliable SoC or OCV estimation is available in the data, simulation, or end application, the anode potential could be estimated using a function $\Phi_{a,est}^0(\mathrm{SoC})$ or $\Phi_{a,est}^0(\mathrm{OCV})$ instead.

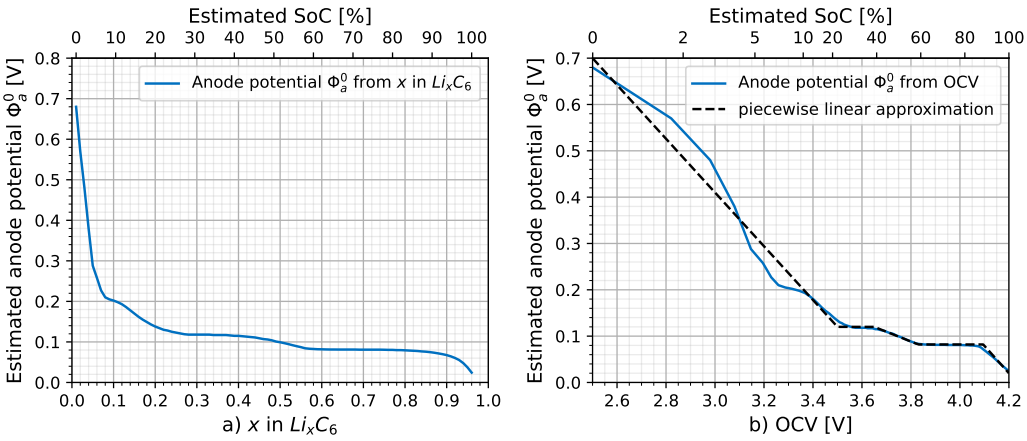

Figure 7.23: Estimated anode potential based on lithiation, SoC, and OCV

regular intercalation becomes increasingly impossible, and even more lithium is plated as a result. The fitting variables summarized in Table 7.7 are used for lithium plating.

Table 7.7: Explanation of lithium plating fitting variables

p_0	effective relative base resistance	higher p_0 $\rightarrow$	plating generally occurs more easily
p_1	temperature-dependent part of r_{eff}	higher p_1 $\rightarrow$	temp.-dependent part more relevant
p_2	temperature (in K) below which p_1 is relevant	higher p_2 $\rightarrow$	temperature-dependent resistance increase already at higher temperatures
p_3	temperature dependency of effective resistance	higher p_3 $\rightarrow$	plating occurs more easily at colder temp. compared to medium temp.
p_4	aging dependency of resistance (tipping behavior)	higher p_4 $\rightarrow$	resistance increases stronger for aged cells
p_5	base plating rate	higher p_5 $\rightarrow$	if plating occurs, plating rate is faster
p_6	C-rate plating rate dependency of plating rate	higher p_6 $\rightarrow$	steeper dependency if relative C-rate > 1, less steep if < 1

In EVs and many other applications, the current rate and cell terminal voltage, which are relevant for cyclic aging, often change relatively frequently. This raises the question of what temporal resolution the aging model should have. Some battery aging models that factor in the DoD as a stress factor use rainflow counting algorithms [633] or a "tolerance belt" [634] to eliminate micro cycles before applying the battery aging model. However, this can significantly complicate and slow down modeling. Instead, the proposed method uses averaged data with reduced temporal resolution before applying the aging model. A resolution of $\Delta t = 30\ s$ was found to be suitable

when applying the aging model to the profile aging cells. For the data of calendar and cyclic aging cells, changing the temporal resolution had almost no impact since the temperatures, voltages, and currents are mostly constant or change only slowly. Hence, the same temporal resolution of $\Delta t = 30\ s$ was used.

The complete capacity fade model is summarized in Figure 7.24. The cell terminal voltage, current, surface temperature, and the model time increment are used as inputs. The model returns the remaining usable capacity $C_{rem,usable}$ after the modeling step and the relative capacity fade increment $\Delta q_{L,tot}$ during the time step. The latter could be used in optimization algorithms to optimize smart unidirectional or bidirectional charging strategies that minimize their impact on battery degradation.

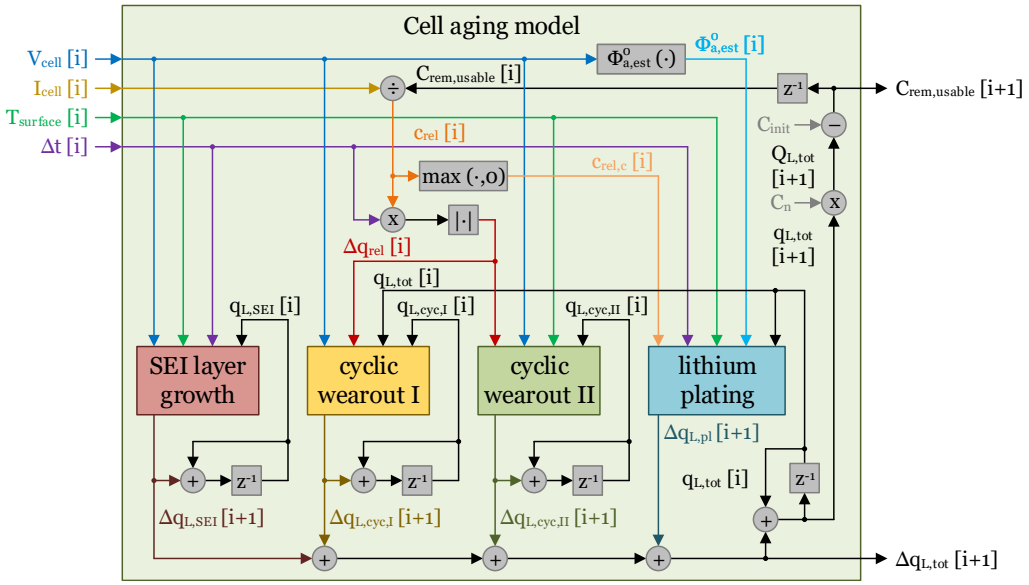

Figure 7.24: Derived battery degradation model for the capacity fade

The 19 variables of the battery model were fitted by running the model with the battery aging log dataset collected for this thesis, using averaged data with the aforementioned temporal resolution of 30 seconds. The root mean square error (RMSE) between the measured and modeled remaining capacity was used as the objective function to minimize and as an indicator to evaluate the model's accuracy. The remaining usable discharge capacities estimated in all CUs of the aging experiment were compared with the predicted capacities of the model at the respective point in time. Since the model error independent of the nominal capacity of the cell is of interest, the RMSE is normalized to the nominal cell capacity. It is referred to as RMSE% in the following and was calculated:

- **for each cell**, using all available CU measurements of the cell j ($N_{CU,cell,j}$):

$$RMSE_{cell,j} = \sqrt{\frac{1}{N_{CU,cell,j}} \sum_{i=1}^{N_{CU,cell,j}} \left(C_{rem,usable,i}^{model} - C_{rem,usable,i}^{meas} \right)^2} \tag{7.11a}$$

$$RMSE\%_{cell,j} = \frac{RMSE_{cell,j}}{C_n} \tag{7.11b}$$

- **for each parameter set**, using all cells operated with the parameter set k ($N_{cells} = 3$):

$$RMSE\%_{param,k} = \sqrt{\frac{1}{N_{cells}} \sum_{j=1}^{N_{cells}} \left(RMSE\%_{cell,j} \right)^2} \tag{7.12}$$

- **for the entire experiment**, using all calendar, cyclic, and profile aging parameter sets investigated in the experiment ($N_{param} = 76$):

$$RMSE\%_{tot} = \sqrt{\frac{1}{N_{param}} \sum_{k=1}^{N_{param}} \left(RMSE\%_{param,k} \right)^2} \tag{7.13}$$

The shelf life of 685 days between the presumed cell production date (see Chapter 7.1.1) and the start of the experiment (see Chapter 7.1.3) was also modeled using the average cell voltage of 3.5558 V measured before the experiment, and a constant estimated average storage temperature of 18°C. The initial cell capacity right after production was assumed to be 3% higher than the nominal capacity, i.e., $C_{init} = 3.09\ Ah$.

The optimization scripts [R3] and the model [R4] were implemented in Python. With 19 fitting variables, exhaustive "brute-force" testing of all combinations of multiple values for each fitting variable using data from all cells of the experiment is unreasonably time-consuming. Using only three values for each fitting variable already results in $3^{19} = 1,162,261,467$ combinations. Gradient-based optimization algorithms may also have difficulties finding a satisfactory solution since there is no monotonic dependency between individual fitting variables and the overall $RMSE\%_{tot}$. Therefore, automated optimization using the *SciPy* optimization library[8] with the Nelder-Mead and SciPy's "L-BFGS-B" method was complemented by many "manual" optimization steps, in which selected fitting variables were varied individually or in combinations. This also allowed guiding individual fitting variables toward ranges in which the model behaved as intended for specific aging model characteristics (e.g., for modeling the tipping point or adjusting

[8] https://scipy.org

the temperature-dependency of the effective resistance based on EIS measurements of the experiment). After each manual optimization iteration, the modeled capacity fade trajectories were visually inspected. This was significantly more informative than the mere consideration of the individual value of $RMSE\%_{tot}$ and thus enabled a more nuanced improvement of the model for each iteration.
The SEI aging model was fitted first, using only calendar aging cells. Next, the cyclic aging cells were included to optimize the cyclic aging and, afterward, the lithium plating model. Finally, the model was fine-tuned by also considering the cells operated with driving profiles.

7.2.2 Results and discussion

The determined variables are summarized in Table 7.8. Using these values, the model accomplished a comparatively low overall error as well as trajectories that reproduce the capacity fade behavior measured in the CUs well for most parameter sets.

Table 7.8: Summary of the optimized fitting variables for the proposed capacity fade model of the LG INR18650HG2

SEI layer growth	Cyclic wearout I	Cyclic wearout II	Resistance for plating	Li plating
$s_0 = 1.49 \cdot 10^{-9}$	$w_0 = 2.67 \cdot 10^{-7}$	$c_0 = 3.6 \cdot 10^{-5}$	$p_0 = 0.07$	$p_5 = 5.3 \cdot 10^{-8}$
$s_1 = -2375$	$w_1 = 2.25$	$c_1 = 1050$	$p_1 = 0.029$	$p_6 = 2.15$
$s_2 = 1.2$	$w_2 = 0.14$	$c_2 = 3.2$	$p_2 = 314.65$	
$s_3 = 1.78 \cdot 10^{-8}$	$w_3 = 9.5 \cdot 10^{-7}$	$c_3 = 2.47 \cdot 10^{-4}$	$p_3 = 3.5$	
			$p_4 = 0.33$	

The modeling results are visualized in the following figures. Each figure contains multiple diagrams, one for each parameter set, described in the graphs' subtitles. An example is shown in Figure 7.25. The x-axis represents the time since the start of the experiment in days. The y-axis shows the measured or modeled remaining capacity of the cells. The points in the graphs indicate the capacities measured in the CUs of the battery aging experiment. Since three cells were tested per parameter set, three sets of points are shown for the CUs, one for each cell (red, green, blue). Even though the cells were operated under similar test conditions, they experienced slight temperature variations, and the charging and discharging profiles (e.g., the duration of the CC phase) eventually drifted apart due to differences in their capacities and impedances. Therefore, the model was simulated for each cell. The colored lines (red, green, and blue) show the remaining capacity calculated by the aging model. The lines may look gray if they overlap each other. The filled areas above the model trajectories indicate to which aging mechanism the capacity loss is attributed. The colors are similar to the ones in Figure 7.24, i.e., red stands for capacity fade due

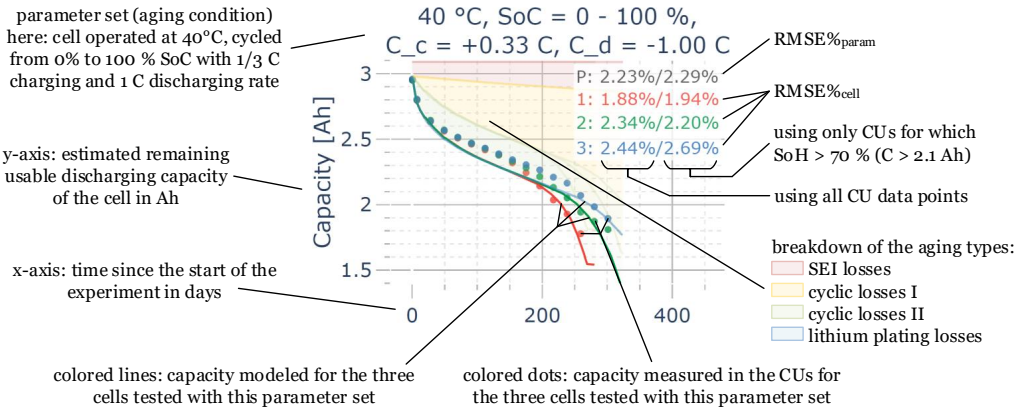

Figure 7.25: Remaining usable discharge capacity of cyclic aging cells measured in the CUs and simulated by the aging model (example)

to SEI layer growth, yellow represents cyclic wearout I, green reflects cyclic wearout II, and blue shows losses due to lithium plating. The latter is not recognizable for most parameter sets.
Since the shelf life of almost two years was also modeled, all cells start with significant SEI losses at the beginning of the experiment. All cells were initialized with the same capacity of 3.09 Ah and modeled with the same constant temperature and voltage before the experiment started. Therefore, their modeled SEI losses are similar at the beginning of the experiment (approximately 0.11 Ah).
The values after the "P" in the diagram, shown in gray, indicate the respective $RMSE\%_{param}$. The $RMSE\%_{cell}$ for each cell tested with this parameter set is shown next to the red "1", green "2", and blue "3" in each diagram. The total error ($RMSE\%_{tot}$) is stated in the title of the figures (not shown in the example). Two RMSE% values are given for each cell, each parameter, and the total RMSE%. The first and usually larger value indicates the RMSE% for all CUs. For the second value, only those CUs were considered for which the SoH from the measurement is higher than 70%, i.e., the remaining capacity is larger than 2.1 Ah. The value is shown because, for many applications, modeling aging is only relevant until this SoH is reached.

Figure 7.26 shows the modeling results for the calendar aging cells. As the overlap of the model trajectories with the measurement points shows, the capacity losses can be modeled very well for most calendar aging cells. The $RMSE\%_{cell}$ between the measurements and the model is less than 1% for most calendar aging cells. The highest discrepancy is found for the cells aging at 25 or 40°C with 90 or 100% (see purple markers "A" to "D"), particularly for a remaining capacity of less than 2.7 Ah (90% SoH). In this region, the capacity losses of the three cells of a parameter set tend to drift apart, indicating manufacturing tolerances between the individual cells or random aging phenomena such as delamination, which cannot be modeled. The maximum $RMSE\%_{cell}$

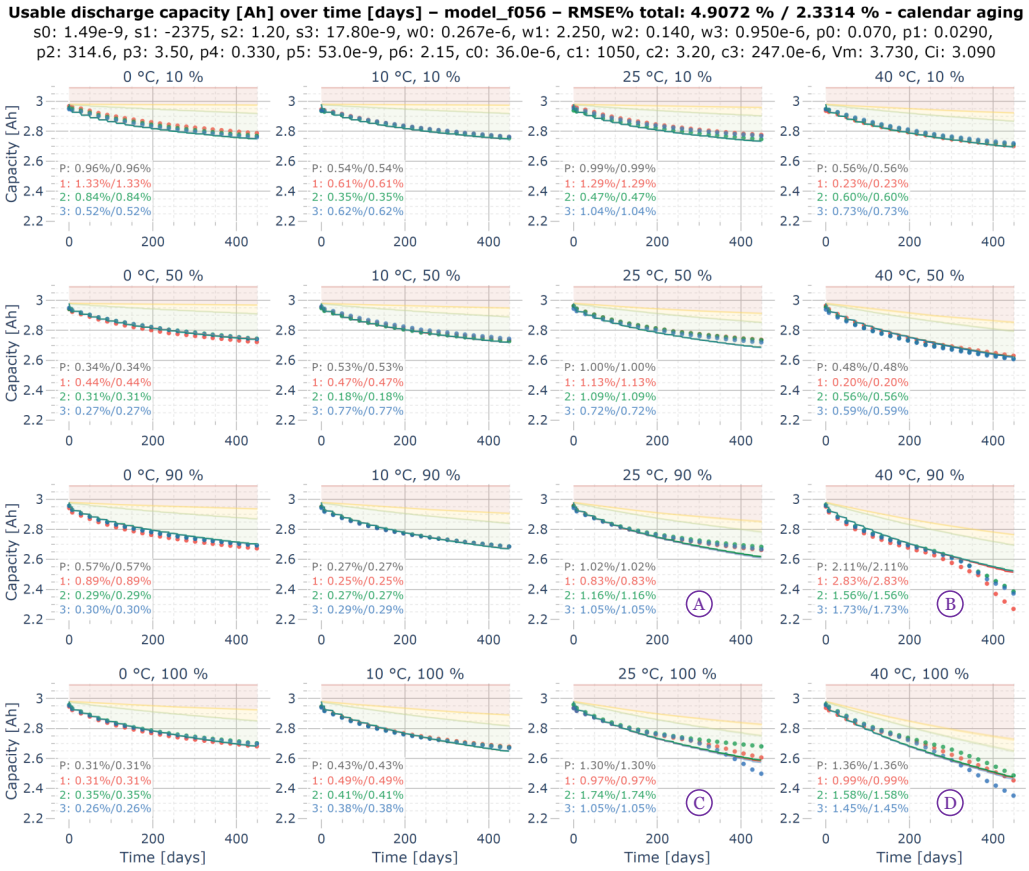

Figure 7.26: Remaining usable discharge capacity of all calendar aging cells measured in the CUs (red, green, and blue points, one color per cell) with aging model simulated for each cell (red, green, and blue lines near points). The areas above the lines indicate which aging mechanisms the capacity loss is attributed to (red: SEI, yellow: cyclic I, green: cyclic II, blue: plating). RMSE% shown for each parameter set (P) and cell (1, 2, 3).

for an individual calendar aging cell is 2.83% for a cell resting at 40°C and 90% (marker "B"). The overall error for this parameter set is 2.11%. As previously mentioned, it is unclear which part of the measured capacity fade is reversible, which might be particularly relevant for this parameter set. However, reversible losses are not considered in the model.

With the optimized fitting variables, a considerable part of the capacity loss that the calendar aging cells experience is attributed to cyclic losses. Due to the frequent CU, these cells undergo between 42 and 61 EFCs, depending on the SoC during regular operation. Most of the processed charge originates from the capacity check cycles between an SoC of 0 to 100%. A complete cycle with a DoD of 100% is comparatively stressful for the cells, even though the C-rate is low. Other fitting variables attributing more SEI losses and less cyclic aging to the cells did not

obtain better results. Therefore, it is assumed that the attribution of considerable cyclic aging losses to the calendar aging of the experiment cells is plausible. This hypothesis can be further analyzed by comparing the cyclic losses of the calendar aging cells with that of the cyclic aging cells charging and discharging with 1/3 C from 0 to 100% at 25°C (marker "E" in Figure 7.27), i.e., test conditions similar to the ones that the calendar aging cells experience during the CUs. These cyclic aging cells had a measured remaining usable capacity of approximately 2.78 Ah after 42 EFCs and 2.75 Ah after 61 EFCs, about two to three weeks after the experiment started. Their remaining usable capacity is similar to that of the calendar aging cells aging at 0°C, for which very low SEI losses are expected. Therefore, it can be concluded that the assumption that the calendar aging cells experience significant cyclic losses in the experiment is plausible.
For future calendar aging experiments, a significantly longer CU period (e.g., three to six months) for the calendar aging cells can reduce this impact for more accurate SEI modeling. In addition, it could be considered to reduce the DoD for all or most of the capacity check cycles, for example, using an SoC range of 20 to 80%.

The model results for the cyclic aging cells are shown in Figure 7.27 (low charging rate) and Figure 7.28 (high charging rates). Note that the minimum values of the y-axes differ from the ones used in the calendar aging figure. Although the model reproduces aging well in many instances, the error is larger than for the calendar aging cells. This is particularly the case toward a lower SoH. While the knee point can be predicted reasonably well for some parameter sets (e.g., 10°C, 0–100%, +0.33 C/−1 C, marker "H", or 25°C, 10–90%, +1 C/−1 C, marker "K" in Figure 7.28), it is incorrectly modeled for many others (e.g., 25°C, 0–100%, +0.33 C/−0.33 C, "E", or 0°C, 10–100%, +0.33 C/−0.33 C, "F").
Interestingly, capacity fade differences between cells cycling at the same parameter set can be modeled well in some instances (e.g., 40°C, 0–100%, +0.33 C/−1 C, "J"), while they are almost not observable in other cases, in which the measured lifetime in the experiment varies significantly between the three cells (e.g., 25°C, 0–100%, +0.33 C/−1 C, "I", or 25°C, 10–90%, +1.67 C/−1 C, "R"). This demonstrates that although the model can simulate the slightly different operating conditions of similarly aging cells, it cannot reproduce random effects such as manufacturing intolerances or local aging phenomena within the cell. As a result, the RMSE% can be fine for one cell but very high for other cells of the same parameter set (e.g., 25°C, 10–90%, +1 C/−1 C, "K", or 10°C, 10–90%, +1.67 C/−1 C, "Q"), impairing the overall model accuracy. This causes a high level of uncertainty with progressed capacity losses. Using models that can at least quantify this uncertainty could help in some applications.
Another issue is the accuracy of the lithium plating model. Particularly under extreme operating conditions (e.g., charging with 1.67 C to 100% at 0 or 10°C, markers "L" to "O"), the capacity fade is massively underestimated. However, this is not very relevant in most real applications, as these operating areas should be avoided at all costs due to the very short battery lifetime.

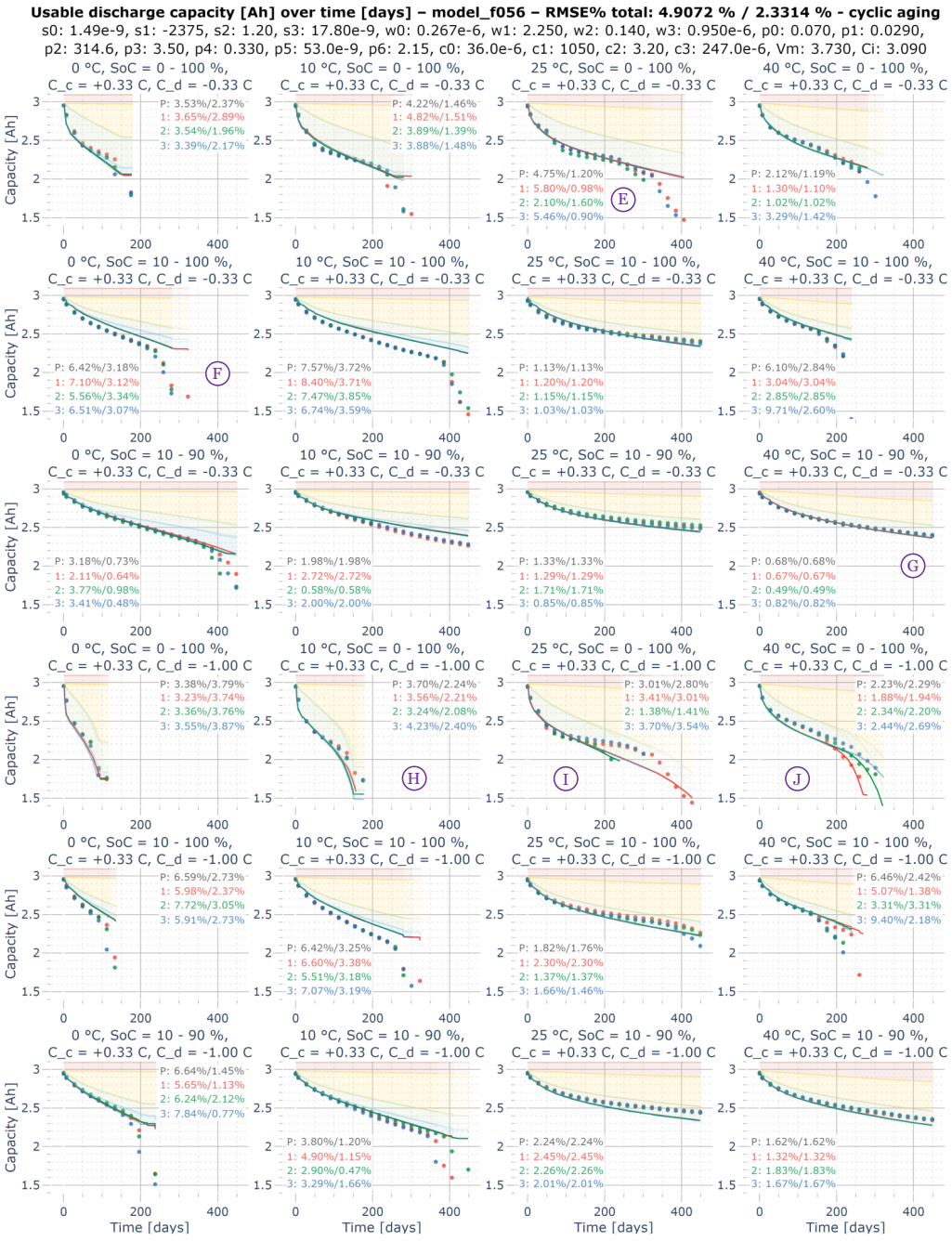

Figure 7.27: Remaining usable discharge capacity of the cyclic aging cells (part 1 of 2) measured in the CUs (points) with simulated aging model (lines) and responsible aging mechanisms (areas)

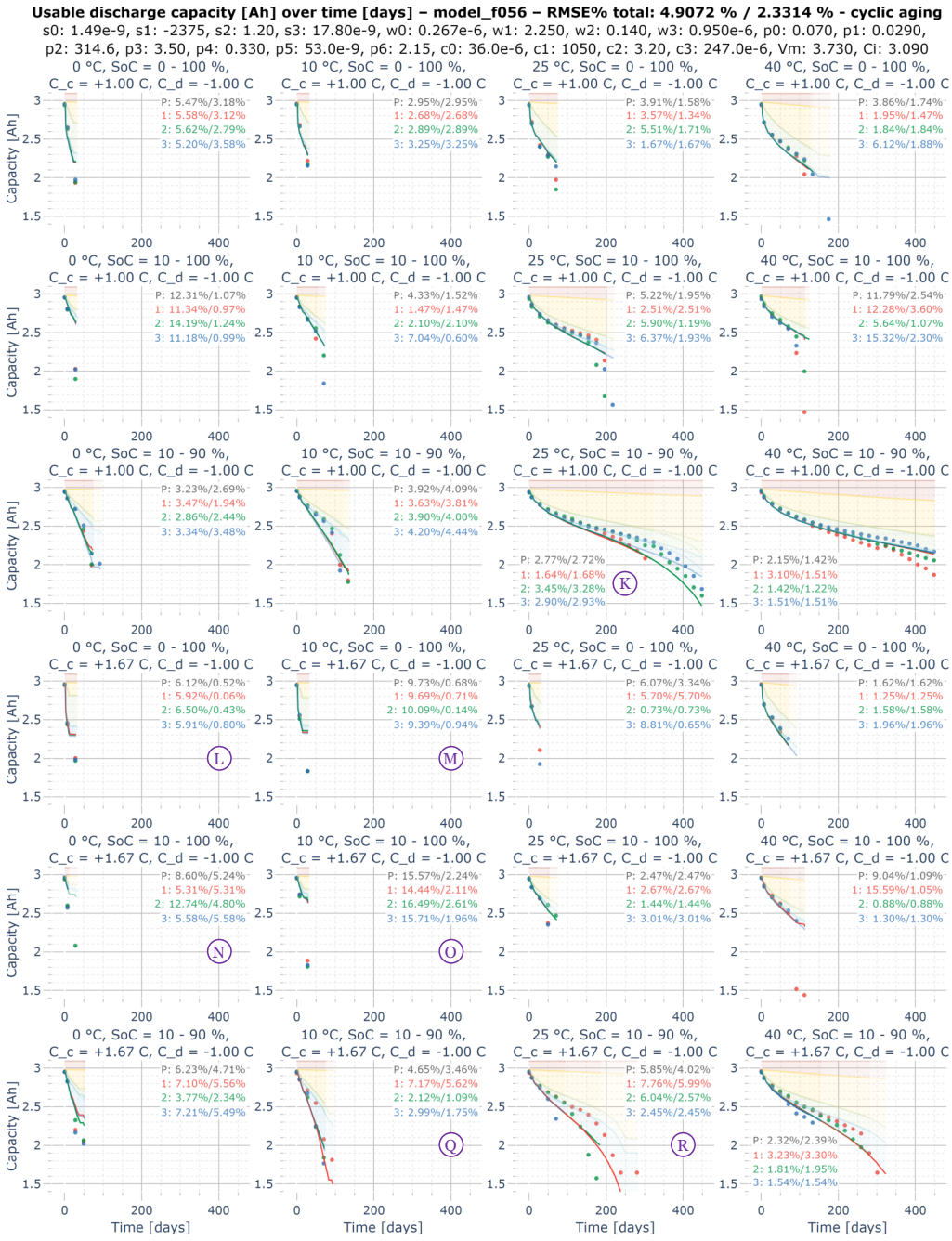

Figure 7.28: Remaining usable discharge capacity of the cyclic aging cells (part 2 of 2) measured in the CUs (points) with simulated aging model (lines) and responsible aging mechanisms (areas)

The parameter set RMSE% values range from 0.68% (40°C, 10–90%, +0.33 C/−0.33 C, “G”) to 15.57% (10°C, 10–100%, +1.67 C/−1 C, “O”). Large RMSE% values are mainly caused by cells for which Li plating is expected to be heavily underestimated or the behavior after the knee point is not modeled correctly. When only considering the CUs in which the SoH is greater than 70% (relevant for many applications) and ignoring the parameter sets with severe plating (charging with 1.67 C at 0 and 10°C), the maximum parameter set RMSE% is 4.09%, and the majority of values are below 2%.

The results for the profile aging cells are shown in Figure 7.29. Here, the model accuracy is generally slightly better than that of the cyclic aging cells. However, aging tends to be overestimated for the driving profiles, i.e., the measured capacity loss is lower than predicted by the model — at least above an SoH of 70%. This is particularly the case for the cell aging at 0°C and charging from 10–90% with +0.33 C (marker “T” in Figure 7.29). After 449 days and 1000 EFCs, the modeled capacity is about 1.87 Ah (62% SoH), while the measured capacity is approximately 2.25 Ah (75% SoH). The capacity fade is significantly underestimated for the cells aging at 25°C and charging from 10-90% with +1.67 C (“U”). The development of measured capacity suggests that lithium plating plays an increasing role in the measured capacity fade for

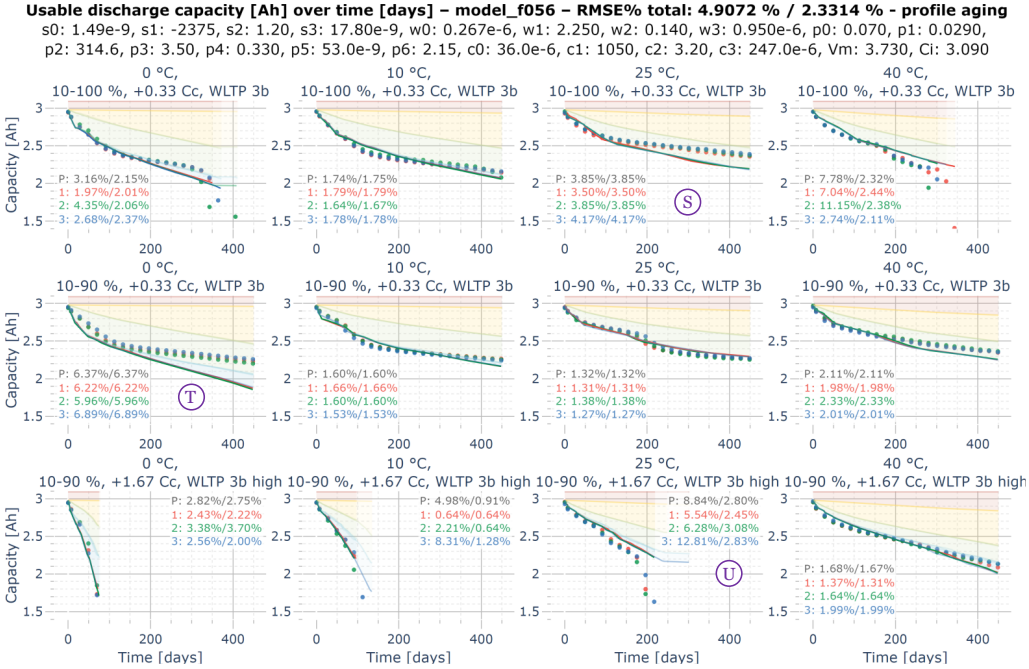

Figure 7.29: Remaining usable discharge capacity of the profile aging cells measured in the CUs (points) with simulated aging model (lines) and responsible aging mechanisms (areas)

this parameter set, but the model does not adequately factor this in.
For the profile aging cells, the parameter set RMSE% ranges from 1.32 to 8.84% when considering all measurements and from 0.91 to 6.37% when only considering the measurement points for which the capacity was greater than 70%.

The overall $RMSE\%_{tot}$ for all cells of the aging experiment using the optimized fitting variables given in Table 7.8 is 4.91%. The total RMSE% is 2.33% when only considering the CUs in which the SoH was greater or equal to 70%. This significant difference between the two values clearly shows that the model accuracy significantly deteriorates toward the EOL of the cell. A histogram of the parameter set $RMSE\%_{param}$ values is shown in Figure 7.30.

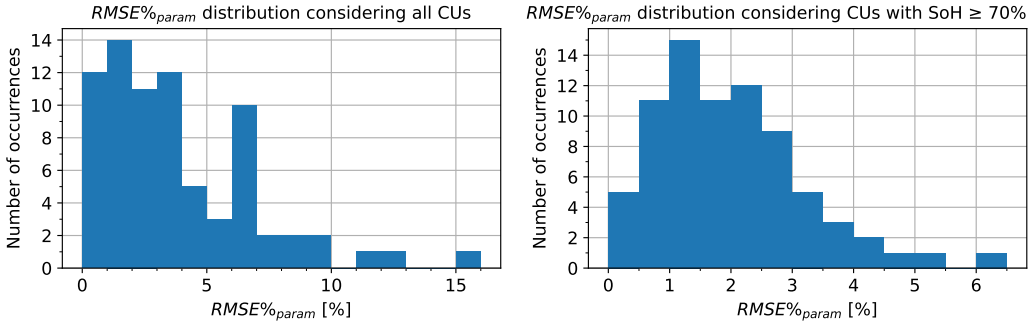

Figure 7.30: Model parameter set RMSE% distribution for all cells of the aging experiment

Although aging models with lower errors have been presented in the literature, they were only demonstrated on smaller, less diverse datasets. Many of these aging models do not even consider parameters for which aging differences were identified in this dataset. In addition, typically, only measurements until an SoH of 70 or even 80% is reached are taken into account, and parameter sets under which severe Li plating occurs are excluded. The considerable variation of measured capacity losses under some operating conditions also increases the RMSE%. For example, the predicted capacity fade for the cells cycled with +1.67 C/−1 C from 10 to 90% at 25°C lies well between the worst-case and best-case cells (marker "R" in Figure 7.28). Nevertheless, the parameter set RMSE% is 5.85%. Therefore, it is unsurprising that the error for the model and data presented in this study is higher than usual in the literature.

Instead of modeling a single capacity fade trajectory for the cell, another approach is to run the model multiple times with different fitting variables and initial capacity conditions. For example, there could be a "realistic", "pessimistic", and "optimistic" model to estimate the uncertainty of the results better and obtain a range in which the capacity is expected to lie. In this case, the "realistic" model could use $C_{init} = 3.09\ Ah$ with the variables shown in Table 7.8, as previously discussed. The pessimistic model could start, for example, with a 2% lower initial capacity C_{init}

and use model variables adjusted by ±2% for increased aging (higher s_0, w_0, w_1, c_0, p_0, p_1, p_2, p_3, p_4, p_5 and lower s_3, w_2, w_3, c_3). The optimistic model could start with a 2% higher initial capacity, and aging variables varied by ∓2% for reduced aging. The model result of this approach is shown in Figure A.11 to Figure A.14 in Appendix A.9.

The proposed model could be further optimized by improving the capacity fade behavior around and after the knee point. The Li plating model could also be improved, for example, with a more accurate determination of the conditions under which plating occurs and by considering lithium stripping. Losses that can be explained with plating were the most challenging to model. They tend to be underestimated for the cyclic aging cells, particularly when charging to an SoC of 100%. At the same time, these losses are overestimated for the profile charging cells when the cell is still relatively new (e.g., 25°C, 10–100%, +0.33 C, or 0°C, 10–90%, +0.33 C, markers "S" and "T" in Figure 7.29).
The model could also be extended by an impedance model. Although this was not implemented in this thesis due to time constraints, the data collected in the aging study required for such an impedance model is publicly available [R1].

As with most other battery aging models, a limitation of the proposed model is that it is only valid and parameterized for the specific cell that was analyzed (LG INR18650HG2). However, the model could be transferred to comparable chemistries using a smaller set of aging experiments. Due to the large number of variables in the model (see Table 7.8), freely automated fitting or even testing all combinations of different variable values is impractical. Therefore, it is advisable to design the operating conditions of the aging experiments in such a way that individual aging mechanisms dominate and the others are minimal. If possible, the tested parameter sets should be selected so that individual variables can be fitted as selectively as possible.
For example, calendar aging experiments with two or three different temperatures and multiple voltages could be repeated to fit the temperature dependency (s_1), voltage dependency (s_2), and temporal aging behavior (s_0 and s_1). For instance, a more stable electrolyte that forms an SEI layer slower will result in a smaller s_0. The cyclic wearout and plating variables could be fitted similarly. For example, a cell with a higher cycle life will likely have smaller values for w_0 and c_0. Cells that experience less plating at cold temperatures may have lower values for p_0, p_1, p_2, and p_3.
However, it is questionable if the cell model can be transferred to entirely other cell chemistries without further adjustments, such as cells with an LFP cathode, an LTO anode, or sodium-ion cells.

7.3 Impact of Vehicle-to-Grid on battery aging

The derived battery aging model shall be used to simulate various smart and bidirectional charging use cases and analyze how they affect aging compared to regular EV usage without V1G or V2G. While the model was applied to cell voltage, current, and temperature measurement data in Chapter 7.2, it shall be applied to synthetic data in this chapter. Therefore, a battery model wrapping the cell aging model and generating its input is needed.

7.3.1 Battery model

The battery model used in this chapter is summarized in Figure 7.31 and described in the following. An implementation of the battery aging model in Python is available on GitHub [R4] in the *bat_model_v01.py* file.

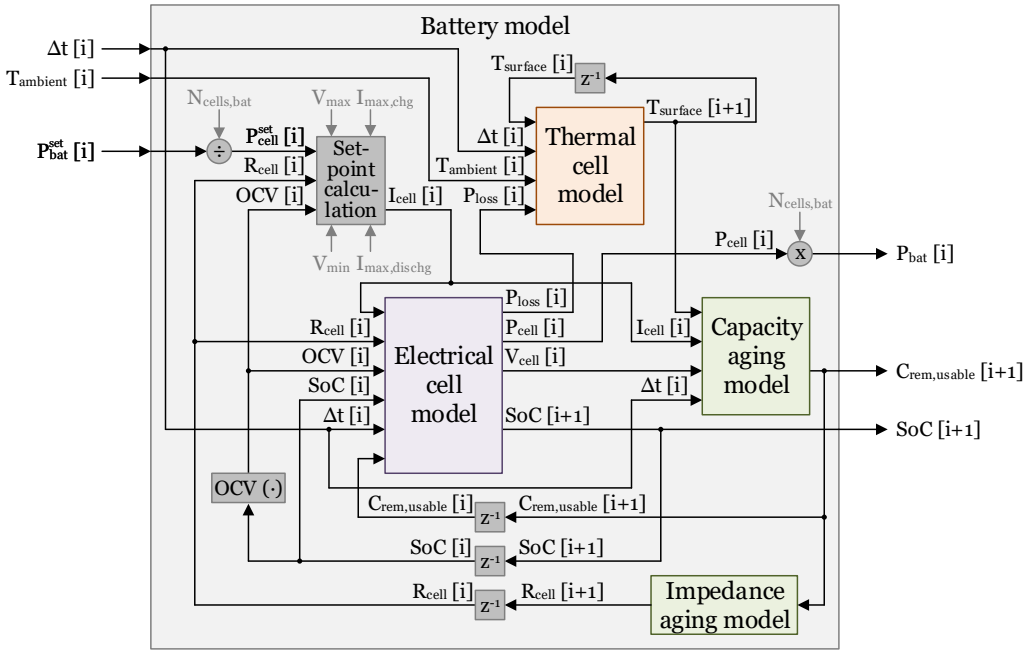

Figure 7.31: Overview of the complete battery model used to simulate the use-case models

In most charging and energy storage applications, a defined power is drawn from or fed into the battery. Thus, a battery power setpoint signal P_{bat}^{set} is a suitable input for the battery model. Besides the power, an ambient temperature $T_{ambient}$ of the environment or coolant is needed. The

duration of a simulation time step Δt is the third input, which allows for faster simulations with variable simulation steps.

The derived aging model only considers a single cell, not the complete battery pack. For a detailed simulation of battery pack aging, including thermal variances within the pack, all individual cells of the pack could be simulated using multiple instances of the aging models and a simulated BMS balancing the cells. For simplicity, it is assumed that all cells in the battery are subject to the same current and ambient temperature, and there are no random manufacturing tolerances. Thus, a single aging model can be used to represent all cells. The power signals are scaled proportionally to the individual cell by dividing the battery power by the number of cells in the pack ($N_{cells,bat}$).

The setpoint calculation module calculates the applied cell current I_{cell} from the setpoint power, the OCV, and the internal resistance R_{cell} of the cell. It also limits the current to the absolute maximum limits ($I_{max,chg}$, $I_{max,dischg}$) or the highest value allowed to respect the maximum and minimum cell voltages (V_{max}, V_{min}). As in the aging data set, a positive current or power in the model indicates charging, and negative values indicate discharging.

An electrical cell model calculates the actual cell power P_{cell} applied during the time step Δt based on the OCV, SoC, and R_{cell}. This power is scaled back to represent the actual battery pack power. It is returned to the use-case model in which the battery model is used. Moreover, the cell voltage V_{cell} is calculated, which is used by the capacity aging model. Furthermore, the power loss P_{loss} of the cell is calculated, and the SoC is updated and output to the application model. The SoC is also used to estimate the OCV using an approximation function.

A simplified thermal model updates the cell surface temperature $T_{surface}$ based on the ambient (or coolant) temperature and the power losses in the cell. As shown in Figure 7.32, the model uses a constant thermal capacity C_{th} of the cell and a fixed thermal resistance R_{th} between the cell surface temperature $T_{surface}$ and the ambient (or coolant) temperature $T_{ambient}$. Internal temperatures inside the cell are not modeled since the aging model was only fitted using the measured surface temperatures of the cells.

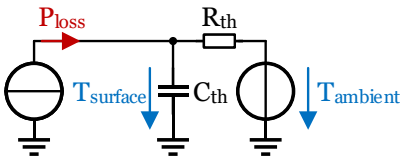

Figure 7.32: Simplified thermal model of the cell

The capacity aging model, already presented in the previous chapter, updates and outputs the remaining capacity of the cell. The aging model uses the latest values for the cell voltage ($V_{cell}[i]$, just after the beginning of the interval i), the cell current ($I_{cell}[i]$, applied during the interval i), and the surface temperature ($T_{surface}[i+1]$, at the end of the interval i, i.e., the start of the next interval i+1). Since no detailed impedance aging model has been derived using the dataset, a

simplified impedance model was used to account for the resistance increase of the cell. Instead of a complex, temperature-, SoC-, and frequency-dependent impedance, a simple resistance R_{cell} is used, which is calculated based on the remaining usable capacity $C_{rem,usable}$ of the cell.

The following equations[9] are used for the setpoint calculation using a power signal as input, whereby the power is specified in watts, the voltages in volts, the currents in ampere, and the resistance in ohms:

$$P_{cell}^{set} = P_{bat}^{set} / N_{cells,bat} \tag{7.14a}$$

$$I_{set} = \frac{-OCV + \sqrt{OCV^2 + 4 \cdot R_{cell} \cdot P_{set}}}{2 \cdot R_{cell}} \tag{7.14b}$$

$$I_{max} = \min\left(I_{max,chg}, \frac{V_{max} - OCV}{R_{cell}}\right) \tag{7.14c}$$

$$I_{min} = \max\left(I_{max,dischg}, \frac{V_{min} - OCV}{R_{cell}}\right) \tag{7.14d}$$

$$I_{cell} = \begin{cases} I_{max} & \text{if } I_{set} > I_{max} \\ I_{min} & \text{if } I_{set} < I_{min} \\ I_{set} & \text{otherwise} \end{cases} \tag{7.14e}$$

The Python model also supports charging to a specific SoC with a defined power. In this case, V_{max} in Equation 7.14c is adjusted to the OCV of the desired SoC.
The simplified electrical cell model consists of the following equations, whereby the time is given in seconds, the remaining capacity in Ah, and the SoC in 100% (i.e., ranging from 0 to 1):

$$V_{cell} = OCV + R_{cell} \cdot I_{cell} \tag{7.15a}$$

$$P_{cell} = V_{cell} \cdot I_{cell} \tag{7.15b}$$

$$P_{loss} = R_{cell} \cdot I_{cell}^2 \tag{7.15c}$$

$$SoC\,[i+1] = SoC\,[i] + \frac{I_{cell}\,[i]}{C_{rem,usable}\,[i]} \cdot \frac{\Delta t\,[i] \cdot 1\ h}{3600\ s} \tag{7.15d}$$

The complex impedance and hysteresis of the cell voltage are not modeled.

The thermal model shown in Figure 7.32 represents a simple thermal equivalent circuit using the power losses as a heat source, a thermal capacity (C_{th} in J/K), and a thermal resistance (R_{th} in

[9] For clarity, the index of simulation step i is omitted if an equation is independent of the simulation step or if all values of an equation belong to the same step.

K/W) between the cell temperature ($T_{surface}$ in °C) and the ambient temperature ($T_{ambient}$ in °C), resulting in:

$$T_{surface}\,[i+1] = T_{surface}\,[i] + \frac{T_{ambient}\,[i] + R_{th} \cdot P_{loss}\,[i] - T_{surface}\,[i]}{R_{th} \cdot C_{th}} \cdot \Delta t\,[i] \quad (7.16)$$

The capacity fade model was already described in Chapter 7.2.1. The aging-dependent internal resistance is modeled using a constant resistance R_0 (in ohms) and an aging-related term. The latter is zero if the remaining capacity is equal to the nominal capacity and equal to $R_0 + R_{age}$ if the remaining capacity is zero.

$$R_{cell} = R_0 + R_{age} * (1 - \frac{C_{rem,usable}}{C_n}) \quad (7.17)$$

The values listed in Table 7.9 are used for the simulation.

Table 7.9: Summary of the parameters used in the battery model of the use case simulations

Voltage limits	Current limits	Impedance model	Thermal model	Battery model
$V_{max} = 4.2\ V$	$I_{max,chg} = +5\ A$	$R_0 = 0.05\ \Omega$	$R_{th} = 15\ K/W$	$N_{cells,bat} = 96{\cdot}60$
$V_{min} = 2.5\ V$	$I_{max,dischg} = -6\ A$	$R_{age} = 0.1\ \Omega$	$C_{th} = 30\ J/K$	$C_n = 3\ Ah$

7.3.2 Use case models

A modular and flexibly extendable modeling framework was implemented in Python for this thesis to simulate different smart and bidirectional EV charging use cases and analyze the resulting battery aging. It is available on GitHub [R4] in the *use_case_model_EV_modular_v01.py* file and can be adapted or extended to simulate custom applications.
The cell aging model is initialized with a remaining usable capacity of 103% of C_n, representing the capacity directly after cell production. It is assumed that the cell rests at an SoC of 25% at 18°C for 30 days between cell production and its use in the EV. This results in a capacity of 102.76% at the beginning of the use case simulation.
Before the simulation starts, one of the following "day types" is assigned to each day of the simulation period. It determines how the EV is used, i.e., which trip it takes and when:

- **Working day:** The EV drives from home to work, rests, and then returns home.
  (220 days per year (Monday to Friday); one complete WLTP driving profile is used per journey, e.g., complete profiles are applied two times per working day; 46.52 km total;

departure: between 7 and 8 AM; duration of stay: between 7.25 and 10.25 hours for scenarios 0 to 32, and 3.5 to 5 hours for scenario 33)

- **Free day:** The EV drives from the home to a leisure or shopping activity location, rests, and then returns home.
  (52 days per year (any day); a "low" and a "medium" WLTP driving profile is combined for each journey; 15.7 km total; departure: between 10 AM and 6 PM; duration of stay: between 0.5 and 7.0 hours)
- **Trip day:** The EV drives from the home to a vacation location and stays there. It returns after one week (three times per year) or two weeks (one time per year).
  (8 days per year (Saturday or Sunday); 48 times "extra high" profile per day — fast-charging in between if SoC falls below 10%; 396 km total; departure: 6 to 11 AM)
- **Day without vehicle usage:** The EV is unused and stays at home or the vacation location, where the same charging strategy is used as at home.
  (remaining 85 days per regular year or 86 days per leap year; 0 km total)

This results in a yearly driving distance of approximately 14,200 km. The model iterates through the days and simulates the driving cycles accordingly. The departure times and rest durations are chosen randomly for each day based on the allowed time or duration range. The driving profiles were derived as already described at the end of Chapter 7.1.1.
The EV can be charged or discharged between the journeys depending on the charging strategy. Different strategies can be chosen for each location (home, work, and leisure activity destination). Examples are:

- **NONE:** The EV is neither charged nor discharged at this location.
- **EARLY:** The EV is immediately charged to a defined SoC limit SoC_{high} as soon as it arrives at the destination (*conventional* or *immediate charging*).
- **EARLY$_{low}$:** Comparable to EARLY, but the EV is only charged if its SoC is below a specified threshold SoC_{low} upon arrival.
- **LATE:** The EV is charged to SoC_{high} right before the earliest departure time defined for this day type (*scheduled* or *delayed charging*).
- **LATE$_{low}$:** Comparable to LATE, but the EV is only charged if its SoC is below SoC_{low} upon arrival.
- **V1G$_{emission}$:** *Smart unidirectional charging* strategy that minimizes emissions. The EV is charged whenever the average emissions of the electricity grid are below a variable threshold, which depends on the current SoC as well as the estimated emissions of the last six days and the next day (in real applications, this is a forecast).

- **V1G$_{\text{cost}}$:** Comparable to V1G$_{\text{emission}}$, but the electricity cost (day-ahead market electricity price) is minimized.
- **V1G$_{\text{renewable}}$:** Comparable to V1G$_{\text{emission}}$, but the EV is charged to minimize residual load in the electricity grid. In other words, the EV is more likely to charge if there is renewable excess energy and less likely to charge if renewable electricity generation is significantly lower than the electricity demand, so there is a lack of energy generated by RES in the grid.
- **V2G$_{\text{emission}}$:** Comparable to V1G$_{\text{emission}}$, but the EV may feed energy back into the grid if the average emissions of the electricity mix are large and the SoC is sufficiently high (*smart bidirectional charging*).
- **V2G$_{\text{cost}}$:** Comparable to V2G$_{\text{emission}}$, but charging when the electricity price is low and discharging while it is high.
- **V2G$_{\text{renewable}}$:** Comparable to V2G$_{\text{emission}}$, but the EV prefers charging when there is excess energy or the residual load is small and the SoC is low. The battery discharges when the grid's residual load is large (lack of RES) and the SoC is high enough.
- **V2G$_{\text{freq}}$:** Based on LATE$_{\text{low}}$, however, the EV supports the grid with frequency control whenever the EV is neither driving nor charging (see "FCR" in Chapter 4.2.3). If the grid frequency is too high, the EV is charged, and if it is too low, the EV battery is discharged. The nominal charging power is applied at the maximum frequency deviation of 200 mHz. Between 10 and 200 mHz, the power is scaled linearly. Below 10 mHz, no power is applied.
- **V2H$_{\text{PV}}$:** The EV is used as a PV storage system to optimize self-sufficiency. The battery is charged if the SoC is below SoC$_{\text{high}}$ and the generated solar power exceeds local electricity consumption. However, if the EV arrives with an SoC below SoC$_{\text{low}}$, it is immediately charged to this lower limit with the regular charging power upon arrival before continuing solar charging. If the SoC is above SoC$_{\text{low}}$ and the generated solar power is insufficient to cover local energy demand, the battery is discharged to match the missing power. The battery is not used if the charging or discharging power is lower than 300 W (about 3% of the simulated nominal charging power) to avoid inefficient operation in real applications.

Examples of the day types and charging strategies are shown in the following images. Conventional charging (EARLY strategy) with a charging limit of $SoC_{high} = 80\%$ is used in Figure 7.33. The power an individual cell experiences in the EV battery is shown in the first row. The grid power, which indicates charging and discharging activity, is shown in the second row. It represents the AC power of the EV charger, i.e., scaled to the complete battery and including charger losses. Next, the cell's SoC and surface temperature are depicted. As described in the previous chapter, the cell temperature depends on the ambient temperature T$_{\text{ambient}}$ and the power dissipation in the cell. In the use case model, T$_{\text{ambient}}$ reflects the battery coolant temperature. The air temperature is used as a baseline for T$_{\text{ambient}}$, but it may be increased when charging or driving.

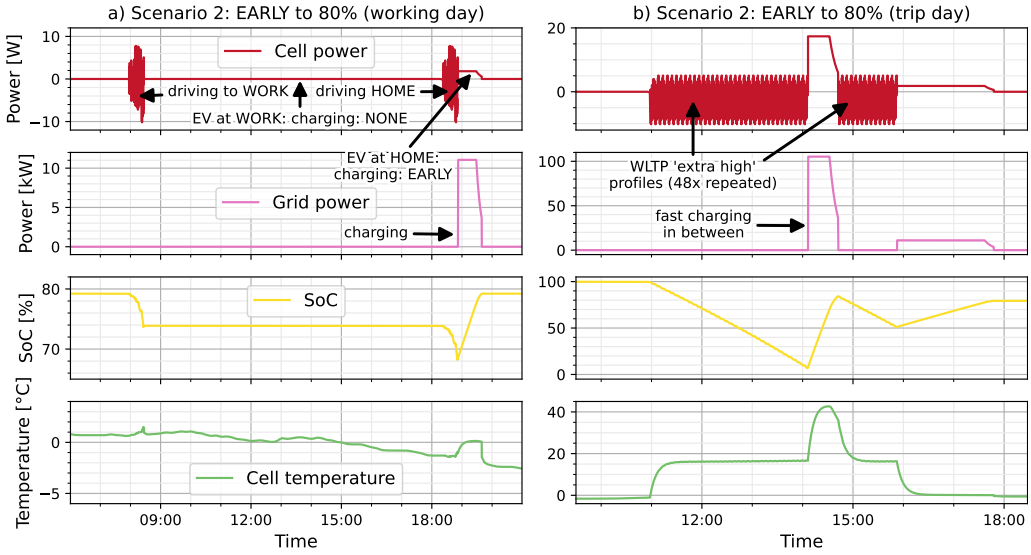

Figure 7.33: Excerpt of the simulation of scenario 2 (EARLY: conventional charging to 80%): a) working day, b) trip day to a vacation location — from top to bottom: cell power, grid power, SoC, and cell surface temperature

Figure 7.33a shows a working day. The EV randomly departs to work between 7 and 8 AM and rests for a random duration of 7.25 to 10.25 hours before returning home. After arrival (here: at around 7 PM), the EV is immediately charged to an SoC of approximately 80%. Constant power, constant voltage (CP-CV) charging is used, using a power of 10.5 kW and the OCV of an SoC of 80% as a voltage limit. The grid power is slightly higher as it considers the charger efficiency of 95%. The final SoC is slightly below 80% since charging is stopped as soon as the current rate falls below the cut-off current rate of 1/20 C.

In the example, the air temperature is below 0°C in the evening due to winter. Whenever the battery is charged from the grid or V2G is used, it is assumed that the thermal management of the battery warms up the cells if their temperature is below $T_{min,chg} = 0°C$, i.e., the coolant temperature ($T_{ambient}$ in the battery model) is at least $T_{min,chg}$ when charging or discharging.

Figure 7.33b shows a trip day. The simulation assumes that the trip was announced to the EV beforehand, and the charging limit was set to 100% for the preceding charging process to use the maximum range of the EV. The EV departs at a random time between 6 and 11 AM. The "extra high" driving cycle is repeated 48 times (ca. 400 km) to simulate the trip. Fast CP-CV charging with 100 kW is used to charge the battery when the SoC after an individual driving cycle falls below 10%. The voltage limit is set to the OCV of an SoC of 95%. Charging stops when a cut-off current rate of 0.5 C is reached, resulting in an SoC of around 85% before the trip continues. After arrival at the destination, the EV is charged using the home charging strategy. In this example, it is immediately charged to 80%.

During regular trips, the air temperature is used as coolant temperature, even if it is below 0°C. However, during long-distance trips, a minimum coolant temperature of $T_{ambient} = 15°C$ is used, i.e., the battery is heated if the temperature falls below this temperature. While the EV is fast-charging, the battery is heated to 30°C (no predictive pre-conditioning is used for simplicity).

Figure 7.34a shows a simulation of two working days and a day without vehicle usage in between them. Scheduled charging (LATE) to an SoC of 90% is used. The EV finishes charging just before the earliest departure time. In the model, the battery is only charged when the vehicle is used, i.e., the day type is known to the EV.
Figure 7.34b shows a weekend in which the EV is used on both days. The charging strategy uses scheduled charging to 90%, but only if the SoC is below 40% after arrival (LATE_{low}), which is the case on the last day shown.

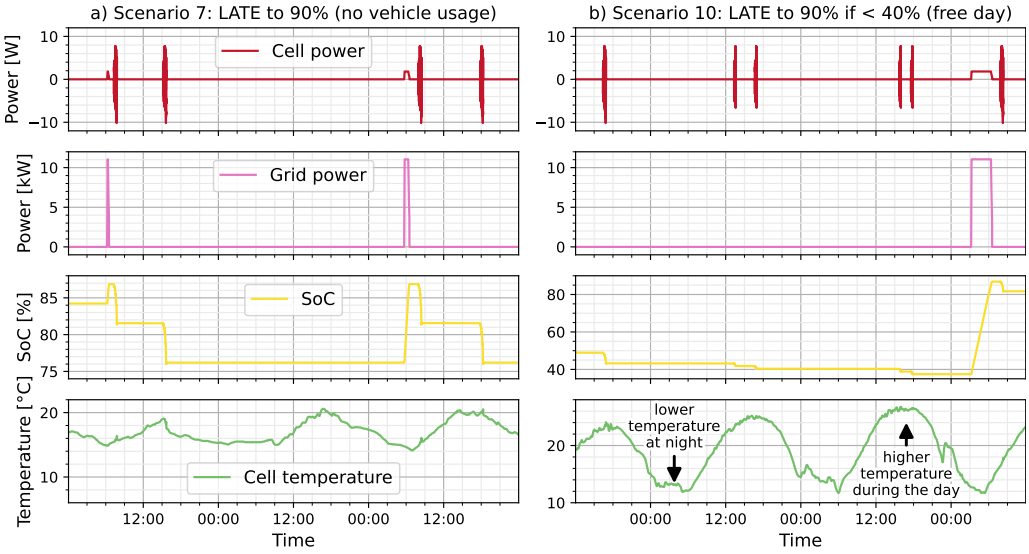

Figure 7.34: Excerpt of a) scenario 7 (LATE: scheduled charging to 90%) and b) scenario 10 (LATE_{low}: scheduled charging to 90% if the SoC falls below 40%) — cell power, grid power, SoC, and cell surface temperature

The smart unidirectional (V1G) and bidirectional (V2G) charging algorithms are explained in the following, using the cost-optimal charging strategy (V1G_{cost}). The day-ahead electricity price "p" is used as a price estimate. When the EV reaches a destination with this charging strategy at the time t_0, a relative "grid condition" g_{rel} is calculated using prices of the last 144 hours (6 days) and the next 24 hours ("forecast"), as shown in Equations 7.18a–c. The grid condition is normalized to a scale from zero (worst condition, i.e., highest price of the interval) to one (best condition,

i.e., lowest price). In other charging strategies, the emission factor (V1G/V2G$_{emission}$) or residual load (V1G/V2G$_{renewable}$) is used to calculate the grid condition instead of the electricity price.

$$g_{best}[t_0] = \min\left(p[t_0 - 144\ h, t_0 + 24\ h]\right) \tag{7.18a}$$

$$g_{worst}[t_0] = \max\left(p[t_0 - 144\ h, t_0 + 24\ h]\right) \tag{7.18b}$$

$$g_{rel}[t] = \frac{p[t] - g_{worst}[t_0]}{g_{best}[t_0] - g_{worst}[t_0]} \tag{7.18c}$$

In the example in Equation 7.19, the cheapest electricity price of the time frame [t_0 − 144 h, t_0 + 24 h) is $-1\frac{\text{ct}}{\text{kWh}}$, and the highest price is $11\frac{\text{ct}}{\text{kWh}}$. If the price p [$t_1$] at $t_1 = t_0 + 1\ h$, i.e., one hour after arriving at the destination, is $2\frac{\text{ct}}{\text{kWh}}$, this results in a grid condition of $g_{rel}[t_1] = 0.75$, i.e., relatively favorable conditions.

$$g_{rel}[t_1] = \frac{p[t_1] - g_{worst}[t_0]}{g_{best}[t_0] - g_{worst}[t_0]} = \frac{2^{ct}/_{kWh} - 11^{ct}/_{kWh}}{-1^{ct}/_{kWh} - 11^{ct}/_{kWh}} = 0.75 \tag{7.19}$$

Using the grid condition g_{rel} and the SoC at arrival, scaled to the SoC range usable for smart or bidirectional charging (SoC$_{scaled}$), a desire/preference to charge "d" is calculated:

$$SoC_{scaled}[t_0] = \frac{SoC[t_0] - SoC_{low}}{SoC_{high} - SoC_{low}} \tag{7.20a}$$

$$d[t] = g_{rel}[t] - SoC_{scaled}[t_0] \tag{7.20b}$$

When d is high, there is a strong desire to charge, e.g., because the current SoC is low, the grid conditions are favorable, or both. For example, if the SoC range of the charging strategy is between $SoC_{low} = 25\%$ and $SoC_{high} = 75\%$, and SoC [t_0] is 55% at arrival, the resulting SoC$_{scaled}$ [t_0] is 0.6. Using the example grid condition of 0.75, the preference to charge results in:

$$d[t_1] = g_{rel}[t_1] - SoC_{scaled}[t_0] = 0.75 - \frac{55\% - 25\%}{75\% - 25\%} = 0.15 \tag{7.21}$$

After reaching the destination at t_0, the smart charging algorithm calculates the approximate energy to reach the upper limit SoC$_{high}$ and the number of 5-minute optimization intervals N_{chg} needed to reach this SoC. Within the period from arrival to the next earliest departure, the N_{chg} intervals with the highest values of d are selected. However, only the N'_{chg} intervals in which d is larger than the threshold $d_{chg} = 0.01$ are selected for charging. This means there can be less than N_{chg} intervals used for charging, or the algorithm can decide not to charge at all (i.e., $0 \leq N'_{chg} \leq N_{chg}$).
In the example, d[t_1] is greater than zero, so there is a desire to charge. However, since the value is comparatively low, the desire is not strong, and the optimization algorithm might prefer other

periods for charging, in which the grid conditions are even better.
For bidirectional charging strategies (e.g., $V2G_{cost}$), the battery can also be discharged if the desire to charge d is significantly smaller than 0 and no long-distance trip is upcoming. The algorithm calculates the maximal number of discharge intervals N_{dischg} to maintain the minimal SoC_{low} and selects the N'_{dischg} lowest intervals in which d is smaller than the threshold d_{dischg}. If bidirectional charging is allowed, N_{chg} is increased by N'_{dischg} before selecting the N'_{chg} charging intervals.
Selecting a threshold with a small amplitude, e.g., $d_{dischg} = -0.01$, would result in very frequent charging and discharging operations, causing significantly more battery cycles and potentially degrading the battery faster. On the other hand, selecting a high negative value (e.g., $d_{dischg} = -0.95$) would result in almost no V2G activity. The thresholds shown in Equations 7.22b-d were selected for the use case simulations. They result in a reasonable use of V2G while balancing the overall processed discharge energy independent of the V2G strategy. The base factor β can be decreased to make the negative thresholds larger in amplitude, resulting in less V2G usage by roughly the same overall processed energy independent of the charging strategy. A higher value for β results in increased V2G usage.

$$\beta = 0.35 \tag{7.22a}$$

$$d_{dischg,cost} = -(1.0 - \beta \cdot 1.09) = -0.6185 \tag{7.22b}$$

$$d_{dischg,emission} = -(1.0 - \beta \cdot 0.77) = -0.7305 \tag{7.22c}$$

$$d_{dischg,renewable} = -(1.0 - \beta \cdot 0.91) = -0.6815 \tag{7.22d}$$

The functionality of the $V1G_{cost}$ strategy is demonstrated using the simulation excerpt in Figure 7.35a. The price in the first two days shown (August 10th and 11th) is comparatively high due to low solar and wind generation. Since the price was significantly lower in the previous days (not shown), the grid condition g_{rel} from August 10 to 11 is comparatively low. Since the SoC is still relatively high, the algorithm decides not to charge. Instead, the EV is charged when the day-ahead electricity price falls below 2 ct/kWh on August 12 to 14.
The $V2G_{emission}$ strategy is depicted in Figure 7.35b. The EV is charged when the emission factor is low and discharged when it is very high.

The $V2G_{renewable}$ charging strategy is shown in Figure 7.36. It calculates the grid condition using the residual load (red line in the bottom row). The lower the residual load, the more likely the EV is charged. If the residual load is exceptionally high (e.g., because of high demand, a lack of renewable energy, or both), the EV feeds energy back into the grid.

Figure 7.37 demonstrates the FCR charging strategy ($V2G_{freq}$). The $LATE_{low}$ strategy is used as a baseline, i.e., scheduled charging to SoC_{high} is used if the SoC is below SoC_{low} when the vehicle arrives. Frequency control is active whenever the EV is not expected to be used, i.e., between the arrival at the destination and the earliest departure time. Since the frequency deviation is

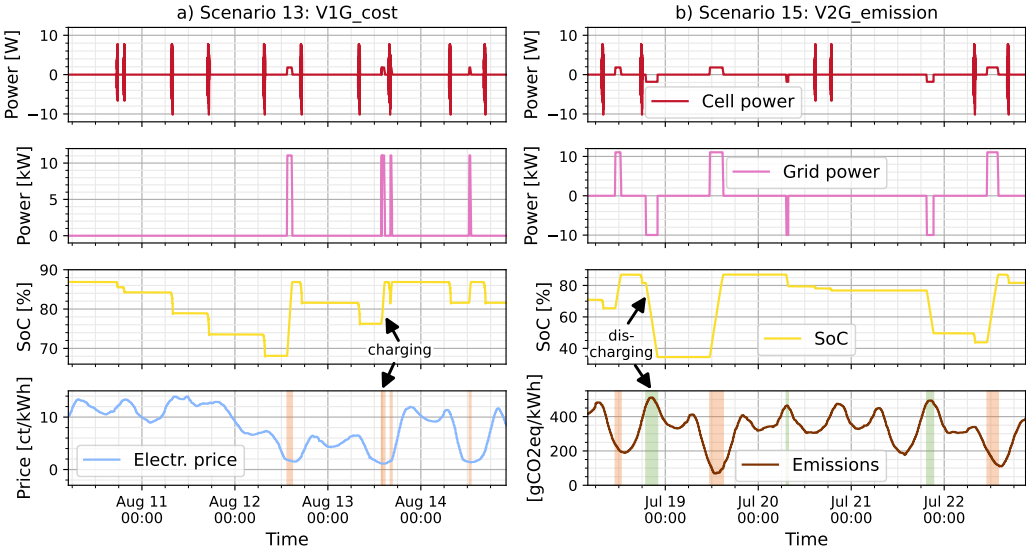

Figure 7.35: Excerpt of a) scenario 13 ($V1G_{cost}$: cost-optimized smart charging) and b) scenario 15 ($V2G_{emission}$: emission-optimized bidirectional charging) — bottom row: day-ahead electricity price or estimated average emissions of the electricity mix with charging (orange areas) or discharging (green areas) activity

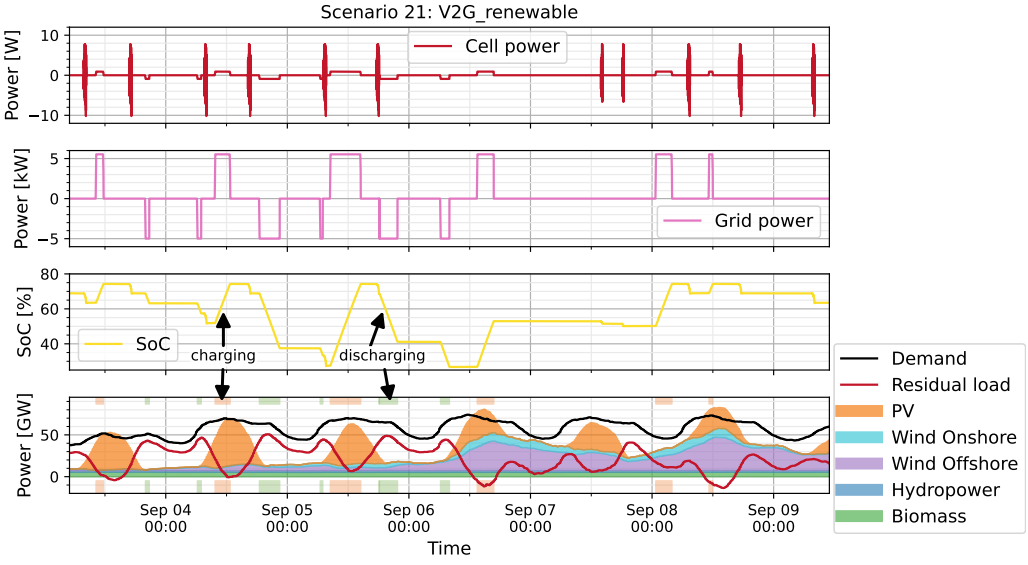

Figure 7.36: Scenario 21 ($V2G_{renewable}$: V2G minimizing residual load) — bottom row: electricity demand (black line), residual load (red line), RE generation (stacked areas), and charging (orange bars) or discharging (green bars) activity

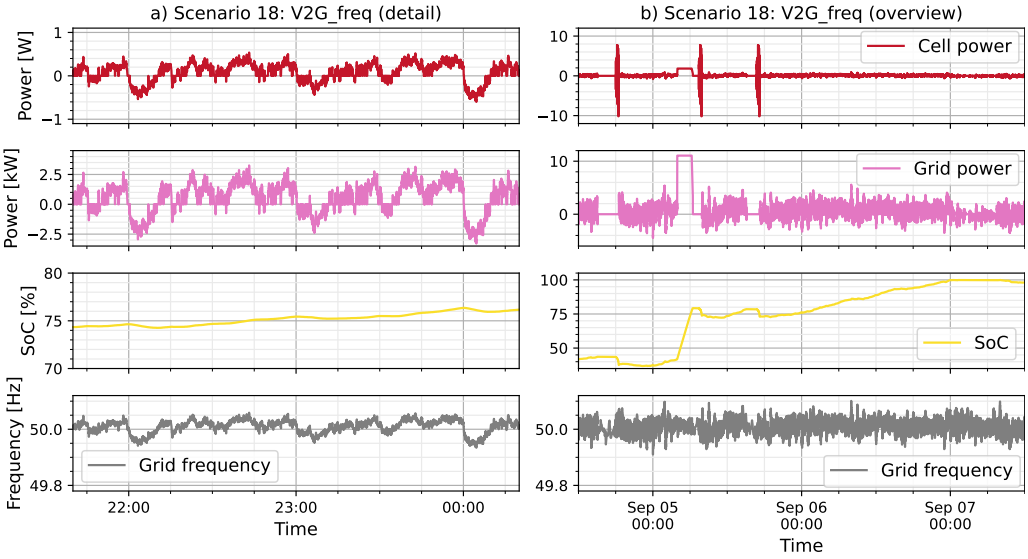

Figure 7.37: Excerpt of scenario 18 ($V2G_{freq}$: frequency control with V2G) — cell power, grid power, SoC, and grid frequency

typically minimal, the charging or discharging power is often low, making it advisable to use a charger with high light-load efficiency. The SoC can drift over time if the frequency deviations are asymmetric. This may cause reaching the SoC limits, which restricts the FCR capability, as seen on September 7 in Figure 7.37. If necessary, FCR power is limited to keep the SoC within 25–100%.

The $V2G_{PV}$ strategy is demonstrated in Figure 7.38. The battery is charged to SoC_{high} with excess energy from a local solar system that is not consumed by the household load (orange area above the blue line). As long as the SoC is above SoC_{low}, energy is fed back to cover household load when not enough solar power is available (green area between the orange and blue lines). In the scenario shown in the figure, it is assumed that the EV can also be charged at work using the same strategy. For simplicity, the same generation and load profiles are used. The EV is charged to the lower SoC threshold with nominal power if its SoC is lower at arrival (seen in Figure 7.38b). This ensures the EV quickly reaches a minimal guaranteed SoC to avoid discomfort for the driver. Since more energy is generated in summer (Figure 7.38a) than in winter (Figure 7.38b), the SoC is often near the higher threshold in summer and near the lower threshold in winter. This suggests using not only V2H but also V2G with hybrid algorithms (not implemented in the simulation). In summer, electricity could be fed into the grid during the evening hours to support the local grid. The lower average SoC reduces battery degradation during warm periods. Additional driving range could be added in winter when electricity is particularly cheap and low in emissions due

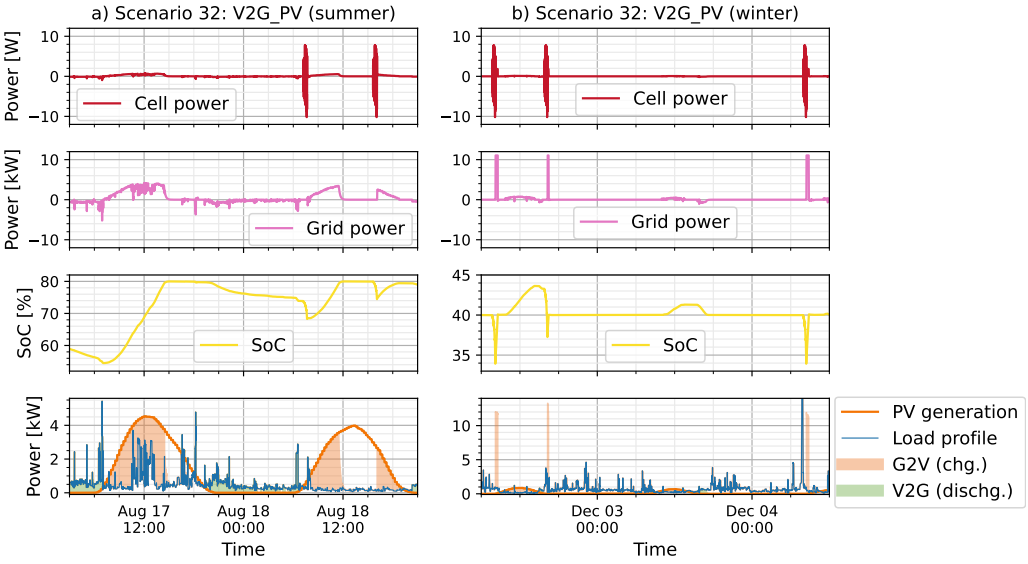

Figure 7.38: Scenario 32 ($V2H_{PV}$: PV-optimized V2H charging): a) in summer, b) in winter — bottom row: locally generated solar power (orange line) and electricity demand (blue line), EV charging (orange area) and discharging (green area) activity

to excess wind energy. The higher average SoC provides increased comfort when driving and a higher supply of electricity from RES for the household.

Independent of the scenario, a variable temporal resolution Δt is used to speed up the simulation while maintaining good model accuracy. When the battery is unused ($P_{bat} = 0$), Δt is five minutes. When charging or discharging the battery, it is 30 seconds. A one-second resolution is used for the driving profiles and when frequency control is active. However, the aging model is applied using 30-second average values in these cases.

Open data from various sources was deployed for the use case models. For electricity generation and demand, as well as the installation capacity of RES, data from the *SMARD* platform[10] is used [39]. The data is normalized using the yearly demand and the respective RES installation capacity. This results in a time series with relative values. For example, a value of 0.5 for the PV generation power means that the output power of solar energy is 50% of the installation capacity. With this method, the data can be scaled to times outside the available range[11]. This method was also used to simulate the future scenarios already presented in Figure 2.4.
For the historical RES installation capacity, data from the *German Federal Ministry for Economic*

[10] "Bundesnetzagentur | SMARD.de", CC BY 4.0 [39]
[11] for this thesis, January 1, 2015, to March 18, 2024

Affairs and Climate Action (BMWK) [43] (hydropower before 2014), SMARD [39] (recent hydropower capacity), and the *German Federal Network Agency* [42] (all other RES) was used. The expansion targets of the current governing coalition [40, 41] are used for the future RES installation capacity.
Data from *SMARD* [39] is used for the historical yearly electricity demand. For future data in 2037 and 2045, the estimated future loads of scenario B (high electrification) of the latest network development plan of the TSOs [44, p. 70] are used. The electricity demand, PtH, and 50% of the power-to-hydrogen demand (representing hydrogen used for industry and mobility) are included. The electricity generation and demand of storage systems (battery, pumped hydro, and the rest of the power-to-hydrogen demand, representing hydrogen used for electricity generation) are excluded. Data for all years in between is linearly interpolated. Before 2015, the demand of 2015 is used, and after 2045, the demand of 2045 is used.
The residual load is calculated by subtracting the resulting RES generation (PV, wind, biomass, and hydropower) from the electricity demand power.

For the PV optimization scenarios, the *SMARD* solar data was scaled to a 10 kWp PV system. The local electricity demand is modeled using high-resolution residential load profile data of "household 31" from a dataset of the *HTW Berlin* [635]. Its yearly energy demand is approximately 5,000 kWh, and the profile closely matches seasonal variations of a standard load profile, according to the authors. The temporal resolution of the load profile was reduced to 30 seconds using average values to speed up the simulation.

For the historical electricity prices (day-ahead market) and emission factors, data from the *Agorameter* [636] is used in the simulation model. Only direct emissions are considered for the emission data (CO_2/kWh). Further details are described in the *Agorameter* documentation [637]. Outside the available data range[12], the electricity prices and emission factors are calculated using a simple approach based on the residual load calculated for this time. For the emission data, a linear dependency between the residual load "r" and the emission factor "e" was fitted using emissions of the last five years in the dataset. It was assumed that the emissions do not fall below 50 gCO_2/kWh. This results in the dependency shown in Figure 7.39a and Equation 7.23:

$$e\left[\frac{gCO_2}{kWh}\right] = \max\left(7.23\ \frac{gCO_2}{kWh \cdot GW} \cdot r\,[GW] + 171.1\ \frac{gCO_2}{kWh},\ 50\ \frac{gCO_2}{kWh}\right) \tag{7.23}$$

[12] for this thesis, January 1, 2012, to March 17, 2024

The electricity price p is determined using the simple dependency shown in Figure 7.39b and Equation 7.24:

$$p\left[\frac{ct}{kWh}\right] = \begin{cases} 0.25\ \frac{ct}{kWh \cdot GW} \cdot r\,[GW] + 2\ \frac{ct}{kWh} & \text{if } r \geq 0\ GW \\ \max\left(0.1\ \frac{ct}{kWh \cdot GW} \cdot r\,[GW] + 2\ \frac{ct}{kWh},\ -2\ \frac{ct}{kWh}\right) & \text{otherwise} \end{cases} \tag{7.24}$$

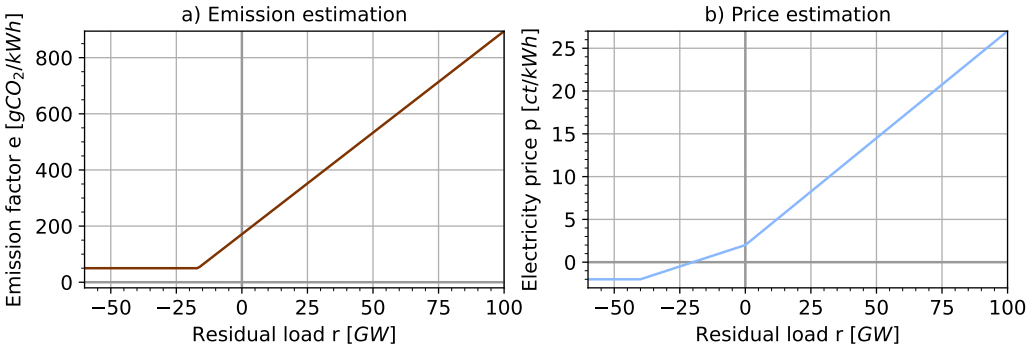

Figure 7.39: Simplified emission and price estimation from projected residual load

For the determination of $T_{ambient}$, data from the *DWD Climate Data Center* [638] of the *German Meteorological Service (Deutscher Wetterdienst)* was used as a baseline. The data comes from a station in Rheinstetten near Karlsruhe in Germany and was measured at a height of two meters. Outside the available range[13], the data is shifted by a multiple of twelve years. For example, if temperature data for 2040 is needed, historical data for 2016 is used.

Grid frequency data from Netztransparenz.de [639] was used with permission. The data is repeated outside the available range[14].

The simulated use cases are summarized in Table 7.10. The first column indicates the scenario ID. For each scenario, the charging strategy, charging/discharging power $P_{chg/dischg}$, and lower and higher SoC limits $SoC_{low/high}$ are presented for the home and work locations. The last column shows the SoC_{high} limit for fast charging during trips. The NONE charging strategy was chosen for the leisure/shopping destination of the "free day", i.e., the EV is not charged. For fast charging during trip days, the charging power is 100 kW with a cut-off current of C/2. For all other regular charging processes, the cut-off current is C/20.

[13] for this thesis, January 1, 2010, to March 13, 2024
[14] for this thesis, June 22, 2022, to March 16, 2024

Table 7.10: Overview of the simulated use-case models

ID	Location: HOME				Location: WORK				Trip
	Strategy	$P_{chg/dischg}$	SoC_{low}	SoC_{high}	Strategy	$P_{chg/dischg}$	SoC_{low}	SoC_{high}	SoC_{high}
0	EARLY	10.5 kW	–	100%	NONE	–	–	–	95%
1	EARLY	10.5 kW	–	90%	NONE	–	–	–	95%
2	EARLY	10.5 kW	–	80%	NONE	–	–	–	95%
3	$EARLY_{low}$	10.5 kW	40%	100%	NONE	–	–	–	95%
4	$EARLY_{low}$	10.5 kW	40%	90%	NONE	–	–	–	95%
5	$EARLY_{low}$	10.5 kW	40%	80%	NONE	–	–	–	95%
6	LATE	10.5 kW	–	100%	NONE	–	–	–	95%
7	LATE	10.5 kW	–	90%	NONE	–	–	–	95%
8	LATE	10.5 kW	–	80%	NONE	–	–	–	95%
9	$LATE_{low}$	10.5 kW	40%	100%	NONE	–	–	–	95%
10	$LATE_{low}$	10.5 kW	40%	90%	NONE	–	–	–	95%
11	$LATE_{low}$	10.5 kW	40%	80%	NONE	–	–	–	95%
12	$V1G_{emission}$	10.5 kW	25%	90%	$V1G_{emission}$	10.5 kW	25%	90%	95%
13	$V1G_{cost}$	10.5 kW	25%	90%	$V1G_{cost}$	10.5 kW	25%	90%	95%
14	$V1G_{renewable}$	10.5 kW	25%	90%	$V1G_{renewable}$	10.5 kW	25%	90%	95%
15	$V2G_{emission}$	10.5 kW	25%	90%	$V2G_{emission}$	10.5 kW	25%	90%	95%
16	$V2G_{cost}$	10.5 kW	25%	90%	$V2G_{cost}$	10.5 kW	25%	90%	95%
17	$V2G_{renewable}$	10.5 kW	25%	90%	$V2G_{renewable}$	10.5 kW	25%	90%	95%
18	$V2G_{freq}$	10.5 kW	40%	80%	$V2G_{freq}$	10.5 kW	40%	80%	95%
19	$LATE_{low}$	5.25 kW	40%	60%	NONE	–	–	–	85%
20	$V2G_{renewable}$	10.5 kW	25%	75%	$V2G_{renewable}$	10.5 kW	25%	75%	95%
21	$V2G_{renewable}$	5.25 kW	25%	75%	$V2G_{renewable}$	5.25 kW	25%	75%	95%
22	$V2G_{renewable}$	5.25 kW	25%	60%	$V2G_{renewable}$	5.25 kW	25%	60%	95%
23	$V1G_{emission}$	10.5 kW	25%	90%	NONE	–	–	–	95%
24	$V1G_{cost}$	10.5 kW	25%	90%	NONE	–	–	–	95%
25	$V1G_{renewable}$	10.5 kW	25%	90%	NONE	–	–	–	95%
26	$V2G_{emission}$	10.5 kW	25%	90%	NONE	–	–	–	95%
27	$V2G_{cost}$	10.5 kW	25%	90%	NONE	–	–	–	95%
28	$V2G_{renewable}$	10.5 kW	25%	90%	NONE	–	–	–	95%
29	$V2G_{renewable}$	10.5 kW	25%	75%	NONE	–	–	–	95%
30	$V2G_{renewable}$	5.25 kW	25%	75%	NONE	–	–	–	95%
31	$V2G_{renewable}$	5.25 kW	25%	60%	NONE	–	–	–	95%
32	$V2H_{PV}$	10.5 kW	40%	80%	$V2H_{PV}$	10.5 kW	40%	80%	95%
33	$V2H_{PV}$	10.5 kW	40%	80%	NONE	–	–	–	95%

Scenarios 0–2 represent conventional charging with SoC limits of 100%, 90%, and 80%, and scenarios 3–5 represent conditional conventional charging when the SoC falls below 40%, using the same upper limits. Scheduled charging with or without a lower SoC condition is analyzed in scenarios 6–11 with otherwise similar settings.
Smart and bidirectional charging is simulated at home and at work in scenarios 12–17, using an SoC range of 25–90%. For the frequency control scenario 18, a range of 40–80% is used to leave a margin for frequency control even when SoC_{high} is reached.
Scenarios 19–22 use scheduled charging and bidirectional RE-optimized charging with settings intended to reduce battery degradation, e.g., lower (dis)charging power and SoC range.
Scenarios 23–31 only use bidirectional charging strategies at home, with otherwise similar conditions to scenarios 12–17 and 20–22.
Scenarios 32 and 33 use PV-optimized V2H charging. In scenario 32, the same strategy is used at work, representing a scenario where someone can charge using a PV system at work and discharge to the private household at night. In scenario 33, the solar charging strategy is only used at home. However, the scenario represents EV usage with part-time employment, in which the vehicle returns around noon, so there is a higher chance that the residential PV system charges the EV in the afternoon. All other scenarios (0–32) reflect EV usage in full-time positions.

7.3.3 Results and discussion

The use case models of all scenarios were configured to simulate EV usage from January 1, 2025, to December 31, 2044, i.e., for a period of 20 years. The computing time required for the simulations depends on the complexity of the charging strategies in the scenario. It varied between one day for the conventional and approximately two weeks for the solar charging strategies.

The development of remaining usable capacity over time in the scenarios is compared in the following. Figure 7.40a shows the capacity fade using different charging limits (SoC_{high}) with conventional charging strategies (EARLY), in which the EV is always immediately charged at the destination, and for scheduled charging strategies (LATE), in which the EV is charged just in time for the earliest departure. The capacity values are indicated relative to the nominal capacity of the modeled cell. Colored horizontal lines mark an SoH of 100% (green) as well as 80% (yellow) and 70% (red), which are commonly used thresholds marking the EOL of a battery. As previously mentioned, all batteries start with 103% of their nominal capacity, i.e., an SoH of 103%.
The simulation results show that the charging limit strongly influences degradation. Batteries charged to 100% daily with conventional EARLY charging (scenario 0) lose almost 11% of their nominal capacity in the first two years. The 80% SoH threshold is reached after ten years, and after 20 years, only 73.7% of the nominal capacity is left.
Daily scheduled LATE charging to 100% (scenario 6) only slightly improves the remaining

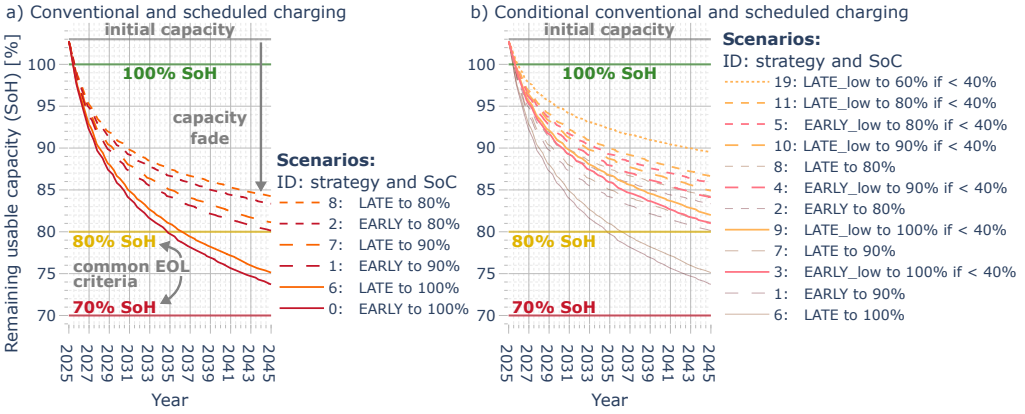

Figure 7.40: Comparison of the simulated remaining usable capacity for *conventional charging* strategies: Immediate (EARLY) or scheduled (LATE) charging, a) on all occasions, b) only if SoC is below 40% upon arrival — legend entries sorted from highest to lowest remaining usable capacity after 20 years of operation

capacity — the final SoH is 75.1%. Even though the battery is only charged just before departing, the average SoC in the EV remains high since the daily trips of the EV do not need much of the battery's energy. Consequently, calendar aging losses are only slightly reduced compared to the EARLY strategy. Immediate (EARLY) and scheduled (LATE) daily charging to an SoC of 80% (scenarios 2 and 8) improve the final SoH to 83.4% and 84.3%, respectively.

A significant reduction of capacity losses is obtained if the EV is not charged daily but only occasionally, e.g., when the SoC falls below 40%, as shown in Figure 7.40b.
For example, the final SoH is 81.0% when using the $\text{EARLY}_{\text{low}}$ strategy with a charging limit of 100% (scenario 3). This is a considerable improvement to the SoH of 73.7% obtained by the EARLY strategy using the same charging limit in scenario 0, shown in gray in the background of Figure 7.40b. The primary reason for the improvement is that the average SoC of the battery is lower, reducing the calendar aging losses caused by SEI layer growth and cyclic aging that is intensified toward extreme SoCs. Accordingly, the losses are further reduced by selecting even lower and shallower SoC ranges. This is demonstrated in the LATE_{low} strategy with a 40–60% SoC range (scenario 19), in which the simulated battery still retains 89.5% of the nominal capacity after 20 years, which is the best of all investigated scenarios. Selecting an even lower SoC range, for example, 35–50%, could further reduce calendar aging losses. However, depending on the usable range of the EV, this could cause inconveniences. Moreover, regularly reaching very low SoCs (e.g., below 15%) could increase cyclic losses (see Chapter 7.2.1).

Smart unidirectional charging (V1G) strategies are compared in Figure 7.41. All strategies use an SoC range of 25 to 90% and optimize either residual load ($\text{V1G}_{\text{renewable}}$), emissions ($\text{V1G}_{\text{emissions}}$), or the electricity price (V1G_{cost}) when charging. In scenarios 23–25, charging is only possible at

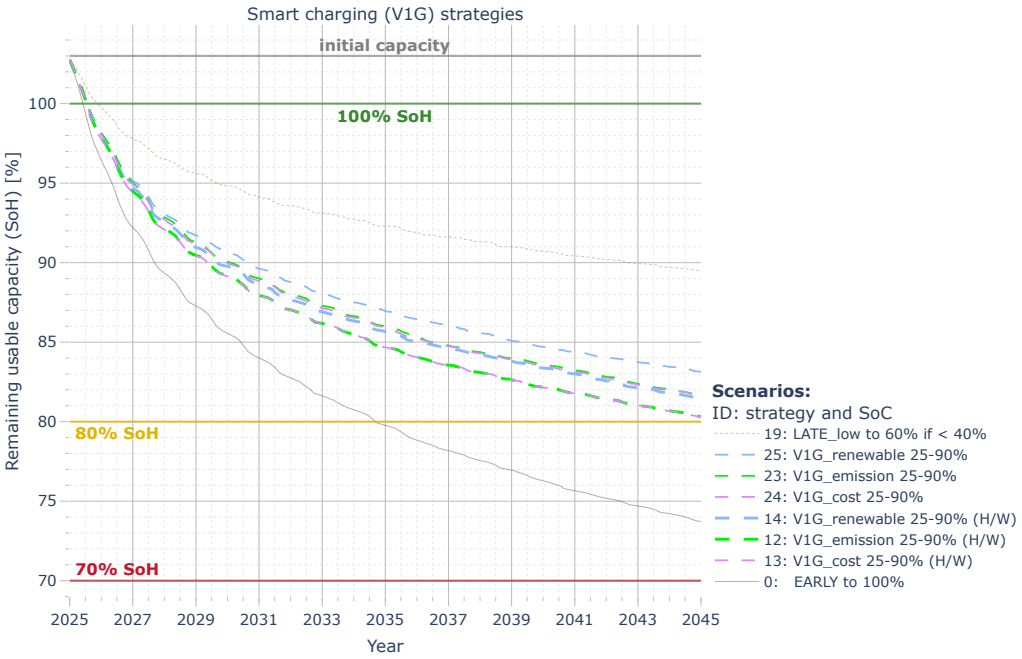

Figure 7.41: Comparison of the remaining capacity for *smart charging (V1G)* strategies — legend entries sorted from highest to lowest remaining capacity, best and worst conventional charging strategy in gray for comparison

home, and in scenarios 12–14, the EV can also charge at work (indicated by "H/W" in the legend). In all simulated smart charging scenarios, the capacity fade lies in between that of the best- and worst-case conventional charging scenarios, which are illustrated by the two gray lines in the figure. Since no energy is fed into the grid and the EVs drive equivalent distances in all scenarios, their total battery energy throughput is almost identical. In the simplified emission and price model used in the simulation, the emissions and prices are closely linked to the residual load (see Figure 7.39). Therefore, it is likely that the EVs are often charged at similar times regardless of the exact V1G charging strategy. Consequently, the capacity losses of these scenarios are relatively similar, ranging from a final SoH of 80.3 to 83.1%. The final SoHs for scenarios 23–25, in which the EV is only charged at home, are about 1.5% higher than the SoHs of scenarios 12–14, in which the EV can also be charged at work. A likely reason is that in the latter case, calendar aging is increased because of a higher average SoC due to more frequent favorable charging conditions.

In Figure 7.42, all simulated bidirectional charging strategies are compared. Like in the smart charging scenarios, bidirectional charging algorithms with similar SoC ranges and charging opportunities (e.g., scenarios 15–17 or 26–28) experience comparable capacity losses. The two V2G scenarios 22 and 31, which use a 25–60% SoC window, experience the lowest capacity fade of all simulated V1G and V2G scenarios. With a final SoH of 87.8% and 88.1%, they perform

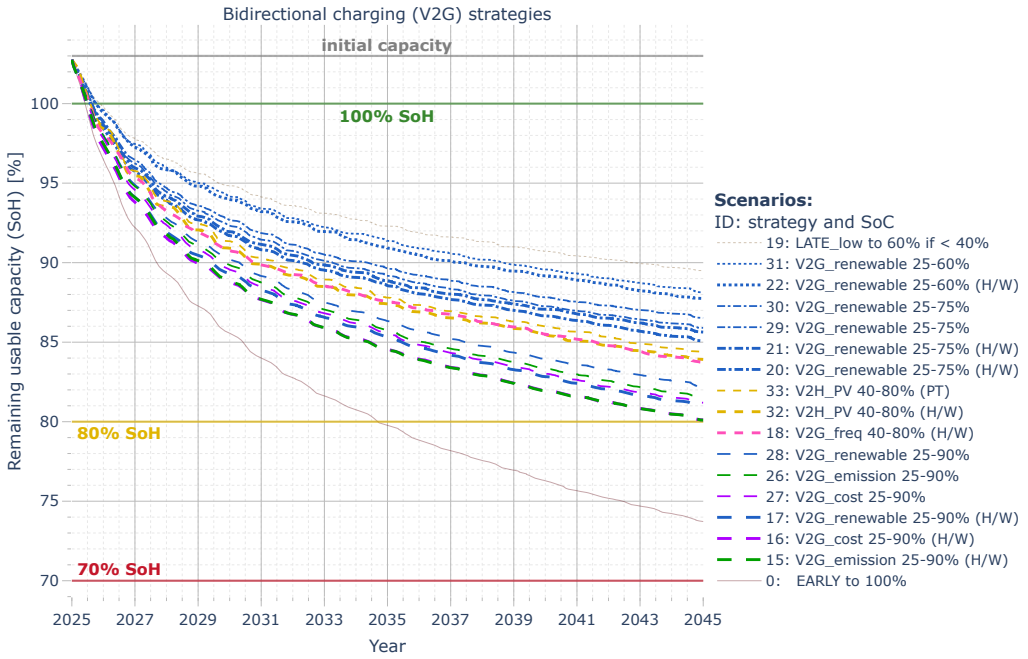

Figure 7.42: Comparison of the remaining capacity for *bidirectional charging (V2G/V2H)* strategies — legend entries sorted from highest to lowest remaining capacity, best and worst conventional charging strategy in gray for comparison

almost as well as the battery-optimized scheduled charging strategy in scenario 19.
Selecting a slightly more extensive SoC range of 25–75% still results in an excellent final SoH of more than 85% after 20 years of operation. With a 40–80% SoC range, even the frequency control scenarios 18 and the PV charging scenarios 32 and 33, in which the battery is used very frequently, experience comparatively low capacity losses, with a final SoH of around 84%. Besides a relatively low average SoC, the charging current is typically low in these scenarios.

An overview of the capacity fade trajectories of all simulated scenarios is shown in Figure 7.43. The direct comparison shows that all investigated V1G and V2G charging strategies cause fewer capacity losses than immediate (EARLY) or scheduled (LATE) charging to an SoC of 100%. Even with a lower charging limit of 90%, most smart and bidirectional scenarios outperform conventional charging.
Strategies and settings that keep the battery at a lower average SoC tend to reduce capacity losses, which is often the case for the V2G scenarios. Nevertheless, degradation due to increased cyclic aging from V2G usage also impacts aging. Therefore, unidirectional scheduled or smart charging strategies maintaining low SoC levels (e.g., scenarios 11 and 19) will experience less capacity fade than V2G strategies operating in similar SoC ranges.

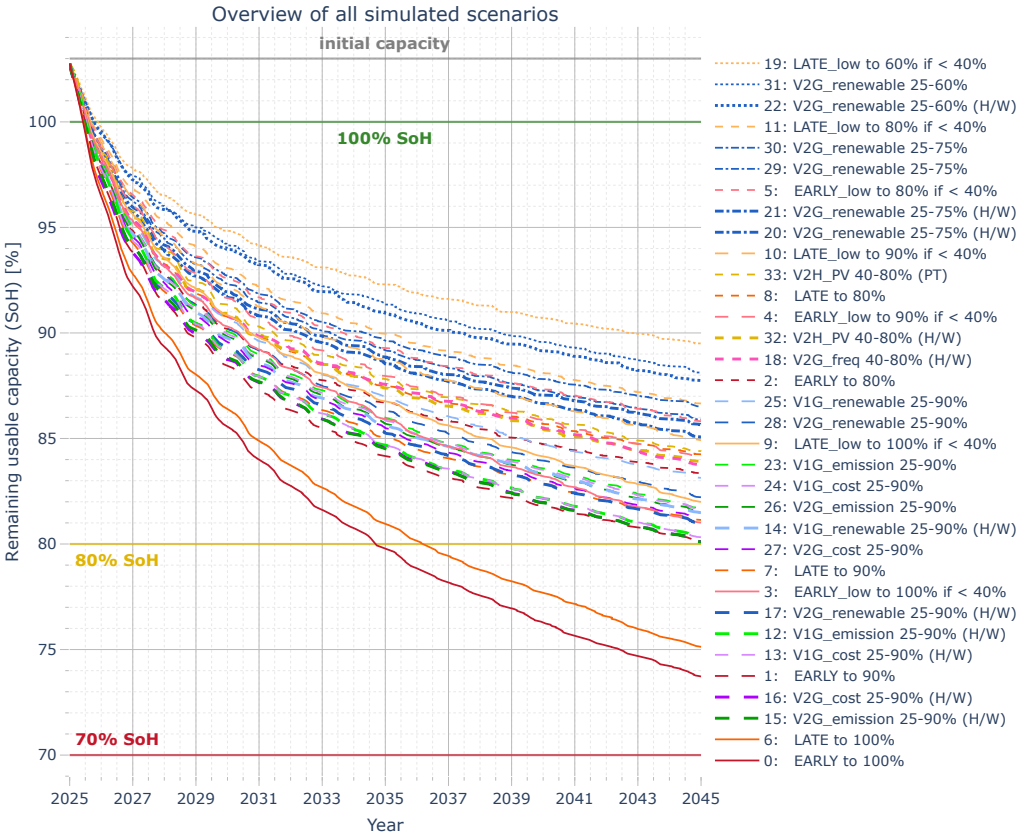

Figure 7.43: Comparison of the remaining capacity for *all* simulated charging strategies — legend entries sorted from highest to lowest remaining capacity

The capacity fade rate of all scenarios varies during the year. It is larger in summer, mainly caused by higher calendar aging at warm temperatures. This seasonal variation is most distinct in PV charging scenarios (32 and 33) since the battery is cycled more frequently in summer and also has a higher average SoC than in winter, increasing both calendar and cyclic aging.

Table 7.11 gives a comprehensive overview of the final SoH after simulation, the number of equivalent full cycles (EFCs) the battery completed, the energy charged from and discharged into the grid, the average and total attributed emissions, as well as the average electricity price and residual load when charging (“chg.”) and discharging (“dis.”).
At the end of the simulation period, the SoH of the scenarios lies between 73.7 and 89.5% after approximately 760 to 1840 EFCs. All unidirectional charging strategies draw around 52 MWh of electrical energy from the grid to cover a total driving distance of about 284,000 kilometers. Bidirectional charging strategies draw up to 126 MWh and feed up to 66 MWh into the grid.

Table 7.11: Summary of the use case model results after a simulation period of 20 years (January 1, 2025, to December 31, 2044, total driving distance: 284,376 km) — scenario ID, SoH, and rank (from highest to lowest SoH), total equivalent full cycles (EFCs) of the cell, overall energy charged from and discharged into the grid, average and overall electricity emissions, electricity price, and residual load while charging and discharging

Scenario ID	Final SoH [%]	SoH rank	Total EFCs	Total grid energy [MWh]		Avg. emission [gCO_2/kWh]		Total emissions [t]	Avg. electricity price [ct/kWh]		Avg. residual load [GW]	
				chg.	dis.	chg.	dis.		chg.	dis.	chg.	dis.
0	73.72	34	772.3	53.86	–	341	–	18.38	5.7	–	23.4	–
1	80.15	30	762.8	51.69	–	348	–	18.01	5.8	–	23.3	–
2	83.35	16	771.1	51.65	–	347	–	17.90	5.8	–	23.0	–
3	81.01	26	785.0	52.53	–	392	–	20.61	6.0	–	30.6	–
4	84.13	13	787.4	52.09	–	392	–	20.43	6.1	–	31.1	–
5	85.82	7	791.7	52.04	–	387	–	20.14	6.0	–	30.1	–
6	75.13	33	771.7	54.31	–	366	–	19.90	5.2	–	28.9	–
7	81.14	25	762.2	52.18	–	376	–	19.60	5.0	–	29.7	–
8	84.25	12	770.5	52.15	–	375	–	19.55	5.1	–	29.5	–
9	82.00	19	784.3	52.61	–	362	–	19.06	4.6	–	27.7	–
10	84.92	10	787.0	52.20	–	361	–	18.86	4.6	–	28.1	–
11	86.66	4	791.8	52.17	–	367	–	19.13	4.7	–	29.0	–
12	80.33	28	763.6	52.19	–	140	–	7.32	4.6	–	-27.1	–
13	80.32	29	763.5	52.19	–	141	–	7.36	4.6	–	-29.6	–
14	81.49	23	768.3	52.19	–	139	–	7.24	4.6	–	-38.6	–
15	80.10	32	1386.1	95.21	-38.15	158	715	-12.25	4.8	6.9	-20.6	75.2
16	80.12	31	1840.9	126.42	-65.84	166	683	-23.94	4.8	6.8	-21.7	70.8
17	80.99	27	1735.5	118.70	-58.94	154	671	-21.30	4.7	6.8	-32.5	69.2
18	83.74	15	1621.1	102.65	-46.15	325	364	16.54	5.0	5.0	17.5	20.5
19	89.50	1	806.9	51.97	–	363	–	18.84	4.6	–	28.6	–
20	85.08	9	1619.1	108.76	-50.17	154	674	-17.02	4.6	6.8	-33.4	69.6
21	85.63	8	1488.3	99.70	-42.61	172	658	-10.86	4.8	6.4	-24.7	67.3
22	87.75	3	1186.1	77.65	-22.89	161	697	-3.44	4.7	6.9	-28.9	72.7
23	81.71	20	769.8	52.19	–	180	–	9.37	4.5	–	-10.6	–
24	81.64	21	769.1	52.19	–	183	–	9.54	4.6	–	-12.1	–
25	83.13	17	776.5	52.20	–	186	–	9.72	4.6	–	-16.3	–
26	81.53	22	1017.3	69.25	-15.11	218	715	4.32	4.6	6.6	-2.3	75.3
27	81.19	24	1281.4	87.12	-30.95	240	696	-0.65	4.5	6.4	-0.5	72.7
28	82.22	18	1155.4	78.03	-22.84	236	683	2.85	4.6	6.7	-3.8	70.7
29	85.90	6	1066.1	70.75	-16.43	227	681	4.88	4.4	6.1	-5.9	70.5
30	86.52	5	1010.6	66.86	-13.21	246	668	7.60	4.5	5.9	-1.0	68.6
31	88.13	2	925.5	59.95	-7.03	235	649	9.51	4.5	5.9	-2.6	66.1
32	83.91	14	1206.8	95.73	-36.89	*(251)*	*(445)*	*(7.63)*	*(5.5)*	*(5.5)*	*(-8.5)*	*(34.0)*
33	84.38	11	1180.4	88.12	-33.61	*(207)*	*(452)*	*(3.07)*	*(5.0)*	*(5.6)*	*(-6.2)*	*(34.3)*

Note: The values in parentheses for the PV use case scenarios 32 and 33 are not representative of the scenarios since they refer to emissions, prices, and residual load of the public electricity grid and not those of the local PV system.

There are remarkable differences between the scenarios' average residual loads while charging and discharging. Lower residual loads or even negative ones, i.e., surpluses from RES, result in significantly lower attributed electricity generation emissions and also tend to cause lower average electricity prices. In the conventional and scheduled charging algorithms (scenarios 0–11 and 19), the EV is almost exclusively charged in the evening or early morning, independent of RE generation. This results in relatively similar total estimated emissions of approximately 18 to 21 tons caused by electricity needed to charge the EV. In the smart charging scenarios (12–14 and 23–25), the average emissions are reduced to around 7.3 tons when charging at home and work is possible and 9.5 tons when only charging at home. On the other hand, even negative emissions can be attributed to most V2G scenarios since the charging algorithm prefers charging when average emissions are low and discharging when the emissions are very high, effectively displacing high-emission fossil fuel power plants. However, it has to be mentioned that the simulation model uses simple approaches to estimate the residual load, prices, and emissions and does not consider a future zero-emission energy grid, in which emissions are also low when the residual load is high. Nevertheless, the actual emissions attributed to V2G charging are expected to be significantly lower than for conventional or smart unidirectional charging strategies.
Even though battery degradation is slightly stronger, average electricity prices and particularly emissions are remarkably lower if the EV can also charge at work (e.g., scenarios 15–17) since optimal grid conditions can be used more often compared to only charging at home (e.g., scenarios 26–28). For example, in summer, the EV can often charge with excess solar energy at work and feed back energy to the grid at home during the evening when the residual load is high. From a technical standpoint, it would be a great opportunity for the energy transition if this were made possible under tax and regulatory law.
The influence of charging power is compared in scenarios 20 and 21 as well as 29 and 30. The $V2G_{renewable}$ strategy is used with the default charging and discharging power of 10.5 kW in scenarios 20 and 29. Scenarios 21 and 30 use a lower power of 5.25 kW with otherwise similar conditions. With an SoH difference of around 0.6%, the lower charging power has a small positive impact on battery lifetime. However, this could partly be attributed to the lower number of cycles in the scenarios with reduced charging power. On the other hand, scenarios with a higher charging power can obtain lower average emissions, electricity prices, and residual load since periods with optimal conditions can be used more effectively. While increasing the charging power from 5.25 kW (approximately 1/12 C charging rate) to 10.5 kW (about 1/6 C) has little effect on aging, a significantly higher charging rate (e.g., above 0.5 C) could negatively impact battery lifetime due to increased lithium plating for aged or cold battery cells. However, this was not analyzed in the scenarios.
While the battery should only be charged at sufficiently high cell temperatures and low C-rates in winter, avoiding high SoCs is particularly beneficial at warmer cell temperatures to maximize battery lifetime.

As mentioned, a limitation of the use case simulation model is the simplified method to estimate residual load, prices, and emissions. Although the electricity price and emission estimates are not accurate, they show clear trends representative of real applications. On the other hand, the sophisticated battery degradation model was derived using the comprehensive battery aging dataset collected for this thesis and is expected to have a higher accuracy.
Nevertheless, the aging model is only valid for the specific NMC cell investigated in the aging study. Even though similar trends are likely to occur, newer cell models typically have an increased lifetime. However, the impact and ratio of calendar and cyclic aging might be very different for other cell chemistries (e.g., cells with an LFP cathode or an LTO anode).
Moreover, cell imbalances within the EV battery are not modeled. Differences in aging due to inhomogeneous temperatures in the battery pack, cell production tolerances, and unsuitable balancing methods could reduce lifetime compared to the simulation. In real applications, it might be necessary for the charging algorithm to allow the BMS to balance the cells, which is typically only done at higher SoCs.
Toward the EOL, i.e., at an SoH below 80% or in extreme operating conditions, such as in scenario 0 with severe SEI losses, the battery aging model might underestimate capacity fade.

7.4 Summary

Li-ion battery aging is a complex topic. The capacity fade and impedance increase of battery cells depends on numerous factors, such as temperature, the discharging, and particularly charging rates, and the SoC range within which the cell is operated or the SoC level at which the cell rests. In simplified terms, aging is often divided into cyclic aging, which takes place when the cell is charging or discharging, and calendar aging, which occurs when the cell is resting. Cyclic aging increases according to how much charge is processed in the cell and is intensified when the cell is charged and discharged close to the maximum or minimum voltage or SoC limits. High charging rates at low internal cell temperatures, high SoCs, or severely aged cells can have an adverse effect on degradation due to lithium plating. Calendar aging is most substantial at the beginning of the cell's life and particularly severe when the cell rests at high voltages and temperatures for long periods.
While these relationships are generally well known in the electrochemistry domain, they are often not considered adequately in other disciplines, such as energy economics, electrical engineering, and computer sciences. For example, many degradation models used in analyses of the profitability of V2G or its effect on battery degradation do not even consider calendar aging, although it tends to have the most significant impact on EV battery aging. Even though aging dependencies might be known, they are hard to factor in due to a lack of accurate yet easily reusable models and comprehensive publicly available datasets on battery degradation.

In this thesis, one of the most extensive publicly available Li-ion battery degradation datasets was generated using a commercial nickel-rich NMC/C+SiO cell. The dataset is publicly available [J1], [R1] and includes capacity fade and impedance measurements, as well as log data with a two-second temporal resolution for up to 449 days. The data largely confirms the aging dependencies known from the literature but also gives new insight into the degradation after the knee point down to an SoH of 40%, which is particularly relevant for aged EV batteries and second-life applications but seldom found in published data. The data was used to derive an accurate open-source aging model of this cell, available for reuse on *GitHub* [R4].
Finally, more than 30 different EV applications were simulated with the new aging model. This use case model is also available on GitHub [R4] to analyze further applications. Conventional, smart, and bidirectional charging strategies with different objectives were simulated for a 20-year operating time. For the analyzed cell, smart unidirectional (V1G) and bidirectional (V2G) charging can significantly reduce electricity generation costs and emissions caused by EV usage while reducing battery aging compared to conventional charging. All investigated V1G and V2G use cases outperform conventional early or late (scheduled) charging to an SoC of 100%. In almost all V2G scenarios, the capacity losses are even lower compared to conventional charging using a reduced SoC limit of 90%. Maintaining a moderately low average SoC is beneficial independent of the charging strategy. Therefore, highly battery-optimized operation with scheduled charging in a comparatively low and shallow SoC range performs slightly better than the best V1G and V2G strategies but limits day-to-day range without other significant advantages.
In summary, when adequately respecting mobility needs and grid capacity, V2G is a win-win-win situation for EV users, the energy transition, and grid stability. Nevertheless, it remains to be investigated how well the aging model applies to other cell chemistries, although similar tendencies are likely to exist. The published aging model could be fitted or adjusted to other datasets reviewed in this thesis or newer datasets for future research. However, it can be assumed that newer cell variants and generally longer-lasting cell chemistries will face an even lower capacity fade and, therefore, live longer despite or even because of V2G.

8 Conclusion

The advantages of bidirectional charging are promising, particularly given the wide range of applications. For instance, coupling electric vehicle (EV) batteries with the electricity grid supports integrating a higher share of renewable energy sources (RES) into the energy system and can improve grid stability through ancillary services. Further, Vehicle-to-Grid (V2G) allows charging an EV when electricity prices and emissions are low and returning energy to the grid when they are high. Given appropriate energy economic policies, this can reduce overall electricity generation costs and yield additional revenue for EV owners. Bidirectional charging can also be used at home (V2H), for example, to improve self-sufficiency in conjunction with a photovoltaic (PV) system or to power devices directly without an electricity grid (V2L). The potential is enormous, as EVs registered in Germany already have two and a half times more energy storage capacity than all domestic pumped hydroelectric energy storage systems. Although the concept of bidirectional charging is already well-known, many challenges still prevent market penetration.

In this thesis, some of the most critical technical challenges hindering market ramp-up are addressed, ranging from the cost and efficiency of the power electronics and achievable revenue through grid stabilization to battery degradation.
A highly efficient V2G charger power electronics system was developed and validated. It comprises a newly designed 22 kW auxiliary resonant commutated pole inverter (ARCPI) and a further developed isolated CLLLC converter with significantly improved efficiency. The maximum overall efficiency is 99.1% for the ARCPI and 98.1% for the CLLLC converter, resulting in an excellent combined peak efficiency of more than 97%. Both converters remain efficient even at light load down to 3% of the nominal load, which is particularly relevant for V2L and V2H. The soft-switching ARCPI and CLLLC converter topologies feature silicon carbide (SiC) MOSFETs with optimized gate timing control to maximize efficiency and switching frequency. This reduces the necessary cooling effort and filter component size, which decreases the cost of the V2G charger.
Different ancillary services were implemented on the inverter of the V2G charging system to increase the obtainable revenue and stabilize the grid. The controller can feed in active power to support balancing electricity supply and demand and reactive power, e.g., to stabilize the local grid voltage. To a limited extent, asymmetrical currents can be intentionally injected to reduce

asymmetries in the grid caused by unbalanced load, for example, single-/two-phase EV chargers and PV plants. Both frequency control (FCR) and virtual inertia (VI) emulation were realized on the controller to stabilize the grid frequency even during severe incidents, reducing the need for synchronous generators of conventional power plants. The bidirectional charger and the control algorithms were successfully validated on a power hardware-in-the-loop test bench. Satisfactory controller stability and reaction times of less than 0.25 s could be achieved for active and reactive power and frequency control, as well as VI emulation. However, the implemented DDSRF-PLL and current controllers only supported a low-voltage ride-through (LVRT) during small voltage faults, and a different inverter hardware and control configuration is necessary if all phase currents shall be arbitrarily controlled.

Even though the cost and lifetime of lithium-ion batteries have improved significantly over the last decades, potentially higher battery degradation caused by V2G and the uncertainty about it still cause skepticism against bidirectional charging. Existing battery degradation models that quantify aging are often too complex to be used outside the electrochemistry domain or too simplified to accurately reflect the nuanced dependencies relevant to modeling the effect of different smart and bidirectional charging strategies on battery lifetime. Openly available, reusable, comprehensive battery degradation datasets suitable for modeling are also scarce.
One of the most extensive publicly available battery degradation datasets to date was generated in this thesis and published for reuse [J1], [R1] to overcome this problem. It features capacity and impedance measurements as well as log data of 228 NMC/C+SiO cells tested under 76 different operating conditions over a period of almost 450 days. The charging and discharging rates, temperature, and State of Charge (SoC) range were varied for cyclic aging cells. Different temperatures and SoCs were analyzed for calendar aging cells. In addition, different WLTP-based driving cycles and charging strategies were applied to the cells to validate the aging behavior under application-specific profiles.
A semi-empirical open-source battery aging model [R4] that considers the effect of SEI layer growth, cyclic aging, and lithium plating was derived using the new dataset. The relative root mean square error between the capacity fade measured in the experiment and the modeled one is 2.3% on average when considering data points with a State of Health (SoH) of more than 70% and 4.9% when considering all data points down to an SoH of 40%.
Finally, the aging model was used to simulate the degradation of EV batteries over a period of 20 years using different charging strategies. Conventional, scheduled, smart, and bidirectional charging strategies with different objectives and boundary conditions were compared. For the NMC cell investigated, conventional and scheduled charging to an SoC of 100% are by far the strategies with the largest capacity loss. Smart (V1G) and bidirectional (V2G) charging strategies optimizing the share of RES, emissions, charging cost, or PV self-sufficiency using moderate SoC ranges (e.g., 25–75% or 40–80%) achieved significantly better results, reducing degradation

by up to 55% compared to conventional, daily immediate charging to an SoC of 100%. Only very degradation-optimized scheduled charging in a 40–60% SoC window without V2G usage obtained slightly better results, reducing capacity fade by 60% compared to conventional charging. The investigations in this thesis have shown that concerns about increased battery aging through the use of V2G are unjustified. The degradation of EV batteries is not only influenced by the higher energy throughput due to V2G but primarily by calendar aging, which can be reduced significantly with appropriate smart (V1G) and particularly bidirectional (V2G) charging algorithms. Thus, the battery life can be increased, reducing overall capacity fade, cost, and emissions compared to conventional charging.

The newly developed hardware of this thesis confirms that resonant switching topologies with wide-bandgap semiconductors, such as SiC MOSFETs, can increase the efficiency and power density of battery chargers while potentially reducing their cost. Compared to a unidirectional charger, the added cost of a bidirectional charger is expected to be in a reasonable range, making it advisable to upgrade the OBC for V2G support. For little extra cost, there are numerous financial and non-monetary benefits for users, many of which can significantly support and accelerate the energy transition and electrification of the transport sector. The comprehensive battery degradation dataset and aging model demonstrate that, with appropriate operation, V2G can even reduce battery degradation compared to conventional charging strategies. Given the rapid global expansion of electric mobility and the resulting immense storage potential, it would be a waste of resources and opportunities if the necessary energy-economic regulatory, normative, fiscal, and political framework conditions were not paved for the fastest possible use of V2G.

A Appendix

A.1 Geographic distribution of apartment types

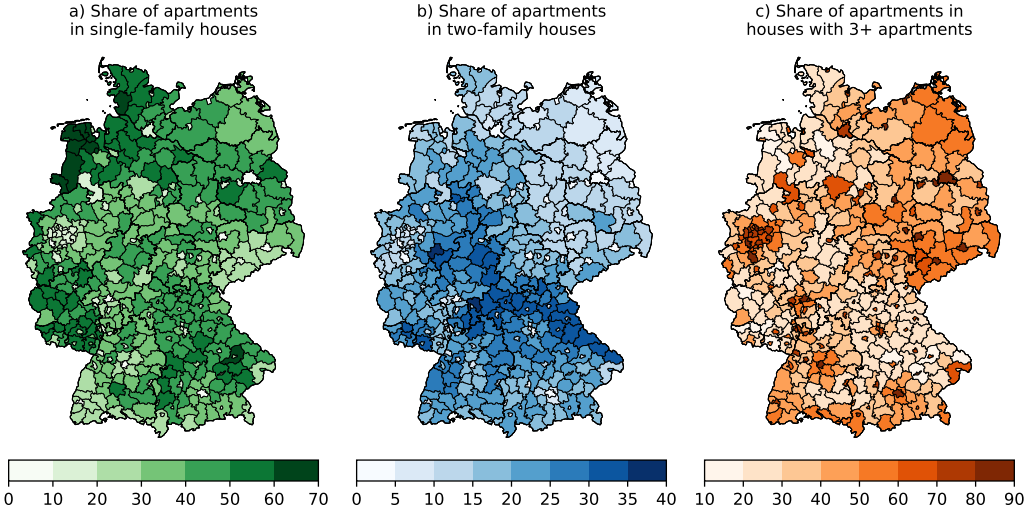

Figure A.1: Share of apartments in a) single-family and b) two-family houses as well as c) residential buildings with three or more apartments (including dormitories and living residences) as a percentage of the number of all apartments. Building data: ©Statistisches Bundesamt (Destatis), 2022 [196, pp. 26-38], [640]. Cartographic data: ©GeoBasis-DE / *BKG* 2023, Data license Germany – attribution – Version 2.0 (dl-de/by-2-0), dataset: https://gdz.bkg.bund.de/index.php/default/digitale-geodaten/verwaltungsgebiete/verwaltungsgebiete-1-2-500-000-stand-31-12-vg2500-12-31.html [127].

A.2 Chargers supporting V2G

Table A.1: Market overview of bidirectional (or "V2G-ready") chargers for EVs (non-exhaustive, as of August 2023)

Sources	Model	Type	Standard	Power	Launch	Notes
[228, 641–644]	Nichicon EV Power Station, Nissan LEAF to Home, Denso DNEVC-D6075	DC	CHAdeMO	6 kW	≈2012	C, J, P
[645, 646]	Tsubakimoto Chain eLINK TPS10	DC	CHAdeMO	5 kW	2013	J, X
[230, 647, 648]	Mitsubishi Electric EV Power Conditioner (SMART V2H)	DC	CHAdeMO	6 kW	2014	J, N
[649–651]	Magnum Cap V2G	DC	CHAdeMO	10 kW	≈2017	–
[652, 653]	Takaoka Toko CFD1-B-V2H1	DC	CHAdeMO	3 kW	2017	J
[654, 655]	Fermata Energy FE-15	DC	CHAdeMO	15 kW	2020	T
[656]	Wallbox Quasar	DC	CHAdeMO	7.4 kW	2020	T, X
[657, 658]	alpitronic HYC50 Wallbox	DC	CHAdeMO, CCS, GB/T	25/50 kW	2022	C
[659]	Eaton Green Motion DC 22	DC	CHAdeMO or CCS	22 kW	≈2022	–
[660–662]	dcbel r16	DC	CHAdeMO or CCS	15.2 kW	2022	I
[663]	GS Yuasa VOXSTAR	DC	CHAdeMO	10 kW	≈2022	J, X
[655]	Fermata Energy FE-20	DC	CHAdeMO	20 kW	2023	T
[664]	Omron	DC	CHAdeMO	6 kW	2023	J, X
[665–667]	Panasonic LJV1671B	DC	CHAdeMO	6 kW	2023	J, X
[668, 669]	Enphase Bidirectional EV Charger	DC	CHAdeMO or CCS	?	2024	U, X
[670, 671]	Delta V2H Bi-directional Charger	DC	CHAdeMO	11/22 kW	?	–

(continued on next page)

Table A.1 (continued)

Sources	Model	Type	Standard	Power	Launch	Notes
[672]	AME V2G 3p10kW V2X Charger	DC	CHAdeMO	10 kW	?	–
[673]	Enovates V2G10kW	DC	CHAdeMO	10 kW	?	–
[674–676]	Indra V2G	DC	CHAdeMO	7.4 kW	?	P
[677, 678]	Nuvve RES-HD125-V2G, BorgWarner RES-DCVC125-480-V2G	DC	CCS	125 kW	≈2020	T, V
[678, 679]	Nuvve RES-HD60-V2G, BorgWarner RES-DCVC60-480-V2G	DC	CCS	60 kW	≈2020	T, V
[680–683]	Evtec sospeso&charge, sun2wheel two-way-10, sun2wheel two-way-digital	DC	CCS	10 kW	2020	C, X
[684, 685]	Enteligent Hybrid DC Bi-Directional Fast EV Charger	DC	CCS	12.5/25 kW	2023	D, X
[686–688]	Ambibox ambiCHARGE DC-Wallbox	DC	CCS	11/22 kW	2023	C, X
[689, 690]	Wallbox Quasar 2	DC	CCS	11.5 kW	2023	P, T
[691]	E3/DC EDISON V2H	DC	CCS	?	2023	M, X
[692]	SolarEdge Bi-Directional DC EV Charger	DC	CCS	24 kW	≈2024	T, X
[693, 694]	Emporia V2X Bi-Directional Charger	DC	CCS	11.5 kW	2024	X
[695, 696]	Silla Duke 44	DC	CCS	2x22 kW	?	–
[697]	Volkswagen DC wallbox	DC	CCS	22 kW	?	–
[698, 699]	Honda Power Manager	DC	CCS	10 kW	?	–
[700–703]	Kostal	DC, AC	?	?	?	C
[704–706]	Nuvve PowerPort3 Ultra	AC	CCS	52.3 kW	?	T, V
[705–707]	Nuvve PowerPort	AC	CCS	19.2 kW	?	T, V
[708]	openWB Pro	AC	CCS	11/22 kW	≈2021	P

(continued on next page)

Table A.1 (continued)

Sources	Model	Type	Standard	Power	Launch	Notes
[709]	DaheimLader Smart/Touch	AC	CCS	11/22 kW	2022	–
[710, 711]	Enovates Single Wallbox	AC	CCS	22 kW	≈2022	–
[233, 712]	Ford Charge Station Pro	AC	CCS	19.2 kW	2022	X
[713, 714]	SENEC.Wallbox premium	AC	CCS	11/22 kW	2023	M, X
[715]	Mobilize Powerbox	AC	CCS	7-22 kW	2024	T
[716]	Webasto Unite	AC	CCS	22 kW	≈2024	–

C also design and manufacture custom/branded charging hardware for other companies
D charges EVs from solar power with a DC/DC charger
I combined system with integrated AC & bidirectional DC charger, solar & stationary battery inverter, and EMS
J only available on the Japanese market
M direct marketing of electricity surpluses supported
N not available anymore / discontinued
P coupling of EMS, PV system & charger supported
T other forms of electricity trading supported
U uninterrupted V2H operation during power outages possible
V capability to combine multiple EVs into a virtual power plant
X coupling of EMS, PV system, home storage & charger supported

Notes: Almost all stations reportedly allow a coupling of the charging station with an EMS.
Actual specifications and capabilities of products may differ from those indicated in the table — they have been compiled based on publicly available information at the time of the market review.
Some dates of market launches are estimated based on available information, such as press releases and certifications.

A.3 CLLLC converter: computer interface and commands

Table A.2: Examples of commands that can be sent to the CLLLC converter via UART

Command	Description
General commands:	
`help`	show help, including a list of valid commands and their usage
`off`	turn off the converter, i.e., stop switching
`stop`	same as `off`, but as an emergency stop
`ack`	acknowledge an emergency stop to continue using the converter
Operation:	
`u 400 dc2`	forward operation with $V_{DC2}^{set} = 400\ V$
`u 400 i 5.5 dc2`	forward operation with $V_{DC2}^{set} = 400\ V$, limited to $I_{DC2}^{set} = 5.5\ A$ (charging the battery)
`u 600 i -3 dc1`	backward operation with $V_{DC1}^{set} = 600\ V$, limited to $I_{DC1}^{set} = -3\ A$ (discharging the battery)
`u1 625 635 i -7 5 u2 300 400 i -10 7.5`	dynamic bidirectional mode with automatic selection of power direction — desired DC1 voltage between 625 and 635 V, I_{DC1} in the range of -7 A (V2G) to +5 A (G2V), battery voltage in the range of 300 to 400 V, 10 A maximum discharging current, 7.5 A maximum charging current
Battery-related commands:	
`bat enable`	enable usage of the *FlexBat* battery
`bat connect`	start *FlexBat* battery connection procedure (converter is turned on, DC2 voltage is set to the battery voltage, relays are connected)
`bat disable`	disable usage of the *FlexBat* battery (turn off relays, continue with manual operation)
Configuration:	
`sr on`	enable synchronous rectifying
`sr off`	disable synchronous rectifying

UART settings:
256 kbaud/s, 8 data bits, 1 stop bit, odd parity, `\n` line separator for inputs and outputs

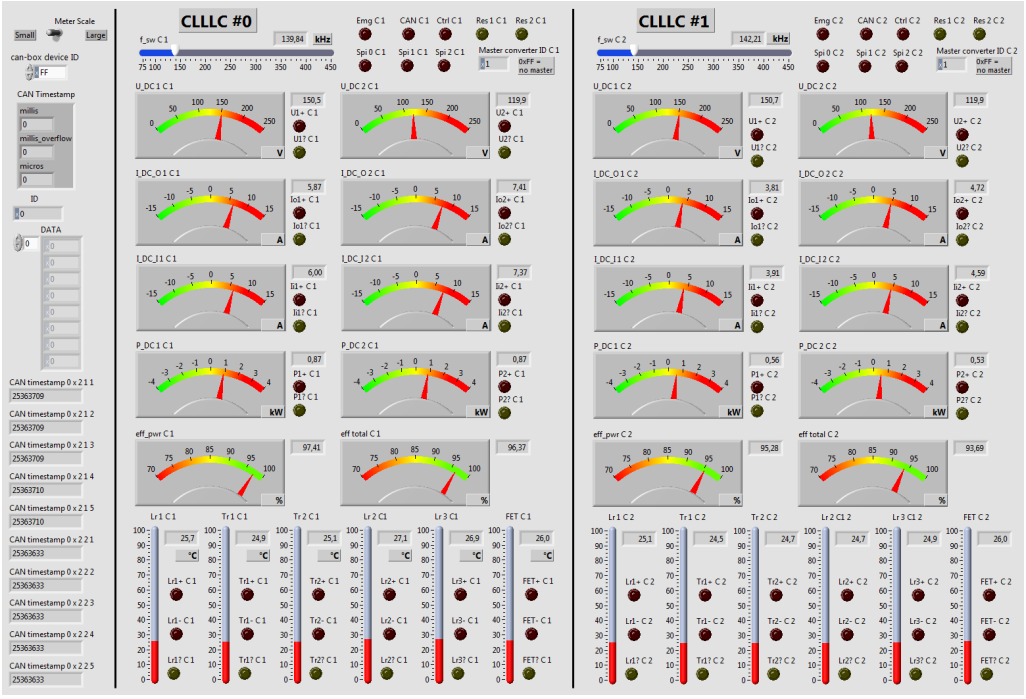

Figure A.2: *LabVIEW* interface to visualize the CLLLC converter measurements and states received via CAN

A.4 Overview of the ARCPI prototype hardware and software

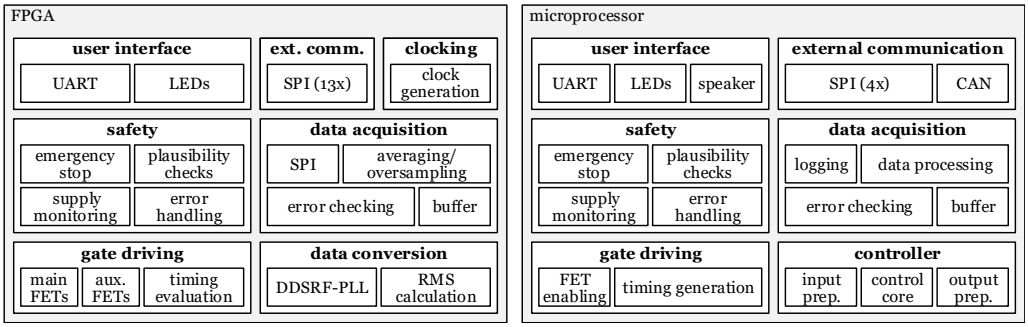

Figure A.3: Overview of the functional blocks of the FPGA and microprocessor used in the ARCPI

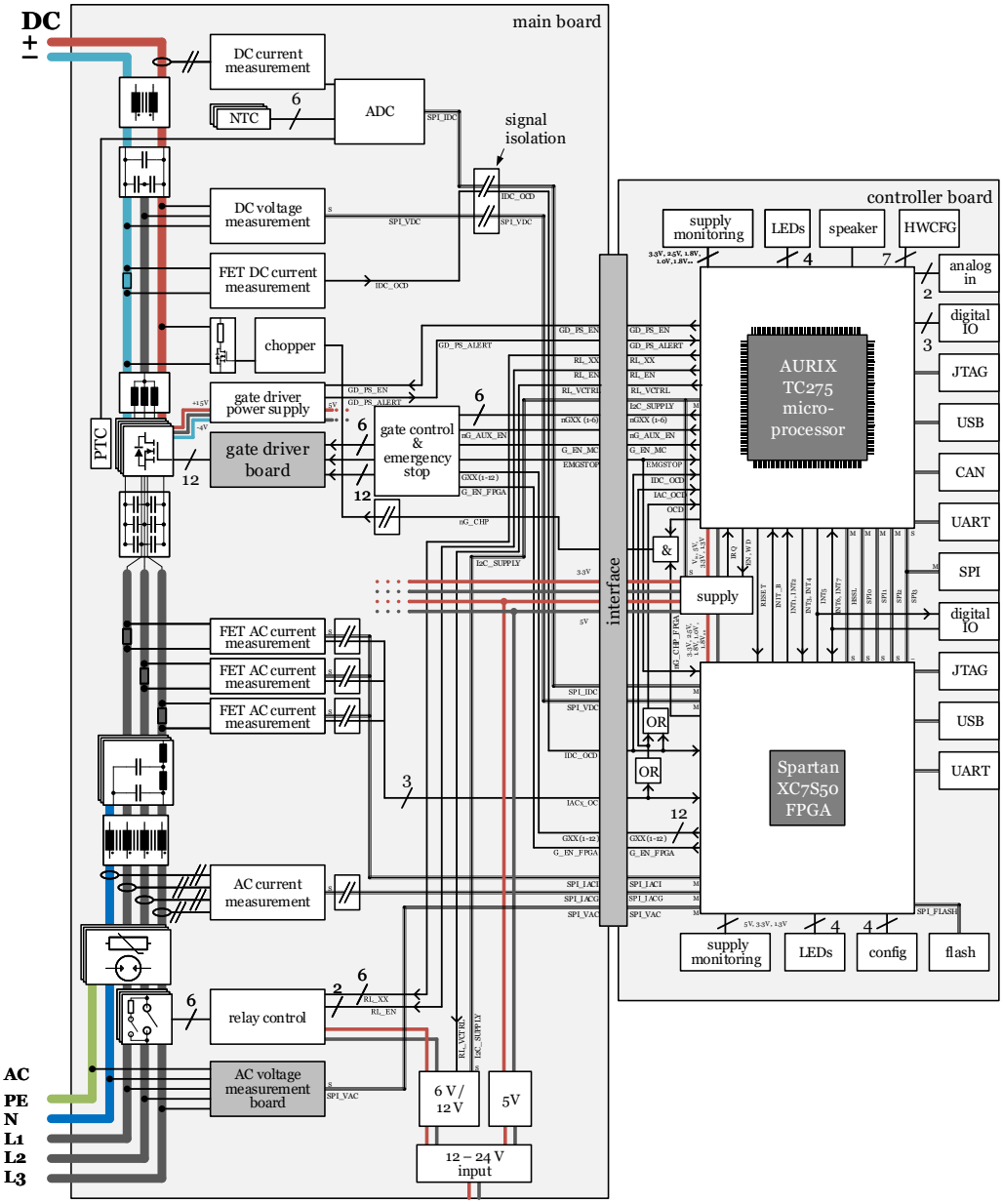

Figure A.4: Overview of the functional blocks and signals of the ARCPI hardware

A.5 UART commands for the ARCPI

Table A.3: Examples of commands that can be sent to the ARCPI via UART

Command	Description
General commands:	
`help`	show help, including a list of valid commands and their usage
`off`	turn off the inverter, i.e., stop switching
`stop`	same as "off", but as an emergency stop
`ack`	acknowledge an emergency stop to continue using the converter
`reset_soft`	application reset of the FPGA (e.g., PLL, error states, ...)
`reset`	power-cycle the FPGA
Configuration:	
`vdc_ctrl m 630 650`	turn on DC link voltage control, 630 to 650 V allowed range — master mode: inverter determines power flow, and external DC/DC converter shall control the DC link voltage
`vdc_ctrl m 650`	turn on DC voltage control, 650 V $\pm 2.5\%$ or $\pm 10\ V$ (whichever is larger) — master mode
`vdc_ctrl m`	turn on DC voltage control (with the last setting) — master mode
`vdc_ctrl s 630 650`	turn on DC voltage control, 630 to 650 V allowed range — slave mode: an external source/sink determines power flow (feedforward control of DC link power is used)
`vdc_ctrl off`	turn off DC voltage control (disabled by default)
`fctrl on 5000 1000`	turn on frequency control ($5\ \frac{kW}{Hz}$) and virtual inertia ($1\ \frac{kW \cdot s}{Hz}$)
`fctrl on`	turn on frequency control with the last/default setting
`fctrl off`	turn off frequency control and virtual inertia (disabled by default)
`vctrl on 3000 230`	turn on grid voltage control, $Q = -3\ kvar$ at 50% of nominal AC voltage ($230\ V_{RMS}$)
`vctrl on 2000`	turn on grid voltage control, $Q = -2\ kvar$ at 50% of last/default nominal voltage
`vctrl off`	turn off grid voltage control (disabled by default)
`ramp pac 50`	limit the rate of change of AC power setpoint to $50\ \frac{W}{ms}$
`ramp pac`	show the maximum rate of change of AC power setpoint
`ramp ... ...`	show or limit other rates of change: `udc` DC link voltage, `uac` grid voltage, `fac` grid frequency, `idq` d/q currents
`soft on`	enable soft switching (enabled by default)
`soft off`	disable soft switching

(continued on next page)

Table A.3 (continued)

Command	Description
Grid-forming operation:	*(e.g., for V2L, islanded operation, or PHIL tests — BPT possible)*
`uacl 230 f 50`	three-phase output voltage with 230 $V_{AC,RMS}$ and 50 Hz, AC voltages are unregulated ("loose" sinusoidal PWM duty cycles)
`uac 230 f 50`	three-phase output voltage with 230 $V_{AC,RMS}$ and 50 Hz, AC voltages are regulated (sinusoidal PWM duty cycles with adjusted amplitudes)
`fevent 4`	start frequency event 4 (modified system separation Europe July 24, 2021) events 1 to 6 are available → see *Config\Frequency_Events.h*
Grid-following operation:	*(e.g., for regular grid-connected operation — automatically connects to the grid)*
`pac 0`	transfer 0 W (but keep switching active → useful for initial turn-on)
`pac 5000`	feed in 5 kW into the grid (discharge battery)
`pac -3600`	draw 3.6 kW from the grid (charge battery)
`pac 500 q 2000`	feed in 500 W into the grid with 2 kvar reactive power (capacitive gen./inductive load)
`pac -500 q -200`	draw 500 W from the grid with −200 var reactive power (inductive gen./capacitive load)
`idqpn 5.0 4.0 3.0 2.0`	set $i_{d+} = 5\ A$, $i_{q+} = 4\ A$, $i_{d-} = 3\ A$, $i_{q-} = 2\ A$ (asymmetric operation)
`ns 0`	turn off negative-sequence control (default)
`ns 3`	turn on negative-sequence control 3: equalizing voltage sequence control (EVSC) — adapted from [331]
`ns 4`	turn on negative-sequence control 4: constant instantaneous active power (CIAP) — adapted from [331]

UART settings for the microprocessor:
256 kbaud/s, 8 data bits, 1 stop bit, odd parity, `\n` line separator for inputs and outputs

UART settings for the FPGA:
256 kbaud/s, 8 data bits, 1 stop bit, no parity, `\n` line separator for outputs (no input supported)

A.6 ARCPI: additional measurements

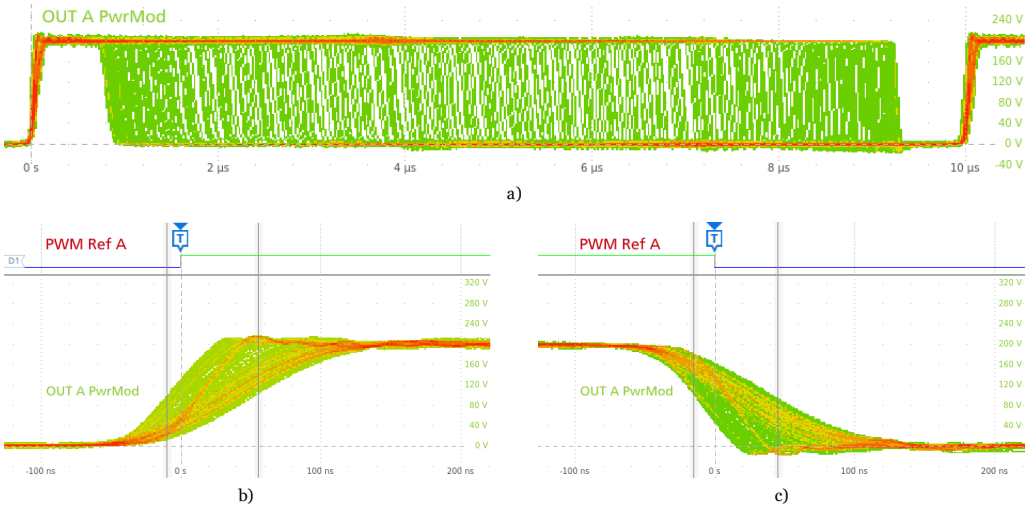

Figure A.5: V_{DS} of the ALS FET during the switching transitions at 200 V_{DC}, 60 $V_{AC,RMS}$, and 12 $A_{AC,RMS}$ with reference PWM (overlay of all transitions in the "fast acquisition mode" of the oscilloscope) — a) complete switching period, b) detailed view of the turn-off (trigger on rising reference PWM edges), and c) the turn-on (trigger on falling edges)

Table A.4: Measurements of the power analyzed at nominal output power (only ARCPI DUT)

setpoint	**AC**	combined	L1	L2	L3	**DC**	
G2V −22 kW	V_{RMS}	229.12 V_{avg}	229.19 V	229.17 V	228.99 V	V_{avg}	600.79 V
	I_{RMS}	31.991 A_{avg}	31.996 A	32.014 A	31.964 A	I_{avg}	−36.210 A
	P	−21.984 kW	−7.332 kW	−7.335 kW	−7.318 kW	P	−21.755 kW
	P.F.	−0.9998	−0.9998	−0.9998	−0.9998	η_{G2V}	98.96%
	THD_i	2.26%	(5th harm.: 1.54%, 7th harm.: 1.04%)			ΔI	±3.1%
V2G +22 kW	V_{RMS}	229.59 V_{avg}	229.68 V	229.64 V	229.44 V	V_{avg}	599.96 V
	I_{RMS}	31.891 A_{avg}	31.887 A	31.912 A	31.875 A	I_{avg}	36.982 A
	P	21.957 kW	7.321 kW	7.325 kW	7.310 kW	P	22.188 kW
	P.F.	±0.9996	+0.9996	−0.9996	−0.9996	η_{V2G}	98.96%
	THD_i	2.33%	(5th harm.: 1.52%, 7th harm.: 1.09%)			ΔI	±3.0%

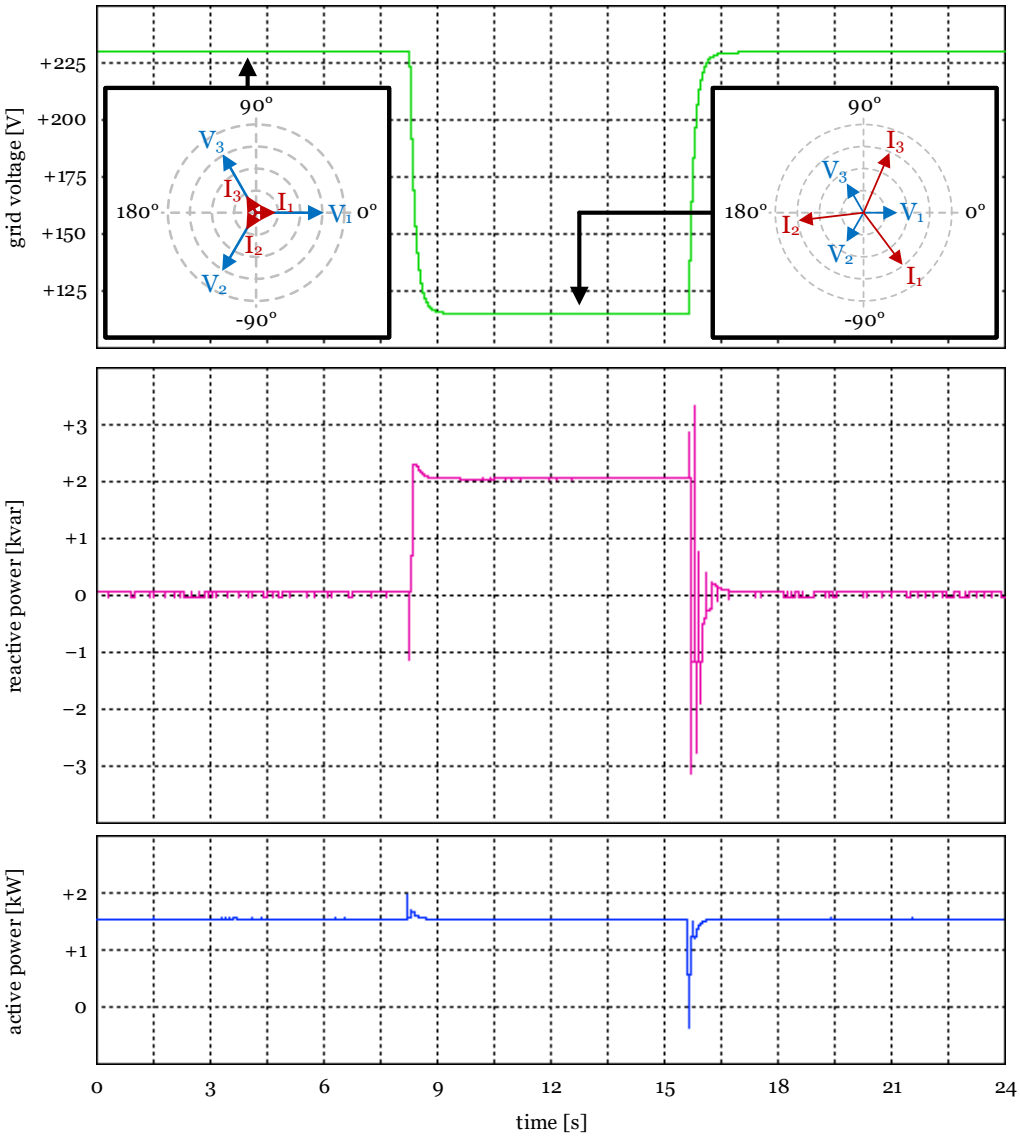

Figure A.6: AC voltage, reactive, and active power during the LVRT with vector diagrams captured by the power analyzer

A.7 Battery aging test bench: test conditions

Table A.5: Assumptions for the calculation of the battery cell power in the WLTP cycle

Input for the *Gearshift Calculation Tool*		**Calculation of the battery power**	
v_{max}	167 km/h	η_{motor}	90%
P_{rated}	150 kW	$\eta_{inverter}$	95%
n_{rated}	11000 1/min	$P_{auxiliary}$	1 kW
n_{idle}	58 1/min	$v_{min,recuperation}$	8 km/h
#g	6	$P_{max,recuperation}$	64 kW
m_{test}	1840 kg	Resulting WLTP consumption: 15.8 kWh/100 km	
f_0	200 N	**Calculation of the cell power**	
f_1	0.35 N/(km/h)	battery capacity	64 kWh
f_2	0.032 N/(km/h)^2	cell capacity	3 Ah
p(n)	$\min(n \cdot 0.04136\ \mathrm{kW \cdot min}, P_{rated})$	cells in series	96
ndv	65.868 (1/min)/(km/h)	cells in parallel	60

Table A.6: Test frequencies for the EIS measurement — current amplitude: 1/6 C = 0.5 A

–	6.757 kHz	675.7 Hz	67.57 Hz	6.757 Hz	–	–
–	5.000 kHz	500.0 Hz	50.00 Hz	5.000 Hz	500.0 mHz	50.00 mHz
–	3.125 kHz	312.5 Hz	31.25 Hz	3.125 Hz	–	–
–	2.083 kHz	208.3 Hz	20.83 Hz	2.083 Hz	208.3 mHz	–
14.71 kHz	1.471 kHz	147.1 Hz	14.71 Hz	–	–	–
10.00 kHz	1.000 kHz	100.0 Hz	10.00 Hz	1.000 Hz	100.0 mHz	–

Table A.7: Data timestamps for the pulse pattern measurement — current amplitude: 1/3 C = 1.0 A

I = 0.0 A	I = +1.0 A	I = −1.0 A	I = 0.0 A	I = +1.0 A	I = −1.0 A	I = 0.0 A
0.000 s	0.001 s	10.001 s	20.001 s	30.001 s	90.001 s	150.001 s
–	0.003 s	10.003 s	20.003 s	30.003 s	90.003 s	150.003 s
–	0.010 s	10.010 s	20.010 s	30.010 s	90.010 s	150.010 s
–	0.030 s	10.030 s	20.030 s	30.030 s	90.030 s	150.030 s
–	0.100 s	10.100 s	20.100 s	30.100 s	90.100 s	150.100 s
–	0.300 s	10.300 s	20.300 s	30.300 s	90.300 s	150.300 s
–	1.000 s	11.000 s	21.000 s	31.000 s	91.000 s	151.000 s
–	3.000 s	13.000 s	23.000 s	33.000 s	93.000 s	153.000 s
–	10.000 s	20.000 s	30.000 s	40.000 s	100.000 s	160.000 s
–	–	–	–	60.000 s	120.000 s	180.000 s
–	–	–	–	90.000 s	150.000 s	210.000 s

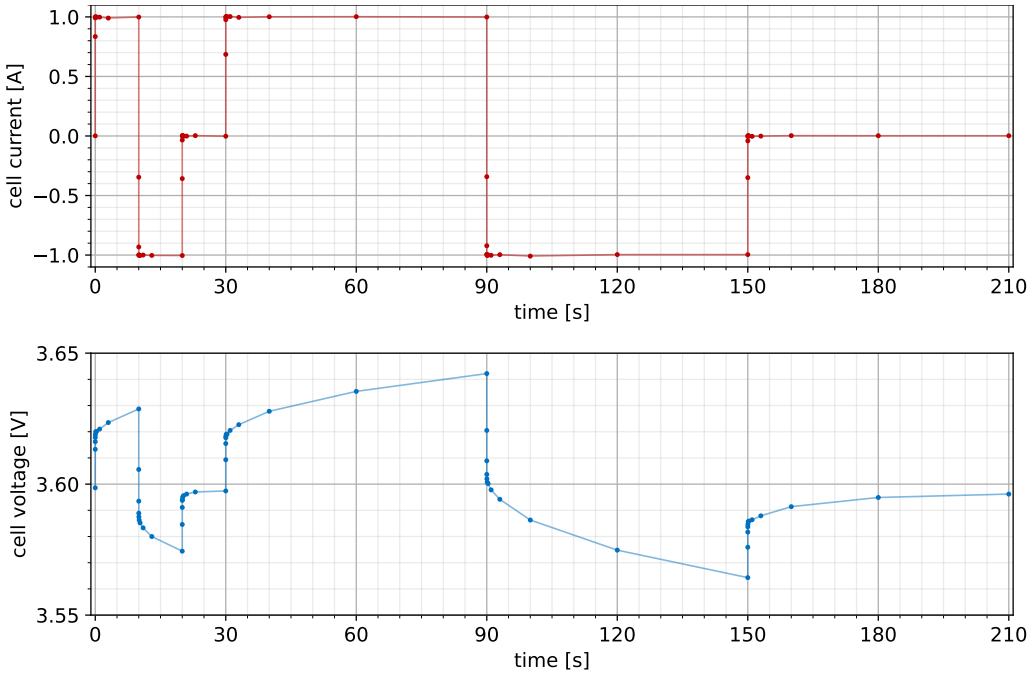

Figure A.7: Example of a pulse pattern measurement: data points connected with linear interpolation

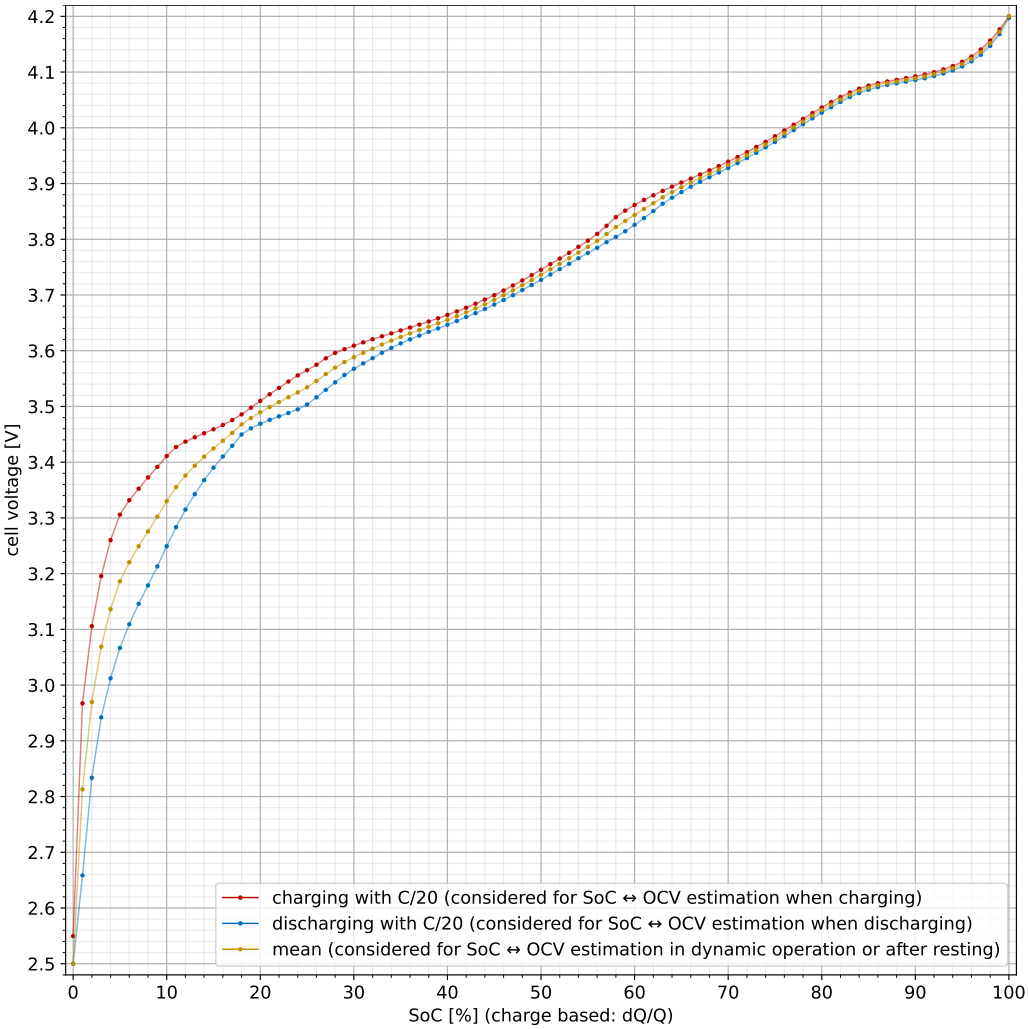

Figure A.8: Cell terminal voltage measured while charging (red) and discharging (blue) the LG INR18650HG2 at C/20 with mean values (yellow). The measurement was taken from a new cell on September 9, 2022. It is stored in an LUT on the cycler board and used for the estimations OCV(SoC) when the cell is in use and SoC(V_{cell}) when the cell rests.

Table A.8: Cell terminal voltage measured while charging and discharging the LG INR18650HG2 at C/20 with mean values (data for Figure A.8) — underlined values were manually edited to match the voltage limits of the cell

SoC [%]	V_{chg} [V]	V_{dischg} [V]	V_{avg} [V]	SoC [%]	V_{chg} [V]	V_{dischg} [V]	V_{avg} [V]	SoC [%]	V_{chg} [V]	V_{dischg} [V]	V_{avg} [V]
0	2.5496	2.5000	2.5000	34	3.6312	3.6050	3.6181	68	3.9236	3.9114	3.9175
1	2.9671	2.6585	2.8128	35	3.6363	3.6131	3.6247	69	3.9313	3.9197	3.9255
2	3.1057	2.8336	2.9696	36	3.6415	3.6204	3.6310	70	3.9393	3.9279	3.9336
3	3.1955	2.9421	3.0688	37	3.6469	3.6271	3.6370	71	3.9475	3.9366	3.9421
4	3.2601	3.0122	3.1362	38	3.6524	3.6338	3.6431	72	3.9562	3.9457	3.9510
5	3.3058	3.0666	3.1862	39	3.6582	3.6400	3.6491	73	3.9655	3.9550	3.9602
6	3.3317	3.1091	3.2204	40	3.6642	3.6467	3.6554	74	3.9748	3.9649	3.9698
7	3.3524	3.1458	3.2491	41	3.6705	3.6533	3.6619	75	3.9848	3.9745	3.9797
8	3.3726	3.1788	3.2757	42	3.6771	3.6603	3.6687	76	3.9952	3.9850	3.9901
9	3.3915	3.2130	3.3022	43	3.6844	3.6674	3.6759	77	4.0055	3.9959	4.0007
10	3.4109	3.2491	3.3300	44	3.6918	3.6749	3.6833	78	4.0160	4.0064	4.0112
11	3.4271	3.2835	3.3553	45	3.6996	3.6829	3.6912	79	4.0264	4.0169	4.0217
12	3.4369	3.3150	3.3759	46	3.7080	3.6911	3.6995	80	4.0364	4.0272	4.0318
13	3.4447	3.3427	3.3937	47	3.7170	3.6995	3.7083	81	4.0460	4.0368	4.0414
14	3.4519	3.3679	3.4099	48	3.7261	3.7089	3.7175	82	4.0552	4.0464	4.0508
15	3.4590	3.3901	3.4246	49	3.7355	3.7179	3.7267	83	4.0633	4.0552	4.0592
16	3.4667	3.4102	3.4385	50	3.7453	3.7271	3.7362	84	4.0702	4.0625	4.0663
17	3.4756	3.4294	3.4525	51	3.7553	3.7368	3.7460	85	4.0757	4.0683	4.0720
18	3.4857	3.4497	3.4677	52	3.7653	3.7464	3.7559	86	4.0800	4.0730	4.0765
19	3.4977	3.4607	3.4792	53	3.7757	3.7560	3.7658	87	4.0832	4.0769	4.0801
20	3.5100	3.4689	3.4894	54	3.7864	3.7658	3.7761	88	4.0861	4.0799	4.0830
21	3.5218	3.4759	3.4988	55	3.7974	3.7753	3.7863	89	4.0891	4.0828	4.0860
22	3.5332	3.4823	3.5077	56	3.8096	3.7846	3.7971	90	4.0923	4.0856	4.0890
23	3.5447	3.4882	3.5165	57	3.8242	3.7947	3.8094	91	4.0958	4.0888	4.0923
24	3.5557	3.4947	3.5252	58	3.8396	3.8043	3.8219	92	4.0997	4.0929	4.0963
25	3.5650	3.5035	3.5342	59	3.8514	3.8144	3.8329	93	4.1048	4.0974	4.1011
26	3.5749	3.5163	3.5456	60	3.8615	3.8259	3.8437	94	4.1108	4.1031	4.1070
27	3.5864	3.5298	3.5581	61	3.8707	3.8380	3.8543	95	4.1183	4.1100	4.1141
28	3.5960	3.5431	3.5696	62	3.8789	3.8505	3.8647	96	4.1279	4.1191	4.1235
29	3.6028	3.5564	3.5796	63	3.8867	3.8637	3.8752	97	4.1406	4.1311	4.1358
30	3.6091	3.5676	3.5883	64	3.8944	3.8746	3.8845	98	4.1565	4.1470	4.1517
31	3.6150	3.5772	3.5961	65	3.9017	3.8846	3.8932	99	4.1765	4.1682	4.1723
32	3.6206	3.5866	3.6036	66	3.9089	3.8942	3.9015	100	4.2000	4.1972	4.2000
33	3.6259	3.5962	3.6111	67	3.9162	3.9031	3.9096				

A.8 Battery aging test bench: experimental setup

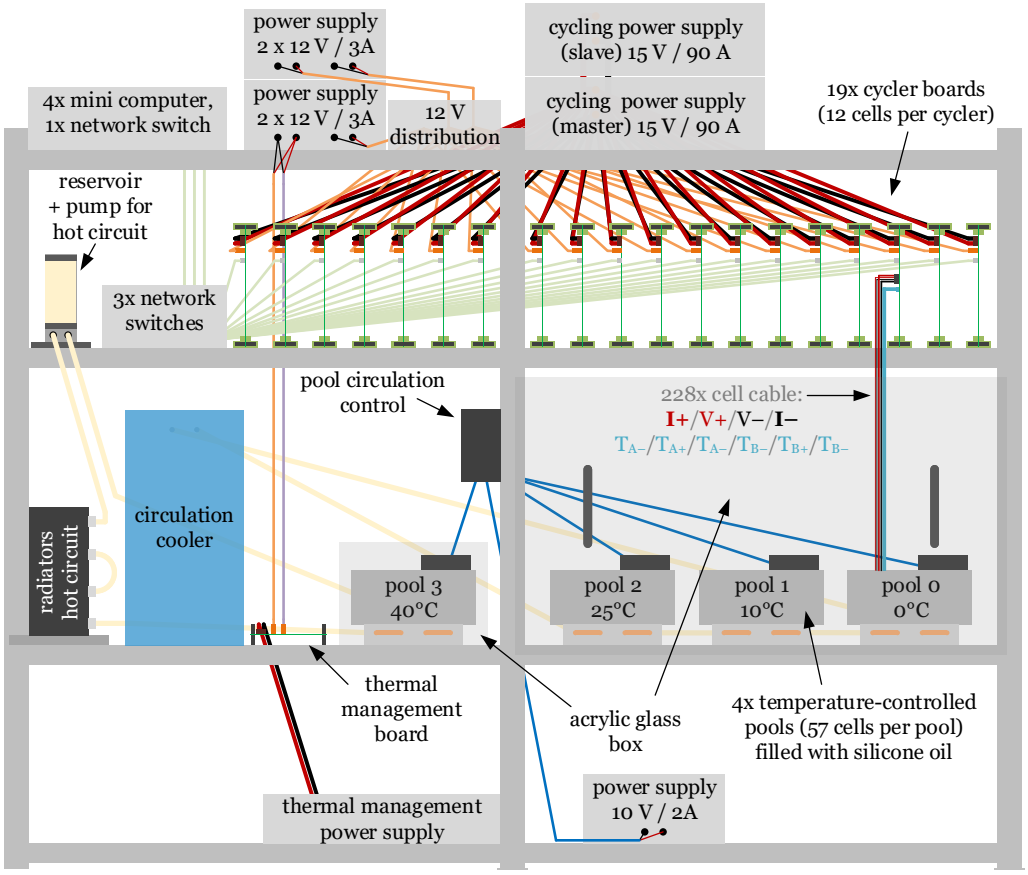

Figure A.9: Detailed overview of the battery aging test bench

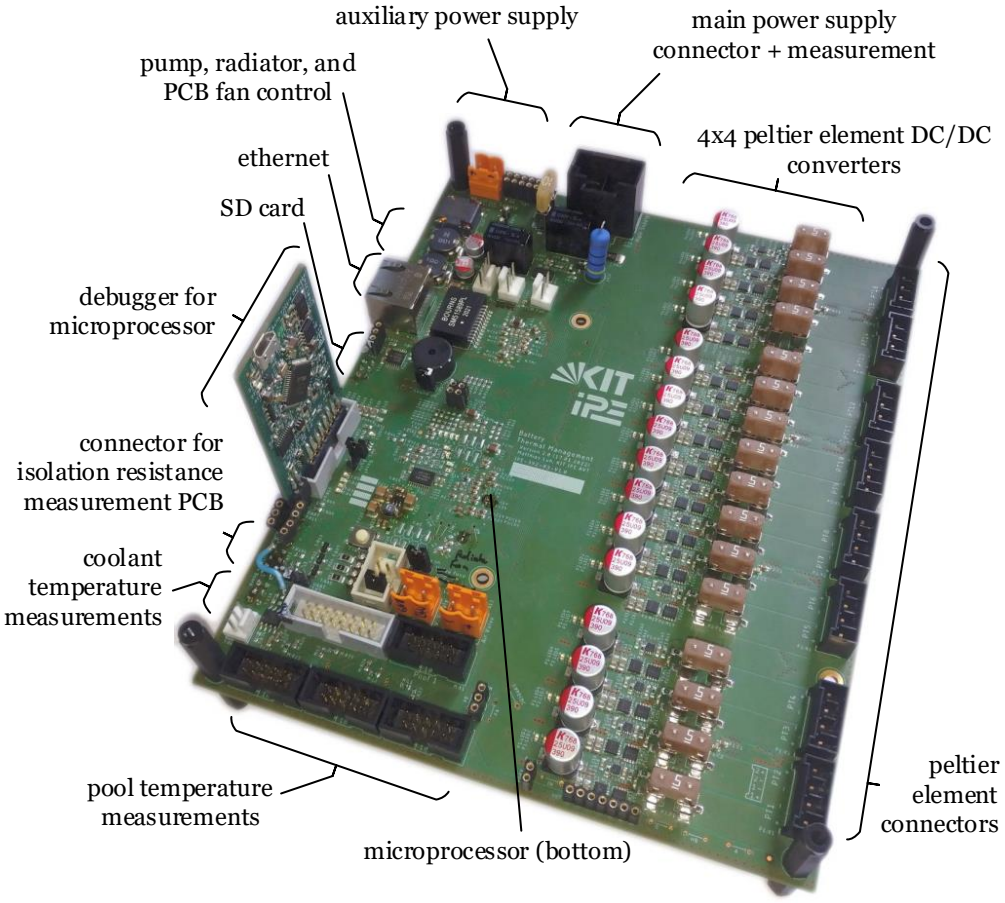

Figure A.10: Battery thermal management board that controls the pool temperatures

A.9 Battery aging model with uncertainty estimation

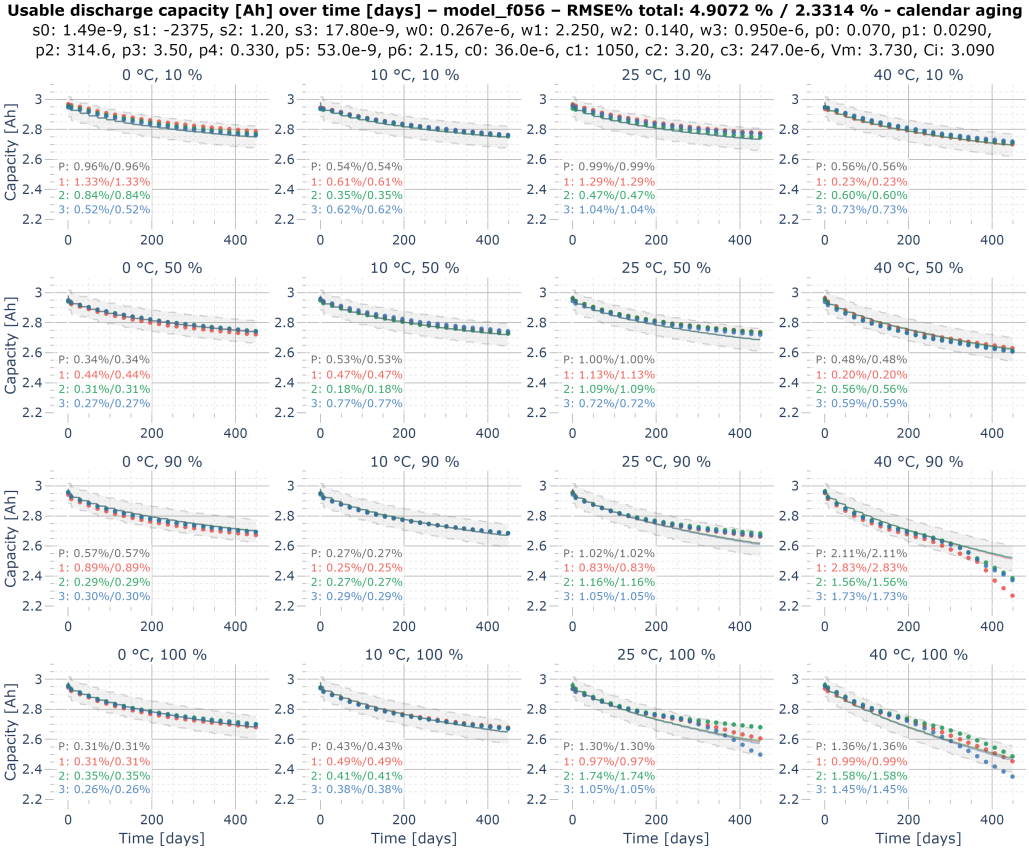

Figure A.11: Remaining usable discharge capacity of the calendar aging cells measured in the CUs (points) with simulated "realistic" aging model (lines) and uncertainty range (gray area — most optimistic model to most pessimistic model)

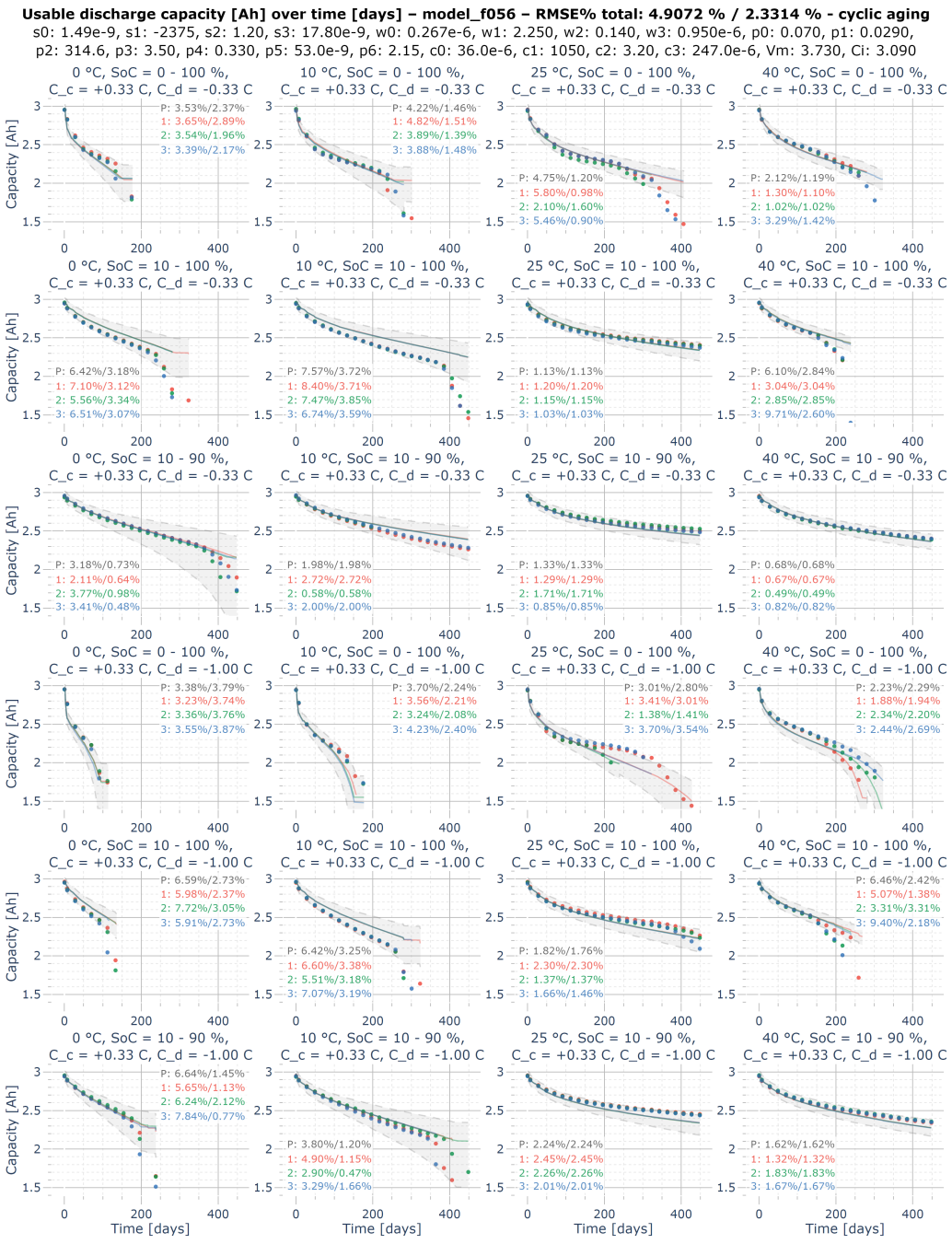

Figure A.12: Remaining usable discharge capacity of the cyclic aging cells (part 1 of 2) measured in the CUs (points) with simulated "realistic" aging model (lines) and uncertainty range (gray area)

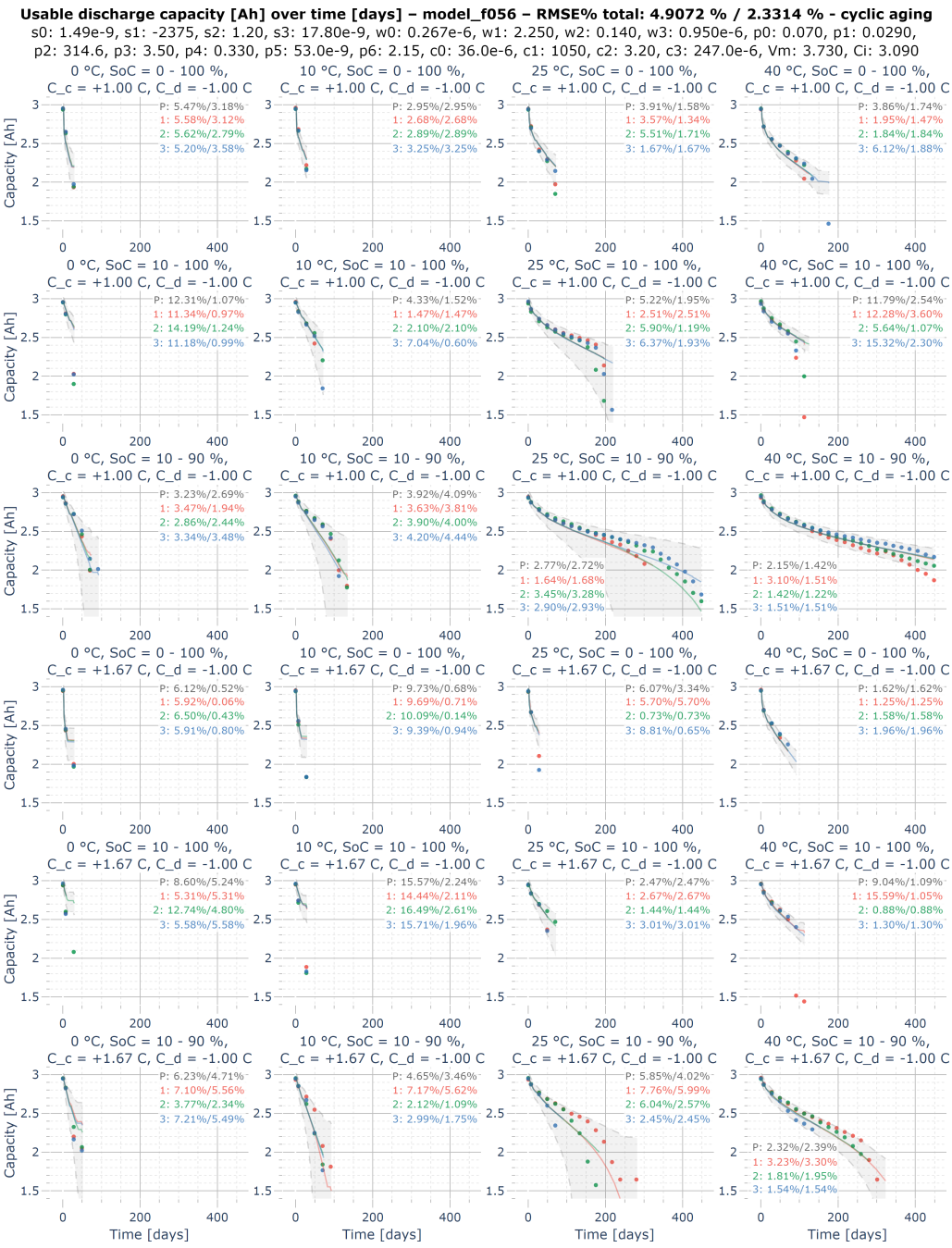

Figure A.13: Remaining usable discharge capacity of the cyclic aging cells (part 2 of 2) measured in the CUs (points) with simulated "realistic" aging model (lines) and uncertainty range (gray area)

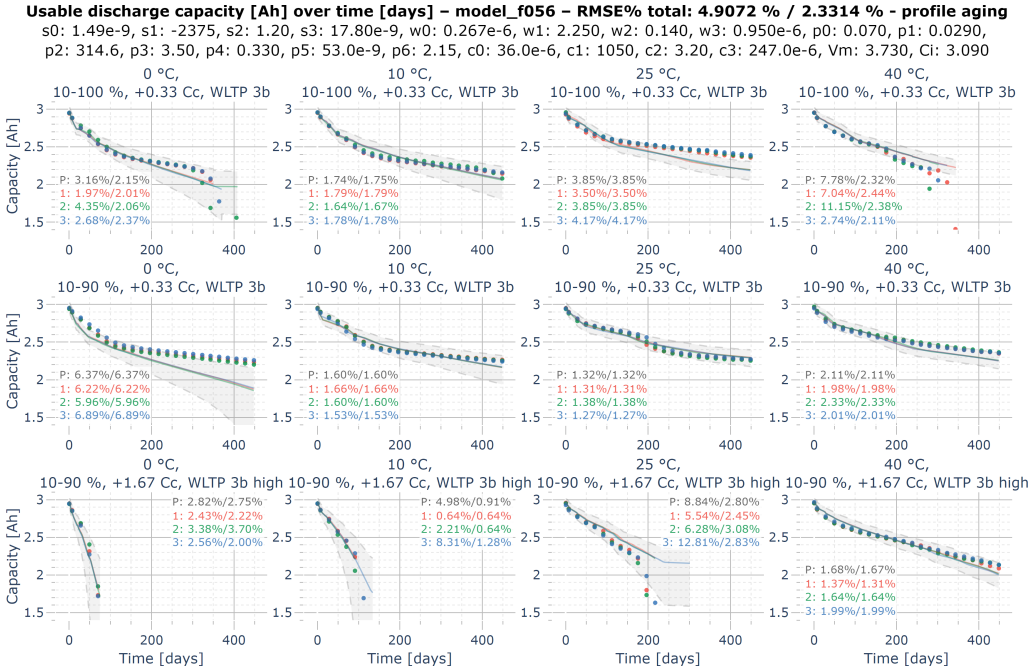

Figure A.14: Remaining usable discharge capacity of the profile aging cells measured in the CUs (points) with simulated "realistic" aging model (lines) and uncertainty range (gray area)

Acronyms and symbols

Acronyms

AC	alternating current
ACD	Automatic Connection Device
ADC	analog-to-digital converter
aFRR	Frequency Restoration Reserve with automatic activation
ANPC	active neutral point clamped
ARCPI	auxiliary resonant commutated pole inverter
BESS	battery electric storage system
BEV	battery electric vehicle
BMDV	Federal Ministry for Digital and Transport (*Bundesministerium für Digitales und Verkehr*)
BMS	battery management system
BOL	beginning of life
BPT	bidirectional power transfer
BTM	behind the meter
CAES	compressed air energy storage
CAN	Controller Area Network
CC	constant current
CCS	Combined Charging System
CEI	cathode-electrolyte interphase
CHAdeMO	Charge de Move
CIAP	constant instantaneous active power
CID	current interrupt device
CL	conductivity loss
CM	common mode
COP	coefficient of performance
CP	control pilot
CP-CV	constant power, constant voltage
CPO	charge point operator
CRC	cyclic redundancy check
CSO	charge system operator
CSR	current source rectifier
CU	check-up

CV	constant voltage
DAB	dual active bridge
DC	direct current
DDSRF	Decoupled Double Synchronous Reference Frame
DER	Distributed Energy Resources
DM	differential mode
DoD	Depth of Discharge
DR	demand response
DSM	demand-side management
DSO	distribution system operator
DSOGI	Double Second-Order Generalised Integrator
DUT	device under test
ECD	equivalent circuit diagram
ECM	equivalent circuit model
EFC	equivalent full cycle
EIS	electrochemical impedance spectroscopy
EMI	electromagnetic interference
EMS	energy management system
EMSP	electromobility service provider
ENTSO-E	European Network of Transmission System Operators for Electricity
EOC	end of charge
EOD	end of discharge
EOL	end of life
EREV	extended-range electric vehicles
EV	electric vehicle
EVSE	electric vehicle supply equipment
FACTS	flexible alternating current transmission systems
FCEV	fuel cell electric vehicle
FCHEV	fuel cell hybrid electric vehicle
FCR	Frequency Containment Reserve
FET	field-effect transistor $\rightarrow$ MOSFET
FHA	first harmonic approximation
FPGA	field-programmable gate array
FPT	forward power transfer
FRR	Frequency Restoration Reserve
FRT	fault ride-through
FTM	front of the meter
GaN	gallium nitride
GEIS	galvanostatic electrochemical impedance spectroscopy
GFCI	ground fault circuit interrupter
GFL	grid-following $\rightarrow$ GFLI
GFLI	grid-following inverter

GFM	grid-forming → GFMI
GFMI	grid-forming inverter
GHG	greenhouse gas
G2V	Grid-to-Vehicle
HEV	hybrid electric vehicle
HRTIM	high resolution timer
IC	integrated circuit
HV	high voltage
HVDC	high-voltage direct current
HVRT	high-voltage ride-through
HW	hardware
IBR	inverter-based resource
ICCB	In-Cable Control Box
IC-CPD	In-Cable Control and Protection Device
ICE	internal combustion engine
ICEV	internal combustion engine vehicle
IGBT	insulated gate bipolar transistor
IPCC	Intergovernmental Panel on Climate Change
ISR	interrupt service routine
IT	isolé terre
LAM	loss of active material
LCO	lithium cobalt oxide
LCOE	levelized cost of energy
LEV	light electric vehicle
LFP	lithium iron phosphate
Li	lithium
Li-ion	lithium-ion
LIB	lithium-ion battery
LLI	loss of lithium inventory
LMO	lithium manganese oxide
LTO	lithium titanium oxide
LPF	low-pass filter
LUT	lookup table
LV	low voltage
LVRT	low-voltage ride-through
mFRR	Frequency Restoration Reserve with manual activation
MMC	modular multilevel converter
MOSFET	metal-oxide-semiconductor field-effect transistor
NACS	North American Charging Standard
NCA	nickel cobalt aluminum
NF	notch filter
NiMH	nickel-metal hydride

NMC	nickel manganese cobalt
NPC	neutral point clamped
NTC	negative temperature coefficient
OBC	onboard charger
OCPP	Open Charge Point Protocol
OCV	open-circuit voltage
OEM	original equipment manufacturer
OT	operating temperature
OVP	over-voltage protection
PbA	lead-acid
PCB	printed circuit board
PCC	point of common coupling
PE	protective earth
PEIS	potentiostatic electrochemical impedance spectroscopy
PEV	plug-in electric vehicle
PFC	power factor correction
PHES	pumped hydroelectric energy storage
PHEV	plug-in hybrid electric vehicle
PHIL	power hardware-in-the-loop
PLC	power line communication
PLL	phase-locked loop
PnC	Plug and Charge
PP	proximity pilot
PSFB	phase-shifted full bridge
PtG	power-to-gas
PtL	power-to-liquid
PtH	power-to-heat
PtX	power-to-X
PV	photovoltaic
PWM	pulse width modulation
RCD	residual-current device
RE	renewable energy
REEV	range-extended electric vehicles
RES	renewable energy sources
RIPT	resonant inductive power transfer
RMS	root mean square
RMSE	root mean square error
RoCoF	Rate of Change of Frequency
RPT	reverse power transfer
RR	replacement reserve
RT	room temperature
RUL	remaining useful life

SEI	solid electrolyte interphase
Si	silicon
SIB	sodium-ion battery
SiC	silicon carbide
SMD	surface-mount device
SMGW	Smart Meter Gateway
SOA	safe operating area
SoC	State of Charge
SoE	State of Energy
SoH	State of Health
SoP	State of Power
SPI	Serial Peripheral Interface
SR	synchronous rectification
SRF	Synchronous Reference Frame
STATCOM	static synchronous compensator
SVM	space vector modulation
SW	software
TNPC	T-type neutral point clamped
TSO	transmission system operator
UART	Universal Asynchronous Receiver/Transmitter
UNFCCC	United Nations Framework Convention on Climate Change
V1G	Smart charging
V2B	Vehicle-to-Building
V2C	Vehicle-to-Community
V2G	Vehicle-to-Grid
V2H	Vehicle-to-Home
V2L	Vehicle-to-Load
V2V	Vehicle-to-Vehicle
V2X	Vehicle-to-X
VI	virtual inertia
VPP	Virtual Power Plant
VSG	Virtual Synchronous Generator
VSI	voltage source inverter
WLTC	Worldwide Light-duty Test Cycle
WLTP	Worldwide harmonized Light vehicles Test Procedure
WPT	wireless power transfer
ZCS	zero-current switching
VGI	Vehicle-Grid Integration
ZEV	Zero-Emission Vehicle
ZVS	zero-voltage switching

Constants

π	Pi: $3.14159\ldots$
F	Faraday constant: $96485.3\ldots\ \frac{C}{mol}$
R_g	universal gas constant: $8.31446\ldots\ \frac{J}{K \cdot mol}$

Operators, math symbols, and indices

X	constant or DC value
x	variable or AC value
$\underline{x}$	complex value or phasor
$\vec{x}$	vector
$\hat{X}$	amplitude
$\|X\|$	absolute value
$Re\{\underline{x}\}$	real part of a complex value
$Im\{\underline{x}\}$	imaginary part of a complex value
$\frac{dx}{dt}$	temporal derivative
x_α	alpha component (Clarke transformation)
x_β	beta component (Clarke transformation)
x_0	zero-sequence component (Clarke transformation)
x_d	direct component (Park transformation)
x_q	quadrature component (Park transformation)
x_{d+}	positive-sequence direct component
x_{q+}	positive-sequence quadrature component
x_{d-}	negative-sequence direct component
x_{q-}	negative-sequence quadrature component
x'	decoupled value
$\bar{x}$	filtered value
$\tilde{x}$	average value or notch-filtered value
X_{bat}	associated with a battery system
X_c	charging
X_{cal}	associated with calendar aging or value for calendar aging cells

X_{cap}	capacity-based
X_{cell}	associated with a battery cell
X_{co}	cut-off (termination of charging/discharging if current falls below this threshold)
X_{CU}	value during check-ups
X_{cyc}	associated with cyclic aging or value for cyclic aging cells
X_{d}	discharging
X_{est}	estimated value
X_{high}	higher threshold
X_{imp}	impedance-based
X_{init}	initial value
X_{L}	losses (e.g., capacity fade)
X_{low}	lower threshold
X_{LSB}	value of the least significant bit (LSB), i.e., the resolution
X_{max}	maximum value
X^{meas}	measured value
X_{mid}	center or average value
X_{min}	minimum value
X^{model}	modeled value
X_{n}	nominal value
X_{param}	associated with a parameter set
X_{peak}	peak value
X_{pl}	associated with lithium plating losses
X_{prf}	value for profile aging cells
X_{ref}	reference value
X_{rel}	relative value
X_{RMS}	root mean square value
X_{SEI}	associated with solid electrolyte interphase (SEI) losses
X^{set}	setpoint value
X_{ths}	threshold value
X_{tot}	total/overall

Latin symbols and variables

Ah	overall charge throughput
C	capacitance or C-rate (relative to the nominal cell capacity)
C_c	charging rate (relative to the nominal cell capacity)
C_d	discharging rate (relative to the nominal cell capacity)
C_n	nominal capacity
c_{rel}	C-rate relative to the remaining usable cell capacity
$C_{rem,usable}$	remaining usable cell capacity
C_{th}	thermal capacity
d	desire/preference to charge or discharge
DoD	Depth of Discharge
e	emission factor of the electricity mix
E_a	activation energy
f	frequency
f_{ctrl}	control loop frequency
f_g	grid frequency
f_{sw}	switching frequency
F_x	normalized switching frequency
g	grid condition
G	gain or transfer function
H	inertia constant
i	current
I_{cell}	battery cell current
i_D	MOSFET drain current
I_{DC}	DC current
I_{in}	DC input current
i_{res}	resonant tank current
I_{out}	DC output current
i_{out}	output current
i_{PCC}	point of common coupling current
J	moment of inertia

K	resonant tank gain
k_D	damping constant of the VSG controller
k_I	inertia constant of the VSG controller
K_i	integral gain of a PI controller
K_p	proportional gain of a PI controller
L	inductance
M	overall gain
N	number of cycles
$N_{CU,cell}$	number of check-ups for a specific cell
N_{cells}	number of cells
N_{param}	number of parameter sets
p	electricity price
P	active power
P_{aux}	auxiliary power demand (e.g., for the controller and cooling)
P_{DC}	DC power
P_{in}	input power
P_{loss}	power loss (dissipation)
P_{out}	output power
Q	reactive power or quality factor of a filter or battery charge/capacity
Δq	relative charged/discharged charge (in % of C_n) in the last time step
ΔQ	charged/discharged charge (in Ah) in the last time step or since charging/discharging began
q_L	relative capacity loss (in % of C_n)
Q_L	absolute capacity loss (in Ah)
Δq_L	relative capacity loss (in % of C_n) in the last time step
ΔQ_L	absolute capacity loss (in Ah) in the last time step
Q_{Li}	capacity loss due to loss of lithium inventory (LLI)
Q_{sites}	capacity loss due to a loss of electrode sites
r	residual load
R	resistance
R_{cell}	internal cell resistance

$R_{DS,on}$	on-state drain-source resistance of a MOSFET
r_{eff}	effective relative cell resistance
R_{load}	load resistance
R_{th}	thermal resistance
$RMSE$	root mean square error (absolute value)
$RMSE\%$	root mean square error (relative to the nominal cell capacity)
S	apparent power
SoC	State of Charge
SoC_{scaled}	State of Charge normalized to a certain operation window
SoC_t	time-dependent State of Charge
SoE	State of Energy
t	time
T	period or temperature
$T_{ambient}$	ambient air/coolant temperature
T_{ctrl}	control loop period
t_{dead}	dead time
T_i	time constant of a PI controller
t_{pd}	propagation delay
T_σ	time constant of a PT1 element
$T_{surface}$	surface temperature
T_{sw}	switching period
THD_i	total harmonic distortion of the current
v	voltage
V_{cell}	battery cell terminal voltage
V_{DC}	DC voltage
v_{DS}	MOSFET drain-source voltage
V_F	diode forward voltage
v_g	grid voltage
V_{GS}	MOSFET gate-source voltage
V_{in}	DC input voltage
v_{LL}	phase-phase voltage

v_{L12}	voltage between phases 1 and 2
v_{LN}	phase-neutral voltage
v_{L1N}	voltage between phase 1 and neutral
V_{out}	DC output voltage
v_{PCC}	point of common coupling voltage
V_R	diode reverse voltage
v_{res}	resonant tank voltage
V_{SD}	MOSFET body diode forward voltage
V_-	anode potential
Wh	overall energy throughput
Z	impedance
Z_g	grid impedance

Greek symbols and variables

η	efficiency
$\eta_{overall}$	overall efficiency (including auxiliary power demand)
η_{power}	power electronics efficiency
θ_g	grid angle
φ	phase
φ_{vi}	phase shift between voltage and current
Φ_a^0	open-circuit/equilibrium anode potential
ω	angular frequency
ω_g	angular grid frequency

List of Figures

List of Tables

List of Publications

Conference contributions

[C1] Matthias Luh and Thomas Blank. Auxiliary Resonant Commutated Pole Inverter (ARCPI) with SiC MOSFETs for efficient Vehicle-to-Grid (V2G) charging. In *2021 23rd European Conference on Power Electronics and Applications (EPE'21 ECCE Europe)*, September 2021. DOI: 10.23919/EPE21ECCEEurope50061.2021.9570620.

[C2] Matthias Luh and Thomas Blank. Design and experimental verification of advanced control strategies to provide ancillary services with a bidirectional Vehicle-to-Grid (V2G) inverter. In *2023 25th European Conference on Power Electronics and Applications (EPE'23 ECCE Europe)*, September 2023. DOI: 10.23919/EPE23ECCEEurope58414.2023.10264565.

[C3] Matthias Luh, Thomas Blank, and Marc Weber. Bidirectional soft-switching DC/DC converter for highly efficient EV chargers: Comprehensive analysis of a 20 kW CLLLC converter prototype for Vehicle-to-Grid (V2G). In *PCIM Europe 2020; International Exhibition and Conference for Power Electronics, Intelligent Motion, Renewable Energy and Energy Management*, pages 1702–1709, Nuremberg, Germany, 2020.

[C4] Matthias Luh and Thomas Blank. Battery cycler to generate open li-ion cell aging data and models. In *2022 24th European Conference on Power Electronics and Applications (EPE'22 ECCE Europe)*, Hannover, Germany, September 2022.

[C5] Matthias Luh, Kaleb Phipps, Anthony Britto, Matthias Wolf, Marek Lutz, et al. High-resolution real-world electricity data from three microgrids in the global south. In *Proceedings of the Thirteenth ACM International Conference on Future Energy Systems*, e-Energy '22, pages 496–514, New York, NY, USA, June 2022. Association for Computing Machinery. ISBN 978-1-4503-9397-3. DOI: 10.1145/3538637.3539763.

Journal articles

[J1] Matthias Luh and Thomas Blank. Comprehensive battery aging dataset: capacity and impedance fade measurements of a lithium-ion NMC/C-SiO cell. *Scientific Data*, 11(1):1004, September 2024. ISSN 2052-4463. DOI: 10.1038/s41597-024-03831-x. Available online: https://www.nature.com/articles/s41597-024-03831-x. Nature Publishing Group.

Data and code repositories

[R1] Matthias Luh and Thomas Blank. Comprehensive battery aging dataset: capacity and impedance fade measurements of a lithium-ion NMC/C-SiO cell [dataset]. *RADAR4KIT*, 2024. DOI: 10.35097/1947.

[R2] Matthias Luh. Example scripts for using and visualizing the battery aging data (bat-age-data-scripts). *GitHub*, 2024. https://github.com/energystatusdata/bat-age-data-scripts, Accessed: 2024-06-01.

[R3] Matthias Luh. Optimization scripts for generating a battery degradation model from battery aging data (bat-age-model-optimization). *GitHub*, 2024. https://github.com/energystatusdata/bat-age-model-optimization, Accessed: 2024-06-18.

[R4] Matthias Luh. Battery aging model with Vehicle-to-Grid (V2G) / Smart Charging (V1G) use case models (bat-age-model). *GitHub*, 2024. https://github.com/energystatusdata/bat-age-model, Accessed: 2024-06-18.

[R5] Matthias Luh, Kaleb Phipps, Anthony Britto, Matthias Wolf, Marek Lutz, et al. High-Resolution Real-World Electricity Data from Three Microgrids in the Global South. *RADAR4KIT*, 2022. DOI: 10.5445/IR/1000143466.

Bibliography

[1] P.R. Shukla, J. Skea, R. Slade, A. Al Khourdajie, R. van Diemen, et al., editors. *IPCC: Climate Change 2022: Mitigation of Climate Change. Contribution of Working Group III to the Sixth Assessment Report of the Intergovernmental Panel on Climate Change*. Cambridge University Press, Cambridge, UK and New York, NY, USA, 2022. DOI: 10.1017/9781009157926.

[2] Willett Kempton and Steven E. Letendre. Electric vehicles as a new power source for electric utilities. *Transportation Research Part D: Transport and Environment*, 2(3):157–175, 1997. ISSN 1361-9209. DOI: 10.1016/S1361-9209(97)00001-1.

[3] Sai Sudharshan Ravi and Muhammad Aziz. Utilization of Electric Vehicles for Vehicle-to-Grid Services: Progress and Perspectives. *Energies*, 15(2):589, 2022. ISSN 1996-1073. DOI: 10.3390/en15020589.

[4] Paul Reynolds, Felicity Jones, Benjamin Lock, Nithin Rajavelu, Joe Phillips, et al. V2G global roadtrip: around the world in 50 projects. http://everoze.com/app/uploads/2018/10/UKPN001-S-01-H-V2G-global-review-compressed.pdf, 2018. Accessed: 2023-08-04.

[5] Benjamin K. Sovacool, Jonn Axsen, and Willett Kempton. The Future Promise of Vehicle-to-Grid (V2G) Integration: A Sociotechnical Review and Research Agenda. *Annual Review of Environment and Resources*, 42(1):377–406, 2017. DOI: 10.1146/annurev-environ-030117-020220.

[6] Lance Noel, Gerardo Zarazua de Rubens, Johannes Kester, and Benjamin K. Sovacool. Navigating expert skepticism and consumer distrust: Rethinking the barriers to vehicle-to-grid (V2G) in the Nordic region. *Transport Policy*, 76:67–77, 2019. ISSN 0967070X. DOI: 10.1016/j.tranpol.2019.02.002.

[7] Amin Ghazanfari and Christian Perreault. The Path to a Vehicle-to-Grid Future: Powering Electric Mobility Forward. *IEEE Industrial Electronics Magazine*, 16(3):4–13, 2022. ISSN 1941-0115. DOI: 10.1109/MIE.2021.3072602.

[8] Håvard Nymoen, Tim Kimpel, and Christopher Kaschade. Initiative „Bidirektionales Laden“: Positionspapier zu notwendigen regulatorischen Anpassungen im Kontext des bidirektionalen Ladens. https://ceco.de/user/pages/downloads/14.bidirektionales-laden-von-eautos-als-schlussel-zur-flexibilisierung-des-energiesystems/Initiative Bidirektionales Laden Positionspapier März 2022.pdf, 2022. Accessed: 2023-08-01.

[9] Our World in Data. Data on Energy. https://github.com/owid/energy-data, 2024. Accessed: 2024-04-08.

[10] Our World in Data. Global primary energy consumption by source. https://ourworldindata.org/grapher/global-energy-substitution, 2022. Accessed: 2023-05-15.

[11] Our World in Data. Electricity production by source. https://ourworldindata.org/grapher/electricity-prod-source-stacked, 2022. Accessed: 2023-05-15.

[12] Dave Jones, Sarah Brown, and Paweł Czyżak. European Electricity Review 2023. https://ember-climate.org/insights/research/european-electricity-review-2023/, 2023. Accessed: 2024-04-08.

[13] Ember. Yearly electricity data. https://ember-climate.org/data-catalogue/yearly-electricity-data/, 2024. Accessed: 2024-04-08.

[14] Energy Institute (EI), KPMG, Kearney, and Heriot-Watt University. *Statistical Review of World Energy 2023*. Energy Institute, 72 edition, 2023. ISBN 978 1 78725 379 7. Accessed: 2023-07-12.

[15] U.S. Energy Information Administration (EIA). Open Data. https://www.eia.gov/opendata/bulkfiles.php, 2024. Accessed: 2024-04-08.

[16] BP. Statistical Review of World Energy 2021 | 70th edition. https://www.bp.com/content/dam/bp/business-sites/en/global/corporate/pdfs/energy-economics/statistical-review/bp-stats-review-2021-full-report.pdf, 2021. Accessed: 2023-05-16.

[17] J. Skea, P. R. Shukla, A. Reisinger, R. Slade, M. Pathak, et al. IPCC: Summary for Policymakers. In P.R. Shukla, J. Skea, R. Slade, A. Al Khourdajie, R. van Diemen, et al., editors, *Climate Change 2022: Mitigation of Climate Change. Contribution of Working Group III to the Sixth Assessment Report of the Intergovernmental Panel on Climate Change*. Cambridge University Press, Cambridge, UK and New York, NY, USA, 2022. DOI: 10.1017/9781009157926.001.

[18] R. P. Allan, P. A. Arias, S. Berger, J. G. Canadell, C. Cassou, et al. Summary for Policymakers. In V. Masson-Delmotte, P. Zhai, A. Pirani, S.L. Connors, C. Péan, et al., editors, *Climate Change 2021: The Physical Science Basis. Contribution of Working Group I to the Sixth Assessment Report of the Intergovernmental Panel on Climate Change*. IPCC, 2021. DOI: 10.1017/9781009157896.001.

[19] David I. Armstrong McKay, Arie Staal, Jesse F. Abrams, Ricarda Winkelmann, Boris Sakschewski, et al. Exceeding 1.5°C global warming could trigger multiple climate tipping points. *Science*, 377 (6611):eabn7950, 2022. ISSN 0036-8075, 1095-9203. DOI: 10.1126/science.abn7950.

[20] United Nations. Paris Agreement - Status of Ratification. https://unfccc.int/process/the-paris-agreement/status-of-ratification. Accessed: 2024-04-08.

[21] United Nations. Paris Agreement. https://unfccc.int/sites/default/files/english_paris_agreement.pdf, 2015. Accessed: 2023-05-16.

[22] Our World in Data. Greenhouse gas emissions. https://ourworldindata.org/grapher/total-ghg-emissions, 2023. Accessed: 2024-04-08.

[23] Our World in Data. Data on CO2 and Greenhouse Gas Emissions. https://github.com/owid/co2-data, 2023. Accessed: 2024-04-08.

[24] Matthew W. Jones, Glen P. Peters, Thomas Gasser, Robbie M. Andrew, Clemens Schwingshackl, et al. National contributions to climate change due to historical emissions of carbon dioxide, methane and nitrous oxide. https://zenodo.org/records/7636699, 2023. DOI: 10.5281/zenodo.7636699.

[25] Matthew W. Jones, Glen P. Peters, Thomas Gasser, Robbie M. Andrew, Clemens Schwingshackl, et al. National contributions to climate change due to historical emissions of carbon dioxide, methane, and nitrous oxide since 1850. *Scientific Data*, 10(1):155, 2023. ISSN 2052-4463. DOI: 10.1038/s41597-023-02041-1.

[26] Pierre Friedlingstein, Michael O'Sullivan, Matthew W. Jones, Robbie M. Andrew, Dorothee C. E. Bakker, et al. Global Carbon Budget 2023. *Earth System Science Data*, 15(12):5301–5369, 2023. ISSN 1866-3508. DOI: 10.5194/essd-15-5301-2023.

[27] Joyeeta Gupta. A history of international climate change policy. *WIREs Climate Change*, 1(5): 636–653, 2010. ISSN 1757-7799. DOI: 10.1002/wcc.67.

[28] Hannah Ritchie. Primary, secondary, final, and useful energy: Why are there different ways of measuring energy? https://ourworldindata.org/energy-definitions, 2022. Accessed: 2023-05-17.

[29] T.W. Brown, T. Bischof-Niemz, K. Blok, C. Breyer, H. Lund, et al. Response to 'Burden of proof: A comprehensive review of the feasibility of 100% renewable-electricity systems'. *Renewable and Sustainable Energy Reviews*, 92:834–847, 2018. ISSN 13640321. DOI: 10.1016/j.rser.2018.04.113.

[30] Aiman Albatayneh, Mohammad N. Assaf, Dariusz Alterman, and Mustafa Jaradat. Comparison of the Overall Energy Efficiency for Internal Combustion Engine Vehicles and Electric Vehicles. *Environmental and Climate Technologies*, 24(1):669–680, 2020. ISSN 2255-8837. DOI: 10.2478/rtuect-2020-0041.

[31] Stuart J. Self, Bale V. Reddy, and Marc A. Rosen. Geothermal heat pump systems: Status review and comparison with other heating options. *Applied Energy*, 101:341–348, 2013. ISSN 0306-2619. DOI: 10.1016/j.apenergy.2012.01.048.

[32] Matthias Schimmel, Pia Kerres, Korinna Jörling, Corinna Klessmann, Jonas Schröder, et al. Making renewable hydrogen cost-competitive: Policy instruments for supporting green H_2. https://static.agora-energiewende.de/fileadmin/Projekte/2020/2020_11_EU_H2-Instruments/A-EW_223_H2-Instruments_WEB.pdf, 2021. Accessed: 2023-05-17.

[33] Falko Ueckerdt, Christian Bauer, Alois Dirnaichner, Jordan Everall, Romain Sacchi, et al. Potential and risks of hydrogen-based e-fuels in climate change mitigation. *Nature Climate Change*, 11(5): 384–393, 2021. ISSN 1758-678X, 1758-6798. DOI: 10.1038/s41558-021-01032-7.

[34] Why did renewables become so cheap so fast? https://ourworldindata.org/cheap-renewables-growth, 2020. Accessed: 2023-05-17.

[35] Christian Breyer, Siavash Khalili, Dmitrii Bogdanov, Manish Ram, Ayobami Solomon Oyewo, et al. On the History and Future of 100% Renewable Energy Systems Research. *IEEE Access*, 10:78176–78218, 2022. ISSN 2169-3536. DOI: 10.1109/ACCESS.2022.3193402.

[36] Henning Meschede, Paul Bertheau, Siavash Khalili, and Christian Breyer. A review of 100% renewable energy scenarios on islands. *WIREs Energy and Environment*, n/a(n/a):e450, 2022. ISSN 2041-840X. DOI: 10.1002/wene.450.

[37] REN21. Global Overview. In *Renewables 2023 Global Status Report Collection*. REN21 Secretariat, Paris, 2023. ISBN 978-3-948393-11-3. Accessed: 2023-09-09.

[38] Lisa Mastny and Kelly Trumbull, editors. *Renewables 2022 Global Status Report*. REN21, Paris, 2022. ISBN 978-3-948393-04-5. Accessed: 2023-05-17.

[39] Bundesnetzagentur für Elektrizität, Gas, Telekommunikation, Post und Eisenbahnen. SMARD | Market data visuals. https://www.smard.de/en/marktdaten, 2024. Accessed: 2024-04-08.

[40] EEG 2023 – Gesetz für den Ausbau erneuerbarer Energien. https://www.gesetze-im-internet.de/eeg_2014/BJNR106610014.html, 2023. Accessed: 2023-06-21.

[41] WindSeeG – Gesetz zur Entwicklung und Förderung der Windenergie auf See. https://www.gesetze-im-internet.de/windseeg/BJNR231000016.html, 2023. Accessed: 2023-06-21.

[42] Bundesnetzagentur für Elektrizität, Gas, Telekommunikation, Post und Eisenbahnen. Statistiken erneuerbarer Energieträger. https://www.bundesnetzagentur.de/DE/Fachthemen/ElektrizitaetundGas/ErneuerbareEnergien/EE-Statistik/start.html, 2024. Accessed: 2024-04-03.

[43] Bundesministerium für Wirtschaft und Klimaschutz (BMWK). Zeitreihen zur Entwicklung der Erneuerbaren Energien in Deutschland. https://www.bmwk.de/Redaktion/DE/Dossier/erneuerbare-energien.html, 2023. Accessed: 2024-04-03.

[44] 50Hertz Transmission GmbH, Amprion GmbH, TenneT TSO GmbH, and TransnetBW GmbH. Netzentwicklungsplan Strom 2037/2045 (2023), zweiter Entwurf. https://www.netzentwicklungsplan.de/sites/default/files/2023-06/NEP_2037_2045_V2023_2_Entwurf_Teil1_2.pdf, 2023. Accessed: 2023-06-21.

[45] Jasmine Ramsebner, Reinhard Haas, Amela Ajanovic, and Martin Wietschel. The sector coupling concept: A critical review. *WIREs Energy and Environment*, 10(4):e396, 2021. ISSN 2041-840X. DOI: 10.1002/wene.396.

[46] Leonard Göke, Jens Weibezahn, and Mario Kendziorski. How flexible electrification can integrate fluctuating renewables. *Energy*, 278:127832, 2023. ISSN 0360-5442. DOI: 10.1016/j.energy.2023.127832.

[47] Volker Quaschning. Sektorkopplung durch die Energiewende. https://www.volker-quaschning.de/publis/studien/sektorkopplung/Sektorkopplungsstudie.pdf, 2016. Accessed: 2023-06-27.

[48] Julian Brandes, Markus Haun, Daniel Wrede, Patrick Jürgens, Christoph Kost, et al. Wege zu einem klimaneutralen Energiesystem - Die deutsche Energiewende im Kontext gesellschaftlicher Verhaltensweisen (Update November 2021: Klimaneutrailtät 2045). https://www.ise.fraunhofer.de/content/dam/ise/de/documents/publications/studies/Fraunhofer-ISE-Studie-Wege-zu-einem-klimaneutralen-Energiesystem-Update-Klimaneutralitaet-2045.pdf, 2021. Accessed: 2022-01-08.

[49] Fraunhofer-Institut für Solare Energiesysteme (ISE). Fraunhofer ISE Study 2021: Installed capacity of variable renewables (VRE) for electricity generation in Germany, scenario reference. https://energy-charts.info/charts/remod_installed_power/chart.htm?l=en&c=DE, 2021. Accessed: 2023-06-27.

[50] Steffen Fattler, Jochen Conrad, Anika Regett, Felix Böing, Andrej Guminski, et al. Dynamis - Dynamische und intersektorale Maßnahmenbewertung zur kosteneffizienten Dekarbonisierung des Energiesystems. https://www.ffe.de/wp-content/uploads/2019/11/Dynamis_Hauptbericht.pdf, 2019. Accessed: 2022-01-16.

[51] Katja Purr, Jens Günther, Harry Lehmann, and Philip Nuss. Wege in eine ressourcenschonende Treibhausgasneutralität (RESCUE - Studie). *Climate Change*, 36/2019(2. Auflage), 2021. ISSN 1862-4359. https://www.umweltbundesamt.de/sites/default/files/medien/1410/publikationen/rescue_studie_cc_36-2019_wege_in_eine_ressourcenschonende_treibhausgasneutralitaet_auflage2_juni-2021.pdf. Accessed: 2022-01-08.

[52] Martin Robinius, Peter Markewitz, Dilara Caglayan, Detlef Stolten, Peter Stenzel, et al. *Wege für die Energiewende: Kosteneffiziente und klimagerechte Transformationsstrategien für das deutsche Energiesystem bis zum Jahr 2050*, volume 499 of *Energie & Umwelt*. Forschungszentrum Jülich GmbH Zentralbibliothek, Verlag, 2020. ISBN 978-3-95806-483-6. Accessed: 2022-01-08.

[53] Thomas Bründlinger, Julian Elizalde König, Oliver Frank, Dietmar Gründig, Christoph Jugel, et al. Dena-Leitstudie Integrierte Energiewende - Impulse für die Gestaltung des Energiesystems bis 2050 (Langfassung). https://www.dena.de/fileadmin/dena/Dokumente/Pdf/9261_dena-Leitstudie_Integrierte_Energiewende_lang.pdf, 2018. Accessed: 2022-01-08.

[54] Philipp Gerbert, Patrick Herhold, Jens Burchardt, Stefan Schönberger, Florian Rechenmacher, et al. Klimapfade für Deutschland. https://www.zvei.org/fileadmin/user_upload/Presse_und_Medien/Publikationen/2018/Januar/Klimapfade_fuer_Deutschland_BDI-Studie_/Klimapfade-fuer-Deutschland-BDI-Studie-12-01-2018.pdf, 2018. Accessed: 2022-01-08.

[55] Fraunhofer ISE. Annual renewable share of public net electricity generation in Germany. https://energy-charts.info/charts/renewable_share/chart.htm?l=en&c=DE&interval=year, 2023. Accessed: 2023-07-11.

[56] Yigang Kong, Zhigang Kong, Zhiqi Liu, Congmei Wei, Jingfang Zhang, et al. Pumped storage power stations in China: The past, the present, and the future. *Renewable and Sustainable Energy Reviews*, 71:720–731, 2017. ISSN 1364-0321. DOI: 10.1016/j.rser.2016.12.100.

[57] Bundesnetzagentur für Elektrizität, Gas, Telekommunikation, Post und Eisenbahnen and Bundeskartellamt. Monitoringbericht 2022. https://www.bundesnetzagentur.de/SharedDocs/Mediathek/Monitoringberichte/MonitoringberichtEnergie2022.pdf?__blob=publicationFile&v=3, 2022. Accessed: 2023-07-11.

[58] WD 8: Umwelt, Naturschutz, Reaktorsicherheit, Bildung und Forschung. Entwicklung der Stromspeicherkapazitäten in Deutschland von 2010 bis 2016. https://www.bundestag.de/resource/blob/496062/759f6162c9fb845aa0ba7d51ce1264f1/wd-8-083-16-pdf-data.pdf, 2017. Accessed: 2023-07-05.

[59] Peter Stenzel, Kevin Knosala, Michael Zier, Jochen Linssen, Martin Robinius, et al. Energiespeicher. *BWK: das Energie-Fachmagazin*, 72(8-9):34–47, 2020. DOI: 10.37544/1618-193X-2020-08-09-34.

[60] Stephan Heimerl and Beate Kohler. Aktueller Stand der Pumpspeicherkraftwerke in Deutschland. *Wasserwirtschaft*, 107(10):77–79, 2017. ISSN 0043-0978, 2192-8762. DOI: 10.1007/s35147-017-0169-2.

[61] Peter Stenzel, Kevin Knosala, Michael Zier, Jochen Linssen, Martin Robinius, et al. Kraftwerkdatenbank PSW Deutschland April 2020. https://www.researchgate.net/publication/344298476_Kraftwerkdatenbank_PSW_Deutschland_April_2020pdf, 2020. Accessed: 2023-07-05.

[62] Thomas Klaus, Carla Vollmer, Kathrin Werner, Harry Lehmann, and Klaus Müschen. Energieziel 2050: 100% Strom aus erneuerbaren Quellen. https://www.umweltbundesamt.de/sites/default/files/medien/378/publikationen/energieziel_2050.pdf, 2010. Accessed: 2023-07-05.

[63] Bjarne Steffen. Prospects for pumped-hydro storage in Germany. *Energy Policy*, 45:420–429, 2012. ISSN 03014215. DOI: 10.1016/j.enpol.2012.02.052.

[64] Energiewirtschaftsgesetz vom 7. Juli 2005 (BGBl. I S. 1970; 3621), das zuletzt durch Artikel 1 des Gesetzes vom 22. Mai 2023 (BGBl. 2023 I Nr. 133) geändert worden ist. https://www.gesetze-im-internet.de/enwg_2005/BJNR197010005.html, 2023. Accessed: 2023-07-11.

[65] Alstom Hydro France, Électricité de France S.A., Elia System Operator, Alstom Grid SAS, Imperial College of Science, Technology and Medicine, et al. Overview of potential locations for new Pumped Storage Plants in EU 15, Switzerland and Norway. http://web.archive.org/web/20201112034701/http://www.estorage-project.eu/wp-content/uploads/2013/06/eStorage_D4.2-Overview-of-potential-locations-for-new-variable-PSP-in-Europe.pdf, 2015. Accessed: 2023-07-06.

[66] Timo Kern, Kirstin Ganz, and Louisa Wasmeier. Deutsche Strompreise im Jahr 2022 an der Börse EPEX Spot. https://www.ffe.de/veroeffentlichungen/deutsche-strompreise-an-der-boerse-epex-spot-im-jahr-2022/, 2023. Accessed: 2023-07-06.

[67] Jan Figgener, Christopher Hecht, and Dirk Uwe Sauer. Battery Charts. https://battery-charts.rwth-aachen.de/main-page/, 2024. Accessed: 2024-04-14.

[68] Jan Figgener, Christopher Hecht, Jakob Bors, Kai Spreuer, Kai-Philipp Kairies, et al. The development of battery storage systems in Germany: A market review (status 2023), 2023. DOI: 10.48550/arXiv.2203.06762.

[69] Fraunhofer-Institut für Solare Energiesysteme (ISE). Fraunhofer ISE Study 2021: Installed storage capacity in Germany, scenario reference. https://energy-charts.info/charts/remod_installed_power/chart.htm?l=en&c=DE&source=storage, 2021. Accessed: 2023-07-10.

[70] Christopher Hecht, Kai Gerd Spreuer, Jan Figgener, and Dirk Uwe Sauer. Market Review and Technical Properties of Electric Vehicles in Germany. *Vehicles*, 4(4):903–916, 2022. ISSN 2624-8921. DOI: 10.3390/vehicles4040049.

[71] Christopher Hecht, Jan Figgener, and Dirk Uwe Sauer. Mobility Charts. https://mobility-charts.rwth-aachen.de/?page_id=531, 2024. Accessed: 2024-04-10.

[72] Kraftfahrt-Bundesamt (KBA). Bestand an Kraftfahrzeugen und Kraftfahrzeuganhängern nach Bundesländern, Fahrzeugklassen und ausgewählten Merkmalen, 1. Januar 2024 (FZ 27). https://www.kba.de/DE/Statistik/Fahrzeuge/Bestand/Umwelt/umwelt_node.html, 2024. Accessed: 2024-04-20.

[73] Henok Behabtu, Maarten Messagie, Thierry Coosemans, Maitane Berecibar, Kinde Fante, et al. A Review of Energy Storage Technologies' Application Potentials in Renewable Energy Sources Grid Integration. *Sustainability*, 12:10511, 2020. DOI: 10.3390/su122410511.

[74] A. G. Olabi, C. Onumaegbu, Tabbi Wilberforce, Mohamad Ramadan, Mohammad Ali Abdelkareem, et al. Critical review of energy storage systems. *Energy*, 214:118987, 2021. ISSN 0360-5442. DOI: 10.1016/j.energy.2020.118987.

[75] Abraham Alem Kebede, Theodoros Kalogiannis, Joeri Van Mierlo, and Maitane Berecibar. A comprehensive review of stationary energy storage devices for large scale renewable energy sources grid integration. *Renewable and Sustainable Energy Reviews*, 159:112213, 2022. ISSN 13640321. DOI: 10.1016/j.rser.2022.112213.

[76] Dirk Günther and Patrick Gniffke. Berechnung der Treibhausgasemissionsdaten für das Jahr 2022 gemäß Bundesklimaschutzgesetz. https://www.umweltbundesamt.de/sites/default/files/medien/361/dokumente/vjs_2022_-_begleitbericht_final_kurzfassung.pdf, 2023. Accessed: 2023-05-04.

[77] Deutsches Zentrum für Luft- und Raumfahrt e.V. (DLR) – Institut für Verkehrsforschung, Deutsches Institut für Wirtschaftsforschung Berlin e.V. (DIW), and Kraftfahrt-Bundesamt. Verkehr in Zahlen 2023/2024. https://bmdv.bund.de/SharedDocs/DE/Anlage/G/verkehr-in-zahlen23-24-pdf.pdf?__blob=publicationFile, 2024. Accessed: 2024-04-10.

[78] Christian Hochfeld, Alexander Jung, Anne Klein-Hitpaß, Dr. Urs Maier, Kerstin Meyer, et al. Transforming Transport to Ensure Tomorrow's Mobility. https://www.agora-verkehrswende.de/fileadmin/Projekte/2017/12_Thesen/Agora-Verkehrswende-12-Insights_EN_WEB.pdf, 2017. Accessed: 2023-05-05.

[79] Auke Hoekstra. The Underestimated Potential of Battery Electric Vehicles to Reduce Emissions. *Joule*, 3(6):1412–1414, 2019. ISSN 2542-4351. DOI: 10.1016/j.joule.2019.06.002.

[80] Claudia Kämper, Hinrich Helms, and Kirsten Biemann. Wie klimafreundlich sind Elektroautos? (Update Bilanz 2020). https://www.bmuv.de/fileadmin/Daten_BMU/Download_PDF/Verkehr/emob_klimabilanz_bf.pdf, 2020. Accessed: 2023-09-22.

[81] Martin Wietschel. Ein Update zur Klimabilanz von Elektrofahrzeugen. https://www.isi.fraunhofer.de/content/dam/isi/dokumente/sustainability-innovation/2020/WP-01-2020_EinUpdatezurKlimabilanzvonElektrofahrzeugen.pdf, 2020. Accessed: 2023-09-22.

[82] Georg Bieker. A global comparison of the life-cycle greenhouse gas emissions of combustion engine and electric passenger cars. https://www.team-bhp.com/forum/attachments/electric-cars/2310712d1653112667-things-consider-when-buying-electric-car-global-lca-passenger-cars-jul2021-0.pdf, 2021. Accessed: 2023-09-22.

[83] Georg Bieker, Cornelius Moll, Steffen Link, Patrick Plötz, and Peter Mock. More bang for the buck: A comparison of the life-cycle greenhouse gas emission benefits and incentives of plug-in hybrid and battery electric vehicles in Germany. https://theicct.org/wp-content/uploads/2022/03/ghg-benefits-incentives-ev-mar22.pdf, 2022. Accessed: 2023-09-22.

[84] Nil Patel, Akash Kumar Bhoi, Sanjeevikumar Padmanaban, and Jens Bo Holm-Nielsen, editors. *Electric Vehicles: Modern Technologies and Trends*. Green Energy and Technology. Springer Singapore, Singapore, 2021. ISBN 978-981-15-9250-8 / 978-981-15-9251-5. DOI: 10.1007/978-981-15-9251-5.

[85] DKE - Deutsche Kommission Elektrotechnik Elektronik Informationstechnik in DIN und VDE, VDE FNN - Forum Netztechnik/Netzbetrieb im VDE (FNN), BDEW - Bundesverband der Energie und Wasserwirtschaft e. V., VDA - Verband der Automobilindustrie e. V., ZVEH - Zentralverband der Deutschen Elektround Informationstechnischen Handwerke, et al. Technischer Leitfaden - Ladeinfrastruktur Elektromobilität. https://www.dke.de/resource/blob/988408/87ed1f99814536d66c99797a4545ad5d/technischer-leitfaden-ladeinfrastruktur-elektromobilitaet---version-4-data.pdf, 2021. Accessed: 2023-05-10.

[86] Wolfgang Hofheinz, Dennis Haub, Michael Zeyen, and VDE Verlag. *Elektrische Sicherheit in der Elektromobilität: Grundlagen, Anwendung und Wirkungsweise von Maßnahmen zum Schutz gegen elektrischen Schlag in der Elektromobilität : DIN VDE 0100-100, DIN VDE 0100-410, DIN VDE 0100-530, DIN VDE 0100-722, DIN EN 61851-23 (VDE 0122-2-3), DIN EN IEC 61851-1 (VDE 0122-1), DIN IEC/TS 60479-1 (VDE V 0140-479-1), ISO 6469-3, ISO 17409 / Dipl.-Ing. Wolfgang Hofheinz, M. Eng. Dennis Haub, Dipl.-Ing. Michael Zeyen*. VDE Verlag GmbH, 2020. ISBN 978-3-8007-5284-3.

[87] Nationale Plattform Elektromobilität (NPE). Die Deutsche Normungs-Roadmap Elektromobilität 2020. https://www.din.de/blob/235248/600bb90a4d09f8ed9ccd4ec4ea7acdcb/roadmap-2020-data.pdf, 2017. Accessed: 2019-04-25.

[88] DIN EN IEC 61851-1:2019-12 (VDE 0122-1:2019-12): Konduktive Ladesysteme für Elektrofahrzeuge - Teil 1: Allgemeine Anforderungen (IEC 61851-1:2017); Deutsche Fassung EN IEC 61851-1:2019, 2019.

[89] Mehrnaz Farzam Far, Mikko Pihlatie, Marko Paakkinen, Marko Antila, and Aida Abdulah. Pre-Normative Charging Technology Roadmap for Heavy-Duty Electric Vehicles in Europe. *Energies*, 15(7):2312, 2022. ISSN 1996-1073. DOI: 10.3390/en15072312.

[90] Geetha Palani and Usha Sengamalai. A critical review on inductive wireless power transfer charging system in electric vehicle. *Energy Storage*, page e407, 2022. ISSN 2578-4862. DOI: 10.1002/est2.407.

[91] Isabel Carrilero, Manuela González, David Anseán, Juan C. Viera, Joaquín Chacón, et al. Redesigning European Public Transport: Impact of New Battery Technologies in the Design of Electric Bus Fleets. *Transportation Research Procedia*, 33:195–202, 2018. ISSN 2352-1465. DOI: 10.1016/j.trpro.2018.10.092.

[92] Arjan Keizer, Hauke Engel, Marte Guldemond, Jasper van, de Staaij, et al. The European electric bus market is charging ahead, but how will it develop? *McKinsey Energy Insights*, 2018.

[93] Jonas Leserer. Charging by Pantograph - Short Charging Break for Electric Commercial Vehicles. https://cdn.vector.com/cms/content/know-how/_technical-articles/Emobility_Pantograph_ElektronikAutomotive_202010_PressArticle_EN.pdf, 2021. Accessed: 2023-05-10.

[94] L. Brunton. The trolleybus story. *IEE Review*, 38(2):57–61, 1992. ISSN 0953-5683. DOI: 10.1049/ir:19920024.

[95] Marcin Połom. Transformations of Trolleybus Transport in Belarus, Russia and Ukraine in 1990–2020. In Walter Leal Filho, Eugene V. Krasnov, and Dara V. Gaeva, editors, *Innovations and Traditions for Sustainable Development*, World Sustainability Series, pages 429–444. Springer International Publishing, Cham, 2021. ISBN 978-3-030-78825-4. DOI: 10.1007/978-3-030-78825-4_26.

[96] Christiane Köllner. Pro und Contra Oberleitungs-Lkw. https://www.springerprofessional.de/schwere-lkw/emissionen/pro-und-contra-oberleitungs-lkw/17781332, 2020. Accessed: 2023-05-10.

[97] Ministerium für Verkehr Baden-Württemberg. Was ist eWayBW? https://ewaybw.de/de/ewaybw/. Accessed: 2023-05-10.

[98] Yongzhong Wu, Siyi Zhuge, Guoxin Han, and Wei Xie. Economics of Battery Swapping for Electric Vehicles—Simulation-Based Analysis. *Energies*, 15(5):1714, 2022. ISSN 1996-1073. DOI: 10.3390/en15051714.

[99] Patrick Schäfer. Nio eröffnet erste Batterietausch-Station in Deutschland. https://www.springerprofessional.de/batterie/ladeinfrastruktur/nio-eroeffnet-erste-batterietausch-station-in-deutschland/23575844, 2022. Accessed: 2023-05-10.

[100] Ralf Schütze. Elektroautos: Die neue Angst vor dem automobilen Stillstand. *DIE WELT*, 2011. https://www.welt.de/motor/article12368502/Die-neue-Angst-vor-dem-automobilen-Stillstand.html. Accessed: 2023-08-03.

[101] CHAdeMO Association. CHAdeMO - Association & protocol. https://www.chademo.com/wp2016/wp-content/uploads/2019/05/2019CHAdeMO_Brochure_web.pdf, 2019. Accessed: 2023-08-03.

[102] Jameson Dow. Europe passes two big laws to make EV charging a whole lot better. *Electrek*, 2023. https://electrek.co/2023/07/11/europe-passes-two-big-laws-to-make-ev-charging-a-whole-lot-better/. Accessed: 2023-08-04.

[103] Stacy Noblet. NACS Versus CCS: It's More Than A Connector. *Forbes*, 2023. https://www.forbes.com/sites/stacynoblet/2023/06/23/nacs-versus-ccs-its-more-than-a-connector/. Accessed: 2023-08-04.

[104] Mohamed Abogadallah. How Electric Vehicle Charging Connectors Differ by Region. *MUO*, 2023. https://www.makeuseof.com/ev-charging-connectors-region-differences/. Accessed: 2023-08-04.

[105] Bundesministerium für Wirtschaft und Energie. Verordnung über technische Mindestanforderungen an den sicheren und interoperablen Aufbau und Betrieb von öffentlich zugänglichen Ladepunkten für elektrisch betriebene Fahrzeuge1 (Ladesäulenverordnung - LSV). https://www.gesetze-im-internet.de/lsv/BJNR045700016.html, 2016. Accessed: 2023-05-10.

[106] DKE - Deutsche Kommission Elektrotechnik Elektronik Informationstechnik in DIN und VDE. DIN EN 62196-2:2017-11 (VDE 0623-5-2:2017-11): Stecker, Steckdosen, Fahrzeugkupplungen und Fahrzeugstecker - Konduktives Laden von Elektrofahrzeugen - Teil 2: Anforderungen und Hauptmaße für die Kompatibilität und Austauschbarkeit von Stift- und Buchsensteckvorrichtungen für Wechselstrom (IEC 62196-2:2016); Deutsche Fassung EN 62196-2:2017, 2017.

[107] DKE - Deutsche Kommission Elektrotechnik Elektronik Informationstechnik in DIN und VDE. DIN EN 62196-3:2015-05 (VDE 0623-5-3:2015-05): Stecker, Steckdosen und Fahrzeugsteckvorrichtungen - Konduktives Laden von Elektrofahrzeugen - Teil 3: Anforderungen an und Hauptmaße für Stifte und Buchsen für die Austauschbarkeit von Fahrzeugsteckvorrichtungen zum dedizierten Laden mit Gleichstrom und als kombinierte Ausführung zum Laden mit Wechselstrom/Gleichstrom (IEC 62196-3:2014); Deutsche Fassung EN 62196-3:2014, 2015.

[108] HARTING Automotive GmbH. Product Data Sheet: Mode-3 – Charging Cable. https://www.harting.com/sites/default/files/2022-03/TechnicalData_Mode3_ChargingCableType2-Type2_EN.pdf, 2022. Accessed: 2023-05-10.

[109] HARTING Automotive GmbH. Product Data Sheet: CCS Type-2 – Charging Cable. https://www.harting.com/sites/default/files/2022-03/Technical%20Data_Charging%20Cable%20CCS%20Type2_EN%20.pdf, 2022. Accessed: 2023-05-10.

[110] Open Charge Alliance (OCA). Downloads. https://www.openchargealliance.org/downloads/. Accessed: 2023-05-11.

[111] EEBus Initiative e.V. EEBUS-Specifications. https://www.eebus.org/media-downloads/. Accessed: 2023-05-11.

[112] OpenADR Alliance. OpenADR 2.0 Specifications. https://www.openadr.org/specification. Accessed: 2023-05-11.

[113] IEEE Communications Society. IEEE Standard for Smart Energy Profile Application Protocol. *IEEE Std 2030.5-2018 (Revision of IEEE Std 2030.5-2013)*, 2018. DOI: 10.1109/IEEESTD.2018.8608044.

[114] International Electrotechnical Commission (IEC). IEC 60870-5-104:2006+AMD1:2016 CSV Consolidated version: Telecontrol equipment and systems - Part 5-104: Transmission protocols - Network access for IEC 60870-5-101 using standardtransport profiles, 2016. Accessed: 2023-05-11.

[115] Severin Sylla, Adrian Ostermann, and Jeremias Hawran. Normenlandschaft für die Elektromobilität. https://www.ffe.de/veroeffentlichungen/normenlandschaft_fuer_die_elektromobilitaet/, 2023. Accessed: 2023-08-08.

[116] Myriam Neaimeh and Peter Bach Andersen. Mind the gap- open communication protocols for vehicle grid integration. *Energy Informatics*, 3(1):1, 2020. ISSN 2520-8942. DOI: 10.1186/s42162-020-0103-1.

[117] Roberto Metere, Myriam Neaimeh, Charles Morisset, Carsten Maple, Xavier Bellekens, et al. Securing the Electric Vehicle Charging Infrastructure. http://arxiv.org/abs/2105.02905, 2022. Accessed: 2023-05-11.

[118] Fabian Angerer. *Smart-Grid-Plattformarchitekturen Für Den Anwendungsbereich E-Mobility*. Diploma Thesis, Technische Universität Wien, Wien, 2022. https://repositum.tuwien.at/handle/20.500.12708/81143. Accessed: 2023-05-11.

[119] Lukas Schriewer and Daniel Reichert. Vehicle-to-Grid: Quo vadis? Readiness check of the technology landscape for integrating electric vehicles into the smart grid. In Johannes Liebl, editor, *Der Antrieb von morgen 2021*, pages 251–262, Berlin, Heidelberg, 2021. Springer. ISBN 978-3-662-63403-5. DOI: 10.1007/978-3-662-63403-5_17.

[120] Zoya Pourmirza and Sara Walker. Electric Vehicle Charging Station: Cyber Security Challenges and Perspective. In *2021 IEEE 9th International Conference on Smart Energy Grid Engineering (SEGE)*, pages 111–116, 2021. DOI: 10.1109/SEGE52446.2021.9535052.

[121] Doris Johnsen, Daniel Strommenger, Henning Schuster, Michael Lehmann, Philipp Laschet, et al. Gesteuertes Laden von Elektrofahrzeugen über Preisanreize - Anwendungsbeispiele und Handlungsbedarf. https://vdivde-it.de/sites/default/files/document/gesteuertes-laden-von-elektrofahrzeugen.pdf, 2020. Accessed: 2023-05-11.

[122] Robert Kohrs, Bernhard Wille-Haussmann, Sönke Rogalla, Roland Singer, Philipp Ernst, et al. Test von netzbildenden Wechselrichtern und rückspeisefähiger Ladeinfrastruktur: Kommunikations- und Hardwaretests für stabile Stromnetze mittels Hardware-in-the-Loop Prüfungen. *at - Automatisierungstechnik*, 70(12):1059–1071, 2022. ISSN 2196-677X. DOI: 10.1515/auto-2022-0036.

[123] European Commission, Directorate-General for Mobility and Transport. Report (Activity 1) of the STF Sub-group on Governance & Standards: Mapping of the discussion concerning standards and protocols for communication exchange in the electromobility ecosystem. *Publications Office*, 2022. DOI: 10.2832/6763.

[124] Lars Ostendorf, Doris Johnsen, Dr Mischa Bechberger, and Sandra Gensch. Steuerung von Ladevorgängen in der Elektromobilität (Darstellung der Kommunikationswege anhand einer Landkarte, Edition I). https://www.iit-berlin.de/wp-content/uploads/2022/10/Whitepaper_Gesteuertes-Laden-Erweiterte-Editin-1.pdf, 2022. Accessed: 2022-11-30.

[125] Kraftfahrt-Bundesamt (KBA). Bestand nach Zulassungsbezirken (FZ 1). https://www.kba.de/DE/Statistik/Produktkatalog/produkte/Fahrzeuge/fz1_b_uebersicht.html, 2024. Accessed: 2024-04-20.

[126] infas, DLR, IVT, and infas 360. Mobilität in Deutschland - MiD Ergebnisbericht (im Auftrag des BMVI). https://www.mobilitaet-in-deutschland.de/archive/pdf/MiD2017_Ergebnisbericht.pdf, 2018. Accessed: 2023-07-11.

[127] Bundesamt für Kartographie und Geodäsie (BKG). Verwaltungsgebiete 1:2 500 000, Stand 31.12. (VG2500 31.12.). https://gdz.bkg.bund.de/index.php/default/digitale-geodaten/verwaltungsgebiete/verwaltungsgebiete-1-2-500-000-stand-31-12-vg2500-12-31.html, 2023. Accessed: 2023-07-25.

[128] Paul Blickle, Christian Endt, David Gutensohn, Carla Grefe-Huge, Julian Stahnke, et al. Gehaltsvergleich: Was man in Deutschland wo verdient. *Die Zeit*, 2022. ISSN 0044-2070. https://www.zeit.de/arbeit/2022-09/gemeinde-gehalt-deutschland-vergleich-daten-entwicklung. Accessed: 2023-07-25.

[129] Carsten Bamberg, Jascha Lackner, Stefan Siegemund, and Alex Auf der Maur. dena-STUDIE: Privates Ladeinfrastrukturpotenzial in Deutschland. https://www.dena.de/fileadmin/dena/Publikationen/PDFs/2020/dena-STUDIE_Privates_Ladeinfrastrukturpotenzial_in_Deutschland.pdf, 2020. Accessed: 2023-07-19.

[130] Kraftfahrt-Bundesamt (KBA). Bestand an Kraftfahrzeugen und Kraftfahrzeuganhängern in den Jahren 1960 bis 2023 nach Fahrzeugklassen. https://www.kba.de/DE/Statistik/Fahrzeuge/Bestand/FahrzeugklassenAufbauarten/2023/b_fzkl_zeitreihen.html, 2023. Accessed: 2023-05-09.

[131] Kraftfahrt-Bundesamt (KBA). Anzahl zugelassener Pkw in Deutschland von 1960 bis 2023. https://de.statista.com/statistik/daten/studie/12131/umfrage/pkw-bestand-in-deutschland/, 2023. Accessed: 2023-05-09.

[132] Daniel Bönnighausen. Elektromobilität: Bestand wächst auf 240.000 E-Fahrzeuge. https://www.electrive.net/2020/03/02/elektromobilitaet-bestand-waechst-auf-240-000-e-fahrzeuge/, 2020. Accessed: 2023-05-09.

[133] Kraftfahrt-Bundesamt (KBA). Anzahl der Plug-In-Hybridautos in Deutschland von 2017 bis 2022. https://de.statista.com/statistik/daten/studie/1241084/umfrage/anzahl-der-hybridautos-in-deutschland/, 2023. Accessed: 2023-05-09.

[134] Mathias Brandt. Infografik: Eine Million E-Autos bis 2022? https://de.statista.com/infografik/4733/anzahl-von-elektroautos, 2019. Accessed: 2023-05-09.

[135] Celine Kuger and Benjamin Kibies. Dataforce Bestandsprognose: 15 Millionen-Ziel der Bundesregierung wird verfehlt. https://www.dataforce.de/news/dataforce-bestandsprognose-15-millionen-ziel-der-bundesregierung-wird-verfehlt/, 2022. Accessed: 2023-05-09.

[136] SPD, Bündnis 90/Die Grünen, and FDP. Mehr Fortschritt wagen - Bündnis für Freiheit, Gerechtigkeit und Nachhaltigkeit (Koalitionsvertrag). https://www.bundesregierung.de/resource/blob/974430/1990812/1f422c60505b6a88f8f3b3b5b8720bd4/2021-12-10-koav2021-data.pdf?download=1, 2021. Accessed: 2023-05-09.

[137] Fraunhofer-Institut für Solare Energiesysteme ISE. Fraunhofer ISE Studie 2021 - Antriebstechnologien im PKW-Verkehr. https://energy-charts.info/charts/remod_sector_data/chart.htm?l=de&c=DE&source=car, 2021. Accessed: 2023-05-09.

[138] Nationale Plattform Zukunft der Mobilität, Arbeitsgruppe 2 „Alternative Antriebe und Kraftstoffe für nachhaltige Mobilität". Roadmap – Markthochläufe alternativer Antriebe und Kraftstoffe aus technologischer Perspektive. https://www.plattform-zukunft-mobilitaet.de/wp-content/uploads/2021/04/NPM_AG2_Technologie_Roadmap.pdf, 2021. Accessed: 2023-05-09.

[139] Detlef Borscheid. Prognose: Mehr als elf Millionen Elektroautos und Plug-Ins bis 2030. https://www.autohaus.de/nachrichten/autohandel/prognose-mehr-als-elf-millionen-elektroautos-und-plug-ins-bis-2030-2697632, 2020. Accessed: 2023-05-09.

[140] Jörg Adolf, Stefan Rommerskirchen, Christoph Balzer, Arndt Joedicke, Uwe Schabla, et al. Shell PKW-Szenarien bis 2040 - Fakten, Trends und Perspektiven für Auto-Mobilität. https://www.prognos.com/sites/default/files/2021-01/140900_prognos_shell_studie_pkw-szenarien2040.pdf, 2014. Accessed: 2023-05-09.

[141] Kraftfahrt-Bundesamt (KBA). Neuzulassungen von Kraftfahrzeugen mit alternativem Antrieb im März 2024 (FZ 28). https://www.kba.de/DE/Statistik/Fahrzeuge/Neuzulassungen/Umwelt/n_umwelt_node.html, 2024. Accessed: 2024-04-20.

[142] Jochen Wieler. Elektroautos im Test: So hoch ist die Reichweite wirklich. https://www.adac.de/rund-ums-fahrzeug/elektromobilitaet/tests/stromverbrauch-elektroautos-adac-test/, 2023. Accessed: 2023-07-11.

[143] BurdaForward GmbH. Elektroautos 2023 - Aktuelle Modelle & Angebote in der Übersicht. https://efahrer.chip.de/elektroautos, 2023. Accessed: 2023-07-11.

[144] Sebastian Rivera, Samir Kouro, Sergio Vazquez, Stefan M. Goetz, Ricardo Lizana, et al. Electric Vehicle Charging Infrastructure: From Grid to Battery. *IEEE Industrial Electronics Magazine*, 15 (2):37–51, 2021. ISSN 1941-0115. DOI: 10.1109/MIE.2020.3039039.

[145] Marija Jankovic, Christian Felgemacher, Kevin Lenz, Aly Mashaly, and Abdelmouneim Charkaoui. Cost and efficiency considerations in On-board Chargers. In *2022 24th European Conference on Power Electronics and Applications (EPE'22 ECCE Europe)*. IEEE, 2022. ISBN 978-90-75815-40-5.

[146] Bundesnetzagentur für Elektrizität, Gas, Telekommunikation, Post und Eisenbahnen. Ladesäulenkarte - Downloads: Liste der Ladesäulen (Stand: 21.03.2024). https://www.bundesnetzagentur.de/DE/Fachthemen/ElektrizitaetundGas/E-Mobilitaet/Ladesaeulenkarte/start.html, 2024. Accessed: 2024-04-10.

[147] Daniel Hoh. Umstieg auf Elektromobilität: Wie viele Ladesäulen braucht Deutschland? *tagesschau*, 2023. https://www.tagesschau.de/wirtschaft/technologie/ladesaeulen-infrastruktur-elektromobilitaet-100.html. Accessed: 2023-07-31.

[148] Antonio Iliceto, Norela Constantinescu, Audrius Baranauskas, Rafal Czapaj, Kari Dalen, et al. ENTSO-E Position Paper on Electric Vehicle Integration into Power

Grids. https://eepublicdownloads.entsoe.eu/clean-documents/Publications/Positionpapersandreports/210331_Electric_Vehicles_integration.pdf, 2021. Accessed: 2023-09-28.

[149] G. T. Heydt. The Impact of Electric Vehicle Deployment on Load Management Straregies. *IEEE Transactions on Power Apparatus and Systems*, PAS-102(5):1253–1259, 1983. ISSN 0018-9510. DOI: 10.1109/TPAS.1983.318071.

[150] Charging Interface Initiative (CharIN) e. V. Grid Integration Levels (V5.2). https://www.charin.global/media/pages/technology/knowledge-base/60d37b89e2-1615552583/charin_levels__grid_integration_v5.2.pdf, 2020. Accessed: 2023-08-07.

[151] Netze BW GmbH. NETZlabore Elektromobilität. https://www.netze-bw.de/unsernetz/netzinnovationen/netzintegration-elektromobilitaet/netzlabore, 2022. Accessed: 2023-07-13.

[152] Netze BW GmbH. Die E-Mobility-Allee – Das Stromnetz-Reallabor zur Erforschung des zukünftigen E-Mobility-Alltags. https://assets.ctfassets.net/xytfb1vrn7of/6gXs8wiRSF0E2SqkwSq406/fc1c9430ba88b81c31e399242b09b17e/20191217_BroschuereE-Mobility_210x275mm_100Ansicht.pdf, 2019. Accessed: 2023-07-13.

[153] Netze BW GmbH. E-Mobility-Allee. https://www.netze-bw.de/e-mobility-allee, 2019. Accessed: 2023-07-13.

[154] Netze BW GmbH. 16 Monate unter Strom – Abschlussbericht zum NETZlabor E-Mobility-Carré. https://assets.ctfassets.net/xytfb1vrn7of/oGRGcuHKm3eaKEA2LDGic/3bd954234bf9339220bc6d6e6512cc6d/netzlabor-e-mobility-carree-abschlussbericht.pdf, 2022. Accessed: 2023-07-13.

[155] Netze BW GmbH. NETZlabor E-Mobility-Carré. https://www.netze-bw.de/unsernetz/netzinnovationen/netzintegration-elektromobilitaet/e-mobility-carre, 2020. Accessed: 2023-07-13.

[156] Netze BW GmbH. Zukunftsorientiert. Elektrisch. Mobil. Abschlussbericht zum NETZlabor E-Mobility-Chaussee. https://assets.ctfassets.net/xytfb1vrn7of/LKFK7LIHxW9nYxFlS1QxC/b8fff50d34043775189cd35c46ed9671/e-mobility-chaussee-abschlussbericht.pdf, 2022. Accessed: 2023-07-13.

[157] Netze BW GmbH. NETZlabor E-Mobility-Chaussee. https://www.netze-bw.de/unsernetz/netzinnovationen/netzintegration-elektromobilitaet/e-mobility-chaussee, 2020. Accessed: 2023-07-13.

[158] Netze BW GmbH. NETZlabor Intelligentes Heimladen. https://www.netze-bw.de/unsernetz/netzinnovationen/netzintegration-elektromobilitaet/intelligentes-heimladen#1-4, 2022. Accessed: 2023-07-13.

[159] ÖAMTC-Test: Wallboxen mit Lastmanagement. https://www.oeamtc.at/tests/elektromobilitaet/lastmanagement-2020/, 2020. Accessed: 2023-07-13.

[160] Melanie Baumann. Die besten Wallboxen mit Lastmanagement im Test Vergleich 2023 - Wallboxen mit Lastmanagement-System: Tests, Bewertung & Funktion. https://www.homeandsmart.de/wallboxen-mit-lastmanagement-test-vergleich, 2022. Accessed: 2023-07-13.

[161] Tom Swallow. Top 10: Charging management software solutions providers. https://evmagazine.com/top10/top-10-charging-management-software-solutions-providers, 2023. Accessed: 2023-07-13.

[162] gridX GmbH. Charging Report 2023. https://de.gridx.ai/resources/ev-charging-infrastructure-report-europe-2023, 2023. Accessed: 2023-07-14.

[163] Ida Marie Henriksen, William Throndsen, Marianne Ryghaug, and Tomas Moe Skjølsvold. Electric vehicle charging and end-user motivation for flexibility: A case study from Norway. *Energy, Sustainability and Society*, 11(1):44, 2021. ISSN 2192-0567. DOI: 10.1186/s13705-021-00319-z.

[164] Jaap Burger, Julia Hildermeier, Andreas Jahn, and Jan Rosenow. The time is now: Smart charging of electric vehicles. https://www.raponline.org/wp-content/uploads/2022/04/rap-jb-jh-smart-charging-europe-2022-april-26.pdf, 2022. Accessed: 2023-07-14.

[165] Jedlix. A sneak peek into tariff rates across countries. https://www.jedlix.com/blog/tariff-rates-accros-countries. Accessed: 2023-07-14.

[166] Department for Business, Energy & Industrial Strategy, Ofgem, and The Rt Hon Graham Stuart MP. New plan for smart electric vehicle (EV) charging could save consumers up to £1000 a year. https://www.gov.uk/government/news/new-plan-for-smart-electric-vehicle-ev-charging-could-save-consumers-up-to-1000-a-year, 2023. Accessed: 2023-07-13.

[167] KfW. Merkblatt: Ladestationen für Elektrofahrzeuge – Kommunen (Zuschuss 439). https://www.kfw.de/PDF/Download-Center/Förderprogramme-(Inlandsförderung)/PDF-Dokumente/6000004503_M_439_Ladestationen.pdf, 2022. Accessed: 2023-07-13.

[168] KfW. Merkblatt: Ladestationen für Elektroautos – Wohngebäude (Zuschuss 440). https://www.kfw.de/PDF/Download-Center/Förderprogramme-(Inlandsförderung)/PDF-Dokumente/6000004534_M_440_Ladestationen_Elektroautos.PDF, 2022. Accessed: 2023-07-13.

[169] KfW. Merkblatt: Ladestationen für Elektrofahrzeuge – Unternehmen (Zuschuss 441). https://www.kfw.de/PDF/Download-Center/Förderprogramme-(Inlandsförderung)/PDF-Dokumente/6000004939_M_441.pdf, 2022. Accessed: 2023-07-13.

[170] Bundesministerium für Wirtschaft und Klimaschutz (BMWK). Smart Meter-Gesetz final beschlossen: Flächendeckender Einsatz intelligenter Stromzähler kommt. https://www.bmwk.de/Redaktion/DE/Pressemitteilungen/2023/05/20230512-smart-meter-gesetz-final-beschlossen.html, 2023. Accessed: 2023-07-13.

[171] U.S. Department of Energy. Timeline: History of the Electric Car. https://www.energy.gov/timeline-history-electric-car. Accessed: 2023-08-07.

[172] California Air Resources Board (CARB). Zero-Emission Vehicle Program. https://ww2.arb.ca.gov/our-work/programs/zero-emission-vehicle-program/about, 2023. Accessed: 2023-08-07.

[173] Willett Kempton, Jasna Tomic, Steven Letendre, Alec Brooks, AC Propulsion, et al. Vehicle-to-Grid Power: Battery, Hybrid, and Fuel Cell Vehicles as Resources for Distributed Electric Power in California, 2001. UCD-ITS-RR-01-03.

[174] John O'Dell. GM Sues to Overturn State's Zero Emission Vehicle Mandate. *Los Angeles Times*, 2001. https://www.latimes.com/archives/la-xpm-2001-feb-24-fi-29699-story.html. Accessed: 2023-08-07.

[175] Benjamin K. Sovacool and Richard F. Hirsh. Beyond batteries: An examination of the benefits and barriers to plug-in hybrid electric vehicles (PHEVs) and a vehicle-to-grid (V2G) transition. *Energy Policy*, 37(3):1095–1103, 2009. ISSN 0301-4215. DOI: 10.1016/j.enpol.2008.10.005.

[176] Mark Vaughn. California's 2035 ZEV Mandate Poses Big Challenges. *Autoweek*, 2022. https://www.autoweek.com/news/green-cars/a39738488/california-wants-new-car-sales-to-be-zero-emissions-by-2035/. Accessed: 2023-08-07.

[177] California Energy Commission. New ZEV Sales in California. https://www.energy.ca.gov/data-reports/energy-almanac/zero-emission-vehicle-and-infrastructure-statistics/new-zev-sales, 2023. Accessed: 2023-08-07.

[178] Stefan Englberger, Kareem Abo Gamra, Benedikt Tepe, Michael Schreiber, Andreas Jossen, et al. Electric vehicle multi-use: Optimizing multiple value streams using mobile storage systems in a vehicle-to-grid context. *Applied Energy*, 304:117862, 2021. ISSN 0306-2619. DOI: 10.1016/j.apenergy.2021.117862.

[179] Nivedita Naik and C. Vyjayanthi. Optimization of Vehicle-to-Grid (V2G) Services for Development of Smart Electric Grid: A Review. In *2021 International Conference on Smart Generation Computing, Communication and Networking (SMART GENCON)*, 2021. DOI: 10.1109/SMARTGENCON51891.2021.9645903.

[180] Kotub Uddin, Tim Jackson, Widanalage D. Widanage, Gael Chouchelamane, Paul A. Jennings, et al. On the possibility of extending the lifetime of lithium-ion batteries through optimal V2G facilitated by an integrated vehicle and smart-grid system. *Energy*, 133:710–722, 2017. ISSN 0360-5442. DOI: 10.1016/j.energy.2017.04.116.

[181] Mathias Müller, Timo Kern, Adrian Ostermann, Patrick Dossow, Yannic Blume, et al. Bidirektionales Lademanagement - Abschlussbericht der FfE. http://ffe.de/wp-content/uploads/2023/03/BDL-Abschlussbericht.pdf, 2023. Accessed: 2023-09-04.

[182] Mehrdad Ehsani, Milad Falahi, and Saeed Lotfifard. Vehicle to Grid Services: Potential and Applications. *Energies*, 5(10):4076–4090, 2012. ISSN 1996-1073. DOI: 10.3390/en5104076.

[183] Lance Noel, Johannes Kester, Benjamin K. Sovacool, and Gerardo Zarazua de Rubens. *Vehicle-to-Grid: A Sociotechnical Transition Beyond Electric Mobility*. Energy, Climate and the Environment. Springer International Publishing : Imprint: Palgrave Macmillan, Cham, 1st ed. 2019 edition, 2019. ISBN 978-3-030-04864-8. DOI: 10.1007/978-3-030-04864-8.

[184] Ramteen Sioshansi and Paul Denholm. Emissions Impacts and Benefits of Plug-In Hybrid Electric Vehicles and Vehicle-to-Grid Services. *Environmental Science & Technology*, 43(4):1199–1204, 2009. ISSN 0013-936X. DOI: 10.1021/es802324j.

[185] Mehrdad Ebrahimi, Mohammad Rastegar, Mohammad Mohammadi, Alejandro Palomino, and Masood Parvania. Stochastic Charging Optimization of V2G-Capable PEVs: A Comprehensive Model for Battery Aging and Customer Service Quality. *IEEE Transactions on Transportation Electrification*, 6(3):1026–1034, 2020. ISSN 2332-7782. DOI: 10.1109/TTE.2020.3005875.

[186] Yang Zhao, Mehdi Noori, and Omer Tatari. Vehicle to Grid regulation services of electric delivery trucks: Economic and environmental benefit analysis. *Applied Energy*, 170:161–175, 2016. ISSN 0306-2619. DOI: 10.1016/j.apenergy.2016.02.097.

[187] Kotub Uddin, Matthieu Dubarry, and Mark B. Glick. The viability of vehicle-to-grid operations from a battery technology and policy perspective. *Energy Policy*, 113:342–347, 2018. ISSN 0301-4215. DOI: 10.1016/j.enpol.2017.11.015.

[188] Johannes Weniger, Nico Orth, Lucas Meissner, Cheyenne Schlüter, Jonas Meyne, et al. Energy Storage Inspection 2023. https://solar.htw-berlin.de/wp-content/uploads/HTW-Energy-Storage-Inspection-2023.pdf, 2023. Accessed: 2023-09-04.

[189] E. D. Tate and Peter J. Savagian. The CO2 Benefits of Electrification E-REVs, PHEVs and Charging Scenarios. In *SAE World Congress & Exhibition*, pages 2009–01–1311, 2009. DOI: 10.4271/2009-01-1311.

[190] Kraftfahrt-Bundesamt (KBA). Bestand an Personenkraftwagen nach Segmenten und Modellreihen am 1. Januar 2023 gegenüber 1. Januar 2022 (FZ 12). https://www.kba.de/DE/Statistik/Fahrzeuge/Bestand/Segmente/segmente_node.html, 2023. Accessed: 2023-07-18.

[191] NUVVE Holding Corp. How Nuvve's Vehicle-to-Grid (V2G) Technology and Electric School Buses Can Help Curb Power Blackouts. https://nuvve.com/v2g-and-electric-buses-can-help-curb-power-blackouts/, 2020. Accessed: 2023-08-02.

[192] Nuvve Holding Corp. Electric Bus Charging Solutions. https://nuvve.com/buses/, 2023. Accessed: 2023-08-02.

[193] Nuvve Holding Corp. Intelligently Electrify Your School Bus Fleet. https://nuvve.com/wp-content/uploads/2022/04/nuvve-school-bus-packet_lcfs_april2022.pdf, 2022. Accessed: 2023-08-02.

[194] Statistisches Bundesamt. Abhängig Erwerbstätige: Deutschland, Jahre (bis 2019), Beschäftigungsumfang, Geschlecht (Ergebnis 12211-9010). https://www-genesis.destatis.de/genesis/online?operation=previous&levelindex=1&step=1&titel=Ergebnis&levelid=1689757296916&acceptscookies=false#abreadcrumb, 2023-07-19T11:01:43+1:00. Accessed: 2023-07-19.

[195] Statistisches Bundesamt. 55 % in kleinen und mittleren Unternehmen tätig. https://www.destatis.de/DE/Themen/Branchen-Unternehmen/Unternehmen/Kleine-Unternehmen-Mittlere-Unternehmen/aktuell-beschaeftigte.html, 2023. Accessed: 2023-07-19.

[196] Statistisches Bundesamt (Destatis). Fachserie 5: Bauen und Wohnen - Reihe 3: Bestand an Wohnungen (31. Dezember 2021). https://www.destatis.de/DE/Themen/Gesellschaft-Umwelt/Wohnen/Publikationen/Downloads-Wohnen/bestand-wohnungen-2050300217005.xlsx?__blob=publicationFile, 2022. Accessed: 2023-07-20.

[197] Karlheinz Bozem, Anna Nagl, Verena Rath, and Alexander Haubrock. *Elektromobilität: Kundensicht, Strategien, Geschäftsmodelle*. Springer Fachmedien, Wiesbaden, 2013. ISBN 978-3-658-02627-1 978-3-658-02628-8. DOI: 10.1007/978-3-658-02628-8.

[198] Hao Tu, Hao Feng, Srdjan Srdic, and Srdjan Lukic. Extreme Fast Charging of Electric Vehicles: A Technology Overview. *IEEE Transactions on Transportation Electrification*, 5(4):861–878, 2019. ISSN 2332-7782, 2372-2088. DOI: 10.1109/TTE.2019.2958709.

[199] Benedict Mortimer, Christopher Olk, Gaurav Kumar Roy, Wilbert Rey Tarnate, Rik W. De Doncker, et al. *Fast-Charging Technologies, Topologies and Standards 2.0*, volume 11 of *E.ON Energy Research Center Series*. E.ON Energy Research Center, RWTH Aachen University, Aachen, 1 edition, 2019. ISSN: 1868-7415.

[200] AG Electrical Technology Co., Ltd. Will Electric Vehicles Remove Car Chargers? https://www.ag-elec.com/will-electric-vehicles-remove-car-chargers.html. Accessed: 2023-07-26.

[201] Sreeraj Arole. An EV Charging system discernment – electric cars without On-Board Chargers? https://evreporter.com/an-ev-charging-system-discernment-electric-cars-without-on-board-chargers/, 2022. Accessed: 2023-07-26.

[202] S.-L. Andersson, A.K. Elofsson, M.D. Galus, L. Göransson, S. Karlsson, et al. Plug-in hybrid electric vehicles as regulating power providers: Case studies of Sweden and Germany. *Energy Policy*, 38(6): 2751–2762, 2010. ISSN 03014215. DOI: 10.1016/j.enpol.2010.01.006.

[203] David Ciechanowicz, Martin Leucker, and Martin Sachenbacher. Ökonomische Bewertung von Vehicle-to-Grid in Deutschland. In *Proceedings of the Multikonferenz Wirtschaftsinformatik (MKWI)*, page 12, 2012.

[204] Alexander Schuller and Fabian Rieger. Assessing the Economic Potential of Electric Vehicles to Provide Ancillary Services: The Case of Germany. *Zeitschrift für Energiewirtschaft*, 37(3):177–194, 2013. ISSN 0343-5377, 1866-2765. DOI: 10.1007/s12398-013-0112-x.

[205] Gerald Broneske and David Wozabal. How Do Contract Parameters Influence the Economics of Vehicle-to-Grid? *Manufacturing & Service Operations Management*, 19(1):150–164, 2017. ISSN 1523-4614. DOI: 10.1287/msom.2016.0601.

[206] Timo Kern, Patrick Dossow, and Serafin von Roon. Integrating Bidirectionally Chargeable Electric Vehicles into the Electricity Markets. *Energies*, 13(21):5812, 2020. ISSN 1996-1073. DOI: 10.3390/en13215812.

[207] André Hackbarth, Benedikt Lunz, Reinhard Madlener, Dirk Uwe Sauer, and Rik W. De Doncker. Plug-in Hybrid Electric Vehicles for CO2-Free Mobility and Active Storage Systems for the Grid (Part 1). http://publications.rwth-aachen.de/record/561979/files/PHEV_Gesamt.pdf, 2010. ISSN: 1868-7415.

[208] Benedikt Tepe, Jan Figgener, Stefan Englberger, Dirk Uwe Sauer, Andreas Jossen, et al. Optimal pool composition of commercial electric vehicles in V2G fleet operation of various electricity markets. *Applied Energy*, 308:118351, 2022. ISSN 0306-2619. DOI: 10.1016/j.apenergy.2021.118351.

[209] John Stevens and Joe Hooker. The Value of Vehicle Grid Integration in California. In *33rd Electric Vehicle Symposium (EVS33)*, Portland, Oregon, 2020. Accessed: 2023-08-14.

[210] C. Heilmann and G. Friedl. Factors influencing the economic success of grid-to-vehicle and vehicle-to-grid applications—A review and meta-analysis. *Renewable and Sustainable Energy Reviews*, 145: 111115, 2021. ISSN 1364-0321. DOI: 10.1016/j.rser.2021.111115.

[211] Jan Figgener, Benedikt Tepe, Fabian Rücker, Ilka Schoeneberger, Christopher Hecht, et al. The influence of frequency containment reserve flexibilization on the economics of electric vehicle fleet operation. *Journal of Energy Storage*, 53:105138, 2022. ISSN 2352152X. DOI: 10.1016/j.est.2022.105138.

[212] Benjamin K. Sovacool, Lance Noel, Jonn Axsen, and Willett Kempton. The neglected social dimensions to a vehicle-to-grid (V2G) transition: a critical and systematic review. *Environmental Research Letters*, 13(1):013001, 2018. ISSN 1748-9326. DOI: 10.1088/1748-9326/aa9c6d.

[213] Nora Baumgartner, Kira Weyer, Lars Eckmann, and Wolf Fichtner. How to integrate users into smart charging – A critical and systematic review. *Energy Research & Social Science*, 100:103113, 2023. ISSN 22146296. DOI: 10.1016/j.erss.2023.103113.

[214] Nora Baumgartner, Franziska Kellerer, Manuel Ruppert, Sebastian Hirsch, Stefan Mang, et al. Does experience matter? Assessing user motivations to accept a vehicle-to-grid charging tariff. *Transportation Research Part D: Transport and Environment*, 113:103528, 2022. ISSN 1361-9209. DOI: 10.1016/j.trd.2022.103528.

[215] Koen van Heuveln, Rishabh Ghotge, Jan Anne Annema, Esther van Bergen, Bert van Wee, et al. Factors influencing consumer acceptance of vehicle-to-grid by electric vehicle drivers in the Netherlands. *Travel Behaviour and Society*, 24:34–45, 2021. ISSN 2214-367X. DOI: 10.1016/j.tbs.2020.12.008.

[216] Joachim Geske and Diana Schumann. Willing to participate in vehicle-to-grid (V2G)? Why not! *Energy Policy*, 120:392–401, 2018. ISSN 0301-4215. DOI: 10.1016/j.enpol.2018.05.004.

[217] Kang Miao Tan, Vigna K. Ramachandaramurthy, and Jia Ying Yong. Integration of electric vehicles in smart grid: A review on vehicle to grid technologies and optimization techniques. *Renewable and Sustainable Energy Reviews*, 53:720–732, 2016. ISSN 1364-0321. DOI: 10.1016/j.rser.2015.09.012.

[218] Sonali Goel, Renu Sharma, and Akshay Kumar Rathore. A review on barrier and challenges of electric vehicle in India and vehicle to grid optimisation. *Transportation Engineering*, 4:100057, 2021. ISSN 2666-691X. DOI: 10.1016/j.treng.2021.100057.

[219] Nanduni I. Nimalsiri, Chathurika P. Mediwaththe, Elizabeth L. Ratnam, Marnie Shaw, David B. Smith, et al. A Survey of Algorithms for Distributed Charging Control of Electric Vehicles in Smart Grid. *IEEE Transactions on Intelligent Transportation Systems*, 21(11):4497–4515, 2020. ISSN 1558-0016. DOI: 10.1109/TITS.2019.2943620.

[220] Andre Leippi, Markus Fleschutz, and Michael D. Murphy. A Review of EV Battery Utilization in Demand Response Considering Battery Degradation in Non-Residential Vehicle-to-Grid Scenarios. *Energies*, 15(9):3227, 2022. ISSN 1996-1073. DOI: 10.3390/en15093227.

[221] Belagavi Viswanath, Dheeraj Kumar Khatod, and Narayana Prasad Padhy. Vehicle-to-Grid (V2G) Optimization for Grid Peak Demand Reduction and Decarbonization: A State-of-the-Art Review. In *2022 IEEE 10th Power India International Conference (PIICON)*, 2022. DOI: 10.1109/PIICON56320.2022.10045118. ISSN: 2642-5289.

[222] Luiz Almeida, Ana Soares, and Pedro Moura. A Systematic Review of Optimization Approaches for the Integration of Electric Vehicles in Public Buildings. *Energies*, 16(13):5030, 2023. ISSN 1996-1073. DOI: 10.3390/en16135030.

[223] Qin Chen and Komla Agbenyo Folly. Application of Artificial Intelligence for EV Charging and Discharging Scheduling and Dynamic Pricing: A Review. *Energies*, 16(1):146, 2023. ISSN 1996-1073. DOI: 10.3390/en16010146.

[224] Jiawei Dong, Abdulsalam Yassine, Andy Armitage, and M. Shamim Hossain. Multi-Agent Reinforcement Learning for Intelligent V2G Integration in Future Transportation Systems. *IEEE Transactions on Intelligent Transportation Systems*, 2023. ISSN 1558-0016. DOI: 10.1109/TITS.2023.3284756.

[225] Shahid Jaman, Boud Verbrugge, Oscar Hernandez Garcia, Mohamed Abdel-Monem, Blum Oliver, et al. Development and Validation of V2G Technology for Electric Vehicle Chargers Using Combo CCS Type 2 Connector Standards. *Energies*, 15(19):7364, 2022. ISSN 1996-1073. DOI: 10.3390/en15197364.

[226] UK Power Networks, Everoze, Innovate UK, and EVConsult. Insights. https://www.v2g-hub.com/insights/, 2023. Accessed: 2024-06-15.

[227] UK Power Networks, Everoze, Innovate UK, and EVConsult. Leaf to home. https://www.v2g-hub.com/projects/leaf-to-home/, 2023. Accessed: 2023-08-07.

[228] Nissan Motor Corporation, Ltd. Nissan and Nichicon to Launch the 'LEAF to Home' Power Supply System With "EV Power Station". http://global.nissannews.com/en/releases/120530-01-e, 2012. Accessed: 2023-08-04.

[229] Dan Passe. Nissan takes major role at 2017 North American International Auto Show's AutoMobili-D exposition. http://global.nissannews.com/en/releases/nissan-takes-major-role-at-2017-north-american-international-auto-shows-automobili-d-exposition, 2017. Accessed: 2023-08-04.

[230] Yuji Ohira and Kento Hirashima. Powering homes with EVs: Panasonic, Omron set to enter Japan's V2H market. https://asia.nikkei.com/Business/Technology/Powering-homes-with-EVs-Panasonic-Omron-set-to-enter-Japan-s-V2H-market, 2023. Accessed: 2023-08-04.

[231] Ricardo Michaelis. Vehicle to Grid (V2G). https://www.charin.global/news/vehicle-to-grid-v2g-charin-bundles-200-companies-that-make-the-energy-system-and-electric-cars-co2-friendlier-and-cheaper/, 2021. Accessed: 2023-08-03.

[232] DIN-Normenausschuss Automobiltechnik (NAAutomobil). ISO 15118-20:2022 Road vehicles — Vehicle to grid communication interface — Part 20: 2nd generation network layer and application layer requirements, 2022.

[233] Ford Motor Company. Ford Charge Station Pro. https://chargers.ford.com/products/ford-charge-station-pro. Accessed: 2023-08-01.

[234] Christopher Hecht, Jan Figgener, and Dirk Uwe Sauer. Vehicle-to-Grid Market Readiness in Europe with a Special Focus on Germany. *Vehicles*, 5(4):1452–1466, 2023. ISSN 2624-8921. DOI: 10.3390/vehicles5040079.

[235] EV Database. Current and Upcoming Electric Vehicles. https://ev-database.org/#sort:path~type~order=.pricesort~number~asc|misc:textGroup=V2XG|paging:number=all, 2024. Accessed: 2024-04-11.

[236] Bundesregierung Deutschland and Bundesministerium für Wirtschaft und Technologie. Verordnung über Allgemeine Bedingungen für den Netzanschluss und dessen Nutzung für die Elektrizitätsversorgung in Niederspannung (Niederspannungsanschlussverordnung - NAV). https://www.gesetze-im-internet.de/nav/BJNR247710006.html, 2006. Accessed: 2023-07-25.

[237] Friedhelm Greis. Wallbox-Programm 440: Mehrere Hunderttausend Anträge bleiben ohne Förderung. https://www.golem.de/news/kfw-programm-440-mehrere-hunderttausend-wallboxen-bleiben-ohne-foerderung-2303-172466.html, 2023. Accessed: 2023-07-19.

[238] KfW. Merkblatt: Solarstrom für Elektroautos (Zuschuss 439). https://www.kfw.de/PDF/Download-Center/Förderprogramme-(Inlandsförderung)/PDF-Dokumente/6000005085_M_442.pdf, 2023. Accessed: 2023-09-22.

[239] Philip Sterchele, Julian Brandes, Judith Heilig, Daniel Wrede, Christoph Kost, et al. Wege zu einem klimaneutralen Energiesystem - Die deutsche Energiewende im Kontext gesellschaftlicher Verhaltensweisen. https://www.ise.fraunhofer.de/content/dam/ise/de/documents/publications/studies/Fraunhofer-ISE-Studie-Wege-zu-einem-klimaneutralen-Energiesystem.pdf, 2020. Accessed: 2022-01-08.

[240] Joe Nocera. Costly Toys, or a New Era for Drivers? *The New York Times*, 2008. ISSN 0362-4331. https://www.nytimes.com/2008/07/19/business/19nocera.html. Accessed: 2023-07-28.

[241] sonnen GmbH Content Team. Netzdienstleistungen mit Batteriespeichern. https://sonnen.de/wissen/netzdienstleistungen-mit-batteriespeichern/. Accessed: 2023-07-28.

[242] Tim Schittekatte, Valerie Reif, and Leonardo Meeus. Welcoming New Entrants into European Electricity Markets. *Energies*, 14(13):4051, 2021. ISSN 1996-1073. DOI: 10.3390/en14134051.

[243] Videgain Barranco, P. and Covrig, C.F. *Vehicle-to-grid and/or vehicle-to-home round-trip efficiency*. Publications Office of the European Union, Luxembourg, eur 30603 en edition, 2021. ISBN 978-92-76-30608-5. DOI: 10.2760/997207. JRC123942.

[244] Lisa Calearo and Mattia Marinelli. Profitability of Frequency Regulation by Electric Vehicles in Denmark and Japan Considering Battery Degradation Costs. *World Electric Vehicle Journal*, 11(3): 48, 2020. DOI: 10.3390/wevj11030048.

[245] Virta Global. Vehicle-to-grid (V2G) technology: Key challenges and developments. https://www.virta.global/blog/v2g-technology-key-challenges-and-developments, 2023. Accessed: 2023-09-21.

[246] Fabian Eisele (Vector Germany). AC Bidirectional Power Transfer with ISO 15118-20. https://cdn.vector.com/cms/content/events/2024/VA/8_Zack_Hendi-Fabian_Eisele_-_AC_Bidirectional_Power.pdf, 2024. Accessed: 2024-04-11.

[247] S. Dusmez, A. Cook, and A. Khaligh. Comprehensive analysis of high quality power converters for level 3 off-board chargers. In *2011 IEEE Vehicle Power and Propulsion Conference*, 2011. DOI: 10.1109/VPPC.2011.6043096.

[248] M. Yilmaz and P. T. Krein. Review of Battery Charger Topologies, Charging Power Levels, and Infrastructure for Plug-In Electric and Hybrid Vehicles. *IEEE Transactions on Power Electronics*, 28 (5):2151–2169, 2013. ISSN 0885-8993. DOI: 10.1109/TPEL.2012.2212917.

[249] Ivan Subotic and Emil Levi. A review of single-phase on-board integrated battery charging topologies for electric vehicles. In *2015 IEEE Workshop on Electrical Machines Design, Control and Diagnosis (WEMDCD)*, pages 136–145, Torino, Italy, 2015. IEEE. ISBN 978-1-4799-8900-3. DOI: 10.1109/WEMDCD.2015.7194522.

[250] Alireza Khaligh and Michael D'Antonio. Global Trends in High-Power On-Board Chargers for Electric Vehicles. *IEEE Transactions on Vehicular Technology*, 68(4):3306–3324, 2019. ISSN 0018-9545, 1939-9359. DOI: 10.1109/TVT.2019.2897050.

[251] Bertrandt, Coroplast Fritz Müller, Delphi Deutschland, Heraeus Materials Technology, Huber & Suhner, et al. Spannungsklassen in der Elektromobilität (Ausgabe 2021). https://www.zvei.org/fileadmin/user_upload/Presse_und_Medien/Publikationen/2021/Juli/ZVEI-Spannungsklassen-in-der-Elektromobilitaet_Ausgabe-2021/ZVEI-Spannungsklassen-in-der-Elektromobilitaet_Ausgabe-2021.pdf, 2021. Accessed: 2023-05-03.

[252] Jiaqi Yuan, Lea Dorn-Gomba, Alan Dorneles Callegaro, John Reimers, and Ali Emadi. A Review of Bidirectional On-Board Chargers for Electric Vehicles. *IEEE Access*, 9:51501–51518, 2021. ISSN 2169-3536. DOI: 10.1109/ACCESS.2021.3069448.

[253] Angshuman Sharma and Santanu Sharma. Review of power electronics in vehicle-to-grid systems. *Journal of Energy Storage*, 21:337–361, 2019. ISSN 2352-152X. DOI: 10.1016/j.est.2018.11.022.

[254] André Kaufung. Position Paper of Charging Interface Initiative e.V.: DC CCS Power Classes V7.2. https://www.charin.global/media/pages/technology/knowledge-base/c6574dae0e-1639130326/charin_dc_ccs_power_classes.pdf, 2021. Accessed: 2023-07-18.

[255] Charging Interface Initiative (CharIN) e.V. CharIN Whitepaper Megawatt Charging System (MCS) – Recommendations and requirements for MCS related standards bodies and solution suppliers (Version 1.0). https://www.charin.global/media/pages/technology/knowledge-base/c708ba3361-1670238823/whitepaper_megawatt_charging_system_1.0.pdf, 2022. Accessed: 2023-09-25.

[256] Jin Wang, Yue Zhang, Mohamed Elshaer, William Perdikakis, Chengcheng Yao, et al. Nonisolated Electric Vehicle Chargers: Their Current Status and Future Challenges. *IEEE Electrification Magazine*, 9(2):23–33, 2021. ISSN 2325-5897, 2325-5889. DOI: 10.1109/MELE.2021.3070935.

[257] Jaeyeon Lee, Hyeonju Jeong, Tat-Thang LE, and Sewan Choi. Three-Phase Single-Stage Bidirectional CCM Soft-Switching AC–DC Converter With Minimum Switch Count. *IEEE Transactions on Power Electronics*, 38(2):2052–2062, 2023. ISSN 1941-0107. DOI: 10.1109/TPEL.2022.3206896.

[258] B. Zhao, Q. Song, W. Liu, and Y. Sun. Overview of Dual-Active-Bridge Isolated Bidirectional DC–DC Converter for High-Frequency-Link Power-Conversion System. *IEEE Transactions on Power Electronics*, 29(8):4091–4106, 2014. ISSN 0885-8993. DOI: 10.1109/TPEL.2013.2289913.

[259] Yun-Sung Kim, Chang-Yeol Oh, Won-Yong Sung, and Byoung Kuk Lee. Topology and Control Scheme of OBC–LDC Integrated Power Unit for Electric Vehicles. *IEEE Transactions on Power Electronics*, 32(3):1731–1743, 2017. ISSN 0885-8993, 1941-0107. DOI: 10.1109/TPEL.2016.2555622.

[260] Qingyun Huang and Alex Q. Huang. Review of GaN Totem-Pole Bridgeless PFC. *CPSS Transactions on Power Electronics and Applications*, 2(3):187–196, 2017. ISSN 2475742X. DOI: 10.24295/CPSSTPEA.2017.00018.

[261] Salil Chellappan. A comparative analysis of topologies for a bridgeless-boost PFC circuit. *Analog Design Journal*, 2018. https://www.ti.com/lit/an/slyt750/slyt750.pdf. Accessed: 2023-09-29.

[262] Adria Marcos-Pastor, Enric Vidal-Idiarte, Angel Cid-Pastor, and Luis Martinez-Salamero. Loss-Free Resistor-Based Power Factor Correction Using a Semi-Bridgeless Boost Rectifier in Sliding-Mode Control. *IEEE Transactions on Power Electronics*, 30(10):5842–5853, 2015. ISSN 0885-8993, 1941-0107. DOI: 10.1109/TPEL.2014.2369431.

[263] Seyfettin Vadi, Ramazan Bayindir, Alperen Mustafa Colak, and Eklas Hossain. A Review on Communication Standards and Charging Topologies of V2G and V2H Operation Strategies. *Energies*, 12(19):3748, 2019. ISSN 1996-1073. DOI: 10.3390/en12193748.

[264] Bruno Burger and Dirk Kranzer. Extreme high efficiency PV-power converters. In *13th European Conference on Power Electronics and Applications*. IEEE, 2009.

[265] Li Zhang, Kai Sun, Lipei Huang, and Seiki Igarashi. Comparison of RB-IGBT and normal IGBT in T-type three-level inverter. In *2013 15th European Conference on Power Electronics and Applications (EPE)*, Lille, France, 2013. IEEE. ISBN 978-1-4799-0116-6. DOI: 10.1109/EPE.2013.6631823.

[266] A Narendrababu, Naveen Yalla, and Pramod Agarwal. A modified T-type single phase five-level inverter with reduced switch voltage stress. In *2018 International Conference on Power, Instrumentation, Control and Computing (PICC)*, Thrissur, 2018. IEEE. ISBN 978-1-5386-2462-3. DOI: 10.1109/PICC.2018.8384775.

[267] Ui-Min Choi and June-Seok Lee. Single-Phase Five-Level IT-Type NPC Inverter With Improved Efficiency and Reliability in Photovoltaic Systems. *IEEE Journal of Emerging and Selected Topics in Power Electronics*, 10(5):5226–5239, 2022. ISSN 2168-6777, 2168-6785. DOI: 10.1109/JESTPE.2021.3103252.

[268] Damoun Ahmadi Khatir. *A Universal Selective Harmonics Elimination Method for High Power Inverters*. Dissertation, The Ohio State University, 2012. https://etd.ohiolink.edu/acprod/odb_etd/etd/r/1501/10?clear=10&p10_accession_num=osu1339611032. Accessed: 2023-10-02.

[269] Faramarz Faraji, S.M. Mousavi G., Aliasghar Hajirayat, Ali Akbar Moti Birjandi, and Kamal Al-Haddad. Single-stage single-phase three-level neutral-point-clamped transformerless grid-connected photovoltaic inverters: Topology review. *Renewable and Sustainable Energy Reviews*, 80:197–214, 2017. ISSN 13640321. DOI: 10.1016/j.rser.2017.05.181.

[270] Mohammad Faisal Akhtar, Siti Rohani S. Raihan, Nasrudin Abd Rahim, Mohammad Nishat Akhtar, and Elmi Abu Bakar. Recent Developments in DC-DC Converter Topologies for Light Electric Vehicle Charging: A Critical Review. *Applied Sciences*, 13(3):1676, 2023. ISSN 2076-3417. DOI: 10.3390/app13031676.

[271] Marco Rivera, Venkata Yaramasu, Ana Llor, Jose Rodriguez, Bin Wu, et al. Digital Predictive Current Control of a Three-Phase Four-Leg Inverter. *IEEE Transactions on Industrial Electronics*, 60(11): 4903–4912, 2013. ISSN 1557-9948. DOI: 10.1109/TIE.2012.2219837.

[272] Yue Zhang, Ge Yang, Xiaoteng He, Mohamed Elshaer, William Perdikakis, et al. Leakage Current Issue of Non-Isolated Integrated Chargers for Electric Vehicles. In *2018 IEEE Energy Conversion Congress and Exposition (ECCE)*, pages 1221–1227, Portland, OR, USA, 2018. IEEE. ISBN 978-1-4799-7312-5. DOI: 10.1109/ECCE.2018.8558133.

[273] V. Yaramasu, J. Rodriguez, B. Wu, M. Rivera, A. Wilson, et al. A simple and effective solution for superior performance in two-level four-leg voltage source inverters: Predictive voltage control. In *2010 IEEE International Symposium on Industrial Electronics*, pages 3127–3132, Bari, Italy, 2010. IEEE. ISBN 978-1-4244-6390-9. DOI: 10.1109/ISIE.2010.5637875.

[274] R.W. De Doncker and J.P. Lyons. The auxiliary resonant commutated pole converter. In *Conference Record of the 1990 IEEE Industry Applications Society Annual Meeting*, pages 1228–1235 vol.2, 1990. DOI: 10.1109/IAS.1990.152341.

[275] Suman Debnath, Jiangchao Qin, Behrooz Bahrani, Maryam Saeedifard, and Peter Barbosa. Operation, Control, and Applications of the Modular Multilevel Converter: A Review. *IEEE Transactions on Power Electronics*, 30(1):37–53, 2015. ISSN 0885-8993, 1941-0107. DOI: 10.1109/TPEL.2014.2309937.

[276] Kumar Nishant, K. Prabha Rani, and K. V. S. R. Murthy. Comparative Analysis of Different Topologies of Vienna Rectifier. In Ranganath M. Singari and Pavan Kumar Kankar, editors, *Advances in Transdisciplinary Engineering*. IOS Press, 2022. ISBN 978-1-64368-336-2 978-1-64368-337-9. DOI: 10.3233/ATDE220736.

[277] T. Bruckner, S. Bernet, and H. Guldner. The Active NPC Converter and Its Loss-Balancing Control. *IEEE Transactions on Industrial Electronics*, 52(3):855–868, 2005. ISSN 0278-0046. DOI: 10.1109/TIE.2005.847586.

[278] Davi. R. Joca, Luiz H.S.C. Barreto, Demercil De S. Oliveira, Ranoyca N. A. L. Silva, and Gustavo A. L. Henn. Modulation technique based on CSV-PWM and HEPWM for THD reduction in flying capacitor multilevel inverters. In *2012 10th IEEE/IAS International Conference on Industry Applications*, Fortaleza, CE, Brazil, 2012. IEEE. ISBN 978-1-4673-2412-0 978-1-4673-2411-3. DOI: 10.1109/INDUSCON.2012.6453491.

[279] DKE Deutsche Kommission Elektrotechnik Elektronik Informationstechnik in DIN und VDE. DIN EN 60038 (VDE 0175-1): 2012-04 – CENELEC-Normspannungen, 2012.

[280] DKE Deutsche Kommission Elektrotechnik Elektronik Informationstechnik in DIN und VDE. DIN EN 50160:2020-11 – Merkmale der Spannung in öffentlichen Elektrizitätsversorgungsnetzen;Deutsche Fassung EN 50160:2010 + Cor.:2010 + A1:2015 + A2:2019 + A3:2019, 2020.

[281] M. Forouzesh, Y. P. Siwakoti, S. A. Gorji, F. Blaabjerg, and B. Lehman. Step-Up DC–DC Converters: A Comprehensive Review of Voltage-Boosting Techniques, Topologies, and Applications. *IEEE Transactions on Power Electronics*, 32(12):9143–9178, 2017. ISSN 0885-8993. DOI: 10.1109/TPEL.2017.2652318.

[282] Md Safayatullah, Mohamed Tamasas Elrais, Sumana Ghosh, Reza Rezaii, and Issa Batarseh. A Comprehensive Review of Power Converter Topologies and Control Methods for Electric Vehicle Fast Charging Applications. *IEEE Access*, 10:40753–40793, 2022. ISSN 2169-3536. DOI: 10.1109/ACCESS.2022.3166935.

[283] Y. Du, S. Lukic, B. Jacobson, and A. Huang. Review of high power isolated bi-directional DC-DC converters for PHEV/EV DC charging infrastructure. In *2011 IEEE Energy Conversion Congress and Exposition*, pages 553–560, 2011. DOI: 10.1109/ECCE.2011.6063818.

[284] Sajib Chakraborty, Hai-Nam Vu, Mohammed Mahedi Hasan, Dai-Duong Tran, Mohamed El Baghdadi, et al. DC-DC Converter Topologies for Electric Vehicles, Plug-in Hybrid Electric Vehicles and Fast Charging Stations: State of the Art and Future Trends. *Energies*, 12(8):1569, 2019. ISSN 1996-1073. DOI: 10.3390/en12081569.

[285] Soedibyo, Budi Amri, and Mochamad Ashari. The comparative study of Buck-boost, Cuk, Sepic and Zeta converters for maximum power point tracking photovoltaic using P&O method. In *2015 2nd International Conference on Information Technology, Computer, and Electrical Engineering (ICITACEE)*, pages 327–332, Semarang, Indonesia, 2015. IEEE. ISBN 978-1-4799-9861-6 978-1-4799-9863-0. DOI: 10.1109/ICITACEE.2015.7437823.

[286] Dierk Schröder and Rainer Marquardt, editors. *Leistungselektronische Schaltungen: Funktion, Auslegung und Anwendung*. Springer Berlin Heidelberg, Berlin, Heidelberg, 2019. ISBN 978-3-662-55324-4 978-3-662-55325-1. DOI: 10.1007/978-3-662-55325-1.

[287] Issa Batarseh and Harb Ahmad. *Power Electronics: Circuit Analysis and Design*. Springer, 2nd ed. edition, 2018. ISBN 978-3-319-68365-2.

[288] Mehnaz Akhter Khan, Adeeb Ahmed, Iqbal Husain, Yilmaz Sozer, and Mohamed Badawy. Performance Analysis of Bidirectional DC–DC Converters for Electric Vehicles. *IEEE Transactions on Industry Applications*, 51(4):3442–3452, 2015. ISSN 0093-9994, 1939-9367. DOI: 10.1109/TIA.2015.2388862.

[289] Zeljko Ivanovic and Mladen Knezic. Modeling Push–Pull Converter for Efficiency Improvement. *Electronics*, 11(17):2713, 2022. ISSN 2079-9292. DOI: 10.3390/electronics11172713.

[290] Sam Abdel-Rahman. Resonant LLC Converter: Operation and Design (Application Note AN 2012-09). https://www.infineon.com/dgdl/Application_Note_Resonant+LLC+Converter+Operation+and+Design_Infineon.pdf?fileId=db3a30433a047ba0013a4a60e3be64a1, 2012. Accessed: 2018-12-03.

[291] STMicroelectronics. ST AN2644: An introduction to LLC resonant half-bridge converter (Rev 2). https://www.st.com/content/ccc/resource/technical/document/application_note/de/f9/17/b7/ad/9f

/4d/dd/CD00174208.pdf/files/CD00174208.pdf/jcr:content/translations/en.CD00174208.pdf, 2008. Accessed: 2018-12-05.

[292] Fariborz Musavi, Murray Edington, and Wilson Eberle. Wireless power transfer: A survey of EV battery charging technologies. In *2012 IEEE Energy Conversion Congress and Exposition (ECCE)*, pages 1804–1810, Raleigh, NC, USA, 2012. IEEE. ISBN 978-1-4673-0803-8 978-1-4673-0802-1 978-1-4673-0800-7 978-1-4673-0801-4. DOI: 10.1109/ECCE.2012.6342593.

[293] A. Hillers, D. Christen, and J. Biela. Design of a Highly efficient bidirectional isolated LLC resonant converter. In *2012 15th International Power Electronics and Motion Control Conference (EPE/PEMC)*, pages DS2b.13–1–DS2b.13–8, 2012. DOI: 10.1109/EPEPEMC.2012.6397282.

[294] Houssein Al Attar, Mohamed Assaad Hamida, Malek Ghanes, and Miassa Taleb. Review on Modeling and Control Strategies of DC–DC LLC Converters for Bidirectional Electric Vehicle Charger Applications. *Energies*, 16(9):3946, 2023. ISSN 1996-1073. DOI: 10.3390/en16093946.

[295] Wei Chen, Ping Rong, and Zhengyu Lu. Snubberless Bidirectional DC–DC Converter With New CLLC Resonant Tank Featuring Minimized Switching Loss. *IEEE Transactions on Industrial Electronics*, 57(9):3075–3086, 2010. ISSN 0278-0046. DOI: 10.1109/TIE.2009.2037099.

[296] B. Sen, Chaohui Liu, Jiabin Wang, C. Gould, and K. Colombage. A CLLC Resonant Converter Based Bidirectional EV Charger with Maximum Efficiency Tracking. In *8th IET International Conference on Power Electronics, Machines and Drives (PEMD 2016)*, Glasgow, UK, 2016. Institution of Engineering and Technology. ISBN 978-1-78561-188-9. DOI: 10.1049/cp.2016.0152.

[297] S. Ditze. Steady-state analysis of the bidirectional CLLLC resonant converter in time domain. In *2014 IEEE 36th International Telecommunications Energy Conference (INTELEC)*, 2014. DOI: 10.1109/INTLEC.2014.6972179.

[298] Jinqiu Song, Dongjiang Yang, Chenghui Zhang, and Bin Duan. Hybrid Control Method for CLLLC Resonant Converter with Low Output Voltage Ripple. *IFAC-PapersOnLine*, 51(31):680–684, 2018. ISSN 2405-8963. DOI: 10.1016/j.ifacol.2018.10.157.

[299] S. Zou, J. Lu, A. Mallik, and A. Khaligh. Bi-Directional CLLC Converter With Synchronous Rectification for Plug-In Electric Vehicles. *IEEE Transactions on Industry Applications*, 54(2): 998–1005, 2018. ISSN 0093-9994. DOI: 10.1109/TIA.2017.2773430.

[300] J. Jung, H. Kim, J. Kim, M. Ryu, and J. Baek. High efficiency bidirectional LLC resonant converter for 380V DC power distribution system using digital control scheme. In *2012 Twenty-Seventh Annual IEEE Applied Power Electronics Conference and Exposition (APEC)*, pages 532–538, 2012. DOI: 10.1109/APEC.2012.6165871.

[301] R. Severns. Topologies for three element resonant converters. In *Fifth Annual Proceedings on Applied Power Electronics Conference and Exposition*, pages 712–722, 1990. DOI: 10.1109/APEC.1990.66374.

[302] Sheng-Yang Yu, Runruo Chen, and Ananthakrishnan Viswanathan. Survey of Resonant Converter Topologies. https://www.ti.com/seclit/ml/slup376/slup376.pdf, 2018. TI Literature Number: SLUP376. Accessed: 2018-12-13.

[303] F. C. Lee. High-frequency quasi-resonant converter technologies. *Proceedings of the IEEE*, 76(4): 377–390, 1988. ISSN 0018-9219. DOI: 10.1109/5.4424.

[304] V. Vorperian. Quasi-square-wave converters: topologies and analysis. *IEEE Transactions on Power Electronics*, 3(2):183–191, 1988. ISSN 0885-8993. DOI: 10.1109/63.4348.

[305] Jun-Young Lee and Byung-Moon Han. A Bidirectional Wireless Power Transfer EV Charger Using Self-Resonant PWM. *IEEE Transactions on Power Electronics*, 30(4):1784–1787, 2015. ISSN 1941-0107. DOI: 10.1109/TPEL.2014.2346255.

[306] Lei Zhao, Duleepa J. Thrimawithana, and Udaya K. Madawala. Hybrid Bidirectional Wireless EV Charging System Tolerant to Pad Misalignment. *IEEE Transactions on Industrial Electronics*, 64(9): 7079–7086, 2017. ISSN 0278-0046, 1557-9948. DOI: 10.1109/TIE.2017.2686301.

[307] Jiejian Dai and Daniel C. Ludois. Capacitive Power Transfer Through a Conformal Bumper for Electric Vehicle Charging. *IEEE Journal of Emerging and Selected Topics in Power Electronics*, 4 (3):1015–1025, 2016. ISSN 2168-6777, 2168-6785. DOI: 10.1109/JESTPE.2015.2505622.

[308] Eric A Walters and Oleg Wasynczuk. Analysis of the Auxiliary Resonant Commutated Pole Inverter. https://docs.lib.purdue.edu/cgi/viewcontent.cgi?article=1144&context=ecetr, 1995. Accessed: 2020-11-10.

[309] Hans-Jürgen Pfisterer. *Der Auxiliary-Resonant-Commutated-Pole-Stromrichter, ein Resonanzstromrichter mit Spannungszwischenkreis, am Niederspannungsnetz*. VDI Verlag, Universität Karlsruhe, 2001. ISBN 3-18-330921-1.

[310] H.-J. Pfisterer. Three phase 160 kVA Auxiliary Resonant Commutated Pole (ARCP) Converter. In *2008 4th IET Conference on Power Electronics, Machines and Drives*, pages 480–484, 2008. DOI: 10.1049/cp:20080568. ISSN: 0537-9989.

[311] Wenzhi Zhou, Xibo Yuan, and Ian Laird. Performance Comparison of the Auxiliary Resonant Commutated Pole Inverter (ARCPI) using SiC MOSFETs or Si IGBTs. In *2019 IEEE Energy Conversion Congress and Exposition (ECCE)*, pages 1981–1987, 2019. DOI: 10.1109/ECCE.2019.8912876. ISSN: 2329-3748.

[312] Behrooz Mirafzal and Aswad Adib. On Grid-Interactive Smart Inverters: Features and Advancements. *IEEE Access*, 8:160526–160536, 2020. ISSN 2169-3536. DOI: 10.1109/ACCESS.2020.3020965.

[313] Dayan B. Rathnayake, Milad Akrami, Chitaranjan Phurailatpam, Si Phu Me, Sajjad Hadavi, et al. Grid Forming Inverter Modeling, Control, and Applications. *IEEE Access*, 9:114781–114807, 2021. ISSN 2169-3536. DOI: 10.1109/ACCESS.2021.3104617.

[314] High Share of Inverter-Based Generation Task Force. Grid-Forming Technology in Energy Systems Integration. https://www.esig.energy/wp-content/uploads/2022/03/ESIG-GFM-report-2022.pdf, 2022. Accessed: 2023-10-20.

[315] Ben Kroposki, Deepak Ramasubramanian, Wenzong Wang, Andy Hoke, Gab-Su Seo, et al. Specifications for Grid-forming Inverter-based Resourcess – Version 1. https://www.energy.gov/sites/default/files/2023-09/Specs%20for%20GFM%20IBRs%20Version%201.pdf, 2022. UNIFI-2022-2-1. Accessed: 2023-10-20.

[316] Guanhong Song, Bo Cao, and Liuchen Chang. Review of Grid-forming Inverters in Support of Power System Operation. *Chinese Journal of Electrical Engineering*, 8(1), 2022. ISSN 2096-1529. DOI: 10.23919/CJEE.2022.000001.

[317] D Venkatramanan, Rodrigo Henriquez-Auba, Rifat Kaisar Rachi, Jennifer T Bui, Manish K Singh, et al. Grid-forming Inverter Technology Specifications: A Review of Research Reports and Roadmaps, 2022. UNIFI-2022-1-1.

[318] Christensen, Peter, Andersen, Gert Karmisholt, Seidel, Matthias, Bolik, Sigrid, Engelken, Sönke, et al. High Penetration of Power Electronic Interfaced Power Sources and the Potential Contribution of Grid Forming Converters. https://euagenda.eu/upload/publications/untitled-292051-ea.pdf, 2020. Accessed: 2023-10-20.

[319] Yashen Lin, Joseph H Eto, Brian B Johnson, Jack D Flicker, Robert H Lasseter, et al. Research Roadmap on Grid-Forming Inverters. https://www.nrel.gov/docs/fy21osti/73476.pdf, 2020. NREL/TP-5D00-73476. Accessed: 2023-10-20.

[320] Sara Anttila, Jéssica S. Döhler, Janaína G. Oliveira, and Cecilia Boström. Grid Forming Inverters: A Review of the State of the Art of Key Elements for Microgrid Operation. *Energies*, 15(15):5517, 2022. ISSN 1996-1073. DOI: 10.3390/en15155517.

[321] A. Nicastri and A. Nagliero. Comparison and evaluation of the PLL techniques for the design of the grid-connected inverter systems. In *2010 IEEE International Symposium on Industrial Electronics*, pages 3865–3870, Bari, Italy, 2010. IEEE. ISBN 978-1-4244-6390-9. DOI: 10.1109/ISIE.2010.5637778.

[322] Alvaro Luna, Joan Rocabert, J. Ignacio Candela, Juan Ramón Hermoso, Remus Teodorescu, et al. Grid Voltage Synchronization for Distributed Generation Systems Under Grid Fault Conditions. *IEEE Transactions on Industry Applications*, 51(4):3414–3425, 2015. ISSN 1939-9367. DOI: 10.1109/TIA.2015.2391436.

[323] M. Barnes and Siyu Gao. Phase-locked loops for grid-tied inverters: comparison and testing. In *8th IET International Conference on Power Electronics, Machines and Drives (PEMD 2016)*, pages 6 .–6 ., Glasgow, UK, 2016. Institution of Engineering and Technology. ISBN 978-1-78561-188-9. DOI: 10.1049/cp.2016.0304.

[324] Saeed Golestan, Josep M. Guerrero, and Juan C. Vasquez. Three-Phase PLLs: A Review of Recent Advances. *IEEE Transactions on Power Electronics*, 32(3):1894–1907, 2017. ISSN 1941-0107. DOI: 10.1109/TPEL.2016.2565642.

[325] Ahmed Meligy, Taoufik Qoria, and Ilknur Colak. Assessment of Sequence Extraction Methods Applied to MMC-SDBC STATCOM Under Distorted Grid Conditions. *IEEE Transactions on Power Delivery*, 37(6):4923–4932, 2022. ISSN 0885-8977, 1937-4208. DOI: 10.1109/TPWRD.2022.3162959.

[326] Remus Teodorescu, Marco Liserre, and Pedro Rodríguez. *Grid converters for photovoltaic and wind power systems*. Wiley, Chichester, 2011. ISBN 978-0-470-66704-0.

[327] P. Rodríguez, R. Teodorescu, I. Candela, A. V. Timbus, M. Liserre, et al. New positive-sequence voltage detector for grid synchronization of power converters under faulty grid conditions. In *2006 37th IEEE Power Electronics Specialists Conference*, 2006. DOI: 10.1109/pesc.2006.1712059. ISSN: 2377-6617.

[328] P. Rodriguez, J. Pou, J. Bergas, J. I. Candela, R. P. Burgos, et al. Decoupled Double Synchronous Reference Frame PLL for Power Converters Control. *IEEE Transactions on Power Electronics*, 22 (2):584–592, 2007. ISSN 1941-0107. DOI: 10.1109/TPEL.2006.890000.

[329] Jianing Li, Botong Li, Qing Zhong, Bin Li, Xiaolong Chen, et al. Comparative Analysis of Dynamic Tracking Ability of Phase-Locked Loop in Case of Sudden Change of Power Grid Voltage. In *2023 5th Asia Energy and Electrical Engineering Symposium (AEEES)*, pages 108–115, 2023. DOI: 10.1109/AEEES56888.2023.10114111.

[330] A. S. Mäkinen and H. Tuusa. Analysis, comparison and performance evaluation of wind turbine grid synchronizing methods. In *Eurocon 2013*, pages 1108–1115, 2013. DOI: 10.1109/EUROCON.2013.6625119.

[331] Salvador Revelo and César A. Silva. Current reference strategy with explicit negative sequence component for voltage equalization contribution during asymmetric fault ride through: Current Strategy with Negative Sequence Component. *International Transactions on Electrical Energy Systems*, 25 (12):3449–3471, 2015. ISSN 20507038. DOI: 10.1002/etep.2045.

[332] IRENA. *Grid codes for renewable powered systems*. International Renewable Energy Agency, Abu Dhabi, 2022. ISBN 978-92-9260-427-1. Accessed: 2023-10-30.

[333] Abhimanyu Kaushal and Dirk Van Hertem. An Overview of Ancillary Services and HVDC Systems in European Context. *Energies*, 12(18):3481, 2019. ISSN 1996-1073. DOI: 10.3390/en12183481.

[334] Kristian Sevdari, Lisa Calearo, Peter Bach Andersen, and Mattia Marinelli. Ancillary services and electric vehicles: An overview from charging clusters and chargers technology perspectives. *Renewable and Sustainable Energy Reviews*, 167:112666, 2022. ISSN 1364-0321. DOI: 10.1016/j.rser.2022.112666.

[335] Consentec GmbH. Beschreibung von Konzepten des Systemausgleichs und der Regelreservemärkte in Deutschland. https://www.regelleistung.net/Portals/1/downloads/modalit%C3%A4ten_rahmenvertraege/marktbeschreibung/BeschreibungSystemausgleichundRegelreservem%C3%A4rkte.pdf, 2022. Accessed: 2023-10-26.

[336] ENTSO-E. Electricity Balancing in Europe – An Overview of the European Balancing Market and Electricity Balancing Guideline. https://docstore.entsoe.eu/Documents/Network%20codes%20documents/NC%20EB/entso-e_balancing_in%20_europe_report_Nov2018_web.pdf, 2018. Accessed: 2023-10-26.

[337] 50Hertz Transmission GmbH, Amprion GmbH, TenneT TSO GmbH, and TransnetBW GmbH. Prequalification Process for Balancing Service Providers (FCR, aFRR, mFRR) in Germany ("PQ conditions"). https://www.regelleistung.net/xsppproxy/api/StaticFiles/Regelleistung/Infos_f%C3%BCr_Anbieter/Wie_werde_ich_Regelenergieanbieter_Pr%C3%A4qualifikation/Pr%C3%A4qualifikationsbedingungen_FCR_aFRR_mFRR/PQ-Bedingungen-03.06.2022(englisch).pdf, 2022. Version: 1.04. Accessed: 2023-10-26.

[338] Commission Regulation (EU) 2017/1485 of 2 August 2017 establishing a guideline on electricity transmission system operation (Text with EEA relevance)Text with EEA relevance. http://data.europa.eu/eli/reg/2017/1485/2021-03-15/eng, 2021. Legislative Body: OP_DATPRO. Accessed: 2023-10-26.

[339] Erik Ørum, Liisa Haarla, Mikko Kuivaniemi, Minna Laasonen, Anders Jerkø, et al. Future System Inertia 2. https://www.statnett.no/globalassets/for-aktorer-i-kraftsystemet/utvikling-av-kraftsystemet/nordisk-frekvensstabilitet/future-system-inertia-phase-2.pdf, 2017. Accessed: 2023-10-27.

[340] Annegret-Cl. Agricola, Hannes Seidl, Reemt Heuke, Christian Rehtanz, Johannes Schwippe, et al. Analyse: Momentanreserve 2030: Bedarf und Erbringung von Momentanreserve 2030. https://www.dena.de/fileadmin/dena/Dokumente/Pdf/9142_Studie_Momentanreserve_2030.pdf, 2016. Accessed: 2022-11-15.

[341] Harold R. Chamorro, Alvaro D. Orjuela-Cañón, David Ganger, Mattias Persson, Francisco Gonzalez-Longatt, et al. Nadir Frequency Estimation in Low-Inertia Power Systems. In *2020 IEEE 29th International Symposium on Industrial Electronics (ISIE)*, pages 918–922, 2020. DOI: 10.1109/ISIE45063.2020.9152296. ISSN: 2163-5145.

[342] A. Moser, Patrick Schwerdt, and Martin Knechtges. Ermittlung der Momentanreserve von Wasserkraftanlagen in Deutschland, 2021.

[343] Luigi Busarello and Rossano Musca. Impact of the high share of converter-interfaced generation on electromechanical oscillations in Continental Europe power system. *IET Renewable Power Generation*, 14(19):3918–3926, 2020. ISSN 1752-1424. DOI: 10.1049/iet-rpg.2020.0489.

[344] M. Dierick, T. Kapetanovic, A. Marques, David Alvira Baeza, Laurent Lamy, et al. Continental Europe Synchronous Area Separation on 24 July 2021 (ICS Investigation Expert Panel » Final Report » 25 March 2022 - Main Report). https://eepublicdownloads.azureedge.net/clean-documents/Publications/2022/entso-e_CESysSep_210724_02_Final_Report_220325.pdf, 2022. Accessed: 2023-01-04.

[345] Commission Regulation (EU) 2017/2196 of 24 November 2017 establishing a network code on electricity emergency and restoration (Text with EEA relevance). http://data.europa.eu/eli/reg/2017/2196/oj/eng, 2017. Legislative Body: COM, ENER. Accessed: 2023-10-27.

[346] European Network of Transmission System Operators for Electricity (ENTSO-E). System Defence Plan. https://eepublicdownloads.entsoe.eu/clean-documents/SOCdocuments/Regional_Groups_Continental_Europe/2022/220215_RGCE_TOP_03.2_D.1_SystemDefencePlan_v8_final.pdf, 2022. Accessed: 2023-10-27.

[347] VDE Verlag. VDE-AR-N 4105:2018-11 Erzeugungsanlagen am Niederspannungsnetz – Technische Mindestanforderungen für Anschluss und Parallelbetrieb von Erzeugungsanlagen am Niederspannungsnetz, 2018.

[348] Ujjwol Tamrakar, Dipesh Shrestha, Manisha Maharjan, Bishnu P. Bhattarai, Timothy M. Hansen, et al. Virtual Inertia: Current Trends and Future Directions. *Applied Sciences*, 7(7):654, 2017. ISSN 2076-3417. DOI: 10.3390/app7070654.

[349] Kah Yung Yap, Charles R. Sarimuthu, and Joanne Mun-Yee Lim. Virtual Inertia-Based Inverters for Mitigating Frequency Instability in Grid-Connected Renewable Energy System: A Review. *Applied Sciences*, 9(24):5300, 2019. ISSN 2076-3417. DOI: 10.3390/app9245300.

[350] Krishnakumar R. Vasudevan, Vigna K. Ramachandaramurthy, Thanikanti Sudhakar Babu, and Aref Pouryekta. Synchronverter: A Comprehensive Review of Modifications, Stability Assessment, Applications and Future Perspectives. *IEEE Access*, 8:131565–131589, 2020. ISSN 2169-3536. DOI: 10.1109/ACCESS.2020.3010001.

[351] Thongchart Kerdphol, Fathin Saifur Rahman, Masayuki Watanabe, and Yasunori Mitani. *Virtual Inertia Synthesis and Control*. Power Systems. Springer International Publishing, Cham, 2021. ISBN 978-3-030-57960-9 978-3-030-57961-6. DOI: 10.1007/978-3-030-57961-6.

[352] Deeksha Singh and K. Seethalekshmi. A Review on Various Virtual Inertia Techniques for Distributed Generation. In *2020 International Conference on Electrical and Electronics Engineering (ICE3)*, pages 631–638, 2020. DOI: 10.1109/ICE348803.2020.9122959.

[353] R. M. da Silva. Power control strategies for grid-connected converters during low voltage ride through operation. Master's thesis, Universidade Federal de Minas Gerais (UFMG) - Escola de Engenharia, 2019. https://repositorio.ufmg.br/bitstream/1843/RAOA-BCDJ49/1/master_thesis_rafael_m_silva.pdf. Accessed: 2022-11-24.

[354] Matthias Luh. Entwicklung eines resonanten, hocheffizienten bidirektionalen Li-Ion Batterieladegerätes mit Silicium-Carbid Halbleitern. Master's thesis, Karlsruhe Institute of Technology, 2019.

[355] Wolfspeed, Inc. CPM3-1200-0013A – Wolfspeed SiC Gen 3 MOSFET (data sheet). https://assets.wolfspeed.com/uploads/2023/08/Wolfspeed_CPM3-1200-0013A_data_sheet_external.pdf, 2023. Rev. 03. Accessed: 2023-12-13.

[356] Cree, Inc. CPW5-1200-Z050B – Silicon Carbide Schottky Diode Chip (data sheet). https://datasheet.octopart.com/CPW5-1200-Z050B-Wolfspeed-datasheet-145438003.pdf, 2014. Rev. A. Accessed: 2023-12-13.

[357] Wolfspeed, Inc. CPM3-1200-0075A – Wolfspeed SiC Gen 3 MOSFET (data sheet). https://assets.wolfspeed.com/uploads/2023/08/Wolfspeed_CPM3-1200-0075A_data_sheet_external.pdf, 2023. Rev. 03. Accessed: 2023-12-13.

[358] Manish Bhardwaj. Software Phase Locked Loop Design Using C2000™ Microcontrollers for Three Phase Grid Connected Applications. https://www.ti.com/lit/an/sprabt4a/sprabt4a.pdf?ts=1714092935548, 2013. Application Report SPRABT4A. Accessed: 2024-04-26.

[359] Cree, Inc. CPM3-0900-0065B Silicon Carbide Power MOSFET (data sheet), 2017. Rev. C.

[360] Dierk Schröder and Joachim Böcker, editors. *Elektrische Antriebe – Regelung von Antriebssystemen*. Springer Berlin Heidelberg, Berlin, Heidelberg, 5 edition, 2021. ISBN 978-3-662-62700-6. DOI: 10.1007/978-3-662-62700-6.

[361] Simon Bischof. *Rekonfigurierbare Lithium-Ionen-Batterien für den Betrieb von industriellen Produktionsstätten*. Dissertation, Karlsruher Institut für Technologie (KIT), Karlsruhe, Germany, 2020. DOI: 10.5445/IR/1000127273.

[362] Bruno Scrosati, Jürgen Garche, and Werner Tillmetz, editors. *Advances in Battery Technologies for Electric Vehicles*. Number 80 in Woodhead Publishing Series in Energy. Woodhead Publishing, Cambridge, UK, 2015. ISBN 978-1-78242-398-0.

[363] Rui Xiong and Weixiang Shen. *Advanced Battery Management Technologies for Electric Vehicles*. Automotive Series. Wiley, Hoboken, NJ, USA, 2019. ISBN 978-1-119-48168-3.

[364] Reiner Korthauer, editor. *Lithium-Ion Batteries: Basics and Applications*. Springer-Verlag GmbH, Berlin, Germany, 1 edition, 2018. ISBN 978-3-662-53071-9. DOI: 10.1007/978-3-662-53071-9.

[365] Alexander Farmann and Dirk Uwe Sauer. A comprehensive review of on-board State-of-Available-Power prediction techniques for lithium-ion batteries in electric vehicles. *Journal of Power Sources*, 329:123–137, 2016. ISSN 0378-7753. DOI: 10.1016/j.jpowsour.2016.08.031.

[366] Gianfranco Pistoia and Boryann Liaw, editors. *Behaviour of Lithium-Ion Batteries in Electric Vehicles: Battery Health, Performance, Safety, and Cost*. Green Energy and Technology. Springer International

Publishing AG, Cham, Switzerland, 1 edition, 2018. ISBN 978-3-319-69950-9. DOI: 10.1007/978-3-319-69950-9.

[367] Magdalena Petrova. Here's why sodium-ion batteries are shaping up to be a big technology breakthrough. *CNBC*, 2023. https://www.cnbc.com/2023/05/10/sodium-ion-batteries-shaping-up-to-be-big-technology-breakthrough.html. Accessed: 2023-10-31.

[368] Maximilian Fichtner. Recent Research and Progress in Batteries for Electric Vehicles. *Batteries & Supercaps*, 5(2):e202100224, 2022. ISSN 2566-6223. DOI: 10.1002/batt.202100224.

[369] Gregory L. Plett. *Battery Management Systems, Volume I: Battery Modeling*. Artech House, 2015. ISBN 978-1-63081-024-5.

[370] Jianlin Li, James Fleetwood, W. Blake Hawley, and William Kays. From Materials to Cell: State-of-the-Art and Prospective Technologies for Lithium-Ion Battery Electrode Processing. *Chemical Reviews*, 122(1):903–956, 2022. ISSN 0009-2665. DOI: 10.1021/acs.chemrev.1c00565.

[371] Matthew Li, Jun Lu, Zhongwei Chen, and Khalil Amine. 30 Years of Lithium-Ion Batteries. *Advanced Materials*, 30(33):1800561, 2018. ISSN 1521-4095. DOI: 10.1002/adma.201800561.

[372] Jürgen Janek and Wolfgang G. Zeier. Challenges in speeding up solid-state battery development. *Nature Energy*, 8(3):230–240, 2023. ISSN 2058-7546. DOI: 10.1038/s41560-023-01208-9.

[373] Aiping Wang, Sanket Kadam, Hong Li, Siqi Shi, and Yue Qi. Review on modeling of the anode solid electrolyte interphase (SEI) for lithium-ion batteries. *npj Computational Materials*, 4(1), 2018. ISSN 2057-3960. DOI: 10.1038/s41524-018-0064-0.

[374] Wiljan Vermeer, Gautham Ram Chandra Mouli, and Pavol Bauer. A Comprehensive Review on the Characteristics and Modeling of Lithium-Ion Battery Aging. *IEEE Transactions on Transportation Electrification*, 8(2):2205–2232, 2022. ISSN 2332-7782, 2372-2088. DOI: 10.1109/TTE.2021.3138357.

[375] Giorgia Zampardi and Fabio La Mantia. Solid–Electrolyte Interphase at Positive Electrodes in High-Energy Li-Ion Batteries: Current Understanding and Analytical Tools. *Batteries & Supercaps*, 3(8): 672–697, 2020. ISSN 2566-6223. DOI: 10.1002/batt.201900177.

[376] Zewen Zhang, Jinlong Yang, William Huang, Hansen Wang, Weijiang Zhou, et al. Cathode-Electrolyte Interphase in Lithium Batteries Revealed by Cryogenic Electron Microscopy. *Matter*, 4(1):302–312, 2021. ISSN 25902385. DOI: 10.1016/j.matt.2020.10.021.

[377] Isidor Buchmann. *Batteries in a portable world: a handbook on rechargeable batteries for non-engineers*. Cadex Electronics Inc., Richmond, British Columbia, 4 edition, 2016. ISBN 978-0-9682118-4-7.

[378] Xuan Liu, Kang Li, and Xiang Li. The Electrochemical Performance and Applications of Several Popular Lithium-ion Batteries for Electric Vehicles - A Review. In Kang Li, Jianhua Zhang, Minyou Chen, Zhile Yang, and Qun Niu, editors, *Advances in Green Energy Systems and Smart Grid*, Communications in Computer and Information Science, pages 201–213, Singapore, 2018. Springer. ISBN 9789811323812. DOI: 10.1007/978-981-13-2381-2_19.

[379] Ghassan Zubi, Rodolfo Dufo-López, Monica Carvalho, and Guzay Pasaoglu. The lithium-ion battery: State of the art and future perspectives. *Renewable and Sustainable Energy Reviews*, 89:292–308, 2018. ISSN 1364-0321. DOI: 10.1016/j.rser.2018.03.002.

[380] Yu Miao, Patrick Hynan, Annette von Jouanne, and Alexandre Yokochi. Current Li-Ion Battery Technologies in Electric Vehicles and Opportunities for Advancements. *Energies*, 12(6):1074, 2019. DOI: 10.3390/en12061074.

[381] Gaizka Saldaña, José Ignacio San Martín, Inmaculada Zamora, Francisco Javier Asensio, and Oier Oñederra. Analysis of the Current Electric Battery Models for Electric Vehicle Simulation. *Energies*, 12(14):2750, 2019. ISSN 1996-1073. DOI: 10.3390/en12142750.

[382] Moodakare B. Sahana and Raghavan Gopalan. Recent Developments in Electrode Materials for Lithium-Ion Batteries for Energy Storage Application. In Yashwant R. Mahajan and Roy Johnson, editors, *Handbook of Advanced Ceramics and Composites: Defense, Security, Aerospace and Energy Applications*, pages 1297–1333. Springer International Publishing, Cham, 2020. ISBN 978-3-030-16347-1. DOI: 10.1007/978-3-030-16347-1_44.

[383] Feixiang Wu, Joachim Maier, and Yan Yu. Guidelines and trends for next-generation rechargeable lithium and lithium-ion batteries. *Chemical Society Reviews*, 49(5):1569–1614, 2020. ISSN 0306-0012, 1460-4744. DOI: 10.1039/C7CS00863E.

[384] Carola Leone, Laura Sturaro, Giacomo Geroli, Michela Longo, and Wahiba Yaici. Design and Implementation of an Electric Skibus Line in North Italy. *Energies*, 14(23):7925, 2021. ISSN 1996-1073. DOI: 10.3390/en14237925.

[385] Matthieu Dubarry, Nan Qin, and Paul Brooker. Calendar aging of commercial Li-ion cells of different chemistries – A review. *Current Opinion in Electrochemistry*, 9:106–113, 2018. ISSN 2451-9103. DOI: 10.1016/j.coelec.2018.05.023.

[386] Muthu Krishna. The EV battery chemistry debate just got more complicated. https://www.fastmarkets.com/insights/the-ev-battery-chemistry-debate-just-got-more-complicated/, 2022. Accessed: 2023-11-03.

[387] Veronika Henze. Lithium-ion Battery Pack Prices Rise for First Time to an Average of $151/kWh. https://about.bnef.com/blog/lithium-ion-battery-pack-prices-rise-for-first-time-to-an-average-of-151-kwh/, 2022. Section: Press Release. Accessed: 2023-11-03.

[388] Xianke Lin, Kavian Khosravinia, Xiaosong Hu, Ju Li, and Wei Lu. Lithium Plating Mechanism, Detection, and Mitigation in Lithium-Ion Batteries. *Progress in Energy and Combustion Science*, 87:100953, 2021. ISSN 0360-1285. DOI: 10.1016/j.pecs.2021.100953.

[389] United Nations (UN). Addendum 15: Global technical regulation No. 15 – Worldwide harmonized Light vehicles Test Procedure (ECE/TRANS/180/Add.15). https://unece.org/fileadmin/DAM/trans/main/wp29/wp29r-1998agr-rules/ECE-TRANS-180a15e.pdf, 2014. Accessed: 2023-11-06.

[390] Min-Hsuan Hung, Chang-Hua Lin, Liang-Cheng Lee, and Chien-Ming Wang. State-of-charge and state-of-health estimation for lithium-ion batteries based on dynamic impedance technique. *Journal of Power Sources*, 268:861–873, 2014. ISSN 0378-7753. DOI: 10.1016/j.jpowsour.2014.06.083.

[391] Benedikt Rzepka, Simon Bischof, and Thomas Blank. Implementing an Extended Kalman Filter for SoC Estimation of a Li-Ion Battery with Hysteresis: A Step-by-Step Guide. *Energies*, 14(13):3733, 2021. ISSN 1996-1073. DOI: 10.3390/en14133733.

[392] Dai Wang, Jonathan Coignard, Teng Zeng, Cong Zhang, and Samveg Saxena. Quantifying electric vehicle battery degradation from driving vs. vehicle-to-grid services. *Journal of Power Sources*, 332:193–203, 2016. ISSN 0378-7753. DOI: 10.1016/j.jpowsour.2016.09.116.

[393] Mehdi Jafari, Antonio Gauchia, Shuaidong Zhao, Kuilin Zhang, and Lucia Gauchia. Electric Vehicle Battery Cycle Aging Evaluation in Real-World Daily Driving and Vehicle-to-Grid Services. *IEEE Transactions on Transportation Electrification*, 4(1):122–134, 2018. ISSN 2332-7782. DOI: 10.1109/TTE.2017.2764320.

[394] Andrew W. Thompson. Economic implications of lithium ion battery degradation for Vehicle-to-Grid (V2X) services. *Journal of Power Sources*, 396:691–709, 2018. ISSN 0378-7753. DOI: 10.1016/j.jpowsour.2018.06.053.

[395] Truong M. N. Bui, Muhammad Sheikh, Truong Q. Dinh, Aniruddha Gupta, Dhammika W. Widanalage, et al. A Study of Reduced Battery Degradation Through State-of-Charge Pre-Conditioning for Vehicle-to-Grid Operations. *IEEE Access*, 9:155871–155896, 2021. ISSN 2169-3536. DOI: 10.1109/ACCESS.2021.3128774.

[396] Maria Stefania Carmeli, Nicola Toscani, and Marco Mauri. Electrothermal Aging Model of Li-Ion Batteries for Vehicle-to-Grid Services Evaluation. *Electronics*, 11(7):1042, 2022. ISSN 2079-9292. DOI: 10.3390/electronics11071042.

[397] Ken Darcovich, Steven Recoskie, Hajo Ribberink, Fleurine Pincet, and Amaury Foissac. Effect on battery life of vehicle-to-home electric power provision under Canadian residential electrical demand. *Applied Thermal Engineering*, 114:1515–1522, 2017. ISSN 1359-4311. DOI: 10.1016/j.applthermaleng.2016.07.002.

[398] Kenechukwu Ginigeme and Zhanle Wang. Distributed Optimal Vehicle-To-Grid Approaches With Consideration of Battery Degradation Cost Under Real-Time Pricing. *IEEE Access*, 8:5225–5235, 2020. ISSN 2169-3536. DOI: 10.1109/ACCESS.2019.2963692.

[399] Christian Schlasza, Peter Ostertag, Daniela Chrenko, Reiner Kriesten, and David Bouquain. Review on the aging mechanisms in Li-ion batteries for electric vehicles based on the FMEA method. In *2014 IEEE Transportation Electrification Conference and Expo (ITEC)*, 2014. DOI: 10.1109/ITEC.2014.6861811.

[400] Shangshang Wang, Jianbo Zhang, Oumaïma Gharbi, Vincent Vivier, Ming Gao, et al. Electrochemical impedance spectroscopy. *Nature Reviews Methods Primers*, 1(1), 2021. ISSN 2662-8449. DOI: 10.1038/s43586-021-00039-w.

[401] BioLogic. Studying batteries with Electrochemical Impedance Spectroscopy (EIS) – White Paper #01. https://www.biologic.net/wp-content/uploads/2019/08/studying-batteries-with-electrochemical-impedance-spectroscopy-wp1-electrochemistry-battery.pdf, 2017. Accessed: 2023-11-07.

[402] Matthieu Dubarry, Arnaud Devie, and Bor Yann Liaw. The Value of Battery Diagnostics and Prognostics. *Journal of Energy and Power Sources*, 1:242–249, 2014.

[403] Christoph R. Birkl, Matthew R. Roberts, Euan McTurk, Peter G. Bruce, and David A. Howey. Degradation diagnostics for lithium ion cells. *Journal of Power Sources*, 341:373–386, 2017. ISSN 0378-7753. DOI: 10.1016/j.jpowsour.2016.12.011.

[404] Xuebing Han, Languang Lu, Yuejiu Zheng, Xuning Feng, Zhe Li, et al. A review on the key issues of the lithium ion battery degradation among the whole life cycle. *eTransportation*, 1:100005, 2019. ISSN 2590-1168. DOI: 10.1016/j.etran.2019.100005.

[405] Carlos Pastor-Fernández, Tung Fai Yu, W. Dhammika Widanage, and James Marco. Critical review of non-invasive diagnosis techniques for quantification of degradation modes in lithium-ion

batteries. *Renewable and Sustainable Energy Reviews*, 109:138–159, 2019. ISSN 1364-0321. DOI: 10.1016/j.rser.2019.03.060.

[406] J. Vetter, P. Novák, M. R. Wagner, C. Veit, K. C. Möller, et al. Ageing mechanisms in lithium-ion batteries. *Journal of Power Sources*, 147(1):269–281, 2005. ISSN 0378-7753. DOI: 10.1016/j.jpowsour.2005.01.006.

[407] Jens Groot. *State-of-Health Estimation of Li-ion Batteries: Cycle Life Test Methods*. Licentiate thesis, Chalmers University of Technology, Göteborg, Sweden, 2012. http://komar.in/files/JensGroot.pdf. Accessed: 2023-11-08.

[408] Christopher Hendricks, Nick Williard, Sony Mathew, and Michael Pecht. A failure modes, mechanisms, and effects analysis (FMMEA) of lithium-ion batteries. *Journal of Power Sources*, 297: 113–120, 2015. ISSN 0378-7753. DOI: 10.1016/j.jpowsour.2015.07.100.

[409] Foad H. Gandoman, Joris Jaguemont, Shovon Goutam, Rahul Gopalakrishnan, Yousef Firouz, et al. Concept of reliability and safety assessment of lithium-ion batteries in electric vehicles: Basics, progress, and challenges. *Applied Energy*, 251:113343, 2019. ISSN 0306-2619. DOI: 10.1016/j.apenergy.2019.113343.

[410] Kazuma Kumai, Hajime Miyashiro, Yo Kobayashi, Katsuhito Takei, and Rikio Ishikawa. Gas generation mechanism due to electrolyte decomposition in commercial lithium-ion cell. *Journal of Power Sources*, 81-82:715–719, 1999. ISSN 0378-7753. DOI: 10.1016/S0378-7753(98)00234-1.

[411] Muthukrishnan Kaliaperumal, Milindar S. Dharanendrakumar, Santosh Prasanna, Kaginele V. Abhishek, Ramesh Kumar Chidambaram, et al. Cause and Mitigation of Lithium-Ion Battery Failure—A Review. *Materials*, 14(19):5676, 2021. ISSN 1996-1944. DOI: 10.3390/ma14195676.

[412] Xiao-Guang Yang, Yongjun Leng, Guangsheng Zhang, Shanhai Ge, and Chao-Yang Wang. Modeling of lithium plating induced aging of lithium-ion batteries: Transition from linear to nonlinear aging. *Journal of Power Sources*, 360:28–40, 2017. ISSN 0378-7753. DOI: 10.1016/j.jpowsour.2017.05.110.

[413] Marco T. F. Rodrigues, Seoung-Bum Son, Andrew M. Colclasure, Ilya A. Shkrob, Stephen E. Trask, et al. How Fast Can a Li-Ion Battery Be Charged? Determination of Limiting Fast Charging Conditions. *ACS Applied Energy Materials*, 4(2):1063–1068, 2021. DOI: 10.1021/acsaem.0c03114.

[414] Polina Brodsky Ringler, Matthew Wise, Prashanth Ramesh, Jung Hyun Kim, Marcello Canova, et al. Modeling of Lithium Plating and Stripping Dynamics during Fast Charging. *Batteries*, 9(7):337, 2023. ISSN 2313-0105. DOI: 10.3390/batteries9070337.

[415] Christian von Lüders, Jonas Keil, Markus Webersberger, and Andreas Jossen. Modeling of lithium plating and lithium stripping in lithium-ion batteries. *Journal of Power Sources*, 414:41–47, 2019. ISSN 0378-7753. DOI: 10.1016/j.jpowsour.2018.12.084.

[416] Weifeng Yao, Junhua Zhao, Fushuan Wen, Yusheng Xue, and Gerard Ledwich. A Hierarchical Decomposition Approach for Coordinated Dispatch of Plug-in Electric Vehicles. *IEEE Transactions on Power Systems*, 28(3):2768–2778, 2013. ISSN 1558-0679. DOI: 10.1109/TPWRS.2013.2256937.

[417] Yue Wang and D. Infield. Optimal Demand Side Response to Real Time Price Signal Using Electric Vehicles. In *International Conference on Renewable Power Generation (RPG 2015)*, 2015. DOI: 10.1049/cp.2015.0325.

[418] Hongcai Zhang, Zechun Hu, Zhiwei Xu, and Yonghua Song. Evaluation of Achievable Vehicle-to-Grid Capacity Using Aggregate PEV Model. *IEEE Transactions on Power Systems*, 32(1):784–794, 2017. ISSN 1558-0679. DOI: 10.1109/TPWRS.2016.2561296.

[419] Abdullah. A. Almehizia and J. M. Snodgrass. Investigation of V2G economical viability. In *2018 IEEE Texas Power and Energy Conference (TPEC)*, 2018. DOI: 10.1109/TPEC.2018.8312048.

[420] Gautham Ram Chandra Mouli, Mahdi Kefayati, Ross Baldick, and Pavol Bauer. Integrated PV Charging of EV Fleet Based on Energy Prices, V2G, and Offer of Reserves. *IEEE Transactions on Smart Grid*, 10(2):1313–1325, 2019. ISSN 1949-3061. DOI: 10.1109/TSG.2017.2763683.

[421] A. Schuller, B. Dietz, C. M. Flath, and C. Weinhardt. Charging Strategies for Battery Electric Vehicles: Economic Benchmark and V2G Potential. *IEEE Transactions on Power Systems*, 29(5): 2014–2022, 2014. ISSN 1558-0679. DOI: 10.1109/TPWRS.2014.2301024.

[422] Zhongjing Ma, Suli Zou, and Xiangdong Liu. A Distributed Charging Coordination for Large-Scale Plug-In Electric Vehicles Considering Battery Degradation Cost. *IEEE Transactions on Control Systems Technology*, 23(5):2044–2052, 2015. ISSN 1558-0865. DOI: 10.1109/TCST.2015.2394319.

[423] Timo Lehtola and Ahmad Zahedi. Cost of EV battery wear due to vehicle to grid application. In *2015 Australasian Universities Power Engineering Conference (AUPEC)*, 2015. DOI: 10.1109/AUPEC.2015.7324824.

[424] Hossein Farzin, Mahmud Fotuhi-Firuzabad, and Moein Moeini-Aghtaie. A Practical Scheme to Involve Degradation Cost of Lithium-Ion Batteries in Vehicle-to-Grid Applications. *IEEE Transactions on Sustainable Energy*, 7(4):1730–1738, 2016. ISSN 1949-3037. DOI: 10.1109/TSTE.2016.2558500.

[425] Justin D. K. Bishop, Colin J. Axon, David Bonilla, Martino Tran, David Banister, et al. Evaluating the impact of V2G services on the degradation of batteries in PHEV and EV. *Applied Energy*, 111: 206–218, 2013. ISSN 0306-2619. DOI: 10.1016/j.apenergy.2013.04.094.

[426] Yifeng He, Bala Venkatesh, and Ling Guan. Optimal Scheduling for Charging and Discharging of Electric Vehicles. *IEEE Transactions on Smart Grid*, 3(3):1095–1105, 2012. ISSN 1949-3061. DOI: 10.1109/TSG.2011.2173507.

[427] Jose Rivera, Philipp Wolfrum, Sandra Hirche, Christoph Goebel, and Hans-Arno Jacobsen. Alternating Direction Method of Multipliers for decentralized electric vehicle charging control. In *52nd IEEE Conference on Decision and Control*, pages 6960–6965, 2013. DOI: 10.1109/CDC.2013.6760992. ISSN: 0191-2216.

[428] Benedikt Lunz, Zexiong Yan, Jochen Bernhard Gerschler, and Dirk Uwe Sauer. Influence of plug-in hybrid electric vehicle charging strategies on charging and battery degradation costs. *Energy Policy*, 46:511–519, 2012. ISSN 0301-4215. DOI: 10.1016/j.enpol.2012.04.017.

[429] A. Hoke, A. Brissette, D. Maksimović, A. Pratt, and K. Smith. Electric vehicle charge optimization including effects of lithium-ion battery degradation. In *2011 IEEE Vehicle Power and Propulsion Conference*, 2011. DOI: 10.1109/VPPC.2011.6043046.

[430] Martin Petit, Eric Prada, and Valérie Sauvant-Moynot. Development of an empirical aging model for Li-ion batteries and application to assess the impact of Vehicle-to-Grid strategies on battery lifetime. *Applied Energy*, 172:398–407, 2016. ISSN 0306-2619. DOI: 10.1016/j.apenergy.2016.03.119.

[431] Ali Ahmadian, Mahdi Sedghi, Behnam Mohammadi-ivatloo, Ali Elkamel, Masoud Aliakbar Golkar, et al. Cost-Benefit Analysis of V2G Implementation in Distribution Networks Considering PEVs Battery Degradation. *IEEE Transactions on Sustainable Energy*, 9(2):961–970, 2018. ISSN 1949-3037. DOI: 10.1109/TSTE.2017.2768437.

[432] Prasad Prakash Malya, Laura Fiorini, Mohammadhadi Rouhani, and Marco Aiello. Electric vehicles as distribution grid batteries: a reality check. *Energy Informatics*, 4(2):29, 2021. ISSN 2520-8942. DOI: 10.1186/s42162-021-00159-3.

[433] Karl Schwenk, Stefan Meisenbacher, Benjamin Briegel, Tim Harr, Veit Hagenmeyer, et al. Integrating Battery Aging in the Optimization for Bidirectional Charging of Electric Vehicles. *IEEE Transactions on Smart Grid*, 12(6):5135–5145, 2021. ISSN 1949-3061. DOI: 10.1109/TSG.2021.3099206.

[434] Matthieu Dubarry, Arnaud Devie, and Katherine McKenzie. Durability and reliability of electric vehicle batteries under electric utility grid operations: Bidirectional charging impact analysis. *Journal of Power Sources*, 358:39–49, 2017. ISSN 0378-7753. DOI: 10.1016/j.jpowsour.2017.05.015.

[435] Jacqueline S. Edge, Simon O'Kane, Ryan Prosser, Niall D. Kirkaldy, Anisha N. Patel, et al. Lithium ion battery degradation: what you need to know. *Physical Chemistry Chemical Physics*, 23(14): 8200–8221, 2021. ISSN 1463-9084. DOI: 10.1039/D1CP00359C.

[436] Anthony Barré, Benjamin Deguilhem, Sébastien Grolleau, Mathias Gérard, Frédéric Suard, et al. A review on lithium-ion battery ageing mechanisms and estimations for automotive applications. *Journal of Power Sources*, 241:680–689, 2013. ISSN 03787753. DOI: 10.1016/j.jpowsour.2013.05.040.

[437] Claudia Meis, Stefan Mueller, Stephan Rohr, Matthias Kerler, and Markus Lienkamp. Guide for the Focused Utilization of Aging Models for Lithium-Ion Batteries - An Automotive Perspective. *SAE International Journal of Passenger Cars - Electronic and Electrical Systems*, 8(1):195–206, 2015. ISSN 1946-4622. DOI: 10.4271/2015-01-0255.

[438] Quentin Badey, Guillaume Cherouvrier, Yvan Reynier, Jean-Marc Duffault, and Sylvain Franger. Ageing forecast of lithium-ion batteries for electric and hybrid vehicles. *Current topics in electrochemistry*, 16:65–79, 2011.

[439] Paul Gasper, Nils Collath, Holger C. Hesse, Andreas Jossen, and Kandler Smith. Machine-Learning Assisted Identification of Accurate Battery Lifetime Models with Uncertainty. *Journal of The Electrochemical Society*, 169(8):080518, 2022. ISSN 1945-7111. DOI: 10.1149/1945-7111/ac86a8.

[440] Jorn M. Reniers, Grietus Mulder, Sina Ober-Blöbaum, and David A. Howey. Improving optimal control of grid-connected lithium-ion batteries through more accurate battery and degradation modelling. *Journal of Power Sources*, 379:91–102, 2018. ISSN 0378-7753. DOI: 10.1016/j.jpowsour.2018.01.004.

[441] Dezhi Li, Dongfang Yang, Liwei Li, Licheng Wang, and Kai Wang. Electrochemical Impedance Spectroscopy Based on the State of Health Estimation for Lithium-Ion Batteries. *Energies*, 15(18): 6665, 2022. ISSN 1996-1073. DOI: 10.3390/en15186665.

[442] Daniel Werner, Sabine Paarmann, Achim Wiebelt, and Thomas Wetzel. Inhomogeneous Temperature Distribution Affecting the Cyclic Aging of Li-Ion Cells. Part II: Analysis and Correlation. *Batteries*, 6(1):12, 2020. ISSN 2313-0105. DOI: 10.3390/batteries6010012.

[443] Jorn M. Reniers, Grietus Mulder, and David A. Howey. Review and Performance Comparison of Mechanical-Chemical Degradation Models for Lithium-Ion Batteries. *Journal of The Electrochemical Society*, 166(14):A3189, 2019. ISSN 1945-7111. DOI: 10.1149/2.0281914jes.

[444] Changyong Lee, Sugyeong Jo, Daeil Kwon, and Michael G. Pecht. Capacity-Fading Behavior Analysis for Early Detection of Unhealthy Li-Ion Batteries. *IEEE Transactions on Industrial Electronics*, 68 (3):2659–2666, 2021. ISSN 0278-0046, 1557-9948. DOI: 10.1109/TIE.2020.2972468.

[445] Damian Burzyński and Leszek Kasprzyk. A novel method for the modeling of the state of health of lithium-ion cells using machine learning for practical applications. *Knowledge-Based Systems*, 219: 106900, 2021. ISSN 0950-7051. DOI: 10.1016/j.knosys.2021.106900.

[446] Ali Ahmadian, Mahdi Sedghi, Ali Elkamel, Michael Fowler, and Masoud Aliakbar Golkar. Plug-in electric vehicle batteries degradation modeling for smart grid studies: Review, assessment and conceptual framework. *Renewable and Sustainable Energy Reviews*, 81:2609–2624, 2018. ISSN 1364-0321. DOI: 10.1016/j.rser.2017.06.067.

[447] Timo A. Lehtola and Ahmad Zahedi. Electric Vehicle Battery Cell Cycle Aging in Vehicle to Grid Operations: A Review. *IEEE Journal of Emerging and Selected Topics in Power Electronics*, 9(1): 423–437, 2021. ISSN 2168-6785. DOI: 10.1109/JESTPE.2019.2959276.

[448] F. Brosa Planella, W. Ai, A. M. Boyce, A. Ghosh, I. Korotkin, et al. A continuum of physics-based lithium-ion battery models reviewed. *Progress in Energy*, 4(4):042003, 2022. ISSN 2516-1083. DOI: 10.1088/2516-1083/ac7d31.

[449] Huixin Tian, Pengliang Qin, Kun Li, and Zhen Zhao. A review of the state of health for lithium-ion batteries: Research status and suggestions. *Journal of Cleaner Production*, 261:120813, 2020. ISSN 0959-6526. DOI: 10.1016/j.jclepro.2020.120813.

[450] Shahid A. Hasib, S. Islam, Ripon K. Chakrabortty, Michael J. Ryan, D. K. Saha, et al. A Comprehensive Review of Available Battery Datasets, RUL Prediction Approaches, and Advanced Battery Management. *IEEE Access*, 9:86166–86193, 2021. ISSN 2169-3536. DOI: 10.1109/ACCESS.2021.3089032.

[451] V. Sulzer, S. G. Marquis, R. Timms, M. Robinson, and S. J. Chapman. Python battery mathematical modelling (PyBaMM). *Journal of Open Research Software*, 9(1), 2021. DOI: 10.5334/jors.309.

[452] J. Neubauer. Battery Lifetime Analysis and Simulation Tool (BLAST) Documentation, 2014. DOI: 10.2172/1167066.

[453] E. Sarasketa-Zabala, I. Gandiaga, E. Martinez-Laserna, L. M. Rodriguez-Martinez, and I. Villarreal. Cycle ageing analysis of a LiFePO4/graphite cell with dynamic model validations: Towards realistic lifetime predictions. *Journal of Power Sources*, 275:573–587, 2015. ISSN 0378-7753. DOI: 10.1016/j.jpowsour.2014.10.153.

[454] E. Sarasketa-Zabala, E. Martinez-Laserna, M. Berecibar, I. Gandiaga, L. M. Rodriguez-Martinez, et al. Realistic lifetime prediction approach for Li-ion batteries. *Applied Energy*, 162:839–852, 2016. ISSN 0306-2619. DOI: 10.1016/j.apenergy.2015.10.115.

[455] Xuebing Han, Minggao Ouyang, Languang Lu, and Jianqiu Li. A comparative study of commercial lithium ion battery cycle life in electric vehicle: Capacity loss estimation. *Journal of Power Sources*, 268:658–669, 2014. ISSN 0378-7753. DOI: 10.1016/j.jpowsour.2014.06.111.

[456] Weiping Diao, Saurabh Saxena, and Michael Pecht. Accelerated cycle life testing and capacity degradation modeling of LiCoO2-graphite cells. *Journal of Power Sources*, 435:226830, 2019. ISSN 0378-7753. DOI: 10.1016/j.jpowsour.2019.226830.

[457] Weiping Diao, Saurabh Saxena, Bongtae Han, and Michael Pecht. Algorithm to Determine the Knee Point on Capacity Fade Curves of Lithium-Ion Cells. *Energies*, 12(15):2910, 2019. ISSN 1996-1073. DOI: 10.3390/en12152910.

[458] Saurabh Saxena, Yinjiao Xing, Daeil Kwon, and Michael Pecht. Accelerated degradation model for C-rate loading of lithium-ion batteries. *International Journal of Electrical Power & Energy Systems*, 107:438–445, 2019. ISSN 01420615. DOI: 10.1016/j.ijepes.2018.12.016.

[459] Saurabh Saxena, Christopher Hendricks, and Michael Pecht. Cycle life testing and modeling of graphite/LiCoO2 cells under different state of charge ranges. *Journal of Power Sources*, 327:394–400, 2016. ISSN 0378-7753. DOI: 10.1016/j.jpowsour.2016.07.057.

[460] John Wang, Ping Liu, Jocelyn Hicks-Garner, Elena Sherman, Souren Soukiazian, et al. Cycle-life model for graphite-LiFePO4 cells. *Journal of Power Sources*, 196(8):3942–3948, 2011. ISSN 03787753. DOI: 10.1016/j.jpowsour.2010.11.134.

[461] Haifeng Dai, Xiaolong Zhang, Weijun Gu, Xuezhe Wei, and Zechang Sun. A Semi-Empirical Capacity Degradation Model of EV Li-Ion Batteries Based on Eyring Equation. In *2013 IEEE Vehicle Power and Propulsion Conference (VPPC)*, 2013. DOI: 10.1109/VPPC.2013.6671660. ISSN: 1938-8756.

[462] Girish Suri and Simona Onori. A control-oriented cycle-life model for hybrid electric vehicle lithium-ion batteries. *Energy*, 96:644–653, 2016. ISSN 0360-5442. DOI: 10.1016/j.energy.2015.11.075.

[463] Lorenzo Milanesi, Matthias K. Scharrer, and Davide Barater. Experimental based Aging Model for Automotive Li-Ion Batteries. In *IECON 2021 – 47th Annual Conference of the IEEE Industrial Electronics Society*, 2021. DOI: 10.1109/IECON48115.2021.9589655. ISSN: 2577-1647.

[464] Joel C. Forman, Scott J. Moura, Jeffrey L. Stein, and Hosam K. Fathy. Optimal Experimental Design for Modeling Battery Degradation. In *Volume 1: Adaptive Control; Advanced Vehicle Propulsion Systems; Aerospace Systems; Autonomous Systems; Battery Modeling; Biochemical Systems; Control Over Networks; Control Systems Design; Cooperativ*, pages 309–318, Fort Lauderdale, Florida, USA, 2012. ASME. ISBN 978-0-7918-4529-5. DOI: 10.1115/DSCC2012-MOVIC2012-8751.

[465] Souleman N. Motapon, Enric Lachance, Louis-A. Dessaint, and Kamal Al-Haddad. A Generic Cycle Life Model for Lithium-Ion Batteries Based on Fatigue Theory and Equivalent Cycle Counting. *IEEE Open Journal of the Industrial Electronics Society*, 1:207–217, 2020. ISSN 2644-1284. DOI: 10.1109/OJIES.2020.3015396.

[466] Yingzhi Cui, Chunyu Du, Geping Yin, Yunzhi Gao, Lingling Zhang, et al. Multi-stress factor model for cycle lifetime prediction of lithium ion batteries with shallow-depth discharge. *Journal of Power Sources*, 279:123–132, 2015. ISSN 0378-7753. DOI: 10.1016/j.jpowsour.2015.01.003.

[467] Valentin Muenzel, Julian de Hoog, Marcus Brazil, Arun Vishwanath, and Shivkumar Kalyanaraman. A Multi-Factor Battery Cycle Life Prediction Methodology for Optimal Battery Management. In *Proceedings of the 2015 ACM Sixth International Conference on Future Energy Systems - e-Energy '15*, pages 57–66, Bangalore, India, 2015. ACM Press. ISBN 978-1-4503-3609-3. DOI: 10.1145/2768510.2768532.

[468] Alan Millner. Modeling Lithium Ion battery degradation in electric vehicles. In *2010 IEEE Conference on Innovative Technologies for an Efficient and Reliable Electricity Supply*, pages 349–356, 2010. DOI: 10.1109/CITRES.2010.5619782.

[469] Saurabh Saxena, Darius Roman, Valentin Robu, David Flynn, and Michael Pecht. Battery Stress Factor Ranking for Accelerated Degradation Test Planning Using Machine Learning. *Energies*, 14 (3):723, 2021. ISSN 1996-1073. DOI: 10.3390/en14030723.

[470] Zhe Li, Languang Lu, Minggao Ouyang, and Yuankun Xiao. Modeling the capacity degradation of LiFePO4/graphite batteries based on stress coupling analysis. *Journal of Power Sources*, 196(22): 9757–9766, 2011. ISSN 0378-7753. DOI: 10.1016/j.jpowsour.2011.07.080.

[471] Josu Olmos, Iñigo Gandiaga, Andoni Saez-de Ibarra, Xabier Larrea, Txomin Nieva, et al. Modelling the cycling degradation of Li-ion batteries: Chemistry influenced stress factors. *Journal of Energy Storage*, 40:102765, 2021. ISSN 2352-152X. DOI: 10.1016/j.est.2021.102765.

[472] E. Sarasketa-Zabala, I. Gandiaga, L. M. Rodriguez-Martinez, and I. Villarreal. Calendar ageing analysis of a LiFePO4/graphite cell with dynamic model validations: Towards realistic lifetime predictions. *Journal of Power Sources*, 272:45–57, 2014. ISSN 0378-7753. DOI: 10.1016/j.jpowsour.2014.08.051.

[473] Sébastien Grolleau, Arnaud Delaille, Hamid Gualous, Philippe Gyan, Renaud Revel, et al. Calendar aging of commercial graphite/LiFePO4 cell – Predicting capacity fade under time dependent storage conditions. *Journal of Power Sources*, 255:450–458, 2014. ISSN 0378-7753. DOI: 10.1016/j.jpowsour.2013.11.098.

[474] Elisa Braco, Idoia San Martín, Pablo Sanchis, and Alfredo Ursúa. Analysis and modelling of calendar ageing in second-life lithium-ion batteries from electric vehicles. In *2022 IEEE International Conference on Environment and Electrical Engineering and 2022 IEEE Industrial and Commercial Power Systems Europe (EEEIC / I&CPS Europe)*, 2022. DOI: 10.1109/EEEIC/ICPSEurope54979.2022.9854784.

[475] I. Baghdadi, O. Briat, J.Y. Delétage, P. Gyan, and J.M. Vinassa. Chemical rate phenomenon approach applied to lithium battery capacity fade estimation. *Microelectronics Reliability*, 64:134–139, 2016. ISSN 00262714. DOI: 10.1016/j.microrel.2016.07.058.

[476] Madeleine Ecker, Jochen B. Gerschler, Jan Vogel, Stefan Käbitz, Friedrich Hust, et al. Development of a lifetime prediction model for lithium-ion batteries based on extended accelerated aging test data. *Journal of Power Sources*, 215:248–257, 2012. ISSN 0378-7753. DOI: 10.1016/j.jpowsour.2012.05.012.

[477] Daniel Werner, Sabine Paarmann, and Thomas Wetzel. Calendar Aging of Li-Ion Cells—Experimental Investigation and Empirical Correlation. *Batteries*, 7(2):28, 2021. ISSN 2313-0105. DOI: 10.3390/batteries7020028.

[478] Eduardo Redondo-Iglesias, Pascal Venet, and Serge Pelissier. Modelling Lithium-Ion Battery Ageing in Electric Vehicle Applications—Calendar and Cycling Ageing Combination Effects. *Batteries*, 6 (1):14, 2020. ISSN 2313-0105. DOI: 10.3390/batteries6010014.

[479] Issam Baghdadi, Romain Mathieu, Olivier Briat, Philippe Gyan, and Jean-Michel Vinassa. Lithium-Ion Battery Ageing Assessment Based on a Reduced Design of Experiments. In *2017 IEEE Vehicle Power and Propulsion Conference (VPPC)*, Belfort, 2017. IEEE. ISBN 978-1-5386-1317-7. DOI: 10.1109/VPPC.2017.8330871.

[480] Issam Baghdadi, Olivier Briat, Jean-Yves Delétage, Philippe Gyan, and Jean-Michel Vinassa. Lithium battery aging model based on Dakin's degradation approach. *Journal of Power Sources*, 325:273–285, 2016. ISSN 0378-7753. DOI: 10.1016/j.jpowsour.2016.06.036.

[481] Romain Mathieu, Issam Baghdadi, Olivier Briat, Philippe Gyan, and Jean-Michel Vinassa. D-optimal design of experiments applied to lithium battery for ageing model calibration. *Energy*, 141:2108–2119, 2017. ISSN 03605442. DOI: 10.1016/j.energy.2017.11.130.

[482] Daniel-Ioan Stroe, Maciej Swierczynski, Ana-Irina Stan, Remus Teodorescu, and Soren Juhl Andreasen. Accelerated Lifetime Testing Methodology for Lifetime Estimation of Lithium-Ion Batteries Used in Augmented Wind Power Plants. *IEEE Transactions on Industry Applications*, 50(6):4006–4017, 2014. ISSN 0093-9994, 1939-9367. DOI: 10.1109/TIA.2014.2321028.

[483] Andrea Marongiu, Marco Roscher, and Dirk Uwe Sauer. Influence of the vehicle-to-grid strategy on the aging behavior of lithium battery electric vehicles. *Applied Energy*, 137:899–912, 2015. ISSN 0306-2619. DOI: 10.1016/j.apenergy.2014.06.063.

[484] Daniel-Ioan Stroe, Maciej Swierczynski, Ana-Irina Stroe, Rasmus Laerke, Philip Carne Kjaer, et al. Degradation Behavior of Lithium-Ion Batteries Based on Lifetime Models and Field Measured Frequency Regulation Mission Profile. *IEEE Transactions on Industry Applications*, 52(6):5009–5018, 2016. ISSN 1939-9367. DOI: 10.1109/TIA.2016.2597120.

[485] John Wang, Justin Purewal, Ping Liu, Jocelyn Hicks-Garner, Souren Soukazian, et al. Degradation of lithium ion batteries employing graphite negatives and nickel–cobalt–manganese oxide + spinel manganese oxide positives: Part 1, aging mechanisms and life estimation. *Journal of Power Sources*, 269:937–948, 2014. ISSN 0378-7753. DOI: 10.1016/j.jpowsour.2014.07.030.

[486] Clemens Guenther, Benjamin Schott, Wilfried Hennings, Paul Waldowski, and Michael A. Danzer. Model-based investigation of electric vehicle battery aging by means of vehicle-to-grid scenario simulations. *Journal of Power Sources*, 239:604–610, 2013. ISSN 0378-7753. DOI: 10.1016/j.jpowsour.2013.02.041.

[487] M. Mauri, F. Castelli-Dezza, M.S. Carmeli, M. Scarforgliero, and G. Marchegiani. Electro-Thermal Aging Model of Li -Ion Batteries for Vehicle-to-Grid Services. In *2019 AEIT International Conference of Electrical and Electronic Technologies for Automotive (AEIT AUTOMOTIVE)*, 2019. DOI: 10.23919/EETA.2019.8804544.

[488] Lisa Calearo, Andreas Thingvad, and Mattia Marinelli. Modeling of Battery Electric Vehicles for Degradation Studies. In *2019 54th International Universities Power Engineering Conference (UPEC)*, 2019. DOI: 10.1109/UPEC.2019.8893474.

[489] E. Sarasketa-Zabala, I. Laresgoiti, I. Alava, M. Rivas, I. Villarreal, et al. Validation of the methodology for lithium-ion batteries lifetime prognosis. In *2013 World Electric Vehicle Symposium and Exhibition (EVS27)*, Barcelona, Spain, 2013. IEEE. ISBN 978-1-4799-3832-2. DOI: 10.1109/EVS.2013.6914730.

[490] J. Schmalstieg, S. Käbitz, M. Ecker, and D. U. Sauer. From accelerated aging tests to a lifetime prediction model: Analyzing lithium-ion batteries. In *2013 World Electric Vehicle Symposium and Exhibition (EVS27)*, 2013. DOI: 10.1109/EVS.2013.6914753.

[491] Johannes Schmalstieg, Stefan Käbitz, Madeleine Ecker, and Dirk Uwe Sauer. A holistic aging model for Li(NiMnCo)O2 based 18650 lithium-ion batteries. *Journal of Power Sources*, 257:325–334, 2014. ISSN 0378-7753. DOI: 10.1016/j.jpowsour.2014.02.012.

[492] Alexander Johannes Warnecke. *Degradation Mechanisms in NMC-Based Lithium-Ion Batteries*. PhD thesis, Rheinisch-Westfälische Technische Hochschule Aachen, Aachen, 2017. DOI: 10.18154/RWTH-2017-09646. ISSN 1437-675X, https://publications.rwth-aachen.de/record/708098/files/708098.pdf. Accessed: 2020-08-10.

[493] Joris de Hoog, Jean-Marc Timmermans, Daniel Ioan-Stroe, Maciej Swierczynski, Joris Jaguemont, et al. Combined cycling and calendar capacity fade modeling of a Nickel-Manganese-Cobalt Oxide Cell with real-life profile validation. *Applied Energy*, 200:47–61, 2017. ISSN 0306-2619. DOI: 10.1016/j.apenergy.2017.05.018.

[494] Bolun Xu, Alexandre Oudalov, Andreas Ulbig, Göran Andersson, and Daniel S. Kirschen. Modeling of Lithium-Ion Battery Degradation for Cell Life Assessment. *IEEE Transactions on Smart Grid*, 9 (2):1131–1140, 2018. ISSN 1949-3061. DOI: 10.1109/TSG.2016.2578950.

[495] Daniel Ioan Stroe. *Lifetime Models for Lithium-ion Batteries used in Virtual Power Plant Applications*. Dissertation, Department of Energy Technology, Aalborg University, Aalborg, 2014. https://vbn.aau.dk/ws/portalfiles/portal/549543532/Lifetime_Models_for_Lithium_ion_Batteries_used_in_Virtual_Power_Plant_Applications.pdf. Accessed: 2023-11-15.

[496] Daniel Stroe, Maciej Świerczyński, Ana-Irina Stan, Remus Teodorescu, and Søren Juhl Andreasen. Experimental investigation on the internal resistance of Lithium iron phosphate battery cells during calendar ageing. In *IECON 2013 - 39th Annual Conference of the IEEE Industrial Electronics Society*, pages 6734–6739, 2013. DOI: 10.1109/IECON.2013.6700247. ISSN: 1553-572X.

[497] Kandler Smith, Paul Gasper, Andrew M. Colclasure, Yuta Shimonishi, and Shuhei Yoshida. Lithium-Ion Battery Life Model with Electrode Cracking and Early-Life Break-in Processes. *Journal of The Electrochemical Society*, 168(10):100530, 2021. ISSN 0013-4651, 1945-7111. DOI: 10.1149/1945-7111/ac2ebd.

[498] M. Schimpe, M. E. von Kuepach, M. Naumann, H. C. Hesse, K. Smith, et al. Comprehensive Modeling of Temperature-Dependent Degradation Mechanisms in Lithium Iron Phosphate Batteries. *Journal of The Electrochemical Society*, 165(2):A181, 2018. ISSN 1945-7111. DOI: 10.1149/2.1181714jes.

[499] Kandler Smith, M. Warleywine, Eric Wood, Jeremy Neubauer, and Ahmad Pesaran. Comparison of Plug-In Hybrid Electric Vehicle Battery Life Across Geographies and Drive-Cycles. *SAE Technical Papers*, 2012. DOI: 10.4271/2012-01-0666.

[500] K Smith, M Earleywine, E Wood, and A Pesaran. Battery Wear from Disparate Duty-Cycles: Opportunities for Electric-Drive Vehicle Battery Health Management: Preprint. In *2012 American Control Conference*, page 9, 2012.

[501] Kandler Smith, Aron Saxon, Matthew Keyser, Blake Lundstrom, Ziwei Cao, et al. Life Prediction Model for Grid-Connected Li-ion Battery Energy Storage System. In *2017 American Control*

Conference (ACC), pages 4062–4068, Seattle, WA, USA, 2017. IEEE. ISBN 978-1-5090-5992-8. DOI: 10.23919/ACC.2017.7963578.

[502] Gonçalo dos Reis, Calum Strange, Mohit Yadav, and Shawn Li. Lithium-ion battery data and where to find it. *Energy and AI*, 5:100081, 2021. ISSN 2666-5468. DOI: 10.1016/j.egyai.2021.100081.

[503] Abolfazl Shahrooei. Comparison of Open Datasets for Lithium-ion Battery Testing. https://medium.com/batterybits/comparison-of-open-datasets-for-lithium-ion-battery-testing-fd0de091ca2, 2020. Accessed: 2023-11-10.

[504] Philipp Dechent, Alexander Epp, Dominik Jöst, Yuliya Preger, Peter M. Attia, et al. ENPOLITE: Comparing Lithium-Ion Cells across Energy, Power, Lifetime, and Temperature. *ACS Energy Letters*, 6(6):2351–2355, 2021. DOI: 10.1021/acsenergylett.1c00743.

[505] Hayder Ali, Hector Beltran, Nancy J. Lindsey, and Michael Pecht. Assessment of the calendar aging of lithium-ion batteries for a long-term—Space missions. *Frontiers in Energy Research*, 11:1108269, 2023. ISSN 2296-598X. DOI: 10.3389/fenrg.2023.1108269.

[506] BatteryArchive.org. https://www.batteryarchive.org/index.html. Accessed: 2022-08-23.

[507] Charlotte Argue. What 6,000 EV batteries tell us about EV battery health. https://www.geotab.com/blog/ev-battery-health/, 2020. Accessed: 2023-09-22.

[508] CALCE. Battery Data. https://calce.umd.edu/battery-data, 2023. Accessed: 2023-11-10.

[509] Valentin Muenzel, Anthony F. Hollenkamp, Anand I. Bhatt, Julian de Hoog, Marcus Brazil, et al. A Comparative Testing Study of Commercial 18650-Format Lithium-Ion Battery Cells. *Journal of The Electrochemical Society*, 162(8):A1592, 2015. ISSN 1945-7111. DOI: 10.1149/2.0721508jes.

[510] Edoardo Catenaro and Simona Onori. Experimental data of lithium-ion batteries under galvanostatic discharge tests at different rates and temperatures of operation. *Data in Brief*, 35:106894, 2021. ISSN 2352-3409. DOI: 10.1016/j.dib.2021.106894.

[511] Edoardo Catenaro. Experimental data of three lithium-ion batteries under galvanostatic discharge tests at different C-rates and operating temperatures, 2021. DOI: 10.17632/KXSBR4X3J2.2.

[512] Scott B. Peterson, Jay Apt, and J. F. Whitacre. Lithium-ion battery cell degradation resulting from realistic vehicle and vehicle-to-grid utilization. *Journal of Power Sources*, 195(8):2385–2392, 2010. ISSN 0378-7753. DOI: 10.1016/j.jpowsour.2009.10.010.

[513] Kotub Uddin, Andrew D. Moore, Anup Barai, and James Marco. The effects of high frequency current ripple on electric vehicle battery performance. *Applied Energy*, 178:142–154, 2016. ISSN 0306-2619. DOI: 10.1016/j.apenergy.2016.06.033.

[514] Shun Sun, Ting Guan, Xinqun Cheng, Pengjian Zuo, Yunzhi Gao, et al. Accelerated aging and degradation mechanism of LiFePO4/graphite batteries cycled at high discharge rates. *RSC Advances*, 8(45):25695–25703, 2018. ISSN 2046-2069. DOI: 10.1039/C8RA04074E.

[515] Thomas Waldmann, Marcel Wilka, Michael Kasper, Meike Fleischhammer, and Margret Wohlfahrt-Mehrens. Temperature dependent ageing mechanisms in Lithium-ion batteries – A Post-Mortem study. *Journal of Power Sources*, 262:129–135, 2014. ISSN 0378-7753. DOI: 10.1016/j.jpowsour.2014.03.112.

[516] Edward Cripps and Michael Pecht. A Bayesian nonlinear random effects model for identification of defective batteries from lot samples. *Journal of Power Sources*, 342:342–350, 2017. ISSN 0378-7753. DOI: 10.1016/j.jpowsour.2016.12.067.

[517] Zhongwei Deng, Le Xu, Hongao Liu, Xiaosong Hu, Zhixuan Duan, et al. Prognostics of battery capacity based on charging data and data-driven methods for on-road vehicles. *Applied Energy*, 339: 120954, 2023. ISSN 0306-2619. DOI: 10.1016/j.apenergy.2023.120954.

[518] Michael Teng. battery-charging-data-of-on-road-electric-vehicles. https://github.com/TengMichael/battery-charging-data-of-on-road-electric-vehicles, 2023. Accessed: 2023-11-10.

[519] Kristen A. Severson, Peter M. Attia, Norman Jin, Nicholas Perkins, Benben Jiang, et al. Data-driven prediction of battery cycle life before capacity degradation. *Nature Energy*, 4(5):383–391, 2019. ISSN 2058-7546. DOI: 10.1038/s41560-019-0356-8.

[520] Kristen A. Severson, Peter M. Attia, Norman Jin, Nicholas Perkins, Benben Jiang, et al. Data-driven prediction of battery cycle life before capacity degradation. https://data.matr.io/1/projects/5c48dd2bc625d700019f3204, 2019. Accessed: 2022-08-23.

[521] Guijun Ma, Songpei Xu, Benben Jiang, Cheng Cheng, Xin Yang, et al. Real-time personalized health status prediction of lithium-ion batteries using deep transfer learning. *Energy & Environmental Science*, 15(10):4083–4094, 2022. DOI: 10.1039/D2EE01676A.

[522] Ye Yuan, Guijun Ma, and Songpei Xu. The Dataset for: Real-time personalized health status prediction of lithium-ion batteries using deep transfer learning, 2022. DOI: 10.17632/NSC7HNSG4S.2.

[523] Peter M. Attia, Aditya Grover, Norman Jin, Kristen A. Severson, Todor M. Markov, et al. Closed-loop optimization of fast-charging protocols for batteries with machine learning. *Nature*, 578(7795): 397–402, 2020. ISSN 0028-0836, 1476-4687. DOI: 10.1038/s41586-020-1994-5.

[524] Peter M. Attia, Aditya Grover, Norman Jin, Kristen A. Severson, Todor M. Markov, et al. Closed-loop optimization of extreme fast charging for batteries using machine learning. https://data.matr.io/1/projects/5d80e633f405260001c0b60a, 2019. Accessed: 2023-11-10.

[525] Jorn M. Reniers, Grietus Mulder, and David A. Howey. Unlocking extra value from grid batteries using advanced models. *Journal of Power Sources*, 487:229355, 2021. ISSN 0378-7753. DOI: 10.1016/j.jpowsour.2020.229355.

[526] J. M. Reniers, G. Mulder, and D. A. Howey. Oxford energy trading battery degradation dataset. https://ora.ox.ac.uk/objects/uuid:9aae61af-2949-49f1-8ad5-6aea448979e5, 2021. University of Oxford. Accessed: 2022-08-23.

[527] Gabriele Pozzato, Anirudh Allam, and Simona Onori. Lithium-ion battery aging dataset based on electric vehicle real-driving profiles. *Data in Brief*, 41:107995, 2022. ISSN 2352-3409. DOI: 10.1016/j.dib.2022.107995.

[528] Gabriele Pozzato, Anirudh Allam, and Simona Onori. Lithium-ion battery aging dataset based on electric vehicle real-driving profiles. https://osf.io/qsabn/?view_only=2a03b6c78ef14922a3e244f3d549de78, 2022. OSF. Accessed: 2023-11-10.

[529] Trishna Raj, Andrew A. Wang, Charles W. Monroe, and David A. Howey. Investigation of Path-Dependent Degradation in Lithium-Ion Batteries**. *Batteries & Supercaps*, 3(12):1377–1385, 2020. ISSN 2566-6223. DOI: 10.1002/batt.202000160.

[530] T. Raj and D Howey. Path Dependent Battery Degradation Dataset Part 1, 2020. DOI: 10.5287/bodleian:v0ervBv6p.

[531] T Raj. Path Dependent Battery Degradation Dataset Part 2, 2021. DOI: 10.5287/BODLEIAN:2ZVYKNYRG.

[532] Andrew Weng, Peyman Mohtat, Peter M. Attia, Valentin Sulzer, Suhak Lee, et al. Predicting the impact of formation protocols on battery lifetime immediately after manufacturing. *Joule*, 5(11): 2971–2992, 2021. ISSN 25424351. DOI: 10.1016/j.joule.2021.09.015.

[533] Andrew Weng, Peyman Mohtat, Peter Attia, Greg Less, Suhak Lee, et al. Battery test data - fast formation study. https://deepblue.lib.umich.edu/data/concern/data_sets/b2773w109, 2021. Accessed: 2023-11-10.

[534] Yang Gao, Jiuchun Jiang, Caiping Zhang, Weige Zhang, and Yan Jiang. Aging mechanisms under different state-of-charge ranges and the multi-indicators system of state-of-health for lithium-ion battery with Li(NiMnCo)O2 cathode. *Journal of Power Sources*, 400:641–651, 2018. ISSN 0378-7753. DOI: 10.1016/j.jpowsour.2018.07.018.

[535] Niall Kirkaldy, Mohammad Amin Samieian, Gregory J. Offer, Monica Marinescu, and Yatish Patel. Lithium-Ion Battery Degradation: Measuring Rapid Loss of Active Silicon in Silicon–Graphite Composite Electrodes. *ACS Applied Energy Materials*, 5(11):13367–13376, 2022. ISSN 2574-0962, 2574-0962. DOI: 10.1021/acsaem.2c02047.

[536] Niall Kirkaldy, Mohammad Amin Samieian, Gregory J Offer, Monica Marinescu, and Yatish Patel. Data from: "Lithium-ion battery degradation: measuring rapid loss of active silicon in silicon-graphite composite electrodes", 2022. DOI: 10.5281/ZENODO.7235857.

[537] Daniel R. Sørensen, Michael Heere, Jiangong Zhu, Mariyam S. D. Darma, Samantha M. Zimnik, et al. Fatigue in High-Energy Commercial Li Batteries while Cycling at Standard Conditions: An In Situ Neutron Powder Diffraction Study. *ACS Applied Energy Materials*, 3(7):6611–6622, 2020. ISSN 2574-0962, 2574-0962. DOI: 10.1021/acsaem.0c00779.

[538] Yongzhi Zhang, Rui Xiong, Hongwen He, Xiaobo Qu, and Michael Pecht. State of charge-dependent aging mechanisms in graphite/Li(NiCoAl)O2 cells: Capacity loss modeling and remaining useful life prediction. *Applied Energy*, 255:113818, 2019. ISSN 03062619. DOI: 10.1016/j.apenergy.2019.113818.

[539] Sabine Paarmann. *How Non-Uniform Temperatures Influence the Performance and Ageing of Lithium-Ion Batteries*. Dissertation, Karlsruhe Institute of Technology (KIT), Karlsruhe, 2021. https://publikationen.bibliothek.kit.edu/1000139983. Accessed: 2023-11-10.

[540] Daniel Werner, Sabine Paarmann, Achim Wiebelt, and Thomas Wetzel. Inhomogeneous Temperature Distribution Affecting the Cyclic Aging of Li-Ion Cells. Part I: Experimental Investigation. *Batteries*, 6(1):13, 2020. ISSN 2313-0105. DOI: 10.3390/batteries6010013.

[541] Jiangong Zhu, Michael Knapp, Daniel R. Sørensen, Michael Heere, Mariyam S. D. Darma, et al. Investigation of capacity fade for 18650-type lithium-ion batteries cycled in different state of charge (SoC) ranges. *Journal of Power Sources*, 489:229422, 2021. ISSN 0378-7753. DOI: 10.1016/j.jpowsour.2020.229422.

[542] Gints Kucinskis, Maral Bozorgchenani, Max Feinauer, Michael Kasper, Margret Wohlfahrt-Mehrens, et al. Arrhenius plots for Li-ion battery ageing as a function of temperature, C-rate, and ageing state – An experimental study. *Journal of Power Sources*, 549:232129, 2022. ISSN 03787753. DOI: 10.1016/j.jpowsour.2022.232129.

[543] Jiahuan Lu, Rui Xiong, Jinpeng Tian, Chenxu Wang, Chia-Wei Hsu, et al. Battery degradation prediction against uncertain future conditions with recurrent neural network enabled deep learning. *Energy Storage Materials*, 50:139–151, 2022. ISSN 2405-8297. DOI: 10.1016/j.ensm.2022.05.007.

[544] Jinpeng Tian, Rui Xiong, Weixiang Shen, Jiahuan Lu, and Xiao-Guang Yang. Deep neural network battery charging curve prediction using 30 points collected in 10 min. *Joule*, 5(6):1521–1534, 2021. ISSN 2542-4351. DOI: 10.1016/j.joule.2021.05.012.

[545] Jiahuan Lu. Battery Degradation Dataset (Fixed Current Profiles & Arbitrary Uses Profiles), 2022. DOI: 10.17632/KW34HHW7XG.3.

[546] Fabio Todeschini, Simona Onori, and Giorgio Rizzoni. An experimentally validated capacity degradation model for Li-ion batteries in PHEVs applications. *IFAC Proceedings Volumes*, 45(20):456–461, 2012. ISSN 1474-6670. DOI: 10.3182/20120829-3-MX-2028.00173.

[547] Jiangong Zhu, Yixiu Wang, Yuan Huang, R. Bhushan Gopaluni, Yankai Cao, et al. Data-driven capacity estimation of commercial lithium-ion batteries from voltage relaxation. *Nature Communications*, 13(1):2261, 2022. ISSN 2041-1723. DOI: 10.1038/s41467-022-29837-w.

[548] Jiangong Zhu, Yixiu Wang, Yuan Huang, R. Bhushan Gopaluni, Yankai Cao, et al. Data-driven capacity estimation of commercial lithium-ion batteries from voltage relaxation, 2022. DOI: 10.5281/ZENODO.6379165.

[549] Weijun Gu, Zechang Sun, Xuezhe Wei, and Haifeng Dai. A Capacity Fading Model of Lithium-Ion Battery Cycle Life Based on the Kinetics of Side Reactions for Electric Vehicle Applications. *Electrochimica Acta*, 133:107–116, 2014. ISSN 0013-4686. DOI: 10.1016/j.electacta.2014.03.186.

[550] Yuliya Preger, Heather M. Barkholtz, Armando Fresquez, Daniel L. Campbell, Benjamin W. Juba, et al. Degradation of Commercial Lithium-Ion Cells as a Function of Chemistry and Cycling Conditions. *Journal of The Electrochemical Society*, 167(12):120532, 2020. ISSN 0013-4651, 1945-7111. DOI: 10.1149/1945-7111/abae37.

[551] Weiping Diao, Yinjiao Xing, Saurabh Saxena, and Michael Pecht. Evaluation of Present Accelerated Temperature Testing and Modeling of Batteries. *Applied Sciences*, 8(10):1786, 2018. ISSN 2076-3417. DOI: 10.3390/app8101786.

[552] CALCE. Battery Accelerated Cycle Life Testing Data. https://calce.umd.edu/battery-accelerated-cycle-life-testing-data, 2023. Accessed: 2023-11-16.

[553] Weiping Diao. Data for: Accelerated Cycle Life Testing and Capacity Degradation Modeling of LiCoO2-graphite Cells, 2019. DOI: 10.17632/c35zbmn7j8.1. Mendeley Data.

[554] Tingkai Li, Zihao Zhou, Adam Thelen, David Howey, and Chao Hu. Predicting Battery Lifetime Under Varying Usage Conditions from Early Aging Data, 2023. DOI: 10.48550/arXiv.2307.08382. preprint.

[555] Adam Thelen, Tingkai Li, Jinqiang Liu, Chad Tischer, and Chao Hu. ISU-ILCC Battery Aging Dataset, 2023. DOI: 10.25380/IASTATE.22582234.V1.

[556] Penelope K. Jones, Ulrich Stimming, and Alpha A. Lee. Impedance-based forecasting of lithium-ion battery performance amid uneven usage. *Nature Communications*, 13(1):4806, 2022. ISSN 2041-1723. DOI: 10.1038/s41467-022-32422-w.

[557] Penelope Jones, Ulrich Stimming, and Alpha Lee. Impedance-based forecasting of battery performance amid uneven usage, 2021. DOI: 10.5281/ZENODO.5704795.

[558] P. Gyan, P. Aubret, J. Hafsaoui, F. Sellier, S. Bourlot, et al. Experimental Assessment of Battery Cycle Life Within the SIMSTOCK Research Program. *Oil & Gas Science and Technology – Revue d'IFP Energies nouvelles*, 68(1):137–147, 2013. ISSN 1294-4475, 1953-8189. DOI: 10.2516/ogst/2013106.

[559] Peter Keil and Andreas Jossen. Charging protocols for lithium-ion batteries and their impact on cycle life—An experimental study with different 18650 high-power cells. *Journal of Energy Storage*, 6: 125–141, 2016. ISSN 2352-152X. DOI: 10.1016/j.est.2016.02.005.

[560] Jens Groot, Maciej Swierczynski, Ana Irina Stan, and Søren Knudsen Kær. On the complex ageing characteristics of high-power LiFePO4/graphite battery cells cycled with high charge and discharge currents. *Journal of Power Sources*, 286:475–487, 2015. ISSN 0378-7753. DOI: 10.1016/j.jpowsour.2015.04.001.

[561] Damian Burzyński and Leszek Kasprzyk. NMC cell 2600 mAh cyclic aging data, 2021. DOI: 10.17632/k6v83s2xdm.1. Mendeley Data.

[562] B. Saha and K. Goebel. Battery Data Set. https://www.nasa.gov/intelligent-systems-division/discovery-and-systems-health/pcoe/pcoe-data-set-repository/, 2007. NASA Ames Research Center. Accessed: 2023-11-20.

[563] Greg Orzech. Prognostics Center of Excellence Data Set Repository. https://www.nasa.gov/intelligent-systems-division/discovery-and-systems-health/pcoe/pcoe-data-set-repository/, 2023. Section: Ames Research Center. Accessed: 2023-11-20.

[564] Simon F. Schuster, Tobias Bach, Elena Fleder, Jana Müller, Martin Brand, et al. Nonlinear aging characteristics of lithium-ion cells under different operational conditions. *Journal of Energy Storage*, 1:44–53, 2015. ISSN 2352-152X. DOI: 10.1016/j.est.2015.05.003.

[565] Peyman Mohtat, Suhak Lee, Jason B. Siegel, and Anna G. Stefanopoulou. Reversible and Irreversible Expansion of Lithium-Ion Batteries Under a Wide Range of Stress Factors. *Journal of The Electrochemical Society*, 168(10):100520, 2021. ISSN 1945-7111. DOI: 10.1149/1945-7111/ac2d3e.

[566] Mohtat, Peyman, Siegel, Jason B., Stefanopoulou, Anna G., and Suhak Lee. UofM Pouch Cell Voltage and Expansion Cyclic Aging Dataset, 2021. DOI: 10.7302/7TW1-KC35.

[567] Brian Bole, Chetan S Kulkarni, and Matthew Daigle. Adaptation of an Electrochemistry-based Li-Ion Battery Model to Account for Deterioration Observed Under Randomized Use. In *Annual conference of the PHM society*, volume 6 of *1*, 2014.

[568] B. Bole, C. Kulkarni, and M. Daigle. Randomized Battery Usage Data Set. https://www.nasa.gov/intelligent-systems-division/discovery-and-systems-health/pcoe/pcoe-data-set-repository/, 2014. NASA Ames Research Center. Accessed: 2023-11-20.

[569] Michael Bosello, Carlo Falcomer, Claudio Rossi, and Giovanni Pau. To Charge or to Sell? EV Pack Useful Life Estimation via LSTMs, CNNs, and Autoencoders. *Energies*, 16(6):2837, 2023. ISSN 1996-1073. DOI: 10.3390/en16062837.

[570] Franz B. Spingler, Maik Naumann, and Andreas Jossen. Capacity Recovery Effect in Commercial LiFePO4 / Graphite Cells. *Journal of The Electrochemical Society*, 167(4):040526, 2020. ISSN 1945-7111. DOI: 10.1149/1945-7111/ab7900.

[571] Laisuo Su, Jianbo Zhang, Caijuan Wang, Yakun Zhang, Zhe Li, et al. Identifying main factors of capacity fading in lithium ion cells using orthogonal design of experiments. *Applied Energy*, 163: 201–210, 2016. ISSN 0306-2619. DOI: 10.1016/j.apenergy.2015.11.014.

[572] Esma Galijatovics, Jelena Rubesa-Zrim, Franz Pichler, and Matthias K. Scharrer. Ageing Data of Lithium-ion "Panasonic NCR18650B" Battery Cells, 2023. DOI: 10.5281/ZENODO.7896428.

[573] Christian Geisbauer, Katharina Wöhrl, Daniel Koch, Gudrun Wilhelm, Gerhard Schneider, et al. Comparative Study on the Calendar Aging Behavior of Six Different Lithium-Ion Cell Chemistries in Terms of Parameter Variation. *Energies*, 14(11):3358, 2021. ISSN 1996-1073. DOI: 10.3390/en14113358.

[574] Christian Geisbauer, Hans-Georg Schweiger, and Yash Kotak. Experimental Calendar Ageing Data for Lithium-Ion Battery Chemistries, 2022. DOI: 10.5281/ZENODO.6546753.

[575] M. Kassem, J. Bernard, R. Revel, S. Pélissier, F. Duclaud, et al. Calendar aging of a graphite/LiFePO4 cell. *Journal of Power Sources*, 208:296–305, 2012. ISSN 03787753. DOI: 10.1016/j.jpowsour.2012.02.068.

[576] A. Eddahech, O. Briat, E. Woirgard, and J.M. Vinassa. Remaining useful life prediction of lithium batteries in calendar ageing for automotive applications. *Microelectronics Reliability*, 52(9-10): 2438–2442, 2012. ISSN 00262714. DOI: 10.1016/j.microrel.2012.06.085.

[577] Akram Eddahech, Olivier Briat, and Jean-Michel Vinassa. Performance comparison of four lithium–ion battery technologies under calendar aging. *Energy*, 84:542–550, 2015. ISSN 0360-5442. DOI: 10.1016/j.energy.2015.03.019.

[578] Dongjiang Li, Dmitri L. Danilov, Jie Xie, Luc Raijmakers, Lu Gao, et al. Degradation Mechanisms of C6/LiFePO4 Batteries: Experimental Analyses of Calendar Aging. *Electrochimica Acta*, 190: 1124–1133, 2016. ISSN 0013-4686. DOI: 10.1016/j.electacta.2015.12.161.

[579] M. Ecker, Jochen Gerschler, J. Vogel, Stefan Käbitz, Friedrich Hust, et al. Analyzing calendar aging data towards a lifetime prediction model for lithium-ion batteries. In *The 26th International Electric Vehicle Symposium (EVS26)*, volume 1, 2012. Accessed: 2023-11-10.

[580] Sebastien Grolleau, Belen Molina-Concha, Arnaud Delaille, Renaud Revel, Julien Bernard, et al. The French SIMCAL Research Network For Modelling of Calendar Aging for Energy Storage System in EVs And HEVs - EIS Analysis on LFP/C Cells. *ECS Transactions*, 45(13):73, 2013. ISSN 1938-5862. DOI: 10.1149/04513.0073ecst.

[581] Bor Yann Liaw, E. Peter Roth, Rudolph G Jungst, Ganesan Nagasubramanian, Herbert L Case, et al. Correlation of Arrhenius behaviors in power and capacity fades with cell impedance and heat generation in cylindrical lithium-ion cells. *Journal of Power Sources*, 119-121:874–886, 2003. ISSN 0378-7753. DOI: 10.1016/S0378-7753(03)00196-4.

[582] Bramy Pilipili Matadi, Sylvie Geniès, Arnaud Delaille, Thomas Waldmann, Michael Kasper, et al. Effects of Biphenyl Polymerization on Lithium Deposition in Commercial Graphite/NMC Lithium-Ion Pouch-Cells during Calendar Aging at High Temperature. *Journal of The Electrochemical Society*, 164(6):A1089, 2017. ISSN 1945-7111. DOI: 10.1149/2.0631706jes.

[583] M Broussely, S Herreyre, P Biensan, P Kasztejna, K Nechev, et al. Aging mechanism in Li ion cells and calendar life predictions. *Journal of Power Sources*, 97-98:13–21, 2001. ISSN 0378-7753. DOI: 10.1016/S0378-7753(01)00722-4.

[584] Peter Keil and Andreas Jossen. Calendar Aging of NCA Lithium-Ion Batteries Investigated by Differential Voltage Analysis and Coulomb Tracking. *Journal of The Electrochemical Society*, 164 (1):A6066–A6074, 2017. ISSN 0013-4651, 1945-7111. DOI: 10.1149/2.0091701jes.

[585] Peter Keil, Simon F. Schuster, Jörn Wilhelm, Julian Travi, Andreas Hauser, et al. Calendar Aging of Lithium-Ion Batteries. *Journal of The Electrochemical Society*, 163(9):A1872, 2016. ISSN 1945-7111. DOI: 10.1149/2.0411609jes.

[586] Eduardo Redondo-Iglesias, Pascal Venet, and Serge Pelissier. Calendar and cycling ageing combination of batteries in electric vehicles. *Microelectronics Reliability*, 88-90:1212–1215, 2018. ISSN 0026-2714. DOI: 10.1016/j.microrel.2018.06.113.

[587] Thomas Waldmann, Michael Kasper, and Margret Wohlfahrt-Mehrens. Optimization of Charging Strategy by Prevention of Lithium Deposition on Anodes in high-energy Lithium-ion Batteries – Electrochemical Experiments. *Electrochimica Acta*, 178:525–532, 2015. ISSN 0013-4686. DOI: 10.1016/j.electacta.2015.08.056.

[588] M. Safari and C. Delacourt. Aging of a Commercial Graphite/LiFePO4 Cell. *Journal of The Electrochemical Society*, 158(10):A1123, 2011. ISSN 1945-7111. DOI: 10.1149/1.3614529.

[589] Erik Goldammer, Marius Gentejohann, Michael Schlüter, Daniel Weber, Wolfgang Wondrak, et al. The Impact of an Overlaid Ripple Current on Battery Aging: The Development of the SiCWell Dataset. *Batteries*, 8(2):11, 2022. ISSN 2313-0105. DOI: 10.3390/batteries8020011.

[590] Daniel Weber. SiCWell Dataset. https://ieee-dataport.org/open-access/sicwell-dataset, 2021. Accessed: 2023-11-22.

[591] Philipp Schröer, Ehsan Khoshbakht, Thomas Nemeth, Matthias Kuipers, Hendrik Zappen, et al. Adaptive modeling in the frequency and time domain of high-power lithium titanate oxide cells in battery management systems. *Journal of Energy Storage*, 32:101966, 2020. ISSN 2352-152X. DOI: 10.1016/j.est.2020.101966.

[592] Meinert Lewerenz, Jens Münnix, Johannes Schmalstieg, Stefan Käbitz, Marcus Knips, et al. Systematic aging of commercial LiFePO4|Graphite cylindrical cells including a theory explaining rise of capacity during aging. *Journal of Power Sources*, 345:254–263, 2017. ISSN 0378-7753. DOI: 10.1016/j.jpowsour.2017.01.133.

[593] Dongjiang Li, Dmitri L. Danilov, Barbara Zwikirsch, Maximilian Fichtner, Yong Yang, et al. Modeling the degradation mechanisms of C6/LiFePO4 batteries. *Journal of Power Sources*, 375:106–117, 2018. ISSN 03787753. DOI: 10.1016/j.jpowsour.2017.11.049.

[594] Madeleine Ecker, Nerea Nieto, Stefan Käbitz, Johannes Schmalstieg, Holger Blanke, et al. Calendar and cycle life study of Li(NiMnCo)O2-based 18650 lithium-ion batteries. *Journal of Power Sources*, 248:839–851, 2014. ISSN 03787753. DOI: 10.1016/j.jpowsour.2013.09.143.

[595] Yukio Miyaki, Kunihiko Hayashi, Tetsuya Makino, Kazuhiko Yoshida, Masumi Terauchi, et al. A Common Capacity Loss Trend: LiFePO4 Cell's Cycle and Calendar Aging. *ECS Meeting Abstracts*, MA2012-02(10):1091, 2012. ISSN 2151-2043. DOI: 10.1149/MA2012-02/10/1091.

[596] Md Sazzad Hosen, Danial Karimi, Theodoros Kalogiannis, Ashkan Pirooz, Joris Jaguemont, et al. Electro-aging model development of nickel-manganese-cobalt lithium-ion technology validated with light and heavy-duty real-life profiles. *Journal of Energy Storage*, 28:101265, 2020. ISSN 2352-152X. DOI: 10.1016/j.est.2020.101265.

[597] Jon P Christophersen, Jeffrey R Belt, Chinh D Ho, Chester G Motloch, Randy B Wright, et al. DOE Advanced Technology Development Program for Lithium-Ion Batteries: INEEL Gen 1 Final Report. *Idaho National Engineering and Environmental Laboratory*, 2001. https://citeseerx.ist.psu.edu/docu

ment?repid=rep1&type=pdf&doi=84574b47cbe46dbb1032b5e7760f132dc3d2188c, INEEL/EXT-2001-00417. Accessed: 2023-11-10.

[598] I Bloom, B. W Cole, J. J Sohn, S. A Jones, E. G Polzin, et al. An accelerated calendar and cycle life study of Li-ion cells. *Journal of Power Sources*, 101(2):238–247, 2001. ISSN 0378-7753. DOI: 10.1016/S0378-7753(01)00783-2.

[599] Randy Ben Wright and Chester George Motloch. Cycle Life Studies of Advanced Technology Development Program Gen 1 Lithium Ion Batteries, 2001. DOI: 10.2172/911513.

[600] K. Amine, C. H. Chen, J. Liu, M. Hammond, A. Jansen, et al. Factors responsible for impedance rise in high power lithium ion batteries. *Journal of Power Sources*, 97-98:684–687, 2001. ISSN 0378-7753. DOI: 10.1016/S0378-7753(01)00701-7.

[601] Randy Ben Wright and Chester George Motloch. Calendar Life Studies of Advanced Technology Development Program Gen 1 Lithium Ion Batteries, 2001. DOI: 10.2172/911512.

[602] R. B Wright, C. G Motloch, J. R Belt, J. P Christophersen, C. D Ho, et al. Calendar- and cycle-life studies of advanced technology development program generation 1 lithium-ion batteries. *Journal of Power Sources*, 110(2):445–470, 2002. ISSN 0378-7753. DOI: 10.1016/S0378-7753(02)00210-0.

[603] Ira Bloom, Scott A. Jones, Edward G. Polzin, Vincent S. Battaglia, Gary L. Henriksen, et al. Mechanisms of impedance rise in high-power, lithium-ion cells. *Journal of Power Sources*, 111(1): 152–159, 2002. ISSN 0378-7753. DOI: 10.1016/S0378-7753(02)00302-6.

[604] Stefan Käbitz, Jochen Bernhard Gerschler, Madeleine Ecker, Yusuf Yurdagel, Brita Emmermacher, et al. Cycle and calendar life study of a graphite|LiNi1/3Mn1/3Co1/3O2 Li-ion high energy system. Part A: Full cell characterization. *Journal of Power Sources*, 239:572–583, 2013. ISSN 03787753. DOI: 10.1016/j.jpowsour.2013.03.045.

[605] Md Sazzad Hosen, Ashkan Pirooz, Theodoros Kalogiannis, Jiacheng He, Joeri Van Mierlo, et al. A Strategic Pathway from Cell to Pack-Level Battery Lifetime Model Development. *Applied Sciences*, 12(9):4781, 2022. ISSN 2076-3417. DOI: 10.3390/app12094781.

[606] Jessie E. Harlow, Xiaowei Ma, Jing Li, Eric Logan, Yulong Liu, et al. A Wide Range of Testing Results on an Excellent Lithium-Ion Cell Chemistry to be used as Benchmarks for New Battery Technologies. *Journal of The Electrochemical Society*, 166(13):A3031–A3044, 2019. ISSN 0013-4651, 1945-7111. DOI: 10.1149/2.0981913jes.

[607] Julius Schmitt, Arpit Maheshwari, Michael Heck, Stephan Lux, and Matthias Vetter. Impedance change and capacity fade of lithium nickel manganese cobalt oxide-based batteries during calendar aging. *Journal of Power Sources*, 353:183–194, 2017. ISSN 0378-7753. DOI: 10.1016/j.jpowsour.2017.03.090.

[608] Arpit Maheshwari, Michael Heck, and Massimo Santarelli. Cycle aging studies of lithium nickel manganese cobalt oxide-based batteries using electrochemical impedance spectroscopy. *Electrochimica Acta*, 273:335–348, 2018. ISSN 0013-4686. DOI: 10.1016/j.electacta.2018.04.045.

[609] Khiem Trad. Everlasting: Electric Vehicle Enhanced Range, Lifetime And Safety Through INGenious battery management. D2.3 – Report containing aging test profiles and test results. https://everlasting-project.eu/wp-content/uploads/2020/03/EVERLASTING_D2.3_final_20200228.pdf, 2020. Accessed: 2022-08-23.

[610] Vlaamse Instelling Voor Technologisch Onderzoek (VITO), Commissariat à L'Energie Atomique Et Aux Energies Alternatives (CEA), Siemens, Technische Universität München (TUM), TÜV SÜD Battery Testing, et al. EVERLASTING: Electric Vehicle Enhanced Range, Lifetime And Safety Through INGenious battery management [collection of datasets], 2021. DOI: 10.4121/C.5065445.V11. 4TU.ResearchData, Version Number: 11.

[611] Peter Keil. *Aging of Lithium-Ion Batteries in Electric Vehicles*. PhD thesis, Technische Universität München, 2017. https://mediatum.ub.tum.de/doc/1355829/1355829.pdf. Accessed: 2021-11-10.

[612] J. Belt, V. Utgikar, and I. Bloom. Calendar and PHEV cycle life aging of high-energy, lithium-ion cells containing blended spinel and layered-oxide cathodes. *Journal of Power Sources*, 196(23): 10213–10221, 2011. ISSN 0378-7753. DOI: 10.1016/j.jpowsour.2011.08.067.

[613] Jean-Marc Timmermans, Alexandros Nikolian, Joris De Hoog, Rahul Gopalakrishnan, Shovon Goutam, et al. Batteries 2020 — Lithium-ion battery first and second life ageing, validated battery models, lifetime modelling and ageing assessment of thermal parameters. In *2016 18th European Conference on Power Electronics and Applications (EPE'16 ECCE Europe)*, Karlsruhe, 2016. IEEE. ISBN 978-90-75815-24-5. DOI: 10.1109/EPE.2016.7695698.

[614] M. Lucu, E. Martinez-Laserna, I. Gandiaga, K. Liu, H. Camblong, et al. Data-driven nonparametric Li-ion battery ageing model aiming at learning from real operation data - Part B: Cycling operation. *Journal of Energy Storage*, 30:101410, 2020. ISSN 2352-152X. DOI: 10.1016/j.est.2020.101410.

[615] M. Lucu, E. Martinez-Laserna, I. Gandiaga, K. Liu, H. Camblong, et al. Data-driven nonparametric Li-ion battery ageing model aiming at learning from real operation data – Part A: Storage operation. *Journal of Energy Storage*, 30:101409, 2020. ISSN 2352-152X. DOI: 10.1016/j.est.2020.101409.

[616] Mattin Lucu. *Development of a data-driven ageing model for Li-ion batteries: a nonparametric approach to learn from real operation data*. doctoral thesis, Universidad del País Vasco, 2020. https://addi.ehu.es/bitstream/handle/10810/50933/TESIS_LUCU_OYHAGARAY_MATTIN.pdf. Accessed: 2023-11-13.

[617] Thomas Bank, Jan Feldmann, Sebastian Klamor, Stephan Bihn, and Dirk Uwe Sauer. Extensive aging analysis of high-power lithium titanate oxide batteries: Impact of the passive electrode effect. *Journal of Power Sources*, 473:228566, 2020. ISSN 0378-7753. DOI: 10.1016/j.jpowsour.2020.228566.

[618] Sébastien Grolleau, Issam Baghdadi, Philippe Gyan, Mohamed Ben-Marzouk, and François Duclaud. Capacity Fade of Lithium-Ion Batteries upon Mixed Calendar/Cycling Aging Protocol. *World Electric Vehicle Journal*, 8(2):339–349, 2016. DOI: 10.3390/wevj8020339.

[619] Mohamed Ben-Marzouk, Agnès Chaumond, Eduardo Redondo-Iglesias, Maxime Montaru, and Serge Pélissier. Experimental Protocols and First Results of Calendar and/or Cycling Aging Study of Lithium-Ion Batteries – the MOBICUS Project. *World Electric Vehicle Journal*, 8(2):388–397, 2016. ISSN 2032-6653. DOI: 10.3390/wevj8020388.

[620] S. Belaid, R. Mingant, M. Petit, J. Martin, and J. Bernard. Strategies to Extend the Lifespan of Automotive Batteries through Battery Modeling and System Simulation: The MOBICUS Project. In *2017 IEEE Vehicle Power and Propulsion Conference (VPPC)*, 2017. DOI: 10.1109/VPPC.2017.8330949.

[621] Maik Naumann, Franz B. Spingler, and Andreas Jossen. Analysis and modeling of cycle aging of a commercial LiFePO4/graphite cell. *Journal of Power Sources*, 451:227666, 2020. ISSN 0378-7753. DOI: 10.1016/j.jpowsour.2019.227666.

[622] Maik Naumann, Michael Schimpe, Peter Keil, Holger C. Hesse, and Andreas Jossen. Analysis and modeling of calendar aging of a commercial LiFePO4/graphite cell. *Journal of Energy Storage*, 17: 153–169, 2018. ISSN 2352-152X. DOI: 10.1016/j.est.2018.01.019.

[623] Maik Naumann. Data for: Analysis and modeling of calendar aging of a commercial LiFePO4/graphite cell, 2021. DOI: 10.17632/KXH42BFGTJ.1. Mendeley Data.

[624] Maik Naumann. Data for: Analysis and modeling of cycle aging of a commercial LiFePO4/graphite cell, 2021. DOI: 10.17632/6HGYR25H8D.1. Mendeley Data.

[625] Leo Wildfeuer, Alexander Karger, Deniz Aygül, Nikolaos Wassiliadis, Andreas Jossen, et al. Experimental degradation study of a commercial lithium-ion battery. *Journal of Power Sources*, 560: 232498, 2023. ISSN 0378-7753. DOI: 10.1016/j.jpowsour.2022.232498.

[626] Leo Wildfeuer, Alexander Karger, Deniz Aygül, Nikolaos Wasiiliadis, Andreas Jossen, et al. Experimental degradation study of a commercial lithium-ion battery, 2023. DOI: 10.14459/2023MP1713382.

[627] LG Chem. Product Specification – Rechargeable Lithium Ion Battery – Model : INR18650HG2 3000mAh. https://www.batteryspace.com/prod-specs/9989.specs.pdf, 2015. PS-HG2-Rev0. Accessed: 2024-01-28.

[628] LG Chem. Technical Information of LG 18650HG2 (3.0Ah). https://www.nkon.nl/sk/k/hg2.pdf, 2014. Accessed: 2024-01-28.

[629] Sustainable Transport Unit, Institute of Energy and Transport, Joint Research Center, European Commission. gearshift_calculation_tool. https://github.com/JRCSTU/gearshift_calculation_tool, 2023. Accessed: 2024-01-29.

[630] Amelie Krupp, Robert Beckmann, Theys Diekmann, Ernst Ferg, Frank Schuldt, et al. Calendar aging model for lithium-ion batteries considering the influence of cell characterization. *Journal of Energy Storage*, 45:103506, 2022. ISSN 2352-152X. DOI: 10.1016/j.est.2021.103506.

[631] Weisi Li, K. R. Crompton, Christopher Hacker, and Jason K. Ostanek. Comparison of Current Interrupt Device and Vent Design for 18650 Format Lithium-ion Battery Caps. *Journal of Energy Storage*, 32:101890, 2020. ISSN 2352-152X. DOI: 10.1016/j.est.2020.101890.

[632] Kevin G. Gallagher, Dennis W. Dees, Andrew N. Jansen, Daniel P. Abraham, and Sun-Ho Kang. A Volume Averaged Approach to the Numerical Modeling of Phase-Transition Intercalation Electrodes Presented for $Li_x C_6$. *Journal of The Electrochemical Society*, 159(12):A2029–A2037, 2012. ISSN 0013-4651, 1945-7111. DOI: 10.1149/2.015301jes.

[633] Thorsten Gruen. *Passiv gekoppelte Lithium-Ionen-Superkondensatorsysteme für 48V Hybridfahrzeuge*. Dissertation, Karlsruher Institut für Technologie, Karlsruhe, Germany, 2020. https://publikationen.bibliothek.kit.edu/1000127761. Accessed: 2023-09-22.

[634] D. Magnor, J.B. Gerschler, M. Ecker, P. Merk, and D.U. Sauer. Concept of a Battery Aging Model for Lithium-Ion Batteries Considering the Lifetime Dependency on the Operation Strategy. *24th European Photovoltaic Solar Energy Conference*, 21-25 September 2009, 2009. DOI: 10.4229/24theupvsec2009-4bo.11.3.

[635] Tjarko Tjaden, Joseph Bergner, Johannes Weniger, and Volker Quaschning. Repräsentative elektrische Lastprofile für Wohngebäude in Deutschland auf 1-sekündiger Datenbasis, 2015. DOI: 10.13140/RG.2.1.5112.0080/1. License: CC-BY-NC-4.0, Version Number: 1.

[636] Agora Energiewende. Agorameter. Model version 3.0, Berlin, 13.09.21. https://www.agora-energiewende.org/data-tools/agorameter/, 2023. Accessed: 2024-04-03.

[637] Katharina Hartz and Hauke Hermann. Agorameter Documentation – Version 13. https://www.agora-energiewende.org/fileadmin/Projekte/Agorameter/2023-10-01_Hintergrunddokumentation_Agorameter_v13_EN.pdf, 2023. Accessed: 2024-04-03.

[638] DWD Climate Data Center (CDC). 10-minütige Stationsmessungen der Lufttemperatur in 2 m Höhe in °C für Deutschland (OBS_deu_pt10m_t2m – ID: 4177 = Rheinstetten), 2024. Accessed: 2024-03-14.

[639] 50Hertz Transmission GmbH, Amprion GmbH, TenneT TSO GmbH, and TransnetBW GmbH. Balancing Capacity data > Data in second resolution. https://www.netztransparenz.de/en/Balancing-Capacity/Balancing-Capacity-data/Data-in-second-resolution. Accessed: 2024-03-18.

[640] Statistisches Bundesamt (Destatis). Fachserie 5: Bauen und Wohnen - Reihe 3: Bestand an Wohnungen (31. Dezember 2021). https://www.destatis.de/DE/Themen/Gesellschaft-Umwelt/Wohnen/Publikationen/Downloads-Wohnen/bestand-wohnungen-2050300217005.xlsx?__blob=publicationFile, 2022. Accessed: 2023-07-26.

[641] NICHICON CORPORATION. EVパワー　ステーションの仕様. https://www.nichicon.co.jp/products/v2h/about/specs/. Accessed: 2023-08-03.

[642] ECHONET Consortium. NICHICON (KAMEOKA) CORPORATION: Grid Interconnection EV Power Station. https://echonet.jp/introduce_en/lz-000119-3/. Accessed: 2023-08-03.

[643] CHAdeMO Association. Denso DNEVC-D6075. https://www.chademo.com/products/v2g/denso, 2023. Accessed: 2023-08-02.

[644] DENSO Corporation. Denso DNEVC-D6075 (Japanese user manual). https://www.denso.com/jp/ja/products-and-services/consumer-products/v2h/images/construction/toriatsukai-setsumeisyo.pdf, 2021. Accessed: 2023-08-02.

[645] Tsubakimoto Chain Co. eLINK: V2X bi-directional EV charging systems. https://tsubakimoto.com/other-products/elink/. Accessed: 2023-08-03.

[646] Tsubakimoto Chain Co. Tsubaki's upgraded eLINK is now a V2X-compatible virtual power plant / EV charging station. https://tsubakimoto.com/company/news/press/2019/03/05/1/, 2019. Accessed: 2023-08-03.

[647] Mitsubishi Electric Corporation. EV用パワーコンディショナ「SMART V2H」モニター販売開始のお知らせ. http://www.mitsubishielectric.co.jp/news/2014/0701.html, 2014. Accessed: 2023-08-03.

[648] Mitsubishi Electric Corporation. EV用パワーコンディショナ. https://www.mitsubishielectric.co.jp/home/smartv2h/. Accessed: 2023-08-03.

[649] CHAdeMO Association. Magnum Cap. https://www.chademo.com/products/v2g/magnum-cap-charger-09, 2023. Accessed: 2023-08-02.

[650] MAGNUM CAP. MC V2G. https://magnumcap.com/v2g/v2g/, . Accessed: 2023-08-03.

[651] MAGNUM CAP. V2G in MAGNUM CAP. https://magnumcap.com/v2g-in-magnum-cap/, . Accessed: 2023-08-03.

[652] Takaoka Toko Co., Ltd. EPower Conditioner for EV (V2H). https://www.tktk.co.jp/en/product/ev-charging/conditioner-ev/. Accessed: 2023-08-03.

[653] Takaoka Toko Co., Ltd. The 5th Fiscal Year Business Report. https://www.tktk.co.jp/en/news/assets/pdf/The5thFiscalYearBusinessReport.pdf, 2017. Accessed: 2023-08-03.

[654] CHAdeMO Association. Fermata Energy FE-15 V2X Charger. https://www.chademo.com/products/v2g/fermata-energy-fe-15-v2x-charger, 2023. Accessed: 2023-08-02.

[655] Fermata Energy LLC. Fermata Energy's Newest V2X Bidirectional Charger — the FE-20 — Available Q1 2023. https://fermataenergy.com/article/fermata-energys-newest-v2x-bidirectional-charger-, 2022. Accessed: 2023-08-02.

[656] Tom Moloughney. Wallbox Quasar Bidirectional Charger Will Power Your Car And Your Home. https://insideevs.com/news/392292/wallbox-introduces-new-chargers-at-ces/, 2020. Accessed: 2023-08-02.

[657] alpitronic GmbH. HYC50. https://www.hypercharger.it/hyc50/, 2022. Accessed: 2023-08-02.

[658] alpitronic GmbH. HYC50 product data sheet (v. 1 - 1). https://www.hypercharger.it/wp-content/uploads/2021/10/HYC50_preliminary_datasheet_V1-5.pdf, 2023. Accessed: 2023-08-02.

[659] Eaton Corporation plc. Green Motion DC 22. https://www.eaton.com/sg/en-us/catalog/emobility/green-motion-dc-22.html. Accessed: 2023-08-02.

[660] dcbel Inc. dcbel r16: The Brightest Home on the Block. https://www.dcbel.energy/uk/our-product-r16/, 2022. Accessed: 2023-08-01.

[661] dcbel Inc. dcbel r16: Your Home Energy Station. https://www.dcbel.energy/uk/r16-specs/, 2022. Accessed: 2023-08-01.

[662] Molly Lempriere. dcbel launch home energy station in the UK as demand for solar and EVs continues to grow. https://www.current-news.co.uk/dcbel-launch-home-energy-station-in-the-uk-as-demand-for-solar-and-evs-continues-to-grow/, 2022. Accessed: 2023-08-01.

[663] GS Yuasa International Ltd. EVOXシステム. https://ps.gs-yuasa.com/products/ev/evox.php. Accessed: 2023-08-03.

[664] OMRON SOCIAL SOLUTIONS. マルチV2Xシステム KPEP-Aシリーズ. https://socialsolution.omron.com/jp/ja/products_service/energy/product/pm/kpep-a.html. Accessed: 2023-08-02.

[665] 諸山泰三. 自家発電　自家消費を促進するパナソニックのV2H蓄電システム「eneplat」. https://news.mynavi.jp/article/20221205-panasonic/, 2022. Accessed: 2023-08-02.

[666] Emiliano Bellini. Panasonic unveils vehicle-to-home system for PV-powered homes. https://www.pv-magazine.com/2022/12/05/panasonic-unveils-vehicle-to-home-system-for-pv-powered-homes/, 2022. Accessed: 2023-08-02.

[667] FUNAI SERVICE CO., LTD. 電気自動車の蓄電システムは豊かな暮らしの電源へ. https://v2h.funai-service.co.jp/, 2023. Accessed: 2023-08-02.

[668] Enphase Energy, Inc. Enphase Energy Demonstrates Bidirectional Electric Vehicle Charger Technology | Enphase Energy. https://newsroom.enphase.com/news-releases/news-release-details/enphase-energy-demonstrates-bidirectional-electric-vehicle/, 2023. Accessed: 2023-08-02.

[669] Enphase Energy, Inc. Bidirectional EV charging. https://enphase.com/ev-chargers/bidirectional-ev-charging, 2023. Accessed: 2023-08-02.

[670] Delta Electronics (Netherlands) BV. V2X Bi-directional Charging Solution. https://cdn.delta-emea.com/cs/download/file/4644217_V2H.pdf, 2021. Accessed: 2023-08-02.

[671] Delta Electronics, Inc. Home Charging. https://explorer.delta-emea.com/apac/#home-charging-apac. Accessed: 2023-08-02.

[672] CHAdeMO Association. AME V2G 3p10kW V2X Charger. https://www.chademo.com/products/v2g/ame, 2023. Accessed: 2023-08-02.

[673] CHAdeMO Association. eNovates. https://www.chademo.com/products/v2g/enovates, 2023. Accessed: 2023-08-02.

[674] CHAdeMO Association. Indra V2G 170911A202. https://www.chademo.com/products/v2g/indra-v2g, 2023. Accessed: 2023-08-02.

[675] Vehicle To Home (V2H) Chargers. https://www.indra.co.uk/v2h/, 2023. Accessed: 2023-08-02.

[676] Vehicle to Grid (V2G) Chargers. https://www.indra.co.uk/v2g/, 2023. Accessed: 2023-08-02.

[677] Nuvve Holding Corp. Nuvve DC Rapid HD Charging Station (Spec Sheet). https://nuvve.com/wp-content/uploads/2022/01/nuvve-dcfc-125kw-rhombus-spec-sheet-jan2022_r2.pdf, 2022. Accessed: 2023-08-02.

[678] BorgWarner Inc. Chargers. https://www.borgwarner.com/technologies/chargers. Accessed: 2023-08-02.

[679] Nuvve Holding Corp. Nuvve PowerPort3 Ultra (Spec Sheet). https://nuvve.com/wp-content/uploads/2022/01/nuvve-dcfc-res-hd60-v2g-spec-sheet-jan2022_r2.pdf, 2022. Accessed: 2023-08-02.

[680] EVTEC GmbH. sospeso&charge. https://www.evtec.ch/en/produkte/sospeso, 2023. Accessed: 2023-08-01.

[681] sun2wheel AG. Unsere Lade- und Speicherlösungen im Überblick. https://sun2wheel.com/produkte/. Accessed: 2023-08-01.

[682] sun2wheel AG. two-way-10. https://sun2wheel.com/wp-content/uploads/two-way-10-a4-de-23-06.pdf, 2023. Accessed: 2023-08-01.

[683] sun2wheel AG. two-way-digital. https://sun2wheel.com/wp-content/uploads/230426-two-way-digital-a4-de-23-04-1.pdf, 2023. Accessed: 2023-08-01.

[684] Enteligent, Inc. Enteligent Hybrid DC Bi-Directional Fast EV Charger. https://enteligent.com/dc-coupled-dc-evses. Accessed: 2023-08-02.

[685] Enteligent, Inc. Enteligent DC-Coupled DC EVSEs. https://img1.wsimg.com/blobby/go/cee57ca6-01e1-4f12-894e-0a3b5bd6c817/downloads/Enteligent_Solar_DC_EVSE_Data_Sheet_v2.1.pdf?ver=1689696189444, 2023. Accessed: 2023-08-02.

[686] Ambibox GmbH. 11 kW DC-Wallbox. https://www.ambibox.de/en/ambicharge/11-kw-dc-wallbox, 2023. Accessed: 2023-08-02.

[687] Ambibox GmbH. 22 kW DC-Wallbox. https://www.ambibox.de/en/ambicharge/22-kw-dc-wallbox, 2023. Accessed: 2023-08-02.

[688] Ambibox GmbH. 11 kW DC-Wallbox (data sheet). https://www.ambibox.de/fileadmin/Ambibox/Dokumente/ambiCHARGE_11kW_DC-Wallbox.pdf, 2022. Accessed: 2023-08-02.

[689] Wallbox USA Inc. Meet Quasar 2. https://wallbox.com/en_us/quasar2-dc-charger. Accessed: 2023-08-01.

[690] Elyce Behrsin. Wallbox Announces its Latest Bidirectional EV Charger, Quasar 2, has Confirmed Compatibility with CUPRA BORN 77kWh. https://wallbox.com/en_us/newsroom/wallbox-

announces-its-latest-bidirectional-ev-charger-quasar-2-has-confirmed-compatibility-with-cupra-born-77kwh.html, 2023. Accessed: 2023-08-01.

[691] HagerEnergy GmbH. Wie Hauskraftwerke heute und morgen 360° autark machen. https://www.e3dc.com/wie-hauskraftwerke-heute-und-morgen-360-autark-machen/, 2023. Accessed: 2023-08-01.

[692] SolarEdge Technologies, Inc. Intersolar 2023: SolarEdge Unveils New Bi-Directional DC-Coupled Electric Vehicle Charger. https://investors.solaredge.com/news-releases/news-release-details/intersolar-2023-solaredge-unveils-new-bi-directional-dc-coupled/, 2023. Accessed: 2023-08-01.

[693] Emporia Corp. Emporia V2X Bi-Directional Charger Coming 2024. https://www.emporiaenergy.com/how-the-emporia-v2x-charger-works. Accessed: 2023-08-02.

[694] Emporia Corp. Smart Home V2X Charger. https://uploads-ssl.webflow.com/5fff2b7694451e66ba2f5a3d/6439d812d720325a86132d5b_V2XChargerTechnicalSpecs.pdf, 2023. Accessed: 2023-08-02.

[695] Valentina De Simone. Duke 44 la ricarica veloce a portata di cavo. https://silla.industries/duke-44-silla-industries-ricarica-veloce/, 2022. Accessed: 2023-08-02.

[696] Valentina De Simone. Silla Industries among the starring voices at K.EY – The Energy Transition Expo. https://silla.industries/en/k-ey-energy-transition-expo-rimini-2023/, 2023. Accessed: 2023-08-02.

[697] Tim Fronzek and Enrico Beltz. Pilot phase for innovative DC wallbox has started. https://www.volkswagen-newsroom.com/en/press-releases/pilot-phase-for-innovative-dc-wallbox-has-started-6715, 2020. Accessed: 2023-08-02.

[698] Nora Manthey. V2X Suisse project launches with V2G-ready Honda e cars. https://www.electrive.com/2022/09/07/v2x-suisse-project-launches-with-v2g-ready-honda-e-cars/, 2022. Accessed: 2023-08-02.

[699] Honda Deutschland. Honda schließt Machbarkeitsprojekt erfolgreich ab. https://www.honda.de/cars/world-of-honda/news-events/2022-11-21-honda-schliesst-machbarkeitsprojekt-erfolgreich-ab.html, 2022. Accessed: 2023-08-02.

[700] KOSTAL Industrie Elektrik GmbH. Charging Solutions: Bidirectional Wallbox. https://www.kostal-charging-solutions.com/en-gb/produkte/bidirektionale-wallbox/, 2023. Accessed: 2023-08-01.

[701] KOSTAL Industrie Elektrik GmbH. Charging Solutions: Powerful and flexible AC wallboxes that support your business – with German quality. https://www.kostal-charging-solutions.com/en-gb/produkte/ac-wallbox/, 2023. Accessed: 2023-08-01.

[702] KOSTAL Industrie Elektrik GmbH. Charging Solutions: Our DC wallboxes for companies. https://www.kostal-charging-solutions.com/en-gb/produkte/dc-wallbox/, 2023. Accessed: 2023-08-01.

[703] KOSTAL Industrie Elektrik GmbH. Smart Charging Solutions. https://www.kostal-charging-solutions.com/en-gb/. Accessed: 2023-08-01.

[704] Nuvve Holding Corp. Nuvve PowerPort3 Ultra (Spec Sheet). https://nuvve.com/wp-content/uploads/2022/01/nuvve-powerport3-ultra-spec-sheet-jan2022.pdf, 2021. Accessed: 2023-08-02.

[705] Nuvve Holding Corp. V1G + V2G Charging Stations. https://nuvve.com/chargers/, 2022. Accessed: 2023-08-02.

[706] Nuvve Holding Corp. Turn your EV fleet into a virtual power plant. https://nuvve.com/wp-content/uploads/2021/08/nuvve-v2g-give-sell-sheet-aug2021.pdf, 2021. Accessed: 2023-08-02.

[707] Nuvve Holding Corp. Nuvve PowerPort (Spec Sheet). https://nuvve.com/wp-content/uploads/2022/01/nuvve-powerport-single-phase-spec-sheet-jan2022.pdf, 2021. Accessed: 2023-08-02.

[708] openWB GmbH & Co. KG. openWB Pro. https://openwb.de/shop/?product=openwb-pro. Accessed: 2023-09-09.

[709] Stephan Schwebe. Bi-direktionales Laden mit einer AC Wallbox. https://www.daheimladen.de/post/bi-direktionales-laden-mit-einer-ac-wallbox, 2022. Accessed: 2023-07-26.

[710] Enovates NV. Single Wallbox. https://www.enovates.com/products/singlewallbox/, 2023. Accessed: 2023-08-02.

[711] Enovates NV. SINGLE WALLBOX SERIES (model 2023). https://www.enovates.com/wp-content/uploads/2022/08/NextGen.pdf, 2022. Accessed: 2023-08-02.

[712] Ford Motor Company. Ford Charge Station Pro (Specifications). https://www.ford.com/cmslibs/content/dam/brand_ford/en_us/brand/trucks/f150/f150-lightning/pdf/FordChargeStationPro-Specs_06_v2.pdf, 2021. Accessed: 2023-08-01.

[713] SENEC GmbH. SENEC.Wallbox: Mobil mit der Kraft der Sonne. https://senec.com/de/produkte/senec-wallbox, 2023. Accessed: 2023-08-01.

[714] SENEC GmbH. SENEC.PowerPilot: Der neue Taktgeber für die Energiewende zuhause. https://senec.com/de/senecpowerpilot-taktgeber-fuer-die-energiewende-zuhause, 2023. Accessed: 2023-07-26.

[715] Célia Potiron and Petra Le Luel. Mobilize V2G: where the future electric Renault 5 becomes a source of energy. https://media.renault.com/mobilize-v2g-where-the-future-electric-renault-5-becomes-a-source-of-energy/, 2023. Accessed: 2023-08-02.

[716] Kai Faulbaum. Power2Drive: Webasto präsentiert vernetzte Wallboxen und erstes Konzept für bidirektionales Laden. https://www.webasto-group.com/de/presse/pressemitteilungen/pressemitteilung/webasto-power2drive-2023/, 2023. Accessed: 2023-07-19.